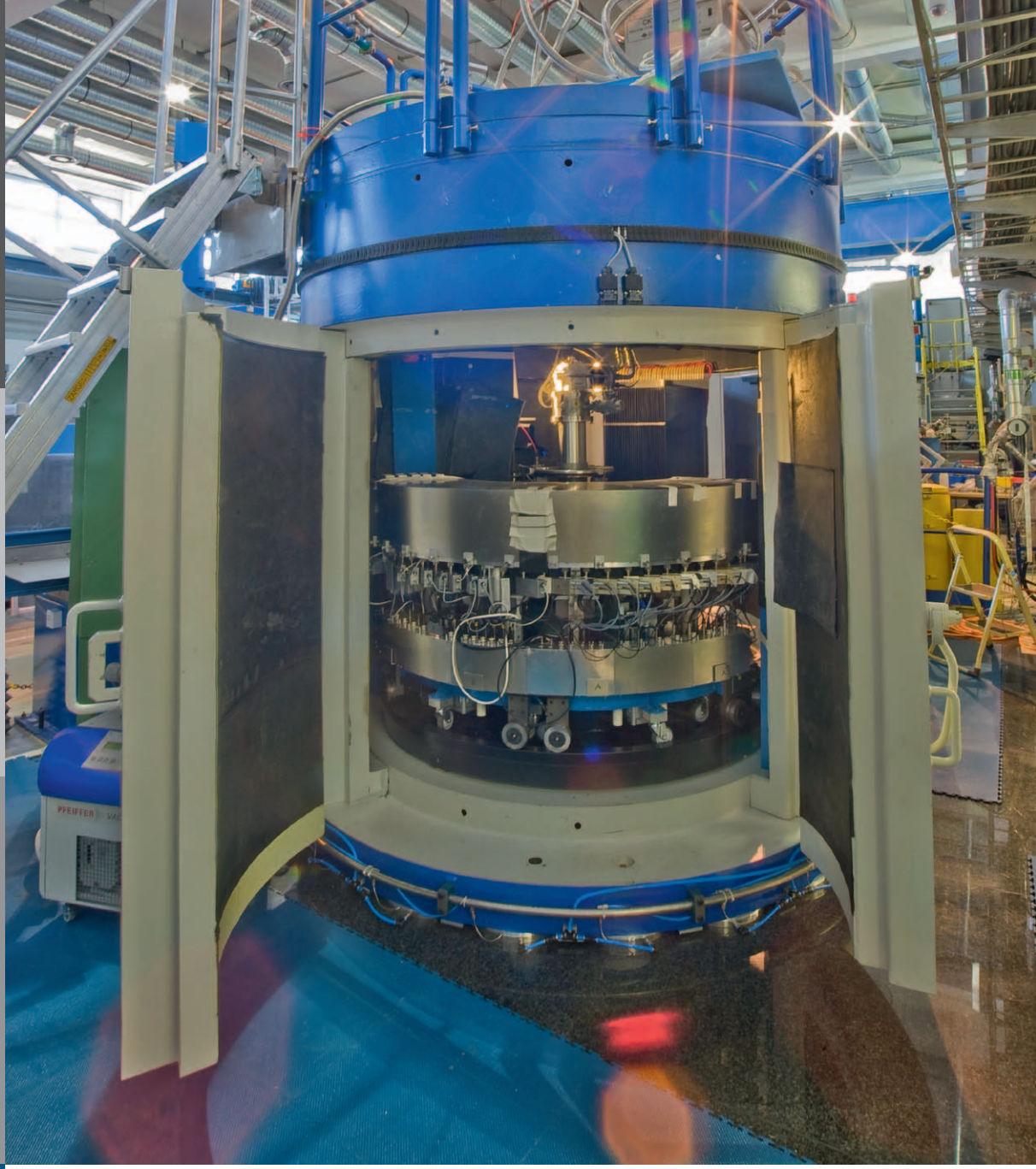

Laboratory Course

Neutron Scattering

Lectures

Thomas Brückel, Gernot Heger, Dieter Richter,
Georg Roth and Reiner Zorn (Editors)

RWTH Aachen
University Münster

JÜLICH
FORSCHUNGSZENTRUM

Schriften des Forschungszentrums Jülich
Reihe Schlüsseltechnologien / Key Technologies Band / Volume 15

Forschungszentrum Jülich GmbH
Institute of Solid State Research (IFF)
Neutron Scattering (IFF-5)

Thomas Brückel, Gernot Heger, Dieter Richter, Georg Roth
and Reiner Zorn (Editors)

Neutron Scattering

Lectures of the JCNS Laboratory Course held at
Forschungszentrum Jülich and the research reactor
FRM II of TU Munich
In cooperation with
RWTH Aachen and University of Münster

Schriften des Forschungszentrums Jülich
Reihe Schlüsseltechnologien / Key Technologies Band / Volume 15

ISSN 1866-1807 ISBN 978-3-89336-635-4

Bibliographic information published by the Deutsche Nationalbibliothek.
The Deutsche Nationalbibliothek lists this publication in the Deutsche Nationalbibliografie; detailed bibliographic data are available in the Internet at http://dnb.d-nb.de.

Publisher and Distributor:	Forschungszentrum Jülich GmbH Zentralbibliothek, Verlag D-52425 Jülich phone:+49 2461 61-5368 · fax:+49 2461 61-6103 e-mail: zb-publikation@fz-juelich.de Internet: http://www.fz-juelich.de/zb
Cover Design:	Grafische Medien, Forschungszentrum Jülich GmbH
Printer:	Grafische Medien, Forschungszentrum Jülich GmbH
Copyright:	Forschungszentrum Jülich 2010

Schriften des Forschungszentrums Jülich
Reihe Schlüsseltechnologien / Key Technologies Band / Volume 15

ISSN 1866-1807
ISBN 978-3-89336-635-4

The complete volume is freely available on the Internet on the Jülicher Open Access Server (JUWEL) at http://www.fz-juelich.de/zb/juwel

Contents

1

Neutron Sources

Alexander Ioffe

Neutron Sources

Alexander Ioffe

1. Introduction

Neutron scattering is a very important tool for studies of fundamental properties of condensed matter as well as material research. It has a special stand among other kinds of radiation as light, X-rays or synchrotron radiation, electrons or ions because of electrical neutrality of neutrons, its large magnetic moment and low kinetic energy. Due to these unique properties of neutrons they became irreplaceable for the investigations of static and dynamic properties of condensed matter, magnetic properties and living biological objects.

The performance of neutron scattering instruments, i.e. the precision of carried out experiments, is primarily determined by the recorded intensity of the scattered beam. The latter is proportional to the unit scattering power of a sample σ_s (the scattering cross-section), to its volume V_s and to the incident neutron flux I_0:

$$I_{\text{det}} = \varepsilon_{pr}\varepsilon_{sec}\varepsilon_{det}\sigma_s V_s I_0$$

where ε_{pr}, ε_{sec} and ε_{det} are efficiencies of primary, secondary spectrometers and detector system, respectively (discussions of these elements of neutron spectrometers will take place in dedicated lectures) (Fig.1). A general tendency in modern science is to investigate smaller samples (such as nanostructures, biological objects, etc.) and weaker effects, so that the unit scattering power of a sample σ_s and the sample volume V_s are very small. Indeed, the flux at the neutron scattering instrument becomes an ultimate parameter that defines the quality of the experiment.

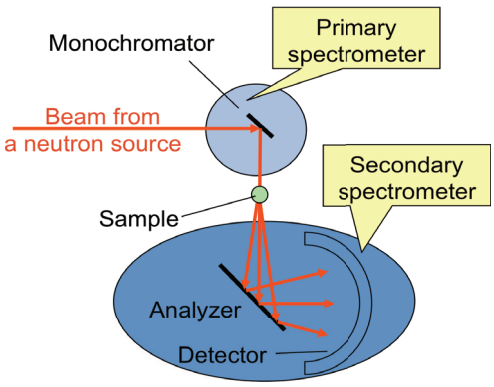

Fig. 1. Layout of a neutron spectrometer.

Usually, under the neutron source one understands a nuclear installation emitting neutrons. However, from the point of view of neutron scattering the neutron source should be considered more generally, including also a spectrum transformer, tailoring the neutron spectrum according to the parameters of the neutron scattering instruments and the neutron transport system that delivers neutrons to the instrument sites (Fig. 2). In this lecture we will discuss all these three components in more details.

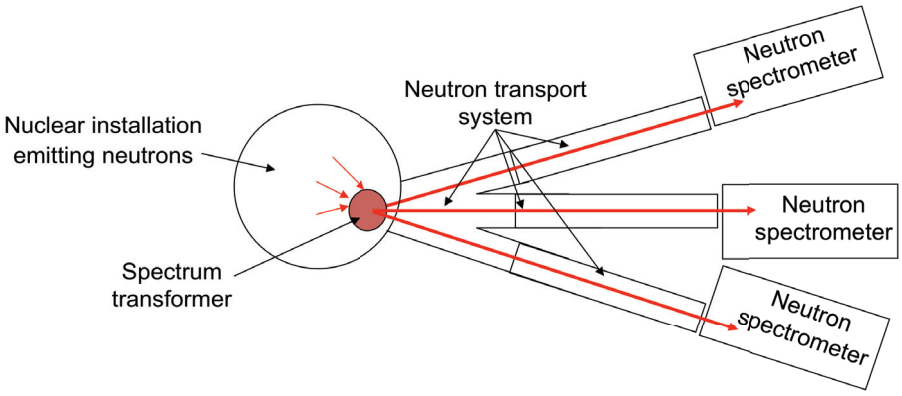

Fig. 2. Layout of a neutron scattering facility.

2. Nuclear reactions

In nature neutrons are strongly bound in the atomic nuclei. Therefore, despite the fact that neutrons constitute about a half of each atom so that nature for a half is comprised of neutrons, it is rather difficult to set them free. Therefore, the only way to free neutrons from the nuclear confinement is to break a nucleus apart by means of a nuclear reaction. Further we will consider two types of such reactions – fission and spallation nuclear reactions – that are used in modern continuous and pulsed neutron sources, respectively.

2.1 Nuclear fission reaction

Namely by this way, bombarding the beryllium nuclei with of α-particles obtained from decay of natural polonium, Chadwick has produced the first free neutrons in 1932:

$$^{9}_{4}\mathrm{Be} + ^{4}_{2}\alpha \rightarrow ^{12}_{6}\mathrm{C} + ^{1}_{0}\mathrm{n}$$

However, the neutron flux available from such sources was far away from being useful for the condensed matter investigation. The breakthrough happened in the 40^{ies}, when nuclear reactors using the nuclear fission reactions have been constructed. Although these reactors have been

primarily developed for purposes of the nuclear weapon industry, a by-product of their operation - an enormous for that time neutron flux, about 10^7 neutrons per square centimetre per second (n/cm^2 s) at the CP-1 reactor in USA - was immediately used for first neutron scattering experiments. Developments in technology of fission reactors during the next 30 years resulted in a tremendous, by 8 orders of magnitude increase of the neutron flux of nuclear research reactors that approached 10^{15} n/cm^2 s for the high-flux reactor of the Institut-Laue-Langevin (Grenoble, France) in 1972.

These reactors are using the fission of the uranium isotope ^{235}U. Following the capture of a slow neutron, this nucleus is deformed and is split into two fragments, simultaneously releasing 2 or 3 (on average 2.5) "prompt" neutrons with energies $E_T \approx 1.29$ MeV (Fig. 1):

$$^{235}\text{U} + \text{neutron} \rightarrow \text{fission fragments} + 2.52\ \text{neutrons} + 180\ \text{MeV}. \qquad (1)$$

Each of these practically instantly (within 10 ns) emitted neutrons can cause the fission of another 2-3 nuclei, so that each of them will also emit 2 to 3 neutrons, and so on (see Fig. 3). This process is called the chain reaction, where the amount of fissile material needed to sustain the chain reaction is called critical mass M_c. If the mass M of fissile material is more than critical, $M>M_c$, the number of neutrons will increase exponentially and the reaction will become uncontrollable very quickly, leading to a huge energy release. If the mass of fissile material is less than critical, $M<M_c$, it will be impossible to sustain a chain reaction: the number of neutrons will decrease over time. Thus, this neutron producing reaction is unstable and will not provide a stable neutron flux.

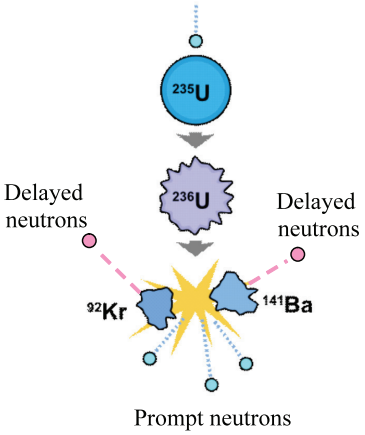

Fig. 3. Schematic representation of the fission process of U-235.

How to obtain a stable neutron flux? Fortunately, there is another additional mechanism that saves the situation - the fission fragments are also rich in neutrons and emit neutrons as a part of their radioactive decay, which can also contribute to the fission of any U-235 nucleus they strike. These so-called “delayed” neutrons, though they make only about 0.64% (!) of the total amount, are extremely important because they are emitted with the average time delay of the order of seconds and thanks to them the chain reaction can be controlled. Practically one runs a reactor sub-critically as far as only prompt neutrons are concerned, i.e. neutron multiplication is suppressed, so that the chain reaction vanishes. The delayed neutrons come a moment later but just in time to sustain the chain reaction when it is going to die out, thus allowing to reach criticality (see Fig. 4). More precisely, the neutrons in the reactor are moderated to decrease their energy and to increase their absorption by control roads that are made of a neutron absorbing material (usually containing boron). When inserted in the reactor core, these roads will reduce the number of slow neutrons to the amount just as necessary for the self–sustaining chain reaction and may be adjusted, so that the reaction remains critical only with the inclusion of the delayed neutrons. Thus, a simple and reliable mechanical control system can be used for the control of the chain reaction in the nuclear reactor.

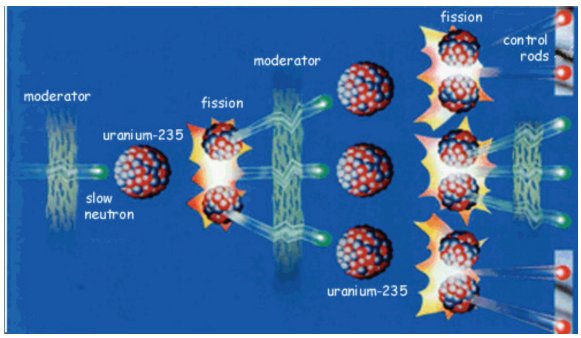

Fig. 4. Controlled chain reaction in the nuclear reactor. Control rods reduce the number of slow neutrons to the amount just as necessary for the self–sustaining chain reaction. By the proper adjustment of the control rods’ position, the reaction may remains critical only with the inclusion of the delayed by a few seconds neutrons.

A change in the reactor power results in changes in temperatures of its fuel. For example, when the power rises, the temperature of the uranium fuel will rise as well. However, the higher

the temperature, the higher the ability of U-238 to absorb neutrons. Indeed, a mass of a fissile material that is exactly critical at room temperature becomes sub-critical if it is warmed and the chain reaction dies out without any external interaction. This so-called negative coefficient of reactivity is an inherent safety factor of nuclear reactors.

2.2 Spallation reaction

The fission is not the only nuclear reaction allowing us to obtain free neutrons. Another kind of nuclear reactions that can be used for neutron production is the spallation reaction (Fig.5), where extremely high energy particles (e.g. protons) hit the target made of a neutron-rich material, "breaking" a heavy nucleus into highly excited fragments. In contrast

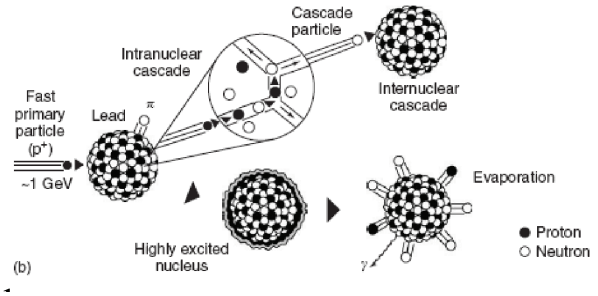

Fig. 5. Schematic representation of the spallation process.

to the fission reaction, the de Broglie wavelength

$$\lambda = \sqrt{h^2/2mE} \tag{2}$$

of the bombarding particles with energy E is shorter than the size of the nuclei, and collisions can take place with individual nuclides in the nucleus rather than with the nucleus as a whole (here h is the Plank constant, m is the neutron mass) . Indeed, a large amount of energy is transferred to the nuclides, which in turn can hit other nuclides in the same nucleus. As the result of this so-called intranuclear cascade, energy is more or less evenly distributed over the nucleus, bringing it to a highly excited state, so that the excited nucleus will "evaporate" neutrons and a smaller amount of protons. However, some energetic particles can escape from the nucleus and either hit another one (internuclear cascade) or just escape from the target.

The energy of these neutrons is extended up to the energy of the incident particles (i.e. up to 1 GeV).

The spallation process is very short and ends within less than 10^{-15} s after the nucleus is hit. Thus, the time distribution of the spallation neutrons is entirely determined by the time distribution of the driving particle pulse, generally provided by a linear accelerator. This pulse that can be made either rather long, about 5 ms (called the long pulse spallation source (LPSS)), or rather short, about 10 μs (called the short pulse spallation source (SPSS)), by compressing charged particles in a compressor ring.

The most intense up-to-day spallation neutron source ISIS at Chilton (Great Britain) provides instantaneous thermal neutron fluxes over 10^{16} n/cm^2 s with short pulse lengths of ~50 μs. Next generation of pulsed neutron sources – SNS in USA and JHP in Japan - with fluxes more than 10^{17} n/cm^2 s have started their operation and gradually approaching their projected parameters. The European project of 5MW spallation source ESS with flux more than 10^{17} n/cm^{2}s is expected to take off within the next years.

Comparing possible nuclear reactions that can be used for neutron production (see Table 1), one should pay attention not only to their efficiency. The heat deposition that accompanies the neutron production results in the cooling problem, which is the real limiting factor for all kinds of neutron sources. From this point of view, fusion is the most attractive process, although it is still a technique of a far future; in the same time, spallation is more attractive than fission.

Table 1. Neutron yields and deposited heat for selected neutron-producing reactions.

Reaction	Energy/event	Yield (neutron/event)	Deposited heat (MeV/neutron)
(T,d) fusion		~1 neutron/fusion	3
^{235}U fission		~1 neutron/fission	200
Pb spallation	1 GeV	~20 neutron/proton	23
^{238}U spallation	1 GeV	~40 neutron/proton	50

3. Neutron spectrum and spectrum transformation

To be useful for condensed matter investigations neutrons wavelength λ should be about few Angstroms, that corresponds to the meV energy range. However, the energy spectrum of neutrons produced by fission or spallation nuclear reactions is in the range of 1 MeV, i.e. the spectrum transformation aiming an energy shift of several orders of magnitude is required. Let us express the neutron energy in the terms of the mean temperature T of the neutron ensemble as $E=k_BT$, where k_B is the conversion coefficient k_B = 11600 K/eV (the Boltzmann constant): then one can say that required energy shift can be achieved by cooling the neutrons down to a much lower temperature. For this purpose neutrons should be brought into the thermal equilibrium with a cold body (moderator): because of multiple inelastic collisions, like billiard balls, with the light atoms (the mass A) of the moderator neutrons are slowing down with energy losses $\Delta E=2A/(A+1)^2$ per collision till $E = E_M = k_BT_M$ (T_M - the moderator temperature), thus achieving thermal equilibrium $T \approx T_M$ with the moderator within 10^{-6} s. This is the so-called thermalization process, which as one can see from the above-mentioned formula most effective for the smallest A. From other hand, depending on the type of neutron source the moderator should provide either the highest possible flux in the largest possible volume (for continuous neutron sources) or in the shortest possible time (for pulsed neutron sources). This can be achieved by using water (A=1) or heavy water moderators (A=2). The neutron energy spectrum is given by the Maxwellian distribution

$$\Phi(E) = \frac{2\sqrt{E}}{\sqrt{\pi k_B{}^3 T_M{}^3}} \exp\left\{-\frac{E}{k_B T_M}\right\} \tag{3}$$

Practically, moderators are big (light or heavy) water volumes (also serving as a biological shielding) surrounding the reactor core or the spallation target and are generally kept at the room temperature of $T_M \approx 300$ K. Because of this reason the corresponding neutrons are called thermal neutrons, with a maximum peak flux around $\lambda \approx 1$ Å (see Fig. 6).

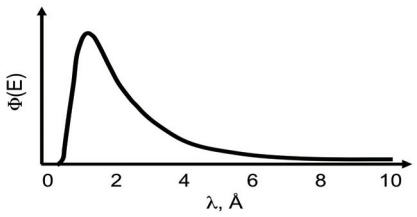

Fig. 6. The energy distribution for neutrons produced by a neutron source for the moderator temperature T_M=300K.

Tables 2 and 3 contain some neutron properties and useful relations between different parameters of neutrons.

Table 2. Neutron properties

Mass	m = 1.675 ·10^{-27} kg
Electrical charge	q = 0
Magnetic dipole moment	μ_n = -1.913 μ_B (μ_B – nuclear magneton)
Life time	$t_{1/2}$ = 820 s

Table 3. Some useful relations.

$\lambda(\text{Å}) = \frac{h}{mv} = \frac{3956}{v(m/s)} = \frac{0.286}{\sqrt{E(eV)}}$	$v(m/s) = \frac{h}{m\lambda} = \frac{3956}{\lambda(\text{Å})}$

4. Nuclear reactor and spallation source.

Now we can consider the construction of a neutron source. In all cases its heart is a core where the nuclear fission reaction takes plays. In the case of the nuclear reactor a set of uranium ^{238}U fuel elements (or a complex single fuel element) is enriched by the isotope ^{235}U. One distinguishes between high-enriched (~95%) and low-enriched (~20%) uranium: because the amount of fission material necessary to support the chain reaction is predetermined (the critical mass), the enrichment of the used uranium fuel actually defines the volume of the core

and the neutron flux density. Compact cores made of high-enriched uranium at the reactors of the Institut-Laue-Langevin (Grenoble, France) and the Maier-Leibnitz Neutron Source (FRM-2) (Garching, Germany) provide the highest flux density and therefore, the highest neutron source luminosity achievable up to this day.

The reactor core is surrounded by (heavy) water (T=300 K) that plays the role of the moderator of high-energy fission neutrons (Fig. 7). Obviously, the full thermalization of these neutrons requires some time necessary for a few collisions with hydrogen (or deuterium) atoms, so that the density of thermal neutrons increases with the distance r_0 from the core. On

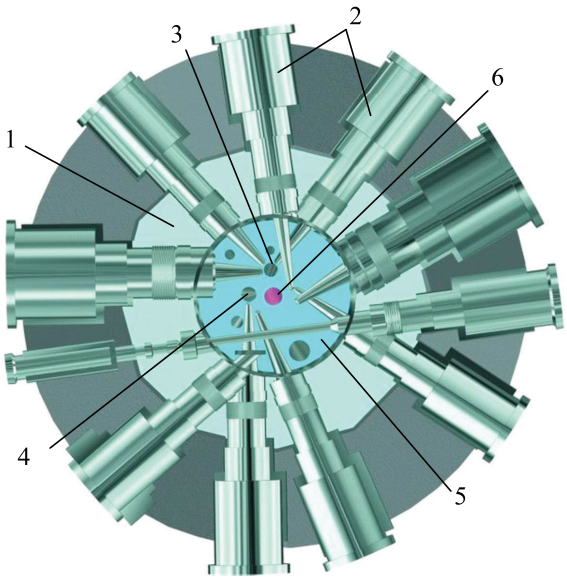

Fig. 7. Horizontal section through the reactor pool of the FRM-2 reactor in Garching, Germany. The reactor tank with internal diameter approx. 5m is filled with light water (1). In the centre of the arrangement the reactor core is situated. The experimental installations as horizontal beam tubes (2), a cold (3) and a hot (4) neutron source are arranged in the heavy water tank (5) around the fuel element (6).

the other hand, the neutron absorption is inverse proportional to the neutron velocity, so that the flux of already thermalized neutrons decreases with r_0. As the result of these two

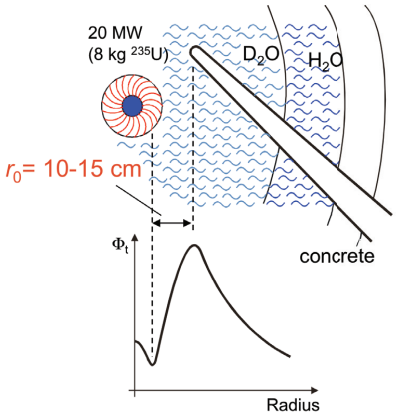

Fig. 8. The density of thermal neutrons vs. the distance r_0 from the core and the tangential arrangement of beam tubes in the reactor core.

competing processes, the thermal neutron flux density achieves its maximum at a certain distance of r_0 = 10-15 cm from the core (Fig. 8). Obviously, to extract thermal neutrons from the reactor, the entrance of a neutron beam tube should be placed exactly in this position. Aiming the decrease in undesirable background of fast (i.e. still not thermalized) neutrons and γ-rays from the core, one should avoid the direct view of the core through the neutron beam tube. All together, it leads to the conclusion that the optimal arrangement of beam tubes is tangential to the reactor core (see Fig. 7).

In case of the spallation source, the role of the reactor core plays a target made of heavy metal as Bi, Pb or Hg. The proton beam is obtained from negatively charged hydrogen ions produced by powerful ion sources (Fig. 9). These ions are accelerated in a linear accelerator (Linac) by a number of subsequent radio-frequency cavities with strong electro-magnetic fields, thus achieving kinetic energies in the GeV range (i.e. about 90% of the speed of light). When these hydrogen ions leave the linac, they are stripped off all their electrons by passing through a thin carbon sieve, so that the negative hydrogen ions become protons. Now, depending on the design of the spallation source, LPSS or SPSS (see Chapter 2) the protons are either sent to the target directly or through a compressor ring, respectively. The latter collects the protons from a large number of successive bunches from the linac into a single very high-intensity proton pulse. It is achieved by an assembly of magnets that send each accelerated proton bunch into a circular orbit of such a large diameter (~50–100 m), so that the travelling time is equal to the time interval between the bunches. Indeed, the next bunch of protons arrives exactly when the previous has made a full turn and both of them are sent

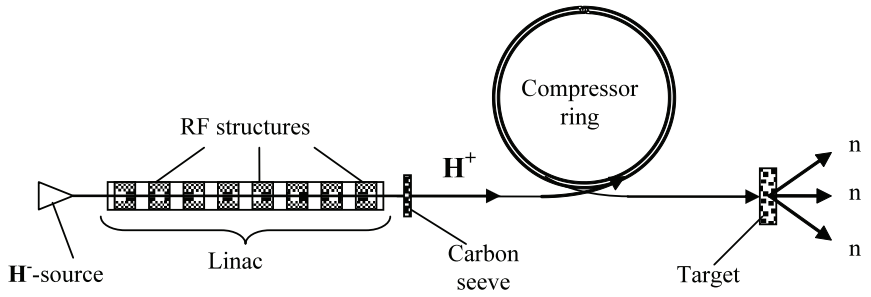

Fig. 9. Layout of the neutron spallation source.

around again. When about 1000 bunches are piled up by such a procedure, sufficient intensity is accumulated and the full proton pulse with a pulse length of about 1 μs is sent to the target. The target is normally a liquid metal (mercury or a lead–bismuth eutectic mixture), placed in special materials to consume the beam power of a few megawatts. The proton pulse repetition rate on the target should be about 10–100 Hz to achieve an optimal use of neutrons in time-of-flight scattering experiments.

Thus, there are two kinds of neutron sources and certainly the question arises, which of them is better answering future trends. These trends, as discussed in the Ch.1 require a significant increase in the luminosity of neutron sources in order to improve the counting statistics of neutron scattering experiments. However, the evolution of nuclear reactors that was very impressive some decades ago, shows no progress since 1972, when the high-flux reactor at the ILL, Grenoble became operative. The reason for this is clearly the technical difficulty of removing the heat from the reactor core.

Let us make some rough estimates. As it was mentioned in Table 1, the deposited heat amounts to 200 Mev/fission with the yield of 1 neutron from 2.5 to be extracted for neutron scattering experiments. Using the relation 1 eV = $1.6 \cdot 10^{-19}$ J, we obtain the source strength (i.e. the number of neutrons emitted per second) $Q = 3 \cdot 10^{16}$ n/s per MW of the reactor power to be removed. However, this is a kind of a "point neutron source" that immersed into the moderator to slow neutrons down till thermal energies (see Ch. 2). Indeed, all neutrons emitted by the point source will be spread over the moderator surface of about 2000 cm^2 (r =10-15 cm), so that the thermal neutron flux will amount to 0.0005 of Q, i.e. about $1.5 \cdot 10^{13}$

n/s·cm^2 per MW of reactor power. Thus, for the 57 MW reactor at the ILL, one may expect the thermal flux of 1 ·10^{15} n/s·cm^2 to be compared with the actual value of 2 ·10^{15} n/s·cm^2 .

Thus, a further increase in the thermal neutron flux from nuclear reactors will require a significant increase in their power. However, such an increase will also require a very sophisticated reactor cooling and result in even stronger radiation damage of the reactor vessel components (beam tube noses, cold source, etc.). Experience gained at the ILL reactor shows that their service time is seven years. Already now new reactors are being designed in a way allowing for a regular exchange of the beam tube noses. Tenfold increase of the reactor power will result in a rather unpractical service time of these elements. Another problem is the worldwide concern about a potential risk associated with nuclear fission installations. On the other hand, pulsed sources are inherently safer because of the absence of any critical configuration that is potentially explosive. The deposited heat is 10 times less with the simultaneous significantly large neutron output (see Table 1) allows for a high peak flux about 50 times higher than the one for the ILL reactor (Table 2). Losses in the average thermal neutron flux will be compensated by the opportunities offered for neutron scattering instrumentation by the time-structured neutron beams, when the instrument performance depends on the peak flux in the pulse rather than on the time-averaged flux.

Therefore, it is not surprising that all new sources under construction, SNS in USA and JHP in Japan as well as planned new European neutron source ESS, are spallation neutron sources. However, SNS and JHP are 1–2 MW spallation sources designed to create rather short neutron pulses of about 100μs and further increase in their power level is rather problematic due to possible target problems. In contrast to this, ESS is planned as 5MW spallation source because it will create neutron pulses of a few milliseconds duration. It was demonstrated that such long pulse provides significant advantages for certain categories of neutron scattering instruments. Although target problems for LPSS also become increasingly severe with the increase of power, nevertheless it seems realistic to approach the ultimate limit of 20MW (i.e. 20 mA proton current at 1 GeV).

5. Cold, thermal and hot neutrons

As it was shown in the previous Chapter, the energies of neutrons produced by neutron sources cover many orders of magnitude. Depending on their energy E, neutrons are classified by commonly used names (see Table 4). Neutrons with $E < 1$ keV are called slow

Table 4. Classification of neutrons according to their energy (wavelength).

Ultra cold	E <0.5 μeV	λ > 400 Å
Very cold	E=0.5μeV-0.05 meV	λ = (40-400) Å
Cold	E=(0.05-5) meV	λ = (4-40) Å
Thermal	E=(5-100) meV	λ = (0.9-4) Å
Hot	E=100 meV -1eV	λ = (0.3-0.9) Å

neutrons; in turn they are classified in 6 groups, but the most relevant for purposes of neutron scattering are hot, thermal and cold neutrons – energy ranges corresponding to these groups are also presented in Table 4. The maximum of the spectrum of thermal neutrons is defined by room temperature of the water moderator and is about $\lambda \approx 1$ Å (see Ch. 3). As one can see from Fig. 10, most of the neutrons are concentrated around this wavelength in the range of (0.8÷2) Å. These neutron wavelengths perfectly match the interatomic distances in solids and therefore, are extensively used for the studies of structure and dynamics of crystalline.

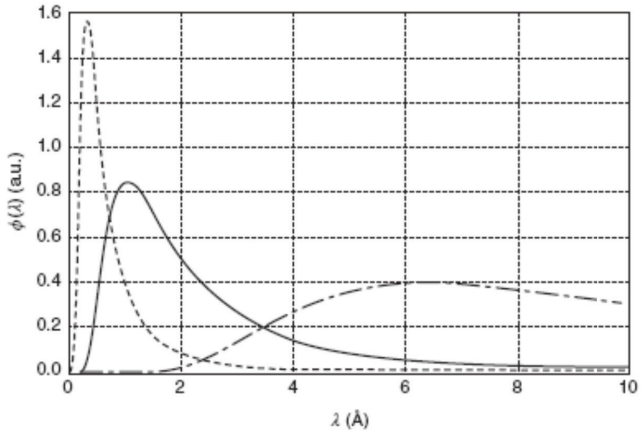

Fig. 10. Neutrons wavelength distribution from cold (dot dashed line, T=50 K), thermal (solid line, T=300K) and hot (dashed line, T=1000 K) moderators.

However, it also means that the amount of hot or cold neutrons in the thermal neutron spectrum is very small, so that any scattering experiment which requires hot or cold neutrons

will suffer from enormous flux losses. To enhance the hot or cold neutron flux one has to transform the thermal neutron spectrum shifting it towards high or low energies: in other words by heating or cooling the thermal neutron spectrum.

To achieve a significant gain factor by such spectrum transformations, the moderator temperature should be as high as 2000K and as low as 20K, respectively. Obviously, it is unrealistic to heat or to cool the whole water in the reactor vessel - tens of cubic meters – to such temperatures. The trick that is used to solve this problem is to insert other small local moderators inside the water and to set their temperatures accordingly. These devices are called hot and cold sources.

The hot source is usually made of a graphite block heated up to T=2400 K, when the cold sources is usually a vessel filled with liquid H_2 or D_2 or their mixture cooled down to 20K. Hot and cold neutron spectra are shown in Fig. 10. Each of them allows for a significant, up to 20 times gain in the corresponding neutron flux. By choosing the adequate neutron spectrum scattering experiments can be optimally tailored to particular experimental requirements.

6. Neutron beam transport

However, it is not enough to produce neutrons in the moderator – they still have to be transported to a neutron scattering instrument. As it was already mentioned in Ch. 4, neutrons are extracted from the moderator by neutron beam tubes, inserted in a heavy biological shielding surrounding the reactor tank and necessary because neutrons are isotropically emitted from the moderator.

The angular acceptance of a neutron beam tube is defined by its diameter (~10 cm) and length (~5m). Thus, the beam divergence of a beam tube is about ~1°, so that the neutron flux available at its output is drastically reduced by about six orders of magnitude, in comparison to the core flux.

This situation can be significantly improved by using neutron optical devices called neutron guides. The principle of their operational is rather similar to the one of light guides, where the light propagating in an optically dense media (i.e. with the refraction index n >1) is totally reflected from the glass air-interface due to the effect of total external reflection (the refraction index of air is equal to unity). In contrast to light, the refraction index of glass for neutrons is n <1, so that the effect of the total external reflection will take place on the air-

glass interface. However, in case of neutrons this phenomenon takes place only for incident angles, i.e. less than the critical angle θ_c , which is given by

$$\theta_c = \lambda\sqrt{\frac{2\rho b_{coh}}{\pi}},$$

where ρ and b_{coh} are the density and the coherent scattering length of the wall material, respectively. To increase θ_c the Ni coating with the critical angle $0.1°\cdot\lambda$ is used. Moreover, the wall of the neutron guide can be coated with so-called supermirrors, with the critical angle up to three times as much as the nickel's one. Indeed, the neutron guide is made as a hollow glass tube, Ni or supermirror coated from the inside (Fig. 11). Because the intensity at the neutron guide output is proportional to θ_c^2, they provide an order of magnitude flux increase as compared to a beam tube.

Fig. 11. To principle of the operation of light guides (a) and neutron guides (b)

Moreover, neutron guides can be bent or shaped. Bent neutron guides allow to avoid direct sight-of-view of the reactor core, drastically reducing γ- and neutron background at the instrument position. The parabolic or elliptic shaping of neutron guides opens exciting possibilities for the concentrating (focusing) of neutrons on a sample, thus providing additional increase in intensity at the position of neutron scattering instruments.

References:

1. G.R. Bauer (1993) Neutron sources. In: A.Furrer (ed.) *Neutron Scattering*, pp. 331–357. PSI-Proceedings No. 93-01, ISSN 1019-6447, Paul Scherrer Institute, Villigen.
2. J.M. Carpenter and W.B. Yelon (1986) Neutron sources. In: K. Sköld and D.L. Price (eds.) *Methods of Experimental Physics*, vol. 23A, pp. 99–196. London: Academic Press.
3. K. Clausen (2001) *Neutron sources*. Office for Official Publications of the European Communities, Luxembourg, ISBN 92-894-0037-4.
4. Utsuro, Masahiko and Ignatovich, Vladimir, *Handbook of Neutron Optics*. ISBN-13: 978-3-527-40885-6 - Wiley-VCH, Berlin.

2

A neutron primer: Elastic scattering and the properties of the neutron

Thomas Brückel

2. A neutron primer: Elastic scattering and the properties of the neutron

Thomas Brückel, IFF, Forschungszentrum Jülich

2.1 Introduction

After we have learnt how neutrons are produced in neutron sources, we will explain in this chapter, how neutrons can be used to study the atomic structure and dynamics of condensed matter systems. We will give a basic introduction into scattering methods in general and then introduce the special properties of neutrons, which make them an invaluable probe for condensed matter research. Neutrons tell us, where the atoms are, how the atoms move and what their atomic magnetic moments do.

Our present understanding of the properties and phenomena of condensed matter science is based on atomic theories. The first question we pose when studying any condensed matter system is the question concerning the internal structure: what are the relevant building blocks (atoms, molecules, colloidal particles, ...) and how are they arranged? The second question concerns the microscopic dynamics: how do these building blocks move and what are their internal degrees of freedom? For magnetic systems, in addition we need to know the arrangement of the microscopic magnetic moments due to spin and orbital angular momentum and their excitation spectra. In principle, the macroscopic response and transport properties, such as specific heat, thermal conductivity, elasticity, viscosity, susceptibility, magnetization etc., which are the quantities of interest for applications, result from the microscopic structure and dynamics. To determine these macroscopic properties from the microscopic information provided by scattering experiments represents a huge challenge to condensed matter theory as we are dealing with an extreme many body problem with typically 10^{23} particles involved. It is a true masterly achievement of mankind that for many solid state systems, such microscopic theories could be developed, based on quantum mechanics and statistical physics.

For the progress of modern condensed matter research, the availability of probes to study structure and dynamics on a microscopic level is therefore essential. Modern scattering techniques can provide all the required information. Radiation, which has a rather weak interaction with the sample under investigation, provides a non-invasive, non-destructive probe for the microscopic structure and dynamics. This has been shown for the first time by W. Friedrich, P. Knipping and M. von Laue in 1912, when interference of x-ray radiation scattered from a single crystal was observed. Max von Laue received the Nobel Prize for the interpretation of these observations. One cannot overestimate this discovery: it was the first definite proof that atoms as the elementary building blocks of condensed matter are arranged in a periodic manner within a crystal. The overwhelming part of our present-day knowledge of the atomic structure of condensed matter is based on x-ray structure investigations. The method has developed rapidly since 1912. With the advent of modern synchrotron x-ray sources, the source brilliance has since then increased by 18 orders of magnitude. Currently X-ray Free Electron Lasers, e. g. the XFEL project (http://xfel.desy.de/), are being realized which will increase this brilliance by another 10 orders of magnitude. Nowadays the structure of highly complex biological macromolecules, like the crystal structure of the ribosome, can be determined with atomic resolution. Extremely weak phenomena such as magnetic x-ray scattering can be exploited successfully at modern synchrotron radiation sources. In soft condensed matter research, where one is interested in the dynamics on larger lengths scales, such

as of colloidal particles in solution, light scattering is an important tool besides x-ray scattering. Finally, intense neutron beams have properties, which make them an excellent probe for condensed matter investigations. Neutron scattering is a unique tool to solve magnetic structures and determine magnetic excitations and fluctuations. In soft matter and life science, neutrons excel due to the possibility to apply contrast variation techniques by selective deuteration of molecules or molecular subunits. Neutrons give access to practically all lengths scales relevant in condensed matter investigations from the sub-atomic level of some pm up to about 1000 nm. They are particularly well suited for investigations of the movement of atoms and molecules. Similar to x-rays, the experimental techniques are in rapid evolution, mainly due to the advent of new neutron optical devices, but also of new sources. The new spallation sources, such as the American Spallation Neutron Source SNS (http://www.sns.gov/) or the proposed European Spallation Source ESS (http://neutron.neutron-eu.net/n_ess) will increase the capabilities of neutron investigations in condensed matter science drastically in the years to come.

This lecture is organized as follows: First we give a very basic introduction into elementary scattering theory for elastic scattering, which is valid for any probe. Then a more rigorous derivation in the framework of the Born series follows. This section can be skipped by beginners, but is provided for completeness.

We will introduce the concepts of coherence and pair correlation functions. Then we will discuss, which probes are most relevant for condensed matter investigations and present in some detail the interaction of neutrons with matter leading to the absorption and scattering cross-sections. More details can be found in [1 - 5].

We will frequently make use of the particle-wave dualism of quantum mechanics, which tells us that the radiation used in the scattering process can be described in a wave picture, whenever we are interested in interference phenomena, and in a particle picture, when the interaction with matter is relevant, e. g. for the detection process.

2.2 Elementary scattering theory: Elastic scattering

Throughout this lecture we assume that the atoms within our sample are rigidly fixed on equilibrium positions in space. Therefore we only look at those processes, in which the recoil is being transferred to the sample as a whole so that the energy change for the radiation is negligible and the scattering process appears to be elastic. In subsequent lectures, this restriction will be dropped and so-called inelastic scattering processes will be discussed. These are due to excitations or internal fluctuations in the sample, which give rise to an energy change of the radiation during the scattering process.

A sketch of the scattering experiment is shown in Figure 2.1.

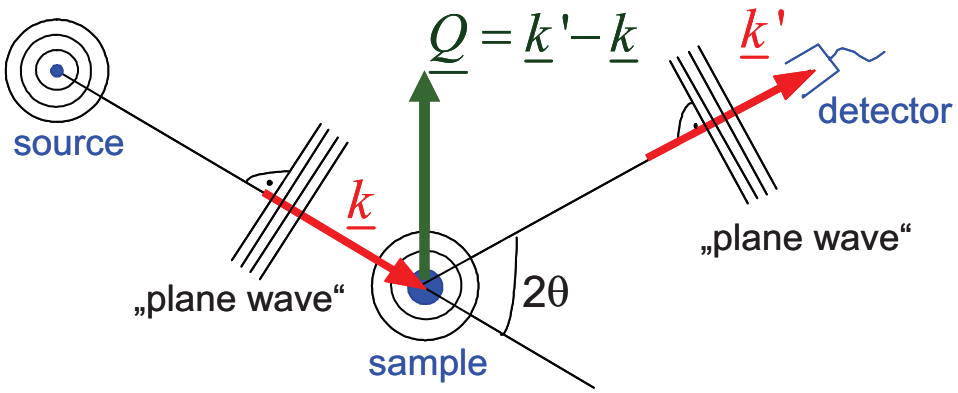

***Fig. 2.1**: A sketch of the scattering process in the Fraunhofer approximation in which it is assumed that plane waves are incident on sample and detector due to the fact that the distances source-sample and sample-detector, respectively, are significantly larger than the size of the sample.*

Here we assume the so-called *Fraunhofer approximation*, where the size of the sample is much smaller than the distance between sample and source and the distance between sample and detector, respectively. This assumption holds in all cases discussed in this lecture. In addition we assume that the source emits radiation of one given energy, i. e. so-called *monochromatic* radiation. Then the wave field incident on the sample can be considered as a plane wave, which is completely described by a wave vector $\underline{k}$. The same holds for the wave incident on the detector, which can be described by a vector $\underline{k}'$. In the case of elastic scattering (diffraction) we have

$$k = |\underline{k}| = |\underline{k}'| = k' = \frac{2\pi}{\lambda} \tag{2.1}$$

Let us define the so-called *scattering vector* by

$$\underline{Q} = \underline{k}' - \underline{k} \tag{2.2}$$

$\hbar\underline{Q}$ represents the momentum transfer during scattering, since according to de Broglie, the momentum of the particle corresponding to the wave with wave vector $\underline{k}$ is given by $\underline{p}=\hbar\underline{k}$. The magnitude of the scattering vector can be calculated from wavelength λ and scattering angle 2θ as follows

$$Q = |\underline{Q}| = \sqrt{k^2 + k'^2 - 2kk'\cos 2\theta} \Rightarrow Q = \frac{4\pi}{\lambda}\sin\theta \tag{2.3}$$

A scattering experiment comprises the measurement of the intensity distribution as a function of the scattering vector $I(Q)$. The scattered intensity is proportional to the so-called *cross section*, where the proportionality factors arise from the detailed geometry of the experiment. For a definition of the scattering cross section, we refer to Figure 2.2.

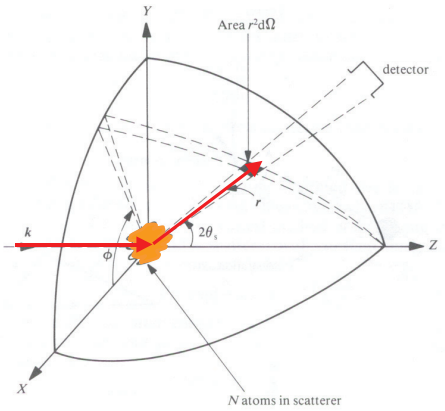

***Fig. 2.2**: Geometry used for the definition of the scattering cross section.*

If n' particles are scattered per second into the solid angle $d\Omega$ seen by the detector under the scattering angle 2θ and into the energy interval between E' and $E' + dE'$, then we can define the so-called *double differential cross section* by:

$$\frac{d^2\sigma}{d\Omega dE'} = \frac{n'}{j d\Omega dE'} \tag{2.4}$$

Here j refers to the incident beam flux in terms of particles per area and time. If we are not interested in the change of the energy of the radiation during the scattering process, or if our detector is not able to resolve this energy change, then we will describe the angular dependence by the so-called *differential cross section:*

$$\frac{d\sigma}{d\Omega} = \int_0^\infty \frac{d^2\sigma}{d\Omega dE'} dE' \tag{2.5}$$

Finally the so-called *total scattering cross section* gives us a measure for the total scattering probability independent of changes in energy and scattering angle:

$$\sigma = \int_0^{4\pi} \frac{d\sigma}{d\Omega} d\Omega \tag{2.6}$$

Therefore our task is to determine the arrangement of the atoms in the sample from the knowledge of the scattering cross section $d\sigma / d\Omega$. The relationship between scattered intensity and the structure of the sample is particularly simple in the so-called *Born approximation*, which is often also referred to as *kinematic scattering approximation*. In this case, refraction of the beam entering and leaving the sample, multiple scattering events and the extinction of the primary beam due to scattering within the sample are being neglected. Following Figure 2.3, the phase difference between a wave scattered at the origin of the coordinate system and at position $\underline{r}$ is given by

$$\Delta\Phi = 2\pi \cdot \frac{\left(\overline{AB} - \overline{CD}\right)}{\lambda} = \underline{k}' \cdot \underline{r} - \underline{k} \cdot \underline{r} = \underline{Q} \cdot \underline{r} \tag{2.7}$$

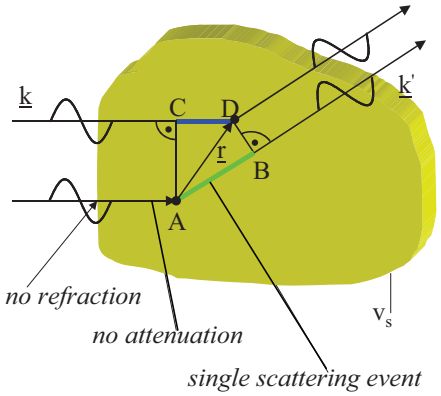

***Fig. 2.3**: A sketch illustrating the phase difference between a beam scattered at the origin of the coordinate system and a beam scattered at the position r.*

The scattered amplitude at the position $\underline{r}$ is proportional to the scattering density $\rho_s(\underline{r})$ at this position. ρ_s depends on the type of radiation used and the interaction of this radiation with the sample. In fact, ρ_s is directly proportional to the interaction potential, as will be shown in the next chapter. Assuming a laterally coherent beam, the total scattering amplitude is given by a coherent superposition of the scattering from all points within the sample, i. e. by the integral

$$A = A_0 \cdot \int_{V_S} \rho_S(\underline{r}) \cdot e^{i\underline{Q}\cdot\underline{r}} d^3r \qquad (2.8)$$

Here A_0 denotes the amplitude of the incident wave field. (2.8) demonstrates that the scattered amplitude is connected with the scattering density $\rho_s(\underline{r})$ by a simple Fourier transform. Knowledge of the scattering amplitude for all scattering vectors $\underline{Q}$ allows us to determine via a Fourier transform the scattering density uniquely. This is the complete information on the sample, which can be obtained by the scattering experiment. Unfortunately, nature is not so simple. On one hand, there is the more technical problem that one is unable to determine the scattering cross section for all values of momentum transfer $\hbar\underline{Q}$. The more fundamental problem, however, is that normally the amplitude of the scattered wave is not measurable. Instead only the scattered intensity

$$I \sim |A|^2 \qquad (2.9)$$

can be determined. Therefore the phase information is lost and the simple reconstruction of the scattering density via a Fourier transform is no longer possible. This is the so-called *phase problem* of scattering. There are ways to overcome the phase problem, e. g. by use of reference waves (e. g. holography). Then the scattering density becomes directly accessible. The question, which information we can obtain from a conventional scattering experiment despite the phase problem will be addressed below.

Which wavelength do we have to choose to obtain the required real space resolution? For information on a length scale L, a phase difference of about $Q \cdot L \approx 2\pi$ has to be achieved. Otherwise according to (2.7) $\underline{k}'$ and $\underline{k}$ will not differ significantly. According to (2.3) $Q \approx 2\pi/\lambda$ for typical scattering angles $(2\theta \sim 60°)$. Combining these two estimates, we end up with the requirement that the wavelength λ has to be in the order of the real space length scale L under investigation. To give an example: with the wavelength in the order of 0.1 nm, atomic resolution can be achieved in a scattering experiment.

2.3 Fundamental scattering theory: The Born series

In this chapter, we will give a simple formulation of scattering theory. Our purpose is to derive (2.8) from fundamental principles. The conditions under which (2.8) holds and the limitations of kinematical scattering theory will thus become clearer. The derivation will be done for particle beams – in particular neutrons - for which the Schrödinger equation holds. Beginners can skip this chapter and continue with 2.4.

In quantum mechanics, neutrons are described as particle wave fields through the Schrödinger equation:

$$H\Psi = \left(-\frac{\hbar^2}{2m}\Delta + V \right)\Psi = i\hbar\frac{\partial}{\partial t}\Psi \tag{2.10}$$

ψ is the probability density amplitude, V the interaction potential. In case of purely elastic scattering $E = E'$, the time dependence can be described by the factor $\exp\left(-i\frac{E}{h}t \right)$. Assuming this time dependence, a wave equation for the spatial part of the probability density amplitude ψ can be derived from (2.10):

$$\Delta\Psi + k^2\left(\underline{r}\right)\Psi = 0 \tag{2.11}$$

In (2.11) we have introduced a spatially varying wave vector with the magnitude square:

$$k^2\left(\underline{r}\right) = \frac{2m}{\hbar^2}\left(E - V\left(\underline{r}\right)\right) \tag{2.12}$$

Solutions of (2.10) in empty space (i. e. $V \equiv 0$) can be guessed immediately. They are given by plane waves $\Psi = \Psi_0 \exp\left[i\left(\underline{k}\cdot\underline{r} - \frac{E}{\hbar}t \right) \right]$ with $k^2 = \frac{2m}{\hbar^2}E$. The relations between magnitude of the wave vector k, wave length λ and energy of the neutron E can be written in practical units:

$$\begin{aligned} k\left[\text{Å}^{-1}\right] &\approx 0.695\sqrt{E\left[meV\right]} \\ \lambda\left[\text{Å}\right] &\approx 9.045/\sqrt{E\left[meV\right]} \\ E\left[meV\right] &\approx 81.8/\lambda^2\left[\text{Å}\right] \end{aligned} \tag{2.13}$$

To give an example, neutrons of wavelength λ=2.4Å=0.24nm have an energy of 14.2 meV with a magnitude of the neutron wave vector of $k = 2.6\ \text{Å}^{-1}$.

To obtain solutions of the wave equation (2.11) in matter, we reformulate the differential equation by explicitly separating the interaction term:

$$\left(\Delta + k^2\right)\Psi = \frac{2m}{\hbar^2}V\cdot\Psi =: \chi \tag{2.14}$$

Here $\underline{k}$ denotes the wave vector for propagation in empty space. The advantage of this formulation is that the solutions of the left hand side are already known. They are the plane waves in empty space. Equation (2.14) is a linear partial differential equation, i. e. the superposition principle holds: the general solution can be obtained as a linear combination of a complete set of solution functions. The coefficients in the series are determined by the boundary conditions. To solve (2.14) one can apply a method developed for inhomogeneous linear differential equations. For the moment, we assume that the right hand side is fixed (given as χ). We define a *Greens-function* by:

$$\left(\Delta + k^2\right)G\left(\underline{r},\underline{r}'\right) = \delta\left(\underline{r} - \underline{r}'\right) \tag{2.15}$$

A solution of (2.15) is given by:

$$G(\underline{r},\underline{r}') = \frac{e^{ik|\underline{r}-\underline{r}'|}}{4\pi|\underline{r}-\underline{r}'|} \tag{2.16}$$

The meaning of (2.16) is immediately clear: the scattering from a point-like scatterer (δ-potential) gives an emitted spherical wave. In a schematic graphical representation:

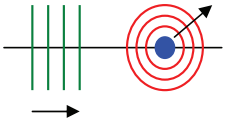

Using the Greens-function $G(\underline{r},\underline{r}')$, we can write down a formal solution of the wave equation (2.14):

$$\Psi = \Psi^o + \int G(\underline{r},\underline{r}')\,\chi(\underline{r}')\,d^3r' \tag{2.17}$$

Here, we have taken the initial conditions of an incident plane wave ψ^0 into account. (2.17) is indeed a solution of (2.14) as can be easily verified by substituting (2.17) into (2.14). If we finally substitute the definition of χ, one obtains the so-called *Lippmann-Schwinger* equation:

$$\Psi(\underline{r}) = \psi^\circ(\underline{r}) + \frac{2m}{\hbar^2}\int G(\underline{r},\underline{r}')V(\underline{r}')\Psi(\underline{r}')\,d^3r' \tag{2.18}$$

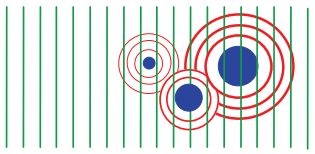

(2.18) has a simple interpretation: the incident plane wave $\psi^0(\underline{r})$ is superimposed by spherical waves emitted from scattering at positions $\underline{r}'$. The intensity of these spherical waves is proportional to the interaction potential $V(\underline{r}')$ and the amplitude of the wave field at the position $\underline{r}'$. To obtain the total scattering amplitude, we have to integrate over the entire sample volume V_s.

However, we still have not solved (2.14): our solution ψ appears again in the integral in (2.18). In other words, we have transformed differential equation (2.14) into an integral equation. The advantage is that for such an integral equation, a solution can be found by iteration. In the zeroth approximation, we neglect the interaction V completely. This gives $\psi = \psi^0$. The next higher order approximation for a weak interaction potential is obtained by substituting this solution in the right hand side of (2.18). The first non-trivial approximation can thus be obtained:

$$\Psi^1(\underline{r}) = e^{i\underline{k}\cdot\underline{r}} + \frac{2m}{\hbar^2}\int \frac{\exp(ik|\underline{r}-\underline{r}'|)}{4\pi|\underline{r}-\underline{r}'|} V(\underline{r}')e^{i\underline{k}\underline{r}'}\,d^3r' \tag{2.19}$$

(2.19) is nothing else but a mathematical formulation of the well-known *Huygens principle* for wave propagation.

The approximation (2.19) assumes that the incident plane wave is only scattered once from the potential $V(\underline{r}')$. For a stronger potential and larger sample, multiple scattering processes will occur. Again, this can be deduced from the integral equation (2.18) by further iteration. For simplification we introduce a new version of equation (2.18) by writing the integral over the "Greens function" as operator $\boldsymbol{G}$:

$$\psi = \psi^o + \mathbf{G}V\psi \tag{2.20}$$

The so-called *first Born approximation*, which gives the *kinematical scattering theory* is obtained by substituting the wave function ψ on the right hand side by ψ^0:

$$\psi^1 = \psi^o + \mathbf{G}V\psi^o \tag{2.21}$$

This first approximation can be represented by a simple diagram as a sum of an incident plane wave and a wave scattered once from the potential V:

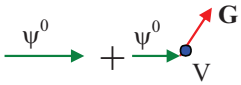

The second approximation is obtained by substituting the solution of the first approximation (2.21) on the right hand side of equation (2.20):

$$\psi^2 = \psi^o + \mathbf{G}V\psi^1 = \psi^o + \mathbf{G}V\psi^o + \mathbf{G}V\mathbf{G}V\psi^o \tag{2.22}$$

Or in a diagrammatic form:

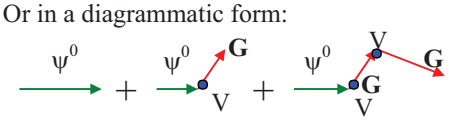

I. e. in the second approximation, processes are being taken into account, in which the neutron is scattered twice by the interaction potential V. In a similar manner, all higher order approximations can be calculated. This gives the so-called *Born series*.[1] For weak potential and small samples, this series converges rather fast. Often, the first approximation, the *kinematic scattering theory*, holds very well. This is especially the case for neutron scattering, where the scattering potential is rather weak, as compared to x-ray- or electron- scattering. Due to the strong Coulomb interaction potential, the probability for multiple scattering processes of electrons in solids is extremely high, making the interpretation of electron diffraction experiments very difficult. But even for neutrons, the kinematic scattering theory can break down, for example in the case of Bragg scattering from large ideally perfect single crystals, where the Born series does not converge. The wave equation has to be solved exactly under the boundary conditions given by the crystal geometry. For simple geometries, analytical solutions can be obtained. This is then called the *dynamical scattering theory*. Since for neutrons, the kinematical theory holds in most cases, or multiple scattering events can often be corrected for, we will no longer discuss dynamical theory in what follows and refer to [3, 6].

Let us return to the first Born approximation (2.19). In a further approximation, the Fraunhofer approximation, we assume that the size of the sample is significantly smaller than the distance sample-detector. The geometry to calculate the far field limit of (2.19) is given in Figure 2.4. Under the assumption $|\underline{R}| >> |\underline{r}'|$, we can deduce from Figure 2.4 the following approximation for the emitted spherical wave:

$$\frac{\exp\left(ik\left|\underline{r}-\underline{r}'\right|\right)}{\left|\underline{r}-\underline{r}'\right|} \approx \frac{\exp\left(ik\left(R-\underline{r}'\cdot\hat{\underline{R}}\right)\right)}{R} \approx \frac{\exp(ikR)}{R}\cdot e^{-i\underline{k}'\cdot\underline{r}'} \tag{2.23}$$

The probability density amplitude for the scattered wave field in the limit of large distances from the sample is thus given by:

$$\Rightarrow \psi^1\left(\underline{R}\right) = e^{i\underline{k}\cdot\underline{R}} + \frac{2m}{\hbar^2}\frac{e^{ikR}}{4\pi R}\int V\left(\underline{r}'\right)e^{i\underline{Q}\cdot\underline{r}'}d^3r' \tag{2.24}$$

[1] Note that Born approximation or the Born series violates energy conservation: scattered waves are created without weakening of the incident plane wave. Born series can therefore only be applied in the limit of very weak scattering potentials.

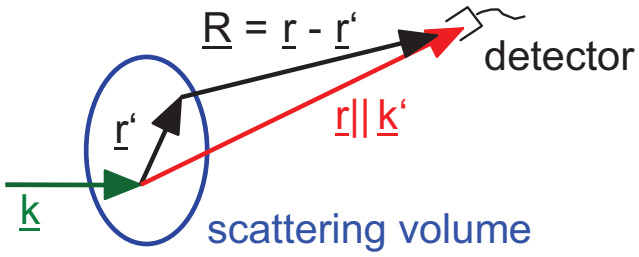

Fig. 2.4*: Scattering geometry for the calculation of the far field limit at the detector. In the Fraunhofer approximation, we assume that* $|\underline{R}| >> |\underline{r}'|$.

This is just the sum of an incident plane wave and a spherical wave emitted from the sample as a whole. The amplitude of the scattered wave is given according to (2.24):

$$A(\underline{Q}) = \frac{m}{2\pi\hbar^2}\int V(\underline{r}) e^{i\underline{Q}\cdot\underline{r}} d^3r \sim F\left[V(\underline{r})\right] \tag{2.25}$$

The integral in the above equation is nothing but the transition matrix element of the interaction potential V between the initial and final plane wave states, therefore:

$$\frac{d\sigma}{d\Omega} = \left(\frac{m}{2\pi\hbar^2}\right)^2 \left|\langle \underline{k}'|V|\underline{k}\rangle\right|^2 \tag{2.26}$$

This formula corresponds to *Fermi's Golden Rule* from time-dependent perturbation theory, where the transition probability per time interval from state k to states k' is given by:

$$W_{k'k} = \frac{2\pi}{\hbar}\left|\langle k'|V|k\rangle\right|^2 \cdot \rho(E_{k'}) \tag{2.27}$$

Here, $\rho(E_{k'})$ denotes the density of states for the final states k'.

With this exact derivation of the scattering cross section, we can now deduce by comparison with (2.8) that the scattering density in the simple derivation of chapter 2.2 is just $\rho_S(\underline{r}) = \frac{m}{2\pi\hbar^2} V(\underline{r})$ for particle beams governed by the Schrödinger equation.

We now allow for inelastic processes, where the sample undergoes a change of its state from α to α' (α denotes a set of quantum numbers characterizing an eigenstate of the sample). In this case, due to the different length of the wavevectors for incoming and outgoing waves, we have to introduce factors k' and k, which arise from the density of states factor in (2.27). Since the scattering event must fulfill energy and momentum conservation, we arrive at the double differential cross section:

$$\frac{d^2\sigma}{d\Omega d\omega} = \frac{k'}{k}\left(\frac{m}{2\pi\hbar^2}\right)^2 \sum_{\alpha} p_\alpha \sum_{\alpha'} \left|\langle \underline{k}', \alpha'|V|\underline{k}, \alpha\rangle\right|^2 \cdot \delta(\hbar\omega + E_\alpha - E_{\alpha'}) \tag{2.28}$$

The first summation is carried out over all possible initial states α of the system, weighted with their thermodynamic occupation probability p_α. The sum over α' is the sum over all final states allowed by energy conservation, which is guaranteed through the δ-function. $\hbar\omega$ denotes the energy transfer of the neutron to the system. This double differential cross section will be discussed in the following lectures on inelastic scattering.

2.4 Coherence

In the above derivation, we assumed plane waves as initial and final states. For a real scattering experiment, this is an unphysical assumption. In the incident beam, a wave packet is produced by collimation (defining the direction of the beam) and monochromatization (defining the wavelength of the incident beam). Neither the direction $\hat{\underline{k}}$, nor the wavelength λ have sharp values but rather have a distribution of finite width about their respective mean values. This wave packet can be described as a superposition of plane waves. As a consequence, the diffraction pattern will be a superposition of patterns for different incident wavevectors $\underline{k}$ and the question arises, which information is lost due to these non-ideal conditions. This *instrumental resolution* is intimately connected with the *coherence* of the beam. Coherence is needed, so that the interference pattern is not significantly destroyed. Coherence requires a phase relationship between the different components of the beam. Two types of coherence can be distinguished.

• *Temporal or longitudinal coherence* due to a wavelength spread.
A measure for the longitudinal coherence is given by the length, on which two components of the beam with largest wavelength difference (λ and $\lambda+\Delta\lambda$) become fully out of phase. According to the following figure, this is the case for $l_{\parallel} = n \cdot \lambda = \left(n - \frac{1}{2} \right)(\lambda + \Delta\lambda)$.

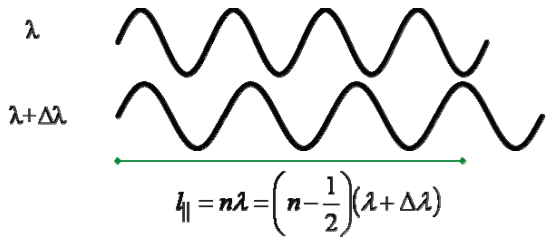

Fig. 2.5*: A sketch illustrating the longitudinal coherence due to a wavelength spread.*

From this, we obtain the *longitudinal coherence length* $l_{\parallel}$ as

$$l_{\parallel} = \frac{\lambda^2}{2\Delta\lambda} \tag{2.29}$$

• *Transversal coherence* due to source extension
Due to the extension of the source (transverse beam size), the phase relation is destroyed for large source size or large divergence. According to the following figure, a first minimum occurs for $\frac{\lambda}{2} = d \cdot \sin\theta \approx d \cdot \theta$.

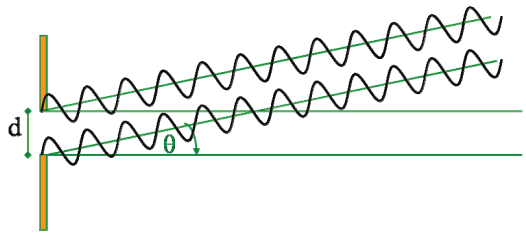

Fig. 2.6*: A sketch illustrating the transverse coherence due to source extension.*

From this, we obtain the *transversal coherence length* $l_\perp$ as

$$l_\perp = \frac{\lambda}{2\Delta\theta} \tag{2.30}$$

Here $\Delta\theta$ is the divergence of the beam. Note that $l_\perp$ can be different along different spatial directions: in many instruments, the vertical and horizontal collimations are different.

Together, the longitudinal and the two transversal coherence lengths (in two directions perpendicular to the beam propagation) define a *coherence volume*. This is a measure for a volume within the sample, in which the amplitudes of all scattered waves superimpose to produce an interference pattern. Normally, the coherence volume is significantly smaller than the sample size, typically a few *100 Å* for neutron scattering, up to *μm* for synchrotron radiation. Scattering between different coherence volumes within the sample is no longer coherent, i. e. instead of the amplitudes the intensities of the contributions to the scattering pattern have to be added. This limits the real space resolution of a scattering experiment to the extension of the coherence volume.

2.5 Pair correlation functions

After having clarified the conditions under which we can expect a coherent scattering process, let us now come back to the question, which information is accessible from the intensity distribution of a scattering experiment. From (2.9) we see that the phase information is lost during the measurement of the intensity. For this reason the Fourier transform of the scattering density is not directly accessible in most scattering experiments (note however that phase information can be obtained in certain cases).

Substituting (2.8) into (2.9) and applying variable substitution $\underline{R}=\underline{r}'-\underline{r}$, we obtain for the magnitude square of the scattering amplitude, a quantity directly accessible in a scattering experiment:

$$I \sim \left| A\left(\underline{Q}\right)\right|^2 \sim \int d^3r'\, \rho_s\left(\underline{r}'\right) e^{i\underline{Q}\cdot\underline{r}'} \int d^3r\, \rho_s^*\left(\underline{r}\right) e^{-i\underline{Q}\cdot\underline{r}} = \iint d^3r'\, d^3r\, \rho_s\left(\underline{r}'\right)\rho_s^*\left(\underline{r}\right) e^{i\underline{Q}\cdot\left(\underline{r}'-\underline{r}\right)}$$
$$= \iint d^3R\, d^3r\, \rho_s\left(\underline{R}+\underline{r}\right)\rho_s^*\left(\underline{r}\right) e^{i\underline{Q}\cdot\underline{R}} \tag{2.31}$$

This shows that the scattered intensity is proportional to the Fourier transform of a function $P(\underline{R})$:

$$I\left(\underline{Q}\right) \sim \int d^3R\, P\left(\underline{R}\right) e^{i\underline{Q}\cdot\underline{R}} \tag{2.32}$$

This function denotes the so-called *Patterson function* in crystallography or more general the *static pair correlation function:*

$$P\left(\underline{R}\right) = \int d^3r\, \rho_s^*\left(\underline{r}\right)\rho_s\left(\underline{r}+\underline{R}\right) \tag{2.33}$$

$P(\underline{R})$ correlates the value of the scattering density at position $\underline{r}$ with the value at the position $\underline{r}+\underline{R}$, integrated over the entire sample volume. If, averaged over the sample, no correlation exists between the values of the scattering densities at position $\underline{r}$ and $\underline{r}+\underline{R}$, then the Patterson function $P(\underline{R})$ vanishes. If, however, a periodic arrangement of a pair of atoms exists in the sample with a difference vector $\underline{R}$ between the positions, then the Patterson function will have an extremum for this vector $\underline{R}$. Thus the Patterson function reproduces all the vectors connecting one atom with another atom in a periodic arrangement.

Quite generally, in a scattering experiment, pair correlation functions are being determined. In a coherent inelastic scattering experiment, we measure the *scattering law* $S(Q,\omega)$, which is the

Fourier transform with respect to space and time of the spatial and temporal pair correlation function:

$$\frac{d^2\sigma}{d\omega d\Omega} \sim S\left(\underline{Q},\omega\right) = \frac{1}{2\pi\hbar}\int_{-\infty}^{+\infty} dt\, e^{-i\omega t}\int d^3r\, e^{i\underline{Q}\cdot\underline{r}} G\left(\underline{r},t\right) \tag{2.34}$$

While the proportionality factor between the double differential cross section and the scattering law depends on the type of radiation and its specific interaction potential with the system studied, the spatial and temporal pair correlation function is only a property of the system studied and independent of the probe used:

$$G\left(\underline{r},t\right) = \frac{1}{N}\sum_{ij}\int d^3r' \left\langle \delta\left(\underline{r}'-\underline{r}_j\left(0\right)\right)\cdot\delta\left(\underline{r}'+\underline{r}-\underline{r}_i\left(t\right)\right)\right\rangle = \frac{1}{N}\int d^3r' \left\langle \rho\left(\underline{r}',0\right)\rho\left(\underline{r}'+\underline{r},t\right)\right\rangle \tag{2.35}$$

Here, the pair correlation function is once expressed as a correlation between the position of N point-like particles (expressed by the delta functions) and once by the correlation between the densities at different positions in the sample for different times. In a magnetic system, we scatter from the atomic magnetic moments, which are vector quantities. Therefore, the scattering law becomes a tensor - the Fourier transform of the spin pair correlations:

$$\mathbf{S}^{\alpha\beta}(\underline{Q},\omega) = \frac{1}{2\pi}\sum_{l}\int dt\, e^{i\left[\underline{Q}\left(\underline{R}_l-\underline{R}_0\right)-\omega t\right]}\left\langle S_0^{\alpha}(0) S_l^{\beta}(t)\right\rangle \tag{2.36}$$

α, β denote the Cartesian coordinates x, y, z; $\underline{R}_0$ and $\underline{R}_l$ are the spatial coordinates of a reference spin 0 and a spin l in the system.

2.6 Form-factor

So far we have not specified the nature of our sample. Now we assume an assembly on N scatterers of finite size, see Figure 2.7.

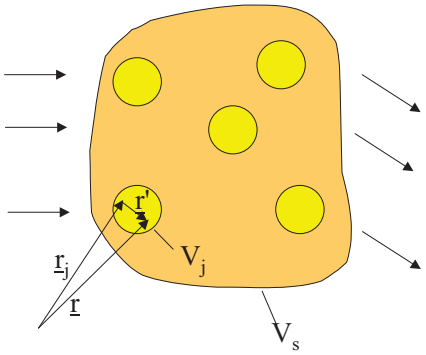

Fig. 2.7: *Sketch showing the assembly of N scatterers of finite size and defining the quantities needed for the definition of the form factor.*

These could be atoms in a solid or colloidal particles in a homogeneous solution. In what follows, we will separate the interference effects from scattering within one such a particle from the interference effects arising from scattering between different particles. With the decomposition of the vector $\underline{r}$ into the centre-of-gravity-vector $\underline{r}_j$ and a vector $\underline{r}'$ within the particle, the scattering amplitude can be written as (all particles are assumed to be identical):

$$A \propto \int_{V_S} d^3r\, \rho_S(\underline{r}) e^{i\underline{Q}\cdot\underline{r}} = \sum_{j=1}^{N} \int_{V_j} d^3r\, \rho_S(\underline{r}) e^{i\underline{Q}\cdot\underline{r}}$$
$$= \sum_{j=1}^{N} e^{i\underline{Q}\cdot\underline{r}_j} \int_{V_j^0} d^3r'\, \rho_S(\underline{r}') e^{i\underline{Q}\cdot\underline{r}'} =: \sum_{j=1}^{N} e^{i\underline{Q}\cdot\underline{r}_j} \rho_j^{tot} f_j(\underline{Q}) \tag{2.37}$$

With (2.37), we have separated the scattering from within the single particles from the interference between different particles. ρ_j^{tot} denotes the total scattering power of the particle. The *form-factor f(Q)* is defined as the normalized amplitude of scattering from within one particle[2] (it describes the "form" of the particle):

$$f(\underline{Q}) \equiv \frac{\int_{V_j^0} d^3r'\, \rho_s(\underline{r}')\, e^{i\underline{Q}\cdot\underline{r}'}}{\int_{V_j^0} d^3r'\, \rho_s(\underline{r}')} \tag{2.38}$$

For a homogeneous sphere

$$\rho_S(\underline{r}) = \begin{cases} 0 & |\underline{r}| > R \\ 1 & |\underline{r}| \le R \end{cases} \tag{2.39}$$

, the form-factor can be calculated by using spherical co-ordinates:

$$\Rightarrow f(Q) = 3 \cdot \frac{\sin QR - QR \cdot \cos QR}{(QR)^3} \tag{2.40}$$

The function (2.40) is plotted in Figure 2.8. In forward direction, there is no phase difference between waves scattered from different volume elements within the sample (note: we assume the Fraunhofer approximation and work in a far field limit). The form-factor takes its maximum value of one. For finite scattering angles 2θ, the form-factor drops due to destructive interference from various parts within one particle and finally for large values of the momentum transfer shows damped oscillations around 0 as a function of QR.

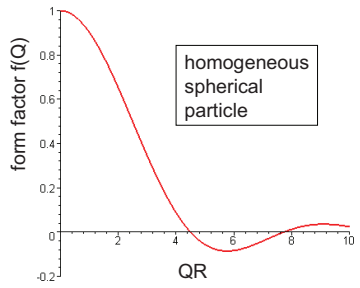

***Fig. 2.8**: Form-factor for a homogeneous sphere according to (2.40).*

2.7 Scattering from a periodic lattice in three dimensions

As an example for the application of (2.8) and (2.9), we will now discuss the scattering from a three dimensional lattice of point-like scatterers. As we will see later, this situation corresponds to the scattering of thermal neutrons from a single crystal. More precisely, we will restrict ourselves to the case of a Bravais lattice with one atom at the origin of the unit cell. To

[2] For simplicity we now drop the index j

each atom we attribute a "scattering power[3] α". The single crystal is finite with *N, M* and *P* periods along the basis vectors $\underline{a}$, $\underline{b}$ and $\underline{c}$. The scattering density, which we have to use in (2.8) is a sum over δ-functions for all scattering centers:

$$\rho_s(\underline{r}) = \sum_{n=0}^{N-1}\sum_{m=0}^{M-1}\sum_{p=0}^{P-1} \alpha \cdot \delta\left(\underline{r} - \left(n\cdot\underline{a} + m\cdot\underline{b} + p\cdot\underline{c}\right)\right) \tag{2.41}$$

The scattering amplitude is calculated as a Fourier transform:

$$A(\underline{Q}) \sim \alpha \sum_{n=0}^{N-1} e^{in\underline{Q}\cdot\underline{a}} \sum_{m=0}^{M-1} e^{im\underline{Q}\cdot\underline{b}} \sum_{p=0}^{P-1} e^{ip\underline{Q}\cdot\underline{c}} \tag{2.42}$$

Summing up the geometrical series, we obtain for the scattered intensity:

$$I(\underline{Q}) \sim \left|A(\underline{Q})\right|^2 = |\alpha|^2 \cdot \frac{\sin^2\frac{1}{2}N\underline{Q}\cdot\underline{a}}{\sin^2\frac{1}{2}\underline{Q}\cdot\underline{a}} \cdot \frac{\sin^2\frac{1}{2}M\underline{Q}\cdot\underline{b}}{\sin^2\frac{1}{2}\underline{Q}\cdot\underline{b}} \cdot \frac{\sin^2\frac{1}{2}P\underline{Q}\cdot\underline{c}}{\sin^2\frac{1}{2}\underline{Q}\cdot\underline{c}} \tag{2.43}$$

The dependence on the scattering vector $\underline{Q}$ is given by the so-called *Laue function*, which factorizes according to the three directions in space. One factor along one lattice direction $\underline{a}$ is plotted in Figure 2.9.

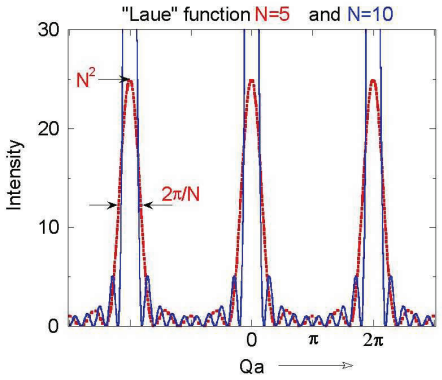

Fig. 2.9: *Laue function along the lattice direction $\underline{a}$ for a lattice with five and ten periods, respectively.*

The main maxima occur at the positions $Q = n \cdot 2\pi/a$. The maximum intensity scales with the square of the number of periods N^2, the half width is given approximately by $\Delta Q = 2\pi/(N\cdot a)$. The more periods contribute to coherent scattering, the sharper and higher are the main peaks. Between the main peaks, there are *N-2* side maxima. With increasing number of periods *N*, their intensity becomes rapidly negligible compared to the intensity of the main peaks. The main peaks are of course the well known *Bragg reflections*, which we obtain for scattering from a crystal lattice. From the position of these Bragg peaks in momentum space, the metric of the unit cell can be deduced (lattice constants *a, b, c* and unit cell angles *α, β, γ*). The width of the Bragg peaks is determined by the size of the coherently scattering volume (parameters *N, M,* and *P*) - and some other factors for real experiments (resolution, mosaic distribution, internal strains, ...).

[3] We will later see that this „scattering power" is connected to the so-called scattering length of the atom.

2.8 Probes for scattering experiments in condensed matter science

In this chapter, we will discuss which type of radiation is suitable for condensed matter investigations. For neutron beams, we will then discuss the relevant interaction processes with matter in detail.

A list of requirements for the type of radiation used in condensed matter investigations looks as follows:

(1) The achievable spatial resolution should be in the order of the inter-particle distances, which implies (see section 2.2) that the wavelength λ is in the order of the inter-particle distance L.
(2) If we want to study volume effects, the scattering has to originate from the bulk of the sample, which implies that the radiation should be at most weakly absorbed within matter.
(3) For a simple interpretation of the scattering data within the Born approximation (see section 2.2), multiple scattering effects should be negligible, i. e. the interaction of the radiation with matter should be weak.
(4) For the sake of simplicity, the probe should have no inner degrees of freedom, which could be excited during the scattering process (i. e. avoid beams of molecules, which have internal vibrational or rotational degrees of freedom).
(5) To study magnetic systems, we need a probe which interacts with the atomic magnetic moments in the sample.
(6) If, in addition to structural studies, we want to investigate elementary excitations, we would like the energy of the probe to be in the order of the excitation energies, so that the energy change during the scattering process is easily measurable.

This list of requirements leads us to some standard probes in condensed matter research. First of all, electromagnetic radiation governed by the Maxwell equations can be used. Depending on the resolution requirements, we will use x-rays with wavelength λ of about *0.1 nm* to achieve atomic resolution or visible light ($\lambda \sim 350 - 700\ nm$) to investigate e. g. colloidal particles in solution. Besides electromagnetic radiation, particle waves can be used. It turns out that thermal neutrons with a wavelength $\lambda \sim 0.1nm$ are particularly well adapted to the above list of requirements. The neutron beams are governed by the Schrödinger equation of quantum mechanics. An alternative is to use electrons, which for energies of around *100keV* have wavelengths in the order of *0.005nm*. As relativistic particles, they are governed by the Dirac equation of quantum mechanics. The big drawback of electrons as a condensed matter probe is the strong Coulomb interaction with the electrons in the sample. Therefore neither absorption, nor multiple scattering effects can be neglected. However the abundance of free electrons and the relative ease to produce optical elements makes them very suitable for imaging purposes (electron microscopy). Electrons, but also atomic beams are very powerful tools for surface science: due to their strong interaction with matter, both types of radiation are very surface sensitive. Low Energy Electron Diffraction LEED and Reflection High Energy Electron Diffraction RHEED are both used for in-situ studies of the crystalline structure during thin film growth, e.g. with Molecular Beam Epitaxy MBE. In what follows we will concentrate on neutron scattering as one of the probes, which is best suited for bulk studies on an atomic scale. We will introduce the properties of the neutron, discuss the absorption of neutrons in matter and derive the scattering cross sections for the main interaction processes with matter.

2.9 Properties of the neutron

We mentioned in the introduction that neutron beams provide a particularly useful probe for condensed matter investigations. The neutron is an elementary particle, a nucleon, consisting of three valance quarks, which are hold together by gluons. It thus has an internal structure, which, however, is irrelevant for condensed matter physics, since the energy scales involved in its internal excitations are much too high. Keeping in mind the difference in lengths scales (diameter of an atom: about $0.1nm=10^{-10}m$; diameter of a neutron: about $1fm=10^{-15}m$), we can safely consider the neutron as a point-like particle without internal structure for our purposes. Due to the weak interaction, the neutron is not a stable particle. A free neutron undergoes a β-decay after an average lifetime of about 15 minutes:

$$n \xrightarrow{15\,\mathrm{min}} p + e^- + \bar{\nu} \tag{2.44}$$

This leaves ample time for scattering investigations. In contrast to the massless photon, the neutron has a mass m of about one atomic mass unit ~ $1.675 \cdot 10^{-27}$ kg. The finite neutron mass is comparable to the mass of a nucleus and thus an appreciable amount of energy can be transferred during the scattering process. The neutron is a charge less particle and thus does not show the strong Coulomb interaction with matter. This results in large penetration depths. Finally, the neutron has a nuclear spin 1/2 giving rise to a magnetic dipolar moment of

$$\mu_n = \gamma\mu_N; \quad \gamma = 1.91; \quad \mu_N = 5.05 \cdot 10^{-27}\, J/T \tag{2.45}$$

Due to this magnetic moment, the neutron can interact with the magnetic field of unpaired electrons in a sample leading to *magnetic scattering*. Thus magnetic structures and excitations can be studied by neutron scattering.

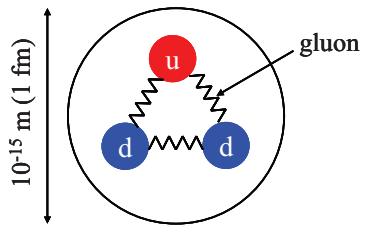

Mass	~ 1u	$1.67495 \cdot 10^{-27}$ kg
Charge	0	$(-0.4 \pm 1.1) \cdot 10^{-21}$ e
Magnetic monopole moment	0	$(0.85 \pm 2.2) \cdot 10^{-20}$ e/2[α]
Electric dipole moment	0	$(-0.1 \pm 0.36) \cdot 10^{-25}$ e·cm
Spin	1/2	

$\Rightarrow$ magnetic dipolar moment

$$\mu_n = -\gamma \cdot \mu_N \quad ; \quad \gamma = 1.913$$

$$\mu_N = \frac{e\hbar}{2\, m_p}$$

Fig. 2.10: *Schematics of the neutron being composed of three quarks and gluons and the main quantities characterizing the neutron as a particle.*

To calculate the interference effects during the scattering process, a neutron has to be described as a matter wave with momentum

$$\underline{p} = m \cdot \underline{v} = \hbar \underline{k}; \; p = h/\lambda \tag{2.46}$$

and energy

$$E = \frac{1}{2} m v^2 = \frac{\hbar^2 k^2}{2m} = \frac{h^2}{2m\lambda^2} \equiv k_B T_{eq} \tag{2.47}$$

Here $\underline{v}$ is the velocity of the neutron and T_{eq} defines the temperature equivalent of the kinetic energy of the neutron. In practical units:

$$\lambda[nm] = \frac{400}{v[m/s]}$$
$$E[meV] = \frac{0.818}{\lambda^2[nm]} \tag{2.48}$$

Let us consider the example of so-called *thermal neutrons* from a moderator at ambient temperature corresponding to a temperature equivalent of T_{eq}~*300K*. According to (2.47), their wavelength is *0.18nm*, matching perfectly the distance between atoms. The energy of thermal neutrons is around *25meV*, which matches well the energy of elementary excitations, such as spin waves (magnons) or lattice vibrations (phonons). Together with the usually large penetration depths (charge = 0) and the magnetic interaction, these properties make neutrons so extremely useful for condensed matter investigations.

In the elementary scattering theory of chapter 2.3, we saw that the relevant quantity is the interaction potential $V(\underline{r})$ of the probe with the system from which the probe is scattered. This potential enters in the cross-section in kinematical theory derived either from Born approximation or from Fermi's golden rule. To determine this interaction potential, we will look in more detail at the interaction of neutrons with matter. For neutrons there exist two dominant interactions: the interaction of the neutron with nuclei and its interaction with the magnetic field in the sample. The nuclear interaction results from the so-called strong interaction of particle physics, which is also responsible for the binding of neutrons and protons in the atomic nuclei. The interaction with the magnetic field is nothing but the magnetic dipole interaction of the neutron due to its dipolar moment with the magnetic field of unpaired electrons. There are other interactions, which are significantly weaker. One is the interaction of the neutron with the electric fields in the sample due to the neutrons magnetic dipole moment. This is a purely relativistic effect. Another is the magnetic dipole interaction of the neutron with the magnetic field produced by the nuclei. Since such interactions are several orders of magnitude weaker than the nuclear and magnetic interaction, they can usually be neglected and we will not discuss them further in this lecture.

2.10 Nuclear interaction: Scattering and absorption

To evaluate the cross section (2.26) for nuclear scattering, we have to specify the interaction potential with the nucleus. To derive this interaction potential from first principles is one of the fundamental challenges of nuclear physics. Fermi has proposed a phenomenological potential based on the argument that the wavelength of thermal neutrons is much larger than the nuclear radius. This means that the nuclei are point-like scatterers which leads to isotropic, Q-independent, (so-called s-wave) scattering. We will therefore use the so-called *Fermi-pseudo-potential:*

$$V(\underline{r}) = \frac{2\pi\hbar^2}{m} b\delta(\underline{r} - \underline{R}) \tag{2.49}$$

to evaluate the cross section (2.26).

Note, that despite the fact that the strong interaction of high energy physics is responsible for the scattering of the neutron with the nucleus, the scattering probability is small due to the small nuclear radius. Therefore, we can apply the first Born approximation. The quantity *b* introduced in (2.49) is a phenomenological quantity describing the strength of the interaction potential and is referred to as the *scattering length*. Tabulated values of *b* can be found in [7] or at http://www.ncnr.nist.gov/resources/n-lengths/. The total cross section of a given nucleus

is $\sigma = 4\pi|b|^2$, corresponding to the surface area of a sphere with radius *b*. Since the interaction potential obviously depends on the details of the nuclear structure, *b* is different for different isotopes of the given element and also for different nuclear spin states. This fact gives rise to the appearance of so-called *coherent* and *incoherent scattering*, see section 2.12. Figure 2.11 shows the variation of the scattering amplitude as a function of atomic weight throughout the periodic table. The scattering length is mostly positive but can also adopt negative values. Since *-1 = exp(iπ)* this negative sign corresponds to a phase shift of π (or 180°) during the scattering process. The scattering length roughly follows the dashed line labeled *potential scattering* contribution, despite the fact that there are rather large excursions from this line.

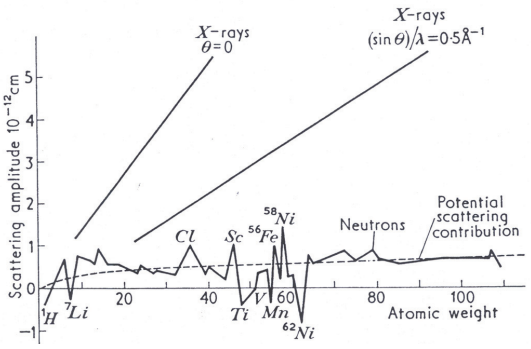

Fig. 2.11: *Scattering length as a function of atomic weight throughout the periodic table (from Research, London 7 (1954), 257).*

In the simplest one dimensional model, we can describe the nucleus as a rectangular potential well, see Figure 2.12.

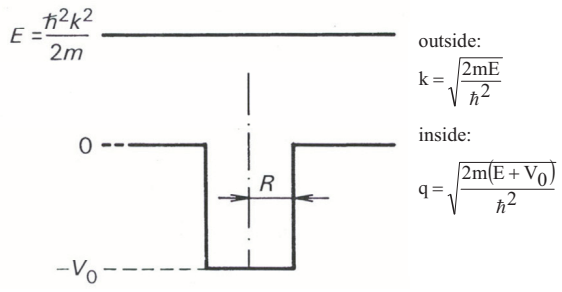

Fig. 2.12: *The nucleus described as a potential well of radius R and depth -V_0, while the neutron has the kinetic energy* $E = \frac{\hbar^2 k^2}{2m}$.

The wave function of the neutron being scattered from such a potential well can be written as:

$$\Psi(\underline{r}) \sim e^{i\underline{k}\underline{r}} + \frac{f}{r} e^{ikr} \qquad (2.50)$$

Here the first term describes the incident plane wave and the second term describes a spherical wave emitted from the nucleus. *f* describes the scattering amplitude. In the limit of a hard sphere, the wave function on the surface of the nucleus has to vanish since the neutron cannot penetrate inside the hard sphere. Mathematically this is described by the condition *ψ(R) = 0* or *-f = R*. The scattering length is defined as *b: = -f*, so that its value is positive for

most nuclei. Therefore for pure potential scattering, where the nucleus is assumed to be a hard sphere, b attains the value of the nuclear radius $b = R$, which is plotted in Figure 2.11 as a dashed line: the *potential scattering* contribution. The marked deviations from this overall behavior are due to so-called *resonance scattering*. In a simplified picture, such resonances occur, when the neutron energy is such that absorption of the neutron in the nucleus produces a bound excited state. This can lead to a resonant absorption process, but it can also lead to resonance scattering, a typical second order perturbation process: in the initial state, the nucleus is in its ground state and the interaction with the neutron can be described as a virtual transition into an excited state of the compound nucleus and back with a re-emission of the neutron, where the nucleus decays back from the excited compound system into its ground state. This process $n+K \rightarrow C^* \rightarrow K+n$ has a cross-section given by the famous *Breit-Wigner-formula*:

$$\sigma_R = 4\pi \left| R + \frac{const}{E - E_R + \frac{1}{2} i\Gamma} \right|^2 \tag{2.51}$$

Here R is the radius of the nucleus, E the neutron energy, E_R the resonance energy and Γ a damping term connected with the life-time of the excited state. As one can see, this formula describes very strong energy dependence with a pronounced maximum, when the neutron energy equals the resonance energy. Moreover, the resonance amplitude has an imaginary part, which describes the *resonance absorption*. In the resonant absorption process, the neutron is captured by the nucleus, leading to a compound nucleus in an excited state, containing one more neutron then the original nucleus. In a subsequent nuclear reaction, the compound nucleus gets rid of its excess energy. Examples for such absorption reactions will be given in the subsequent section. Finally the Breit-Wigner-formula gives an indication that the scattering length can be negative whenever the resonant term is negative (i. e. $E < E_R$), and its magnitude is larger than the contribution from potential scattering.

2.11 Neutron absorption

As explained above, neutron absorption can occur during nuclear reactions. Far away from the resonance, the absorption cross section is given by

$$\sigma_a \sim \lambda \sim \frac{1}{v} \tag{2.52}$$

This proportionality to the wavelength λ or the inverse velocity $1/v$ is a result of the density of states appearing in Fermi's golden rule. One can argue that wavelength and neutron velocity v are inversely proportional and thus, for longer wavelength i. e. smaller velocity, the neutron remains correspondingly longer close to the nucleus, which leads to a higher absorption cross-section. Table 2.1 gives examples for neutron absorption processes connected with nuclear reactions.

Examples:		
σ_a (25 meV) [barn]		
5333	$n + {}^3He \rightarrow {}^4He^* \rightarrow p + {}^3T$	neutron detection
940	$n + {}^6Li \rightarrow {}^7Li^* \rightarrow {}^3T + {}^4He$	
3837	$n + {}^{10}B \rightarrow {}^{11}B^* \rightarrow {}^4He + {}^7Li + \gamma$	
681	$n + {}^{235}U \rightarrow$ fission	

Tab. 2.1: *Examples for neutron absorption processes due to nuclear reactions. The absorption cross-section is given for neutrons of energy 25 meV in barn = 10^{-28} m^2 = 100 fm^2.*

As an example, there is a high probability of neutrons to be absorbed by ^{3}He nuclei, because the ^{4}He or α-particle is very stable, since it corresponds to a closed nuclear shell. However, during the absorption of the neutron, the ^{4}He nucleus is produced in an excited state. It gets rid of its surplus energy by decay into a proton and a triton[4] ^{3}T. Since these two particles have very high energies of about 0.5 MeV due to the nuclear reaction, charged particles are created during this decay, which can be used for neutron detection in a proportional counter. In a similar manner, the reaction with ^{6}Li, ^{10}B or ^{235}U can be used to build neutron detectors. It should be mentioned, however, that the neutron absorption in ^{3}He is very strongly dependent on the relative orientation of the nuclear spins of both particles. While for anti parallel spin direction, the absorption cross-section is ≈ 6000 barn, it reduces to 2 barn for parallel spin direction. This effect can be used to build efficient neutron polarization filters. By optical pumping with laser light, the nuclear moment of the ^{3}He nuclei can be aligned along one direction (so-called hyperpolarized ^{3}He gas). If an unpolarized neutron beam passes a filter cell filled with hyperpolarized ^{3}He, the neutrons with spin moment anti parallel to the nuclear moment of the ^{3}He have a high probability to be absorbed, while neutrons with the other spin direction have a high probability to be transmitted. For an appropriate thickness of the filter cell, a very high neutron beam polarization can be achieved in this manner.

Another class of absorption processes are so-called *(n, γ)-resonances*. Examples are given in Table 2.2. In these processes, a nucleus is produced, which contains one additional neutron and this compound nucleus decays into the ground state by emission of γ-radiation. Prominent (n,γ)-resonances occur for Cadmium or Gadolinium where, depending on the isotope, the absorption cross-section can be very high, see Table 2.2. These metals are often used as neutron absorbers in shieldings or diaphragms, which define the size of the neutron beam. One should, however, be aware that in these reactions, γ-radiation of very high energy is being released, which requires additional lead shielding for radiation protection.

	nucleide	σ_{γ}[barn]	$E_{resonance}$[meV]
(n, γ)-resonances:	^{113}Cd	20600	178
	^{151}Eu	9200	321
	^{155}Gd	60900	26.8
	^{157}Gd	254000	31.4

Tab. 2.2: *Examples for (n, γ)-resonances with the cross-section in barn and the resonance energy in meV.*

As described by the Breit-Wigner-Formula, these resonance absorption cross-sections have very strong energy dependences. The simple proportionality to the wavelength given in equation (2.52) no longer holds close to the resonance energies. As an example, we show the energy dependence of the absorption cross-section for Cadmium in Figure 2.13. Such data can be found in the compilation [8].

[4] The triton ^{3}T nucleus is a hydrogen isotope with one proton and 2 neutrons.

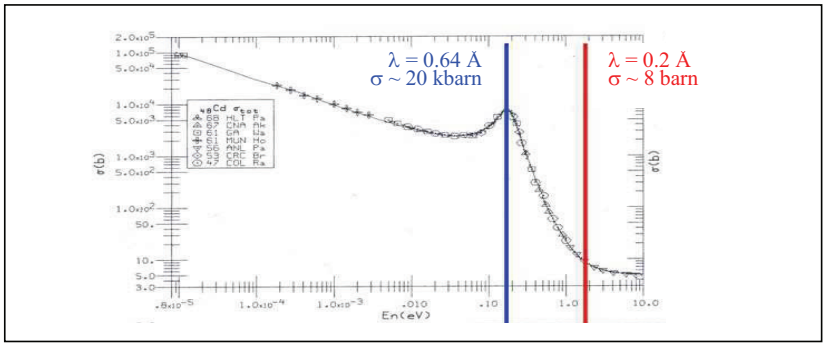

Fig. 2.13: *Absorption cross-section of the element Cadmium as a function of energy in a double logarithmic representation (from 8).*

Figure 2.13 shows that for lower energies, i. e. long wavelengths, the proportionality of the absorption cross-section to the wavelength holds to very good approximation. However, there is a strong resonance for a wavelength of 0.64 Å, where the cross-section attains a maximum of about 20 kbarn. Above this energy, i. e. for shorter wavelengths, the absorption cross-section drops drastically. At a wavelength of 0.2 Å, it attains a value of only 8 barn. This shows that in the thermal energy range, Cadmium can be used as an efficient neutron absorber. However, one has to be careful and not use it for the same purpose in case of hot neutrons, where Cadmium becomes virtually transparent. There are many more resonances for higher neutron energies, which are not relevant for neutron scattering, where only hot, thermal and cold neutrons are being used.

A similar strong energy dependence occurs for the element Gadolinium. Usually, neutron scatterers try to avoid samples containing Gadolinium since it is the most absorbing element, especially the isotope ^{157}Gd. However, the resonances lay right in the thermal neutron energy range. If the scattering experiment is performed with hot neutrons, the absorption cross-section of Gadolinium becomes much smaller and scattering experiments become feasible[5].

2.12 Coherent and incoherent scattering

As mentioned above, the nuclear interaction potential depends on the details of the nuclear structure and thus, the scattering length b is different for different isotopes of a given element and also for different nuclear spin states. In this section, we will discuss the effects of these special properties of the interaction of neutrons and nuclei for the scattering from condensed matter.

Let us assume an arrangement of atoms with scattering lengths b_i on fixed positions $\underline{R}_i$. For this case, the scattering potential writes:

$$V(\underline{r}) = \frac{2\pi\hbar^2}{m_n} \sum_i b_i \delta(\underline{r} - \underline{R}_i) \tag{2.53}$$

The scattering amplitude is obtained from a Fourier transform:

[5] Another possibility is to use isotope enriched Gadolinium. While the isotope ^{157}Gd with natural abundance 15.7% has a thermal absorption cross section of 259000 barn, the isotope ^{158}Gd, which is the most abundant with 24.8%, and has an absorption cross section of only 2.2 barn.

$$A(\underline{Q}) = \sum_i b_i e^{i\underline{Q}\cdot\underline{R}_i} \tag{2.54}$$

When we calculate the scattering cross section, we have to take into account that the different isotopes are distributed randomly over all sites. Also the nuclear spin orientation is random, except for very low temperatures in external magnetic fields. Therefore, we have to average over the random distribution of the scattering length in the sample:

$$\frac{d\sigma}{d\Omega}(\underline{Q}) \sim \left|A(\underline{Q})\right|^2 = \left\langle \sum_i b_i \; e^{i\underline{Q}\cdot\underline{R}_i} \cdot \sum_j b_j^* e^{-i\underline{Q}\underline{R}_j} \right\rangle \tag{2.55}$$

In calculating the expectation value of the product of the two scattering lengths at sites i and j, we have to take into account that according to the above assumption, the distribution of the scattering length on the different sites is completely uncorrelated. This implies that for $i \neq j$, the expectation value of the product equals to the product of the expectation values. Only for $i = j$ a correlation occurs, which gives an additional term describing the mean quadratic deviation from the average:

$$\left\langle b_i b_j \right\rangle = \begin{cases} \langle b\rangle\langle b\rangle = \langle b\rangle^2 & i \neq j \\ \left\langle b^2 \right\rangle = \langle b\rangle^2 + \left\langle \left(b - \langle b\rangle\right)^2 \right\rangle & i = j \end{cases}$$

The line for i = j results from the identity:

$$\left\langle \left(b - \langle b\rangle\right)^2 \right\rangle = \left\langle b^2 - 2b\langle b\rangle + \langle b\rangle^2 \right\rangle = \left\langle b^2 \right\rangle - \langle b\rangle^2 \tag{2.56}$$

Therefore, we can write the cross section in the following form:

$$\begin{aligned} \frac{d\sigma}{d\Omega}(\underline{Q}) &= \langle b\rangle^2 \left| \sum_i e^{i\underline{Q}\cdot\underline{R}_i} \right|^2 \qquad \text{"}coherent\text{"} \\ &+ N\left\langle \left(b - \langle b\rangle\right)^2 \right\rangle \qquad \text{"}incoherent\text{"} \end{aligned} \tag{2.57}$$

The scattering cross section is as a sum of two terms. Only the first term contains the phase factors $e^{i\underline{Q}\cdot\underline{R}}$, which result from the coherent superposition of the scattering from pairs of scatterers. This term takes into account interference effects and is therefore named *coherent scattering*. The scattering length averaged over the isotope- and nuclear spin- distribution enters this term. The second term in (2.57) does not contain any phase information and is proportional to the number N of atoms (and not to N^2!). This term is not due to the interference of scattering from different atoms. As we can see from (2.56) (line $i = j$), this term corresponds to the scattering from single atoms, which subsequently superimpose in an incoherent manner (adding intensities, not amplitudes!). This is the reason for the intensity being proportional to the number N of atoms. Therefore the second term is called *incoherent scattering*. Coherent and incoherent scattering are illustrated in Figure 2.14.

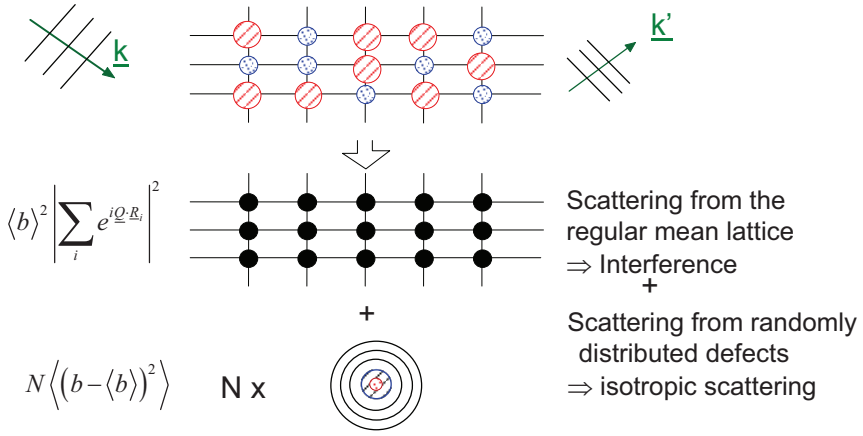

Fig. 2.14: *Two-dimensional schematic illustration of the scattering process from a lattice of N atoms of a given chemical species, for which two isotopes (small dotted circles and large hatched circles) exist. The area of the circle represents the scattering cross section of the single isotope. The incident wave (top part of the figure for a special arrangement of the isotopes) is scattered coherently only from the average structure. This gives rise to Bragg peaks in certain directions. In the coherent scattering only the average scattering length is visible. Besides these interference phenomena, an isotropic background is observed, which is proportional to the number N of atoms and to the mean quadratic deviation from the average scattering length. This incoherent part of the scattering is represented by the lower part of the figure.*

The most prominent example for *isotope incoherence* is elementary nickel. The scattering lengths of the nickel isotopes are listed together with their natural abundance in Table 2.3 [7]. The differences in the scattering lengths for the various nickel isotopes are enormous. Some isotopes even have negative scattering lengths. This is due to resonant bound states, as compared to the usual potential scattering.

Isotope	Natural Abundance	Nuclear Spin	Scattering Length [fm]
^{58}Ni	68.27 %	0	14.4(1)
^{60}Ni	26.10 %	0	2.8(1)
^{61}Ni	1.13 %	$^3/_2$	7.60(6)
^{62}Ni	3.59 %	0	-8.7(2)
^{64}Ni	0.91 %	0	-0.37(7)
Ni			10.3(1)

Tab. 2.3: *The scattering lengths of the nickel isotopes and the resulting scattering length of natural $_{28}$Ni [7].*

Neglecting the less abundant isotopes ^{61}Ni and ^{64}Ni, the average scattering length is calculated as:

$$\langle b \rangle \approx \left[0.68 \cdot 14.4 + 0.26 \cdot 2.8 + 0.04 \cdot (-8.7)\right] fm \approx 10.2\, fm \qquad (2.58)$$

, which gives the total coherent cross section of:

$$\Rightarrow \sigma_{coherent} = 4\pi \langle b \rangle^2 \approx 13.1\, barn\ (exact: 13.3(3) barn) \qquad (2.59)$$

The incoherent scattering cross section per nickel atoms is calculated from the mean quadratic deviation:

$$\sigma_{incoherent}^{Isotope} = 4\pi\left[0.68\cdot(14.4-10.2)^2 + 0.26\cdot(2.8-10.2)^2 + 0.04\cdot(-8.7-10.2)^2\right] fm^2 \approx 5.1 barn\ (exact: 5.2(4) barn) \quad (2.60)$$

Values in parentheses are the exact values taking into account the isotopes ^{61}Ni and ^{64}Ni and the nuclear spin incoherent scattering (see below). From (2.59) and (2.60), we learn that the incoherent scattering cross section in nickel amounts to more than one third of the coherent scattering cross section.

The most prominent example for *nuclear spin incoherent scattering* is elementary hydrogen. The nucleus of the hydrogen atom, the proton, has the nuclear spin $I = ½$. The total nuclear spin of the system H + n can therefore adopt two values: $J = 0$ and $J = 1$. Each state has its own scattering length: b_- for the singlet state $(J = 0)$ and b_+ for the triplet state $(J = 1)$ - compare Table 2.4.

Total Spin	Scattering Length	Abundance
J = 0	b_- = - 47.5 fm	$\frac{1}{4}$
J = 1	b_+ = 10.85 fm	$\frac{3}{4}$
<b> = - 3.739(1) fm		

Tab. 2.4: *Scattering lengths for hydrogen [7].*

As in the case of isotope incoherence, the average scattering length can be calculated:

$$\langle b\rangle = \left[\frac{1}{4}(-47.5) + \frac{3}{4}\cdot(10.85)\right] fm = -3.74\, fm \quad (2.61)$$

This corresponds to a coherent scattering cross section of about ≈ 1.76 barn [7]:

$$\Rightarrow \sigma_{coherent} = 4\pi\langle b\rangle^2 = 1.7568(10)\ barn \quad (2.62)$$

The nuclear spin incoherent part is again given by the mean quadratic deviation from the average:

$$\sigma_{incoherent}^{nuclear\ spin} = 4\pi\left[\frac{1}{4}(-47.5+3.74)^2 + \frac{3}{4}(10.85+3.74)^2\right] fm^2 = 80.2\ barn$$

(*exact:* 80.26(6) *barn*) (2.63)

Comparing (2.62) and (2.63), it is immediately clear that hydrogen scatters mainly incoherently. As a result, we observe a large background for all samples containing hydrogen. We should avoid all hydrogen containing glue for fixing our samples to a sample stick. Finally, we note that deuterium with nuclear spin $I = 1$ has a much more favorable ratio between coherent and incoherent scattering:

$$\sigma_{coh.}^{D} = 5.592(7) barn; \quad \sigma_{inc.}^{D} = 2.05(3) barn \quad (64)$$

The coherent scattering lengths of hydrogen (-3.74 fm) and deuterium (6.67 fm) are significantly different. This can be used for contrast variation by isotope substitution in all samples containing hydrogen, i. e. in biological samples or soft condensed matter samples, see corresponding chapters.

A further important element, which shows strong nuclear incoherent scattering, is vanadium. Natural vanadium consists to 99,75 % of the isotope ^{51}V with nuclear spin 7/2. By chance, the

ratio between the scattering lengths b_+ and b_- of this isotope are approximately equal to the reciprocal ratio of the abundances. Therefore, the coherent scattering cross section is very small and the incoherent cross section dominates [7]:

$$\sigma_{coh}^{V} = 0.01838(12)\ barn; \quad \sigma_{incoh}^{V} = 5.08(6)\ barn \tag{2.65}$$

For this reason, Bragg scattering of vanadium is difficult to observe above the large incoherent background. However, since incoherent scattering is isotropic, the scattering from vanadium can be used to calibrate multi-detector arrangements.

Here, we will not discuss scattering lengths for further elements and refer to the values tabulated in [7].

2.13 Magnetic neutron scattering

So far, we have only discussed the scattering of neutrons by the atomic nuclei. Apart from nuclear scattering, the next important process is the scattering of neutrons by the magnetic field created within the sample from the moments of unpaired electrons. This so-called magnetic neutron scattering comes about by the magnetic dipole-dipole interaction between the magnetic dipole moment of the neutron and the magnetic field of the unpaired electrons, which has spin and orbital angular momentum contributions. This magnetic neutron scattering allows us to study the magnetic properties of a sample on an atomic level, i. e. with atomic spatial- and atomic energy- resolution. In what follows, we will give an introduction into the formalism of magnetic neutron scattering, restricting ourselves to the case of elastic magnetic scattering. Inelastic magnetic scattering will we discussed in subsequent lectures.

To derive the magnetic scattering cross section of thermal neutrons, we consider the situation shown in Figure 2.15: a neutron with the nuclear moment μ_n is at position $\underline{R}$ with respect to an electron with spin $\underline{S}$, moving with a velocity $\underline{v}_e$.

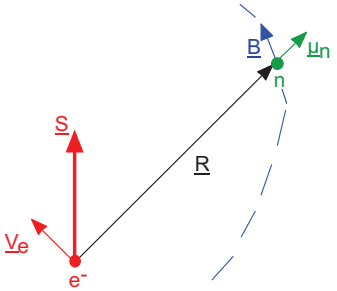

Fig. 2.15*: Geometry for the derivation of the interaction between neutron and electron.*

Due to its magnetic dipole moment, the neutron interacts with the magnetic field of the electron according to ("Zeeman-potential"):

$$\mathbf{V}_m = -\underline{\mu}_n \cdot \underline{B} \tag{2.66}$$

Here, the magnetic moment of the neutron is given by:

$$\underline{\mu}_n = -\gamma_n \mu_N \cdot \underline{\sigma} \tag{2.67}$$

$\underline{\sigma}$ denotes the spin operator, μ_N the nuclear magneton and $\gamma_N = -1.913$ the gyromagnetic factor of the neutron. The magnetic field $\underline{B}$ of an electron is due to a spin- and orbital- part $\underline{B} = \underline{B}_S + \underline{B}_L$. The dipole field of the spin moment is given by:

$$\underline{B}_S = \underline{\nabla} \times \left(\frac{\underline{\mu}_e \times \underline{R}}{R^3} \right) \quad ; \quad \underline{\mu}_e = -2\mu_B \cdot \underline{S} \tag{2.68}$$

The field due to the movement of the electron is given according to Biot-Savart:

$$\underline{B}_L = \frac{-e}{c} \frac{\underline{v}_e \times \underline{R}}{R^3} \tag{2.69}$$

The magnetic scattering cross section for a process, where the neutron changes its wave vector from $\underline{k}$ to $\underline{k}'$ and the projection of its spin moment to a quantization axis z from σ_z to σ_z' can be expressed within the first Born approximation:

$$\frac{d\sigma}{d\Omega} = \left(\frac{m_n}{2\pi\hbar^2} \right)^2 \left| \left\langle \underline{k}' \sigma_z' \middle| \mathbf{V}_m \middle| \underline{k} \sigma_z \right\rangle \right|^2 \tag{2.70}$$

As mentioned, we only consider the single differential cross section for elastic scattering. Introducing the interaction potential from (2.66) to (2.69) in (2.70) we obtain after some algebra [1, 4]:

$$\frac{d\sigma}{d\Omega} = \left(\gamma_n r_0 \right)^2 \left| -\frac{1}{2\mu_B} \left\langle \sigma_z' \middle| \underline{\sigma} \cdot \underline{M}_\perp \left(\underline{Q} \right) \middle| \sigma_z \right\rangle \right|^2 \tag{2.71}$$

The pre-factor $\gamma_n r_0$ has the value $\gamma_n r_0 = 0.539 \cdot 10^{-12} cm = 5.39 fm$. Here, $\underline{M}_\perp(\underline{Q})$ denotes the component of the Fourier transform of the sample magnetization, which is perpendicular to the scattering vector $\underline{Q}$ (see Figure 2.16):

$$\underline{M}_\perp \left(\underline{Q} \right) = \hat{\underline{Q}} \times \underline{M} \left(\underline{Q} \right) \times \hat{\underline{Q}} \tag{2.72}$$

$$\underline{M} \left(\underline{Q} \right) = \int \underline{M} \left(\underline{r} \right) e^{i \underline{Q} \cdot \underline{r}} d^3 r \tag{2.73}$$

The total magnetization is given as a sum of the spin- and orbital-angular- momentum part according to:

$$\begin{aligned} \underline{M} \left(\underline{r} \right) &= \underline{M}_S \left(\underline{r} \right) + \underline{M}_L \left(\underline{r} \right) \\ \underline{M}_S \left(\underline{r} \right) &= -2\mu_B \cdot \underline{S} \left(\underline{r} \right) = -2\mu_B \sum_i \delta \left(\underline{r} - \underline{r}_i \right) \underline{S}_i \end{aligned} \tag{2.74}$$

(2.71) tells us that with magnetic neutron scattering, we are able to determine the magnetization $\underline{M}(\underline{r})$ in microscopic atomic spatial co-ordinates $\underline{r}$. This gives a lot more information than a simple macroscopic measurement, where we obtain the ensemble average of the magnetization over the entire sample. We also see from (2.71) that the orientation of the nuclear spin momentum of the neutron (represented by σ_z) plays an important role in magnetic scattering. This is not surprising, since magnetism is a vector property of the sample and obviously there should be an interaction with the vector property of the neutron, its nuclear magnetic moment. Therefore, the analysis of the change of the direction of the neutron nuclear moment in the scattering process should give us valuable additional information as compared to a determination of the change of energy and momentum direction of the neutron alone. These so-called polarization analysis experiments are discussed in a following lecture. Finally, to obtain an idea of the size of magnetic scattering relative to nuclear scattering, we can replace the matrix element in (2.71) for a spin ½ particle by the value *1* μ_B. This gives us an "equivalent" scattering length for magnetic scattering of *2.696 fm* for a spin ½ particle. This value corresponds quite well to the scattering length of cobalt, which means that magnetic scattering is comparable in magnitude to nuclear scattering.

In contrast to nuclear scattering, we obtain for magnetic scattering a directional term: neutrons only "see" the component of the magnetization perpendicular to the scattering vector (see Figure 2.16).

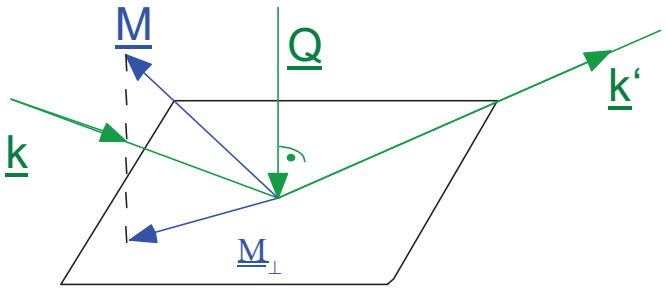

Fig. 2.16: *For magnetic neutron scattering, only the component $\underline{M}_\perp$ of the magnetization perpendicular to the scattering vector $\underline{Q}$ is of relevance.*

A second specialty of magnetic scattering as compared to nuclear scattering is the existence of the *magnetic form factor*. How the form factor comes about is most easily understood in the simple case of pure spin scattering, i. e. for atoms with spherical symmetric *(L = 0)* ground state, such as Mn^{2+} or Fe^{3+}. Moreover, the derivation is simplified for ionic crystals, where the electrons are located around an atom. We denote the spin operators of the electrons of atom *i* with $\underline{s}_{ik}$. The spatial co-ordinates of the electron number *k* in atom *i* are $\underline{r}_{ik} = \underline{R}_i + \underline{t}_{ik}$, where $\underline{R}_i$ denotes the position vector to the nucleus of atom *i*. Now we proceed to separate the intra-atomic quantities. We can write the operator for the magnetization density as:

$$\underline{M}_S(\underline{r}) = -2\mu_B \sum_{ik} \delta(\underline{r} - \underline{r}_{ik}) \cdot \underline{s}_{ik} \tag{2.75}$$

The Fourier transform of this magnetization density is calculated to:

$$\underline{M}(\underline{Q}) = \int \underline{M}_S(\underline{r}) e^{i\underline{Q}\cdot\underline{r}} d^3r = \sum_{ik} e^{i\underline{Q}\cdot\underline{r}_{ik}} \underline{s}_{ik} = \sum_i e^{i\underline{Q}\cdot\underline{R}_i} \sum_k e^{i\underline{Q}\cdot\underline{t}_{ik}} \cdot \underline{s}_{ik} \tag{2.76}$$

To calculate the scattering cross section, we now have to determine the expectation value of this operator for the quantum mechanical state of the sample averaged over the thermodynamic ensemble. This leads to

$$\underline{M}(\underline{Q}) = -2\mu_B \cdot f_m(\underline{Q}) \cdot \sum_i e^{i\underline{Q}\cdot\underline{R}_i} \cdot \underline{S}_i \tag{2.77}$$

The single differential cross section for elastic scattering is thus given by:

$$\frac{d\sigma}{d\Omega} = (\gamma_n r_0)^2 \left| f_m(\underline{Q}) \sum_i S_{i\perp} e^{i\underline{Q}\underline{R}_i} \right|^2 \tag{2.78}$$

Here, $f_m(\underline{Q})$ denotes the form factor, which is connected with the spin density of the atom via a Fourier transform:

$$f_m(\underline{Q}) = \int_{Atom} \rho_s(\underline{r}) e^{i\underline{Q}\cdot\underline{r}} d^3r \tag{2.79}$$

With the form (2.78), we have expressed the cross section in simple atomic quantities, such as the expectation values of the spin moment $\underline{S}_i$ at the various atoms. The distribution of the spin density within an atom is reflected in the magnetic form factor (2.79).

For ions with spin and orbital angular momentum, the cross section takes a significantly more complicated form [4]. Under the assumption that spin- and orbital- angular momentum of each atom couple to the total angular momentum $\underline{J}_i$ (*L/S*-coupling) and for rather small momentum transfers (the reciprocal magnitude of the scattering vector has to be small compared to the size of the electron orbits), we can give a simple expression for this cross section in the so-called *dipole approximation*:

$$\frac{d\sigma}{d\Omega} = (\gamma_n r_o)^2 \cdot \left| \frac{g_J}{2} f_m(Q) \sum_i J_{i\perp} e^{i\underline{Q}\cdot\underline{R}_i} \right|^2 \tag{2.80}$$

Here the magnetic form factor writes:

$$f_m(Q) = \langle j_o(Q) \rangle + C_2 \langle j_2(Q) \rangle \tag{2.81}$$

g_J denotes the Lande g-factor, $C_2 = \frac{2}{g_J} - 1$ and

$$\langle j_l(Q) \rangle = 4\pi \int_0^\infty j_l(Qr) R^2(r) r^2 dr \tag{2.82}$$

are the spherical transforms of the radial density distributions *R(r)* with the spherical Bessel functions $j_l(Qr)$. For isolated atoms, the radial part *R(r)* has been determined by Hartree-Fock-calculations and the functions $\langle j_0(Q) \rangle$ and $\langle j_2(Q) \rangle$ in (2.82) have been tabulated [9].

Since the distribution of the magnetic field for spin and orbital angular momentum is completely different, different Q-dependencies of the corresponding form factors result. Moreover, because only the outer electrons in open shells contribute to magnetic scattering, the magnetic form factor also differs from the x-ray form factor, which is the Fourier transform of the entire electron density distribution within an atom, see Figure 2.17.

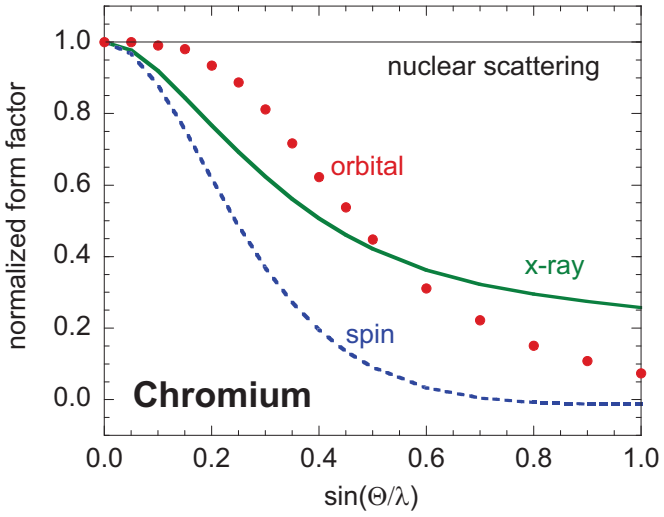

Fig. 2.17: *Form-factor of Cr [10, 11]. Due to the different distribution of the magnetic field for spin S and orbital angular momentum L, a more rapid decrease of the scattering amplitude as a function of momentum transfer results for the spin form factor. For the x-ray form factor, the inner electrons play an important role, too. Therefore, the x-ray form factor drops slower as compared to the magnetic form factor. On the Å length scale of the thermal neutron wavelength, the nucleus is point-like. Therefore, nuclear scattering is independent of the momentum transfer. Finally, we want to mention that the magnetic form factor can in general be anisotropic, if the magnetization density distribution is anisotropic.*

2.14 Comparison of probes

In this lecture, we have so far introduced the elementary formalism to describe the scattering process and discussed the interaction of neutrons with matter. We now want to ask the questions, for which problems in condensed matter research, neutrons can be utilized successfully also in comparison to other probes, such as x-ray scattering or electron microscopy and electron scattering. To answer these questions, we have to look at the ranges of energies, wavelength or scattering vector, which can be covered by various probes as well as the different contrast mechanisms.

Figure 2.18 shows a double logarithmic plot of the dispersion relation "wavelength versus energy" for the three probes neutrons, electrons and photons. The plot demonstrates, how thermal neutrons of energy 25 meV are ideally suited to determine interatomic distances in the order of 0.1 nm, while the energy of x-rays or electrons for this wavelength is much higher. However with modern techniques at a synchrotron radiation source, energy resolutions in the meV-region become accessible even for photons of around 10 keV corresponding to a relative energy resolution $\Delta E/E \approx 10^{-7}$! The graph also shows that colloids with a typical size of 100 nm are well suited for the investigation with light of energy around 2 eV. These length scales can, however, also be reached with thermal neutron scattering in the small angle region. While Figure 18 thus demonstrates for which energy-wave-length combination a certain probe is particularly useful, modern experimental techniques extend the range of application by several orders of magnitude.

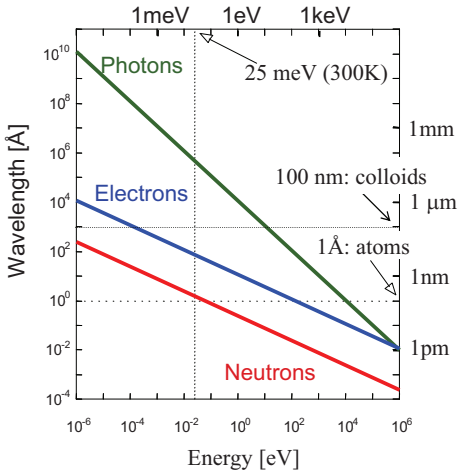

Fig. 2.18: *Comparison of the three probes - neutrons, electrons and photons - in a double logarithmic energy-wavelength diagram.*

It is therefore useful to compare the scattering cross sections as it is done in Figure 2.19 for x-rays and neutrons. Note that the x-ray scattering cross sections are in general a factor of 10 larger as compared to the neutron scattering cross sections. This means that the signal for x-ray scattering is stronger for the same incident flux and sample size. But caution has to be applied that the conditions for kinematical scattering are fulfilled. For x-rays, the cross section depends on the number of electrons and thus varies in a monotonic fashion throughout the periodic table. Clearly it will be difficult to determine hydrogen positions with x-rays in the presence of heavy elements such as metal ions. Moreover, there is a very weak contrast between neighboring elements as can be seen from the transition metals Mn, Fe and Ni in Figure

2.19. However, this contrast can be enhanced by anomalous scattering, if the photon energy is tuned close to the absorption edge of an element. Moreover, anomalous scattering is sensitive to the anisotropy of the local environment of an atom. For neutrons the cross section depends on the details of the nuclear structure and thus varies in a non-systematic fashion throughout the periodic table. As an example, there is a very high contrast between Mn and Fe. With neutrons, the hydrogen atom is clearly visible even in the presence of such heavy elements as Uranium. Moreover there is a strong contrast between the two Hydrogen isotopes H and D. This fact can be exploited for soft condensed matter investigations by selective deuteration of certain molecules or functional groups. This will vary the contrast within the sample.

Finally, both neutrons and x-rays allow the investigation of magnetism on an atomic scale. Magnetic neutron scattering is comparable in strength to nuclear scattering, while non-resonant magnetic x-ray scattering is smaller than charge scattering by several orders of magnitude[6]. Despite the small cross sections, non-resonant magnetic x-ray Bragg scattering from good quality single crystals yields good intensities with the brilliant beams at modern synchrotron radiation sources. While neutrons are scattered from the magnetic induction within the sample, x-rays are scattered differently from spin and orbital momentum and thus allow one to measure both form factors separately. Inelastic magnetic scattering e.g. from magnons or so called quasielastic magnetic scattering from fluctuations in disordered magnetic systems is a clear domain of neutron scattering and cannot be done with x-rays up to now. Finally, resonance exchange scattering XRES allows one not only to get enhanced intensities, but also to study magnetism with element- and band sensitivity [12].

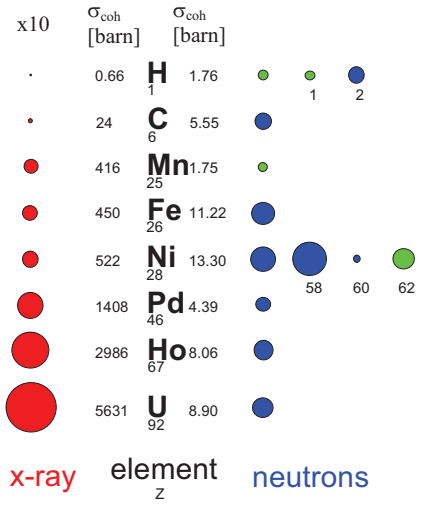

Fig. 2.19: *Comparison of the coherent scattering cross-sections for x-rays and neutrons for a selection of elements. The area of the colored circles represent the scattering cross section, where in the case of x-rays a scale factor 10 has to be applied. For neutrons, the blue and green circles distinguish the cases where the scattering occurs with or without a phase shift of π. For $_1$H and $_{28}$Ni, scattering cross sections for certain isotopes are given in addition to the averaged values for the natural abundancies.*

[6] Typically between 6 to 9 orders of magnitude.

With appropriate scattering methods, employing neutrons, x-rays or light, processes in condensed matter on very different time and space scales can be investigated. Which scattering method is appropriate for which region within the "scattering vector Q - energy E plane" is plotted schematically in Figure 2.20. A scattering vector Q corresponds to a certain length scale, an energy to a certain frequency, so that the characteristic lengths and times scales for the various methods can be directly determined from the Figure. Examples for applications and information on instrumentation will follow in subsequent lectures.

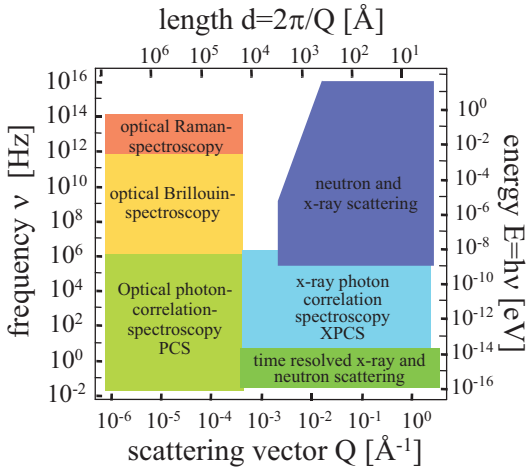

Fig. 2.20: *Regions in frequency ν and scattering vector Q or energy E and length d, which can be covered by various scattering methods.*

References

[1] G. L. Squires "Introduction to the Theory of Thermal Neutron Scattering" Dover 1997

[2] K. Sköld, D. Price (Eds.) "Methods of Experimental Physics" Neutron Scattering Part A-C Academic Press 1987

[3] J. M. Cowley "Diffraction Physics" North Holland, Amsterdam 1995

[4] S. W. Lovesey "Theory of neutron scattering from condensed matter" Clarendon Press, Oxford, 1987

[5] A. Furrer, J. Mesot, T. Strässle "Neutron Scattering in Condensed Matter Physics" World Scientific, London, 2009

[6] B. W. Batterman, H. Cole "Dynamical Diffraction of X-Rays by Perfect Crystals" Rev. Mod. Phys. 36 (1964), 681 - 717.

[7] A. Dianoux, G. Lander (Eds.) "Neutron Data Booklet", Institute Laue-Langevin (2002) - see also [8] -

[8] D. E. Garber, R. R. Kinsey "Neutron Cross-Section II" BNL-Report (1976), also: S. Mughabghab "Atlas of Neutron Resonances" Elsevier (2006)

[9] E. Price (Ed.) "International Tables for Crystallography, Volume C" International Union of Crystallography (2004) - see also [6] -

[10] J. Strempfer et al. Eur. Phys. J B **14** (2000), 63 - 72

[11] J. Strempfer et al. Physica B **267 - 268** (1999), 56 - 59

[12] Th. Brückel "Scattering Techniques II: Magnetic X-Ray Scattering" Schriften des Forschungszentrum Jülich, Materie und Material **26** (2006), B5.1 - B5.34

3

Correlation functions measured by scattering experiments

Reiner Zorn

3. Correlation functions measured by scattering experiments

Reiner Zorn

3.1 Introduction

In this lecture a more formal derivation of the scattering laws will be presented. It is based on the fact that scattering experiments indirectly measure correlation functions. The usual derivation of scattering laws is based on the fact that the scattering law (for neutrons, photons or any other radiation) is essentially the absolute square of the Fourier transform of a scattering density. In Fig. 3.1 this is shown as the left way from the density $\rho(\mathbf{r})$ to $S(Q)$. The Wiener-Khintchine theorem

$$|\mathcal{F}[f(x)]|^2 = \mathcal{F}[\langle f(0)f(x)\rangle] \tag{3.1}$$

(with the Fourier transform $\mathcal{F}$ defined as in the appendix[1]) now states that the absolute square of a Fourier transform is the Fourier transform of the autocorrelation function. This opens another way (the right one in Fig. 3.1) to calculate the scattering law. Apart from elucidating the meaning of the scattering law in another way, this gives an alternative to calculate it even if the density itself is not known.

In section 3.2, the scattering law of a static system will be calculated in both ways. In section 3.3, the analogous calculation is done for a system of moving scatterers. The resulting scattering is *inelastic* and its frequency dependence depends on the dynamics via a Fourier transform.

In the literature [3, 4] inelastic neutron scattering is usually derived in three steps:

1. quantum-mechanical formulation of the scattering process (Schrödinger equation),
2. (first) Born approximation for weak scattering,

[1] For a more in-depth introduction into the properties of Fourier transforms relevant for scattering see lecture I in the previous edition of this course [1].

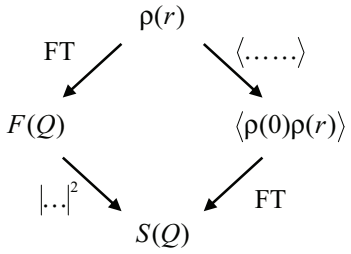

Figure 3.1: The two ways to calculate the scattering law from the microscopic density, left: as the absolute-squared Fourier transform of the density, right: as the Fourier transform of the correlation function.

3. classical approximation revealing relation to microscopic atomic motions.

It is clear that for a rigorous derivation one has to start with a quantum-mechanical treatment. Even if one considers the scattering system classically at least the neutron has to be treated quantum-mechanically. Otherwise its wave nature, which is essential for the interference connected with scattering, will not be captured.

But experience has shown that this way cannot be followed in a lecture series of the current extent without 'comprehension gaps'. Therefore, this lecture will use a simplified approach circumventing the mathematical problems caused by a quantum-mechanical treatment. (This approach is in many points similar to the the Huygens principle used already in lecture 2.) The differences of the actual scattering law from that derived in this classical approximation will be pointed out in section 3.4 without an explicit derivation.

Without specifying the exact nature of the scattered radiation, a propagating plane wave will be described by a wave function

$$\psi(\mathbf{r}, t) = A \exp(\mathrm{i}(\varpi t - \mathbf{k} \cdot \mathbf{r}))\,. \tag{3.2}$$

Here $\varpi = 2\pi f$ is the angular frequency[2] of the wave and $k = 2\pi/\lambda$ the wave vector inverse proportional to the wavelength λ. For neutrons, this is the quantum-mechanical wave function, for light or x-rays it would be the electric field. Therefore, the results derived

[2] The symbol ϖ (which is actually not an omega but a variant writing of pi) is used to avoid confusion with ω used in the energy transfer $\hbar\omega$ in section 3.3.

are qualitatively the same for any kind of radiation with only the relation between k and ϖ making a quantitative difference.

We furthermore take for granted that the intensity of the radiation is given by the absolute square of the wave function:

$$I = |\psi(\mathbf{r}, t)|^2 \,. \tag{3.3}$$

Again this is obviously for quantum-mechanics the probability of the observation of a particle and for light or x-rays the power of the electromagnetic field.

Finally, we will assume for the elementary scattering process that it is determined by a single parameter so that the wave scattered by a single scattering centre is given by

$$\psi(\mathbf{r}', t) = \frac{\exp(-\mathrm{i}(k|\mathbf{r}' - \mathbf{r}_j|))}{|\mathbf{r}' - \mathbf{r}_j|} \, b_j \psi(\mathbf{r}_j, t) \,. \tag{3.4}$$

Here, $\mathbf{r}'$ denotes the point of observation of the scattered wave (location of the detector) $\mathbf{r}_j$ the position of the scattering centre (nucleus or atom), and b_j is a property of this scattering centre, the scattering length. b_j may be complex, the amplitude determines the probability of the scattering process (scattering cross section). The sign, or more general the angle in the complex plane, represents a possible phase shift during the scattering. In the prefactor, $\exp(-\mathrm{i}(k|\mathbf{r}' - \mathbf{r}_j|))$ expresses the additional oscillations between the scattering process and detection. Because the scattered wave is spherical centred around $\mathbf{r}_j$ it decays with $1/|\mathbf{r}' - \mathbf{r}_j|$. After applying (3.3) this leads to the $1/r^2$ law in intensity.

3.2 Scattering from a static system[3]

In this section it is assumed that the scattering centres are fixed in space, i.e. $\mathbf{r}_j(t) = \text{const.} = \mathbf{r}_\mathrm{j}$. In that case the scattering will be *elastic*, i.e. the energy of the scattered particles will not change due to the scattering process. This is clear from classical mechanics because a system which is static before and after the scattering process cannot exchange energy. The equivalent argument from the wave picture would be that upon scattering by fixed centres there is no Doppler shift of the frequency.

[3] This section could also be headed 'elastic scattering' or 'static scattering' which are often used terms for the type of scattering discussed here.

Without loss of generality[4] one can define the direction of the incident beam as the z direction: $\mathbf{k} = (0, 0, k)$. By using equation (3.2) for the incident and (3.4) for the scattered wave the wave scattered by particle j into the detector can be expressed as

$$\psi(\mathbf{r}', t) = \frac{\exp(-\mathrm{i}(k|\mathbf{r}' - \mathbf{r}_j|))}{|\mathbf{r}' - \mathbf{r}_j|} b_j A \exp(\mathrm{i}(\varpi t - \mathbf{k} \cdot \mathbf{r})) = A b_j \frac{\exp(\mathrm{i}(\varpi t - k(l_j + l'_j))}{l'_j} \quad (3.5)$$

where l_j is the distance from the source to the scatterer and l'_j that from the scatterer to the detector. We now assume that the distance between the detector and the centre of the sample, R, is large compared to the size of the sample (Fraunhofer diffraction). Then, an expansion to first order in the scatterer's position yields

$$\psi(\mathbf{r}', t) = A b_j \frac{\exp(\mathrm{i}(k(\mathbf{R} \cdot \mathbf{r}_j - (L + R + z_j)) + \varpi t))}{R} = \frac{A}{R} \mathrm{e}^{\mathrm{i}\varpi t} \mathrm{e}^{\mathrm{i}k(R+L))} b_j \exp(\mathrm{i}\mathbf{Q} \cdot \mathbf{r}_j)\,. \quad (3.6)$$

(L is the distance from the source to the centre of the sample.) In the second expression the *scattering vector*

$$\mathbf{Q} = \left(\frac{x'}{R}, \frac{y'}{R}, \frac{z'}{R} - 1\right) k = \mathbf{k}' - \mathbf{k} \quad (3.7)$$

is introduced[5]. It is the vectorial difference of the final and incident wave vectors with the final being a vector of the same length k (elastic scattering) in the direction pointing towards the detector:

$$\mathbf{k}' = \left(\frac{x'}{R}, \frac{y'}{R}, \frac{z'}{R}\right) k\,. \quad (3.8)$$

From (3.7) it is clear that quantum-mechanically $\hbar\mathbf{Q}$ is the *momentum transfer* because $\hbar\mathbf{Q} = \hbar\mathbf{k}' - \hbar\mathbf{k} = \mathbf{p}' - \mathbf{p}$. Geometrically, equation (3.7) means that $\mathbf{k}$, $\mathbf{k}'$, and $\mathbf{Q}$ form a triangle, the *scattering triangle* (Fig. 3.2). Because of $k = k'$ it is isosceles for elastic scattering and the scattering vector is related to the scattering angle 2θ and the wavelength λ by

$$Q = \frac{4\pi}{\lambda} \sin\theta\,. \quad (3.9)$$

---

[4] German: ohne Beschränkung der Allgemeinheit

[5] In the British and American literature the definition usually is $\mathbf{Q} = \mathbf{k} - \mathbf{k}'$ and analogously $\Delta E = E - E'$ instead of (3.44). This can be seen as a consequence of starting with reversed signs in the exponential in (3.2). Because the measurement does not reveal the phase, this does not change any of the results.

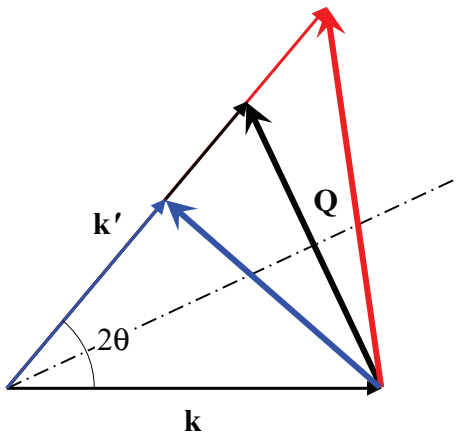

Figure 3.2: Definition of the scattering vector $\mathbf{Q}$ in terms of the incident and final wave vectors $\mathbf{k}$ and $\mathbf{k}'$. The black (isosceles) triangle corresponds to elastic scattering. The blue and red ones correspond to inelastic scattering with energy loss or gain of the scattered radiation, respectively.

Inserting (3.6) into (3.3) leads to a great simplification because $|\mathrm{e}^{\mathrm{i}\phi}| = 1$ for real ϕ. The actual lengths L and R only influence the unobservable phase of the wave. The intensity only depends on the positions of the scatterers in the sample except for the obvious $1/R^2$ factor:

$$I = \frac{A^2}{R^2} \left| \sum_{j=1}^{N} b_j \exp(\mathrm{i}\mathbf{Q} \cdot \mathbf{r}_j) \right|^2 . \tag{3.10}$$

In neutron scattering this result is usually expressed in terms of the *differential cross-section* which is the probability density that a neutron is scattered into a solid angle element $\mathrm{d}\Omega$ normalised to the intensity of the incident beam:

$$\frac{\mathrm{d}\sigma}{\mathrm{d}\Omega} = \left\langle \left| \sum_{j=1}^{N} b_j \exp(\mathrm{i}\mathbf{Q} \cdot \mathbf{r}_j) \right|^2 \right\rangle . \tag{3.11}$$

At this point it is necessary to explain the meaning of the average $\langle \ldots \rangle$ and justify it. Of course for a completely arrested system and completely coherent radiation, (3.11) would be valid without the average. Experimentally, this situation is only realised in laser light scattering from rigid objects. The experiments as well as the calculation do not yield a smooth function $\mathrm{d}\sigma/\mathrm{d}\Omega$ but an assembly of so-called speckles. For two reasons this situation is exceptional and especially not realised for neutron scattering:

1. If a dynamics exists which is sufficiently slow not to cause a noticeable inelasticity, the particles will rearrange over the time of the experiment T. In this sense, $\langle \ldots \rangle$ expresses a temporal average over the experimental time.

2. If the radiation used is not highly coherent, the sum over the amplitudes in (3.11) has to be restricted to the coherence volume which is usually much smaller than the sample volume. The results from the individual regions have to be added as intensities, i.e. after the absolute-square. This implies the same average but to be interpreted as a thermodynamic average over different realisations of the particle positions. In the case of ergodic systems both averages have the same result.

A system of identical scatterers[6] can be described by the local density $\rho(\mathbf{r})$. In a strict microscopic sense this is a sum of delta functions concentrated at the positions of the scatterers:

$$\rho(\mathbf{r}) = \sum_{j=1}^{N} \delta(\mathbf{r} - \mathbf{r}_j)\,. \tag{3.12}$$

In many cases, systems are homogeneous (liquids, glasses, crystal powders). Then the average density of scatterers is just their total number divided by the sample volume:

$$\langle \rho(\mathbf{r}) \rangle = N/V \equiv \rho_0\,. \tag{3.13}$$

The scattering from such a system of identical scatterers can now be expressed in terms of the density:

$$\frac{\mathrm{d}\sigma}{\mathrm{d}\Omega} = |b|^2 \left\langle \left| \int_V \mathrm{d}^3 r \exp(\mathrm{i}\mathbf{Q}\cdot\mathbf{r})\rho(\mathbf{r}) \right|^2 \right\rangle . \tag{3.14}$$

One may ask what the gain of replacing the sum by an integral over a sum of delta functions is. Of course this expression is not helpful for an experiment aiming at resolving the atomistic structure. Then the experimental scattering vector Q is chosen such that $2\pi/Q$ is in the order of the particle distance d. But in many experiments only a 'coarse-grained' structure on a length scale $\gg d$ is of interest. Then $Q \ll 2\pi/d$ and as a good approximation the atomistic $\rho(\mathbf{r})$ of (3.12) can be replaced by a smoothed continuous

[6] For neutrons this means same isotopes and parallel spin directions. This is obviously not often fulfilled. The consequence of isotopic- or spin-disorder is more interesting for inelastic scattering (incoherent scattering) and will be discussed in the next section.

function. In that case equation (3.14) can be used to calculate the scattering without exact knowledge of the atomic positions.

A simple way (neglecting incoherent scattering) to introduce mixed scatterers is to start with the *scattering length density*

$$\rho_b(\mathbf{r}) = \sum_{j=1}^{N} b_j \delta(\mathbf{r} - \mathbf{r}_j)\,. \tag{3.15}$$

instead of the density. By including the scattering properties in the density equation (3.14) simplifies further to

$$\frac{\mathrm{d}\sigma}{\mathrm{d}\Omega} = \left\langle \left| \int_V \mathrm{d}^3 r \exp(\mathrm{i}\mathbf{Q}\cdot\mathbf{r})\rho_b(\mathbf{r}) \right|^2 \right\rangle . \tag{3.16}$$

The use of the scattering length density is very popular in the description of small-angle scattering data which often come from complicated mixtures of chemical components.

The second way to derive the scattering starts with applying the definition of the absolute square, $|X|^2 = X^*X$ to equation (3.11):

$$\begin{aligned} \frac{\mathrm{d}\sigma}{\mathrm{d}\Omega} &= \left\langle \left(\sum_{j=1}^{N} b_j^* \exp(-\mathrm{i}\mathbf{Q}\cdot\mathbf{r}_j) \right) \left(\sum_{k=1}^{N} b_k \exp(\mathrm{i}\mathbf{Q}\cdot\mathbf{r}_k) \right) \right\rangle \\ &= \sum_{j,k=1}^{N} b_j^* b_k \left\langle \exp(\mathrm{i}\mathbf{Q}\cdot(\mathbf{r}_k - \mathbf{r}_j)) \right\rangle . \end{aligned} \tag{3.17}$$

Here, we introduce the two-particle density

$$\rho(\mathbf{r}_1)\rho(\mathbf{r}_2) = \sum_{j,k=1}^{N} \delta(\mathbf{r}_1 - \mathbf{r}_j)\delta(\mathbf{r}_2 - \mathbf{r}_k) \tag{3.18}$$

which is the joint probability that particle j is found at $\mathbf{r}_1$ and particle k at $\mathbf{r}_2$. It is important that in general the average of this probability density is not just the product of the average densities:

$$\langle \rho(\mathbf{r}_1)\rho(\mathbf{r}_2) \rangle \neq \langle \rho(\mathbf{r}_1) \rangle \langle \rho(\mathbf{r}_2) \rangle = {\rho_0}^2 . \tag{3.19}$$

The reason for this is that usually there is an interaction between particles which enhances or reduces the probability for particles close to each other. E.g. if one imagines particles with a hard core of radius R then $\langle \rho(\mathbf{r}_1)\rho(\mathbf{r}_2) \rangle$ vanishes for all $\mathbf{r}_1$ and $\mathbf{r}_2$ which would imply a 'collision' of the particles, $0 < |\mathbf{r}_2 - \mathbf{r}_1| < 2R$. Nevertheless, in a translationally

invariant system one of the positions can be chosen arbitrarily, especially as the origin, so that

$$\langle \rho(\mathbf{r}_1)\rho(\mathbf{r}_2)\rangle = \langle \rho(\mathbf{0})\rho(\mathbf{r}_2-\mathbf{r}_1)\rangle = \rho_0 \left\langle \sum_{j,k=1}^{N} \delta(\mathbf{r}_j - \mathbf{r}_k + \mathbf{r}_2 - \mathbf{r}_1) \right\rangle . \tag{3.20}$$

For a system of identical scatterers the two-particle density (3.18) can now be used to express the scattering:

$$\begin{aligned} \frac{\mathrm{d}\sigma}{\mathrm{d}\Omega} &= |b|^2 \left\langle \int_V \mathrm{d}^3 r_1 \int_V \mathrm{d}^3 r_2 \exp(\mathrm{i}\mathbf{Q}\cdot(\mathbf{r}_2-\mathbf{r}_1))\rho(\mathbf{r}_1)\rho(\mathbf{r}_2) \right\rangle \\ &= |b|^2 V \int_{V_d} \mathrm{d}^3 r \exp(\mathrm{i}\mathbf{Q}\cdot\mathbf{r})\langle \rho(\mathbf{0})\rho(\mathbf{r})\rangle . \end{aligned} \tag{3.21}$$

Note that in this last expression $\mathbf{r}$ does not have the meaning of an absolute position but that of a vectorial distance and consequently the volume of integration is not the sample volume but the volume of possible distances within the sample.

In the literature the pair correlation function[7] is usually defined as

$$g(\mathbf{r}) = \frac{\langle \rho(\mathbf{0})\rho(\mathbf{r})\rangle}{{\rho_0}^2} - \frac{\delta(\mathbf{r})}{\rho_0} . \tag{3.22}$$

The normalisation by ${\rho_0}^2$ has the effect that for non-interacting particles or at distances where the interaction is weak, $g(\mathbf{r}) = 0$. The subtraction of the delta function removes the singularity of $\langle \rho(\mathbf{0})\rho(\mathbf{r})\rangle$ at $\mathbf{r} = \mathbf{0}$ due to the $j = k$ terms in (3.18). With this pair correlation function the differential scattering cross-section can be written as

$$\frac{\mathrm{d}\sigma}{\mathrm{d}\Omega} = |b|^2 N \left(1 + \rho_0 \int_{V_d} \mathrm{d}^3 r \exp(\mathrm{i}\mathbf{Q}\cdot\mathbf{r})(g(\mathbf{r})-1) \right) . \tag{3.23}$$

(Note that (3.23) and (3.21) differ at $\mathbf{Q} = \mathbf{0}$ corresponding to the—unobservable—scattering at zero angle): While (3.21) has a delta function contribution there, it is removed by subtracting 1 from $g(\mathbf{r})$ in (3.23).)

The scattering from a static system is often formulated in terms of a dimensionless quantity which does not depend on the scattering lengths and number of particles:

$$S(\mathbf{Q}) = \frac{1}{N} \left\langle \left| \sum_{j=1}^{N} \exp(\mathrm{i}\mathbf{Q}\cdot\mathbf{r}_j) \right|^2 \right\rangle = \frac{1}{N} \sum_{j,k=1}^{N} \langle \exp(\mathrm{i}\mathbf{Q}\cdot(\mathbf{r}_j - \mathbf{r}_k))\rangle$$

[7] This quantity is dimensionless in contrast to (3.20) with the dimension volume^{-2}. The Patterson function used in crystallography, $P(\mathbf{r}) = \langle \rho(\mathbf{0})\rho(\mathbf{r})\rangle/\rho_0$ lies in between with the dimension volume^{-1}. But note that this is only a question of notation, all three approaches are equivalent.

$$= \quad 1 + \rho_0 \int_{V_d} \mathrm{d}^3 r \exp(\mathrm{i}\mathbf{Q}\cdot\mathbf{r})(g(\mathbf{r})-1)\,. \tag{3.24}$$

The relation to the differential scattering cross section is $\mathrm{d}\sigma/\mathrm{d}\Omega = N|b|^2 S(\mathbf{Q})$ which assumes implicitly that the scatterers are identical. $S(\mathbf{Q})$ is usually called the *structure factor* because it expresses how the structure of the sample given by the $\mathbf{r}_j$ or $g(\mathbf{r})$ determines the scattering. On the other hand equation (3.14) can also be used to calculate the scattering of a single particle. In this case the quantity corresponding to (3.24) is the *form factor* $P(\mathbf{Q})$ with the slightly different convention $\mathrm{d}\sigma/\mathrm{d}\Omega = N^2|b|^2 P(\mathbf{Q})$ implying that $P(0) = 1$.

In many physical systems the interaction between particles is not directional with the consequence that $g(\mathbf{r})$ depends only on the distance $r = |\mathbf{r}|$. In this case by symmetry follows that also $S(\mathbf{Q})$ is only a function of $Q = |\mathbf{Q}|$. Formula (3.145) from the appendix can be applied resulting in

$$S(Q) = 1 + \frac{4\pi\rho_0}{Q}\int_0^\infty (g(r)-1)\sin(Qr) r \mathrm{d}r\,. \tag{3.25}$$

3.2.1 Example 1: form factor of a sphere

In this example, the two ways to calculate the scattering (via the density and the density correlation) will be demonstrated. On a length scale larger than the distance of the individual scatterers, the density of a sphere of radius R is given as

$$\rho(r) = \begin{cases} \tilde{\rho} & \text{for } r < R \\ 0 & \text{for } r > R \end{cases} \tag{3.26}$$

where $\tilde{\rho} = N/V_{\text{sphere}} = 3N/4\pi R^3$. Because of the spherical symmetry the Fourier transform of the density can be carried out using (3.145):

$$\int_V \mathrm{d}^3 r \exp(\mathrm{i}\mathbf{Q}\cdot\mathbf{r})\rho(\mathbf{r}) = \frac{4\pi}{Q}\int_0^R \tilde{\rho} r \sin(Qr)\mathrm{d}r\,. \tag{3.27}$$

Substitution $x = Qr$ yields

$$= \frac{4\pi\tilde{\rho}}{Q^3}\int_0^{QR} x\sin x \mathrm{d}x\,.$$

This integral can be calculated using integration by parts:

$$\begin{aligned} &= \frac{4\pi\tilde{\rho}}{Q^3}\left(-x\cos x\Big|_0^{QR} + \int_0^{QR}\cos x \mathrm{d}x\right) \\ &= \frac{3N}{Q^3R^3}\left(\sin(QR) - QR\cos(QR)\right)\,. \end{aligned}$$

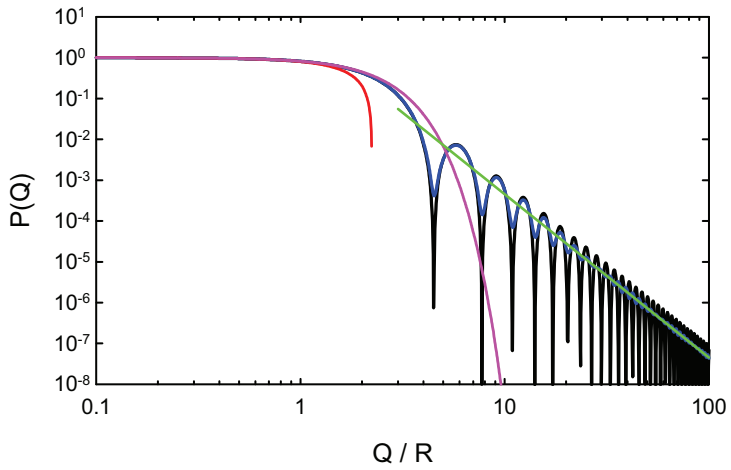

Figure 3.3: Form factor of a sphere (black), average for spheres distributed equally over $R = 0.95 \ldots 1.05$ (blue), low Q expansion (3.30) (red), Guinier approximation (3.33) (magenta), Porod limit (3.35) (green).

In the last result the density is expressed via the number of scatterers within the sphere. Knowing the Fourier transform of the density, the differential scattering cross-section (3.16) is

$$\frac{\mathrm{d}\sigma}{\mathrm{d}\Omega} = \frac{9N^2|b|^2}{Q^6R^6}\left(\sin(QR) - QR\cos(QR)\right)^2 \tag{3.28}$$

and the form factor

$$P(Q) = \frac{9}{Q^6R^6}\left(\sin(QR) - QR\cos(QR)\right)^2 . \tag{3.29}$$

Fig. 3.3 shows the form factor of the sphere. The zeros predicted by (3.29) are usually not found in the experiment but only more-or-less pronounced minima. The reason is that experimental samples usually consist of spheres of slightly different radii (polydispersity). This leads to a smearing out which is simulated by a $\pm 5\%$ variation in R in the blue curve of Fig. 3.3.

A series expansion of (3.28) yields

$$\frac{\mathrm{d}\sigma}{\mathrm{d}\Omega} = N^2|b|^2\left(1 - \frac{Q^2R^2}{5} + \mathcal{O}(Q^4)\right) . \tag{3.30}$$

One can see that the low Q limit is proportional to N^2. This is so because at low Q the waves scattered by the individual particles add up *coherently*, i.e. by amplitude. The

linear increase of the amplitude corresponds to a quadratic one in intensity. It is therefore possible to determine the particle size from the low Q scattering. E.g. in a small-angle scattering experiment on a sample of uncorrelated spheres one obtains the scattering intensity defined by the SANS convention as

$$I_{\mathrm{SANS}}(Q) = \frac{1}{V_{\mathrm{sample}}} \frac{\mathrm{d}\sigma}{\mathrm{d}\Omega} \tag{3.31}$$

with dimension length^{-1}:

$$\lim_{Q\to 0} I_{\mathrm{SANS}}(Q) = N_{\mathrm{spheres}} N^2 |b|^2 = \phi V_{\mathrm{sphere}} \tilde{\rho}^2 |b|^2 \tag{3.32}$$

From this expression for a given volume fraction ϕ the volume of the scatterer can be calculated. It can be shown [8] that this formula holds for arbitrarily shaped particles as well[8]. The Q^2 term in the expansion (3.30) also has a more general significance. It is actually related to the fact that for any form factor to second order in Q the *Guinier approximation* holds:

$$\frac{\mathrm{d}\sigma}{\mathrm{d}\Omega} \approx N^2 |b|^2 \mathrm{e}^{-Q^2 {R_{\mathrm{g}}}^2/3} \approx N^2 |b|^2 \left(1 - \frac{Q^2 {R_{\mathrm{g}}}^2}{3}\right) \tag{3.33}$$

where

$${R_{\mathrm{g}}}^2 = \frac{\int_V r^2 \rho(r) \mathrm{d}^3 r}{\int_V \rho(r) \mathrm{d}^3 r} = \frac{1}{2} \frac{\int_{V_d} r^2 g(r) \mathrm{d}^3 r}{\int_{V_d} g(r) \mathrm{d}^3 r} \tag{3.34}$$

is the *radius of gyration* of the particle. As Fig. 3.3 shows, the Guinier approximation approximates the sphere from factor slightly better than the second order approximation (3.30) because it contains higher order terms in Q despite with incorrect coefficients.

Finally, a general high Q property of the scattering can be demonstrated with the example of a sphere. For large Q the $\sin(QR)$ term in (3.29) becomes negligible compared to $QR\cos(QR)$. Also, assuming some polydispersity or finite instrumental resolution which are always present in a real experiment, $(\cos(QR))^2$ can be replaced by its average $\overline{\cos^2 x} = 1/2$, so that:

$$\overline{\lim_{Q\to\infty}} P(Q) = \frac{9}{2} \frac{1}{Q^4 R^4} \,. \tag{3.35}$$

---

[8] From the derivation formula (3.32) corresponds to the unrealistic case of spheres consisting of monisotopic scatterers *in vacuo*. For the realistic situation of molecular particles suspended in a solvent $\tilde{\rho}^2|b|^2$ has to be replaced by $\left|\rho_b^{\mathrm{spheres}} - \rho_b^{\mathrm{solvent}}\right|^2$, the squared scattering length density difference between solvent and particle.

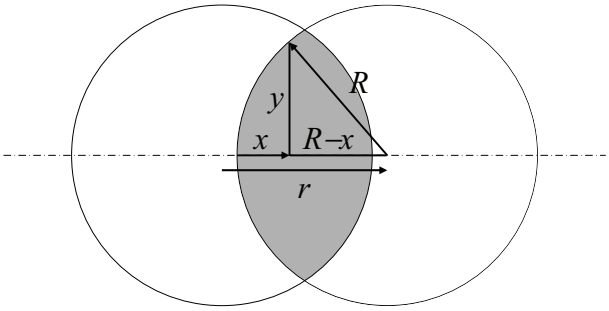

Figure 3.4: Intersection volume of two spheres of radius R offset by a distance r. The volume has to be imagined as a body of rotation around the dot-dashed axis.

Again, this is the special case of a general relation, the *Porod law* which relates the high Q scattering to the ratio surface area S_{particle} / volume V_{particle}:

$$\overline{\lim_{Q\to\infty}} P(Q) = \frac{2\pi S_{\text{particle}}}{{V_{\text{particle}}}^2}\frac{1}{Q^4}\,; \tag{3.36}$$

or in terms of the SANS intensity:

$$\overline{\lim_{Q\to\infty}} I_{\text{SANS}}(Q) = 2\pi\tilde{\rho}^2|b|^2\frac{S}{V}\frac{1}{Q^4} \tag{3.37}$$

where it is now irrelevant whether S and V refer to a single particle or the whole system because the particle number cancels out in the ratio.

Although the calculation by Fourier transform of the density is simpler in the case of the sphere, for didactical purposes, the calculation via the correlation function $g(\mathbf{r})$ will be presented too: Being the probability that a certain distance $\mathbf{r}$ is represented within an object with sharp boundaries it can be obtained by a simple geometrical construction proposed by Glatter [9]. It is proportional to the volume of the intersection of the object with itself shifted by $\mathbf{r}$. The situation is drafted in Fig. 3.4 for a sphere. The intersection volume is a body of revolution[9] whose volume can be calculated as

$$V_d(r) = \int_0^{2R-r} \pi y^2(x)\mathrm{d}x\,. \tag{3.38}$$

Because of symmetry this is the double of the left half-volume obtained by restricting the integral to $x = 0\ldots(2R-r)/2$. From simple geometrical considerations

[9] German: Rotationskörper

$y = \sqrt{R^2 - (R-x)^2}$ and therefore

$$\begin{aligned} V_d(r) &= 2\pi \int_0^{(2R-r)/2} \left(R^2 - (R-x)^2\right) \mathrm{d}x \\ &= \pi \left(\frac{4}{3}R^3 - R^2 r + \frac{1}{12}r^3\right) . \end{aligned} \tag{3.39}$$

The proportionality factor between $V_d(r)$ and $g(r)$ can be calculated from the requirement that the volume integral over $g(r)$ is one:

$$\int_0^{2R} V_d(r) 4\pi r^2 \mathrm{d}r = \frac{16\pi^2 R^6}{9} \Rightarrow g(r) = \frac{3\left(16R^3 - 12R^2 r + r^3\right)}{64\pi R^6} . \tag{3.40}$$

Inserting this expression into (3.25) results in an integral over terms $x^n \sin x$ which are all calculable by integration by parts resulting in

$$P(Q) = \frac{9}{2} \frac{1 + Q^2R^2 + Q^2R^2\cos(2QR) - \cos(2QR) - 2QR\sin(2QR)}{Q^6R^6} \tag{3.41}$$

which after using some trigonometric function identities turns out to be the same result as expression (3.29).

3.2.2 Example 2: structure factor of a liquid

This second example is not an exact calculation as the preceding one but more a rough description of the features to be expected for scattering from a liquid (Fig. 3.5). A liquid also does not fulfil the requirement that the structure is static in the strict sense required above. Nevertheless, as will be derived in the following section, a diffraction experiment will yield an $S(Q)$ corresponding to the instantaneous structure. But what is more a problem for the mathematical treatment is that for a given interparticle potential $V(r)$ there is no exact way to derive the pair correlation function $g(r)$. There are only approximative analytical methods [10] and numerical methods available for this purpose. Nevertheless it can be expected that there is a preferential nearest-neighbour distance r_{nn} which is roughly defined by the minimum of the interparticle potential and corresponds to a maximum in $g(r)$. As explained before $g(r)$ will drop sharply for too short distances because of the strong repulsion. For large r there will be no significant interaction between the particles so that the joint probability $\langle \rho(\mathbf{0})\rho(\mathbf{r}) \rangle$ will become the product of the average densities ${\rho_0}^2$ and in consequence $\lim_{r\to\infty} g(r) = 1$.

From $g(r)$ by use of equation (3.25) the structure factor can be calculated. Although again an exact result cannot be given, several general features can be stated: For $Q \to \infty$,

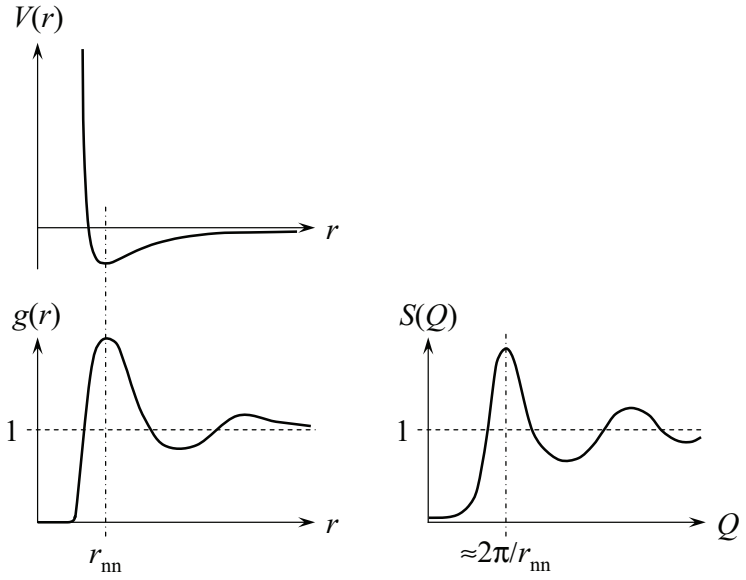

Figure 3.5: Schematic representation of interaction potential $V(r)$, pair correlation function $g(r)$, and scattering function $S(Q)$.

$\exp(\mathrm{i}\mathbf{Q}\cdot\mathbf{r})$ becomes a rapidly oscillating function and the integral vanishes. Then one has

$$\lim_{Q\to\infty} S(Q) = 1\,. \tag{3.42}$$

For $Q \to 0$, $S(Q)$ measures only the overall density fluctuation, i.e. the fluctuation of the particle number:

$$\lim_{Q\to 0} S(Q) = \frac{V^2\langle\delta\rho^2\rangle}{N} = \frac{\langle N^2\rangle - \langle N\rangle^2}{\langle N\rangle} = \rho_0 k_\mathrm{B} T \kappa_T\,. \tag{3.43}$$

Here, k_B denotes the Boltzmann factor, T the temperature and κ_T the isothermal compressibility. At intermediate Q, the structure factor of liquids shows a diminishing series of broad peaks, remainders of the Bragg peaks of a crystalline structure. The first peak occurs at a scattering vector roughly corresponding to the next neighbour distance by $Q_\mathrm{max} = 2\pi/r_\mathrm{nn}$.

3.3 Scattering from a dynamic system[10]

Here, the more realistic situation will be considered in which the particles of the sample are moving. Their dynamics will be described by *trajectories* $\mathbf{r}_j(t)$ which implies that the result is only valid in classical approximation, i.e. does not contain effects of quantum mechanics[11]. Therefore, all results in this section should be labelled by "cl" for "classical". But in order to avoid undue complication of the formulae, this is only done where the result is blatantly false in comparison to the quantum-mechanical calculation. For moving particles energy may be transferred to or from the scattered particle or in the wave picture the frequency is changed by the Doppler effect. Thus an energy transfer

$$\Delta E = E' - E = \hbar\varpi' - \hbar\varpi \equiv \hbar\omega \tag{3.44}$$

occurs, the scattering is in general *inelastic*, and $k' \neq k$.

An experimental observation of inelastic scattering requires that the energy of the scattered particle $E' = \hbar\varpi'$ is measured. This is usually done by a filter-detector combination which determines the Fourier component at a single frequency ϖ' over some (long) registration time T:

$$\psi_{\varpi'}(\mathbf{r}) = \lim_{T\to\infty} \frac{1}{\sqrt{2\pi T}} \int_0^T \psi(\mathbf{r},t)\mathrm{e}^{-\mathrm{i}\varpi' t}\mathrm{d}t\,. \tag{3.45}$$

The reason for the seemingly odd normalisation factor is that this component is defined such that the integral of the intensities of the components

$$I_{\varpi'} = |\psi_{\varpi'}(\mathbf{r})|^2 \tag{3.46}$$

over all frequencies coincides with the total intensity in (3.3): $\int_{-\infty}^{\infty} I_{\varpi'}\mathrm{d}\varpi' = I$.

It is now possible to calculate the intensity of a frequency component from the scattering particles' trajectories from (3.2) and (3.4) using the Fraunhofer diffraction approximation as before:

$$I_{\varpi'} = \frac{|A|^2}{R^2}\left|\lim_{T\to\infty}\frac{1}{\sqrt{2\pi T}}\int_0^T \sum_{j=1}^{N} b_j \mathrm{e}^{\mathrm{i}\varpi t}\mathrm{e}^{\mathrm{i}\mathbf{Q}\cdot\mathbf{r}_j(t)}\mathrm{e}^{-\mathrm{i}\varpi' t}\mathrm{d}t\right|^2 . \tag{3.47}$$

---

[10] This section could also be headed 'inelastic scattering' or 'dynamic scattering'.

[11] of course, apart from the fact that the description of a neutron beam as a wave requires quantum mechanics.

Here, the $e^{i\varpi t}$ stems from the definition of the incident wave (3.2) and $e^{-i\varpi' t}$ from the selection of the scattered wave (3.45). The two factors can be united by using the energy transfer (3.44):

$$= \frac{|A|^2}{R^2} \left| \lim_{T\to\infty} \frac{1}{\sqrt{2\pi T}} \int_0^T \sum_{j=1}^N b_j e^{-i\omega t} e^{i\mathbf{Q}\cdot\mathbf{r}_j(t)} dt \right|^2 . \tag{3.48}$$

As in the static case the calculation continues by expressing the absolute square as the product of conjugate complex quantities:

$$\begin{aligned} &= \frac{|A|^2}{2\pi R^2} \lim_{T\to\infty} \frac{1}{T} \int_0^T \sum_{j=1}^N b_j^* e^{i\omega t_1} e^{-i\mathbf{Q}\cdot\mathbf{r}_j(t_1)} dt_1 \int_0^T \sum_{k=1}^N b_k e^{-i\omega t_2} e^{i\mathbf{Q}\cdot\mathbf{r}_k(t_2)} dt_2 \\ &= \frac{|A|^2}{2\pi R^2} \lim_{T\to\infty} \frac{1}{T} \int_0^T dt_1 \int_0^T dt_2 e^{i\omega(t_1-t_2)} \sum_{j,k=1}^N b_j^* b_k e^{-i\mathbf{Q}\cdot(\mathbf{r}_k(t_2)-\mathbf{r}_j(t_1))} . \end{aligned} \tag{3.49}$$

$\lim_{T\to\infty} \frac{1}{T} \int_0^T dt X(t)$ expresses the average over time of a quantity X. Assuming *ergodicity*[12] it can be replaced by the thermodynamic average at time zero, $\langle X(0)\rangle$. In addition, the integration over t_2 can be replaced by one over the temporal distance $t = t_2 - t_1$:

$$= \frac{|A|^2}{2\pi R^2} \left\langle \int_{-\infty}^{\infty} e^{-i\omega t} \sum_{j,k=1}^N b_j^* b_k e^{i\mathbf{Q}\cdot(\mathbf{r}_k(t)-\mathbf{r}_j(0))} dt \right\rangle . \tag{3.50}$$

This result is the intensity as density of the wave *per volume*. What is actually measured is usually the intensity of a beam *per area and time*. Because the number of particles crossing a surface in a time unit is the density multiplied by their velocity, one has to correct (3.50) by a factor $v'/v = k'/k$ for non-relativistic particles (i.e. for neutrons but not for light):

$$I_{\varpi'} = \frac{|A|^2}{2\pi R^2} \frac{k'}{k} \int_{-\infty}^{\infty} e^{-i\omega t} dt \sum_{j,k=1}^N b_j^* b_k \left\langle e^{i\mathbf{Q}\cdot(\mathbf{r}_k(t)-\mathbf{r}_j(0))} \right\rangle . \tag{3.51}$$

Another place where $k' \neq k$ has to be taken into account is that Q now does not anymore result from the isosceles construction in Fig. 3.2 drafted in black but from scattering triangles as those in blue and red. Application of the cosine theorem leads to the following expression for Q in the inelastic situation:

$$Q = \sqrt{k^2 + k'^2 - 2kk'\cos(2\theta)} \tag{3.52}$$

[12] Roughly speaking this means that the system 'explores' the whole phase space during the observation period T. This may not be fulfilled for certain dynamic light scattering experiments; for a discussion see ref. 13.

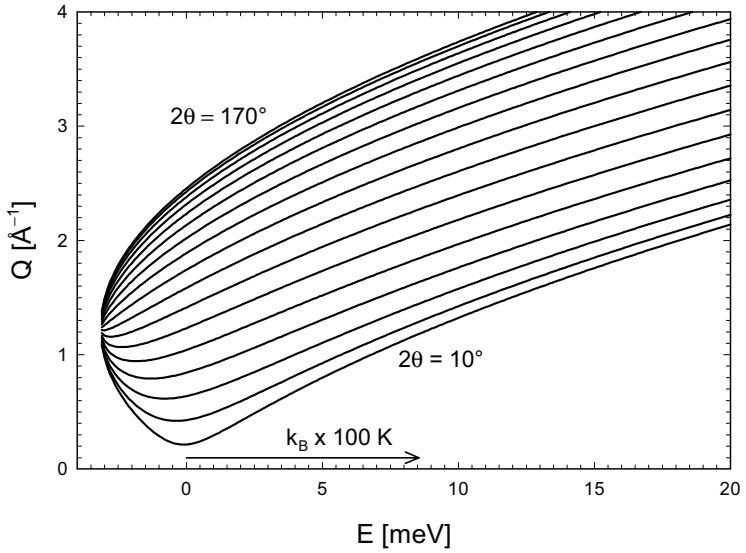

Figure 3.6: Scattering vectors Q accessed by a neutron scattering experiment with the detector at scattering angles $2\theta = 10 \ldots 170°$ vs. the energy transfer $\hbar\omega$ (incident wavelength $\lambda = 5.1$ Å). For comparison the thermal energy $k_\mathrm{B}T$ corresponding to 100 K is indicated by an arrow.

$$= \sqrt{\frac{8\pi^2}{\lambda^2} + \frac{2m\omega}{\hbar} - \frac{4\pi}{\lambda}\sqrt{\frac{4\pi^2}{\lambda^2} + \frac{2m\omega}{\hbar}}\cos(2\theta)} \quad \text{for neutrons.} \tag{3.53}$$

Especially, it has to be observed now that Q also depends on $\hbar\omega$ implying that Q is not anymore constant for a single scattering angle. Fig. 3.6 shows the magnitude of this effect for typical parameters of a neutron scattering experiment. It can be seen that it is by no means negligible for typical thermal energies of the sample even at temperatures as low as 100 K.

In analogy to (3.11) the *double differential cross-section* is defined as the probability density that a neutron is scattered into a solid angle element $\mathrm{d}\Omega$ with an energy transfer $\hbar\omega \ldots \hbar(\omega + \mathrm{d}\omega)$. From (3.51) it is

$$\frac{\mathrm{d}\sigma}{\mathrm{d}\Omega\mathrm{d}\omega} = \frac{1}{2\pi}\frac{k'}{k}\int_{-\infty}^{\infty} \mathrm{e}^{-\mathrm{i}\omega t}\mathrm{d}t \sum_{j,k=1}^{N} b_j^* b_k \left\langle \mathrm{e}^{\mathrm{i}\mathbf{Q}\cdot(\mathbf{r}_k(t)-\mathbf{r}_j(0))}\right\rangle . \tag{3.54}$$

In order to derive a quantity similar to the structure factor (3.24), one assumes again a system of N *chemically* identical particles. But in order to capture the feature of incoherent scattering, present in neutron scattering, it is assumed that these particles do not have

identical scattering lengths but individual randomly distributed scattering lengths with the average $\overline{b} = (1/N)\sum_j b_i$ and the variance $\overline{|b|^2} - \left|\overline{b}\right|^2 = \overline{\left|b - \overline{b}\right|^2} = (1/N)\sum_i \left|b_j - \overline{b}\right|^2$. The most obvious reason for the variance of scattering lengths is that chemically identical atoms may be different isotopes. Because the neutron scattering length is a nuclear property it may differ from isotope to isotope. But even in monisotopic systems there may be such a variance due to disorder of the nuclear spin orientations because the scattering length also depends on the combined spin state of the scattered neutron and the scattering nucleus[13]. The sum in expression (3.54) can be decomposed into one over different indices and one over identical indices,

$$\sum_{j,k=1}^{N} b_j^* b_k \mathrm{e}^{\mathrm{i}\mathbf{Q}\cdot(\mathbf{r}_k(t)-\mathbf{r}_j(0))} = \sum_{j\neq k=1}^{N} b_j^* b_k \mathrm{e}^{\mathrm{i}\mathbf{Q}\cdot(\mathbf{r}_k(t)-\mathbf{r}_j(0))} + \sum_{j=1}^{N} |b_j|^2 \mathrm{e}^{\mathrm{i}\mathbf{Q}\cdot(\mathbf{r}_j(t)-\mathbf{r}_j(0))}\,, \tag{3.55}$$

which have to be averaged in a different way with respect to the distribution of scattering lengths. In the first term b_j^* and b_k can be averaged separately because the different particle scattering lengths are uncorrelated: $\overline{b^*}\,\overline{b} = \overline{b}^*\overline{b} = |\overline{b}|^2$. In the second term one has to average *after* taking the absolute square:

$$= \sum_{j\neq k=1}^{N} |\overline{b}|^2 \mathrm{e}^{\mathrm{i}\mathbf{Q}\cdot(\mathbf{r}_k(t)-\mathbf{r}_j(0))} + \sum_{j=1}^{N} \overline{|b|^2} \mathrm{e}^{\mathrm{i}\mathbf{Q}\cdot(\mathbf{r}_j(t)-\mathbf{r}_j(0))}\,. \tag{3.56}$$

In order to avoid the sum over distinct particles, the first sum is complemented by the $j = k$ terms, $|\overline{b}|^2 \mathrm{e}^{\mathrm{i}\mathbf{Q}\cdot(\mathbf{r}_j(t)-\mathbf{r}_j(0))}$, and to compensate, these terms are subtracted in the second sum:

$$= \sum_{j,k=1}^{N} |\overline{b}|^2 \mathrm{e}^{\mathrm{i}\mathbf{Q}\cdot(\mathbf{r}_k(t)-\mathbf{r}_j(0))} + \sum_{j=1}^{N} \left(\overline{|b|^2} - |\overline{b}|^2\right) \mathrm{e}^{\mathrm{i}\mathbf{Q}\cdot(\mathbf{r}_j(t)-\mathbf{r}_j(0))}\,. \tag{3.57}$$

With this result it is possible to express the double differential cross section as

$$\frac{\partial\sigma}{\partial\Omega\partial\omega} = N\frac{k'}{k}\left(\left|\overline{b}\right|^2 S_{\mathrm{coh}}(\mathbf{Q},\omega) + \left(\overline{|b|^2} - \left|\overline{b}\right|^2\right) S_{\mathrm{inc}}(\mathbf{Q},\omega)\right) \tag{3.58}$$

with

$$S_{\mathrm{coh}}(\mathbf{Q},\omega) = \frac{1}{2\pi N}\int_{-\infty}^{\infty} \mathrm{e}^{-\mathrm{i}\omega t}\mathrm{d}t \sum_{j,k=1}^{N} \left\langle \mathrm{e}^{\mathrm{i}\mathbf{Q}\cdot(\mathbf{r}_k(t)-\mathbf{r}_j(0))}\right\rangle \tag{3.59}$$

and

$$S_{\mathrm{inc}}(\mathbf{Q},\omega) = \frac{1}{2\pi N}\int_{-\infty}^{\infty} \mathrm{e}^{-\mathrm{i}\omega t}\mathrm{d}t \sum_{j=1}^{N} \left\langle \mathrm{e}^{\mathrm{i}\mathbf{Q}\cdot(\mathbf{r}_j(t)-\mathbf{r}_j(0))}\right\rangle\,. \tag{3.60}$$

---

[13] In this lecture only nuclear non-magnetic scattering will be considered. For a full treatment of magnetic scattering see e.g. vol. 2 of ref. 3.

The quantities defined by (3.59) and (3.60) are called *coherent* and *incoherent scattering function* or *dynamic structure factors*. It is a peculiarity of neutron scattering that there is also the incoherent term solely depending on the *single particle dynamics* due to the variance of the scattering lengths.

The prefactors of the scattering functions in expression (3.58) are often replaced by the scattering cross sections

$$\sigma_{\mathrm{coh}} = 4\pi \left|\bar{b}\right|^2, \quad \sigma_{\mathrm{inc}} = 4\pi \left(\overline{|b|^2} - \left|\bar{b}\right|^2\right) \tag{3.61}$$

which (for the incoherent part in general and for the coherent in the limit $Q \to \infty$) give the scattering into all directions, i.e. the solid angle 4π.

In some cases it is interesting to consider the part of expression (3.59) before the time-frequency Fourier transform, called *intermediate coherent scattering function*:

$$I_{\mathrm{coh}}(\mathbf{Q}, t) = \frac{1}{N} \sum_{jk} \left\langle \mathrm{e}^{\mathrm{i}\mathbf{Q}\cdot(\mathbf{r}_k(t) - \mathbf{r}_j(0))} \right\rangle . \tag{3.62}$$

Its value for $t = 0$ expresses the correlation between atoms *at equal times*. A theorem on Fourier transforms tells that this is identical to the integral of the scattering function over all energy transfers:

$$I_{\mathrm{coh}}(\mathbf{Q}, 0) = \frac{1}{N} \sum_{jk} \left\langle \mathrm{e}^{\mathrm{i}\mathbf{Q}\cdot(\mathbf{r}_k - \mathbf{r}_j)} \right\rangle = S(\mathbf{Q}) = \int_{-\infty}^{\infty} S_{\mathrm{coh}}(\mathbf{Q}, \omega) \mathrm{d}\omega \, . \tag{3.63}$$

The concrete significance of this relation is that a diffraction experiment, which does not discriminate energies and thus implicitly integrates over all $\hbar\omega$, only shows the instantaneous correlation of the atoms, viz the structure of the sample[14]. $S(\mathbf{Q})$ is the structure

[14] Strictly speaking, this is only an approximation. There are several reasons why the integration in the diffraction experiment is not the 'mathematical' one of (3.63): (1) On the instrument the integral is taken along a curve of constant 2θ in Fig. 3.6 while constant Q would correspond to a horizontal line. (2) The double differential cross-section (3.58) contains a factor k'/k which depends on ω via (3.52). (3) The detector may have an efficiency depending on wavelength which will introduce another ω-dependent weight in the experimental integration. All these effects have been taken into account in the so-called Placzek corrections [2, 11, 12].

factor as derived in section 3.2 for the static situation. The dynamic information is lost in the integration process.

Similarly the *incoherent intermediate scattering function* is

$$I_{\mathrm{inc}}(\mathbf{Q},t) = \frac{1}{N}\sum_{j=1}^{N}\left\langle \mathrm{e}^{\mathrm{i}\mathbf{Q}\cdot(\mathbf{r}_j(t)-\mathbf{r}_j(0))}\right\rangle \tag{3.64}$$

with

$$I_{\mathrm{inc}}(\mathbf{Q},0) = \frac{1}{N}\sum_{j=1}^{N}\left\langle \mathrm{e}^{\mathrm{i}\mathbf{Q}\cdot(\mathbf{r}_j-\mathbf{r}_j)}\right\rangle = 1 = \int_{-\infty}^{\infty} S_{\mathrm{inc}}(\mathbf{Q},\omega)\mathrm{d}\omega\,. \tag{3.65}$$

Note that this result is independent of the actual structure of the sample. Also it is the same result as the high Q limit $S(Q) \to 1$ (3.42). This is a consequence of the more general fact that coherent and incoherent scattering become indistinguishable for large Q. Integration of the double-differential cross section (3.58) over ω shows that also the static scattering contains an incoherent contribution. But because of (3.65), this term is constant in Q. It constitutes a flat background in addition to the $S(Q)$-dependent scattering. In some cases (e.g. small-angle scattering) it may be necessary to correct for this, in other cases (e.g. diffraction with polarisation analysis) it may even be helpful to normalise the coherent scattering.

In the paragraphs before it was shown that the value of the intermediate scattering functions at $t = 0$ corresponds to the integral of the scattering function over an infinite interval. This is a consequence of a general property of the Fourier transform. There is also the inverse relation that the value of $S(\mathbf{Q},\omega)$ at $\omega = 0$ is related to the integral of $I(\mathbf{Q},t)$ over all times. The most important case is here when $I(\mathbf{Q},t)$ does not decay to zero for infinite time but to a finite value $f(\mathbf{Q})$. In that case the integral is infinite implying that $S(\mathbf{Q},\omega)$ has a delta function contribution at $\omega = 0$. This means that the scattering contains a strictly elastic component. Its strength can be calculated by decomposing the intermediate scattering function into a completely decaying part and a constant for the coherent and the incoherent scattering:

$$I_{[\mathrm{coh|inc}]}(\mathbf{Q},t) = I^{\mathrm{inel}}_{[\mathrm{coh|inc}]}(\mathbf{Q},t) + f_{[\mathrm{coh|inc}]}(\mathbf{Q})\,. \tag{3.66}$$

Because the Fourier transform of constant one is the delta function this corresponds to

$$S_{[\mathrm{coh|inc}]}(\mathbf{Q},\omega) = S^{\mathrm{inel}}_{[\mathrm{coh|inc}]}(\mathbf{Q},\omega) + S^{\mathrm{el}}_{[\mathrm{coh|inc}]}(\mathbf{Q})\delta(\omega)\,. \tag{3.67}$$

where $S^{\mathrm{el}}_{[\mathrm{coh|inc}]}(\mathbf{Q}) = f_{[\mathrm{coh|inc}]}(\mathbf{Q})$, the *elastic coherent/incoherent structure factor*, can be written as

$$S^{\mathrm{el}}_{\mathrm{coh}}(\mathbf{Q}) = \frac{1}{N}\sum_{j,k=1}^{N}\left\langle \mathrm{e}^{\mathrm{i}\mathbf{Q}\cdot(\mathbf{r}_k(\infty)-\mathbf{r}_j(0))}\right\rangle , \tag{3.68}$$

$$S^{\mathrm{el}}_{\mathrm{inc}}(\mathbf{Q}) = \frac{1}{N}\sum_{j=1}^{N}\left\langle \mathrm{e}^{\mathrm{i}\mathbf{Q}\cdot(\mathbf{r}_j(\infty)-\mathbf{r}_j(0))}\right\rangle . \tag{3.69}$$

Here, $t = \infty$ indicates a time which is sufficiently long that the correlation with the position at $t = 0$ is lost. For the elastic incoherent structure factor (EISF) this lack of correlation implies that the terms with initial and final positions can be averaged separately:

$$\begin{aligned} S^{\mathrm{el}}_{\mathrm{inc}}(\mathbf{Q}) &= \frac{1}{N}\sum_{j=1}^{N}\left\langle \mathrm{e}^{\mathrm{i}\mathbf{Q}\cdot\mathbf{r}_j}\right\rangle\left\langle \mathrm{e}^{-\mathrm{i}\mathbf{Q}\cdot\mathbf{r}_j}\right\rangle \\ &= \frac{1}{N}\sum_{j=1}^{N}\left|\mathrm{e}^{-\mathrm{i}\mathbf{Q}\cdot\mathbf{r}_j}\right|^2 \qquad (3.70) \\ &= \frac{1}{N}\sum_{j=1}^{N}\left|\int_V \mathrm{d}^3r\,\exp\left(\mathrm{i}\mathbf{Q}\cdot\mathbf{r}\right)\rho_j(\mathbf{r})\right|^2 . \qquad (3.71) \end{aligned}$$

Here, $\rho_j(\mathbf{r})$ denotes the 'density of particle j', i.e. the probability density of the individual particle j being at $\mathbf{r}$. One can see that the elastic incoherent structure factor differs from the structure factor (3.24) itself mainly by the order of summation and averaging. It has the normalisation $S^{\mathrm{el}}_{\mathrm{inc}}(0) = 1$, that of a form factor. One can say that the EISF is the form factor of the volume confining the motion of the particles. E.g. for particles performing any kind of motion within a sphere, the EISF would be $S^{\mathrm{el}}_{\mathrm{inc}}(Q) = 9\left(\sin(QR) - QR\cos(QR)\right)^2/Q^6R^6$ as given by (3.29).

As in the static situation, the scattering law can be traced back to distance distribution functions, the *van Hove correlation functions*, which are time-dependent:

$$G(\mathbf{r},t) = \frac{1}{N}\left\langle\sum_{j,k=1}^{N}\delta(\mathbf{r}-\mathbf{r}_k(t)+\mathbf{r}_j(0))\right\rangle , \tag{3.72}$$

$$G_{\mathrm{s}}(\mathbf{r},t) = \frac{1}{N}\left\langle\sum_{j=1}^{N}\delta(\mathbf{r}-\mathbf{r}_j(t)+\mathbf{r}_j(0))\right\rangle . \tag{3.73}$$

Insertion into

$$I_{[\mathrm{coh|inc}]} = \int_{V_d} G_{[\mathrm{s}]}(\mathbf{r},t)\exp(\mathrm{i}\mathbf{Q}\cdot\mathbf{r})\mathrm{d}^3r \tag{3.74}$$

directly proves that the spatial Fourier transforms of the van Hove correlation function are the intermediate scattering functions.

The two particle version can—as in the static case—be reduced to the microscopic density,

$$\rho(\mathbf{r},t) = \sum_{j=1}^{N} \delta(\mathbf{r} - \mathbf{r}_j(t)) \,. \tag{3.75}$$

Its autocorrelation function in space and time is

$$\langle \rho(\mathbf{0},0)\rho(\mathbf{r},t)\rangle \,. \tag{3.76}$$

The $\mathbf{0}$ is again showing that translational symmetry is assumed. So the correlation function can be replaced by its average over all starting points $\mathbf{r}_1$ in the sample volume:

$$\langle \rho(\mathbf{0},0)\rho(\mathbf{r},t)\rangle = \frac{1}{V}\int_V \mathrm{d}^3 r_1 \langle \rho(\mathbf{r}_1,0)\rho(\mathbf{r}_1+\mathbf{r},t)\rangle \,. \tag{3.77}$$

Insertion of (3.75) gives

$$\begin{aligned} \langle \rho(\mathbf{0},0)\rho(\mathbf{r},t)\rangle &= \frac{1}{V}\left\langle \sum_{j,k=1}^{N} \int_V \mathrm{d}^3 r_1 \delta(\mathbf{r}_1 - \mathbf{r}_k(t))\delta(\mathbf{r}_1 + \mathbf{r} - \mathbf{r}_j(t)) \right\rangle & (3.78)\\ &= \frac{1}{V}\left\langle \sum_{j,k=1}^{N} \delta(\mathbf{r}_k(t) + \mathbf{r} - \mathbf{r}_j(t)) \right\rangle & (3.79) \end{aligned}$$

which with (3.72) implies

$$G(\mathbf{r},t) = \frac{1}{\rho_0}\langle \rho(\mathbf{0},0)\rho(\mathbf{r},t)\rangle \,. \tag{3.80}$$

Again setting $t = 0$ results in the static scattering situation:

$$G(\mathbf{r},0) = \frac{\langle \rho(\mathbf{0},0)\rho(\mathbf{r},0)\rangle}{\rho_0} = \delta(\mathbf{r}) + \rho_0 g(\mathbf{r}) \tag{3.81}$$

with $g(\mathbf{r})$ from equation (3.22).

As in the case of static scattering there is an alternative way (Fig. 3.1, left) to derive the scattering function by first Fourier-transforming the density

$$\rho_{\mathbf{Q}}(t) = \int \mathrm{d}^3 r \mathrm{e}^{\mathrm{i}\mathbf{Q}\cdot\mathbf{r}} \rho(\mathbf{r},t) = \sum_{j=1}^{N} \mathrm{e}^{\mathrm{i}\mathbf{Q}\cdot\mathbf{r}_j(t)} \tag{3.82}$$

and then multiplying its conjugated value at $t = 0$ with that at t:

$$I_{\mathrm{coh}}(\mathbf{Q},t) = \frac{1}{N}\left\langle \rho^*_{\mathbf{Q}}(0)\rho_{\mathbf{Q}}(t)\right\rangle \tag{3.83}$$

and

$$S_{\mathrm{coh}}(\mathbf{Q},\omega) = \frac{1}{2\pi N}\int_{-\infty}^{\infty} \mathrm{e}^{-\mathrm{i}\omega t}\left\langle \rho^*_{\mathbf{Q}}(0)\rho_{\mathbf{Q}}(t)\right\rangle \mathrm{d}t\,. \tag{3.84}$$

(This is a general consequence of the *cross-correlation theorem* of Fourier transform (3.163) which is the generalisation of the Wiener-Khintchine theorem for two different correlated quantities.)

Note that a reduction of the self correlation function $G_{\mathrm{s}}(\mathbf{r},t)$ is *not* possible in the same way because the multiplication $\rho(\mathbf{0},0)\rho(\mathbf{r},t)$ inevitably includes all combinations of particles j,k and not only the terms for identical particles j,j.

From the definitions (3.72) and (3.73) it is immediately clear that the van Hove correlation functions are symmetric with respect to a *combined* inversion of space and time. (Note that the following relations are *not* valid in a correct quantum-mechanical treatment.):

$$G^{\mathrm{cl}}_{[\mathrm{s}]}(-\mathbf{r},-t) = G^{\mathrm{cl}}_{[\mathrm{s}]}(\mathbf{r},t)\,. \tag{3.85}$$

But in many cases the system is dynamically symmetric to an inversion of space (meaning that the distance between two particles is changing by $-\mathbf{r}$ in the time interval t with equal probability as changing by $\mathbf{r}$)[15]:

$$G^{\mathrm{cl}}_{[\mathrm{s}]}(-\mathbf{r},t) = G^{\mathrm{cl}}_{[\mathrm{s}]}(\mathbf{r},t) \tag{3.86}$$

which implies symmetry in time

$$G^{\mathrm{cl}}_{[\mathrm{s}]}(\mathbf{r},-t) = G^{\mathrm{cl}}_{[\mathrm{s}]}(\mathbf{r},t)\,. \tag{3.87}$$

From (3.86) and general properties of the Fourier transform it follows that $I_{[\mathrm{coh|inc}]}(\mathbf{Q},t)$ is real and from (3.87) that it is also symmetric in time:

$$I^{\mathrm{cl}}_{[\mathrm{coh|inc}]}(\mathbf{Q},-t) = I^{\mathrm{cl}}_{[\mathrm{coh|inc}]}(\mathbf{Q},t)\,. \tag{3.88}$$

[15] A simple counterexample would be a solid moving at constant velocity as a car in a Doppler radar. In that case $G_{\mathrm{s}}(\mathbf{r},t) = \delta(\mathbf{r}-\mathbf{v}t)$ but $G_{\mathrm{s}}(-\mathbf{r},t) = \delta(\mathbf{r}+\mathbf{v}t)$ and $S(\mathbf{Q},\omega)$ will only have a component for positive *or* negative frequency shift ω, depending on whether $\mathbf{Q}$ and $\mathbf{v}$ are parallel or antiparallel, the former arrangement usually being the choice of the police.

In turn this implies that the scattering functions are real and symmetric in energy transfer $\hbar\omega$:

$$S^{\rm cl}_{[\rm coh|inc]}(\mathbf{Q},-\omega) = S^{\rm cl}_{[\rm coh|inc]}(\mathbf{Q},\omega)\,. \tag{3.89}$$

Without the dynamical symmetry to inversion in space (3.86) from (3.85) would only follow that $S_{[\rm coh|inc]}(\mathbf{Q},\omega)$ is real.

3.3.1 Example 3: diffusion

For simple diffusion the density develops in time following Fick's second law,

$$\frac{\partial\rho}{\partial t} = D\Delta\rho \equiv D\left(\frac{\partial^2\rho}{\partial x^2}+\frac{\partial^2\rho}{\partial y^2}+\frac{\partial^2\rho}{\partial z^2}\right)\,. \tag{3.90}$$

Because the underlying mechanism is Brownian motion, random collisions with solvent molecules, it can be concluded from the central limit theorem of statistics that the density of particles initially assembled at the origin is a Gaussian in all coordinates:

$$\begin{aligned}\rho_1 &= \frac{1}{\sqrt{2\pi}\sigma}\exp\left(-\frac{x^2}{2\sigma^2}\right)\frac{1}{\sqrt{2\pi}\sigma}\exp\left(-\frac{y^2}{2\sigma^2}\right)\frac{1}{\sqrt{2\pi}\sigma}\exp\left(-\frac{z^2}{2\sigma^2}\right)\\ &= \frac{1}{(2\pi)^{3/2}\sigma^3}\exp\left(-\frac{r^2}{2\sigma^2}\right)\,.\end{aligned} \tag{3.91}$$

The index 1 should remind that the prefactor is chosen such that the total particle number $\int\rho_1\,{\rm d}^3r$ is normalised to one. The width of the distribution, σ has the dimension length. The only way to construct a length out of D (dimension length^{2}time^{-1}) and time is $\sigma = c\sqrt{Dt}$ where c is a dimensionless constant. Inserting this into (3.91) yields:

$$\rho_1 = \frac{1}{c^3(2\pi Dt)^{3/2}}\exp\left(-\frac{r^2}{2c^2Dt}\right)\,. \tag{3.92}$$

The derivatives of this expression with respect to t and x,y,z can be calculated and inserted into (3.90):

$$\frac{\sqrt{2}\,(r^2-3c^2Dt)}{8\pi^{3/2}c^5D^{5/2}t^{7/2}}\exp\left(-\frac{r^2}{2c^2Dt}\right) = \frac{\sqrt{2}\,(r^2-3c^2Dt)}{4\pi^{3/2}c^7D^{7/2}t^{7/2}}\exp\left(-\frac{r^2}{2c^2Dt}\right)\,. \tag{3.93}$$

One can see that the right- and left-hand side are identical if $c=\sqrt{2}$. This proves that the 'guess' (3.91) is indeed a solution of Fick's second law and also determines the unknown c. With the value of c substituted, the 'single particle density' is

$$\rho_1 = \frac{1}{(8\pi Dt)^{3/2}}\exp\left(-\frac{r^2}{4Dt}\right)\,. \tag{3.94}$$

In passing it is noted that from this distribution the *mean-square displacement* due to diffusion can be calculated:

$$\langle r^2 \rangle = \int \rho_1 r^2 4\pi r^2 \mathrm{d}^3 r = 6Dt\,. \tag{3.95}$$

For incoherent scattering the starting position $\mathbf{r}(0)$ is irrelevant. Therefore, expression (3.94) is also $G_\mathrm{s}(r,t)$. Because the Fourier transform of a Gaussian function is a Gaussian (see appendix) the corresponding incoherent intermediate scattering function is

$$I_\mathrm{inc}(Q,t) = \exp\left(-DQ^2 t\right)\,, \tag{3.96}$$

and because the Fourier transform of an exponential decay is a Lorentzian the incoherent scattering function is

$$S_\mathrm{inc}(Q,\omega) = \frac{1}{\pi}\frac{DQ^2}{\omega^2 + \left(DQ^2\right)^2}\,. \tag{3.97}$$

From these expression one can see that $I_\mathrm{inc}(Q,t)$ decays faster with time for larger Q and $S_\mathrm{inc}(Q,\omega)$ is getting broader. This is understandable because Q defines the spatial resolution of a neutron scattering experiment in a reciprocal way. So a larger Q means observation on shorter distances which can be travelled faster by the diffusing particle.

Finally, one can see that

$$I_\mathrm{inc}(Q,t) = \exp\left(-\frac{Q^2\langle r^2\rangle}{6}\right)\,. \tag{3.98}$$

Because this expression is derived independently of the specific form of $\sigma(t)$ in (3.91) it is generally valid if the distribution of displacements $G_\mathrm{s}(r,t)$ is a Gaussian. Even if this is not the case, equation (3.98) is often a good low-Q approximation called the *Gaussian approximation*[16] and is the dynamical analogue of to the Guinier approximation (3.33) of static scattering.

In general, the incoherent intermediate scattering function cannot be derived from the mean-square displacement alone. Because equation (3.98) is the first term of the cumulant

[16] In the literature, denominators 1, 2, and 3 are also found in this expression. Most of these formulae are nevertheless correct. If $\langle r^2\rangle$ has the meaning of a mean-square displacement from an average position, 3 is correct. In this case often $\langle u^2\rangle$ is written for distinction, but some authors instead rename $\langle r^2\rangle$ into $\langle \Delta r^2\rangle$. If only the displacement in one coordinate is taken ($\langle x^2\rangle$), then 2 is the right denominator.

expansion $\exp(aQ^2 + bQ^4 + \ldots)$ of $I_{\rm inc}(Q,t)$ [14] the mean-square displacement can be calculated as

$$\langle r^2 \rangle = -\lim_{Q\to 0} \frac{6}{Q^2} \ln I_{\rm inc}(Q,t) \quad \text{or} \tag{3.99}$$

$$\langle r^2 \rangle = -\left. \frac{\mathrm{d} \ln I_{\rm inc}(Q,t)}{\mathrm{d}Q^2} \right|_{Q=0} . \tag{3.100}$$

By replacing $I_{\rm inc}(Q,t)$ by its value at infinite time, the EISF $S^{\rm el}_{\rm inc}(Q)$, in this way the limiting mean-square displacement of a confined motion can be obtained. This is the principle of the *elastic scan* technique often used on neutron backscattering spectrometers [15].

3.3.2 Example 4: dynamics of a liquid

(As for the discussion of the static structure factor of liquids before, this is only a qualitative presentation because exact results in closed form cannot be derived and even approximations are much more complicated than in the static case.) Figure 3.7 schematically shows on the left side the behaviour of the correlation functions $G(r,t)$ and $G_{\rm s}(r,t)$ for a simple liquid in classical approximation. On the right side the corresponding intermediate scattering functions $I_{\rm coh}(Q,t)$ and $I_{\rm inc}(Q,t)$ are displayed:

- For $t = 0$ the self correlation function is given by a delta function at $r = 0$. The pair correlation function follows the static correlation function $g(r)$. The intermediate scattering functions are constant one for the incoherent and the static structure factor for the coherent.

- For intermediate times the self correlation function broadens to a bell-shaped function while the pair correlation function loses its structure. The intermediate scattering functions decay with respect to the $t = 0$ value. The decay is faster for higher Q and (in the coherent case) less pronounced at the structure factor maximum (De Gennes narrowing).

- The long time limit of the pair correlation function is the average density ρ_0 while the self correlation simply vanishes (in a liquid). In consequence both the coherent and the incoherent intermediate scattering function decay to zero for long times and any Q.

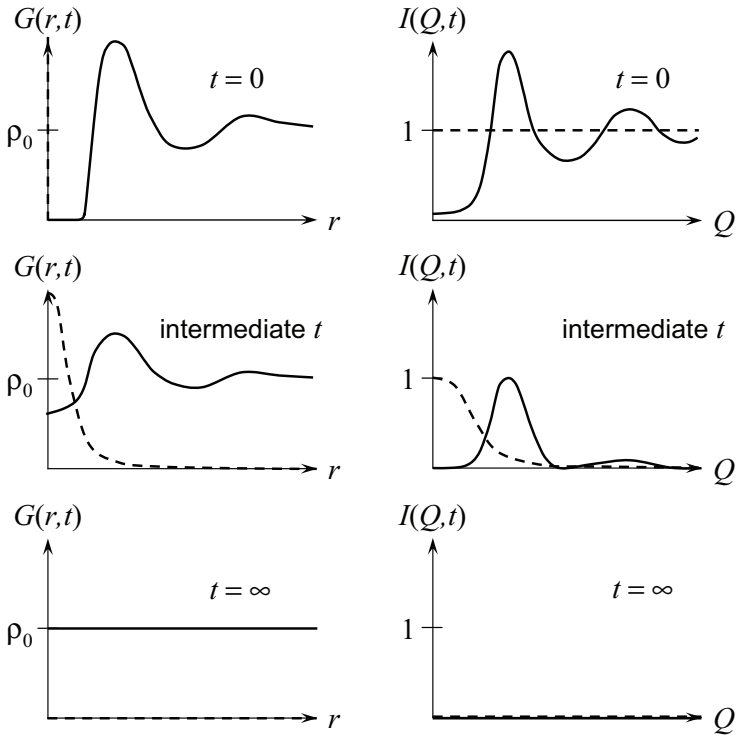

Figure 3.7: Schematic Comparison of the correlation functions $G(r,t)$, $G_{\rm s}(r,t)$ and the intermediate scattering functions $I_{\rm coh}(Q,t)$, $I_{\rm inc}(Q,t)$ for a simple liquid at different times. The solid lines denote the coherent case, the dashed lines the self/incoherent.

3.4 Quantum mechanical considerations

In this section the exact quantum-mechanical results will be presented without a rigorous derivation. For such a derivation see lecture 4 in the previous edition of this course [2] or refs 3, 4. The quantum-mechanical result for the coherent scattering function is (equations (3.8) and (3.6) in ref. 3[17]):

$$S_{\rm coh}(\mathbf{Q},\omega) = \frac{1}{2\pi N}\int_{-\infty}^{\infty} {\rm e}^{-{\rm i}\omega t}{\rm d}t \sum_{j,k=1}^{N} \left\langle {\rm e}^{-{\rm i}\mathbf{Q}\cdot\hat{\mathbf{r}}_j(0)}{\rm e}^{{\rm i}\mathbf{Q}\cdot\hat{\mathbf{r}}_k(t)}\right\rangle . \qquad (3.101)$$

[17] In ref. 3 $S(Q,\omega)$ is defined with the dimension energy^{-1} implying an additional factor $\hbar^{-1}$ with respect to the definition here. This makes sense for an original quantum-mechanical derivation, but in the classical approach used here the appearance of $\hbar$ is unmotivated.

In this expression $\hat{\mathbf{r}}_j(t)$ are the (time-dependent) *Heisenberg operators* of the particle positions. The result would be identical to expression (3.59) if the rule $\mathrm{e}^A\mathrm{e}^B = \mathrm{e}^{A+B}$ could be used. But for operators this would require that $\hat{A}\hat{B} = \hat{B}\hat{A}$, i.e. that the operators *commute*, which is only the case for the $\hat{\mathbf{r}}_j(t)$ at equal times. Therefore, (only) in the static case ($t = 0$) the classical result is exact and the results of section 3.2 do not need any quantum-mechanical corrections. Similarly, the incoherent scattering function is:

$$S_{\mathrm{inc}}(\mathbf{Q},\omega) = \frac{1}{2\pi N}\int_{-\infty}^{\infty}\mathrm{e}^{-\mathrm{i}\omega t}\mathrm{d}t\sum_{j=1}^{N}\left\langle \mathrm{e}^{-\mathrm{i}\mathbf{Q}\cdot\hat{\mathbf{r}}_j(0)}\mathrm{e}^{\mathrm{i}\mathbf{Q}\cdot\hat{\mathbf{r}}_j(t)}\right\rangle . \tag{3.102}$$

The intermediate scattering functions are:

$$I_{\mathrm{coh}}(\mathbf{Q},t) = \frac{1}{N}\sum_{j,k=1}^{N}\left\langle \mathrm{e}^{-\mathrm{i}\mathbf{Q}\cdot\hat{\mathbf{r}}_j(0)}\mathrm{e}^{\mathrm{i}\mathbf{Q}\cdot\hat{\mathbf{r}}_k(t)}\right\rangle \quad \text{and} \tag{3.103}$$

$$I_{\mathrm{inc}}(\mathbf{Q},t) = \frac{1}{N}\sum_{j=1}^{N}\left\langle \mathrm{e}^{-\mathrm{i}\mathbf{Q}\cdot\hat{\mathbf{r}}_j(0)}\mathrm{e}^{\mathrm{i}\mathbf{Q}\cdot\hat{\mathbf{r}}_j(t)}\right\rangle . \tag{3.104}$$

The van Hove correlation functions are:

$$G(\mathbf{r},t) = \frac{1}{N}\sum_{j,k=1}^{N}\int_V \mathrm{d}^3r\langle\delta(\mathbf{r}-\mathbf{r}_1+\hat{\mathbf{r}}_j(0))\delta(\mathbf{r}_1-\hat{\mathbf{r}}_k(t))\rangle \quad \text{and} \tag{3.105}$$

$$G_{\mathrm{s}}(\mathbf{r},t) = \frac{1}{N}\sum_{j=1}^{N}\int_V \mathrm{d}^3r\langle\delta(\mathbf{r}-\mathbf{r}_1+\hat{\mathbf{r}}_j(0))\delta(\mathbf{r}_1-\hat{\mathbf{r}}_j(t))\rangle \tag{3.106}$$

A further simplification as in the classical expressions (3.72) and (3.73) is again not possible because the Heisenberg position operators do not commute. Nevertheless, the pair-correlation function $G(\mathbf{r},t)$ can be reduced to the density which is now an operator:

$$G(\mathbf{r},t) = \frac{1}{\rho_0}\langle\hat{\rho}(\mathbf{0},0)\hat{\rho}(\mathbf{r},t)\rangle \tag{3.107}$$

with

$$\hat{\rho}(\mathbf{r},t) = \sum_{j=1}^{N}\delta(\mathbf{r}-\hat{\mathbf{r}}_j(t)) . \tag{3.108}$$

Note that for $t = 0$ also here the classical result is correct and the relation $G(\mathbf{r},0) = \delta(\mathbf{r})+\rho_0 g(\mathbf{r})$ (3.81) to the static pair correlation is valid for the exact quantum-mechanical treatment too.

As in the classical treatment, the Fourier components of the density operator can also be used to derive the coherent scattering:

$$\hat{\rho}_{\mathbf{Q}}(t) = \int \mathrm{d}^3r\mathrm{e}^{\mathrm{i}\mathbf{Q}\cdot\mathbf{r}}\hat{\rho}(\mathbf{r},t) = \sum_{j=1}^{N}\mathrm{e}^{\mathrm{i}\mathbf{Q}\cdot\hat{\mathbf{r}}_j(t)} . \tag{3.109}$$

In terms of this quantity the coherent intermediate scattering function is

$$I_{\mathrm{coh}}(\mathbf{Q},t) = \frac{1}{N}\left\langle \hat{\rho}_{-\mathbf{Q}}(0)\hat{\rho}_{\mathbf{Q}}(t)\right\rangle = \frac{1}{N}\left\langle \hat{\rho}^{\dagger}_{\mathbf{Q}}(0)\hat{\rho}_{\mathbf{Q}}(t)\right\rangle \tag{3.110}$$

and the coherent scattering function itself

$$S_{\mathrm{coh}}(\mathbf{Q},\omega) = \frac{1}{N}\int_{-\infty}^{\infty} \mathrm{e}^{-\mathrm{i}\omega t}\left\langle \hat{\rho}^{\dagger}_{\mathbf{Q}}(0)\hat{\rho}_{\mathbf{Q}}(t)\right\rangle \mathrm{d}t\,. \tag{3.111}$$

Note that these equations are the same as in the classical calculation (3.83) and (3.84) just with the Fourier transformed density replaced by the operator and the conjugate * changed to the adjoint †.

The most prominent consequence of the correct quantum-mechanical treatment is that the scattering functions are asymmetric with respect to the energy transfer $\hbar\omega$:

$$S_{[\mathrm{coh|inc}]}(-\mathbf{Q},-\omega) = \exp\left(\frac{\hbar\omega}{k_{\mathrm{B}}T}\right) S_{[\mathrm{coh|inc}]}(\mathbf{Q},\omega) \tag{3.112}$$

in contrast to (3.89). This means that the probability for a neutron to be scattered with energy loss is always higher than the probability to be scattered with energy gain[18] (Fig. 3.8). This can be understood as a *detailed balance* factor: In equilibrium, the probability for the scattering system to be in the lower energy state is higher by the factor $\exp(\hbar\omega/k_{\mathrm{B}}T)$. Therefore the probability of scattering into a state with higher energy is more probable by the same factor than scattering into the lower energy state. The effect of the asymmetry will be noticeable for low temperatures and high energy transfers unless $T \gg \hbar\omega/k_{\mathrm{B}}$ [19]. Considering that for room temperature $k_{\mathrm{B}} \cdot 300\,\mathrm{K} \approx 26$ meV it is clear that the condition for a classical treatment is often not fulfilled in neutron scattering. As in the classical calculation, the minus sign in front of $\mathbf{Q}$ can be omitted for a dynamically time-reversal-symmetric system:

$$S_{[\mathrm{coh|inc}]}(\mathbf{Q},-\omega) = \exp\left(\frac{\hbar\omega}{k_{\mathrm{B}}T}\right) S_{[\mathrm{coh|inc}]}(\mathbf{Q},\omega)\,. \tag{3.113}$$

---

[18] This is one of the few instances where the sign of ω in its definition matters. Therefore, one should memorise the meaning of this sentence instead of formula (3.112).

[19] There is another condition for the validity of the classical calculation concerning the momentum transfer, $Q \ll \sqrt{2Mk_{\mathrm{B}}T}/\hbar$, where M is the mass of the scattering particle. The meaning of this condition is that the De Broglie wavelength of the scatterer should be sufficiently small compared to the length scale of the scattering experiment $1/Q$.

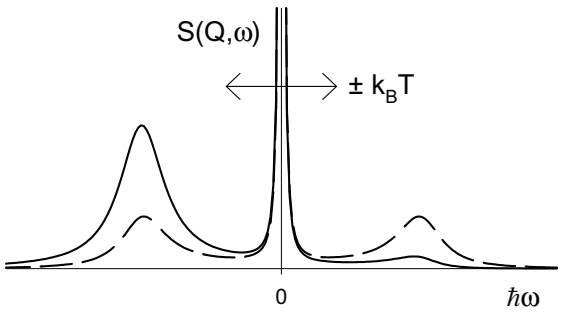

Figure 3.8: Example of the asymmetry of the scattering function due to the detailed balance factor. The (neutron) energy loss side is enhanced compared to the energy gain side for the correct quantum-mechanical result (continuous curve). The classical result (dashed curve) in contrast is mirror symmetric. The arrow indicates for comparison the thermal energy $\pm k_{\mathrm{B}}T$.

From the asymmetry of $S(\mathbf{Q},\omega)$ follows that the intermediate scattering function $I(\mathbf{Q},t)$ and the van Hove correlation function $G(\mathbf{r},t)$ are *complex*. This is surprising but allowed because they are (in contrast to within the classical treatment) no observable quantities[20] as $S(\mathbf{Q},\omega)$ which still has to be real. By inversion of the Fourier transform in time it follows for the intermediate scattering functions and the van Hove correlation functions:

$$I_{[\mathrm{coh|inc}]}(\mathbf{Q},-t) = I_{[\mathrm{coh|inc}]}\left(\mathbf{Q},t-\frac{\mathrm{i}\hbar}{k_{\mathrm{B}}T}\right) \tag{3.114}$$

$$G_{[\mathrm{s}]}(\mathbf{r},-t) = G_{[\mathrm{s}]}\left(\mathbf{r},t-\frac{\mathrm{i}\hbar}{k_{\mathrm{B}}T}\right) \tag{3.115}$$

The latter relations follow from the quantum-mechanical peculiarity that time-dependent operators in a correlation function may not be interchanged but $\langle\hat{A}(0)\hat{B}(t)\rangle = \langle\hat{B}(t-\mathrm{i}\hbar/k_{\mathrm{B}}T)\hat{A}(0)\rangle$ and $\langle\hat{A}(0)\hat{B}(t)\rangle^* = \langle\hat{B}^\dagger(t)\hat{A}^\dagger(0)\rangle$.

In many cases, the classical particle trajectories are much easier to derive that their quantum-mechanical counterparts. If a full quantum-mechanical result is not available, at least an approximation to the correct scattering functions can be derived [16] which

[20] Note that the neutron spin echo spectrometer, which is said to measure the intermediate scattering function, performs an inverse *cosine* Fourier transform instead of an exponential one. Therefore it actually measures only the real part of the intermediate scattering function.

fulfills the detailed balance relation (3.113). It is based on simply multiplying the square root of the prefactor in equation (3.113) neutron energy loss side and dividing it out of the energy gain side:

$$S_{[\mathrm{coh|inc}]}(\mathbf{Q},\omega) \approx \exp\left(-\frac{\hbar\omega}{2k_\mathrm{B}T}\right) S^{\mathrm{cl}}_{[\mathrm{coh|inc}]}(\mathbf{Q},\omega)\,. \tag{3.116}$$

The corresponding result for the intermediate scattering functions and the van Hove correlation functions results from shifting by half the imaginary time of expressions (3.114) and (3.115):

$$I_{[\mathrm{coh|inc}]}(\mathbf{Q},t) \approx I^{\mathrm{cl}}_{[\mathrm{coh|inc}]}\left(\mathbf{Q}, t+\frac{\mathrm{i}\hbar}{2k_\mathrm{B}T}\right) \tag{3.117}$$

$$G_{[\mathrm{s}]}(\mathbf{r},t) \approx G^{\mathrm{cl}}_{[\mathrm{s}]}\left(\mathbf{r}, t+\frac{\mathrm{i}\hbar}{2k_\mathrm{B}T}\right)\,. \tag{3.118}$$

3.4.1 Example 5: ideal gas

In order to demonstrate a full quantum-mechanical calculation, the calculation of the scattering function for an ideal gas is presented. Although this is possibly the simplest system one can imagine, the calculation is already rather intricate and relies on some knowledge of quantum-mechanical relations which cannot be derived here. The simplicity of the model is mainly based on the definition of an ideal gas, that particles do not interact. This implies that there are no correlations between different particles and the $i \neq j$ terms vanish in expressions as (3.59). Therefore, the incoherent and coherent quantities are equal for the ideal gas:

$$S_{\mathrm{coh}}(Q,\omega) = S_{\mathrm{inc}}(Q,\omega)\,,\; I_{\mathrm{coh}}(Q,t) = I_{\mathrm{inc}}(Q,t)\,,\; G(r,t) = G_{\mathrm{s}}(r,t)\,. \tag{3.119}$$

(Because the ideal gas is isotropic, r and Q are scalars.) In addition, all particles behave statistically in the same way and therefore the averages over all particles can be replaced by a single representative particle:

$$I(Q,t) = \frac{1}{N}\sum_{j=1}^{N}\left\langle \mathrm{e}^{-\mathrm{i}\mathbf{Q}\cdot\hat{\mathbf{r}}_j(0)}\mathrm{e}^{\mathrm{i}\mathbf{Q}\cdot\hat{\mathbf{r}}_j(t)}\right\rangle = \left\langle \mathrm{e}^{-\mathrm{i}\mathbf{Q}\cdot\hat{\mathbf{r}}_1(0)}\mathrm{e}^{\mathrm{i}\mathbf{Q}\cdot\hat{\mathbf{r}}_1(t)}\right\rangle\,. \tag{3.120}$$

Writing out the Heisenberg operator $\hat{\mathbf{r}}_1(t)$ in its explicit form one obtains

$$I(Q,t) = \left\langle \mathrm{e}^{-\mathrm{i}\mathbf{Q}\cdot\hat{\mathbf{r}}_1(0)}\mathrm{e}^{\mathrm{i}\hat{\mathcal{H}}_1 t/\hbar}\mathrm{e}^{\mathrm{i}\mathbf{Q}\cdot\hat{\mathbf{r}}_1(t)}\mathrm{e}^{-\mathrm{i}\hat{\mathcal{H}}_1 t/\hbar}\right\rangle \tag{3.121}$$

where $\hat{\mathcal{H}}_1$ is the Hamiltonian of the representative particle which is simply the square of the momentum operator divided by twice the scattering particle's mass:

$$\hat{\mathcal{H}}_1 = \frac{1}{2M}\hat{\mathbf{p}}^2 \,. \tag{3.122}$$

Taking into account that the operator $\mathrm{e}^{-\mathrm{i}\mathbf{Q}\cdot\hat{\mathbf{r}}_1}$ shifts the momentum

$$\mathrm{e}^{-\mathrm{i}\mathbf{Q}\cdot\hat{\mathbf{r}}_1}\hat{p}\mathrm{e}^{\mathrm{i}\mathbf{Q}\cdot\hat{\mathbf{r}}_1} = \hat{p} + \hbar\mathbf{Q} \tag{3.123}$$

one gets

$$I(Q,t) = \left\langle \mathrm{e}^{\mathrm{i}\hat{\mathcal{H}}_1' t/\hbar}\mathrm{e}^{-\mathrm{i}\hat{\mathcal{H}}_1 t/\hbar}\right\rangle \tag{3.124}$$

where $\hat{\mathcal{H}}_1'$ denotes the single-particle Hamiltonian with shifted momentum:

$$\hat{\mathcal{H}}_1' = \frac{1}{2M}\left(\hat{\mathbf{p}} + \hbar\mathbf{Q}\right)^2 = \hat{\mathcal{H}}_1 + \frac{\hbar}{M}\mathbf{Q}\cdot\hat{\mathbf{p}} + \frac{\hbar^2 Q^2}{2M} \,. \tag{3.125}$$

Insertion of (3.125) into (3.124) yields:

$$I(Q,t) = \mathrm{e}^{\mathrm{i}\hbar t Q^2/2M}\left\langle \mathrm{e}^{\mathrm{i}t\mathbf{Q}\cdot\hat{\mathbf{p}}/M}\right\rangle \tag{3.126}$$

The thermodynamic average in this expression can be calculated with the equilibrium distribution of momenta. Here, a Boltzmann distribution is assumed:

$$\left\langle \mathrm{e}^{\mathrm{i}t\mathbf{Q}\cdot\hat{\mathbf{p}}}\right\rangle = \int \mathrm{d}^3p\, \mathrm{e}^{-\frac{p^2}{2Mk_\mathrm{B}T}}\mathrm{e}^{\mathrm{i}t\mathbf{Q}\cdot\mathbf{p}} \Big/ \int \mathrm{d}^3p\, \mathrm{e}^{-\frac{p^2}{2Mk_\mathrm{B}T}} = \mathrm{e}^{-Q^2t^2k_\mathrm{B}T/2M} \,. \tag{3.127}$$

From (3.126) and (3.127) the intermediate scattering function is finally obtained:

$$I(Q,t) = \exp\left(-\frac{Q^2}{2M}\left(k_\mathrm{B}Tt^2 + \mathrm{i}\hbar t\right)\right) \,. \tag{3.128}$$

In the same way as the Fourier transform of the Gaussian (3.168), the Fourier transform of (3.128) can be calculated yielding

$$S(Q,\omega) = \sqrt{\frac{M}{2\pi k_\mathrm{B}TQ^2}}\exp\left(-\frac{M}{2\pi k_\mathrm{B}TQ^2}\left(\omega + \frac{\hbar Q^2}{2M}\right)^2\right) \,. \tag{3.129}$$

The scattering function is a Gaussian distribution around $-\hbar Q^2/2M$ (Fig. 3.9) showing that on average the neutrons lose the 'recoil energy' $E_\mathrm{r} = \hbar^2Q^2/2M$ during the scattering event. The width of the Gaussian, $\sqrt{k_\mathrm{B}T/M}\hbar Q$ increases with temperature and scattering 'vector' Q.

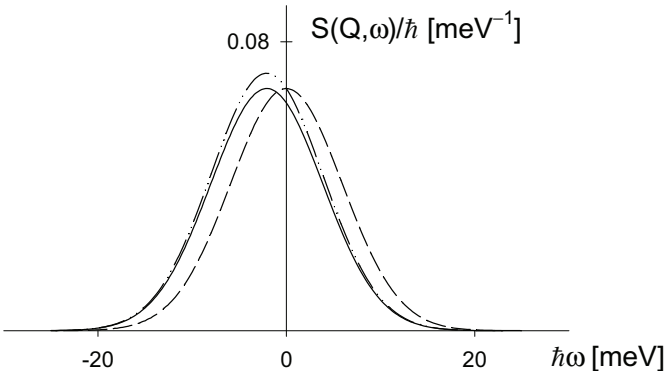

Figure 3.9: Scattering from an ideal gas calculated with the parameters of helium at 100 K for $Q = 2$ Å^{-1}. The continuous curve shows the correct quantum-mechanical result, the dashed curve that of a classical calculation. The dot-dashed curve represents the approximation resulting from applying (3.116) to the classical result.

The van Hove correlation function can be calculated immediately by inverse Fourier transform from (3.128) because $I(Q,t)$ is also a Gaussian in Q:

$$G(r,t) = \left(\frac{M}{2\pi k_\mathrm{B}Tt(t+\mathrm{i}\hbar/k_\mathrm{B}T)}\right)^{3/2} \exp\left(-\frac{Mr^2}{2k_\mathrm{B}Tt(t+\mathrm{i}\hbar/k_\mathrm{B}T)}\right) . \tag{3.130}$$

To demonstrate the differences arising from a classical calculation, the classical intermediate scattering function will be derived too. Because of the identity of the particles (3.64) reduces to

$$I^\mathrm{cl}(Q,t) = \left\langle \mathrm{e}^{\mathrm{i}\mathbf{Q}\cdot(\mathbf{r}_1(t)-\mathbf{r}_1(0))}\right\rangle . \tag{3.131}$$

In an ideal gas the trajectory of a particle is $\mathbf{r}_1(t) = \mathbf{r}_1(0) + \mathbf{v}t$ yielding:

$$I^\mathrm{cl}(Q,t) = \left\langle \mathrm{e}^{\mathrm{i}\mathbf{Q}\cdot\mathbf{v}t}\right\rangle . \tag{3.132}$$

This thermodynamic average can be calculated using the Maxwell distribution of velocities:

$$P(v) = \sqrt{\frac{2\pi k_\mathrm{B}T}{M}} \exp\left(-\frac{Mv^2}{2k_\mathrm{B}T}\right) \tag{3.133}$$

resulting in

$$I^\mathrm{cl}(Q,t) = \exp\left(-\frac{k_\mathrm{B}TQ^2t^2}{2M}\right) . \tag{3.134}$$

In contrast to the quantum-mechanical $I(Q,t)$ (3.128), this quantity is real and (accidentally for the ideal gas) $= |I(Q,t)|$. Because $I^\mathrm{cl}(Q,t)$ is a Gaussian in both Q and r,

the Fourier transforms can be calculated by direct application of (3.168). The scattering function is

$$S^{\mathrm{cl}}(Q,\omega) = \sqrt{\frac{M}{2\pi k_{\mathrm{B}} T Q^2}} \exp\left(-\frac{M\omega^2}{2\pi k_{\mathrm{B}} T Q^2}\right) . \tag{3.135}$$

a Gaussian of the same width as the quantum-mechanical result (3.129) but centred around zero energy transfer (Fig. 3.9). Thus, classically neutrons are scattered with no average energy transfer. The classical van Hove correlation function

$$G^{\mathrm{cl}}(r,t) = \left(\frac{m_{\mathrm{sc}}}{2\pi k_{\mathrm{B}} T t^2}\right)^{3/2} \exp\left(-\frac{m_{\mathrm{sc}} r^2}{2k_{\mathrm{B}} T t^2}\right) \tag{3.136}$$

conveys the meaning that at any time the distribution of distances travelled by particles of an ideal gas is Gaussian with a width increasing linearly in time.

Finally, the approximations of the correct quantum-mechanical results from the classical using (3.117) and (3.116) are

$$\tilde{I}(Q,t) = \exp\left(-\frac{k_{\mathrm{B}} T Q^2}{2M}\left(t + \frac{\mathrm{i}\hbar}{2k_{\mathrm{B}} T}\right)^2\right) \quad \text{and} \tag{3.137}$$

$$\tilde{S}(Q,\omega) = \sqrt{\frac{M}{2\pi k_{\mathrm{B}} T Q^2}} \exp\left(-\frac{M}{2\pi k_{\mathrm{B}} T Q^2}\left(\omega^2 + \frac{\hbar Q^2}{M}\omega\right)\right) . \tag{3.138}$$

It can be seen (Fig. 3.9) that the approximation captures the shift by the recoil energy correctly but the normalisation is wrong: $\int \tilde{S}(Q,\omega)\mathrm{d}\omega = \tilde{I}(Q,0) = \exp(\hbar^2 Q^2/8Mk_{\mathrm{B}}T) \neq 1$. Nevertheless, equations (3.137) and (3.138) are different from (3.128) and (3.129) only in the order $\hbar^2$, which makes them better approximations that the purely classical results deviating already in $\hbar^1$ terms.

3.5 Appendix: elementary properties of the Fourier transform

In this section only those properties of the Fourier transform will be recapitulated which are relevant for the understanding of the results on scattering presented in the lecture. A broader introduction to Fourier transforms (still with an emphasis on the applications in scattering theory) is presented in the previous edition of this course [1]. The proofs of the theorems will mostly only be sketched. For the mathematically more inclined reader refs. 17–19 are recommended.

According to the dominant standard in neutron scattering the Fourier transform will be defined as

$$F(X) = \int_{-\infty}^{\infty} f(x) \exp(\mathrm{i}Xx)\mathrm{d}x\,. \tag{3.139}$$

Wherever possible I will use the functional notation

$$\mathcal{F}_{X|\,x}[f(x)] = \int_{-\infty}^{\infty} f(x) \exp(\mathrm{i}Xx)\mathrm{d}x\,. \tag{3.140}$$

to abbreviate the Fourier integral. The inversion of the FT (3.139) is:

$$f(x) = \mathcal{F}^{-1}_{x|\,X}[F(X)] = \frac{1}{2\pi}\int_{-\infty}^{\infty} F(X) \exp(-\mathrm{i}Xx)\mathrm{d}X\,. \tag{3.141}$$

The proof that (3.141) is the inverse of (3.139) is not simple and can be found in ref. 17.

A straightforward generalisation of the FT is that to multiple dimensions. The most important case of three dimensions is:

$$F(X,Y,Z) = \int_{-\infty}^{\infty}\mathrm{d}x\int_{-\infty}^{\infty}\mathrm{d}y\int_{-\infty}^{\infty}\mathrm{d}z \exp(\mathrm{i}Xx)\exp(\mathrm{i}Yy)\exp(\mathrm{i}Zz)f(x,y,z)\,. \tag{3.142}$$

The arguments of the exponentials can be grouped together and replaced by the scalar product of the vector $\mathbf{r} = (x,y,z)$ and the 'reciprocal space' vector $\mathbf{Q} = (X,Y,Z)$:

$$F(\mathbf{Q}) = \int \exp(\mathrm{i}\mathbf{Q}\cdot\mathbf{r})f(\mathbf{r})\mathrm{d}^3r\,. \tag{3.143}$$

The inversion is obviously

$$f(\mathbf{r}) = \frac{1}{(2\pi)^3}\int \exp(-\mathrm{i}\mathbf{Q}\cdot\mathbf{r})F(\mathbf{Q})\mathrm{d}^3r \tag{3.144}$$

with one $1/2\pi$ pre-factor for each of the individual coordinates' transform.

An important special case of the 3D FT is that of isotropic functions, where the functions only depend on the absolute values $r = \|\mathbf{r}\| = \sqrt{x^2+y^2+z^2}$ and $Q = \|\mathbf{Q}\|$. In spherical polar coordinates (3.143) reads:

$$F(Q) = \int_0^{\infty}\mathrm{d}r\int_0^{\pi}\mathrm{d}\theta\int_0^{2\pi}\mathrm{d}\phi\; r^2\sin\theta\exp(\mathrm{i}\mathbf{Q}\cdot\mathbf{r})f(\mathbf{r}) =$$

Because of the symmetry one can assume $\mathbf{Q} = (0,0,Q)$ without loss of generality. Then $\mathbf{Q}\cdot\mathbf{r} = Qr\cos\theta$. In addition, because $f(\mathbf{r})$ does not depend on ϕ the integral over this angle can be carried out: $\int_0^{2\pi}\mathrm{d}\phi = 2\pi$. With this we get:

$$= \int_0^{\infty}\mathrm{d}r\int_0^{\pi}\mathrm{d}\theta\; 2\pi r^2\sin\theta\exp(\mathrm{i}Qr\cos\theta)f(r) =$$

Here, we substitute $\cos\theta \to t$ with the consequence that $\mathrm{d}t = -\sin\theta \mathrm{d}\theta$:

$$= -\int_0^\infty \mathrm{d}r\; 2\pi r^2 \int_1^{-1} \mathrm{d}t \exp(\mathrm{i}Qrt) f(r) =$$

Because only $\exp(\mathrm{i}Qrt)$ depends on t the integration can be carried out resulting in

$$= \int_0^\infty \frac{\sin(Qr)}{Qr} f(r) 4\pi r^2 \mathrm{d}r = \frac{4\pi}{Q} \int_0^\infty f(r) r \sin(Qr) \mathrm{d}r \,. \tag{3.145}$$

Similarly it can be shown that the inverse FT is

$$f(r) = \frac{1}{2\pi^2 r} \int_0^\infty F(Q) Q \sin(Qr) \mathrm{d}Q \,. \tag{3.146}$$

Often the function to be transformed, $f(x)$, corresponds to a physical observable and thus is a real function $f(x) \in \mathbb{R}$. It can be easily shown from the definition (3.139) that in this case

$$\mathcal{F}_{X|x}[f(-x)] = \mathcal{F}_{-X|x}[f(x)] = \left(\mathcal{F}_{X|x}[f(x)]\right)^* \tag{3.147}$$

where the star denotes the complex conjugate defined as $(a + b\mathrm{i})^* = a - b\mathrm{i}$. In words: The Fourier transform of the mirror image of a *real* function is the complex conjugate of the original function. This implies that the Fourier transform of an even function is real and that of a real function is even.

In order to describe point scatterers (e.g. nuclei being orders of magnitude smaller than the scattered wave) it is convenient to introduce the delta 'function' as the following limit:

$$\delta(x) = \lim_{a \to 0} \begin{cases} 1/a & \text{for } |x| < a/2 \\ 0 & \text{everywhere else} \end{cases} \,. \tag{3.148}$$

When the limit is carried out the delta function is everywhere zero except for $x = 0$ where it has an infinite value. What is important is that the area under the function is always one during the whole limiting process. Therefore, it can be concluded that $\int_{-\infty}^{\infty} \delta(x) \mathrm{d}x = 1$. This integral condition and the fact that only the value at $x = 0$ does not vanish are the only characteristics of the delta function. Therefore, different definitions by limits are possible, e.g. by narrowing Gaussian functions. It is somehow justified to say that the delta function is the Black Hole of mathematics, where every individuality of the function is lost as that of a star when it collapses.

The property making the delta function interesting is that it is able to pull out a single value of a function from a definite integral:

$$\int_{-\infty}^{\infty} \delta(x) f(x) \mathrm{d}x = \lim_{a \to 0} \frac{1}{a} \int_{-a/2}^{a/2} f(x) \mathrm{d}x =$$

Because in the limit of small a the function does not vary much over the interval $[-a/2, a/2]$ it can be replaced by its value at the centre, $f(0)$:

$$= \lim_{a\to 0} \frac{1}{a}\, a f(0) = f(0)\,. \tag{3.149}$$

From the basic property of the delta function (3.149) follows that the FT as the integral (3.139) is

$$\mathcal{F}_{X|\,x}[\delta(x)] = \int_{-\infty}^{\infty} \exp(\mathrm{i}Xx)\delta(x)\mathrm{d}x = 1\,, \tag{3.150}$$

i.e. the FT of the delta function is the constant function $F(X) = 1$. By writing down the inversion formula (3.141) one obtains that the iFT of a constant is a delta function:

$$\mathcal{F}^{-1}_{x|\,X}[1] = \frac{1}{2\pi}\int_{-\infty}^{\infty} \exp(-\mathrm{i}Xx)\mathrm{d}x = \delta(x)\,. \tag{3.151}$$

(At this point it is important not to forget the 2π!) Because in the last two formulae $\mathrm{i}Xx$ can be replaced by $-\mathrm{i}Xx$ it is of course also true that the iFT of the delta function is a constant $(1/2\pi)$ and the FT of a constant a delta function multiplied by 2π:

$$\mathcal{F}^{-1}_{x|\,X}[\delta(X)] = \frac{1}{2\pi}\,, \tag{3.152}$$

$$\mathcal{F}_{X|\,x}[1] = 2\pi\delta(x)\,. \tag{3.153}$$

There are a couple of theorems on definite integrals including FTs which in physics are usually called 'sum rules'. The simplest of these is that for the infinite integral of the FT itself:

$$\begin{aligned}\int_{-\infty}^{\infty} \mathcal{F}_{X|\,x}[f(x)]\mathrm{d}X &= \int_{-\infty}^{\infty}\mathrm{d}X\int_{-\infty}^{\infty}\mathrm{d}x\exp(iXx)f(x)\\ &= \int_{-\infty}^{\infty} f(x)2\pi\delta(x)\mathrm{d}x = 2\pi f(0)\,.\end{aligned} \tag{3.154}$$

(using that $\int_{-\infty}^{\infty}\mathrm{d}x\exp(iXx)$ is the FT of constant 1, see (3.153).) Here, it is assumed that the integrals over X and x are interchangeable which may cause problems for certain functions. Often it may be necessary to interpret the integral over X as Cauchy principal value and handle discontinuities in $f(x)$ by imposing Dirichlet's condition, $f(a) = (\lim_{x\searrow a} f(x) + \lim_{x\nearrow a} f(x))/2$.

The complementary sum rule is even simpler to derive:

$$\mathcal{F}_{0|\,x}[f(x)] = \int_{-\infty}^{\infty} f(x)\exp(\mathrm{i}0x)\mathrm{d}x = \int_{-\infty}^{\infty} f(x)\mathrm{d}x\,. \tag{3.155}$$

We see that the infinite integral of a FT corresponds to the value of the original function at zero (up to a factor 2π) and vice versa.

The *convolution*[21] of two functions is defined as follows:

$$f \otimes g(x) = \int_{-\infty}^{\infty} f(t)g(x-t)\mathrm{d}t\,. \tag{3.156}$$

One of the most important theorems on FTs is that the FT of a convolution is the product of the individual FTs:

$$\mathcal{F}_{X|x}[f \otimes g(x)] = \mathcal{F}_{X|x}[f(x)] \cdot \mathcal{F}_{X|x}[g(x)] = F(X)G(X) \tag{3.157}$$

or vice versa:

$$\mathcal{F}_{X|x}[f(x)g(x)] = \mathcal{F}_{X|x}[f(x)] \otimes \mathcal{F}_{X|x}[g(x)] = F(X) \otimes G(X)\,. \tag{3.158}$$

Proof of relation (3.157): From the definition (3.139) follows straightforwardly:

$$\begin{aligned}
\mathcal{F}_{X|x}[f \otimes g(x)] &= \int_{-\infty}^{\infty} \exp(\mathrm{i}Xx) \left(\int_{-\infty}^{\infty} f(t)g(x-t)\mathrm{d}t \right) \mathrm{d}x \\
&= \int_{-\infty}^{\infty} \mathrm{d}x \int_{-\infty}^{\infty} \mathrm{d}t \exp(\mathrm{i}Xx) f(t)g(x-t) \\
&= \int_{-\infty}^{\infty} \mathrm{d}x \int_{-\infty}^{\infty} \mathrm{d}t \exp(\mathrm{i}X(x-t)) \exp(\mathrm{i}Xt) f(t)g(x-t) \\
&= \int_{-\infty}^{\infty} \mathrm{d}t \int_{-\infty}^{\infty} \mathrm{d}x \exp(\mathrm{i}X(x-t)) \exp(\mathrm{i}Xt) f(t)g(x-t) \qquad (3.159)
\end{aligned}$$

Substituting $x - t \to x'$ leaves the infinite bounds of the first integral unchanged:

$$\begin{aligned}
&= \int_{-\infty}^{\infty} \mathrm{d}t \int_{-\infty}^{\infty} \mathrm{d}x' \exp(\mathrm{i}Xx') \exp(\mathrm{i}Xt) f(t)g(x') \\
&= \int_{-\infty}^{\infty} \exp(\mathrm{i}Xt) f(t)\mathrm{d}t \int_{-\infty}^{\infty} \exp(\mathrm{i}Xx')g(x')\mathrm{d}x' \\
&= \mathcal{F}_{X|x}[f(x)] \cdot \mathcal{F}_{X|x}[g(x)] \qquad (3.160)
\end{aligned}$$

Note that the critical step of this proof is the exchange of integrations at line (3.159). For some 'crazy' functions this may not be allowed and in consequence the convolution theorem does not hold. Nevertheless, for 'physical' functions this is usually no issue.

Closely related to the convolution is the correlator (or correlation function) of two functions:

$$\langle f(0)g(x) \rangle = \int_{-\infty}^{\infty} f(t)g(x+t)\mathrm{d}t\,. \tag{3.161}$$

---

[21] German: Faltung (sometimes also used in English)

By a substitution $t \to -t'$ it is easy to show that

$$\langle f(0)g(x)\rangle = f(-x) \otimes g(x) \tag{3.162}$$

so that the correlator is just the convolution with one of the functions mirrored. Using the convolution theorem and (3.147) in succession, it follows that the FT of the correlator of real functions is the product of the FTs of the correlated functions with one FT conjugated, i.e.

$$\mathcal{F}_{X|x}[\langle f(0)g(x)\rangle] = \mathcal{F}_{-X|x}[f(x)]\mathcal{F}_{X|x}[g(x)] = F^*(X)G(X)\,. \tag{3.163}$$

In physics the most important special case is the autocorrelation function where $f = g$:

$$\mathcal{F}_{X|x}[\langle f(0)f(x)\rangle] = F^*(X)F(X) = |F(X)|^2\,. \tag{3.164}$$

This relation, which expresses that the autocorrelation function $\langle f(0)f(t)\rangle$ and the power spectrum $|F(\omega)|^2$ of a signal $f(t)$ are related by a FT, is known as the Wiener-Khintchine theorem.

Only two concrete examples of FTs will be presented here, the exponential/Lorentzian FT pair and the Gaussian function. Interestingly, together with clever use of the rules on Fourier transforms these may cover 90 % of all physical problems. If there is really the necessity to obtain the FT of other functions they may be found in table books as ref. 20. In some cases it may even be more effective to look up the Fourier integral (3.139) in a table of definite integrals. The (according to the experience of the author) most extensive compilation of such integrals can be found in ref. 21.

Exponential decay: Because the exponential $\exp(-ax)$ diverges for x going to negative infinity one cannot FT it with the two-sided transform. One has either to use a one sided transform or define a function

$$f(x) = \begin{cases} 0 & \text{for } x < 0 \\ \exp(-ax) & \text{for } x > 0 \end{cases} \tag{3.165}$$

which is cut-off at $x = 0$. This makes also sense in most of the physical contexts, e.g. thinking of the current of a capacitor which is discharged by closing a circuit with a resistor at time zero. The Fourier integral (3.139) becomes then

$$\int_0^\infty \exp(\mathrm{i}Xx)\exp(-ax)\mathrm{d}x = \int_0^\infty \exp((\mathrm{i}X - a)x)\mathrm{d}x = \tag{3.166}$$

The indefinite integral of the exponential is known, $\int \exp(Ax) = \exp(Ax)/A$, thus one continues the calculation

$$= \left.\frac{\exp((\mathrm{i}X - a)x)}{\mathrm{i}X - a}\right|_0^\infty = \frac{1}{a - \mathrm{i}X} = \frac{a}{a^2 + X^2} + \frac{X}{a^2 + X^2}\,\mathrm{i}\,.$$

The real part (which is usually the physically relevant) is a so-called Lorentzian function which peaks at $X = 0$ and has a full width at half maximum of $2a$. Reverting to the interpretation as a decay in time, a is related to the time constant by $a = 1/\tau$. This means that the decay time and the width of the Lorentzian in frequency are inversely proportional.

Gaussian: The bell-shaped curve of the Gaussian (or 'normal') distribution

$$f(x) = \frac{1}{\sqrt{2\pi}\sigma} \exp\left(-\frac{x^2}{2\sigma^2}\right) \tag{3.167}$$

decays to both sides rapidly enough and can thus be FTed two-sidedly. The Fourier integral is:

$$\int_{-\infty}^{\infty} \exp(\mathrm{i}Xx) \frac{1}{\sqrt{2\pi}\sigma} \exp\left(-\frac{x^2}{2\sigma^2}\right) \mathrm{d}x = \frac{1}{\sqrt{2\pi}\sigma} \int_{-\infty}^{\infty} \exp\left(\mathrm{i}Xx - \frac{x^2}{2\sigma^2}\right) \mathrm{d}x =$$

In order to simplify the integral we are going to 'complete the square'[22] inside the exponential by adding $\sigma^2 X^2/2$ and compensating this by a factor in front of the integral:

$$\begin{aligned} &= \frac{1}{\sqrt{2\pi}\sigma} \exp\left(-\frac{\sigma^2 X^2}{2}\right) \int_{-\infty}^{\infty} \exp\left(-\frac{x^2}{2\sigma^2} + \mathrm{i}Xx + \frac{\sigma^2 X^2}{2}\right) \mathrm{d}x \\ &= \frac{1}{\sqrt{2\pi}\sigma} \exp\left(-\frac{\sigma^2 X^2}{2}\right) \int_{-\infty}^{\infty} \exp\left(-\frac{(x - \mathrm{i}\sigma^2 X)^2}{2\sigma^2}\right) \mathrm{d}x = \end{aligned}$$

The definite integral of the Gaussian distribution always fulfills the normalisation property $(1/\sqrt{2\pi}\sigma) \int_{-\infty}^{\infty} \exp(-(x - A)^2/2\sigma^2)\mathrm{d}x = 1$, irrespectively of its centre A. Therefore, the simple result is:

$$= \exp\left(-\frac{\sigma^2 X^2}{2}\right)\,. \tag{3.168}$$

This means that the FT of a Gaussian is a Gaussian, a property which is called 'self-reciprocity'. It is shared by all Hermite functions of which the Gaussian is the simplest [18]. Nevertheless, the Fourier transform is not the *same* Gaussian but one with the reciprocal standard deviation $1/\sigma$ of the original Gaussian. Also the FT is not normalised to one but its maximum is fixed to one. This in turn causes that the area under the FT Gaussian is $\int_{-\infty}^{\infty} \exp(-\sigma^2 X^2/2)\mathrm{d}x = \sqrt{2\pi}/\sigma$.

[22] German: quadratische Ergänzung

References

[1] R. Zorn: "Fourier Transforms" in T. Brückel, G. Heger, D. Richter, R. Zorn (eds.): "Neutron Scattering" (Forschungszentrum Jülich, 2008, `http://hdl.handle.net/2128/37180`), chapter I.

[2] R. Zorn, D. Richter: "Correlation Functions Measured by Scattering Experiments", ibidem, chapter 4.

[3] S. W. Lovesey: "Theory of Neutron Scattering from Condensed Matter" (Clarendon Press, Oxford, 1984).

[4] G. L. Squires: "Introduction to the theory of thermal neutron scattering" (Cambridge University Press, Cambridge, 1978).

[5] G. E. Bacon: "Neutron Diffraction" (Clarendon Press, Oxford, 1975).

[6] G. E. Bacon (ed.): "Fifty Years Of Neutron Diffraction: The Advent Of Neutron Scattering" (Adam Hilger, Bristol, 1986).

[7] M. Bée: "Quasielastic neutron scattering" (Adam Hilger, Bristol, 1988).

[8] O. Spalla: "General Theorems in Small-Angle Scattering" in P. Lindner, Th. Zemb (eds.): "Neutrons, X-rays and Light: Scattering Methods Applied to Soft Condensed Matter" (Elsevier, Amsterdam, 2002), pp. 49–72

[9] O. Glatter: "The Inverse Scattering Problem in Small-Angle Scattering", ibidem, pp. 73–102.

[10] R. Klein: "Interacting Colloidal Suspensions", ibidem, pp. 351–380.

[11] G. Placzek, *Phys. Rev.* **86** 377 (1952).

[12] J. L. Yarnell, M. J. Katz, R. G. Wenzel, S. H. Koenig, *Phys. Rev. A* **7** 2130 (1973).

[13] W. van Megen, T. C. Mortensen, S. R. Williams, and J. Müller, Phys. Rev. E **58**, 6073 (1998)

[14] A. Rahman, K. S. Singwi, A. Sjölander, *Phys. Rev.* **126**, 986 (1962).

[15] R. Zorn, *Nucl. Instr. Meth. A* **603**, 439 (2009)

[16] P. Schofield, *Phys. Rev. Lett.* **4**, 239 (1960).

[17] K. B. Howell: "Principles of Fourier Analysis" (Chapman & Hall/CRC, Boca Raton, 2001).

[18] H. J. Weaver: "Theory of discrete and continuous Fourier analysis" (John Wiley & Sons, New York, 1988).

[19] J. Kauppinen, J. Partanen: "Fourier Transforms in Spectroscopy" (Wiley-VCH, Berlin, 2001).

[20] F. Oberhettinger: "Tables of Fourier Transforms and Fourier Transforms of Distributions" (Springer, Berlin, 1990).

[21] A. P. Prudnikov, Yu. A. Brychkov, O. I. Marichev: "Integrals and Series" (Gordon and Breach, New York 1986–1992).

4

Symmetry of Crystals

Gernot Heger

4. Symmetry of Crystals

G. Heger

4.1 Introduction

The term “crystal” comes from the Greek κρύσταλλος , which was first used as description of ice and later on - more general - of transparent minerals with regular morphology (regular crystal faces and edges).

Fig. 1. Example: rock crystal – quartz (SiO_2), mineral from the Gotthard-Massif.

Matter is usually classified into three states: gaseous – liquid – solid. Crystals are representatives of the solid state. **Crystalline solids are thermodynamically stable** in contrast to glasses and are **characterised by a regular three-dimensional periodic arrangement of atoms (ions, molecules) in space**.

4.2 Crystal lattices

The three-dimensional periodicity of crystals can be represented by the so-called crystal lattice. The repeat unit in form of a parallelepiped - known as the **unit cell** – is defined by 3 non-linear basis vectors $\boldsymbol{a_1}$, $\boldsymbol{a_2}$, and $\boldsymbol{a_3}$, whose directions form the reference axes *X*, *Y*, and *Z* of the corresponding right-handed crystallographic coordination system. The 6 lattice parameters are given as the lengths of the basis vectors $a = |\boldsymbol{a_1}|$, $b = |\boldsymbol{a_2}|$, $c = |\boldsymbol{a_3}|$ and the angles between the basis vectors: angle $(\boldsymbol{a_1},\boldsymbol{a_2}) = \gamma$, angle $(\boldsymbol{a_2},\boldsymbol{a_3}) = \alpha$, angle $(\boldsymbol{a_3},\boldsymbol{a_1}) = \beta$. The faces of the unit cell are named as face $(\boldsymbol{a_1},\boldsymbol{a_2})$ = C**,** face $(\boldsymbol{a_2},\boldsymbol{a_3})$ = A**,** face $(\boldsymbol{a_3},\boldsymbol{a_1})$ = B.

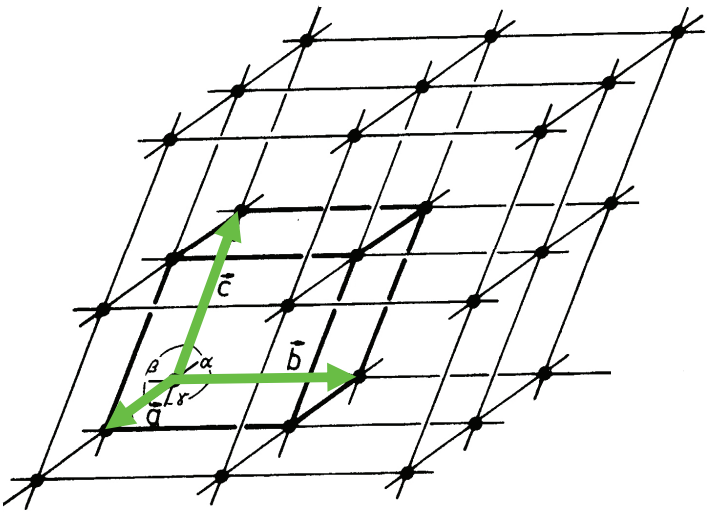

Fig. 2. Notation for a unit cell and a point lattice.

If the vertices of all repeat units (unit cells) are replaced by points, there results the crystal lattice in the form of a **point lattice**. Each lattice point is given by a vector $\boldsymbol{a} = u\boldsymbol{a}_1+v\boldsymbol{a}_2+w\boldsymbol{a}_3$, with u, v, w being integers. As a symmetry operation of parallel displacement, $\boldsymbol{a}$ – also known as **translation vector** – maps the atomic arrangement of the crystal (crystal structure) onto itself.

A **lattice point** is named "*uvw*", according to the coefficients (integers) of the translation vector $\boldsymbol{a} = u\boldsymbol{a}_1+v\boldsymbol{a}_2+w\boldsymbol{a}_3$ from the origin to the lattice point. A **lattice direction** - given by the symbol [*uvw*] - is defined by the direction of the corresponding translation vector.

A plane passing through three lattice points is known as a **lattice plane**. Since all lattice points are equivalent (by translation symmetry) there will be infinitely many parallel planes passing through all the other points of the lattice. Such a set of equally spaced planes is known as a **set of lattice planes**. If the first plane from the origin of a set of lattice planes makes intercepts a/h, b/k, c/l on the X, Y, Z axes, respectively, where h, k, l are integers, then the **Miller indices** of this set of lattice planes are (hkl), the three factors h, k, l being enclosed in parentheses.

The equation of lattice planes can be written in intercept form as

$$(h\mathrm{x}/a) + (k\mathrm{y}/b) + (l\mathrm{z}/c) = \mathrm{n}, \qquad (1)$$

where n is an integer. If n = 0 the lattice plane passes through the origin; if n = 1 the plane makes intercepts a/h, b/k, c/l on the X, Y, Z axes respectively; if n = 2 the intercepts are $2a/h$, $2b/k$, $2c/l$; and so on.

The line of intersection of any two non-parallel lattice planes is a row of lattice-points common to both planes. This lattice point row defines a lattice direction [*uvw*] which is known as **zone axis**. All lattice planes intersecting in a common lattice-point row are said to lie in the same **zone**. The condition for lattice planes to be parallel to a lattice vector $\boldsymbol{a} = u\boldsymbol{a_1}+v\boldsymbol{a_2}+w\boldsymbol{a_3}$ is the **zone equation**

$$uh + vk + wl = 0 \qquad (2)$$

The zone axis symbol [*uvw*] for the zone containing the two planes ($h_1k_1l_1$) and ($h_2k_2l_2$) is obtained by solving the simultaneous equations $uh_1 + vk_1 + wl_1 = 0$ and $uh_2 + vk_2 + wl_2 = 0$,

$$[uvw] = [k_1l_2\text{-}k_2l_1,\ l_1h_2\text{-}l_2h_1,\ h_1k_2\text{-}h_2k_1]. \qquad (3)$$

4.3 Crystallographic coordinate systems

The description of a crystal structure consists first of the choice of a unit cell as smallest repeat unit of the crystal with its basis vectors. In this way a crystal-specific coordinate system is defined which is used to localize all the atoms in the unit cell. Whereas in physics and chemistry usually Cartesian coordinate systems are used, in crystallography quite different systems are applied. The conventional crystallographic coordinate systems are based on the symmetry of the crystals. In three dimensions there exist 7 different crystal systems and hence 7 crystallographic coordinate systems:

system name	minimum symmetry	conventional unit cell
triclinic	1 or $\bar{1}$	$a \neq b \neq c$; $\alpha \neq \beta \neq \gamma$
monoclinic (unique axis b)	one diad – 2 or m ($\parallel Y$)	$a \neq b \neq c$; $\alpha=\gamma=90°$, $\beta>90°$
orthorhombic	three mutually perpendicular diads – 2 or m ($\parallel X$, Y and Z)	$a \neq b \neq c$; $\alpha=\beta=\gamma=90°$
tetragonal	one tetrad – 4 or $\bar{4}$ ($\parallel Z$)	$a = b \neq c$; $\alpha=\beta=\gamma=90°$
trigonal (hexagonal cell)	one triad – 3 or $\bar{3}$ ($\parallel Z$)	$a = b \neq c$; $\alpha=\beta=90°$, $\gamma=120°$
hexagonal	one hexad – 6 or $\bar{6}$ ($\parallel Z$)	$a = b \neq c$; $\alpha=\beta=90°$, $\gamma=120°$
cubic	four triads – 3 or $\bar{3}$ ($\parallel$ space diagonals of cube)	$a = b = c$; $\alpha=\beta=\gamma=90°$

The choice of the origin of the coordinate system is free in principle, but for convenience it is usually chosen in a centre of symmetry (inversion centre), if present, otherwise in a point of high site symmetry of the space group.

In order to complete the symmetry conventions of the coordinate systems it is necessary to add to the 7 so-called primitive unit cells of the crystal systems (primitive lattice types with only one lattice point per unit cell) 7 centred unit cells with two, three or four lattice points per unit cell (centred lattice types). These centred unit cells are consequently two, three or four times larger than the smallest repeat units of the crystals. The resulting 14 **Bravais lattice types** with their centring conditions are collected in Fig. 3.

A set of lattice planes (*hkl*) is separated by a characteristic interplanar spacing *d*(*hkl*). According to the different crystallographic coordinate systems these *d*(*hkl*) values are calculated in a specific manner:

For the cubic lattice ($a = b = c$, $\alpha = \beta = \gamma = 90°$), ex. NaCl

$$d(hkl) = a \cdot \left(h^2 + k^2 + l^2\right)^{-\frac{1}{2}}$$

For the hexagonal lattice ($a = b$, c, $\alpha = \beta = 90°$, $\gamma = 120°$), ex. Graphite

$$d(hkl) = \left(\frac{4}{3}\frac{h^2 + k^2 + hk}{a^2} + \frac{l^2}{c^2}\right)^{-\frac{1}{2}}$$

For the tetragonal lattice ($a = b$, c, $\alpha = \beta = \gamma = 90°$)

$$d(hkl) = \left(\frac{h^2 + k^2}{a^2} + \frac{l^2}{c^2}\right)^{-\frac{1}{2}}$$

For the orthorhombic lattice (a, b, c, $\alpha = \beta = \gamma = 90°$)

$$d(hkl) = \left(\frac{h^2}{a^2} + \frac{k^2}{b^2} + \frac{l^2}{c^2}\right)^{-\frac{1}{2}}$$

For the monoclinic lattice (a, b, c, $\alpha = \gamma = 90°$, $\beta > 90°$)

$$d(hkl) = \left(\frac{h^2}{a^2\sin^2\beta} + \frac{k^2}{b^2} + \frac{l^2}{c^2\sin^2\beta} - \frac{2hl\cos\beta}{ac\sin^2\beta}\right)^{-\frac{1}{2}}$$

For the triclinic lattice (a, b, c, α, β, γ), the most general case,

$$d(hkl) = \left(1 - \cos^2\alpha - \cos^2\beta - \cos^2\gamma + 2\cos\alpha \cdot \cos\beta \cdot \cos\gamma\right)^{\frac{1}{2}}$$

$$\left(\begin{array}{l} \dfrac{h^2}{a^2}\sin^2\alpha + \dfrac{k^2}{b^2}\sin^2\beta + \dfrac{l^2}{c^2}\sin^2\gamma \\ + \dfrac{2kl}{bc}\left(c \cdot \cos^2\beta - \cos\alpha\right) + \dfrac{2lh}{ca}\left(c \cdot \cos^2\gamma - \cos\beta\right) + \dfrac{2hk}{ab}\left(c \cdot \cos^2\alpha - \cos\gamma\right) \end{array}\right)^{-\frac{1}{2}} \quad (4)$$

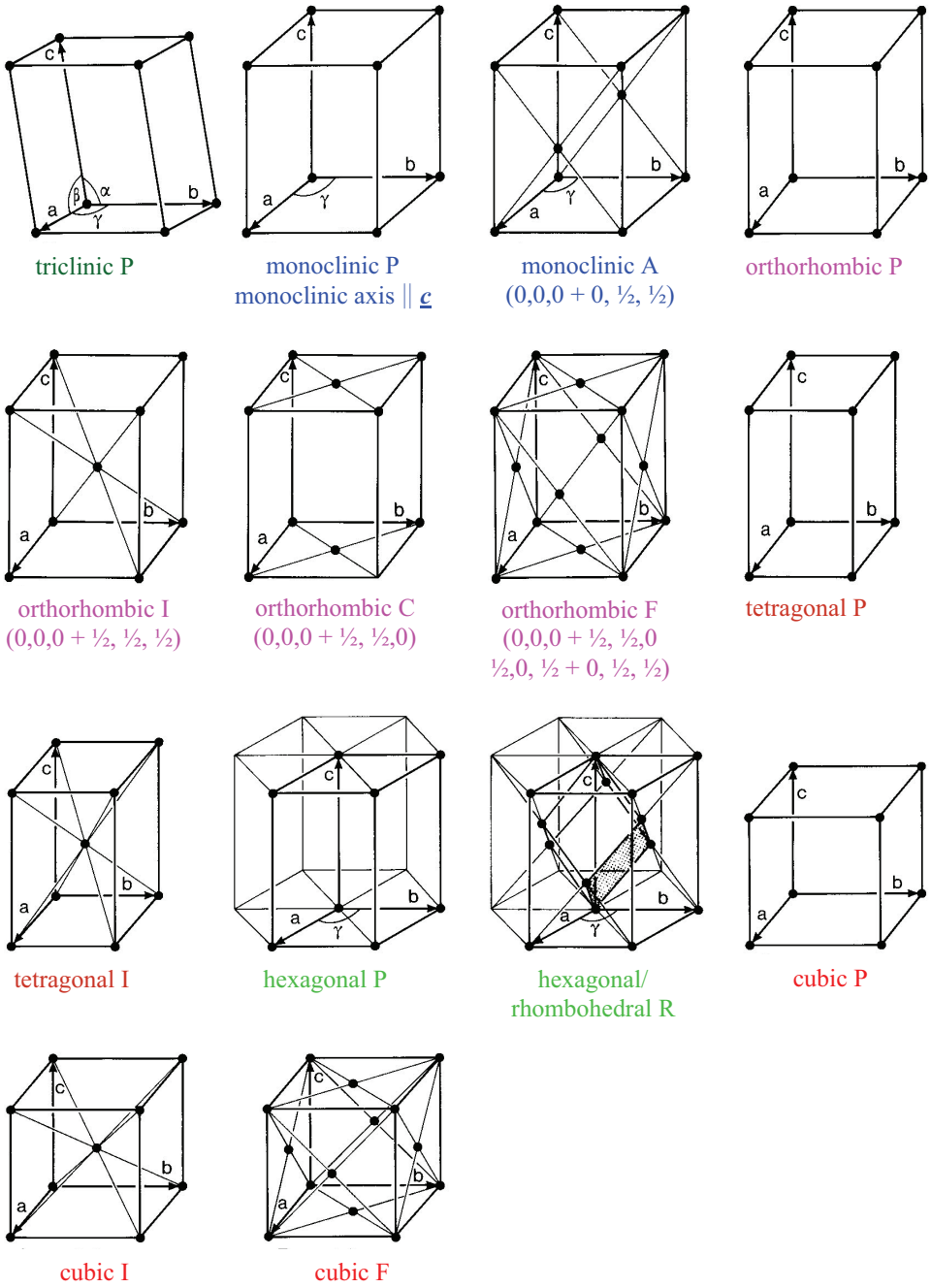

Fig. 3. The 14 Bravais lattices consisting of the 7 primitive lattices P for the 7 crystal systems with only one lattice point per unit cell + the 7 centred (multiple) lattices A, B, C, I, R and F with 2, 3 and 4 lattice points per unit cell.

4.4 Crystallographic symmetry operations and symmetry elements

The **symmetry operations** of a crystal are isometric transformations or motions, i.e. mappings which preserve distances and, hence, also angles and volumes. An object and its transformed object superpose in a perfect manner, they are indistinguishable.

The simplest crystallographic symmetry operation is the **translation**, which is a parallel displacement of the crystal by a translation vector $\boldsymbol{a}$ (see chapt. 4.2). There is no fixed point, the entire lattice is shifted and therefore, theoretically, the crystal lattice is considered to be infinite.

Crystallographic **rotations** n around an axis by an angle $\varphi = 360°/n$ (n-fold rotations) and **rotoinversions** (combination of rotations and inversions) $\bar{n}$ are called point symmetry operations because they leave at least one point of space invariant (at least one fixed point). An important fact of crystallographic symmetry is the restriction of the rotation angles by the three-dimensional crystal lattice to $\varphi = 360°$ (n = 1), 180° (n = 2), 120° (n = 3), 90° (n = 4), 60° (n = 6). Only for these crystallographic rotations the space can be covered completely without gaps and overlaps. The rotoinversion $\bar{n} = \bar{1}$ is an **inversion** in a point, $\bar{n} = \bar{2} \equiv m$ (mirror) describes a **reflection** across a plane.

The combination of n-fold rotations with $m/n \cdot \boldsymbol{a}$ translation components ($m < n$) $\parallel$ to the rotation axis leads to the so-called **screw rotations** n_m, e.g. 2_1, 3_2, 4_2, 6_5. These symmetry operations have no fixed points.

The combination of a reflection through a plane (glide plane) with translation components (glide vectors) of $\boldsymbol{a}_1/2$, $\boldsymbol{a}_2/2$, $\boldsymbol{a}_3/2$, $(\boldsymbol{a}_1+\boldsymbol{a}_2)/2$, … $\parallel$ to this plane are known as **glide reflections** a, b, c, n, …, d. Again no fixed points exist for these symmetry operations.

In addition to the symmetry operations which represent isometric motions of an object, symmetry can also be described in (static) geometrical terms by **symmetry elements**. They form the geometrical locus, oriented in space, on which a symmetry operation is performed (line for a rotation, plane for a reflection, and point for an inversion) together with a description of this operation. Symmetry elements are mirror planes, glide planes, rotation axes, screw axes, rotoinversion axes and inversion centres. The geometrical descriptions of the crystallographic symmetry operations are illustrated in Figs. 4-6.

Point symmetry operations

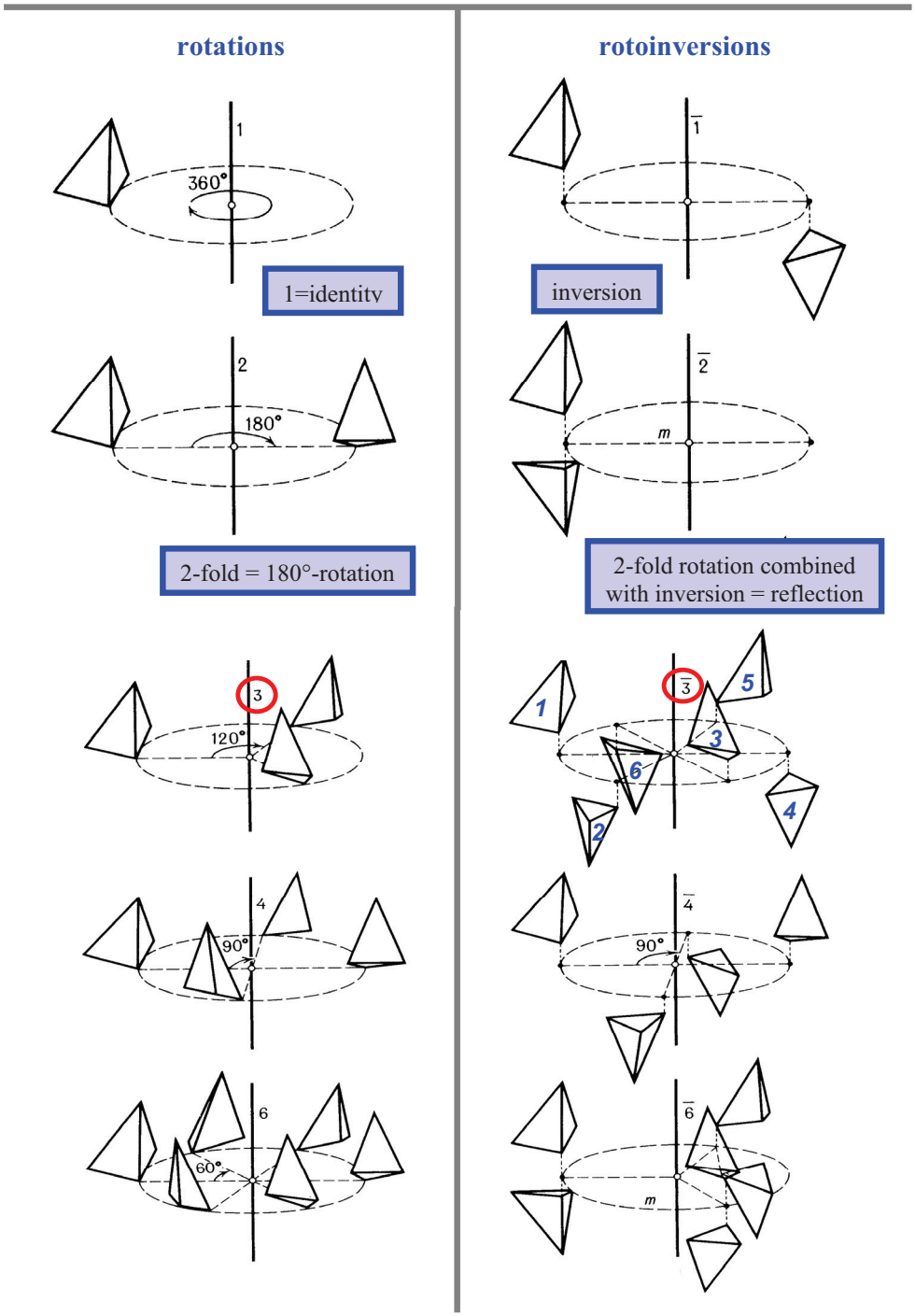

Fig. 4. Rotations: n=1 (identity), n=2 (rotation angle 180°), n=3 (120°), n=4 (90°), n=6 (60°). Rotoinversions: $\bar{1}$ (inversion), $\bar{2} \equiv m$ (reflection), $\bar{3} = 3 + \bar{1}$, $\bar{4}$, $\bar{6} = 3/m$.

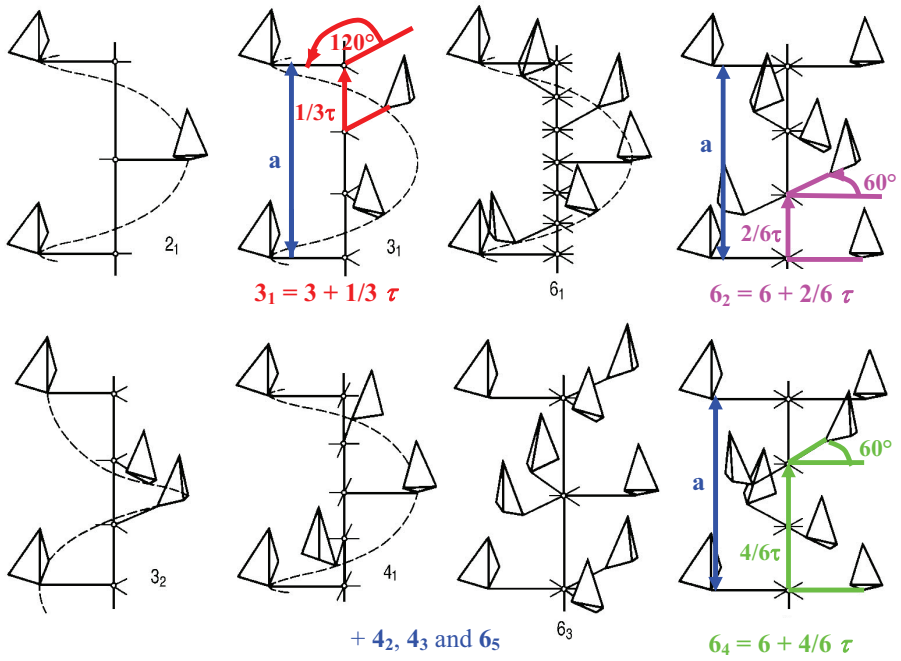

*Fig. 5. Screw rotations n_m: combination of rotations n and translation components m/n·**a** // to the rotation axis.*

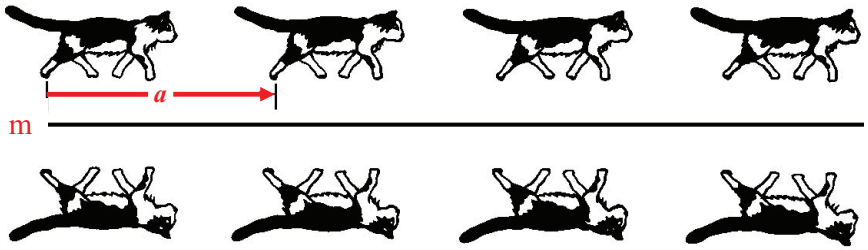

reflection: mirror plane m ⊥ image plane (plane of the paper)

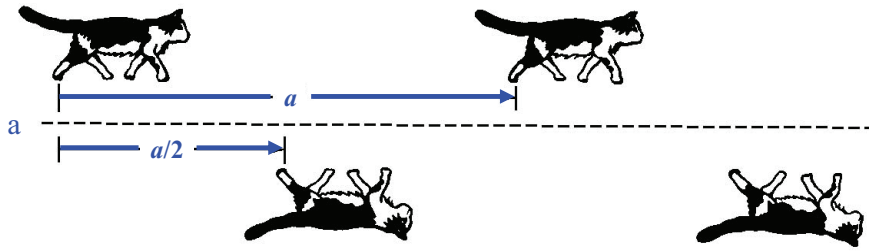

glide reflection: glide plane a ⊥ with glide vector ***a***/2

Fig. 6. Examples of reflections and glide reflections.

A symmetry operation transforms a point X with coordinates x, y, z (according to a position vector $\boldsymbol{X} = x\boldsymbol{a_1} + y\boldsymbol{a_2} + z\boldsymbol{a_3}$) into a symmetrically equivalent point X' with coordinates x', y', z' mathematically by the linear equations

$$\begin{aligned} x' &= W_{11}x + W_{12}y + W_{13}z + w_1 \\ y' &= W_{21}x + W_{22}y + W_{23}z + w_2 \\ z' &= W_{31}x + W_{32}y + W_{33}z + w_3 \end{aligned} \qquad (5)$$

or, in matrix notation:

$$\begin{pmatrix} x' \\ y' \\ z' \end{pmatrix} = \begin{pmatrix} W_{11} & W_{12} & W_{13} \\ W_{21} & W_{22} & W_{23} \\ W_{31} & W_{32} & W_{33} \end{pmatrix} \circ \begin{pmatrix} x \\ y \\ z \end{pmatrix} + \begin{pmatrix} w_1 \\ w_2 \\ w_3 \end{pmatrix}; \quad \boldsymbol{X}' = \mathbf{W} \circ \boldsymbol{X} + \boldsymbol{w} = (\mathbf{W}, \mathbf{w}) \circ \boldsymbol{X}. \qquad (6)$$

The (3×3) matrix **W** is the rotation part and the (3×1) column matrix $\boldsymbol{w}$ the translation part of the symmetry operation. The two parts **W** and $\boldsymbol{w}$ can be assembled into an augmented (4×4) matrix $\boldsymbol{W}$ according to

$$\begin{pmatrix} x' \\ y' \\ z' \\ 1 \end{pmatrix} = \begin{pmatrix} W_{11} & W_{12} & W_{13} & w_1 \\ W_{21} & W_{22} & W_{23} & w_2 \\ W_{31} & W_{32} & W_{33} & w_3 \\ 0 & 0 & 0 & 1 \end{pmatrix} \circ \begin{pmatrix} x \\ y \\ z \\ 1 \end{pmatrix} = \boldsymbol{W} \circ \boldsymbol{X} \qquad (7)$$

Since every symmetry transformation is a "rigid-body" motion, the determinant of all matrices **W** and $\boldsymbol{W}$ is det **W** = det $\boldsymbol{W}$ = ± 1 (+ 1: preservation of handedness; - 1: change of handedness of object).

The sequence of two symmetry operations (successive application) is given by the product of their matrices $\boldsymbol{W_1}$ and $\boldsymbol{W_2}$:

$$\boldsymbol{W_3} = \boldsymbol{W_1} \circ \boldsymbol{W_2}\,, \qquad \text{whereby } \boldsymbol{W_3} \text{ is again a symmetry operation.} \qquad (8)$$

4.5 Crystallographic point groups and space groups

The symmetry of a crystal and of its crystal structure can be described by mathematical group theory. The symmetry operations are the group elements of a crystallographic group G and the combination of group elements is the successive execution of symmetry operations. All possible combinations of crystallographic point-symmetry operations in three-dimensional space lead to exactly 32 crystallographic point groups (≡ crystal classes) which all are of finite order (the maximum order is 48 for the cubic crystal class $m\bar{3}m$). For the different crystal systems they are represented by stereographic projections in Fig. 7. There are two types of

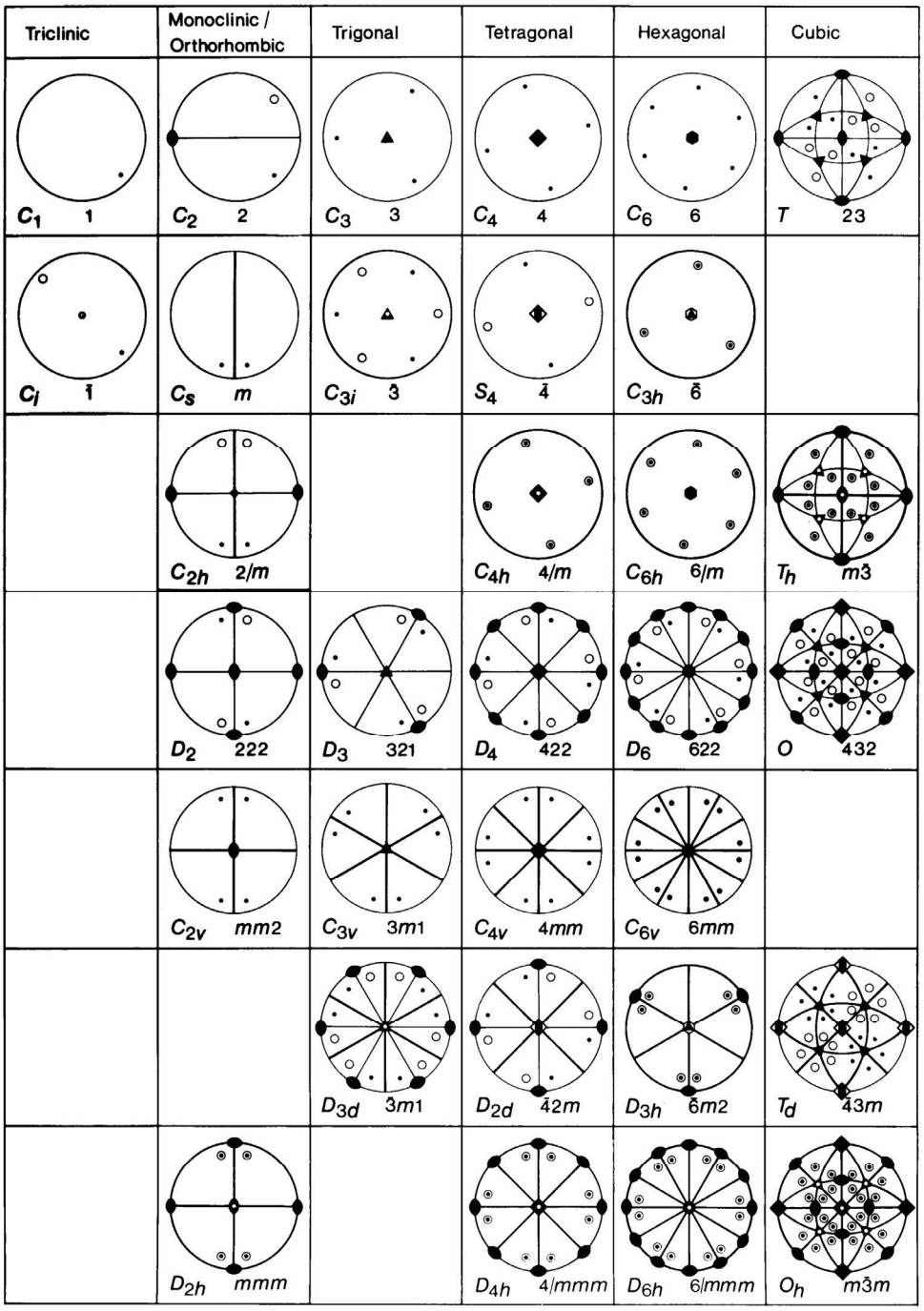

Fig. 7. The 32 crystallographic point groups (crystal classes) in three-dimensional space represented by their stereographic projections. The group symbols are given according to Schoenflies (bottom left) and to Hermann-Mauguin (bottom right).

group symbols in use: for each crystal class the corresponding Schoenflies symbol is given at the bottom left and the Hermann-Mauguin (international) symbol at the bottom right. A maximum of 3 independent main symmetry directions ("Blickrichtungen") is sufficient to describe the complete symmetry of a crystal. These Blickrichtungen are specifically defined for the 7 crystal systems (Hermann-Mauguin symbols). As an example the Blickrichtungen of the cubic system are shown in Fig. 8.

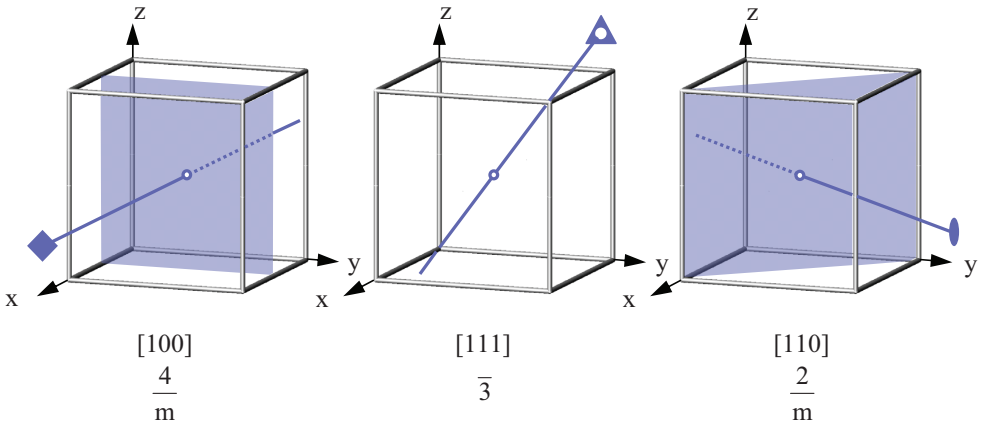

Fig. 8. Symmetry directions ("Blickrichtungen") of the cubic lattice (a=b=c, α=β=γ=90°). Along [100]: 4/m, along [111]: $\bar{3}$, along [110]: 2/m.

The point-group symmetries determine the anisotropic (macroscopic) physical properties of crystals, i. e. mechanical, electrical, optical and thermal properties. By diffraction methods normally only the 11 centrosymmetric Laue classes can be determined:

crystal system	Laue class
triclinic	$\bar{1}$
monoclinic	1 2/m 1 = 2/m
orthorhombic	2/m 2/m 2/m = m m m
tetragonal	4/m 4/m 2/m 2/m = 4/m m m
trigonal	$\bar{3}$ $\bar{3}$ 2/m = $\bar{3}$ m
hexagonal	6/m 6/m 2/m 2/m = 6/m m m
cubic	2/m $\bar{3}$ = m $\bar{3}$ 4/m $\bar{3}$ 2/m = m $\bar{3}$ m

In three dimensions all possible combinations of the point symmetries of the 32 crystallographic point groups with the lattice translations of the 14 Bravais lattices lead to exactly 230 space groups, all of infinite order. As already mentioned, there result new symmetry operations: screw rotations and glide reflections. The conventional graphical symbols for the symmetry elements according to the International Tables for Crystallography Vol. A (ITA, 2002 [1]) are shown in Fig. 9.

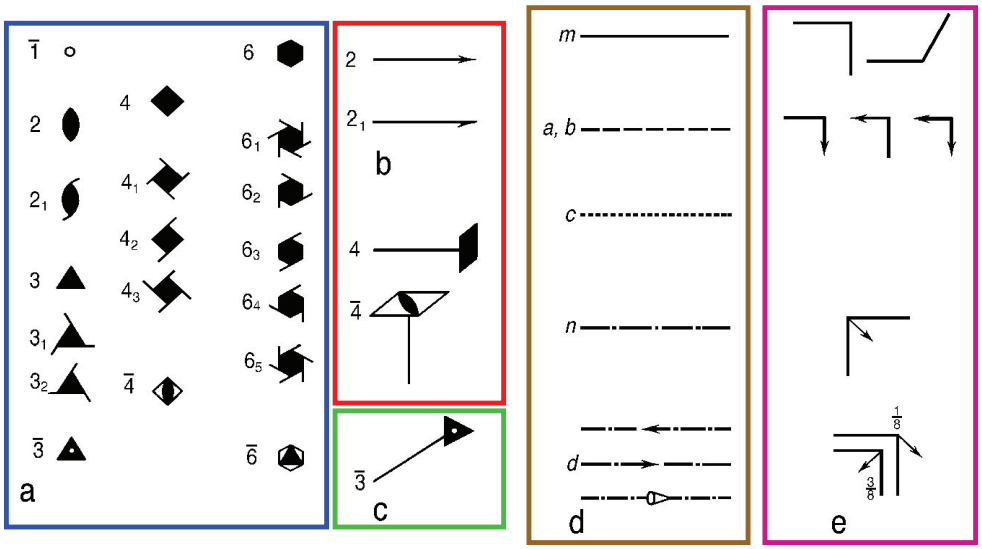

Fig. 9. Conventional graphical symbols for symmetry elements:

- *symmetry axes (a) perpendicular, (b) parallel, and (c) inclined to the image plane*
- *symmetry planes (d) perpendicular and (e) parallel to the image plane.*

In the International Tables for Crystallography Vol. A [1] all space groups are described in detail with their Hermann-Mauguin symbols and corresponding crystal classes, the relative locations and orientations of the symmetry elements with respect to a chosen origin and the crystal-specific basis vectors, a listing of the general and all special positions (with their symmetrically equivalent points) and the related reflection conditions.

4.6 Example of the crystal structure description of $YBa_2Cu_3O_{7-\delta}$ using the ITA

The crystal structure determination with atomic resolution is achieved by diffraction experiments with X-rays, electron or neutron radiation. As an example, the results of a structure analysis by neutron diffraction on a single crystal of the ceramic high-T_C superconductor $YBa_2Cu_3O_{7-\delta}$ with T_C = 92 K are presented. The atomic arrangement of the orthorhombic structure, space group Pmmm, and the temperature-dependent electrical resistivity is shown in Fig. 10.

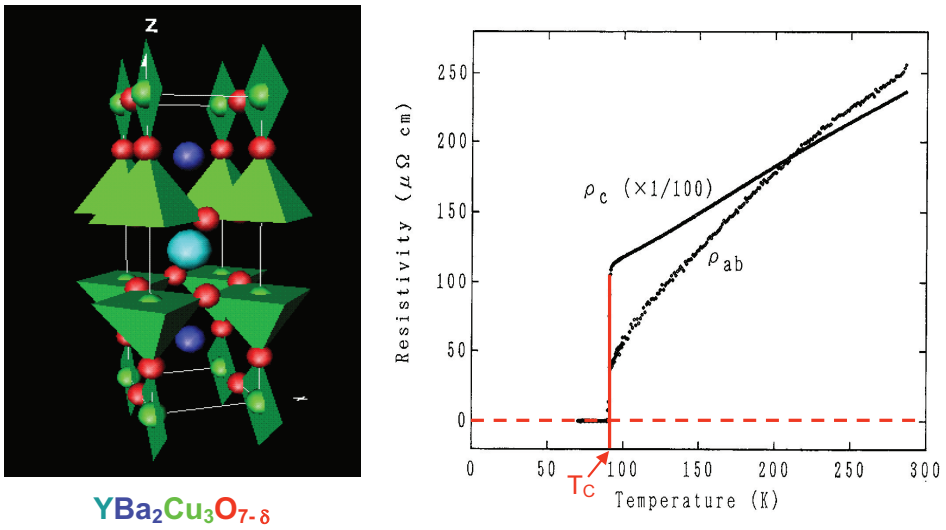

Fig. 10. Crystal structure (unit cell) of $YBa_2Cu_3O_{7-\delta}$ with the CuO_x-polyhedra (left) and the electrical resistivity as a function of temperature // and ⊥ to the [001] direction.

$Pmmm$ **D^1_{2h}** **mmm** **Orthorhombic**

No. 47 $P\,2/m\,2/m\,2/m$ Patterson symmetry $Pmmm$

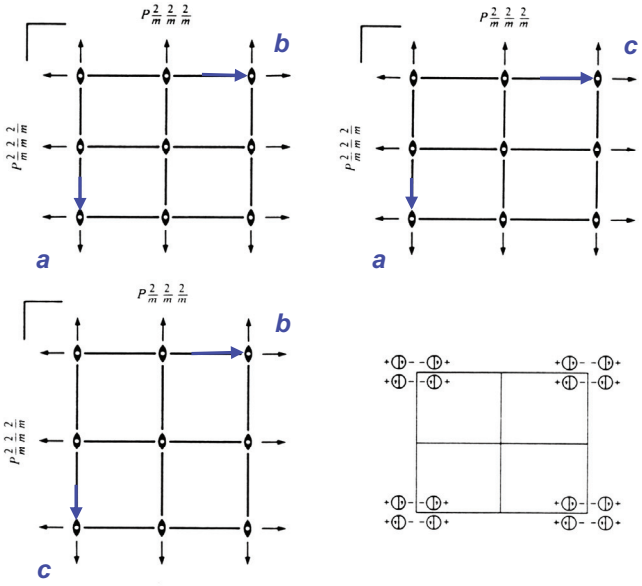

Origin at centre (mmm)

Asymmetric unit $0\le x\le\frac{1}{4};\ 0\le y\le\frac{1}{4};\ 0\le z\le\frac{1}{4}$

Symmetry operations

(1) 1	(2) 2 0,0,z	(3) 2 0,y,0	(4) 2 x,0,0
(5) $\bar{1}$ 0,0,0	(6) m x,y,0	(7) m x,0,z	(8) m 0,y,z

Fig. 11. Description of the orthorhombic space group Pmmm in ITA (2002).

Information from ITA on the relative locations and orientations of the symmetry elements (symmetry operations 1, 2_z, 2_y, 2_x, $\bar{1}$, m_z, m_y, m_x) of the orthorhombic space group Pmmm, together with the choice of the origin (in an inversion centre), is shown in Fig. 11. The general position (site symmetry 1) of multiplicity 8 and all special positions with their site symmetries are listed in Fig. 12. There are no special reflection conditions for this space group.

CONTINUED $YBa_2Cu_3O_{7-\delta}$ No. 47 *Pmmm*

Generators selected (1); $t(1,0,0)$; $t(0,1,0)$; $t(0,0,1)$; (2); (3); (5)

Positions

Multiplicity, Wyckoff letter, Site symmetry			Coordinates				Reflection conditions
8	α	1	(1) x,y,z	(2) $\bar{x},\bar{y},z$	(3) $\bar{x},y,\bar{z}$	(4) $x,\bar{y},\bar{z}$	General:
			(5) $\bar{x},\bar{y},\bar{z}$	(6) $x,y,\bar{z}$	(7) $x,\bar{y},z$	(8) $\bar{x},y,z$	no conditions
4	z	$..m$	$x,y,\frac{1}{2}$	$\bar{x},\bar{y},\frac{1}{2}$	$\bar{x},y,\frac{1}{2}$	$x,\bar{y},\frac{1}{2}$	Special: no extra conditions
4	y	$..m$	$x,y,0$	$\bar{x},\bar{y},0$	$\bar{x},y,0$	$x,\bar{y},0$	
4	x	$.m.$	$x,\frac{1}{4},z$	$\bar{x},\frac{1}{4},z$	$\bar{x},\frac{1}{4},\bar{z}$	$x,\frac{1}{4},\bar{z}$	
4	w	$.m.$	$x,0,z$	$\bar{x},0,z$	$\bar{x},0,\bar{z}$	$x,0,\bar{z}$	
4	v	$m..$	$\frac{1}{4},y,z$	$\frac{1}{4},\bar{y},z$	$\frac{1}{4},y,\bar{z}$	$\frac{1}{4},\bar{y},\bar{z}$	
4	u	$m..$	$0,y,z$	$0,\bar{y},z$	$0,y,\bar{z}$	$0,\bar{y},\bar{z}$	
2	t	$mm2$	$\frac{1}{4},\frac{1}{4},z$	$\frac{1}{4},\frac{1}{4},\bar{z}$			
2	s	$mm2$	$\frac{1}{4},0,z$	$\frac{1}{4},0,\bar{z}$			
2	r	$mm2$	$0,\frac{1}{4},z$	$0,\frac{1}{4},\bar{z}$			
2	q	$mm2$	$0,0,z$	$0,0,\bar{z}$			
2	p	$m2m$	$\frac{1}{4},y,\frac{1}{2}$	$\frac{1}{4},\bar{y},\frac{1}{2}$			
2	o	$m2m$	$\frac{1}{4},y,0$	$\frac{1}{4},\bar{y},0$			
2	n	$m2m$	$0,y,\frac{1}{2}$	$0,\bar{y},\frac{1}{2}$			
2	m	$m2m$	$0,y,0$	$0,\bar{y},0$			
2	l	$2mm$	$x,\frac{1}{4},\frac{1}{2}$	$\bar{x},\frac{1}{4},\frac{1}{2}$			
2	k	$2mm$	$x,\frac{1}{4},0$	$\bar{x},\frac{1}{4},0$			
2	j	$2mm$	$x,0,\frac{1}{2}$	$\bar{x},0,\frac{1}{2}$			
2	i	$2mm$	$x,0,0$	$\bar{x},0,0$			
1	h	mmm	$\frac{1}{2},\frac{1}{2},\frac{1}{2}$				
1	g	mmm	$0,\frac{1}{2},\frac{1}{2}$				
1	f	mmm	$\frac{1}{2},\frac{1}{2},0$				
1	e	mmm	$0,\frac{1}{2},0$				
1	d	mmm	$\frac{1}{2},0,\frac{1}{2}$				
1	c	mmm	$0,0,\frac{1}{2}$				
1	b	mmm	$\frac{1}{2},0,0$				
1	a	mmm	$0,0,0$				

Fig. 12. General and special positions (coordinates of all symmetrically equivalent positions) of space group Pmmm with their site symmetries and multiplicities as well as reflection conditions. The special positions of the $YBa_2Cu_3O_{7-\delta}$ structure are indicated by frames.

The atomic parameters of the structure refinement of $YBa_2Cu_3O_{6..96}$ at room temperature [2] are given in the following Table:

Atomic positions of $YBa_2Cu_3O_{6.96}$ orthorhombic, space group type P *2/m 2/m 2/m* *a* = 3.858 Å, *b* = 3.846 Å, *c* = 11.680 Å (at room temperature)					
atom/ion	**multiplicity**	**site symmetry**	**x**	**y**	**z**
$Cu1/Cu^{2+}$	1	*2/m 2/m 2/m*	0	0	0
$Cu2/Cu^{2+}$	2	*m m 2*	0	0	0.35513(4)
Y/Y^{3+}	1	*2/m 2/m 2/m*	½	½	½
Ba/Ba^{2+}	2	*m m 2*	½	½	0.18420(6)
$O1/O^{2-}$	2	*m m 2*	0	0	0.15863(5)
$O2/O^{2-}$	2	*m m 2*	0	½	0.37831(2)
$O3/O^{2-}$	2	*m m 2*	½	0	0.37631(2)
$O4/O^{2-}$	1	*2/m 2/m 2/m*	0	½	0

References

[1] International Tables for Crystallography Vol. A, Space-group Symmetry, edited by Th. Hahn, Dordrecht: Kluwer Academic Publishers (5. Edition, 2002).

[2] P. Schweiss, W. Reichardt, M. Braden, G. Collin, G. Heger, H. Claus, A. Erb, Phys. Rev. **B49**, 1387 – 1396 (1994).

5

Applications of neutron scattering

Thomas Brückel

5. Applications of neutron scattering

Thomas Brückel, IFF, Forschungszentrum Jülich

5.1 Introduction

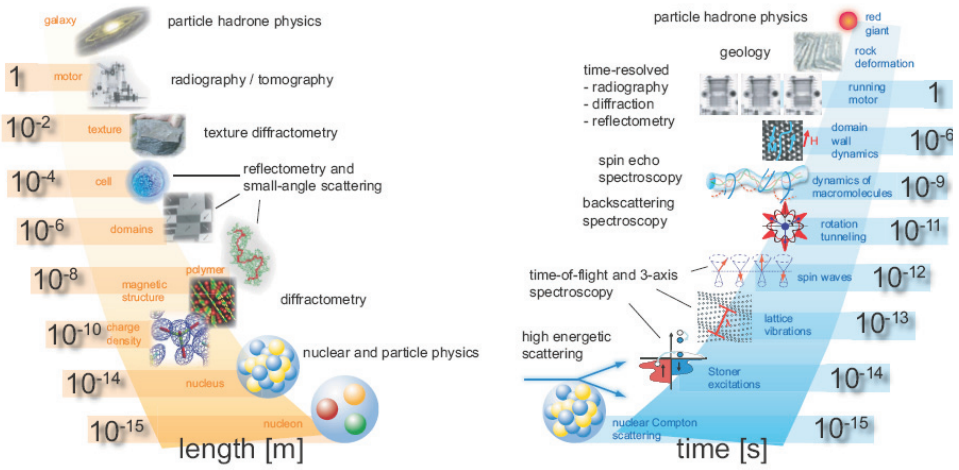

Fig 5.1: *Length- and time scales covered by research with neutrons giving examples for applications and neutron techniques [1].*

Research with neutrons covers an extraordinary range of length- and time scales as depicted in figure 5.1. The very extremes of length scales - below 10^{-12} m - are the domain of nuclear and particle physics, where e. g. measurements of the charge or electric dipole moment of the neutron provide stringent tests of the standard model of particle physics without the need of huge and costly accelerators. On the other extreme, neutrons also provide information on length- and time scales relevant for astronomical dimensions, e. g. the decay series of radioactive isotopes produced by neutron bombardment give information on the creation of elements in the early universe. In this course, however, we are only concerned with neutrons as a probe for condensed matter research and therefore restrict ourselves to a discussion of neutron scattering. Still, the various neutron scattering techniques cover an area in phase space from picometers pm up to meters and femtoseconds fs up to hours, a range, which probably no other probe can cover to such an extend.

Different specialized neutron scattering techniques are required to obtain structural information on different length scales:

- With *wide angle neutron diffractometry*, magnetization densities can be determined within single atoms on a length scale of ca. 10 pm[1]. The position of atoms can be determined on a similar length scale, while distances between atoms lie in the 0.1 nm range[2].

[1] In this sense, neutrons are not only nanometer nm, but even picometer pm probes!
[2] In what follows, we use as "natural atomic unit" the Ångstrøm, with 1 Å=0.1 nm.

- The sizes of large macromolecules, magnetic domains or biological cells lie in the range of nm to μm or even mm. For such studies of large scale structures, one applies *reflectometry* or *small angle scattering* techniques.
- Most materials relevant for engineering or geo-science occur neither in form of single crystals, nor in form of fine powders. Instead they have a grainy structure, often with preferred orientation of the grains. This so called texture determines the macroscopic strength of the material along different directions. *Texture diffractometry* as a specialized technique allows one to determine this grainy structure on length scales of up to mm.
- Finally, for even larger structures, one uses imaging techniques, such as neutron *radiography* or *tomography*, which give a 2dimensional projection or full 3-dimensional view into the interior of a sample due to the attenuation of the neutron beam, the phase shift or other contrast mechanisms.

In a similar way, different specialized neutron scattering techniques are required to obtain information on the system's dynamics on different time scales:

- *Neutron Compton scattering*, where a high energy neutron in the eV energy range makes a deep inelastic collision with a nucleus in so-called impulse approximation, gives us the momentum distribution of the atoms within the solid. Interaction times are in the femtosecond fs time range.
- In magnetic metals, there exist single particle magnetic excitations, so-called Stoner excitations, which can be observed with inelastic scattering of high energy neutrons using the so-called *time-of-flight spectroscopy* or the *triple axis spectroscopy* technique. Typically, these processes range from fs to several hundred fs.
- Lattice vibrations (phonons) or spin waves in magnetic systems (magnons) have frequencies in the picosecond ps time range. Again these excitations can be observed with *time-of-flight* or *triple axis spectroscopy*.
- Slower processes in condensed matter are the tunneling of atoms, for example in molecular crystals or the slow dynamics of macromolecules. Characteristic time scales for these processes lie in the nanosecond ns time range. They can be observed with specialized techniques such as *backscattering spectroscopy* or *spin-echo spectroscopy*.
- Even slower processes occur in condensed matter on an ever increasing range of length scales. One example is the growth of domains in magnetic systems, where domain walls are pinned by impurities. These processes may occur with typical time constants of microseconds μs. Periodic processes on such time scales can be observed with *stroboscopic neutron scattering* techniques.
- Finally, *kinematic neutron scattering* or imaging techniques, where data is taken in consecutive time slots, allow one to observe processes from the millisecond ms to the hour h range.

In this chapter, we will overview the various techniques used in neutron scattering and provide some examples for their application. We will start by repeating the properties of the different correlation functions, in order to be able to judge what kind of information we can obtain from a certain neutron scattering experiment. We will introduce neutron scattering techniques used to obtain information on "where the atoms are" (diffractometry) and "what the atoms do" (spectroscopy). We will finish by reviewing the range of applicability of various neutron scattering methods and compare them to other experimental techniques.

5.2 Scattering and correlation functions

In the chapter on "Correlation Functions" it has been shown that the neutron scattering cross section for nuclear scattering can be expressed in the following form (for simplicity, we restrict ourselves to a mono-atomic system):

$$\frac{\partial^2\sigma}{\partial\Omega\partial\omega} = \frac{k'}{k}\cdot N\cdot\left[\left(\overline{|b|^2}-|\bar{b}|^2\right)S_{inc}(\underline{Q},\omega)+|\bar{b}|^2\ S_{coh}(\underline{Q},\omega)\right] \tag{5.1}$$

The cross section is proportional to the number N of atoms. It contains a kinematical factor k'/k, i. e. the magnitude of the final wave vector versus the magnitude of the incident wave vector, which results from the phase-space density. The scattering cross section contains two summands: one is the coherent scattering cross section, which depends on the magnitude square of the average scattering length density $|\bar{b}|^2$ and the other one is the incoherent scattering, which depends on the variance of the scattering length $\left(\overline{|b|^2}-|\bar{b}|^2\right)$. The cross section (5.1) has a very convenient form: it separates the interaction strength between probe (the neutrons) and sample from the properties of the system studied. The latter is given by the so-called scattering functions $S_{coh}(\underline{Q},\omega)$ and $S_{inc}(\underline{Q},\omega)$, which are completely independent of the probe and a pure property of the system under investigation [2]. The *coherent scattering function* $S_{coh}(\underline{Q},\omega)$ (also called *dynamical structure factor* or *scattering law*) is a Fourier transform in space and time of the pair correlation function:

$$S_{coh}(\underline{Q},\omega) = \frac{1}{2\pi\hbar}\int G(\underline{r},t)e^{i(\underline{Q}\cdot\underline{r}-\omega t)}d^3rdt \tag{5.2}$$

Here the *pair correlation function* $G(\underline{r},t)$ depends on the time dependent positions of the atoms in the sample:

$$\begin{aligned} G(\underline{r},t) &= \frac{1}{N}\sum_{ij}\int\left\langle\delta(\underline{r}'-\underline{\mathrm{r}}_{\mathrm{i}}(0))\cdot\delta(\underline{r}'+\underline{r}-\underline{\mathrm{r}}_{\mathrm{j}}(t))\right\rangle d^3r' \\ &= \frac{1}{N}\int\left\langle\rho(\underline{r}',0)\cdot\rho(\underline{r}'+\underline{r},t)\right\rangle d^3r' \end{aligned} \tag{5.3}$$

$\underline{r}_i(0)$ denotes the position of atom i at time 0, while $\underline{r}_j(t)$ denotes the position of another atom j at time t. The angle brackets denote the thermodynamic ensemble average, the integral extends over the entire sample volume and the sum runs over all atom pairs in the sample. Instead of correlating the positions of two point-like scatterers at different times, one can rewrite the pair correlation function in terms of the particle density as given in the second line of (5.3). Coherent scattering arises from the superposition of the amplitudes of waves scattered from one particle at time *0* and a second particle at time *t*, averaged over the entire sample volume and the thermodynamic state of the sample. In contrast, incoherent scattering arises from the superposition of waves scattered from the same particle at different times. Therefore the *incoherent scattering function* $S_{inc}(\underline{Q},\omega)$ is given in the following form:

$$S_{inc}(\underline{Q},\omega) = \frac{1}{2\pi\hbar}\int G_s(\underline{r},t)e^{i(\underline{Q}\cdot\underline{r}-\omega t)}d^3rdt \tag{5.4}$$

which is the Fourier transform in space and time of the *self correlation function* $G_S(\underline{r},t)$:

$$G_s(\underline{r},t) = \frac{1}{N}\sum_{j}\int\left\langle\delta(\underline{r}'-\underline{\mathrm{r}}_{\mathrm{j}}(0))\cdot\delta(\underline{r}'+\underline{r}-\underline{\mathrm{r}}_{\mathrm{j}}(t))\right\rangle d^3r' \tag{5.5}$$

We next define the *intermediate scattering function* $S(\underline{Q},t)$ as the purely spatial Fourier transform of the correlation function (here we have dropped the index "coh" and "inc", re-

spectively, as the intermediate scattering function can be defined for coherent as well as for incoherent scattering in the same way):

$$\begin{aligned} S(\underline{Q},t) &:= \int G(\underline{r},t)e^{i\underline{Q}\cdot\underline{r}}d^3r \\ &= S(\underline{Q},\infty) + S'(\underline{Q},t) \end{aligned} \tag{5.6}$$

For reasons, which will become apparent below, we have separated in the second line the intermediate scattering function for infinite time

$$S(\underline{Q},\infty) = \lim_{t\to\infty} S(\underline{Q},t) \tag{5.7}$$

from the time development at intermediate times. Given this form of the intermediate scattering function $S(\underline{Q},t)$, we can now calculate the scattering function as the temporal Fourier transform of the intermediate scattering function:

$$\begin{aligned} S(\underline{Q},\omega) &= \frac{1}{2\pi\hbar}\int_{-\infty}^{+\infty} S(\underline{Q},t)e^{-i\omega t}dt \quad = \frac{1}{2\pi\hbar}\int_{-\infty}^{+\infty}\left[S(\underline{Q},\infty) + S'(\underline{Q},t)\right]e^{-i\omega t}dt \\ &= \underbrace{\frac{1}{\hbar}\delta(\omega)S(\underline{Q},\infty)}_{elastic\ scattering} + \underbrace{\frac{1}{2\pi\hbar}\int_{-\infty}^{+\infty} S'(\underline{Q},t)e^{-i\omega t}dt}_{inelastic\ scattering} \end{aligned} \tag{5.8}$$

In this way, the scattering function has been separated into one term for frequency 0, i. e. vanishing energy transfer $\Delta E = \hbar\omega = 0$ and one term for non-vanishing energy transfer. The first term is the purely elastic scattering, which is given by the correlation function at infinite times. Correlation at infinite times is obtained for particles at rest. A prominent example is the Bragg scattering from a crystalline material, which is purely elastic, while the scattering from liquids is purely inelastic, since the atoms in liquids are moving around freely and thus the correlation function vanishes in the limit of infinite time differences.

Often times the energy of the scattered neutron is not discriminated in the detector. In such experiments, where the detector is set at a given scattering angle, but does not resolve the energies of the scattered neutrons, we measure an *integral cross section* for a fixed direction $\hat{\underline{k}}'\ of\ \underline{k}'$:

$$\left(\frac{d\sigma}{d\Omega}\right)_{coh,\mathrm{int}} = \int \left.\frac{\partial^2\sigma}{\partial\Omega\partial\omega}\right|_{\hat{\underline{k}}'=const} \cdot d\omega \tag{5.9}$$

Momentum and energy conservation are expressed by the following kinematic equations of scattering:

$$\underline{Q} = \underline{k}' - \underline{k} \quad ; \quad \hbar\omega = E - E' = \frac{\hbar^2}{2m}\left(k^2 - k'^2\right) \tag{5.10}$$

Due to these kinematic conditions, the scattering vector $\underline{Q}$ will vary with the energy of the scattered neutron E' or the energy transfer $\hbar\omega$ as the integral in (5.9) is performed. The so-called *quasi-static approximation* neglects this variation and uses the scattering vector Q_0 for elastic scattering $(\hbar\omega = 0)$ in (5.9). This approximation is valid only if the energy transfer is small compared to the initial energy. This means that the movements of the atoms are negligible during the propagation of the radiation wave front from one atom to the other. In this case, the above integral can be approximated as follows:

$$\begin{aligned} \left(\frac{d\sigma}{d\Omega}\right)_{coh,QSA} &= \frac{k'}{k}\frac{N}{2\pi\hbar}\int\left(\int G(\underline{r},t)e^{i(\underline{Q}_0\cdot\underline{r}-\omega\cdot t)}d^3rdt\right)d\omega \\ &= \frac{k'}{k}\frac{N}{2\pi\hbar}\int G(\underline{r},t)e^{i\underline{Q}_0\cdot\underline{r}}\delta(t)d^3rdt = \frac{k'}{k}\frac{N}{2\pi\hbar}\int G(\underline{r},0)e^{i\underline{Q}_0\cdot\underline{r}}d^3r \end{aligned} \tag{5.11}$$

which shows that the integral scattering in quasi-static approximation depends on the *instantaneous spatial correlation function* only, i. e. it measures a snapshot of the arrangement of atoms within the sample. This technique is e. g. very important for the determination of short-range order in liquids, where no elastic scattering occurs (see above).

Our discussion on correlation functions can be summarized in a schematic diagrammatic form, see figure 5.2.

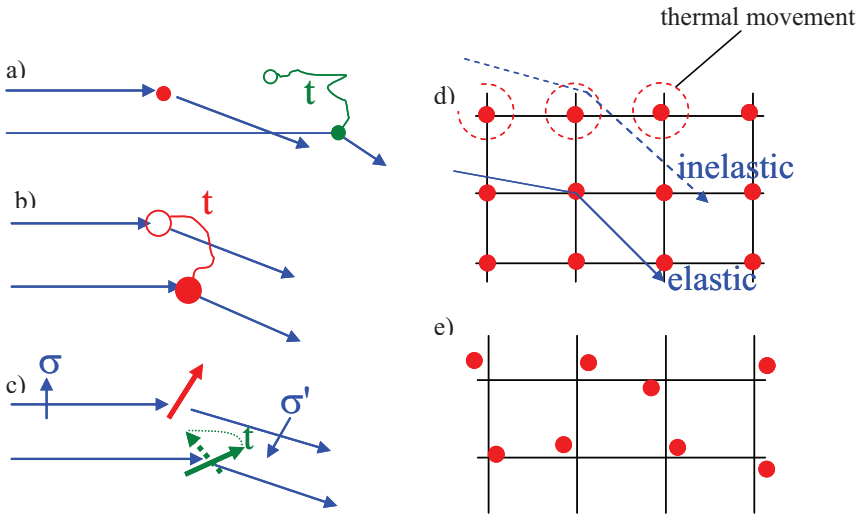

Fig. 5.2: *Schematic diagrams depicting the various scattering processes: a) coherent scattering is connected with the pair correlation function in space-and time; b) incoherent scattering is connected with the self-correlation function; c) magnetic scattering is connected with the spin pair correlation function; d) elastic and inelastic scattering from a crystal measures average positions and movements of the atoms, respectively, e) inelastic scattering in quasistatic approximation sees a snapshot of the sample.*

Figure 5.2 shows that coherent scattering is related to the pair correlation between different atoms at different times (5.2a), while incoherent scattering relates to the one particle self correlation function at different times (5.2b). In analogy to nuclear scattering, magnetic scattering depends on the correlation function between magnetic moments of the atoms. If the magnetic moment is due to spin only, it measures the *spin pair correlation function*. Since the magnetic moment is a vector quantity, this correlation function strongly depends on the neutron polarization. For this reason, in magnetic scattering we often perform a polarization analysis as discussed in the corresponding chapter. Figure 5.2d depicts elastic and inelastic scattering from atoms on a regular lattice. Elastic scattering depends on the infinite time correlation and thus gives us information on the time averaged structure. Excursions of the atoms from their time averaged positions due to the thermal movement will give rise to inelastic scattering, which allows one e. g. to determine the spectrum of lattice vibrations, see chapter on “inelastic neutron scattering”. Finally, an experiment without energy analysis in quasi-static approximation will give us the instantaneous correlations between the atoms, see figure 5.2e. This schematic picture shows a snapshot of the atoms on a regular lattice. Their positions differ from the time averaged positions due to thermal movement.

5.3 The generic scattering experiment

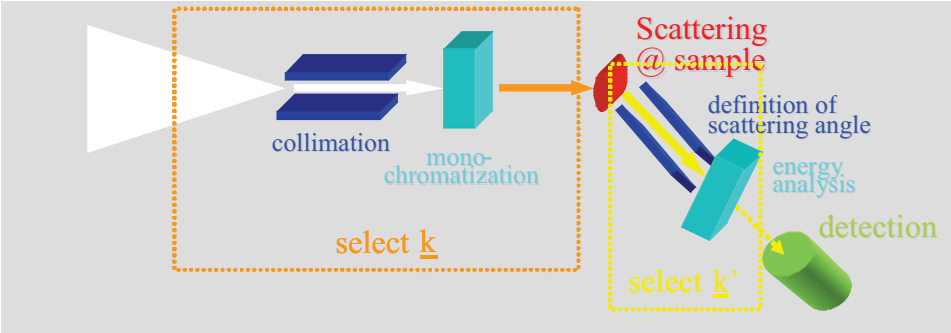

Fig. 5.3: *Schematic diagram of a generic scattering experiment; the primary spectrometer in front of the sample serves to select an incident wave vector distribution by means of collimation and monochromatization; the secondary spectrometer after the sample selects a final wave vector; the number of neutrons for a given distribution of incident wave vector $\underline{k}$ and final wave vector $\underline{k}'$ is counted in the detector.*

A generic scattering experiment is depicted schematically in figure 5.3. The incident beam is prepared by collimators, which define the direction of the beam and monochromators, which define the energy of the incident neutrons. Together these optical elements select an incident wave vector $\underline{k}$. In reality, since these neutron-optical elements are never perfect, a certain distribution of incident wave vectors around an average wave vector is selected in the primary spectrometer. In an analogous manner, a final wave vector - or better a distribution of final wave vectors - is being selected from all scattered waves after the sample by the secondary spectrometer. Finally the scattered neutrons are being counted in the detector. Since our neutron-optical elements are never perfect, the measured intensity in the detector is not simply proportional to the scattering function $S(\underline{Q},\omega)$ (or more precisely, the cross section), but it is proportional to the convolution of the scattering function (or cross section) with the *experimental resolution function R*:

$$I(\underline{Q}_0,\omega_0) \sim \iint S(\underline{Q},\omega)R(\underline{Q}_0-\underline{Q},\omega_0-\omega)d^3Qd\omega \qquad (5.12)$$

Here, the resolution function R appears due to the limited ability of any experimental setup to define an incident or final wave vector $\underline{k}$ or $\underline{k}'$, respectively. R therefore depends purely on the instrumental parameters and not on the scattering system under investigation. The art of any neutron scattering experiment is to adjust the instrument - and with it the resolution function - to the problem under investigation. If the resolution of the instrument is too tight, the intensity in the detector becomes too small and counting statistics will limit the precision of the measurement. If, however, the resolution is too relaxed, the intensity will be smeared out and will not allow one to determine the scattering function properly.

The simplest way to collimate an incident beam is to put two slits with given openings in a certain distance in the beam path and thus define the angular spread of the incident beam. For monochromatization of a neutron beam, usually one of two different methods is applied:

- One can use the wave property of the neutron and diffract the neutron beam from a single crystal. According to Braggs' law $2d\sin\theta = \lambda$, a certain wave length λ is being selected for a given lattice d-spacing under a scattering angle 2θ.

- One can use the particle property of the neutron and use the neutron time-of-flight to determine its velocity and thus its kinetic energy. How this is being done technically will be discussed in subsequent chapters.

Following our discussion of the correlation functions, we will now distinguish two principally different types of neutron scattering instruments:

- Diffractometers: these are scattering instruments, which either perform no energy analysis at all, or which measure only the truly elastic scattering. As discussed in chapter 5.2, the truly elastic scattering allows one to determine the time averaged structure. The prominent example is Bragg scattering from single crystals. If, however, no energy analysis is performed, one usually makes sure that one works in quasistatic approximation to facilitate the interpretation of the scattered intensity distribution. Quasistatic approximation corresponds to a snapshot of the scatterers in the sample and is important for example to determine short-range order in a liquid. Be it elastic scattering or integral scattering in quasistatic approximation, a diffraction experiment allows one to determine the position of the scatterers only. The movement of the scatterers is not accessible with such a diffraction experiment. Similarly, in a diffraction experiment for magnetic scattering, the arrangement of magnetic moments within the sample, i. e. its magnetic structure, can be determined, while the spin dynamics is not accessible in a diffraction experiment[3].
- Spectrometers: a neutron spectrometer is dedicated to measure inelastic scattering, i. e. to determine the change of the neutrons' kinetic energy $E = \frac{\hbar^2 k^2}{2m}$ during the scattering process. Such an experiment requires the analysis of the energy of the scattered neutrons, in contrast to a conventional diffractometer. Now the intensity measured in the detector depends on momentum- and energy- transfer and is proportional to the convolution of the double differential scattering cross section (5.1) with the resolution function of the instrument (5.12). Therefore a neutron spectrometer gives us information on the scattering functions (coherent or incoherent) and thus on the truly time dependent pair- or self correlation functions. This is why spectrometers are used to determine the dynamics of a system after its structure has been determined in a previous diffraction experiment[4].

[3] In fact there is a way to access also spin- or lattice- dynamics in a diffraction experiment: lattice vibrations will give rise to diffuse scattering around Bragg peaks, so-called thermal diffuse scattering, which can be modelled and thus the spectrum of excitations can be determined in an indirect, but not model-free direct way.
[4] Of course, spectrometers could also be used to determine the structure, but usually their resolution is not at all adapted to this purpose.

5.4 Diffractometers

5.4.1 Wide angle diffraction versus small angle scattering

According to (5.10), the momentum transfer during a scattering experiment is given by $\hbar\underline{Q} = \hbar\underline{k}' - \hbar\underline{k}$. Remembering that $k = \frac{2\pi}{\lambda}$, the magnitude of the scattering vector Q can be expressed in terms of wavelength λ and scattering angle 2θ as:

$$Q = \frac{4\pi}{\lambda}\sin\theta \tag{5.13}$$

As we have seen in chapter 5.2, the scattering cross section is related to the Fourier transform of the spatial correlation function and therefore a reciprocal relation exists between characteristic real space distances d and the magnitude of the scattering vector Q, for which intensity maxima appear:

$$\Delta Q \sim \frac{2\pi}{d} \tag{5.14}$$

Bragg scattering from crystals provides an example for this equation (compare chapter: "A neutron primer"): the distance between maxima of the Laue function is determined by $\Delta Q \cdot d = 2\pi$, where d is the corresponding real space periodicity. Reflectometry provides another example (see below): the Q-distance between Kiessig fringes is given by the relation $\Delta Q \cdot d \sim 2\pi$ (compare (5.19)), where d is the layer thickness.

(5.14) is central for the choice of an instrument or experimental set-up, since it tells us which Q-range we have to cover in order to get information on a certain length range in real space. (5.13) tells us, at which angles we will observe the corresponding intensity maxima for a given wavelength. This angle has to be large enough in order to separate the scattering event clearly from the primary beam. This is why we need different instruments to study materials on different length scales. Table 5.1 gives two examples.

Example	d	ΔQ	2θ (λ=1 Å)	2θ (λ=10 Å)	Technique
Distance between atoms in crystals	2 Å	3.14 $Å^{-1}$	29°	"cut-off"	wide angle diffraction
Precipitates in metals (e.g. Co in Cu)	400 Å	0.016$Å^{-1}$	0.14°	1.46°	small angle scattering

Tab. 5.1: *Examples for scattering from structures on different characteristic real space length scales d. ΔQ is the corresponding characteristic scattering vector according to (5.14), 2θ the scattering angle according to (5.13), calculated for two different wavelength λ.*

1. The study of structures on atomic length scales is typically done with a wavelength of around 1 Å (comparable to the distance between the atoms) and the scattered intensity is observed at rather large angles between 5° and 175°. Therefore one speaks of *wide angle diffraction*, which is employed for the study of atomic structures.
2. For the study of large scale structures (precipitates, magnetic domains, macromolecules in solution or melt) on length scales of 10 up to 10,000 Å (1 up to 1000 nm), the magnitude of the relevant scattering vectors as well as the corresponding scattering

angles are small. Therefore one chooses a longer wavelength in order to expand the diffractogram. The suitable technique is *small angle scattering*, which is employed to study large scale structures.

In what follows we will first focus on the study of large scale structures. In the corresponding conceptually very simple instruments, some typical considerations for the design of an instrument can be exemplified. We will distinguish between small angle neutron scattering instruments and reflectometers, discuss the basic instrument concepts and list some possible applications. After having discussed how large scale structures can be studied with neutron diffraction, we will then introduce instruments for wide angle scattering and their possible applications.

5.4.2 Small angle neutron scattering SANS

As mentioned in chapter 5.4.1, small angle scattering is employed whenever structures on length scales between typically 10 Å and 10,000 Å (1 nm and 1,000 nm) are of interest. This range of real space lengths corresponds to a scattering vector of magnitude between about 10^{-1} Å^{-1} and 10^{-4} Å^{-1} (1 nm^{-1} and 10^{-3} nm^{-1}). In order to observe the scattering events under reasonable scattering angles, one chooses a rather long wavelength. However, due to the moderator spectrum (see chapter "Neutron Sources"), there is very little neutron flux at wavelengths above 20 Å. Therefore typically neutrons of wavelength between 5 and 15 Å are employed for small angle neutron scattering.

Two different principles of small angle neutron scattering will be distinguished in this chapter: the pinhole SANS and the focusing SANS depicted in figures 5.4 and 5.5, respectively. Other types of instruments, e.g. with multi-pinhole grid collimation, are variants of these techniques and will not be discussed here.

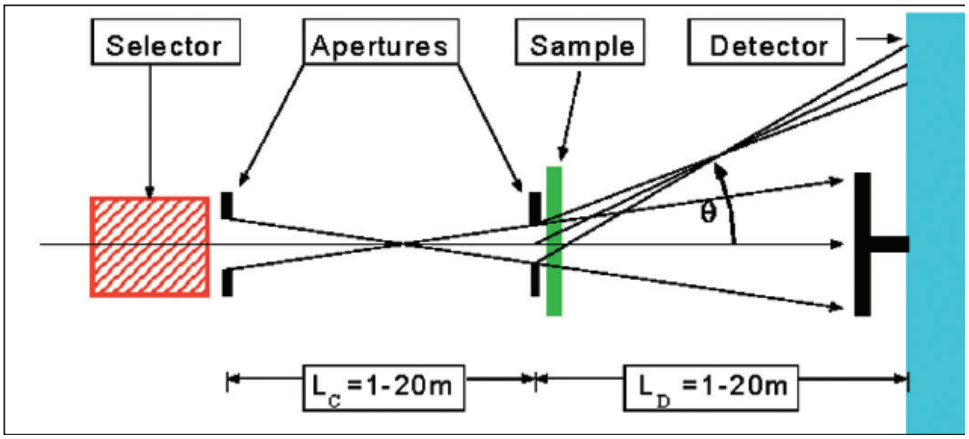

Fig. 5.4: *Schematics of a pinhole SANS, where the incident wave vector is defined through distant apertures (KWS-1 or KWS-2 of JCNS [3]).*

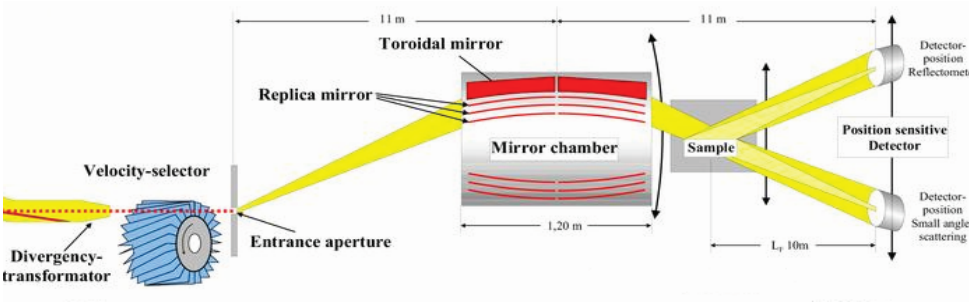

***Fig. 5.5**: Schematics of a focusing SANS, where an image of the entrance aperture is produced on the detector by a focusing mirror (KWS-3 of JCNS [3]).*

For both instrument concepts, the wavelength band is usually defined by a so-called velocity selector. Figure 5.6 shows a photo of a velocity selector drum build in Jülich for the instrument KWS-3.

***Fig. 5.6**: Drum of a velocity selector made from a light-weight, neutron absorbing alloy (MgLi). A velocity selector works on the "screw threat principle": it is rotating at high speeds and only neutrons in a certain velocity band can travel undisturbed in the channels between the absorbing partition walls; neutrons outside this velocity band are stopped in the walls. Thus only a certain velocity- or wavelength band can pass this device.*

In the pinhole SANS, the incident wave vector $\underline{k}$ is defined by two distant apertures of comparable size. The longer the distance between the diaphragms, the higher is the collimation for a given cross section of the beam. The sample is placed right next to the second aperture and the scattered neutrons are being recorded in a detector, which is at a large distance from the sample; typically the sample-detector distance is comparable to the collimation distance. The overall length of such an instrument can amount to 40 m, up to 80 m.

In contrast to the pinhole SANS, the focusing SANS uses a divergent incident beam and a focusing optical element produces an image of the entrance aperture on the detector. The sample is positioned directly behind the focusing element. Small angle scattering from the sample appears on the position-sensitive area detector around the primary beam spot. Such a set-up with a focusing element would be the natural solution in light optics, where focusing lenses are readily available. Due to the weak interaction of neutrons with matter, the index of refraction for neutrons is very close to one, and it is difficult to produce efficient focusing elements. In case of the focusing SANS realized by Forschungszentrum Jülich [4], a toroidal[5] mirror is employed as focusing element. Locally, the toroidal shape is a good approximation to an ellipsoid with its well-known focusing properties. The challenge in realizing such a device lies in the fact that small angle scattering from the focusing element has to be avoided i.e.

[5] A torus is a surface of revolution generated by revolving a circle about an axis coplanar with the circle, which does not touch the circle (examples: doughnuts, inner tubes).

the mirror has to be flat on an atomic scale (root-mean square roughness of about 3 Å !), which became possible due to the developments of optical industry for x-ray satellites.[6]

As an example of the considerations leading to the design of a neutron scattering instrument, we will now discuss the resolution of a pinhole SANS machine. In general terms, the resolution of an instrument denotes the smearing out of the signal due to the instruments' finite performance (5.12). As neutron scattering is a flux limited technique, there is need for optimization: the better the resolution of the instrument, i. e. the better the angular collimation $\Delta\theta$, the smaller the wavelength spread $\Delta\lambda$, the smaller is the intensity recorded on the detector. Therefore resolution has to be relaxed to such an extent that the features of interest are still measurable and not smeared out entirely by the resolution of the instrument, while at the same time the intensity is maximized. In order to determine the resolution of a SANS instrument, we start from (5.13): $Q = \frac{4\pi}{\lambda}\sin\theta$. The influence of angular- and wavelength spread can be determined by differentiation of this equation, where the different contributions have to be added quadratically:

$$\Delta Q^2 = \left(\frac{\partial Q}{\partial \theta}\right)^2 (\Delta\theta)^2 + \left(\frac{\partial Q}{\partial \lambda}\right)^2 (\Delta\lambda)^2 = \left(\frac{4\pi}{\lambda}\right)^2 \cos^2\theta (\Delta\theta)^2 + \left(\frac{4\pi \sin\theta}{\lambda^2}\right)^2 \Delta\lambda^2$$
$$\underset{\theta\to 0}{\overset{\uparrow}{=}} \left(\frac{4\pi}{\lambda}\right)^2 \left[(\Delta\theta)^2 + \theta^2\left(\frac{\Delta\lambda}{\lambda}\right)^2\right] = \frac{k^2}{12}\left[\left(\frac{d_D}{L_D}\right)^2 + \left(\frac{d_E}{L_C}\right)^2 + \left(\frac{d_S}{L_C} + \frac{d_S}{L_D}\right)^2 + \theta^2\left(\frac{\Delta\lambda}{\lambda}\right)^2\right] \quad (5.15)$$

ΔQ^2 is the variance of the scattering vector due to the finite collimation and monochromatization. d_E and d_S are the diameters of the entrance and sample aperture, respectively. d_D denotes the detector pixel size. L_C and L_D are collimation length and sample-detector distance, respectively. An optimization can be achieved, if all terms in (5.15) contribute the same amount, which leads to the condition

$$L_D = L_C \ , \ \ d_E = d_D = 2d_S \quad (5.16)$$

(5.16) shows that a pinhole SANS has to be designed such that sample-to-detector distance L_D is equal to the collimation length L_C. Typical values are $L_D = L_C = 10$ m with openings of $d_E = 3$ cm for the entrance- and $d_S = 1.5$ cm for the sample aperture. Note that one can chose the opening of the entrance aperture to be twice as large as the opening of the sample aperture - or sample size - without sacrificing markedly in resolution, while gaining in neutron count rate! The detector needs a minimum pixel resolution $d_D \approx d_E$; A detector with a radius of about $R_D \approx 30$ cm is necessary to cover the required Q-range up to 0.05 Å^{-1} at $L_D = 10$ m and for $\lambda = 8$ Å. Having defined the incident collimation, we can now determine the appropriate wavelength spread with the same argument as above: the last term in the sum in (5.15), corresponding to the wavelength spread, should contribute the same amount to the variance of the scattering vector as the corresponding terms for the collimation, i. e.:

$$\frac{\Delta\lambda}{\lambda} = \frac{d_E}{L_C}\cdot\frac{L_D}{r_D} \approx \frac{d_E}{r_D} \approx \frac{1}{10} = 10\% \quad (5.17)$$

(5.17) demonstrates that in general for small angle scattering we don't need a very high degree of monochromatization. A 10 % wavelength band is acceptable, since for small angles the smearing due to the wavelength spread is quite comparable to the smearing due to the incident divergence. This is the reason why usually a velocity selector is employed as monochromatizing element for small angle scattering, as it lets a wavelength band of typically 10 % pass.

[6] It should be mentioned that nowadays focusing lenses for neutron scattering have also been realised. These have a very long focal distance, but can be employed to improve intensity or resolution in pinhole SANS.

Let us give a short introduction into the analysis of small angle scattering experiments. As in any scattering experiment, the detected intensity is proportional to the scattering cross section, which in the SANS case is usually normalised to the sample volume and therefore has the unit [cm^{-1}]:

$$\frac{d\Sigma}{d\Omega} = \frac{1}{V_{sample}} \cdot \frac{d\sigma}{d\Omega} \tag{5.18}$$

Here we discuss the so-called "two phase model" only, where homogeneous particles are dispersed in a matrix (e. g. precipitates in metals or nanoparticles in solution etc.). The cross section will then be proportional to the contrast between particles and solution

$$\Delta b = \sum_j b_j \left(\rho_{j,P} - \rho_{j,M} \right) \tag{5.19}$$

where j labels atom species j of scattering length b_j with number density $\rho_{j,P}$ in the particle and $\rho_{j,M}$ in the matrix, respectively. The differential cross section per particle is given by the interference term (note: we use a continuum description for the small Q limit):

$$\begin{aligned} \frac{d\Sigma}{d\Omega}(\underline{Q}) &= \left| \int_V \Delta b \cdot e^{i\underline{Q}\cdot\underline{r}} d^3r \right|^2 \\ &= \Delta b^2 V^2 \underbrace{\left| \frac{1}{V} \int_V e^{i\underline{Q}\cdot\underline{r}} d^3r \right|^2}_{f(\underline{Q})} \end{aligned} \tag{5.20}$$

Here $f(\underline{Q})$ denotes the *particle form factor* for a homogeneous particle of volume V:

$$f(\underline{Q}) = \frac{1}{V} \int e^{i\underline{Q}\cdot\underline{r}} d^3r \tag{5.21}$$

(5.20) is the differential cross section for a single particle. For very dilute solutions of identical particles, the cross section will be given by (5.20) times the number N of particles ("single particle approximation"). However, in more concentrated solutions, there will be additional interference effects between the particles, which are described by the so-called *structure factor S* and we obtain the modified cross section for dense solutions:

$$\frac{d\sigma}{d\Omega} = N \cdot \Delta b^2 \cdot V^2 \cdot \left| f(\underline{Q}) \right|^2 \cdot S(\underline{Q}) \tag{5.22}$$

where $S(\underline{Q})$ is related to the Fourier Transform of the pair correlation function $g(\underline{R})$ between the single particles at distance $\underline{R}$:

$$S(\underline{Q}) = 1 + \frac{1}{V_{sample}} \int_{V_{sample}} g(\underline{R}) e^{i\underline{Q}\cdot\underline{R}} d^3r \tag{5.23}$$

(Note: for vanishing pair correlations $g(\underline{R}) \equiv 0$, i. e. random distributed particles, the structure factor has to be unity: $S(\underline{Q}) \equiv 1$).

The isotropic form factor of a homogeneous sphere of radius R has already been given in the chapter "Neutron Primer":

$$f(Q) = 3 \frac{\sin QR - QR\cos QR}{(QR)^3} \tag{5.24}$$

For foreward scattering $f(Q=0)=1$ per definition. For small values of the scattering vector, this expression can be approximated by:

"*Guinier Law*" for *QR≤2*:

$$\left|f(Q)\right|^2 \approx e^{-\frac{(QR_G)^2}{3}} \approx 1-\frac{Q^2R_G^2}{3} \tag{5.25}$$

Here the quantity R_G is the so-called *radius of gyration* of the particle. For a spherical particle $R_G^2=\frac{3}{5}R^2$, but R_G can defined in a more general way also for non-spherical particles.

For *QR=3* the form factor squared has dropped to about 10 %. In the larger *Q* region - neglecting the sharp minima of the form factor (5.24), which are often not visible due to particle size distribution and instrumental resolution - the form factor follows the behaviour:

"*Porod Law*" for *QR≥4.5*:

$$\left|f(Q)\right|^2 \approx 2\pi\frac{A}{V^2}Q^{-4} \tag{5.26}$$

where $A=4\pi R^2$ is the surface, and $V=\frac{4\pi}{3}R^3$ the volume of the sphere of radius *R*. In small angle scattering, often times one does not deal with simple geometrically smooth particles in a second phase. In stochastical growth processes or soft matter system, irregular *fractal* structures can appear, which show self-similarity on multiple length scales. For such structures, power laws with other exponents are observed:

$$\begin{aligned}\frac{d\sigma}{d\Omega}(mass\ fractal) &\sim Q^{-D} = Q^{-1}...Q^{-3}\\ \frac{d\sigma}{d\Omega}(surface\ fractal) &\sim Q^{D_s-6} = Q^{-3}...Q^{-4}\end{aligned} \tag{5.27}$$

where *D* denotes the so-called *fractal dimension* for porous objects. *D* is in general smaller than 3 and non-integer. If the particles have a dense core, but a rough self-similar surface, they are called *surface fractals* with a surface area of $A \sim R^{Ds}$. From the above discussion we see that characteristic regions can be distinguished in a small angle scattering experiment:

1. Close to forward direction in the very small *Q* limit and for dilute solutions, we observe constant scattering proportional to the number of particles *N*, the square of the particle volume V^2 and contrast (5.19). For known contrast, we can deduce the product $N\cdot V^2$, if the scattering is measured in absolute units by comparing to a known scatterer e. g. water. For dense solutions, the structure factor form correlations between particles becomes apparent.

2. In the region up to *QR≤2*, the Guinier Law (5.25) holds for compact particles. From a *Guinier-Plot* $\ln\frac{d\sigma}{d\Omega}$ versus Q^2 one can determine the radius of gyration

$$R_G = \frac{\int_V r^2\Delta b(r)d^3r}{\int_V \Delta b(r)d^3r} \tag{5.28}$$

3. In the Porod-region *QR≥4.5*

$$\frac{d\sigma}{d\Omega} = \Delta b^2 2\pi NAQ^{-4} \tag{5.29}$$

we can, independent of particle shape, determine the total surface area $N \cdot A$ of all particles with sharp surfaces from a *Porod Plot* $\frac{d\sigma}{d\Omega} \cdot Q^4$ versus Q^4.

4. Finally, if Q approaches the value $1/a$ where a corresponds to typical atomic distances, we approach the region of Bragg scattering from atomic structures (wide angle scattering).

Let us now turn to applications of small angle scattering. One example is given in figure 5.7, which is concerned with the self-organization of crystalline amorphous diblock-copolymers [4]. Combining three different instruments, small angle scattering has been observed over ten orders of magnitude in cross section and nearly four orders of magnitude in momentum transfer. In different regions, different power laws apply, corresponding to different structures observed: the Q^{-2} power law corresponds to *2d* structures on the shortest length scale, the Q^{-1} power law corresponds to the organization of rods in bundles, while the Q^{-3} power law corresponds to a network of bundles with a mass fractal aspect and finally, correlations become visible in the very low Q-range.

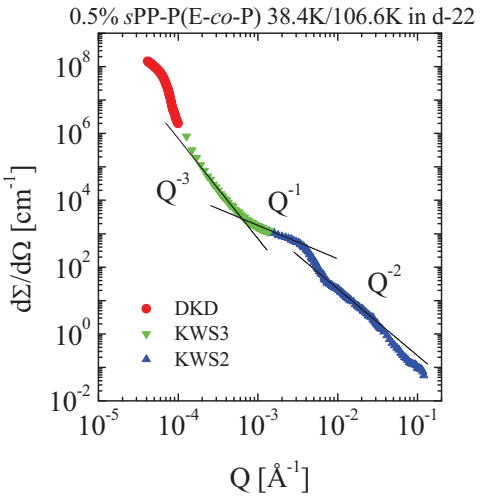

Fig. 5.7: *SANS investigation of the self-organization of a crystalline-amorphous diblock-copolymer measured with three different instruments of different resolution: double crystal diffractometer, focussing SANS and pinhole SANS for the low, medium and larger Q range, respectively. Plotted is the cross section in absolute units versus the magnitude of the scattering vector. For details see [4].*

We will end this short introduction into the principles of small angle scattering by listing some examples for applications of small angle scattering in different fields of science:

- *soft matter*: polymers and colloids, e. g. micelles, dendrimers, liquid crystals, gels, reaction kinetics of mixed systems, …
- *materials science*: phase separation in alloys and glasses, morphologies of superalloys, microporosity in ceramics, interfaces and surfaces of catalysts
- *biological macromolecules*: size and shape of proteins, nucleic acids and of macromolecular complexes, biomembranes, drug vectors
- *magnetism*: ferromagnetic correlations and domains, flux line lattices in superconductors, …

5.4.3 Large scale structures: Reflectometry

As elaborated in chapter 5.4.2, neutron small angle scattering is applied to determine large scale structures, e. g. scattering length density fluctuations on length scales of some 100 Å in bulk material. There is another type of instruments, which is dedicated to the study of large scale structures in thin film systems, on surfaces and in multilayers. Such an instrument is called a *neutron reflectometer*. This conceptually simple instrument is depicted schematically in figure 5.8.

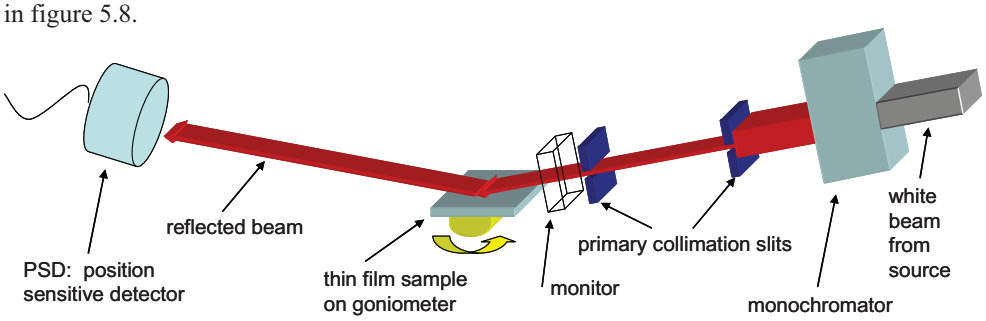

Fig. 5.8: *Schematics of a neutron reflectometer. Monochromatization can be done in many different ways: by a velocity selector, by a crystal monochromator, or by a chopper in a time-of-flight instrument. Collimation slits define the direction of the incident beam. The monitor is a low efficient detector of high transmission, which measures the incident flux on the sample. The reflected neutrons are either detected in a position sensitive detector, or a secondary collimation track in front of a point detector selects the direction of the reflected beam. For magnetic samples, a polarizer, a polarization analyzer and guide fields can be inserted for polarization analysis experiments.*

Similar to a pinhole SANS instrument, the incident beam is collimated through a set of two well separated slits. However, since in reflectometry, one is mainly interested in the momentum transfer perpendicular to the planar sample surface, the collimation of a reflectometer is tight only in this direction. Along the sample surface the beam can be wide and have a larger divergence in order to gain intensity. This collimated beam impinges on the sample under a grazing angle (typically fractions of a degree up to a few degrees) and is reflected into a single point detector or a position sensitive detector. To define the angle of exit for a point detector, a secondary collimation is needed between sample and detector. The incident beam is monochromatized using different techniques, depending on the resolution requirements: velocity selector, time-of-flight chopper or crystal monochromator.

With such an instrument, the layer structure of a sample can be determined, such as layer composition, layer thickness and surface- or interfacial roughness. This information is obtained in so-called specular reflection, for which the incident angle is equal to the final angle like in a reflection from a perfect optical mirror. In this case, the momentum transfer of the neutrons is perpendicular to the surface of the sample and thus only laterally averaged information can be obtained. In order to determine lateral correlations within the layers, for example magnetic domain sizes, a momentum transfer within the layer has to occur, which implies that angle of incidence and final angle have to be different. Short range correlation within the layers will then give rise to so-called off specular diffuse scattering as well know in optics from a bad optical mirror.

The scattering geometry is shown in Fig. 5.9.

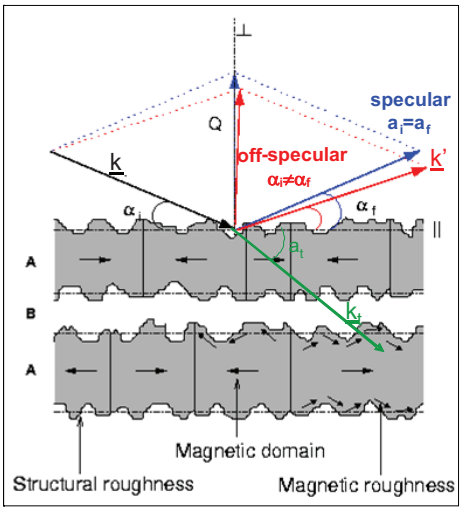

Fig. 5.9: *Scattering geometry for grazing incidence neutron scattering. Specular reflections are obtained, if the angle of incidence equals the final angle $\alpha_i = \alpha_f$. Off-specular scattering is observed at $\alpha_i \neq \alpha_f$.*

In fact, the theoretical description of neutron reflectometry follows exactly along the lines of conventional optics, except that for neutrons in most cases the index of refraction is smaller than one and thus external total reflection occurs for neutrons coming from vacuum towards matter[7]: The index of refraction n of neutrons of wavelength λ from a layer composed of elements with scattering length b_i and number density ρ_i and linear absorption coefficient μ_n is given by:

$$n = 1 - \frac{\lambda^2}{2\pi}\sum_j b_j \rho_j - i\frac{\lambda}{4\pi}\mu_n =: 1 - \delta - i\beta \tag{5.30}$$

Refraction and total reflection are described by the well-known *Snell's Law* of optics:

Snells law: $$\frac{\cos\alpha_i}{\cos\alpha_t} = \frac{k_t}{k} = n \tag{5.31}$$

angle of total reflection: $\cos\theta_c = n$ (5.32)

The intensities of reflected and transmitted beam can be determined from the optical *Fresnel equation* (A_0, A_1, B_0: amplitudes of incident, transmitted and reflected waves, respectively; k_z, k_{tz}: component of wavevector $\underline{k}$ and $\underline{k}_z$, respectively, perpendicular to average surface):
Fresnel equation:

Reflectivity $$R = \left|\frac{B_0}{A_0}\right|^2 = \left|\frac{k_z - k_{tz}}{k_z + k_{tz}}\right|^2 = \left|\frac{\alpha_i - n\cdot\alpha_t}{\alpha_i + n\cdot\alpha_t}\right|^2 \tag{5.33}$$

Transmissivity $$T = \left|\frac{A_1}{A_0}\right|^2 = \left|\frac{2k_z}{k_z + k_{t,z}}\right|^2 = \left|\frac{2\alpha_i}{\alpha_i + n\cdot\alpha_t}\right|^2 \tag{5.34}$$

[7] This is exactly what happens in neutron guides, evacuated tubes of usually rectangular cross section, where neutrons are totally reflected from the smooth glass side walls, often coated, e.g. with ^{58}Ni, to enhance the angle of total reflection. Since for total reflection conditions, reflectivity is close to 100%, neutrons are transported nearly without loss from the source to the instruments by bouncing back- and forth from the guide side walls.

Fig. 5.10 shows as an example the reflectivity and transmissivity of a Ni layer.

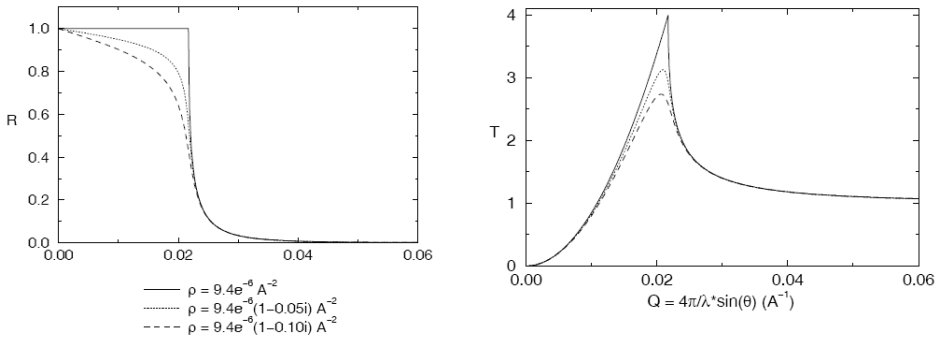

Fig. 5.10: *Reflectivity and transmissivity of neutrons from a Ni surface.*

Here we just want to demonstrate with very simple arguments how interference effects from layered structures arise and how the intensity modulation in Q-space are related to real space length scales. Figure 5.11 shows how interference can occur from a beam being reflected at the surface and at the internal interface of a double layer stack.

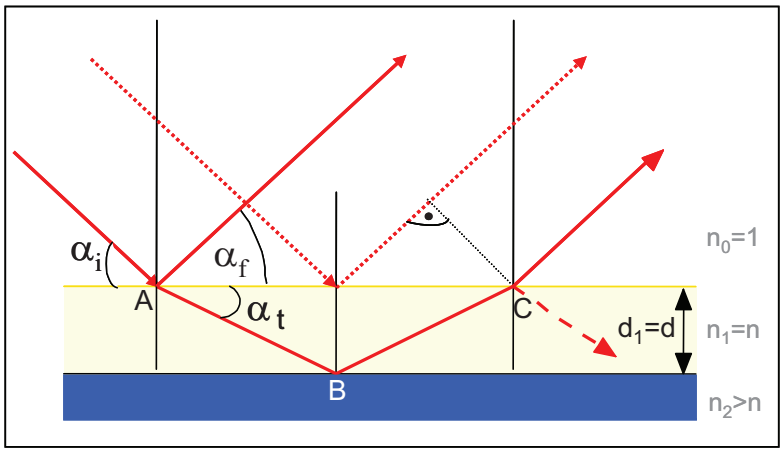

Fig. 5.11*: Schematics of the reflection of a neutron beam from a single layer on a substrate. There exists an optical path length difference Δ between the rays drawn with a solid line and those drawn with a dotted line.*

For simplicity we consider only the case of a specular reflection, i. e. the incident angle α_i is equal to the angle of exit α_f: $\alpha_i = \alpha_f = \alpha$. Interference occurs between beams reflected from the surface (dotted line in Fig. 5.11) and those first transmitted into the layer, reflected from the interface between layer 1 and substrate and then leaving the layer into vacuum (solid line). To a good approximation, refraction at the top surface can be neglected for incident angles larger than about twice the critical angle of total reflection. In this case $\alpha_t = \alpha_i = \alpha_f = \alpha$ holds. Since the index of refraction for neutrons is very close to one, this approximation is

valid even for rather small angles of incidence. Then the optical path length difference for the two beams is:

$$\Delta = 2d \sin\alpha \tag{5.35}$$

Here d is the thickness of the layer 1. We can now determine the distance between interference maxima from the condition that the path length difference has to differ by one wavelength: $\lambda = 2d \cdot \Delta(\sin\alpha) \approx 2d \cdot \Delta\alpha$. With $Q = \frac{4\pi}{\lambda}\sin\alpha \approx \frac{4\pi}{\lambda}\alpha$ we finally obtain:

$$\Delta Q \approx \frac{2\pi}{d} \tag{5.36}$$

Again we can see that the interference phenomena in Q-space are connected with real space length scales in a reciprocal way. (5.36) tells us that there will be a number of interference maxima at distances in Q of $\frac{2\pi}{d}$. These interference phenomena are called "*Kiessig fringes*" and are well known to us in conventional optics for example as the beautiful colors observed in soap bubbles. Figure 5.12 shows as an example the reflectivity of neutrons from a thin nickel layer on a glass substrate, which is nothing else but a section of a neutron guide employed to transport the neutrons from the source to the instrument over long distances by multiple total reflections. The Kiessig fringes are nicely visible in this example and the thickness of the nickel layer can be determined from the distance between adjacent intensity maxima.

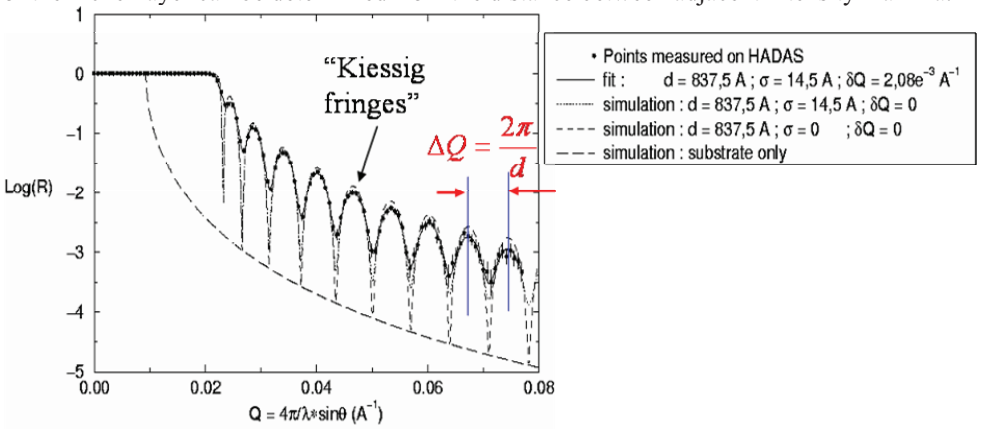

Fig. 5.12: *Reflectivity of neutrons from a nickel layer on glass substrate on a logarithmic scale. Data points were measured on the HADAS reflectometer of the late FRJ-2 reactor. The solid line shows a fit, where the layer thickness was determined to be 837.5 Å with a root mean square roughness of 14.5 Å and where the resolution of the instrument of $\delta Q = 2.08 \cdot 10^{-3}$ Å^{-1} has been taken into account; the dotted line shows a simulation for the same structural parameters, but for an ideal instrument without resolution broadening; the short dashed line shows the simulation for the same layer thickness but without roughness; the long dashed line shows the simulation for the glass substrate only.*

Neutron reflectometry has many applications in different fields of science of which we can only list a few:

- *soft matter science*: thin films e. g. polymer films; polymer diffusion, self-organization of diblock copolymers; surfactants; liquid-liquid-interfaces, …
- *life science*: structure of biomembranes

- *materials science*: surface of catalysts; kinetic studies of interface evolution; structure of buried interfaces
- *magnetism*: thin film magnetism e. g. exchange bias, laterally structured systems for magnetic data storage, multilayers of highly correlated electron systems, …

5.4.4 Atomic structures: Single crystal and powder neutron diffraction

As explained in chapter 5.4.1, wide angle scattering with neutrons of wavelength typically 1 Å is applied for the determination of atomic structures. Due to the periodicity of the lattice, Bragg peaks appear under diffraction angles given by the Bragg equation (compare reflectometry: (5.35) and (5.36)!):

$$2d\sin\theta = \lambda \qquad (5.37)$$

The intensity of the Bragg peaks is governed by the arrangement of the atoms within the unit cell (structure factor) and the scattering from the single atom (form factor). By collecting a large set of scattered intensities for many Bragg peaks, modeling the atomic structure and refining the parameters in order to get an optimum agreement between calculated and observed intensities, the arrangement of atoms within the unit cell as well as the arrangements of spins for magnetic samples can be determined. Figure 5.13 shows the schematics of a single crystal diffractometer.

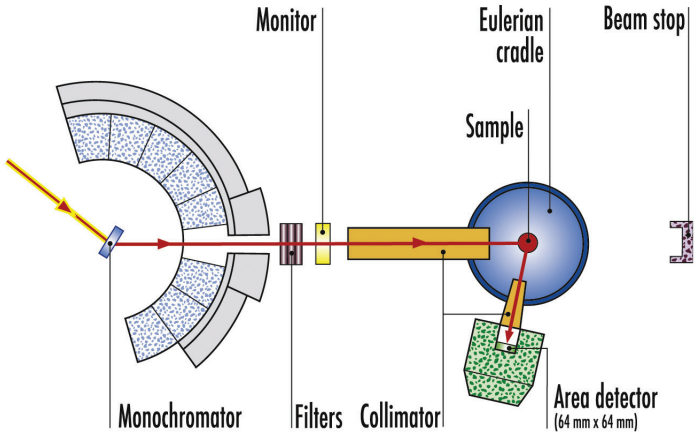

Fig. 5.13: *Schematics of a single crystal diffractometer. The drawing shows the layout of the diffractometer D9 at the Institute Laue-Langevin and has been taken from http://www.ill.eu/.*

In contrast to small angle scattering, where a broad wavelength band is employed to enhance the scattered intensity, a better monochromatization of typically $\frac{\Delta\lambda}{\lambda} \sim 1\%$ has to be achieved for wide angle scattering to avoid the broadening of the Bragg reflections due to the wavelength spread according to (5.37). This monochromatization is typically done by Bragg diffraction from a single crystal. The direction of the incident beam is determined by a set of slits. As Bragg reflections only occur when the corresponding lattice planes have a definite orientation with respect to the incident beam, the single crystal sample is usually mounted on a so-called Eulerian cradle, which allows one to orient the sample using the three Eulerian

angles ω, χ and ϕ. Finally the scattered beam is detected in a point- or small area detector. Care must be taken to collect the entire integrated intensity for a scan through the Bragg reflection.

A conceptually simpler experiment for the determination of atomic structures is the neutron powder diffractometer. In this case, since the powder grains in the sample usually have random orientations with respect to the incident beam, there is no need for orienting the sample with respect to the beam. Scattering will always occur for some of the grains, which by chance fulfill the Bragg condition. As scattering occurs for all allowed Bragg reflections simultaneously, it would be very inefficient to detect it by a single point detector, which would have to be positioned recursively for the correct 2θ values. Therefore in powder diffraction one usually uses a large linear - or even better area - position sensitive detector, which is arranged on a circular arch around the sample position.

While neutron powder diffraction is conceptually simple, it poses the problem that Bragg reflections will overlap for larger unit cells e. g. due to the finite peak width. Among other factors, the peak width is determined by the resolution of the instrument. One can show that the resolution function for a neutron powder diffractometer on a beam being monochromized by a Bragg reflection from a monochromator crystal is given by:

$$\left(\Delta 2\theta\right)^2 = U\tan^2\theta + V\tan\theta + W \qquad (5.38)$$

In such a situation, one cannot determine the intensities of the various Bragg reflections separately. The solution to the problem is the so-called *Rietveldt*- or profile refinement, where structural parameters (unit cell metric *a,b,c,α,β,γ,* atom positions and site occupations, the Debye-Waller-factors, etc) are refined together with the instrumental parameters (zero point of the scattering angle $2\theta_0$, parameters of the resolution function *U, V, W*, etc). Assuming a certain peak shape function, this allows one to model the entire powder diffractogram and determine the corresponding parameters from a refinement, which aims at minimizing the weighted sum of the quadratic deviations of calculated and observed intensities for all data points. Figure 5.14 shows an example of such a Rietveldt analysis for data taken from a colossal magnetoresistance manganite.

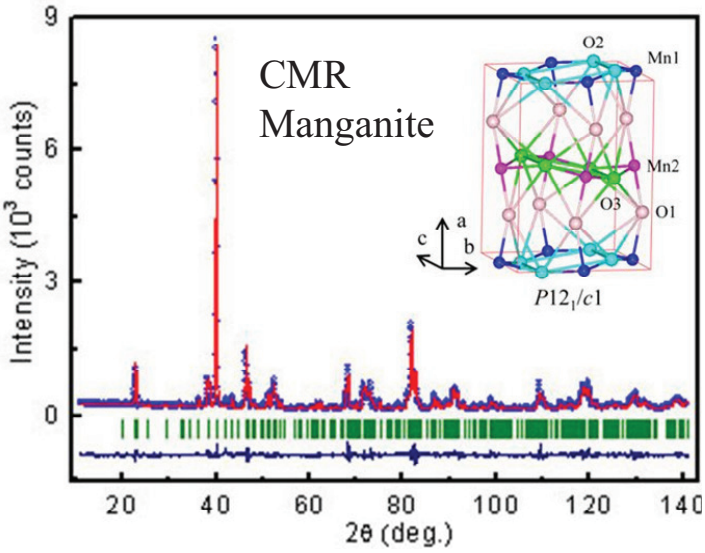

Fig. 5.14: *Powder neutron diffraction from a colossal magnetoresistance manganite. Points represent the measured intensities, the solid line the calculated profile function. The green bars below the diffractogram indicate the positions of the Bragg reflections and the line beneath shows the difference between observed and calculated intensities [5].*

As one can see, there is a very strong overlap of Bragg reflections, especially at larger scattering angles. Still, by using the above mentioned profile refinement technique, the atomic structure of the compound could be determined to a great position.

Applications of wide angle diffractions are manifold:

- *lifescience*: structure of biological macromolecules, e. g. Hydrogen (crystal water!) in protein structures
- *chemistry*: structure determination of new compounds, position of light atoms; time resolved reaction kinetics
- *materials science*: stress-strain determination; texture of materials
- *geo-science*: phase and texture analysis
- *solid state physics*: structure - function relations e. g. in high T_C superconductors; magnetic structures and spin densities, e. g. in molecular magnets

5.5 Spectroscopy

So far, we have only explored the purely elastic - or the quasistatic correlation functions, which give us structural information on various length scales only. We will now turn to the general case of correlation functions in space and time, which allow us to determine in addition the microscopic dynamics of the sample under investigation. Again, different instrument types exist for different applications. First of all, if we consider the neutron as a particle, we can determine the time of flight it needs to travel from the sample to the detector and thus its velocity or energy after the scattering process. With the knowledge of the incident energy, the

energy transfer during the scattering process can be determined. This kind of neutron spectrometer is called a *time-of-flight or TOF spectrometer*. A special case of the TOF spectrometer is the so-called *neutron spin echo spectrometer*, where the time-of-flight of each single neutron is being determined through the Larmor precession of the nuclear spin of the neutron in an external magnetic field. Neutron spin echo spectroscopy has the highest energy resolution and measures the intermediate scattering function directly. Therefore it is well suited to study slow relaxation processes. An alternative approach to spectroscopy is to determine the energy of the scattered neutrons by means of Bragg reflection from an analyzer crystal. Such an instrument is called a *crystal spectrometer* and if the selection of the incident wavelength is done by a crystal monochromator, it is called a *triple axis spectrometer*. A variant of a crystal spectrometer is the high resolution *backscattering spectrometer*. Of course there are various combinations of these techniques, which exist in particular at spallation sources. A discussion of all of the various instrument concepts goes well beyond the scope of this introductory chapter.

5.5.1 Time-of-Flight or TOF spectrometry

Figure 5.15 depicts schematically a generic time-of-flight spectrometer.

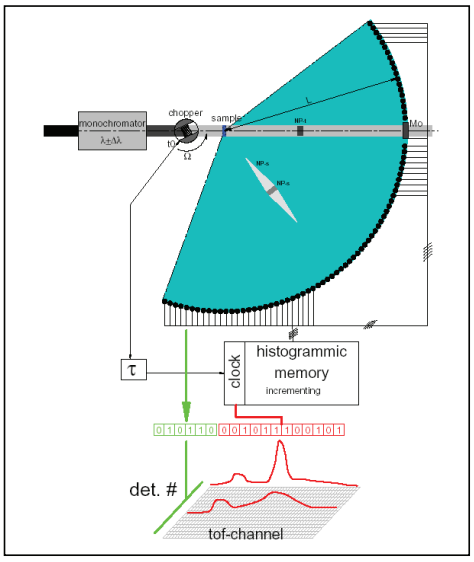

***Fig. 5.15**: Generic TOF spectrometer. The neutron beam is monochromatized, either by a crystal monochromator (X-TOF) or by time-of-flight (TOF-TOF) with choppers and / or the pulse from a spallation source. A chopper creates monochromatic neutron beam pulses incident on the sample. The scattered neutrons are collected in an array of detectors surrounding the sample. For each detector pixel, the neutrons are counted into a histogram as a function of their arrival time. These intensity – time histograms can be converted into the scattering function S(Q,ω) by using a reference sample for absolute calibration and simple kinematic relations between scattering angle and flight time on one hand and scattering vector and energy on the other hand.*

Neutrons are being monochromized either by reflection from a monochromator crystal or by time-of-flight techniques (X-TOF or TOF-TOF instruments). Monochromatic neutron pulses are produced by a chopper, which can be a fast rotating (up to e.g. 600 Hz) disc or drum made from neutron absorbing material, which has a slit that lets neutron pass only during a short time interval of typically some microseconds. This pulsed neutron beam impinges on the sample and is scattered under all possible scattering angles. Neutrons are recorded on a two dimensional position sensitive detector (nowadays, this is often an array of linear position sensitive ^{3}He detector tubes) surrounding the sample typically on the surface of a cylinder. From the arrival time of the neutrons in the detector with respect to the starting time given by the opening of the chopper, an intensity spectrum can be recorded for each scattering angle separately as a function of the arrival time of the neutrons in the detector. Using simple kine-

matic equations for the neutron as a particle and a calibration obtained by measuring a reference sample, this time-of-flight spectrum can be converted into the scattering function $S(\underline{Q},\omega)$. Figure 5.16 illustrates the scattering process in a flight path versus time diagram.

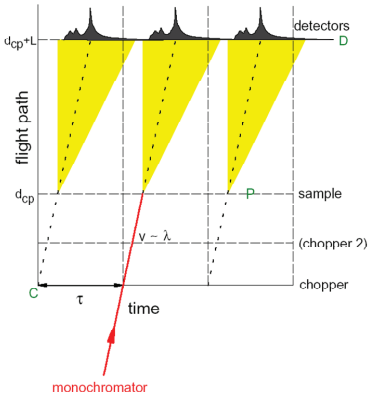

Fig. 5.16: *Flight-path-versus-time-diagram for a generic time-of-flight instrument (see text).* (*Courtesy of Dr. M. Monkenbusch)*

In such a diagram, a monochromatic neutron beam has a certain slope, which can be derived from the de Broglie equation $p = \frac{h}{\lambda} = m \cdot v = m \cdot \frac{s}{t}$:

$$t = \frac{m}{h} \cdot s \cdot \lambda \tag{5.39}$$

Typical velocities for thermal neutrons lie in the range of meter per millisecond. In figure 5.16 the neutrons coming from a monochromator enter the chopper with a certain slope in the path-vs.-time diagram corresponding to the velocity of the monochromatic neutrons. With a repetition rate of $1/\tau$ given by the chopper frequency, pulses of monochromatic neutrons leave the chopper. A second chopper can be applied to suppress higher order reflections. The neutron scattered from the sample can either gain energy, resulting in a steeper slope in the path-vs.-time diagram or loose energy resulting in a shallower slope. The number of neutrons entering the detector in a certain time interval is counted into a histogram with the elastic line usually being strongest and inelastic events being visible in neutron energy gain or -loss.

A nice example for a powder neutron time-of-flight spectrum is given by the excitation spectrum of a molecular magnet, namely Mn_{12} acetat, see figure 5.17 [6]. Here the time-of-flight axis has been converted into an energy scale. Clearly visible are nicely separated excitations, which result in the energy level diagram depicted on the middle of figure 5.17. Transitions between these levels correspond to transitions between different values of the magnetic quantum number of the total spin of the molecule. Modeling this energy level spectrum allows one to determine the magnetic interaction parameters, here mainly the magnetic anisotropy.

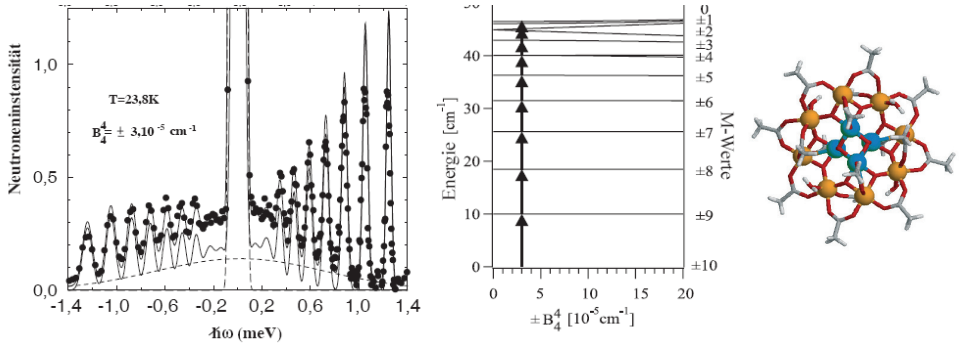

Fig. 5.17: *Left: Time-of-flight spectrum of the molecular magnet Mn_{12} acetat converted into an energy scale; middle: the corresponding energy level diagram; right: the magnetic molecule consisting of an outer ring of 8 Mn atoms with parallel coupled spins and an inner ring of 4 Mn atoms with opposite spin orientation. Taken from [6].*

Typical applications of time-of-flight spectroscopy can be found in various fields of science:

- *soft matter and biology*: dynamics of gels, proteins and biological membranes; diffusion of liquids, polymers; dynamics in confinement
- *chemistry*: vibrational states in solids and adsorbed molecules on surfaces; rotational tunneling in molecular crystals
- *materials science*: molecular excitations in materials of technological interest (e. g. zeolithes) and especially in diluted systems (matrix isolation); local and long range diffusion in superionic glasses, hydrogen-metal systems, ionic conductors
- *solid state physics*: quantum liquids; crystal field splitting in magnetic systems; spin dynamics in high T_C superconductors; phase transitions and quantum critical phenomena; phonon density of states.

5.5.2 Triple axis spectroscopy

An alternative approach for the study of dynamics of condensed matter systems is the so-called *triple axis spectroscopy*. The schematic of a triple axis spectrometer is depicted in figure 5.18.

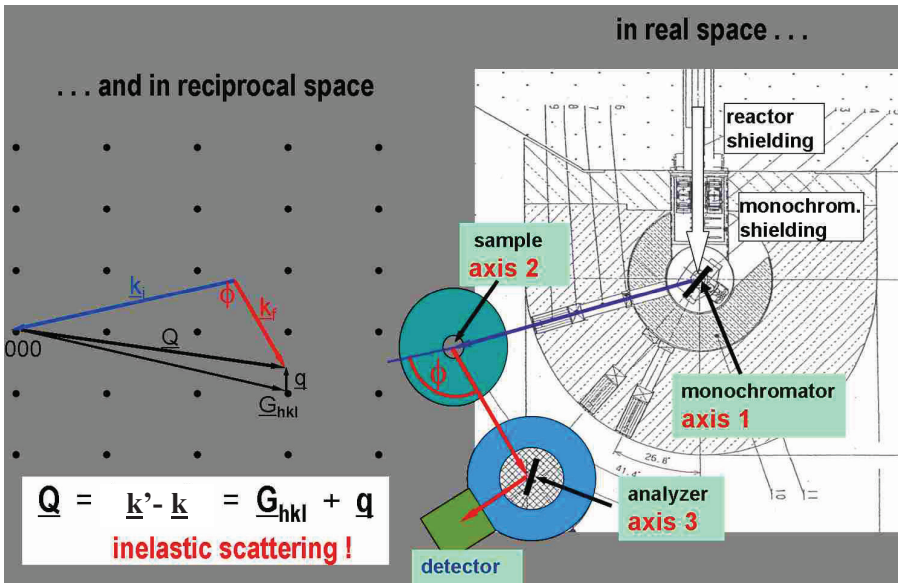

Fig. 5.18: *right: schematics of a triple axis spectrometer showing the three axes; left: scattering diagram in reciprocal space. (Courtesy of Dr. H. Conrad)*

In this case the energies of the incident and scattered neutrons are selected by means of a single crystal monochromator and - analyzer, respectively. Also the sample is usually in single crystalline form. These crystals (monochromator, sample, analyser) are on rotation tables, which form axis 1, axis 2 and axis 3 of the triple axis spectrometer. If we compare this instrument with the time-of-flight spectrometer shown in figure 5.15, one difference becomes immediately clear: while the time-of-flight spectrometer with its large detector bank allows one to obtain an overview over the excitation spectrum in reciprocal space, the triple axis spectrometer is the instrument of choice, if a certain narrow region in $\underline{Q}$ and ω is of interest. This is the case, if sharp excitations like lattice vibrations (phonons) or spin waves (magnons) are being investigated. A propagation vector of such an excitation together with a certain energy transfer can be selected by setting monochromator, sample and analyzer to the corresponding values as depicted in the scattering diagram of figure 5.18, left. Here the energy transfer is given by $\Delta E = \frac{\hbar^2}{2m}(k'^2 - k^2)$, while the momentum transfer is given as $\hbar\underline{Q} = \hbar\underline{k}' - \hbar\underline{k} = \hbar\underline{G}_{hkl} + \hbar\underline{q}$.

Figure 5.19 shows as an example spin wave dispersion relations determined for the garnet $Fe_2Ca_3Ge_3O_{12}$ by triple axis spectroscopy.

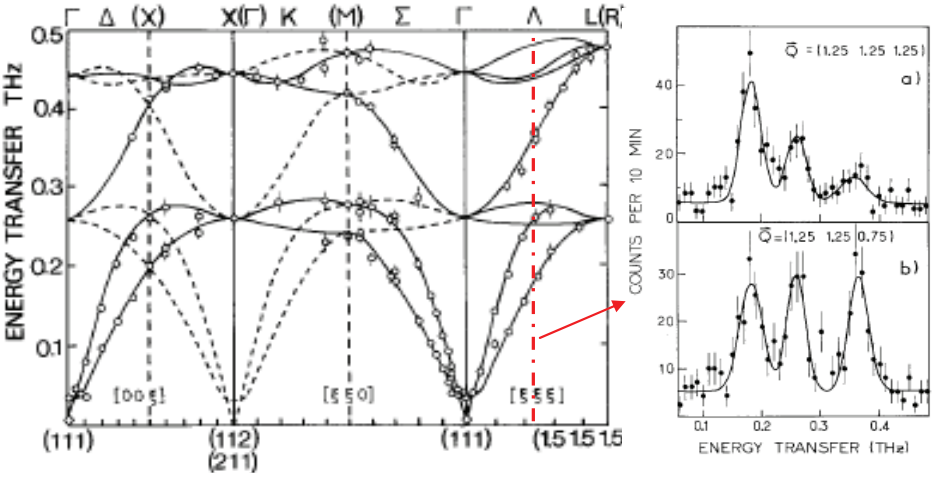

Fig. 5.19: *Spin wave dispersion relations for the garnet $Fe_2Ca_3Ge_3O_{12}$ along main symmetry directions in reciprocal space. The data points are obtained from scans keeping the momentum transfer Q constant. The figure on the right shows examples of such "constant Q scans". The solid lines are model calculations, from which the interaction (exchange) parameters between the spins in the unit cells can be determined; figure taken from [7].*

Typical examples of triple axis spectroscopy lie mainly in solid state physics:

- phonon dispersions in crystalline material, from which the interatomic forces can be determined
- spin wave dispersions, which allow one to determine exchange and anisotropy parameters
- dynamics of biological model membranes
- lattice and spin excitations in quantum magnets, superconductors, …
- phase transitions: critical behavior.

5.5.3 High resolution spectroscopy

Both, time-of-flight and triple axis spectroscopy, have typical energy resolutions of a few percent of the incident neutron energy. While such energy resolutions are sufficient in many cases, there is need for higher energy resolutions, for example to investigate the rather slow movements of large macromolecules, the slow spin dynamics of frustrated spin systems, diffusion of atoms or tunneling processes in molecular crystals. In order to improve the energy resolution, one could just narrow the energy band width of the neutrons incident on the sample. However, such an improvement of resolution goes hand-in-hand with the decrease of the signal in the detector and is therefore not practicable. There are, however, alternative approaches to increase the energy resolution: *neutron spin echo spectroscopy* and *backscattering spectroscopy*.

Neutron spin echo spectroscopy can be understood as a further development of the time-of-flight spectroscopy, where the flight time of each single neutron is encoded and thus a broad wavelength band of incident neutron energies can be used. Encoding of the flight-time is done

by the Larmor precession of the nuclear spin of the neutrons in an external magnetic field. Loosely speaking "each neutron carries its own clock" to measure its individual time-of-flight. Figure 5.20 demonstrates the principle of neutron spin echo spectroscopy: the incident neutron beam with a broad wavelength band of typically 10 % is being polarized with the polarization along the neutron flight direction. A so-called $\frac{\pi}{2}$-flipper turns the neutron polarization into the vertical direction, just before the neutrons enter a strong magnetic field, which is designed in such a way that the field integral $\int \underline{B}(\underline{s})d\underline{s}$ is identical for all neutron flight paths (an absolute non-trivial requirement!!). In the external filed, the nuclear magnetic moment of the neutron starts to precess in this field with a Larmor precession frequency determined by:

$$\frac{d\underline{s}}{dt} = \gamma \underline{s} \times \underline{B} \tag{5.40}$$

Due to the different neutron velocities and thus different flight times in the magnetic field area, the neutron beam reaching the sample is entirely depolarized. Typical field integrals are in the range of *0.5 T·m* giving rise to some 10,000 precessions of the neutron spin. At the sample, the polarization of each neutron is inverted by a so-called π-flipper. In the second arm of the neutron spin echo spectrometer, the scattered neutrons travel through an identical solenoid as on the incident side. If the neutrons are scattered elastically and the field integrals in the two coils are precisely identical, then the full polarization of the neutron beam will be restored and a full intensity will be recorded in the detector after a further $\frac{\pi}{2}$ flip and a polarization analyzer. This maximum intensity is called the spin echo. This spin echo is due to the fact that in the second coil, each neutron performs as many revolutions as in the first coil and thus has to end up with the initial spin direction. If an inelastic scattering event happens at the sample, the spin echo will be destroyed i. e. the intensity in the detector will be lowered. The echo signal can be measured by scanning the field of the second coil with respect to the field of the first coil. Since the echo signal depends directly on the time-of-flight which neutrons need to travel through the magnetic field region, the spin echo technique directly measures the intermediate scattering function $S(\underline{Q},t)$ instead of $S(\underline{Q},\omega)$. This type of spectroscopy is therefore well suited to measure slow relaxation processes like the magnetization dynamics in spin glasses or the dynamics of large macromolecules. This aspect will be detailed in the lecture “Dynamics of Macromolecules”.

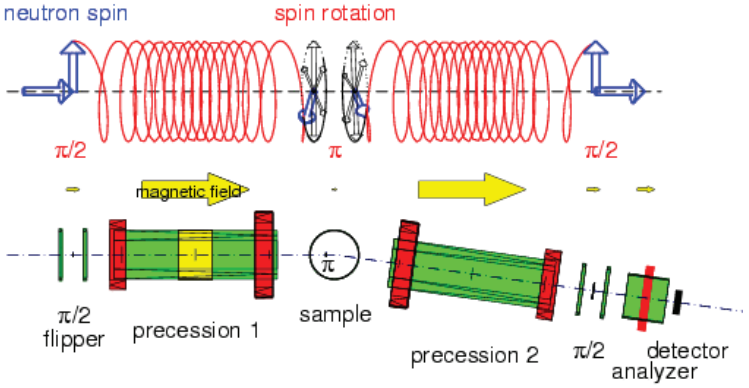

Fig. 5.20: *Schematics of the neutron spin echo spectrometer of JCNS at the FRM II reactor in Munich [3]. The incident neutron beam has wavelength – or energy band of* $\Delta\lambda/\lambda = 10\%$.

Another instrument for high resolution spectroscopy, based on a crystal analyzer and thus related to the triple axis spectrometer, is the so-called neutron *backscattering instrument*. Starting from the Bragg equation $\lambda = 2d\sin\theta$ one can derive the wavelength spread of a Bragg reflection from a monochromator or analyzer crystal by simple derivation:

$$\Delta\lambda = \left(\frac{\partial\lambda}{\partial d}\right)^2 (\Delta d)^2 + \left(\frac{\partial\lambda}{\partial\theta}\right)^2 (\Delta\theta)^2 \Rightarrow \left(\frac{\Delta\lambda}{\lambda}\right)^2 = \left(\frac{\Delta d}{d}\right)^2 + \cot^2\theta\cdot(\Delta\theta)^2 \qquad (5.41)$$

(5.41) shows that the wavelength spread results from two factors: an uncertainty in the lattice d-spacing, which can be minimized for perfect crystals such as silicon or germanium and a term resulting from the divergence of the beam. For backscattering i. e. $2\theta = 180°$ or $\theta = 90°$ this latter contribution vanishes due to the *cot(θ)* dependence. Thus in backscattering, one can work with a very divergent beam and still achieve a very good wavelength- or energy- resolution – of course at the prize of a poor *Q* resolution. This principle is applied for backscattering instruments. An example of such a spectrometer from a neutron spallation source is shown in figure 5.21.

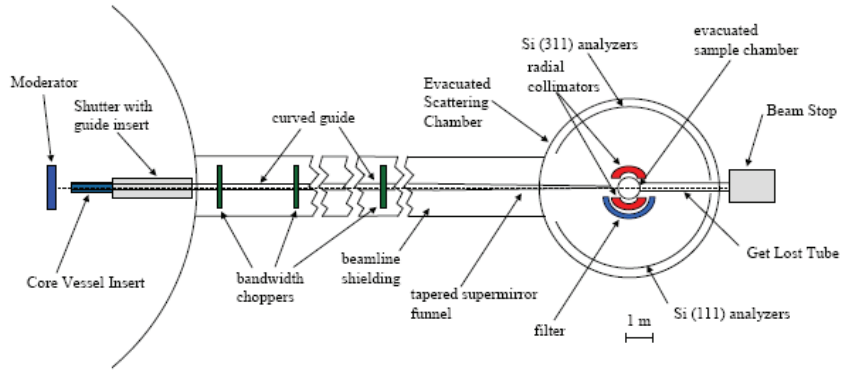

Fig. 5.21: *Schematics of the neutron backscattering spectrometer BASIS at the Spallation Neutron Source SNS in Oak Ridge, USA, taken from [8].*

Neutron pulses are produced in the supercritical hydrogen moderator. These pulses have a width of about *45 μs* for $\lambda = 6.267\,\text{Å}$ wavelength neutrons (this wavelength corresponds with silicon *(111)* backscattering analyzer). Bandwidth choppers are used to select a certain wavelength band from the pulsed white neutron beam. A long incident flight path of *84 m* between moderator and sample allows one to define with great precision the wavelength of the incident neutrons arriving at the sample at a certain time after the initial neutron pulse. Neutrons are scattered from the sample onto *Si (111)* analyzers, reflected from these analyzers into detectors in a close-to-backscattering geometry. In this way the final neutron wavelength is fixed to *6.267 Å*, while the incident neutron wavelength varies with time after the pulse and thus the energy transfer can be determined like in a time-of-flight instrument. An energy resolution of about *2.2 μeV* can be achieved with the dynamic range of ± *250 μeV*. Typical applications of such a backscattering spectrometer lie in the investigation of tunneling in molecular crystals, spin diffusion or slow spin relaxation in frustrated spin systems, or atomic diffusion processes.

5.12 Summary and conclusions

In this chapter we have given a rough overview over the different neutron scattering techniques and their applications. Many details will be discussed in the practical part of this course. In addition to the instrument concepts presented, there are many variants, which could not be discussed within the scope of this introduction. Besides neutron scattering there are of course many other techniques, which cover similar length and time scales for research in condensed matter. All these techniques are complementary since all of them can only access a certain range of length or time scales and since the contrast mechanisms are quite different for the different techniques. Figures 5.22 and 5.23 depict the relevant length and time scales accessible with the various neutron- and non-neutron techniques.

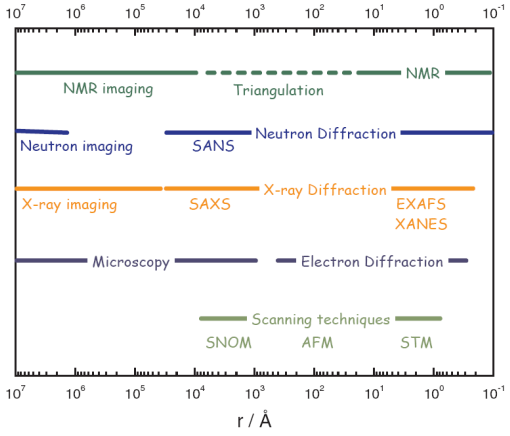

Fig. 5.22: *Experimental techniques with spatial resolution: neutron diffraction compared to other experimental techniques; taken from [9].*

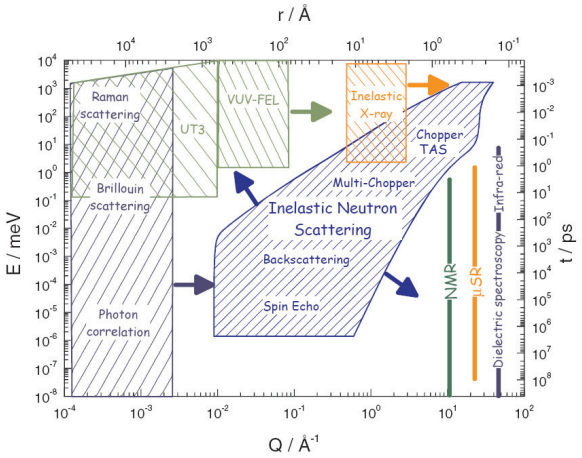

Fig. 5.23: *Experimental techniques with time and energy resolution, respectively: neutron spectroscopy compared to other experimental techniques; taken from [9].*

As these figures clearly demonstrate, neutron techniques cover a very large range of length and time scales relevant for research on condensed matter systems. Together with the typical assets of neutrons - sensitivity to magnetism, gentle non-destructive probe, sensitivity to light elements, contrast for neighboring elements etc. - it is clear why neutrons are such an important probe in many fields of research. Figure 5.24 shows how research with neutrons is relevant in many areas of fundamental research and how this in turn is highly relevant for many developments of modern technologies, which are the basis to solve current challenges of mankind.

Fig. 5.24: *Significance of research with neutrons in fundamental research and modern technologies, which finally shape our environment and help solve pressing problems of modern societies, like energy supply, transport or communication; taken from [9].*

References:

[1] Th. Brückel (Ed.) *Forschung mit Neutronen in Deutschland - Status und Perspektiven* Brochure of the German Committee for Research with Neutrons KFN; 2005
see also http://www.neutronenforschung.de

[2] G.L. Squires *Introduction to the Theory of Thermal Neutron Scattering* Dover Publications Inc.; Reprint 1997
or
S.W. Lovesey Theory *of Neutron Scattering from Condensed Matter: Vol. 1 & 2* (International Series of Monographs of Physics)
Clarendon Press; 1986

[3] http://www.jcns.info/jcns_instruments/

[4] A. Radulescu, E. Kentzinger, J. Stellbrink, L. Dohmen, B. Alefeld, U. Rücker, M. Heiderich, D. Schwahn, Th. Brückel, D. Richter; *KWS-3: The New (Very) Small-Angle Neutron Scattering Instrument Based on Focusing-Mirror-Optics*; Neutron News 16 (2005), 18 - 21

[5] H. F. Li, Y. Su, Y. Xiao, J. Perßon, P. Meuffels, Th. Brückel; "*Crystal and Magnetic Structure of Single Crystal* $La_{1-x}Sr_xMnO_3$ *(x ~ 1/8)*; European Physical Journal B 67 (2009), 149 - 157

[6] R. Bircher, G. Chaboussant, A. Sieber, H.U. Güdel and H. Mutka; *Transverse magnetic anisotropy in* Mn_{12} *acetate: Direct determination by inelastic neutron scattering*; Phys. Rev. B 70 (2004), 212413-6

[7] Th. Brückel, B. Dorner, A. Gukasov, V. Plakhty, W. Prandl, E. Shender, O. Smirnow; *Dynamical interaction of antiferromagnetic subsystems: a neutron scattering study of the spinwave spectrum of the garnet* $Fe_2Ca_3(GeO_4)_3$; Z. Phys. B 72 (1988), 477 - 485

[8] http://neutrons.ornl.gov/ ;
http://neutrons.ornl.gov/instrument_systems/beamline_02_basis/index.shtml

[9] ESS project reports 2003 and update 2004;
http://neutron.neutron-eu.net/n_documentation/n_reports/n_ess_reports_and_more

6

Polarized neutron scattering and polarization analysis

Werner Schweika

6 Polarized neutron scattering and polarization analysis

Werner Schweika

Institut für Festkörperforschung, Forschungszentrum Jülich

6.1 Introduction

The neutron has no electric charge, however, the neutron is a fermion with spin 1/2, and the observation of a magnetic moment is related to an internal structure with a moving charge distribution that gives rise to a magnetic moment. This neutron property has important consequences for neutron scattering, firstly because the strong nuclear interaction with the nucleus of an isotope is actually sensitive to the either parallel or antiparallel alignment of the spins of neutron and nucleus, and secondly, because the magnetic dipole interaction between the neutron's magnetic moment and the unfilled electron shells of atoms or ions leads to magnetic scattering. Both effects are not small compared to the average nuclear scattering considered in the previous lectures. Therefore, the neutron's magnetic moment is an ideal probe to study magnetic structures and excitations in condensed matter physics. We will see that this adds complexity to the scattering process, but at the same time we benefit from the larger amount of information available to us. The impact for magnetic scattering studies seems to be quite obvious, however, with respect to the high spin-dependent cross-section of hydrogen, polarization analysis opens up new possibilities for interesting soft-matter research. The case that there is more information available is particularly true, if by experimental means we are able to define and distinguish the spin state of the neutron probe before and after the scattering process, which leads us to the subject of this lecture: neutron scattering with polarization analysis. The history of polarized neutron work started early; essentially all principles experimentally and theoretically were developed in the 50s and early 60s of the past century. With still ongoing improvements in instrument performance for using polarized neutrons and polarization analysis, a steadily increasing number of research is published utilizing neutron polarization techniques.
This lecture will introduce first some basic properties of neutrons in magnetic fields, knowledge needed for a proper experimental set-up. Secondly, we will cover the scattering process itself including the changes of neutron polarization and which information can be extracted. The first part is also relevant for spin-echo-techniques, where the neutron spin precession in a magnetic field is used for coding the neutron energy. For particularly interested readers in the present subject I recommend exploring the homepage of Otto Schärpf [1].

6.2 Neutron spins in magnetic fields

In the following we define a quantization axis by an applied magnetic field along z-direction, $\boldsymbol{H} = (0, 0, H_z)$. The operator of a nuclear magnetic moment $\hat{\boldsymbol{\mu}}$ is related to its nuclear spin operator $\hat{\mathbf{I}}$ and can be expressed in nuclear magneton μ_N in the form

$$\hat{\boldsymbol{\mu}} = g\frac{e}{2m_p}\hat{\mathbf{I}}, \text{ with } \mu_z = g\frac{e\hbar}{2m_p}m_I = g\mu_N m_I, \text{and } \mu_N = 5.05078324(13)10^{-27}JT^{-1}.$$

Here m_p denotes the proton mass, e the electron charge, and $\hbar$ is Planck's constant divided by 2π. For neutrons the Landé g-factor is large $g = -3.8260837(18)$, and m_I takes the spin values $S = \pm\frac{1}{2}$. The origin of a magnetic moment is the orbital angular momentum of a particle with mass and charge.

Precession of neutron spins

The characteristic **motion** of the neutron magnetic moment in a magnetic field is Larmor precession, which for simplicity can be considered in a classical treatment [2]. In fact, even the quantum mechanical treatment, which introduces Pauli spin matrices $\hat{\boldsymbol{\sigma}}$ into the Schrödinger equation, is effectively a classical treatment considering the origin of these matrices. They result from the problem of mapping three dimensions onto two by introducing a complex component and were treated by Cayley and Klein (1897) [3] describing the classical problem of a spinning top.

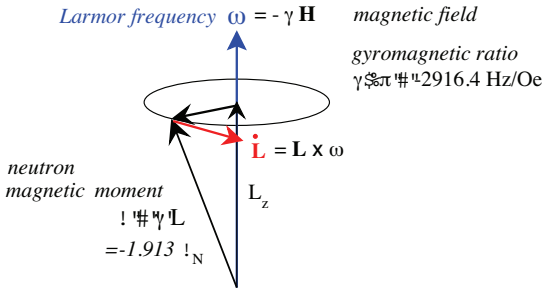

Fig. 1: *Larmor precession: the motion of the neutron in a constant magnetic field.*

Classical mechanics shows that a torque exerted on a magnetic moment $\boldsymbol{\mu}$ by a magnetic field $\mathbf{H}$ inclined at an angle θ relative to the magnetic moment causes the magnetic moment of the neutron to precess about the direction of the field with the *Larmor* frequency ω_L. The precession frequency is independent of the angle of inclination θ. Different to the motion of a spinning top in a gravity field the neutron's motion shows no nutation. The operator of angular momentum $\hat{\mathbf{L}} = \hbar\hat{\mathbf{S}}$ and its energy is a constant of motion. Hence we shall obtain the correct quantum-mechanical results even from a simplified classical treatment. The ratio of angular momentum $\mathbf{L}$ and magnetic moment $\boldsymbol{\mu}$ defines the *gyromagnetic ratio* $\gamma = g/2 \approx -1.91$, $\boldsymbol{\mu} = \gamma\mathbf{L}$. An applied magnetic field will tend to align this magnetic moment and exerts a torque. No force is exerted by a homogeneous field, therefore, the resulting equation of motion

$$\frac{d\mathbf{L}}{dt} = \dot{\mathbf{L}} = -\gamma\,\mathbf{L} \times \mathbf{H} \tag{1}$$

simply describes a precession of the magnetic moment around the magnetic field, see Fig.1, in which L_z, and hence the polarization along the field axis, is a constant of motion, which is contrary to the relaxation of an electric dipole in an electric field.

Motion in time dependent fields

Thermal neutrons move with a speed of thousands of meters per second. When passing through magnetic fields, the neutrons experience time-depedent changes in the field. Replacing $\mathbf{H}$ by $\mathbf{H}(t)$, the differential equation Eq. (1) can be used to calculate numerically the effect of all relevant field variations in an experimental set-up. Usually, it is possible to work within two simple limiting cases of either **(i) slow adiabatic field variation**, in which the non-precessing spin component parallel to the field smoothly follows the field direction, or of **(ii) sudden field reversal**, in which the non-precessing spin component has no time to reorient itself, when traversing abruptly from a parallel to anti-parallel field or vice versa. Slow field variation means that the field $\mathbf{H}$ changes or rotates in the coordinate system of the neutron with a frequency that is small compared to the Larmor frequency.

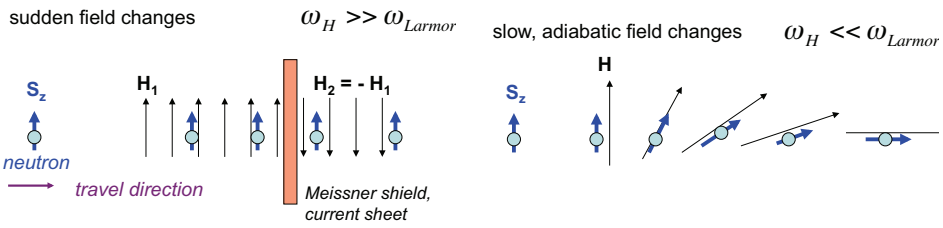

Fig. 2: *Neutron motion in changing fields.*

Polarized neutron beams

Polarization of a neutron beam is defined by the average over the neutron spin operators divided by its modulus $\hat{\mathbf{S}}$

$$\mathbf{P} = 2\langle\hat{\mathbf{S}}\rangle \tag{2}$$

Polarization will be measured with respect to a magnetic field defining a quantization axis and any device for polarization analysis will take the projection of the spins in up- and down state state, $n_\uparrow$ and $n_\downarrow$ respectively

$$\mathrm{P} = \frac{n_\uparrow - n_\downarrow}{n_\uparrow + n_\downarrow} \tag{3}$$

Typical neutron beams have a cross-section of a few cm^2. In order to preserve the beam polarization $\mathbf{P}$ one could try to avoid and screen any disturbing magnetic fields, however, it is more convenient to use magnetic fields to guide the polarization. These fields may even show smooth field variations.

6.3 Experimental set-up for neutron polarization analysis

Already in the 60s of the last century, in a classical paper by Moon, Riste and Koehler [4] the principles of neutron scattering with polarization analysis and possible applications were beautifully demonstrated, and their pioneering studies are particularly recommended to the interested reader. Their method of polarization analysis is also sometimes called longitudinal polarization analysis, which means that the analysis is taken only with respect to the component parallel to the initially defined direction. In general, scattering leads to a tensor relation between the two vectors of incoming and scattered polarization and today the tools for a complete spherical polarization analysis have been fully developed. For the sake of brevity, the methods will not be discussed here, and the reader is referred to the literature [5, 6, 7] As will be shown, longitudinal polarization analysis provides a wealth of information, and allows for a complete separation of the scattering terms. In the following, polarization analysis on the DNS instrument, which is also part of the practical laboratory course, is described. With respect to efficiency, the DNS being a multi-detector instrument represents a major improvement compared to the original single detector experiment [4]. It is worthwhile to note that there is a comparable instrument at the ILL Grenoble, the D7, described in an excellent recent review [10].

The DNS instrument

The diffuse neutron scattering spectrometer DNS at the FRM2 in Munich is equipped with polarization analysis and is particularly devoted to elastic and inelastic diffuse scattering that may arise from spin correlations and magnetic disorder and ordering in materials. A layout of the instrument is shown in Fig. 3. DNS is a time-of-flight instrument[8] with a multi-detector system similar to the D7 instrument at the ILL [10, 9]. The monochromatic incident beam is polarized with a focusing supermirror bender, xyz-field coils allow for a change of the polarization at the sample, and the polarization analysis is performed with supermirror analyzers in focusing arrangement in front of each detector.

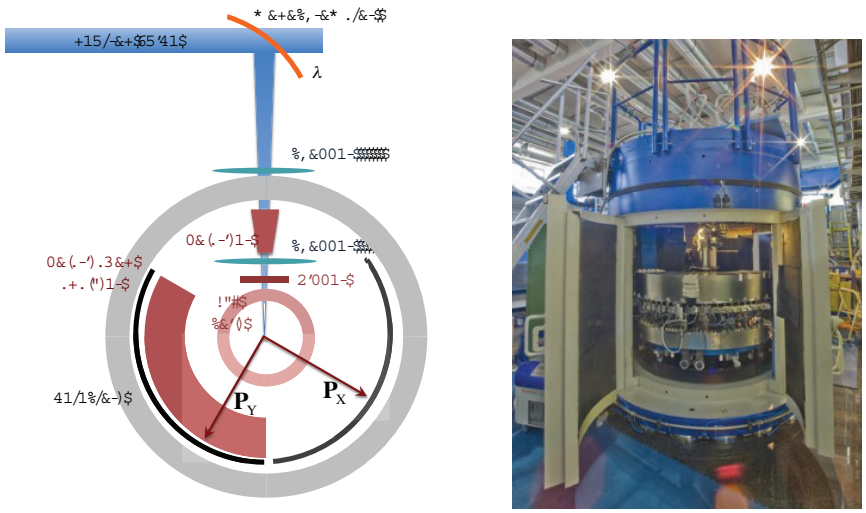

Fig. 3: *Scheme of the DNS instrument.*

Polarization analyzers

The most common methods to polarize neutrons are (i) using the total reflection from magnetic multi-layers, (ii) using Bragg reflection of polarizing single crystals (typically Heusler crystals) and (iii) polarized He-3 filters, in which for anti-parallel spins the (n,^{3}He)-compound has a large absorption cross-section while all neutrons with parallel spins may pass the filter cell. The first two methods use an interference effect of nuclear and magnetic scattering amplitudes having the same absolute value.
The polarization analysis at the DNS is performed with supermirrors using total reflection. The angle of total reflection for a single ferromagnetic (FM) layer is given by

$$\Theta_c^{\pm} = \lambda\sqrt{n(b-p)/\pi}. \tag{4}$$

Here n denotes the particle density and b and p the nuclear and magnetic scattering lengths, respectively. However, the critical angle can be further increased by artificial multi-layers (supermirrors) of alternating FM and non-magnetic layers of varying thickness [11]. The alternating layers of the DNS polarizers consist of the materials $Fe_{50}Co_{48}V_2$ / TiN_x, with critical angles up to $\Theta_c = 0.3^o \times \lambda/\text{Å}$. The degree of polarization that can be achieved is rather high, typically 98%.
Both the polarizer in the initial flight-path and the polarization analyzers in front of the detectors are made out of supermirrors being curved to avoid any direct flight path without reflection, and in addition the curvature is such that neutrons are focussed on the sample. The common polarization axis of initial and final polarizers is vertical.

Guide-fields

A magnetic *guide field* is used to maintain the direction of the spin and the polarization of the neutron beam. The guide field preserves the quantization axis to which the neutron moments have align either parallel or anti-parallel. Guide fields are typically weak so that the sample magnetization is not significantly influenced, but sufficiently stronger than for instance the magnetic field of the earth or any other stray magnetic fields from the surrounding. In the DNS instrument the polarizers and polarization analyzers are kept in a permanent vertical field that is not screened. This vertical stray-field is used as a guide field throughout the instrument. While near the permanent magnets at the polarizers, the field reaches several hundred Gauss, at the sample position its strength is still about 5 Gauss and sufficient to dominate the earth magnetic field, which is weaker by an order of magnitude .

π-Flipper

The purpose of a π-flipper is to reverse the polarization and to detect whether the sample causes spin-flip scattering.
When applying a magnetic field perpendicular to the polarized neutron beam, the polarization immediately starts its Larmor precession. A flipper that reverses the neutron polarization with respect to the guide field has to induce a well-defined field pulse so that the polarization precesses by an angle π. For this purpose one can use the homogeneous field of a long rectangular coil, see Fig. 4. Neutrons see a sudden field change when they enter and exit the coil, in between they precess around the flipping field, whose magnitude is tuned with respect to the time of flight that the neutrons spend inside the coil.

In the DNS set-up the initial polarization is along the vertical guide field. In a combination of two perpendicular coils, one is used to compensate the guide field and the second is used for flipping. (To give an example for typical flipping fields, a π-flip is achieved by 17 Gauss for neutrons with a wave length of $\lambda = 4$Å and a flight path of 1 cm through the coil.)

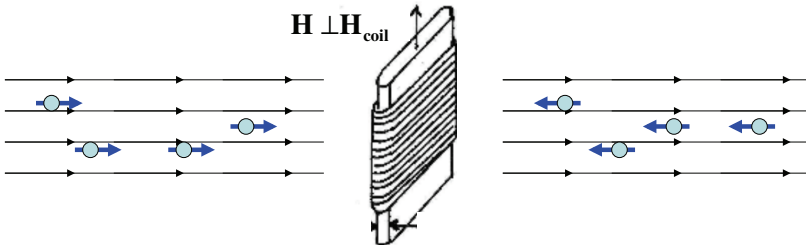

Fig. 4: *Principle of a neutron π-spin flipper. The neutrons perform half of a Larmor-precession inside a long rectangular coil. The field $\boldsymbol{H}_\pi$ is perpendicular to spin orientation and to the travel direction of the neutron and has to be adjusted to the speed of the neutrons.*

XYZ-coils

In order to align the polarization to any desired direction at the sample position, there is (in the simplest version) a set-up of three orthogonal pairs of so-called xyz-coils. Fig. 5 illustrates the field setting along x-direction. One can see that the z-coil has been used to compensate the guide field at the sample position, and that the x-coils produce a field of a few Gauss. The field is sufficiently strong so that the neutron polarization can follow the smooth variation of the field adiabatically, finally turning back into the z-direction of the guide field outside the xyz-coils.

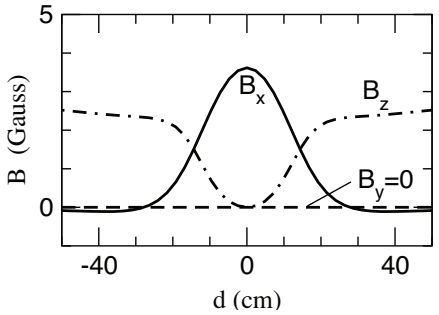

Fig. 5: *Magnetic field setting by the xyz-coils for an adiabatic nutation of the polarization in x-direction at the sample.*

6.4 Scattering and polarization - principles and applications

Interaction of neutrons with matter

The total scattering amplitude consists of two parts, a nuclear and a magnetic term, that are often comparable in magnitude

$$F_Q = N_{\mathbf{Q}} + \hat{\boldsymbol{\sigma}} \cdot \mathbf{M}_{\mathbf{Q}}^{\perp}. \tag{5}$$

The **nuclear interaction** can be described by a point-like Fermi potential, which is isotope-specific. For nuclei with zero spin (*e.g.* ^{12}C, ^{16}O ..., and many *"gg"* isotopes with even number of protons and neutrons) the scattering will be independent of the neutron spin orientation. In the previous lecture we have defined **the coherent scattering amplitude** or scattering length as an average for different isotopes and possible spin states, an average that again **is independent of the neutron polarization**, see Appendix.

The interaction is spin-dependent if the scattering nuclei have a non-zero spin $\mathbf{I}$. Since nuclear spins are usually randomly oriented, this fluctuating part leads to spin-incoherent scattering. The average part gives the coherent nuclear scattering which does not change the neutron polarization. In contrast, spin-incoherent scattering effects the neutron polarization. As shown in detail in the Appendix, the component of $\mathbf{I}$ parallel to $\mathbf{P}$, say $I_z \parallel P_z$, does not affect $\mathbf{P}$, but the two perpendicular components I_x and I_y change P_z to $-P_z$ upon scattering. Therefore, two thirds of the spin-incoherent scattering is spin-flip scattering, and the final polarisation $\mathbf{P}' = -\frac{1}{3}\mathbf{P}$, has changed in sign, is reduced in magnitude, but shows no inclination towards $\mathbf{P}$. In summary, we can distinguish three contributions to the nuclear scattering

$$\frac{d\sigma}{d\Omega}^{N}_{\mathbf{Q}} = |N_{\mathbf{Q}}|^2, \text{ with } N_{\mathbf{Q}} = \sum_j b_j e^{i\mathbf{Q}\cdot\mathbf{R}_j} \tag{6}$$

$$\frac{d\sigma}{d\Omega}^{N}_{\mathbf{Q}} = \frac{d\sigma}{d\Omega}^{N}_{\mathbf{Q},coh} + \frac{d\sigma}{d\Omega}^{N}_{isotop-inc} + \frac{d\sigma}{d\Omega}^{N}_{spin-inc}.$$

In absence of magnetic scattering, the coherent part of the nuclear scattering plus the isotopic incoherent part can be separated from the spin-incoherent scattering by measuring spin-flip and non-spin-flip scattering.

$$\frac{d\sigma}{d\Omega}^{N}_{\mathbf{Q},coh} + \frac{d\sigma}{d\Omega}^{N}_{isotop-inc} = \frac{d\sigma}{d\Omega}^{NSF} - \frac{1}{2}\frac{d\sigma}{d\Omega}^{SF} \tag{7}$$

$$\frac{d\sigma}{d\Omega}_{spin-inc} = \frac{3}{2}\frac{d\sigma}{d\Omega}^{SF} \tag{8}$$

The **magnetic interaction** arises from the scattering potential $-\mu \cdot \mathbf{H}$ describing the dipole-dipole interaction between the magnetic moment of the neutron μ and a magnetic field $\mathbf{H}$ that is due to the spins $\mathbf{s}_j$ of the unpaired electrons j and their orbital momentum $\mathbf{p}_j = -i\nabla_j$. The Fourier transform of the interacting magnetic moments is given by

$$\mathbf{M}_{\mathbf{Q}} = r \int d\tau \psi_b^*(\tau) \sum_j e^{i\mathbf{Q}\cdot\mathbf{R}_j} (\mathbf{s}_j - i(\mathbf{Q} \times \mathbf{p}_j)) \psi_a^*(\tau) \tag{9}$$

where $r = |\gamma| e^2/mc^2$ is the magnetic scattering length of an electron and e^2/mc^2 is the classical electron radius. As illustrated in Fig. 6 the component of a magnetic dipole field parallel to the scattering vector $\mathbf{Q}$ cancels out. Therefore, in contrast to the spin-incoherent scattering,

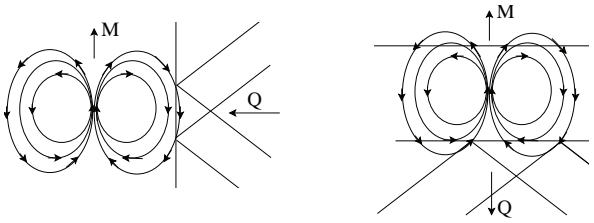

Fig. 6: *Illustration why only* $\mathrm{M}_\mathbf{Q}^\perp$ *is measured. Magnetic field amplitudes of the dipole field left: constructive interference for* $\mathbf{M} \perp \mathbf{Q}$*, and right: destructive interference for* $\mathbf{M} \parallel \mathbf{Q}$*.*

magnetic scattering is anisotropic with respect to $\mathbf{Q}$ and only $\mathrm{M}_\mathbf{Q}^\perp$, the component perpendicular to $\mathbf{Q}$ can be observed. There is another simple rule (see Appendix), which is illustrated in Fig. 7: the component of $\mathbf{P}$ parallel to $\mathrm{M}_\mathbf{Q}^\perp$ remain unchanged, while the component of $\mathbf{P}$ perpendicular to $\mathrm{M}_\mathbf{Q}^\perp$ reverse its sign. This selection rule combined with the $\mathbf{Q}$-dependence provides another simple rule: If $\mathbf{P} \parallel \mathbf{Q}$, all magnetic scattering will be spin-flip.

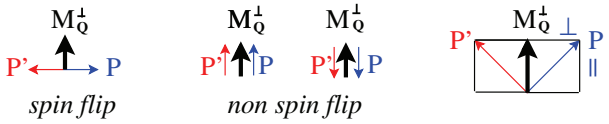

Fig. 7: *Change of initial polarization* $\mathbf{P}$ *to final polarization* $\mathbf{P}'$*: the component perpendicular to* $\mathrm{M}_\mathbf{Q}^\perp$ *reverses sign, the parallel component of* $\mathbf{P}$ *is invariant.*

Separating nuclear scattering

Polarization analysis can be used to distinguish the spin-dependent and spin-independent part of the nuclear scattering, as has been demonstrated by Moon, Riste, Koehler for Ni and V. If we look up the scattering properties of these two elements, see Ref. [13], both elements have a similar incoherent scattering 5.2 and 5.1 barn respectively, yet of different origin. Ni consists of different isotopes with different scattering lengths, however, most nuclei have no spin, leading to isotopic incoherent scattering. In addition there is an average coherent scattering length. On the other hand, ^{51}V represents 99.75% of the element, the average coherent scattering amplitude is accidentally close to zero and the variation due to the spin dependence causes the spin-incoherent scattering. Therefore, first, Ni should give essentially no spin-flip scattering in agreement with Fig. 8; this holds for both the coherent scattering and for isotopic -incoherent scattering. Second, V should exhibit both spin-flip and non-spin-flip scattering with an ideal ratio of 2:1. Furthermore, the spin-incoherent scattering is independent of how we choose the direction of the polarization, which is in contrast to magnetic scattering. The example for Ni is actually not as simple as it may look at first glance. Ni is a ferromagnet, which should give rise also to Bragg magnetic scattering, however, Bragg scattering can easily be avoided by an appropriate setting of Q. The real problem is that typically ferromagnets have a domain structure and the strong magnetic fields will cause undesired Larmor precessions of the polarized neutrons, often leading to a complete depolarization of the beam. Therefore, Moon,

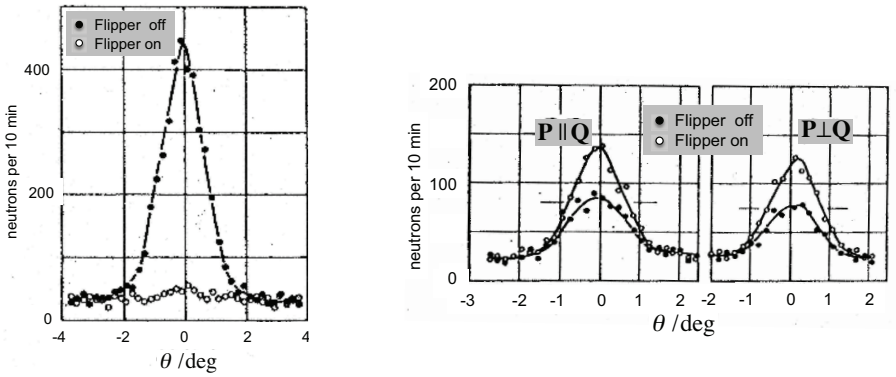

Fig. 8: Left*: Nuclear isotopic incoherent scattering from nickel obtained by rocking the analyzer crystal through the elastic position, which is essentially all non-spin-flip scattering.*
Right: *Nuclear spin-incoherent scattering from vanadium show 2/3 and 1/3 contributions in the spin-flip and non-spin-flip channel respectively. There is no dependence on the direction of* $\mathbf{P}$ *relative to* $\mathbf{Q}$ *for all nuclear scattering.*

Riste and Koehler applied a saturating magnetic field in direction of the $\mathbf{Q}$ vector, the direction in which the magnetic moments are invisible due to the dipolar interaction.

Applications to local order in disordered, hydrogeneous materials

Typical soft matter samples contain hydrogen which causes a huge spin-incoherent background ($\sigma_{inc}(H) = 80\,\mathrm{b}$) in the wide-angle scattering that contains information about local correlations ($\sigma_{coh}(H) = 1.76\,\mathrm{b}$). Here, a precise determination of coherent scattering can be achieved by measuring spin-flip and non-spin-flip scattering. It is particularly valuable to combine this further with the method of contrast variation using H and D isotopes, having rather distinct scattering lengths, $b_{coh}(H) = -0.374 \cdot 10^{-12}\mathrm{cm}$ and $b_{coh}(D) = 0.667 \cdot 10^{-12}\mathrm{cm}$. Fig. 9 shows the separated coherent scattering of a polymer glass. Such results can be compared to those obtained in molecular dynamics simulations of theoretical polymer models [14]. A recent application to water also showed that the simplest type of polarization analysis provides a new, unprecedented quality of data and a better insight into local correlations in water with characteristic signatures of hydrogen bridge bonding and tetrahedral coordination of oxygen[15].

Applications to dynamics in liquids

Since in a liquid all atoms are moving around, the scattering is not elastic as in the case of Bragg peaks from a solid, single crystal. Diffraction - the energy integrated scattering - provides us with structural properties from a snap-shot of typical atomic configurations. Since neutron energies are comparable to thermal energies involved in atomic motions, it is relatively simple to achieve an adequate energy resolution to study the dynamics for instance in liquids. Therefore, a typical instrument set-up uses the time-of-flight technique: the monochromatic beam is pulsed by a mechanical chopper and the measured *time-of-flight* of the neutrons can be related to an energy transfer in the sample. Note, the separation by polarization analysis in *coherent* scattering and spin-*incoherent* scattering distinguishes *pair-correlations* from *single particle*

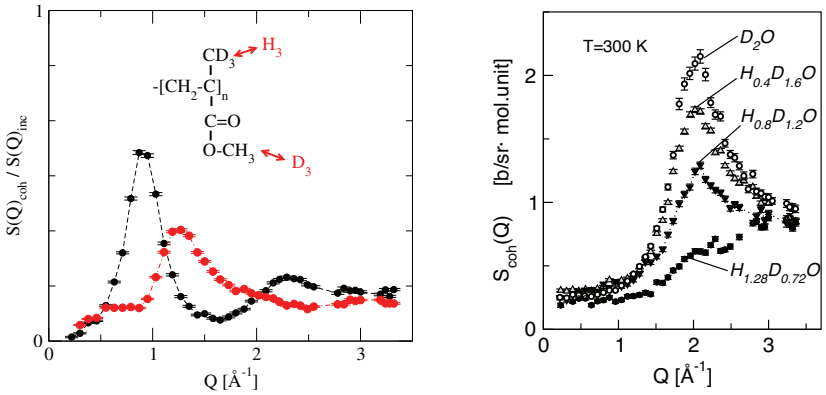

Fig. 9: *Neutron polarisation analysis separates coherent scattering from spin-incoherent scattering which is typically a disturbing large background in materials that contain hydrogen. The examples show results for the coherent scattering of (left) a polymer glasses [14] and (right) water [15]. Both experiments also show the effect of H/D contrast.*

correlations, respectively. The following example of liquid sodium [16] demonstrates in a very instructive way the complementary information that can be obtained. The data have been obtained by Schärpf at the D7 instrument at the ILL-Grenoble, an instrument that is quite similar to the DNS at FRM2 in Munich. From simple liquid models one expects that the incoherent scattering has a Lorentzian shape in energy at constant Q, related to exponential relaxations in time, with a width that for the macroscopic limit, $Q \rightarrow 0$, is related to the macroscopic diffusion constant. On the other hand, the coherent scattering is rather different and exhibits a pronounced peak related to typical nearest neighbor distances and reflecting precursors of Bragg peaks and crystalline order. Finally, time-of-flight analysis reveals that for typical neutron energies diffraction is not equivalent to an integration in energy at truly constant Q, see Fig. 10, and more accurate $S(Q)$ can be obtained from time-of-flight results.

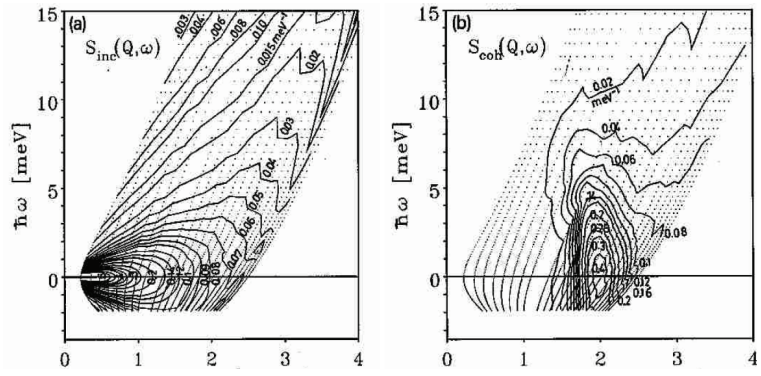

Fig. 10: *Contour plot of a) spin-incoherent and b) coherent scattering of liquid sodium at T=840 K separated by polarization analyis (taken from Ref.[16]). The dotted mesh corresponds to the coordinates of time-of-flight and scattering angles.*

Separating magnetic scattering

In order to separate magnetic scattering, one needs a polarization analysis with directional dependence. The example in Fig. 11 taken again from Moon, Riste, Koehler's seminal paper shows a nice and clean separation of nuclear and magnetic Bragg peaks by non-spin-flip scattering and spin-flip scattering for the case $\mathbf{P} \parallel \mathbf{Q}$, collecting all magnetic scattering. Apparently the data has been taken by a *single detector*, scanning the scattering angle with an appropriate setting of the incoming polarization.

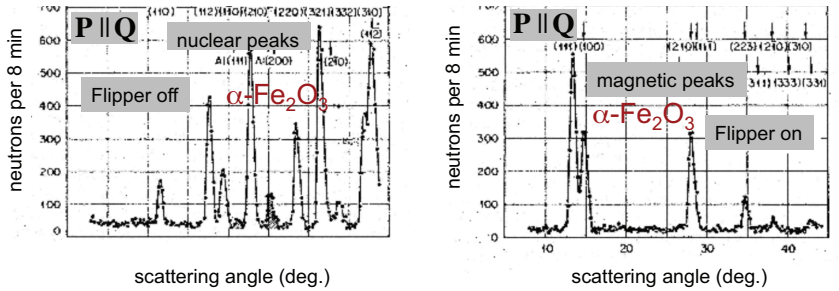

Fig. 11: *Separation of magnetic and nuclear Bragg peaks for powder diffraction from* Fe_2O_3 *by non-spin-flip and spin-flip scattering with* $\mathbf{P} \parallel \mathbf{Q}$.

XYZ-polarization analysis for multi-detectors

It is straightforward to generalize the separation for magnetic powder diffraction for the use of multi-detectors, a case in which it is not possible to set the polarization parallel to all $\mathbf{Q}$ simultaneously. Therefore, one uses the method of **xyz-polarization analysis** [18], and measurements of spin-flip and non-spin-flip intensities are taken with the polarization set into three orthogonal directions, say with z perpendicular to the scattering plane. The following linear combinations eliminate all nuclear scattering contributions and yield the magnetic scattering only[18]. The pre-condition is isotropy, valid for powder samples, and the method is applicable to paramagnets and antiferromagnetic ordered systems (ferromagnets cause depolarization).

$$\frac{d\sigma}{d\Omega}_{pm} = 2\left(\frac{d\sigma}{d\Omega}^{SF}_{\mathrm{x}} + \frac{d\sigma}{d\Omega}^{SF}_{\mathrm{y}} - 2\frac{d\sigma}{d\Omega}^{SF}_{\mathrm{z}}\right) = -2\left(\frac{d\sigma}{d\Omega}^{NSF}_{\mathrm{x}} + \frac{d\sigma}{d\Omega}^{NSF}_{\mathrm{y}} - 2\frac{d\sigma}{d\Omega}^{NSF}_{\mathrm{z}}\right) , \qquad (10)$$

In many cases, polarization analysis is not requested to study antiferromagnetic order, because typically the ordering vector is found at the zone boundary and therefore different from the fundamental structural peaks. However, there are few relevant issues for polarization analysis. The magnetic origin can be uniquely identified and distinguished from other, possibly accompanying phase transitions; one can achieve a higher accuracy in determination of complex structures [19], if the moments and the magnetic scattering are weak; the signal to background ratio maybe significantly improved by polarization analysis as exemplified further below. Furthermore, there are antiferromagnetic structures, in which the magnetic peak positions coincide with the fundamental structural peaks. These are the so-called q=0 structures, typically noncollinear spin structures, frustrated magnetic systems [21].

Applications to magnetic order in nanoparticles

Recently, the magnetic ordering and phase transition in MnO nanoparticles confined in a porous glass have been investigated using polarized neutron scattering. These MnO nanoparticles are best described as extended wormlike structures with a mean diameter of 70 Å. By polarization analysis, separating the magnetic scattering, it is found that within the individual MnO nanoparticles about 60% of atoms remain disordered in the low-temperature limit, presumably due to interactions between nanoparticles and glass walls. In contrast to the well-known discontinuous phase transition in bulk MnO, it is found that there is an an apparent continuous magnetic phase transition in these MnO nanoparticles. The continuous character of the phase transition and the unusual temperature dependence suggests a surface-induced disorder phenomenon.[22]

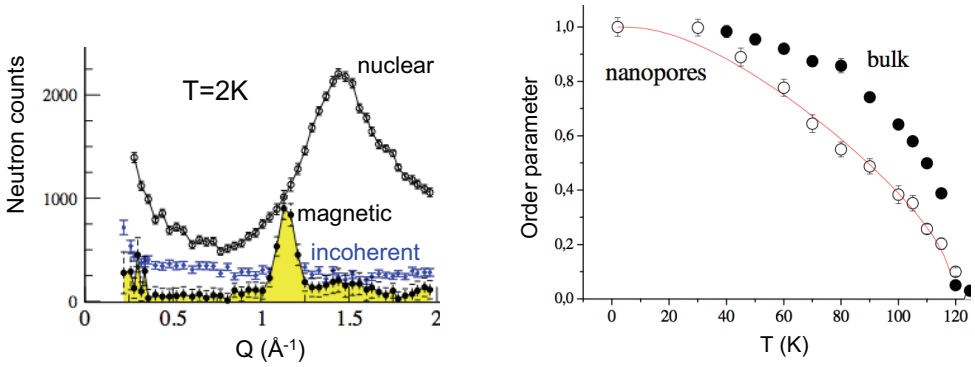

Fig. 12: *MnO nanoparticles.* Left: *Separation of scattering by polarization analysis reveals ordered fraction at low T.* Middle: *TEM picture of worm-like nano-structures.* Right: *Temperature dependence of the order parameter obtained from magnetic peak intensities. [22]*

Applications to diffuse magnetic scattering and spin correlations from disordered systems

Above the ordering phase transition, the paramagnetic scattering may still show interesting characteristic features related to short-range correlations among the spins. The example depicted in Fig. 13, is the separated magnetic scattering from a strongly frustrated and essentially two-dimensional system. In this new Co-compound the magnetic ions are situated on layers with kagome geometry, see insert. There is a very strong antiferromagnetic exchange, as inferred from the susceptibility within the Curie-Weiss approximation, which usually would yield ordering at high temperatures - in the order of 1000 K-, however, the low dimensionality prohibits ordering even at low temperature of 1.4 K. The peak shape is peculiar, its asymmetric shape is characteristic for two dimensional systems. Its full width at half maximum is rather broad, while the comparably sharp top of the peak indicates that many Fourier components $\langle \mathbf{S_R} \cdot \mathbf{S_{R'}} \rangle$ for larger distances $\mathbf{R} - \mathbf{R}'$ have to be taken into account. These spin-correlations seem to approach a ground state with a larger magnetic unit cell, named as $\sqrt{3} \times \sqrt{3}$ order. Here the geometric frustration due to triangular spin arrangements leads to a manifold of degenerate spin arrangements, which seems to prevent true long range order even at ideal T = 0 K condition.[23]

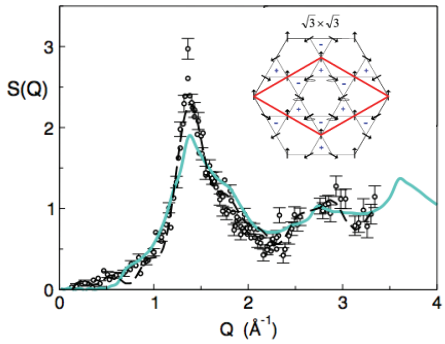

Fig. 13: *Magnetic scattering due to Two dimensional spin correlations in the kagome-sublattice layers of $Y_{0.5}Ca_{0.5}BaCo_4O_7$. Separation and absolute calibration is obtained by xyz-polarization analysis. The light blue line represents Monte Carlo simulations for the kagome Heisenberg antiferromagnet at low T. [23]*

Single crystals studies - *diffuse magnetic scattering from "spin-ice"*

The standard xyz-separation given by Eq. 10, implies orientational average and hence does not hold for single crystals. However, specific measurements with polarization analysis will be conclusive and valuable. The following example will illustrate the spin-correlations in pyrochlores, whose geometry with tetrahedral network and Ising spin-anisotropy leads to strong frustration even for ferro-type exchange. In the ordered state the local spin-correlations can be described for each tetrahedra by a simple rule: two spins are pointing along the ¡111¿ body diagonals towards the center of the tetrahedra and two spins point outwards. Actually this rule is the perfect analogue to the ice rules in hexagonal ice, describing the hydrogen bonds around the tetrahedral environment of the O ions, which give the magnetic systems the name spin-ice. Hence Pauling's famous ice model also explains why there should be a residual entropy due to remaining disorder in spin-ice. The example in Fig. 14 displays diffuse magnetic scattering obtained from

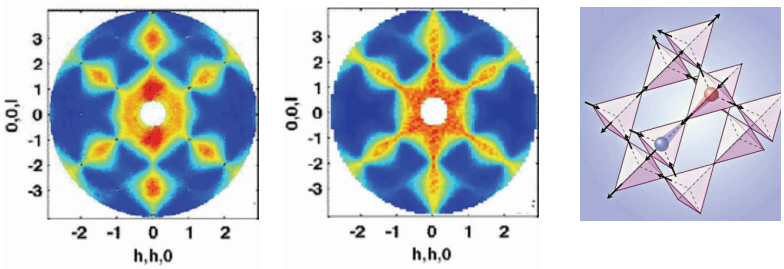

Fig. 14: *Diffuse scattering maps from spin ice, Ho_2Ti_2O, (*middle*) experimental SF scattering at T = 1.7 K with pinch points at (0,0,2), (1,1,1), and (2,2,2); (*right*) Monte Carlo simulations of the near neighbour model. [24]*

spin-flip scattering with polarization perpendicular to the scattering plane. Apparently, there is broad diffuse scattering at low temperatures, due to the remaining disorder. The z-spin-flip polarization setup probes spin-correlation in plane and with the projection of magnetic moments onto this plane. The extraordinary features of this diffuse scattering are so-called pinch-points, the saddle-points in intensity at (111) and (200) positions; on one hand the intensity variation radially, along the modulus of Q, is rather smooth, involving short-range correlations, on the other hand the transverse variation at constant Q is almost discontinuous and singular, which involves many Fourier coefficients and long-range correlations. The explanation is that the ice-topology creates effectively long-range interactions, – any local decision for a specific two-in two-out spin configuration imposes far-reaching constraints for the other tetrahedra –, an effective interaction that can be mapped to Coulomb interaction between monopoles and provides a picture, where the dipole moments in their local sums over four tetrahedral sites can be viewed as two separated monopoles.[24]

Nuclear-magnetic interference: application to anisotropy and single site susceptibility

There are further applications and experimental techniques using polarized neutrons, which will not be discussed here. For a general understanding of the possibilities it is recommended to study the complete polarized scattering terms, see Appendix, and further literature (e.g. [21]).

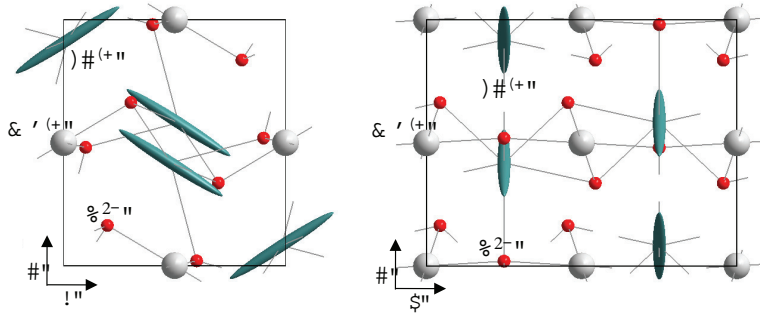

Fig. 15: *Spin susceptibilities in the paramagnetic phase of $TbMnO_3$ as obtained from the directional field dependence of the polarized neutron Bragg scattering. Magnetic moments of the Mn-ions exhibit isotropic susceptibilies, whereas the Tb-site crystal fields cause a highly anisotropic, needle-like susceptibility.[25].*

One important technique is related to measurements in magnetic fields much higher than the guide-fields that lead to a significant magnetization. Thereby, it is possible to measure the field-induced magnetization in paramagnetic single crystals, which provides the anisotropy of the susceptibility on the atomic level for spins at specific lattice sites.
For a paramagnet in a magnetic fields the moments will partly align with the applied field direction according to their susceptibility. Considering the square of the total scattering amplitude, given in Eq. 5, the pure magnetic scattering will usually be small compared to the nuclear scattering and typically also small compared to the interference term of nuclear and magnetic amplitudes. By measuring the difference in intensities for two opposite field directions, according to Eq. 5, we separate the interference term $N\mathbf{M}_{\mathbf{Q}}^{\perp}$, changing sign with field direction from

the invariant terms N^2 and $|\mathbf{M}_{\mathbf{Q}}^{\perp}|^2$.
The signal will be the additional scattering due to NM on the fundamental atomic Bragg peaks arising from nuclear-magnetic interference. Therefore we do not need to analyze the final polarization. The scattering will actually be non-spin-flip, however, *polarization analysis is not required*, because the separation results already from the field reversal. If we now vary the field direction, we can probe the anisotropy of the susceptibility for each Bragg peak, and for a known structure one knows the contributions of each atomic site to the various measured Bragg peaks. An example is given in Fig. 15, showing a needle like moment distribution for Tb moments tilted within the ab-plane and a spherical distribution of moments for the Mn-site.

6.5 Final remarks

This lecture and the selection of examples is certainly biased by own research, thus ignoring many other beautiful results that have been obtained by polarized neutron scattering and polarization analysis. There is still a lot of progress being made in instrumentation and method development, also stimulated by new research fields. We have not discussed the "cryopad", a versatile tool for complete "tensor" polarization analysis of the scattering. Here, the sample is kept in a "zero-field" by superconducting ("cryo"genic) shields for magnetic fields, which has the advantage that the polarization of the scattered neutrons is determined by avoiding a possible precession of neutrons upon a scattering process with an arbitrary rotation of the polarization. Alternatively, a screening of external magnetic fields can also be achieved by μ-metals. The crypad provides all flexibility to measure polarization changes [5]. There is a caveat, that this principle works fine for a single S(Q), however, is not appropriate for multi-detector instruments. In view of the improved performance of instruments like DNS or D7 and increasing interest in single crystal studies of complex magnetic phenomena, it is interesting to point to a recent paper [26], which demonstrates that a complete separation from the diagonal part of the polarization tensor is possible and can be realized also for multi-detectors. Hence, there are new and promising prospects to further exploit the full potential of the longitudinal polarization analysis.

Appendix

Nuclear scattering

The interaction of thermal and cold neutrons with the nuclei of of scattering system is given by the sum of Fermi potentials $V(r) = \frac{2\pi\hbar^2}{m_N} b\delta(r)$, where b is a scalar complex parameter called scattering length. Tabulated values comprise average scattering lengths for each element, with further distinction of scattering lengths of isotopes [13]. The interaction potential depends also on the spin of the scattering compound of nucleus and neutron. Therefore, if the nucleus has a non-zero spin, one can distinguish further the scattering lengths b_+ and b_- for parallel and anti-parallel spin alignment. If the nucleus has zero spin, there is of course no spin-dependent interaction potential.
In general, we can decompose the nuclear scattering into two parts, the average coherent nuclear scattering and the spin-dependent and spin-incoherent scattering. The reason why the latter part is incoherent, except for some unusual cases, is because the orientation of nuclear spins is given by a random distribution.

Therefore, in general, the scattering length needs to be replaced by the scattering length operator $\mathbf{b} = A + B\,\boldsymbol{\sigma}\cdot\mathbf{I}$ with $A = \frac{(I+1)\,b_+ + I\,b_-}{2I+1}$ and $B = \frac{b_+ - b_-}{2I+1}$ where $\mathbf{I}$ denotes the nuclear spin operator. One may calculate the transition probability from the initial spin state $|S\rangle$ to the final spin state $\langle S'|$, which yields the scattering amplitude $\mathrm{A}_\mathbf{Q}$, assuming an arbitrary orientation of the neutron spin, say along z-direction,

$$\mathrm{A}_\mathbf{Q} = \langle S'_{(z)}|A + B\boldsymbol{\sigma}\cdot\mathbf{I}|S_{(z)}\rangle = \begin{cases} \langle +|A + B\boldsymbol{\sigma}\cdot\mathbf{I}|+\rangle & = A + B\mathrm{I_z} \\ \langle -|A + B\boldsymbol{\sigma}\cdot\mathbf{I}|-\rangle & = A - B\mathrm{I_z} \\ \langle -|A + B\boldsymbol{\sigma}\cdot\mathbf{I}|+\rangle & = B(\mathrm{I_x} + \mathrm{iI_y}) \\ \langle +|A + B\boldsymbol{\sigma}\cdot\mathbf{I}|-\rangle & = B(\mathrm{I_x} - \mathrm{iI_y}) \end{cases} \tag{11}$$

Thermal averaging yields, for random orientation of nuclear spins $\langle \mathrm{I_x}\rangle = \langle \mathrm{I_y}\rangle = \langle \mathrm{I_z}\rangle = 0$, so that the (coherent) scattering amplitude is given only by the non-spin flip matrix element equal to $A \equiv b_{coh} = \bar{b}$ and the coherent nuclear scattering is proportional to the square of $\bar{b}^2$

$$\frac{d\sigma}{d\Omega}^{(NSF)}_{coherent} = \bar{b}^2 \sum_{\mathbf{r},\mathbf{r}'} \mathrm{e}^{\mathrm{i}\mathbf{Q}\cdot(\mathbf{r}'-\mathbf{r})}. \tag{12}$$

The coherent nuclear scattering does not change the polarization of the neutrons.
We have used that the neutron spin operator σ can be described by the Pauli-spin matrices $\underline{\underline{\sigma}}_\alpha$

$$\underline{\underline{\sigma}}_\mathrm{x} = \begin{pmatrix} 0 & 1 \\ 1 & 0 \end{pmatrix}, \underline{\underline{\sigma}}_\mathrm{y} = \begin{pmatrix} 0 & -\mathrm{i} \\ \mathrm{i} & 0 \end{pmatrix}, \underline{\underline{\sigma}}_\mathrm{z} = \begin{pmatrix} 1 & 0 \\ 0 & -1 \end{pmatrix} \tag{13}$$

When applied to spin-up and down states $|+\rangle = \begin{pmatrix} 1 \\ 0 \end{pmatrix}$ and $|-\rangle = \begin{pmatrix} 0 \\ 1 \end{pmatrix}$ respectively, one obtains the following relations:

$$\begin{array}{lll} \underline{\underline{\sigma}}_\mathrm{x}|+\rangle = \ |-\rangle & , & \underline{\underline{\sigma}}_\mathrm{x}|-\rangle = \ \ |+\rangle \\ \underline{\underline{\sigma}}_\mathrm{y}|+\rangle = \mathrm{i}\,|-\rangle & , & \underline{\underline{\sigma}}_\mathrm{y}|-\rangle = -\mathrm{i}\,|+\rangle \\ \underline{\underline{\sigma}}_\mathrm{z}|+\rangle = \ |+\rangle & , & \underline{\underline{\sigma}}_\mathrm{z}|-\rangle = \ -|-\rangle\,. \end{array} \tag{14}$$

The incoherent scattering intensity is determined only by the thermal average of the squares of the matrix elements. With $\langle \mathrm{I_x^2}\rangle = \langle \mathrm{I_y^2}\rangle = \langle \mathrm{I_z^2}\rangle = \frac{1}{3}\mathrm{I}\langle|\mathrm{I}+1\rangle$ and Eq. (11), the spin-incoherent scattering (per atom)

$$\frac{d\sigma}{d\Omega}^{(\substack{+\to+\\-\to-},NSF)}_{spin-incoherent} = (\bar{b^2} - \bar{b}^2)^{NSF} = \frac{1}{3}\langle B^2\mathrm{I}(\mathrm{I}+1)\rangle \tag{15}$$

$$\frac{d\sigma}{d\Omega}^{(\substack{+\to-\\-\to+},SF)}_{spin-incoherent} = (\bar{b^2} - \bar{b}^2)^{SF} = \frac{2}{3}\langle B^2\mathrm{I}(\mathrm{I}+1)\rangle \tag{16}$$

The result is that 1/3 of the spin-incoherent part of the nuclear scattering is non-spin flip scattering and 2/3 of it is spin-flip scattering, and it is independent of the (direction) of an external field $\mathbf{H}$.

Magnetic scattering

For pure magnetic scattering we consider the interaction of the neutron magnetic moment $\boldsymbol{\mu_N}$ with the magnetic field of the electrons $\mathbf{B} = \mathbf{B}_{spin} + \mathbf{B}_{orbital}$ due to spin and orbital momentum contributing to the magnetization $\mathbf{M}$. The magnetic interaction potential is given by

$$V_m = -(\gamma_n r_0/2)\boldsymbol{\sigma} \cdot \mathbf{M}_{\mathbf{Q}}^{\perp}, \tag{17}$$

where $\mathbf{M}_{\mathbf{Q}}^{\perp}$ is the so-called magnetic interaction vector,

$$\mathbf{M}_{\mathbf{Q}}^{\perp} = \mathbf{Q} \times \mathbf{M} \times \mathbf{Q}. \tag{18}$$

The magnetic scattering amplitude is obtained from the transition matrix elements

$$A_{\mathbf{Q}} = \langle S_z'| \frac{-\gamma_n r_o}{2} \boldsymbol{\sigma} \cdot \mathbf{M}_{\mathbf{Q}}^{\perp}) |S_z\rangle = \frac{-\gamma_n r_o}{2} \sum_{\alpha} \langle S_z'| \underline{\sigma}_{\alpha} |S_z\rangle \, M_{\alpha,\mathbf{Q}} \tag{19}$$

where $r_0 = e^2/(m_e c^2)$ is the classical electron radius. Inserting the relations of Eq.(14) into Eq. (19) we obtain the matrix elements (scattering amplitudes) for spin-flip and non-spin flip scattering:

$$A_{\mathbf{Q}} = \frac{-\gamma_n r_o}{2\mu_B} \times \begin{cases} \mathbf{M}_{z,\mathbf{Q}}^{\perp} \\ -\mathbf{M}_{z,\mathbf{Q}}^{\perp} \\ (\mathbf{M}_{x,\mathbf{Q}}^{\perp} - \mathrm{i}\mathbf{M}_{y,\mathbf{Q}}^{\perp}) \\ (\mathbf{M}_{x,\mathbf{Q}}^{\perp} + \mathrm{i}\mathbf{M}_{y,\mathbf{Q}}^{\perp}) \end{cases} \text{for} \begin{cases} + \rightarrow + \quad (\mathrm{NSF}) \\ - \rightarrow - \quad (\mathrm{NSF}) \\ + \rightarrow - \quad (\mathrm{SF}) \\ - \rightarrow + \quad (\mathrm{SF}) \end{cases} \tag{20}$$

Recall that $\mathbf{M}_{\mathbf{Q}}^{\perp}$ is the perpendicular component of $\mathbf{M}_{\mathbf{Q}}$ with respect to the scattering vector $\mathbf{Q}$, and the neutron polarization has been chosen parallel to an external field $\mathbf{H}_z$. If we choose the cartesian coordinate system xyz, with $\mathbf{x}||\mathbf{Q}$, the equation simplifies with $\mathbf{M}_{x,\mathbf{Q}}^{\perp} = 0$. We obtain two rules for the magnetic scattering:

The "spin-flip" processes are observed for the component $\mathbf{M}_{\mathbf{Q}}^{\perp}$ that is perpendicular to the neutron polarization. The "non-spin flip" processes are observed for the component of $\mathbf{M}_{\mathbf{Q}}^{\perp}$ that is parallel to the neutron polarization.

Scattering cross-section for polarized neutrons

A theoretical description of neutron scattering including magnetic interactions has been derived by Blume [27] and Maleyev [28]. The scattering process can be completely described by two master equations, (i) for the scattering cross-section σ and (ii) for $\mathbf{P}'\sigma$, where $\mathbf{P}'$ denotes the final polarization:

$$\begin{aligned} \sigma_{\mathbf{Q}} \;=\; & \sigma_{\mathbf{Q},coh}^{N} + \sigma_{isotop-inc}^{N} + \sigma_{spin-inc}^{N} \\ & + |\mathbf{M}_{\mathbf{Q}}^{\perp}|^2 + \mathbf{P}(N_{-\mathbf{Q}}\mathbf{M}_{\mathbf{Q}}^{\perp} + \mathbf{M}_{-\mathbf{Q}}^{\perp}N_{\mathbf{Q}}) + \mathrm{i}\mathbf{P}(\mathbf{M}_{-\mathbf{Q}}^{\perp} \times \mathbf{M}_{\mathbf{Q}}^{\perp}) \end{aligned} \tag{21}$$

$$\begin{aligned} \mathbf{P}'\sigma_{\mathbf{Q}} \;=\; & \mathbf{P}\sigma_{\mathbf{Q},coh}^{N} + \mathbf{P}\sigma_{isotop-inc}^{N} - \frac{1}{3}\mathbf{P}\sigma_{spin-inc}^{N} \\ & + \mathbf{M}_{\mathbf{Q}}^{\perp}(\mathbf{P}\mathbf{M}_{-\mathbf{Q}}^{\perp}) + \mathbf{M}_{-\mathbf{Q}}^{\perp}(\mathbf{P}\mathbf{M}_{\mathbf{Q}}^{\perp}) - \mathbf{P}\mathbf{M}_{\mathbf{Q}}^{\perp}\mathbf{M}_{-\mathbf{Q}}^{\perp} \\ & + \mathbf{M}_{\mathbf{Q}}^{\perp}N_{-\mathbf{Q}} + \mathbf{M}_{-\mathbf{Q}}^{\perp}N_{\mathbf{Q}} + \mathrm{i}\mathbf{M}_{\mathbf{Q}}^{\perp} \times \mathbf{M}_{-\mathbf{Q}}^{\perp} + \mathrm{i}(\mathbf{M}_{\mathbf{Q}}^{\perp}N_{-\mathbf{Q}} - \mathbf{M}_{-\mathbf{Q}}^{\perp}N_{\mathbf{Q}}) \times \mathbf{P} \end{aligned} \tag{22}$$

The first equation shows that for unpolarized neutrons, $\mathbf{P}$=0, one can measure the square of $N_{\mathbf{Q}}$ and the square of $\mathbf{M}_{\mathbf{Q}}^{\perp}$ but some of the scattering terms are not detectable. These terms are related to *nuclear-magnetic interference* and the cross-products of $\mathbf{M}_{\mathbf{Q}}^{\perp}$ to *chiral correlations* $\langle \mathbf{s}_i \times \mathbf{s}_j \rangle$ that can be found in many more complex magnetic materials; as follows from the second equation, due to such terms, polarization can be created in a scattering process.
For $\mathbf{P} = 0$, the scattering contribution due to the interference term of nuclear and magnetic scattering amplitudes as well as the chiral term vanish. On the other hand, polarization may be created by Bragg scattering with nuclear-magnetic interference. For example, for $\mathbf{P} = 0$ and vanishing chiral terms, one obtains

$$\sigma_{\mathbf{Q}} = |N_{\mathbf{Q}}|^2 + |\mathbf{M}_{\mathbf{Q}}^{\perp}|^2 \quad \text{and} \quad \mathbf{P}'\sigma_{\mathbf{Q}} = \mathbf{M}_{\mathbf{Q}}^{\perp} N_{-\mathbf{Q}} + \mathbf{M}_{-\mathbf{Q}}^{\perp} N_{\mathbf{Q}},$$

yielding a polarization

$$\mathbf{P}' = \frac{\mathbf{P}'\sigma_{\mathbf{Q}}}{\sigma_{\mathbf{Q}}} = \frac{\mathbf{M}_{\mathbf{Q}}^{\perp} N_{-\mathbf{Q}} + \mathbf{M}_{-\mathbf{Q}}^{\perp} N_{\mathbf{Q}}}{|N_{\mathbf{Q}}|^2 + |\mathbf{M}_{\mathbf{Q}}^{\perp}|^2} = 1, \ \text{ if } \ N_{\mathbf{Q}} = \mathbf{M}_{\mathbf{Q}}^{\perp}.$$

Polarization creation is also possible by scattering from chiral structures, with

$$\mathbf{P}' = \frac{\mathrm{i}\mathbf{M}_{\mathbf{Q}}^{\perp} \times \mathbf{M}_{-\mathbf{Q}}^{\perp}}{\mathbf{M}_{\mathbf{Q}}^{\perp} \cdot \mathbf{M}_{-\mathbf{Q}}^{\perp}},$$

and it can be seen also that scattering is sensitive to the sign of the chirality, for instance the helicity of a magnetic spiral.
By spherical polarization analysis it is possible to measure an arbitrary rotation and a change in magnitude of the polarization in a scattering process [5]. The relationship between initial and final polarization vectors, $\mathbf{P}$ and $\mathbf{P}'$ can be conveniently described by a tensor equation

$$P_i' = P_{ij} P_j + P_i'', \tag{23}$$

defining a 3×3 polarization matrix P_{ij} that rotates the initial polarization $\mathbf{P}$, while $\mathbf{P}''$ is the polarization that is created by the scattering process. The polarization matrix P_{ij} and $\mathbf{P}''$ can be determined experimentally.

References

[1] http://82.135.31.182/

[2] O. Schärpf, in *Neutron Spin Echo* Lecture Notes in Physics **128**, Ed. F. Mezei, Springer (1980) 27-52.

[3] F. Klein, *The mathematical theory of the top*, Princeton 1897; see also H. Goldstein, *Klassische Mechanik*, Akademische Verlagsges. Frankfurt am Main (1974).

[4] R.M. Moon, T. Riste, W.C. Koehler, Phys. Rev. **181**, 920 (1969).

[5] P. J. Brown, J. B. Forsyth, and F. Tasset, Proc. Roy. Soc. London A 442 (1993) 147;
P.J. Brown, *Polarimatric Neutron Scattering*, in lecture notes on *Polarized Neutron Scattering* (Eds. Th. Brückel and W. Schweika), Schriften des Forschungszentrums Jülich, Series Matter and Materials Vol.12, Forschungszentrums Jülich (2002).

[6] W. Schweika, Physica B **335** (1-4), (2003) 157-163.

[7] W. Schweika, S. Easton, and K.-U. Neumann, Neutron News **16** (2005) 14.

[8] W. Schweika and P. Böni, Physica B **297**, 155 (2001).

[9] O. Schärpf, Physica B **182** (1992) 376.

[10] J. R. Stewart *et al*, *J. Appl. Cryst.* **42**, 69 2009.

[11] O. Schärpf, J. Physics E: Sci. Instrum. **8** (1975) 268; F. Mezei, Commun. Phys. **1** (1976) 81; P. Böni, J. Neutron Research **5** (1996) 63.

[12] G.L. Squires, *Introduction to the theory of thermal neutron scattering*, Cambridge University Press, Cambridge (1978).

[13] V. Sears, Neutron News, Vol. **3**, No. 3, 29-37 (1992) ; http://www.ncnr.nist.gov/resources/n-lengths/

[14] A. C. Genix *et. al.* Macromolecules **39** (2006) 3947.

[15] L. Temleitner, L. Pusztai, and W. Schweika, J. Phys. Cond. Mat., (2007).

[16] O. Schärpf, *The spin of the neutron as a measuring probe*, Chapter 11, http://82.135.31.182/neutronpol.pdf

[17] G. Shirane, Y.J. Uemura, J.P.Wicksted, Y. Endoh, Y. Ishikawa, Phys. Rev. B **31** (1985) 1227.

[18] O. Schärpf, H. Capellmann, Phys. Stat. Sol. (a) **135** (1993) 359.

[19] M. Krott *et al.* Phys. Rev. B **80**, 024117 (2009).

[20] J. Herrero-Martn, V. Scagnoli, C. Mazzoli, Y. Su, R. Mittal, Y. Xiao, T. Brueckel, N. Kumar, S. K. Dhar, A. Thamizhavel, and L. Paolasini, Phys. Rev. B **80**, 134411 (2009).

[21] T. Chatterji, *Neutron scattering from magnetic materials* edited T. Chatterji (Amsterdam: Elsevier) (2006).

[22] M. Feygenson, W. Schweika, A. Ioffe, S. B. Vakhrushev, and Thomas Brückel, Phys. Rev. B **81**, 064423 (2010).

[23] W. Schweika, M. Valldor, P. Lemmens, Phys. Rev. Lett. **98**, 067201 (2007).

[24] T. Fennell *et al.* Science **326**, 415 (2009).

[25] J. de Groot *et al.*, manuscript in preparation.

[26] W. Schweika, J. Phys. Conf. Ser. **211**, 012026 (2010).

[27] M. Blume, *Phys. Rev.* **130** 1670 (1963).

[28] S. V. Maleyev, V. G. Baryakhtar P. A. and Suris, *Fiz. Tv. Tela* **4** 3461 (1962); *Soviet Phys. Solid State* **4** 2533 (1963).

7

Structural Analysis

Georg Roth

7. Structural Analysis

G. Roth

7.1 Introduction

The analysis of crystal structures and magnetic ordering is usually based on diffraction phenomena caused by the interaction of matter with X-rays, neutrons, or electrons. Even though modern electron microscopy (HRTEM) can achieve atomic resolution, more detailed and quantitative information on the 3-dim. atomic arrangement in crystals and on 3-dim. magnetic structures and spin densities, requires diffraction methods. In a more general nomenclature, diffraction is equivalent to coherent, elastic scattering. The basic theory of diffraction used for structural analysis (the so called kinematical theory) is similar for all types of radiation. Due to the different properties of X-rays, neutrons and electrons and their specific interaction with matter, complementary information is obtained from experiments with different types of radiation.

Considering only X-rays and thermal neutrons one finds that their wavelengths are similar (0.5 Å < λ < 2.4 Å) but they are scattered very differently by matter: While the electromagnetic X-radiation is scattered from the electrons and yields the total electron density distribution in the crystal, the nuclear scattering of neutrons is sensitive to the density distribution of the nuclei and the magnetic neutron scattering probes the magnetisation density of unpaired electrons.

X-ray diffraction using conventional laboratory equipment and/or synchrotron installations is the most important method for structure analysis. The purpose of this chapter is to discuss particularly those cases, for which, instead of or complementary to X-rays, neutrons are required to solve structural problems.

7.2 Structure factor and Bragg intensities

The characteristic feature of the crystalline state is its periodic order, which may be represented by a (translation) lattice. In the 3-dim. case, three basis vectors $\boldsymbol{a}_1$, $\boldsymbol{a}_2$, $\boldsymbol{a}_3$ define a parallelepiped, called unit cell. The general lattice vector

$$\boldsymbol{a} = u\,\boldsymbol{a}_1 + v\,\boldsymbol{a}_2 + w\,\boldsymbol{a}_3. \qquad (1)$$

results from a linear combination of the basis vectors with coefficients u, v, and w being positive or negative integers (incl. 0).

The position of atom j in the unit cell is given by the vector

$$\boldsymbol{r_j} = x_j\,\boldsymbol{a_1} + y_j\,\boldsymbol{a_2} + z_j\,\boldsymbol{a_3}. \tag{2}$$

The coefficients x_j, y_j, and z_j are called atomic coordinates ($0 \le x_j < 1$; $0 \le y_j < 1$; $0 \le z_j < 1$).

Lattice planes (that means a set of parallel planes containing lattice points) defined by three integers (*hkl*), called Miller indices, have the characteristic interplanar spacing d_{hkl}.

For scattering studies of crystals the concept of the reciprocal lattice with the basis vectors $\boldsymbol{\tau_1}$, $\boldsymbol{\tau_2}$, $\boldsymbol{\tau_3}$ has been developed. In crystallography, the lattice vector of the reciprocal lattice is defined by

$$\boldsymbol{\tau} = h\,\boldsymbol{\tau_1} + k\,\boldsymbol{\tau_2} + l\,\boldsymbol{\tau_3}. \tag{3}$$

In solid state physics,

$$\boldsymbol{Q} = 2\pi\,\boldsymbol{\tau} \tag{4}$$

is used instead of $\boldsymbol{\tau}$ ($|\boldsymbol{\tau}| = 1/d_{hkl}$ with d_{hkl}: lattice spacing).

7.2.1 Nuclear scattering

In the kinematical approximation, which assumes that the magnitude of the incident wave amplitude is the same at all points in the specimen (this implies a small sample size, weak scattering intensities, no multiple diffraction and negligible absorption), the diffracted intensity is proportional to the square of the amplitude of the scattered wave for each individual reflection; it can be regarded as a weight ascribed to the reciprocal-lattice nodes

$$I(\boldsymbol{\tau}) \sim |\boldsymbol{F}(\boldsymbol{\tau})|^2. \tag{5}$$

The structure factor $\mathbf{F}(\boldsymbol{\tau})$ is the Fourier transform of the scattering density within the unit cell, and contains the complete structural information, including the atomic coordinates x_j, y_j, z_j and the thermal vibrations T_j.

$$\boldsymbol{F}(\boldsymbol{\tau})(= \sum_j b_j \exp[2\pi i(\boldsymbol{\tau}\boldsymbol{r_j})]\cdot T_j(\boldsymbol{\tau}) = |\boldsymbol{F}(\boldsymbol{\tau})|\cdot\exp[i\varphi(\boldsymbol{\tau})]. \tag{6}$$

In the case of nuclear scattering of neutrons the structure factor has the dimension of a length, as has the scattering length $b_j(\boldsymbol{\tau}) = b_j$ = const. of nucleus j. $T_j(\boldsymbol{\tau})$ is the Debye-Waller factor which takes into account dynamical and static displacements of the nucleus j from its average position $\boldsymbol{r_j}$ in the unit cell (see Eq. 2). With the fractional coordinates x_j, y_j and z_j the scalar product in the exponential function can be written as

$$\boldsymbol{\tau}\cdot\boldsymbol{r_j} = hx_j + ky_j + lz_j. \tag{7}$$

Note: The measurement of diffraction intensities ("Bragg intensities") $I(\boldsymbol{\tau})$ yield only the modulus of the structure factors, $|\boldsymbol{F}(\boldsymbol{\tau})| \propto \sqrt{I(\boldsymbol{\tau})}$, and not their phases $\varphi(\boldsymbol{\tau})$ (see Eq. 6), which would be required for the inverse Fourier transform of the data (Fourier synthesis) to give directly the arrangement of the atoms in the unit cell. The lack of the phase information is known as the *phase problem of crystallography*.

In a diffraction experiment normally only relative Bragg intensities are measured. A scale factor SCALE takes into account all parameters which are constant for a given set of diffraction intensities. Additional corrections have to be applied, which are a function of the scattering angle. For nuclear neutron diffraction from single crystals the integrated relative intensities are given by

$$I(\boldsymbol{\tau}) = \text{SCALE} \cdot \text{L} \cdot \text{A} \cdot \text{E} \cdot |\boldsymbol{F}(\boldsymbol{\tau})|^2. \qquad (8)$$

The Lorentz factor L is instrument specific. The absorption correction A depends on the geometry and linear absorption coefficient of the sample and the extinction coefficient E takes into account a possible violation of the assumed conditions for the application of the kinematical diffraction theory.

Information on the crystal system, the Bravais lattice type and the basis vectors $\boldsymbol{a}_1$, $\boldsymbol{a}_2$, $\boldsymbol{a}_3$ of the unit cell (lattice parameters a, b, c, α, β, γ) may be directly deduced from the reciprocal lattice. The $|\boldsymbol{F}(\boldsymbol{\tau})|^2$ values associated as weights to the nodes of the reciprocal lattice give the diffraction symbol and hence valuable information on the space-group symmetry. Here, systematic absences (zero structure factors) can be used to determine non-primitive Bravais lattices or detect the presence of non-symmorphic symmetry operations (symmetry operations with translation components). Most of these statements apply equally well to single crystal X-ray as well as neutron diffraction.

The peculiarities of the coherent elastic neutron scattering length b_j of atom type j have been discussed in previous chapters. For the purpose of structural analysis, one important point is the absence of the form-factor fall-off of the intensities with increasing scattering angle, an effect that is well known from X-ray diffraction and is related to the fact that for X-rays, the scattering object (the electron cloud around the atom) has a size comparable to the wavelength of the scattered radiation leading to increasingly destructive interference with increasing scattering angle. In nuclear neutron scattering, the object (the nucleus of the atom) is almost a point scatterer compared to the wavelength of the radiation. This allows the

measurement of diffraction data with good counting statistics even at very large scattering angles. This extra data improves considerably the precision of atomic coordinates x_j, y_j, z_j and (anisotropic) thermal displacement parameters T_j (see equation (6)) derived form neutron data as compared to those from X-ray data.

7.2.2 Magnetic scattering

The dipolar interaction between the neutron magnetic moments and the magnetic moments of atoms/ions (and nuclei) $\boldsymbol{M}_j$ leads to the magnetic neutron scattering in addition to the nuclear contribution. In the case of an ordering of the magnetic moments over the whole crystal (periodic magnetic structure) the magnetic structure factor is given by

$$\boldsymbol{F}_M(\boldsymbol{\tau}) = \sum_j b_{Mj}(\boldsymbol{\tau})\cdot\exp[2\pi i(\boldsymbol{\tau}\cdot\boldsymbol{r}_j)]\cdot T_j(\boldsymbol{\tau}) \qquad (9)$$

with the magnetic scattering amplitude

$$b_{Mj}(\boldsymbol{\tau}) = (e^2\gamma/2m_ec^2)\cdot f_{Mj}(\boldsymbol{\tau})\cdot\sigma\cdot\boldsymbol{M}_{\perp j}(\boldsymbol{\tau}). \qquad (10)$$

$\frac{1}{2}\sigma$ is the neutron spin operator and $\mathbf{M}_{\perp j}(\boldsymbol{\tau})$ the projection of the magnetic moment vector $\boldsymbol{M}_j$ onto the scattering plane (*hkl*). The magnetic form factor $f_{Mj}(\boldsymbol{\tau})$ is the Fourier transform of the normalised magnetisation density $M_j(\underline{\boldsymbol{r}})$ of the atom or ion j:

$$f_{Mj}(\boldsymbol{\tau}) = \int_V \boldsymbol{M}_j(\boldsymbol{r})\cdot\exp[2\pi i(\boldsymbol{\tau}\cdot\boldsymbol{r})]\cdot d\boldsymbol{r} \qquad (11)$$

$$\text{with } f_M(0) = \int_V \boldsymbol{M}_j(\boldsymbol{r})\cdot d\boldsymbol{r} = 1.$$

This is a function of the reciprocal lattice vector $\boldsymbol{\tau}$, whereas the similarly defined atomic scattering factor f_j of X-ray diffraction

$$f_j(|\boldsymbol{\tau}|) = \int_V \rho_j(\boldsymbol{r})\cdot\exp[2\pi i(\boldsymbol{\tau}\cdot\boldsymbol{r})]\cdot d\boldsymbol{r}, \qquad (12)$$

for a spherical electron density $\rho_j(\boldsymbol{r})$, depends only on the length of $\boldsymbol{\tau}$.

The intensity of magnetic and nuclear neutron scattering is of the same order of magnitude. For unpolarised neutrons the Bragg intensity of nuclear and magnetic neutron diffraction is simply an incoherent superposition

$$I(\boldsymbol{\tau}) = I_N(\boldsymbol{\tau}) + I_M(\boldsymbol{\tau}) \sim |\boldsymbol{F}_N(\boldsymbol{\tau})|^2 + |\boldsymbol{F}_M(\boldsymbol{\tau})|^2. \qquad (13)$$

For polarised neutrons on the other hand the coherent superposition gives

$$[|\boldsymbol{F}(\boldsymbol{\tau})|^2]^{\pm} = |\boldsymbol{F}_N(\boldsymbol{\tau}) \pm \boldsymbol{F}_M(\boldsymbol{\tau})|^2 \qquad (14)$$

with the interference terms $\pm 2\cdot|\boldsymbol{F}_N(\boldsymbol{\tau})\cdot\boldsymbol{F}_M(\boldsymbol{\tau})|$ according to the two possible directions of polarisation (+ and -). In measuring the flipping ratio at superimposed Bragg reflections, that

means the ratio of the intensities for the two polarisations up and down, even small magnetic structure factors can be determined quite accurately.

The analysis of a magnetic structure starts with the determination of its periodicity with respect to that of the crystal structure. The identification of magnetic reflections is usually accomplished by a careful comparison of powder diagrams recorded below and above the magnetic phase transition temperatures. A more detailed study of the scattering vectors, e.g. for incommensurate structures, may require also single-crystal experiments. The nuclear structure factors $\boldsymbol{F}_N(\boldsymbol{\tau})$ can be calculated from the known crystal structure. In this way the scale factor of the data set can be obtained and the absolute values of the magnitudes of the magnetic structure factors $|\boldsymbol{F}_M(\boldsymbol{\tau})|$ can be determined. The individual orientations of the magnetic moments $\boldsymbol{M}_j$ with respect to the basis vectors of the crystal lattice and their magnitudes are then to be calculated from a model of the magnetic structure. Symmetry again plays an important role in the field of magnetic structure determination: The symmetry of the high temperature paramagnetic phase above the magnetic phase transition can be exploited to derive symmetrically feasible ordered candidate structures below the phase transition. This process reduces the number of candidate structures dramatically; the underlying theory (magnetic space groups, representation theory etc.) is beyond the scope of this chapter.

Magnetic structure determination is still one of the domains of neutron diffraction, although (resonant) magnetic X-ray scattering, performed at synchrotron sources, has recently been catching up for some favourable cases.

7.3 Diffraction contrast variation

Another great advantage of neutrons over X-rays in the context of structural analysis is the very much different variation of the scattering length of atoms within the periodic system of the elements: The contrast in conventional X-ray diffraction is directly related to the ratio of the number of electrons Z_j of the different atoms or ions j involved. The atomic scattering factor f_j in the structure-factor formula, which represents the Fourier transform of the atomic electron density distribution, is proportional to Z_j ($f_j = Z_j$ for $\sin\theta/\lambda = 0$). Standard X-ray techniques can hardly differentiate between atoms/ions with a similar number of electrons (like Si and Al or Cr and Mn). Even if the atoms are fully ordered on different sites, X-ray diffraction just ‘sees’ average structure.

For neutrons the atomic scattering factor f_j is replaced by the nuclear scattering length (or coherent scattering amplitude) b_j, which is of the same order of magnitude for all nuclei but

varies from nucleus to nucleus in a non-systematic way. b_j values can be either positive or negative and depend on the isotopes and nuclear spin states of the element j. A nucleus of an isotope with spin I may have two different neutron scattering lengths: one for the combined spin state $J = I + ½$ and one with $J = I - ½$.

An important and fundamental example is provided by the simplest of all nuclei, the proton with spin $I = ½$. The two combined spin states, $J = 1$ (triplet) and $J = 0$ (singlet), with statistical weights ¾ and ¼ respectively, lead to the scattering lengths for a *free* proton:

b^s_H = -23.7 fm, b^t_H = +5.38 fm, $b_{freeH} = ¼b^s_H + ¾b^t_H$ = -1.89 fm (with 10^{-15} m = 1 fm).

The value for the *bound* proton in a crystal structure, which is to be used in the structure-factor calculations, amounts to $b_H = 2 \cdot b_{freeH}$ = -3.741 fm. The existence of two different scatterings lengths for hydrogen also leads to a considerable amount of incoherent scattering ('spin-incoherence') causing a strong diffuse background scattering for hydrogen-containing compounds. Deuterium D (heavy hydrogen), on the other hand, has spin $I = 1$, a positive scattering length of +6.67 fm and show only very small spin incoherent scattering. Very often deuterated compounds are preferred in order to profit from the larger b_D value, but also to reduce the background from incoherent scattering. This volume-dependent background may become crucial for neutron powder diffraction experiments, but is usually not a problem in single crystal experiments.

7.4 Example: Contrast variation:

Crystal structure, site occupation and magnetic phase diagram of $(Mn_{1-x}Cr_x)_{1+\delta}Sb$

As an example of contrast variation, the combination of X-ray and neutron diffraction information is demonstrated for the intermetallic compounds $(Mn_{1-x}Cr_x)_{1+\delta}Sb$, with $0 \le x \le 1$ [1]. This solid solution system is interesting for its magnetic properties: One end member of the solid solution series ($Mn_{1+\delta}Sb$) shows isotropic ferromagnetic behaviour while the other one ($Cr_{1+\delta}Sb$) is a uniaxial antiferromagnet. Intermediate compositions are characterized by competing magnetic interactions leading to a complex magnetic phase diagram. The crystal structure is closely related to the hexagonal NiAs-type structure (space group: $P6_3/mmc$) with some additional partial occupation (≤ 0.14) of the interstitial site 2(d) (see Fig. 1):

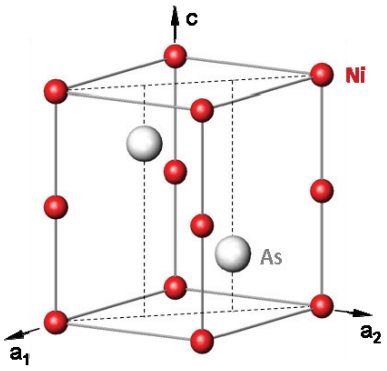

Fig. 1(a). NiAs structure

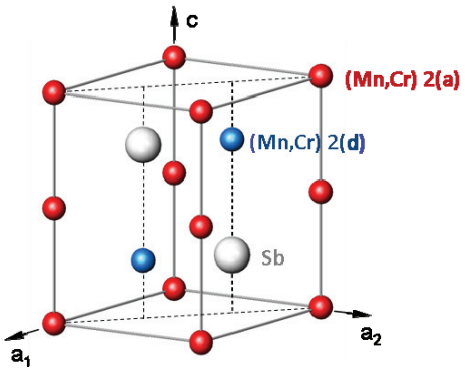

Fig. 1(b). $(Mn_{1-x}Cr_x)_{1+\delta}Sb$ structure

Conventional X-ray diffraction can hardly differentiate between chromium (Z_{Cr}= 24) and manganese (Z_{Mn}= 25) but still yields information on the overall occupation probabilities by (Mn,Cr) for site 2(a) (denoted as a) and site 2(d) (denoted as d). The Sb position is assumed to be fully occupied, thus serving as an internal standard for the scattering power.

The compound formula can now be reformulated site-specifically as:

$$(Mn_{1-y}Cr_y)_a(Mn_{1-z}Cr_z)_dSb$$

site 2(a) site 2(d)

corresponding to a chemical composition of $Mn_{[(1-y)a+(1-z)d]}Cr_{[ya+zd]}Sb$.

On the other hand, the nuclear scattering lengths of Cr and Mn for neutron diffraction are extremely different with b_{Cr} = +3.52 fm and b_{Mn} = -3.73 fm.

Note: A positive value of b_j means that there is a phase shift of 180° between the incident and scattered neutron waves as a consequence of predominant potential scattering. Negative b_j values – corresponding to no phase change - result from resonant scattering.

In the structure analysis of the neutron data site-specific effective scattering lengths b_{eff} (2a) and b_{eff} (2d) are refined, which in turn are expressed as:

$$b_{eff}(2a) = a\cdot[(1-y)\cdot b_{Mn} + y\cdot b_{Cr}] \quad \text{and} \quad b_{eff}(2d) = d\cdot[(1-z)\cdot b_{Mn} + z\cdot b_{Cr}]$$

solving for the unknown parameters y and z gives:

$$y = [b_{eff}(2a)/a - b_{Mn}] / [b_{Cr} - b_{Mn}] \quad \text{and} \quad z = [b_{eff}(2d)/d - b_{Mn}] / [b_{Cr} - b_{Mn}].$$

The combination of the overall occupation probabilities a and d - from conventional X-ray studies – with the effective scattering lengths b_{eff}(2a) and b_{eff}(2d) determined in a neutron dif-

fraction experiment allows the evaluation of the Cr and Mn concentrations on the different sites 2(a) and 2(d).

It is evident, that the individual (Cr,Mn) distributions on the two crystallographically different sites 2(a) and 2(d) are not accessible merely by a chemical analysis. For most of the samples studied, the site 2(a) was found to be fully occupied: a ≈ 1.0. But the formula $(Mn_{1-x}Cr_x)_{1+\delta}Sb$ used normally is only correct for the special case of equal Cr : Mn ratios on both sites:

$$x = y = z \quad \text{and} \quad 1 + \delta = a + d.$$

The detailed information on the (Cr,Mn) distribution is needed to explain the magnetic properties of these intermetallic compounds, for which only the spins localised on the 2(a) sites are involved in the magnetic ordering leading to a complex magnetic phase diagram of the MnSb – CrSb system (see Fig. 3). An overall Cr : Mn ratio from chemical analysis is not sufficient. The ferromagnetic $Mn_{1+\delta}Sb$ changes its axis of easy magnetisation from parallel to the hexagonal ***c***-axis at high temperatures to $\perp \boldsymbol{c}$ at low temperatures. The magnetic spins of the uniaxial antiferromagnetic $Cr_{1+\delta}Sb$ are oriented parallel (or antiparallel) to ***c***. For solid solutions $(Mn_{1-x}Cr_x)_{1+\delta}Sb$ between the pure end members there exist various ferro- and antiferromagnetic states with inclined spin orientations, with non-colinear magnetic arrangements, and regions with co-existing magnetic ordering. Several magnetic structures of the intermetallic MnSb – CrSb system are shown in Fig. 2.

Note: In general, a statistical occupation of one crystallographic site with three kinds of scatterers - e.g. Mn, Cr and "vacancies" - requires at least two independent experiments with sufficiently different relative scattering power of the atoms involved to determine the fractional occupancies.

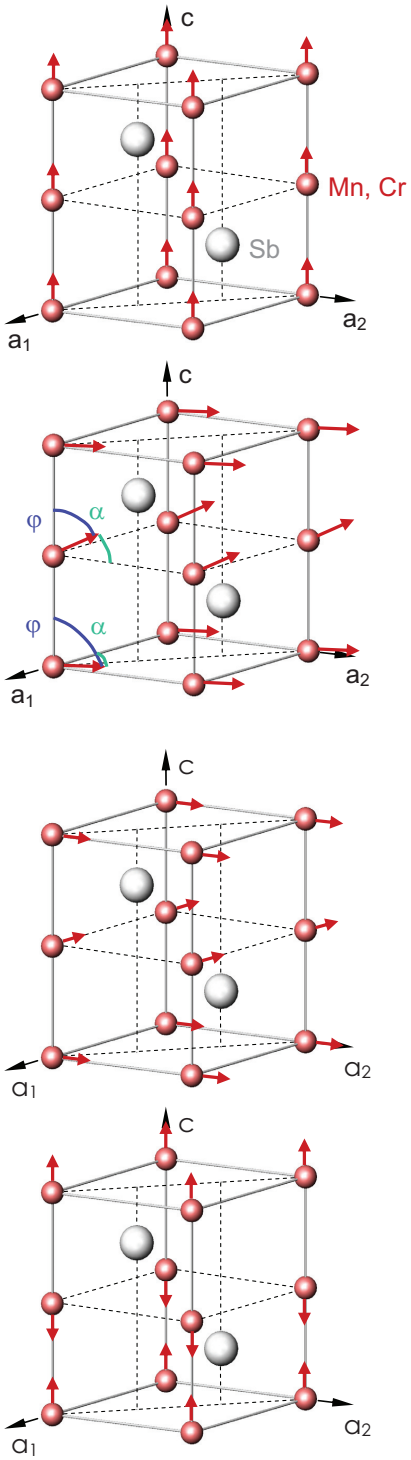

Ferromagnetism:
spin orientation ||***c***

Canted magnetic structure
(weak ferromagnet):
the spins are turned away from [001]
by an angle φ and within the (001) planes with
an antiphase rotation around ***c*** by α

Canted magnetic structure:
canting angle α = 60°
all spins lie in (001) planes

Antiferromagnetism:
spin orientation ||***c***

Fig. 2. Various types of magnetic structures in the intermetallic system ($Mn_{1-x}Cr_x$)Sb (NiAs structure type)

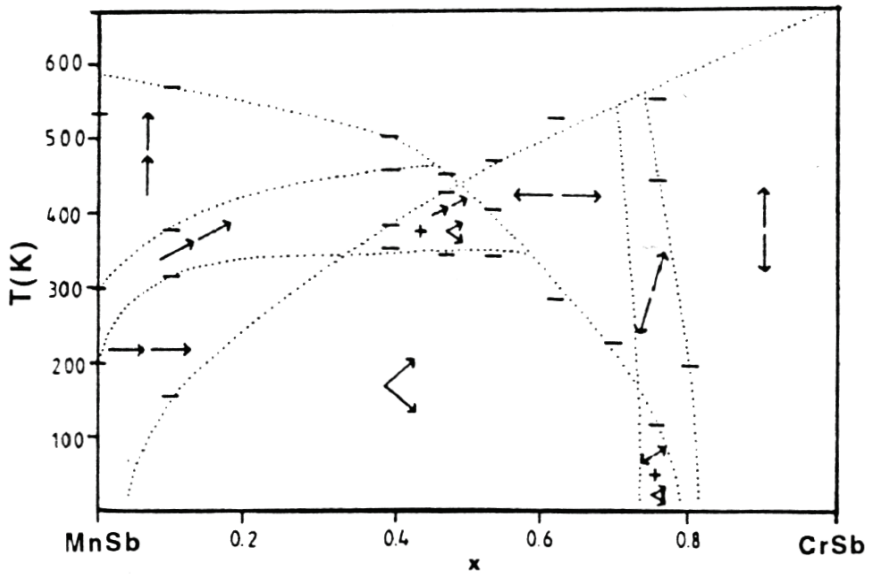

Fig. 3. Magnetic phase diagram of the intermetallic system MnSb – CrSb. The vectors indicate the spin orientations in the different magnetic structures.

7.5 The hydrogen problem in structural analysis

The determination of the structural parameters (coordinates, displacement parameters) of hydrogen atoms in crystals is a special problem involving again the different properties of X-rays and neutrons. It is obvious that H or D atoms with Z = 1 give only a small contribution to the electron density and, therefore, they are hardly visible in X-ray structure analysis, particularly if heavy atoms are also present in the structure. However, there is an even more fundamental problem: The single electron of H or D is engaged in the chemical bonding and is by no means localised at the proton/deuteron position. Therefore, bond distances from X-ray diffraction involving hydrogen are notoriously wrong and any comparison with quantum mechanical calculations is quite hard to perform. This lack of sound experimental information is in sharp contrast to the importance of hydrogen bonding in solids, particularly in biological molecules like proteins, where hydrogen bonds govern to a large extent structures and functionalities of these 'bio-catalysts'. A combination with neutron diffraction experiments is important to determine the structural parameters of the H/D atoms properly. More generally, the structure analysis by neutron diffraction yields separately and independently from the X-ray data the structure parameters of all atoms including the mean square displacements due to static and dynamic (even anharmonic) effects.

7.5.1 Example of a study of H/D ordering:

Ferroelectric phase transition in RbH_2PO_4 (RDP)

The hydrogen problem in crystal structure analysis is of special importance for structural phase transitions driven by proton ordering. KH_2PO_4 (KDP) is the most well-known representative of hydrogen-bonded ferroelectrics. Here, we discuss the isotypic RbH_2PO_4 (RDP). The crystal structure consists of a three-dimensional network of PO_4-groups linked by strong hydrogen bonds (Fig. 4).

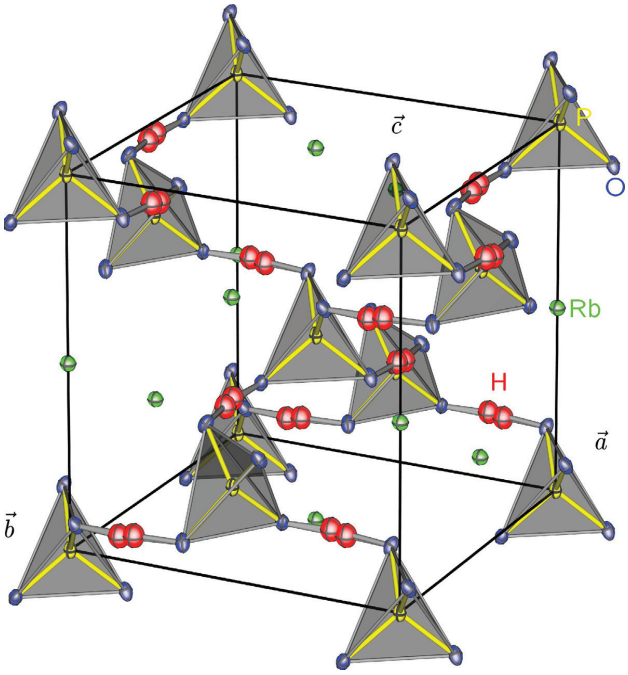

Fig. 4: Crystal structure of the paraelectric phase of RDP (RbH_2PO_4) with a split-model representation of the hydrogen disorder [3].

In the paraelectric phase at room temperature KDP as well as RDP crystallise in the tetragonal space group I $\bar{4}$2d, where the H-atoms are dynamically disordered in symmetric O···H···O bonds, which are almost linear with short O–O distances, typically in the range of 2.5 Å. The disordered H-distribution may be interpreted as corresponding to a double-well potential [2]. Figures 5 and 6 show the corresponding results for RDP, obtained from single crystal neutron diffraction [3].

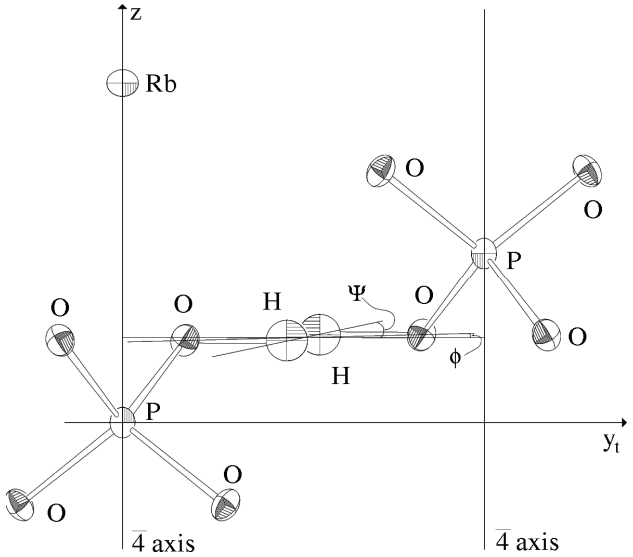

Fig. 5: Hydrogen disorder (split-model description) in the PO_4···H-H···PO_4 hydrogen bond of RDP at T_C + 4 K (atoms are represented by their mean-square displacement ellipsoids) [3].

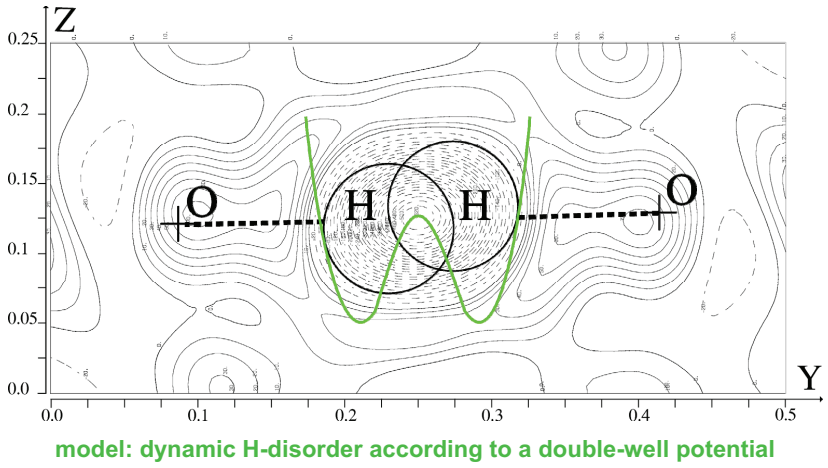

Fig. 6. Difference-Fourier-plot of the negative proton density in the hydrogen bond of paraelectric RDP (fig. 5) indicated by broken contour lines.

The two very close hydrogen positions with 50% occupation probability are, of course, an artefact of the time-space averaging that is inherent to diffraction. In this case, the hydrogen disorder is assumed to be a dynamic hopping process between the two energetically degenerate sites.

At T_c = 147 K, RDP transforms to a ferroelectric phase of orthorhombic symmetry (space group: Fdd2) in which the protons order in short asymmetric O-H···O bonds (Fig. 7). The PO_4-tetrahedra show a characteristic deformation with two shorter and two longer P-O distances due to a transfer of electron density to the covalent O–H bonds. The electrical dipole moments are oriented ||z which give rise to a polarisation along the ***c***-direction.

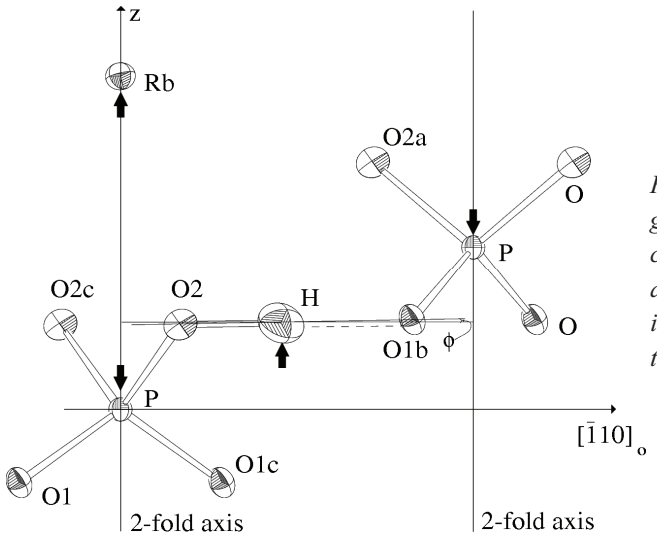

Fig. 7: Ferroelectric, hydrogen-ordered structure of RDP close to the phase transition at T_C – 1 K (major changes indicated by arrows, presentation as in Fig.5) [3].

The phase transition temperatures of KDP-type compounds changes drastically when H is substituted by D. For $K(H,D)_2PO_4$, for instance, the para- to ferroelectric T_C changes from 122 K in the protonated to 229 K in the deuterated compound. This huge H/D-isotope effect proves that hydrogen-ordering and -dynamics is the major factor controlling this phase transition. Another type of H/D-isotope effect was found for $Tl(H,D)_2PO_4$ (TDP/DTDP) and $Rb(H,D)_2PO_4$ (RDP/DRDP), where a different polymorphism between the protonated and deuterated phases exists.

Clearly, the use of neutron diffraction is detrimental to a better understanding of these compounds and their interesting physical properties.

7.6 Accurate atomic coordinates and displacement parameters from neutron diffraction:
As discussed in chapter 7.2.1, neutron diffraction is very useful for obtaining precise atomic coordinates and displacement parameters. The improved accuracy (compared to X-rays) stems mainly from the absence of the form-factor fall-off. We will use measurements on Cobalt-olivine, Co_2SiO_4, (crystal size 3 x 2 x 2 mm) taken at the four-circle diffractometer HEiDi at the hot-neutron source of the FRM II reactor (λ = 0.552 Å) for demonstrating this advantage for the thermal displacements:

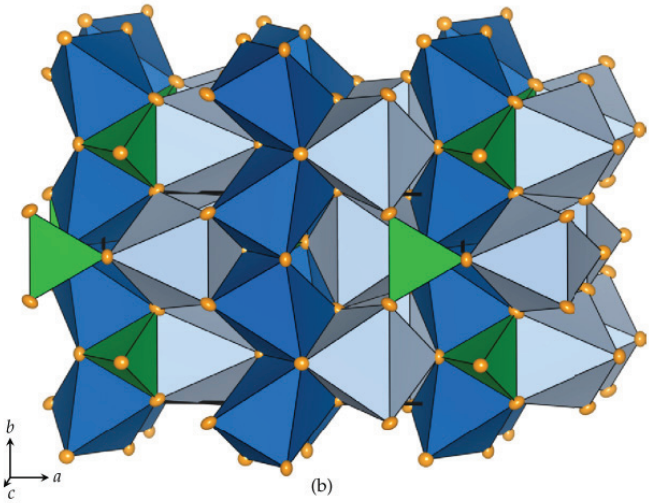

Fig. 8: Structure of Co_2SiO_4 olivine at room temperature, projected along c.
Green: SiO_4-tetrahedra, Dark blue: Co(1)O_6-octahedra, light blue: Co(2)O_6-octahedra
Displacement ellipsoids are plotted at the 95% probability level (from [4]).

The olivine structure consists of chains of two types of edge-sharing CoO_6-octahedra connected by SiO_4-tetrahedra. A large data set with 1624 independent reflections up to sin θ/λ = 1.05 Å^{-1} had been measured. The data were then successively cut off in shells of sin θ/λ and the resulting partial data sets were used to analyse the displacement parameters. Figure 9 shows two interesting observations: First of all, the precision improves significantly with increasing $(\sin \theta/\lambda)_{max}$, as is evident from the decreasing error bars. In the X-ray case, high angle reflections are usually very weak and their measurement does often not lead to improved precision. Secondly, there is a systematic change of the displacement values themselves, resulting from systematic errors that vary with $(\sin \theta/\lambda)_{max}$.

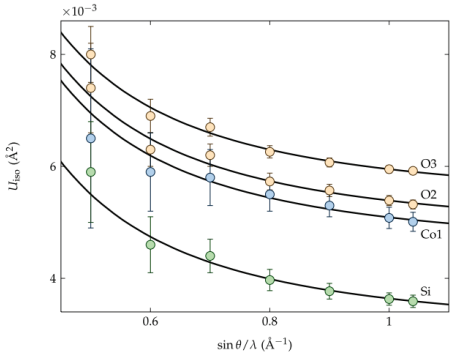

Fig. 9: Statistical (error bars) and systematic errors of isotropic displacements parameters in Co_2SiO_4 as a function of measured sin θ/λ range from single-crystal neutron diffraction data at room temperature [4].

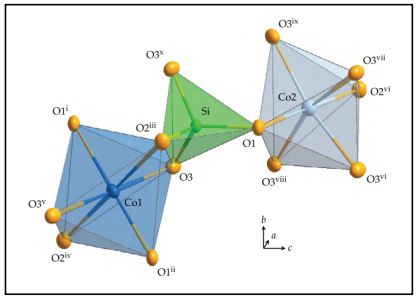

Fig. 10: Clinographic view of the CoO_6 and SiO_4 polyhedra in Co_2SiO_4 at room temperature [4].

High d_{hkl}-value resolution data from neutron diffraction is also useful to derive precise temperature dependent displacement parameters:

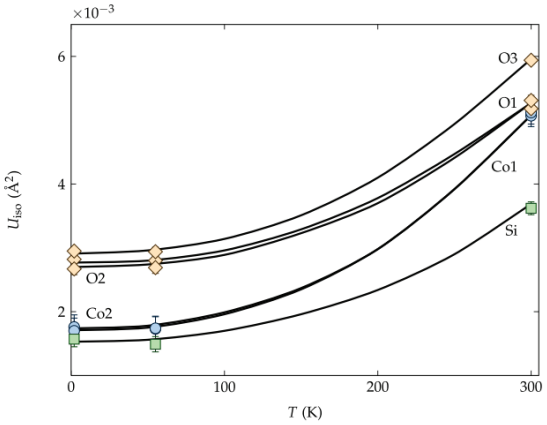

Fig. 11: Temperature dependence of the isotropic displacement parameters of Co_2SiO_4 [4].

Just as in the case of high quality single crystal X-ray diffraction data, anisotropic displacement parameters can be determined as well. In addition to that, the quality of single crystal neutron data allows to refine anharmonic displacement parameters.

Note: Due to the absence of the form-factor fall-off, neutron diffraction data can be collected to large sin θ/λ resulting in improved precision (error bars) and accuracy (convergence to resolution-independent values) of coordinates and displacement parameters.

7.7 Magnetic structures from neutron diffraction: Co_2SiO_4

Cobalt-Olivine, Co_2SiO_4, orders magnetically below about 50 K. The magnetic moments of the Co^{2+}-ions turn from a paramagnetic phase with no long range order of the magnetic moments into an antiferromagnetically ordered arrangement. We use Co_2SiO_4 again to briefly demonstrate the application of neutron diffraction to the structural analysis of magnetic structures. This time, a powder neutron diffraction experiment has been performed at the diffractometer D20 (ILL, France) in its high-resolution mode, at temperatures between 70K and 5K, with a neutron wavelength of $\lambda = 1.87$ Å and approximately 2 g of powdered Co_2SiO_4 [4].

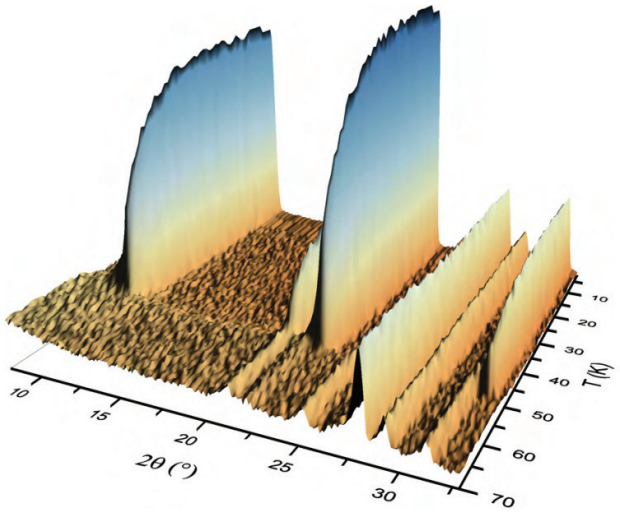

Fig. 12: Thermal evolution of the neutron powder diffraction pattern (low angle part) of Co_2SiO_4 [4].

At about 50 K, new magnetic reflections (001), (100), (110), (300) etc. appear. The nuclear reflections don't change much at the magnetic phase transition. The new reflections can be indexed with the same unit cell als the nuclear reflections, but they were forbidden in the paramagnetic phase with space group P n m a. Obviously, the symmetry has changed at the magnetic ordering transition. The task is then - just as in 'ordinary' structure determination - to find a structural model (that is: magnetic moments and their orientation on the magnetic ions, here Co^{2+}) that fits the observed positions and intensities of the magnetic Bragg peaks. Magnetic structure determination is outside the scope of this chapter (see also 7.3), but assumed such a model has been constructed, it can be refined by (in the case of powder data) the Rietveld method.

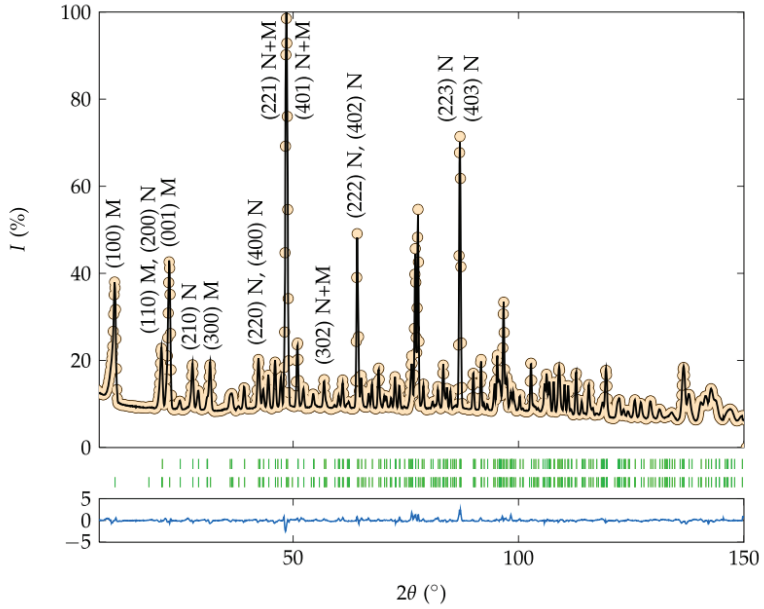

Fig. 13: Neutron powder diffraction pattern (dots), Rietveld fit (black line) and allowed Bragg reflections (green marks) at 5 K of Co_2SiO_4 [4].

The lower trace (blue) is the difference *Iobs* - *Icalc* on the same scale. The upper row of the green marks shows Bragg reflections corresponding to the nuclear phase and the lower row represents the allowed positions of the magnetic peaks. Some of the Bragg peaks are indexed. 'N' and 'M' denote the nuclear and magnetic contributions, respectively [4]. Note that the magnetic Bragg peaks are only visible at low diffraction angles.

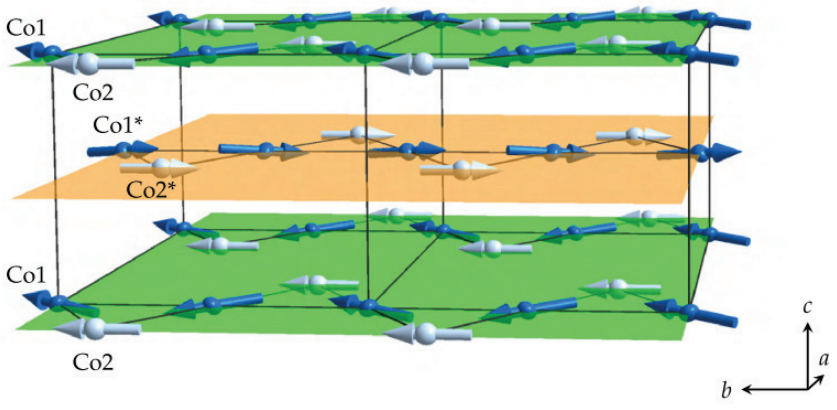

Fig. 14: Graphical representation of the magnetic structure of Co_2SiO_4 below 50 K. The non-magnetic atoms (Si and O) are excluded for simplicity. The figure shows the zigzag chains of Co(1) and Co(2) in layers perpendicular to the ***c*** *axis [4].*

From the Rietveld refinements, one can derive parameters describing quantitatively the magnetic moments on the two symmetrically non-equivalent Co^{2+}-sites. However, magnetic neutron diffraction from single crystals often gives additional and more accurate information:

	Co1 (0,0,0)	Co2 (x,1/4,z)
M_x (μ_B)	1.18 ± 0.05	—
M_y (μ_B)	3.61 ± 0.04	3.37 ± 0.04
M_z (μ_B)	0.66 ± 0.18	—
M (μ_B)	3.86 ± 0.05	3.37 ± 0.04
ϕ (°)	71.9 ± 0.7	90
θ (°)	80.2 ± 2.7	90

$\chi^2 = 2.23$, $R[F^2 > 2\sigma(F^2)] = 0.033$, $wR(F^2) = 0.044$.

Table: Cartesian (M_x, M_y and M_z) and spherical (M, φ and θ) components of the Co1 and Co2 magnetic moments according to the single-crystal neutron diffraction data at 2.5 K. The directions of the magnetic moments for other cobalt ions in the unit cell can be obtained by applying the symmetry operations of the magnetic space group (Schubnikov group) Pnma.

7.8 Electron density determination from X-ray and neutron diffraction: Co_2SiO_4

Another advanced application of neutron diffraction in structural analysis is the determination of 3-dimensinal high resolution maps of the electron density in the unit cell to study, for instance, details of the chemical bonding. The most involved method of electron density studies (called X-N-synthesis) uses a combination of high quality single crystal neutron and X-ray diffraction experiments. In the present case, a single crystal of Co_2SiO_4 with dimensions 3 x 2 x 2 mm, was measured on the four-circle diffractometer HEiDi at the hot-neutron source of the FRM II reactor (Garching) at λ = 0.552 Å, the single crystal X-ray (synchrotron) experiment was performed on Diffractometer D3 at the synchrotron facility HASYLAB/DESY (Hamburg) with a Co_2SiO_4-sphere, diameter 150 µm as the sample and an X-ray wavelength of λ = 0.5 Å. The next step is to take the X-ray-data, do a Fourier-transform (Fourier-synthesis) to obtain the electron density map:

$$\rho(\boldsymbol{r}) = 1/V \cdot \sum_{\tau} \boldsymbol{F}(\boldsymbol{\tau}) \cdot \exp[2\pi i(\boldsymbol{\tau r})] \qquad \text{with} \qquad \boldsymbol{F}(\boldsymbol{\tau}) = |\boldsymbol{F}(\boldsymbol{\tau})| \cdot \exp[i\varphi(\boldsymbol{\tau})]. \qquad (14)$$

The phases $\varphi(\boldsymbol{\tau})$ are calculated from the atomic model (eqn. (6)), the moduli $|\boldsymbol{F}(\boldsymbol{\tau})|$ are taken from the measured X-ray intensities after correction analogous to eqn. (8). The result is a 3-dimensinal map of the total electron density $\rho(\boldsymbol{r})$ within the unit cell:

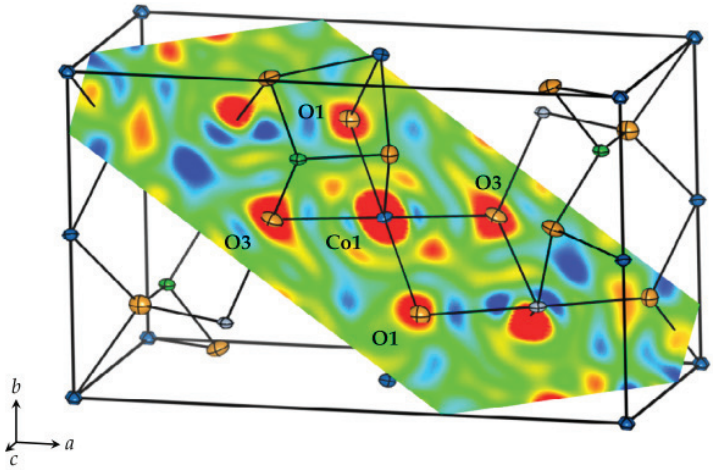

Fig. 15: Electron density distribution $\rho(\boldsymbol{r})$ of Co_2SiO_4 at 12 K from Fourier synthesis of X-ray data. Contours range from −8 e/Å^3 (blue) to 10 e/Å^3 (red). A plane which intersects the $Co1O_6$ octahedron and contains the Co1, O1 and O3 atoms is shown together with a sketch of the crystal structure [4].

In favourable cases, such a map already shows interesting features of the (anisotropic) bonding electron density, however, the map can be very significantly improved by taking the coordinates and displacement parameters from the more accurate neutron diffraction experiment (see above for the reasons) and calculate, in a second step, the so called deformation density. This is done by subtracting from the total electron density $\rho(\boldsymbol{r})$ the density $\rho(\boldsymbol{r})_{\text{spherical}}$ corresponding to a superposition of spherical atoms at the nuclear positions. More specifically: atomic positions x_j, y_j, z_j and thermal displacements T_j of atoms j derived from the neutron experiment, 'decorated' with the calculated spherical single atom electron densities.

$\rho(\boldsymbol{r})_{\text{deform}} = \rho(\boldsymbol{r}) - \sum \rho(\boldsymbol{r})_{\text{spherical}}$, where the sum runs over all atoms in the unit cell. (15)

This deformation density represents the deformation of the charge distribution as a result of the formation of chemical bonds:

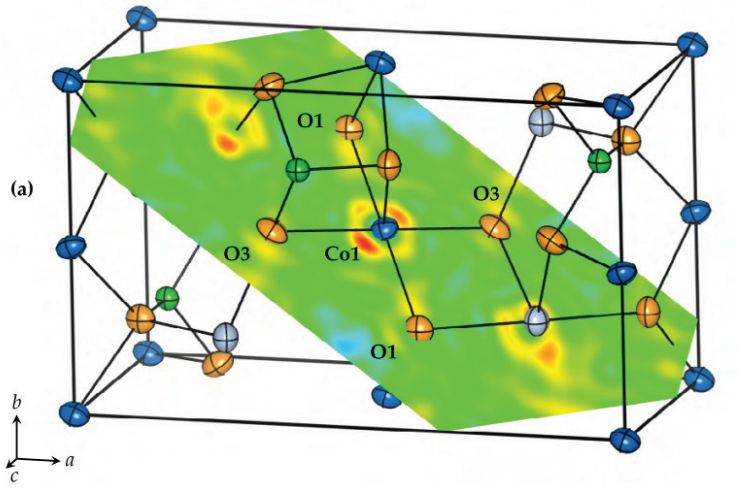

Fig. 16: Deformation density from the X-N-difference Fourier map of Co_2SiO_4 at 300 K: Section through the O1–Co1–O3 plane The difference density varies from −1.25 e/Å^3 (blue) to 1.15 e/Å^3 (red) [4].

7.9 Magnetization density distribution from neutron diffraction: Co_2SiO_4

As a final example for the application of neutron diffraction in structural analysis, we briefly sketch how a 3-dimensional map of the magnetization density, that is: the density of magnetic moments (spin- as well as orbital-moments) within the unit cell can be determined. These maps are sometimes lucidly called 'spin density maps', but in systems with non-vanishing orbital moments, the term magnetization density is really the correct one.

The experiment is performed by polarized neutron diffraction on a single crystal using the flipping ratio method (see 7.2.2). For details on the experimental method see chapters 2 and 6. The flipping ratio method allows to separate nuclear and magnetic contributions to the diffracted intensities. It is performed *above* the magnetic phase transition in the paramagnetic state (in the case of Co_2SiO_4 above T_N=50K) and the sample is in a strong external magnetic field (here: 7 T). 207 Bragg reflection flipping ratios were measured at diffractometer 5C1 of the ORPHÉE reactor (Laboratory Léon Brillouin, CEA Saclay, France) for Co_2SiO_4 at 70K up to sin $\theta/\lambda \approx 0.62$ Å^{-1} at a neutron wavelength of $\lambda = 0.845$ Å. Given the flipping ratios and the nuclear structure factors, the magnetic structure factors can be calculated which are then Fourier transformed to give the spatially resolved magnetization density.

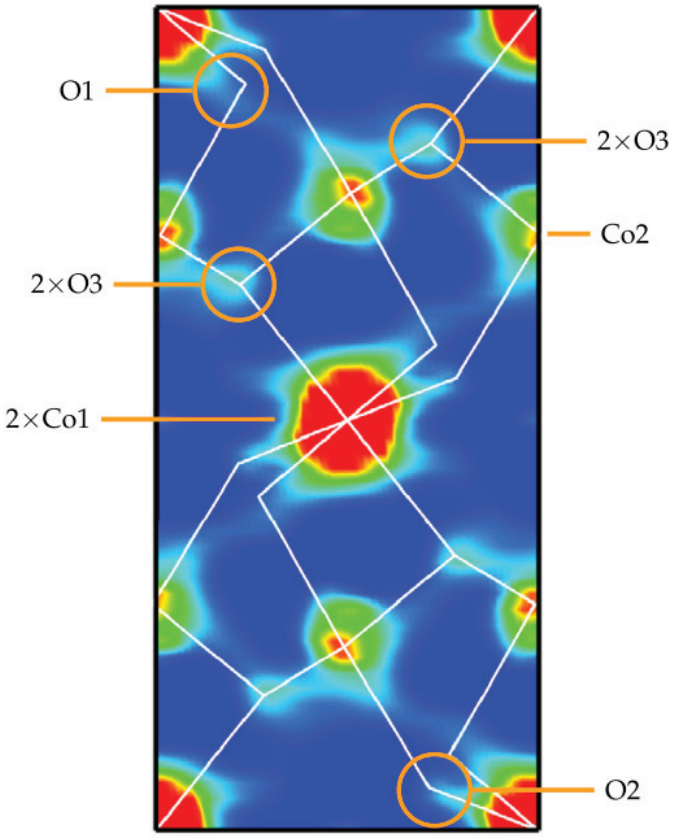

*Fig. 17: Reconstruction of the density (projected along the **b** axis) corresponding to the observed magnetization distribution of Co_2SiO_4 at 70 K with contours ranging from 0 $\mu_B/Å^3$ (blue) to 2 $\mu_B/Å^3$ (red) [4].*

Among the interesting features of this map is the observation of magnetization density on the, nominally non-magnetic, oxygen atoms coordinating the Co^{2+}-ions. These 'transferred moments' are direct experimental evidence for the magnetic exchange interaction along the covalent Co-O-bonds.

References

1. W. Reimers, E. Hellner, W. Treutmann and G. Heger,
J. Phys. C: Solid State Phys. **15**, 3597 (1982).

2. R. J. Nelmes, W. F. Kuhs, C. J. Howard, J. E. Tibballs and T. W. Ryan,
J. Phys. C: Solid State Phys. **18**, L711 (1985).

3. S. Mattauch, G. Heger, and K. H. Michel, Cryst. Res. Technol. **39**, 1027 (2004)

4. A. Sazonov, Ph.D.-thesis, RWTH Aachen (2009)
A. Sazonov et al., Acta Cryst. B65, 664-675 (2009).

Textbooks

- G. E. Bacon, Neutron Diffraction, Clarendon Press, Oxford (1975).
- HERCULES: Neutron and Synchrotron Radiation for Condensed Matter Studies,
Vol. I and II (edited by J. Baruchel, J. L. Hodeau, M. S. Lehmann, J. R. Regnard and
C. Schlenker), Les Editions de Physique, Les Ulis & Springer-Verlag, Berlin (1993-1994).
- L. Dobrzynski and K. Blinowski, Neutrons and Solid State Physics,
Ellis Horwood Series in Physics and its Applications, New York (1994).
- A. Furrer et al.: Neutron Scattering in Condensed Matter Physics,
World Scientific Publ. Comp. (2009).

8

Magnetic and lattice excitations: Inelastic neutron scattering

Jörg Voigt

8 Magnetic and lattice excitations: Inelastic neutron scattering

Jörg Voigt
Institut für Streumethoden, IFF
Forschungszentrum Jülich, 52425 Jülich

Contents

1 Introduction

A structure determination using e.g. neutron or x-ray diffraction yields the equilibrium position of the atoms in a single crystal. The positions can be addressed by the respective unit cell and the atom position within the unit cell. Beside the position of the nuclei, neutron diffraction is the classical method to determine the magnetic structure, i.e. the order unpaired electron spins. While the *static lattice model* can explain many material features, e.g. shapes of single crystals, electronic structure, optical properties ..., it fails, when the properties depend on temperature. Examples include the heat capacity, thermal expansion structural phase transitions including melting or transport properties such as thermal conductivity or sound propagation. All these features are related to the atomic motions, which are described by *lattice dynamics*. We will see, that the crystal symmetry is an important tool to classify the motions, which are due to the forces the atoms exert on each other. For magnetic systems the basic question addresses why and at which temperature ordering appears. The answer requires a detailed knowledge about the interactions between the spins, which determine the magnetic excitations.

Most of our knowledge about dynamics in the solid state stems from investigations of inelastic scattering by a probe. Inelastic neutron scattering is a particular valuable tool, as the neutrons exchange energy in the cold and thermal energy range with the sample. Furthermore it yields not only information about the energy of lattice and magnetic excitations (and hence correlations in time), but also about spatial correlations on the atomic length scale.

2 Scattering

2.1 Kinematics

In a scattering experiment the probe exchanges energy, momentum and possibly angular momentum with the sample. Grace to the conservations laws, the relation between energy and momentum within the studied system can be deduced by analysis of the energy and momentum of the probe particles.

Inelastic scattering Most of the lectures so far concerned the elastic scattering. The Ewald construction has been introduced to explain the Bragg scattering of the static crystal lattice, see Fig 1. Since energy is transferred between the sample and the neutron, the norm of the initial and final wave vector, $\boldsymbol{k}$ and $\boldsymbol{k}'$, are different for inelastic scattering. In that case, the diagram 1a) has to be modified as shown in Fig. 1b). Writing down momentum and energy conservation

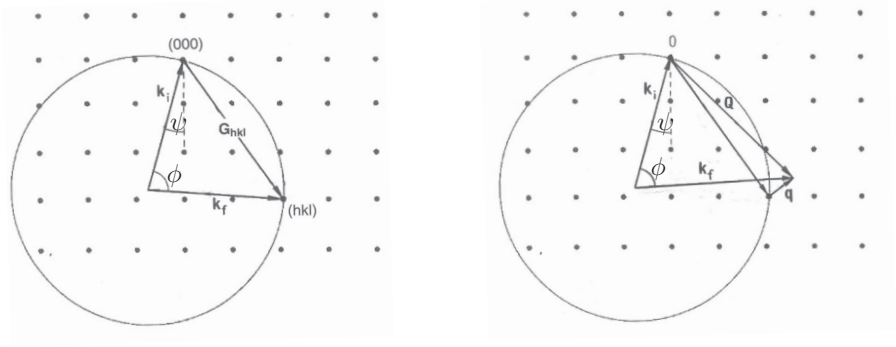

a) b)

Fig. 1: a) Reciprocal space and vector representation for elastic scattering: the $\{100\}$ zone of a simple cubic lattice showing Ewald's construction for Bragg reflection. The number (letters) in brackets denote the Miller indices of the reciprocal lattice vector $\boldsymbol{\tau}$. b) Reciprocal space and vector representation for inelastic scattering: The momentum transferred to the sample is the sum of the reciprocal lattice vector $\boldsymbol{\tau}$ and the momentum transfer $\boldsymbol{q}$ to a phonon within the Brillouin zone around $\boldsymbol{\tau}$.

gives:

$$\boldsymbol{Q} = \boldsymbol{k'} - \boldsymbol{k} \tag{1}$$

$$Q^2 = k^2 + k'^2 - 2kk' \cos\phi \tag{2}$$

$$\hbar\omega = E_i - E_f = \frac{\hbar^2}{2m}(k^2 - k'^2) \tag{3}$$

Combining these equations yields the accessible region in the Q, ω space for a given incident energy E_i, which is limited for neutron scattering (see Fig. 2). The highest accessible energy transfer for a given momentum transfer is given by the cases of forward scattering ($\phi = 0$) and exact backscattering ($\phi = 180$). In a periodic lattice any harmonich deviation from the equilibrium position can be described by a wave vector $-\frac{\pi}{a} < q < \frac{\pi}{a}$, see Fig. 3. Adding a reciprocal lattice vector τ yields a wave that has the same effect at the position of the atoms. Due to the discrete nature of the lattice, the deviations from the equilibrium position can be studied at a momentum transfer

$$\boldsymbol{Q} = \boldsymbol{\tau} + \boldsymbol{q} \tag{4}$$

around any reciprocal lattice vector τ as depicted in Fig. 1b). An acoustic phonon branch has been included in Fig. 2 for several Brillouin zones.

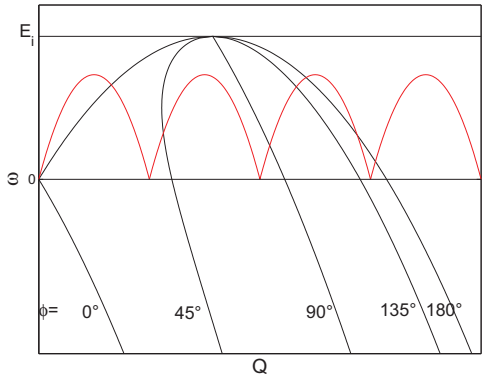

Fig. 2: Relation between norm of the momentum transfer $\hbar Q$ and $\hbar\omega$ for different values of the scattering angle ϕ. The outer contour encloses the accessible Q, ω space. Positive values of ω correspond to energy loss of the neutron. Acoustic phonon branches in several Brillouin zones are shown as well. Note: For small momentum transfer, a phonon cannot be observed, if the sound velocity within the sample is higher than the neutron velocity (the velocities are given by the slope of the respective curves at $Q = 0$).

2.2 The neutron triple axis spectrometer

The most common instrument using Bragg diffraction to prepare and analyse the neutron wavelength is the triple axis spectrometer (TAS). In 1994 the Nobel price has been awarded to its inventor Bertram Brockhouse ”for pioneering contributions to the development of neutron scattering techniques for studies of condensed matter” and in particular ”for the development of neutron spectroscopy”.
The particular instrument name stems from the existence of three axes around which important components of the instrument can be rotated (see Fig. 4). In order to select the desired wavelength according to the Bragg equation, the monochromator as well as the sample table have to

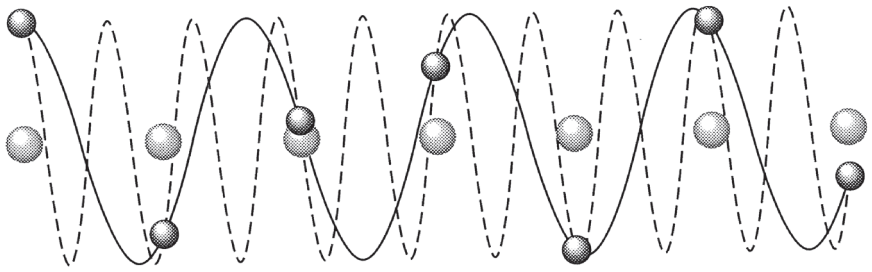

Fig. 3: The atomic motions associated with two waves that have wave vectors that differ by a reciprocal lattice vector. Obviously the two wave have the same effect at the position of the atoms. From [6]

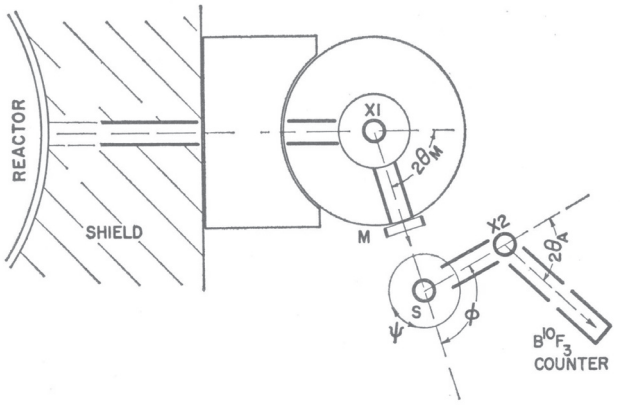

Fig. 4: Schematic of a triple axis spectrometer

be rotated around the first axis in a $\theta - 2\theta$ mode (X1 in Fig. 4). Around the second axis (the sample axis) the analyser/detector unit can be rotated, whereby the sample scattering angle ϕ is selected with respect to the direction of the incoming neutron wave vector $\boldsymbol{k}$. Around the third axis (X2 in Fig. 4), both the analyser crystal and the detector are rotated in a $\theta - 2\theta$ mode in order to probe the wavelength (energy) of the scattered neutrons. An additional rotation around the sample axis (angle ψ) allows to scan any desired path within the reciprocal space plane spanned by $\boldsymbol{k}$ and $\boldsymbol{k'}$.

The resolution of a triple axis instrument depends on the relative sense of rotation at the instrument spectrometer axes, as shown in Fig. 5a). The resolution function of a TAS has been derived analytically by Cooper and Nathans [3] and by Popovici [4]. By an appropriate choice of the scattering geometry, the resolution ellipsoid can be oriented nearly parallel to the dispersion. In that case the folding of the scattering function with the resolution function will be as narrow as possible (cp. Fig 5b)).

2.3 Time-of-flight spectroscopy

The energy of the neutron can also be analyzed by measuring the time-of-flight to determine the neutron velocity. If we know, when the neutron of well defined energy arrives at the sample, we can measure the velocity and hence the energy by measuring the time the neutron takes to travel to the detector at a fixed distance from the sample, see Fig. 6a. In contrast to three axis spectroscopy, the energy can then be determined simultaneously for all scattering angles ϕ. Therefore by covering a large solid angle with detectors, one could measure the complete $\boldsymbol{Q}, \omega$ space very effectively. However, the decoupling of energy and scattering angle comes for a price: one can use only neutrons in a short burst time $\tau < 20\mu$s and has then to wait until all neutrons arrive at the detector to record the full energy spectrum, before the next pulse can

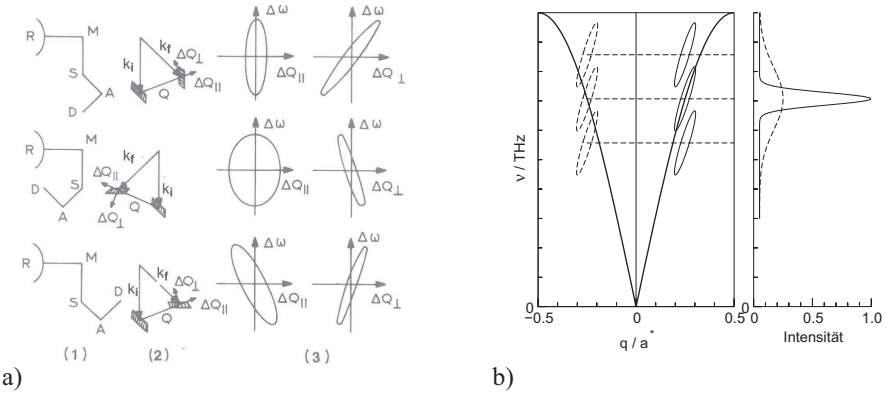

a) b)

Fig. 5: a)Resolution volumes of a TAS in different geometries. From [5]. b) Effect of focusing: If the orientation of the resolution ellipsoid is adopted to the slope of the dispersion, the peak shape of the inelastic signal can be optimized.

start, see Fig. 6b. So for a time-of-flight instrument at a continuous source, one can use the neutron beam during 1-2% of the time. At short pulse spallation sources, all neutron are created in a short pulse. For time-of-flight experiments on can therefore us the full peak flux and gain over constant beam sources a factor ≈ 100, even if the time averaged flux is comparable or lower. The intensity scattered into the solid angle $d\Omega$ defined by the desired $\boldsymbol{Q}$ resolution is still sometimes at the limit of detection. Traditionally time-of-flight spectroscopy is used mainly to study excitations that are not sharply defined in momentum transfer. Then the intensity can be integrated over a larger solid angle. One example is the incoherent one phonon scattering cross section as a measure for the phonon density of states, as it integrates all scattering vectors $\boldsymbol{Q}$ for a given energy ω. Crystalline electric field excitations that depend mainly on the local environment are another typical application for time-of-flight spectroscopy.
With the new Megawatt spallation sources but also with new instruments at reactor sources, as the new TOPAS instrument at the FRM2, the flux limit will be lifted and the full potential of TOF spectroscopy will be available.

3 Lattice excitations

Lattice dynamics describe how atoms can move in the force field due to the bonding in the crystal. Apparently, symmetry will strongly restrict possible motions and is therefore vital to simplify the mathematical description of the problem.
If an atom is displaced from the equilibrium position, the lattice energy is increased. Since in a perfect single crystal the positions of all atoms are correlated, all atoms will respond to the displacement of the special atom. As long as the displacement is small enough, the energy of the displaced system can be described by a harmonic potential, i.e. all atoms are bonded to their neighbors by specific force constants, which depend on the symmetry of the atom position.

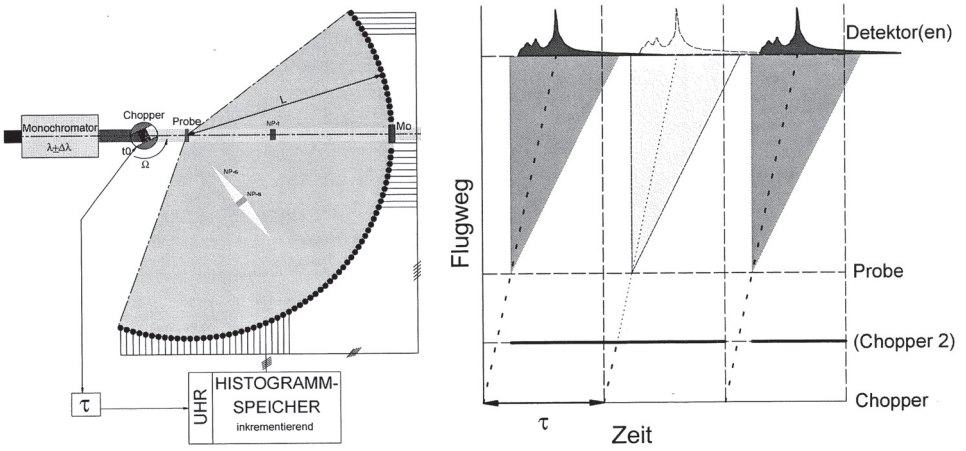

(a) Generic setup of a time-of-flight spectrometer.

(b) Path-time diagram for a configuration with frame overlap choppers

Fig. 6: ToF spectroscopy.

The equation of motion can then be written for the displacement of the atom at position $\mathbf{r}_j$ in direction α:

$$M\ddot{u}_\alpha(\mathbf{r})_j = -\sum_{\beta,\mathbf{r}_{j'}} D_{\alpha,\beta}(\mathbf{r}_j,\mathbf{r}_{j'})u_\beta(\mathbf{r})_{j'}. \tag{5}$$

The force that is exerted onto an atom at $\mathbf{r}_j$, if an atom at $\mathbf{r}_{j'}$ moves away from the equilibrium position in direction β is described by

$$D_{\alpha,\beta}(\mathbf{r}_j,\mathbf{r}_{j'}) = \frac{d^2\Phi(\mathbf{r}_j,\mathbf{r}_{j'})}{du_\alpha(\mathbf{r}_j)du_\beta(\mathbf{r}_{j'})}. \tag{6}$$

Considering the crystalline periodicity, one has to consider only the atoms within one unit cell, which reduces the degrees of freedom to a treatable level of $3N$, where N is the number of atoms in the unit cell. For each of the atoms in the one unit cell one makes a plane wave ansatz for the displacement at time zero:

$$u_\alpha(\mathbf{r}_j) = e_\alpha M^{-1/2} \cdot \exp[i(\mathbf{q}\mathbf{r}_j - \omega_s t)] \tag{7}$$

giving the Eigen-value problem

$$\omega_s^2 e_\alpha = M^{-1}\sum_{\mathbf{r}_j,\beta} D_{\alpha,\beta}(\mathbf{r}_j,0)\exp(-i\mathbf{q}\mathbf{r}_j)e_\beta. \tag{8}$$

with 3 solutions for each $\mathbf{q}$ vector. $\mathbf{e}$ denotes a unit vector, which describes along which direction the atoms are displaced. This property is called the polarization of the displacement. Here we use the fact, that only the distance between to atoms $(\mathbf{r}_j - \mathbf{r}_{j'})$ determines the force constant. If we define the *dynamical matrix*

$$\hat{D}_{\alpha,\beta}(\mathbf{q}) = M^{-1}\sum_{\mathbf{r}_j,\beta} D_{\alpha,\beta}(\mathbf{r}_j,0)\exp(-i\mathbf{q}\mathbf{r}_j), \tag{9}$$

we can re-write Eq. (8) in matrix form:

$$\omega_s(\mathbf{q})^2\mathbf{e} = \hat{D}(\mathbf{q})\mathbf{e} \tag{10}$$

How can we express these mathematical results in a physical picture? The dispersion relation (8), (10) describes the energy that is needed to deform the crystal lattice by a plane wave that is characterized by the propagation vector $\mathbf{q}$. Arbitrary displacements may be expressed as superpositions of plane waves. For any atom in the unit cell one gets 3 possible Eigen-values. While our considerations so far have been completely classical, the atomistic dynamics is determined by quantum mechanics. For the details such derivations we refer to more specialised literature,e.g. [6]. One result we will use throughout the reminder of the lecture, is the concept of phonons. In eq. (7) we have seen, that the displacement in crystals can be described as travelling waves. In analogy to the concept of photons for the electro-magnetic field, the normal modes of lattice vibrations are called phonons with a defined dispersion and polarization $\omega_s(\mathbf{q}), \mathbf{e}(j, \mathbf{q}, \nu)$. The 3 acoustic phonon branches are characterized by the fact, that the respective energy goes to zero, when the propagation vector approaches zero, i.e. when the wavelength of the displacement becomes infinite. The sound velocity in a crystal is equivalent to the phase velocity of the wave for $\mathbf{q} \to 0$. In contrast the branches with a finite energy for vanishing propagation vector are called optical branches. The definition is due to the fact that the dipolar moment in a (partly) ionic crystal oscillate with the displacement.

Neutron scattering by phonons The interaction of the neutron with the nuclei in a sample is comprised by two contributions, giving rise to coherent and incoherent scattering [7]. The former depends on correlations between the position of *one* nucleus at different times and correlations between the positions of different nuclei at different times. It is related to the average nuclear scattering length of the different isotopes of a given atom. The latter probes only the correlations between the positions of the *same* nucleus at different times. It originates from the root mean square deviation of the scattering length for the different isotopes. Since the incoherent scattering probes only a single site, it integrates over all allowed momentum transfers for a given energy. Its intensity is therefore proportional to the phonon density of states. The incoherent nuclear scattering is frequently an annoying background that can be suppressed by isotope pure samples, if the incoherence is due to isotope mixture. Spin incoherent scattering might be separated from the coherent signal by polarization analysis.

Due its good resolution in momentum transfer and energy transfer, the TAS is ideally suited for the measurement of coherent scattering. The coherent scattering function for one phonon

scattering becomes [7]:

$$\left(\frac{\mathrm{d}^2\sigma}{\mathrm{d}\Omega\mathrm{d}\omega}\right)^{\pm}_{\mathrm{coh}} = \frac{k'}{k}\frac{(2\pi)^3}{v_0}\sum_{\boldsymbol{\tau}}\sum_{j,\boldsymbol{q}}$$

$$\cdot|\sum_i \frac{\bar{b}_i}{\sqrt{m_i}}\exp[-W_i(\boldsymbol{Q}) + i\boldsymbol{Q}\cdot\boldsymbol{R_i}](\boldsymbol{Q}\cdot\boldsymbol{e_i^j})|^2 \quad (11)$$

$$\cdot\omega_j^{-1} \quad (12)$$

$$\cdot(n(\omega_j(\boldsymbol{q})) + \frac{1}{2} \pm \frac{1}{2}) \quad (13)$$

$$\cdot\delta(\omega \mp \omega_j(\boldsymbol{q}))\delta(\boldsymbol{Q} \mp \boldsymbol{q} - \boldsymbol{\tau}) \quad (14)$$

Expression 11 is called the dynamical structure factor, in analogy to the structure factor in elastic scattering. It includes the Debye-Waller factor $\exp[-W], W = \langle\boldsymbol{Q}\cdot\boldsymbol{u}\rangle^2$. The intensity is proportional to a factor $|\boldsymbol{Q}\cdot\boldsymbol{e_i^j}|^2$, with the polarization vector of the phonon mode $\boldsymbol{e_i^j}$. This factor has 2 consequences. First, it becomes favorable to measure phonons with large $\boldsymbol{Q}$, because the factor increases quadratically with increasing $|\mathbf{Q}|$. Second, only the component of the displacement along the direction of the momentum transfer is probed. One can imagine, that the neutron excites a phonon with a polarization in the direction of the momentum transfer.
The intensity of a phonon mode depends inversely on its energy (eq. 12). Thus high energy phonons become difficult to measure. Expression 13 describes the occupation of a phonon mode. The $+$ sign refers to a phonon creation, the $-$ sign to annihilation.

$$n(\omega_j(\boldsymbol{q}) = (\exp[\hbar\omega_j(\boldsymbol{q})/k_bT] - 1)^{-1} \quad (15)$$

is the familiar Bose factor. Finally, the expression 14 describes energy and momentum conservation of the scattering process. The coherent cross section is peaked, when the energy and momentum transfer is identical to $\omega_s(\mathbf{q})$ determined by the dispersion relation.
In Fig. 7 (b) the neutron intensity is shown for some example scans at a triple axis spectrometer. For all of this scans, the scattering vector $\mathbf{Q}$ is fixed and the energy transfer is varied by coupled motions of the angles $2\theta_M, \psi, \Phi, 2\theta_A$ in Fig. 4. These type of scans are called constant-Q scans. The other common scan type at a triple axis instrument is a constant-E scan. In that case, the energy transfer is fixed and the momentum transfer is scanned along a arbitrary direction. Usually k' is fixed for inelastic scans, because the reflectivity of the monochromator and the analyzer changes with neutron energy. For the monochromator this effect is accounted for by the monitor that determines the incoming flux on the sample. For a fixed k' the analyzer properties do not change. The peak in the scans gives the information about the $\omega_s(\mathbf{q})$ in the δ functions of double differential cross section (14). One can now follow the phonon branch throughout the Brillouin zone and determine the dispersion relation.

3.1 Bravais lattice

For a simple crystal lattice one may determine the polarization patterns without detailed model calculations. The dispersion of a copper single crystal is shown in Fig. 7b) along the three main

symmetry directions. According to the common use they are labeled Δ for the $[100]$ direction, Σ for the $[011]$ direction and Λ for the $[111]$ direction.
Copper crystallizes in the fcc lattice with one atom per primitive unit cell. Therefore one expects three acoustic branches for a given $\boldsymbol{q}$. However, in Δ and Λ direction appear only two branches. In the Δ direction the transverse polarization means, that the displacement is along the $[010]$ or the $[001]$ direction. In a cubic symmetry these directions are of course equivalent. The respective dispersion branches are degenerate. The same is true for the Λ direction with a three-fold axis of the lattice. The Σ direction is a two-fold axis, the $[0\overline{1}1]$ and the $[100]$ directions are not identical. As a consequence, three distinct dispersion branches exist.
At the X point ($(1\ 0\ 0)$ =$(0\ 1\ 1)$) Δ and Σ branches coincide (cp. Fig 7a)). If we consider the scattering plane spanned by the $[100]$ and $[011]$ direction one cane reach the X point going from $\Gamma(422)$ in Δ direction or from $\Gamma(511)$ in Σ direction. The symmetry determines, which branches coincide: for example the longitudinal mode as seen from $\Gamma(422)$ is transverse as seen from $\Gamma(511)$. The degenerate modes at X join the two degenerate transverse modes along Δ with the longitudinal $[011]$ and transverse $[10\overline{1}]$ mode.
Fig. 7 further shows how to measure the Δ branches. The momentum transfer may be varied along $(4+\xi\ 0\ 0)$ for the study of the longitudinal phonons, whereas one may determine the transverse frequencies in the $(0\ 2\ 2)$ Brillouin zone at $(\xi\ 2\ 2)$.

3.2 Non-Bravais lattice

The NaCl structure is a simple example for a lattice with 2 atoms in the elementary unit cell. It consists of two fcc lattices shifted against each other by $(0.5\ 0.5\ 0.5)$. The entire crystal structure possesses fcc symmetry, too. Only the Σ direction shows the 6 branches expected for a two-atomic structure. The transverse branches in Δ and Λ direction are degenerate because of the fcc symmetry. The longitudinal acoustic and the transverse acoustic branches coincide at the zone boundary, as in the mono-atomic crystal.
The polarization pattern of an optical mode corresponds to an anti-phase axial movement of the ion pairs connected in $[100]$, $[010]$ or $[001]$ direction. The three vibrations polarized in the crystal direction should be degenerate due to the cubic symmetry; one might expect only one optical frequency. The optical vibrations in an ionic lattice posses a polar character, i.e. a local dielectric polarization due to the opposite shifts of cations and anions. For large wavelength, i.e. close to the zone center, the local polarizations add to a macroscopic polarization in the case of the longitudinal mode. This requires an additional energy. Hence the longitudinal optical mode is always higher in energy than the transverse optical as $q \to 0$. This splitting is called Lydane-Sachs-Teller (LST) splitting. It is related by the LST relation to the dieelectrical constant.

3.3 Phonon softening

Changes in the phonon dispersion are hints for structural transitions. As an example we discus a fictive two-dimensional lattice with two atoms in the primitive cell, see Fig 9. In the high

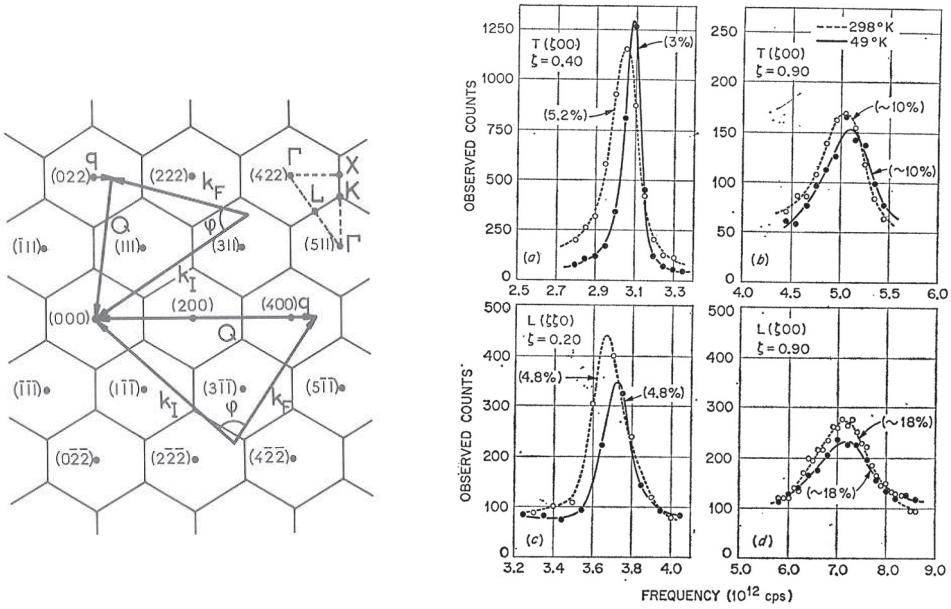

Fig. 7: (a) Reciprocal lattice of the fcc lattice with (hkk) scattering plane. Scattering triangles optimized for transverse (top) and longitudinal (bottom) phonons are inserted. In the top right corner, the directions Δ (Γ to X), Σ (Γ to K to X) and Λ (Γ to L) are indicated. (b) Several typical phonon peaks for copper obtained in constant $\mathbf{Q}$ scans. (c) Dispersion relation of Cu along the main symmetry directions determined by neutron TAS. From [5]

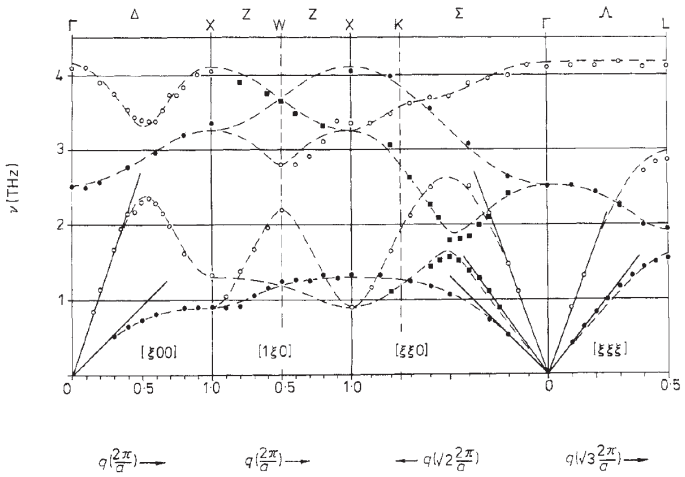

Fig. 8: Phonon dispersion curves in AgBr at 85 K measured by TAS. Open symbols: longitudinal modes. Filled symbols: transverse modes. From [8].

symmetry high temperature phase, the black ion occupies a site with inversion symmetry. This symmetry is broken at the phase transition due to a displacement of the black ion in one lattice direction. The static distortion leads to a splitting of the optical phonon branch at the zone center, since the two directions are not any more equivalent. The phonon frequency of this mode is lowered therefore called a soft mode. The structural instability can also seen in the dispersion quite above T_C: the frequency of the relevant mode at Γ is lower than those of modes with $\boldsymbol{q}$ values in the Brillouin zone. Es an example we show the temperature dependence of a transverse optic mode at the Γ point. Below the transition temperature the mode splits in two branches. The anions are displaced against the cations. When approaching T_C the corresponding phonon frequency vanishes almost completely. The polarization pattern has a strong polar character and is connected to the dieelectric constan through the LST relation. The softening of the TO mode leads finally to a divergence of the dielectric constant and the formation of a ferroelectric polarization below T_C.

In addition to the phonon softening one expects a broadening of the linewidth in frequency, because the life time of the phonon is decreased. Finally the width of a phonon mode may surpass its frequency. Such overdamped modes may no longer be described in the harmonic approximation.

If the unit cell is enlarged by a structural phase transition, e.g. because equivalent atoms in neighboring units cells move to different position, the phonon is softened at the zone boundary.

3.4 Electron-phonon coupling

The lattice dynamics can be drastically changed, if the phonons couple to the charge carriers in a crystal. Since largest effects are expected in the Brillouin zone, inelastic scattering method

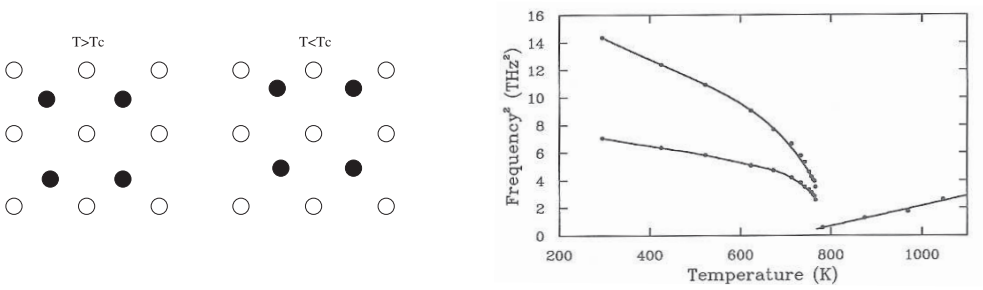

a) b)

Fig. 9: a) Schematic picture of a displacive phase transition occurring at the zone centre. b) Phonon softening above T_C in $PbTiO_3$, below T_c the soft transverse optic mode splits in two branches. The data were taken from Raman spectroscopy below T_C and INS above T_C. From [6]

are most often the method of choice. The screening of the interatomic potentials through free charge carriers is determined by the topology of the Fermi surface. Charge carriers can be scattered by a phonon from one region on the Fermi surface to another. If the momentum transfer connects parallel regions on the Fermi surface, the electron-phonon scattering is increased for that particular value of $\boldsymbol{q}$, which is called the *nesting* vector. The susceptibility will be enhanced for this vector. The respective phonon frequency is renormalized by the electron phonon coupling.

The effect of the renormalization is also seen in the lifetime of a phonon, which is inversely proportional to the width of the lifetime in the energy domain. In a recent experiment this has been investigated for the superconducting phase transition in Pb [9, 10]. The energy resolution in this experiment is only a few μeV. It was achieved by a combination of TAS and neutron resonance spin echo technique [11]. In an spin echo experiment, the spin of the neutron precesses in an magnetic field before the sample (see lecture about neutron spin echo techniques). After the scattering , the neutron passes in an identical but reversed magnetic field and the original spin orientation is restored if the velocity of the spin was not changed. For more details we refer to [11, 10, 9].

In Fig. 10 the phonon width decreases abruptly, when the superconducting gap opens and the phonon energy is smaller than the gap for the given $\mathbf{q}$. The electron phonon scattering is decreased, because the energy transferred from the phonon to the electron is not sufficient to break a Cooper pair. Thus the life time of the phonon is increased.

4 Magnetic excitations

When it comes to investigations of the dynamics in ordered magnetic crystals, inelastic neutron scattering is the unique tool to study the magnetic excitations throughout the whole Brillouin zone. While phonons can nowadays also be measured by inelastic x-ray scattering, no other

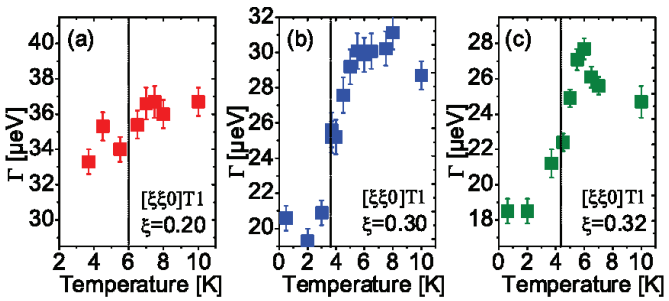

Fig. 10: Temperature dependence of the phonon line width for different ξ along the Σ direction, measured by high resolution TAS. The linewidth is increased, when the phonon energy $\omega(\boldsymbol{q})$ is smaller than the superconducting gap. The solid lines indicate the temperature at which the superconducting gap opens. The gap decreases with increasing temperature. When the gap becomes smaller, also the respective phonon wave vector becomes smaller. Therefore the broadening is shifted to higher temperature for smaller q. From [9]

probe is sensitive to the dispersion of magnetic excitations in bulk materials.

If we consider only the exchange between magnetic ions, the ground state and hence the magnetic structure is defined by the Heisenberg Hamiltonian

$$H = -\sum_{i,j} J_{ij} \boldsymbol{S_i} \boldsymbol{S_j} \tag{16}$$

Therefore by measuring the dispersion one can determine the exchange parameters in a magnetic compound that can give further insight not only in the magnetic properties but also into related features as electronic structure etc..

The double differential cross section takes a similar form as in the case of the coherent 1-phonon scattering:

$$\left(\frac{\mathrm{d}^2\sigma}{\mathrm{d}\Omega \mathrm{d}\omega}\right)^{\pm} = \frac{k'}{k} \cdot S \cdot const \cdot \exp[-2W(\mathbf{Q})] F^2(Q)(1+\tfrac{Q_z^2}{Q^2}) \cdot \tag{17}$$

$$\textstyle\sum_{\tau,\mathbf{q}} (n(\omega_j(\mathbf{q})) + \frac{1}{2} \pm \frac{1}{2}) \delta(\omega \mp \omega_j(\boldsymbol{q})) \delta(\boldsymbol{Q} \mp \boldsymbol{q} - \boldsymbol{\tau}). \tag{18}$$

The conservation of momentum and energy gives again rise to the intensity, when the energy and momentum transfer are equal to dispersion relation of the magnetic excitation. Also the Debye-Waller factor appears again as in the case of phonons. There are also distinct differences: The cross section does not contain the dynamic structure factor, but the spin S affects the intensity. Since the spin distribution is not point-like as the nucleus, the form factor $F(Q)$ leads to a suppression of intensity, when the scattering vector becomes large. Beside the temperature dependence, this fact is often used to distinguish, whether an excitation is magnetic or not: While the intensity is rising with increasing Q for phonon scattering, it vanishes for magnon scattering.

Fig. 11: Schematic picture of a magnon in a ferromagnetic chain. The magnon possesses the spin $\frac{1}{2}$ as if one spin would be flipped.

4.1 Ferromagnet

In a ferro-magnetically ordered crystal the ground state is defined by the parallel alignment of all spins, as this is the lowest energy of the Hamiltonian for a positive exchange constant J. Now the neutron that possesses a spin can interact with the magnetic field created by the spins in the sample. Intuitively one would expect, that the first excitation in a ferromagnet is realized by the flip of a single spin. However, such a state is not an Eigenstate of the Heisenberg Hamiltonian. For a ferromagnetic linear chain, the Eigenstate can be written as a spin wave

$$|q,\omega\rangle = N^{-\frac{1}{2}} \sum_j e^{i(\boldsymbol{qR_j}-\omega t)} |... \uparrow\uparrow\uparrow \nearrow_j \uparrow\uparrow ...\rangle. \tag{19}$$

This state is sketched in Fig. 11. In total the spin of the chain is reduced by 1 μ_B, but the change is distributed over all magnetic lattice sites. This quantized excitation by one μ_B is called a magnon. The dispersion relation for a ferromagnetic linear chain with spacing a is given as:

$$\hbar\omega(q) = 4JS(1-\cos qa) \tag{20}$$

For small q this can be approximated to $\hbar\omega = 2JS(qa)^2$, in contrast to an acoustic phonon, which disperses linearly. The measurement of the dispersion relation allows the determination of the exchange constant. As an example I present the magnon dispersion in the ferromagnetic Rare Earth elements Gd and Tb in Fig 12. The crystal structure is hexagonal closed packed. We see, that the quadratic dispersion close to the Γ point is a general feature of a ferromagnetic structure.

At the Γ point, the frequency does not vanish as one would expect from eq. 20. In the Heisenberg Hamiltonian eq. 16 we did not take into account further contribution besides the exchange between spins. Therefore a common rotation of all spins, that would be described by an infinite wavelength or a vanishing wave vector, wouldn't cost any energy, in analogy to the long wavelength limit of an acoustic phonon. But if a crystalline anisotropy is present, a finite energy is necessary to rotate all spins. This energy is seen as the gap in the dispersion. Apparently the anisotropy is stronger in Tb than in Gd. Gd has a half-filled $4f$ shell. According to Hund's rule, the orbital momentum vanishes and hence the electron density, which creates the anisotropy, is isotropic.

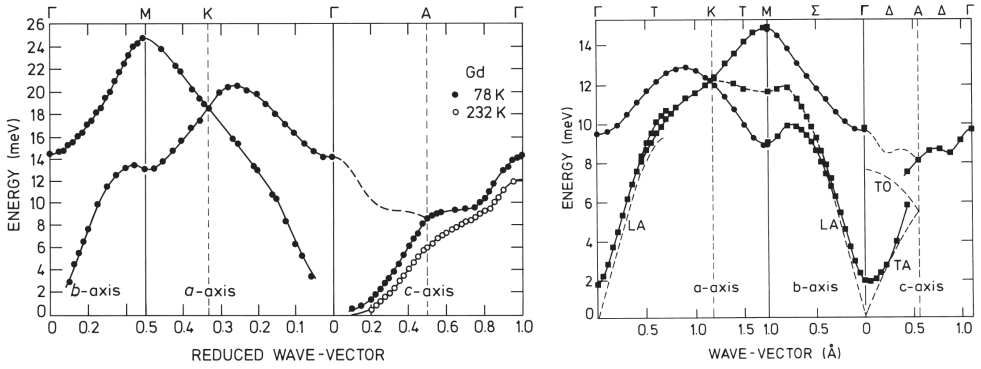

Fig. 12: Magnon dispersion in FM Gd measured at 78 K and in FM Tb at 4 K measured by TAS. From [12]

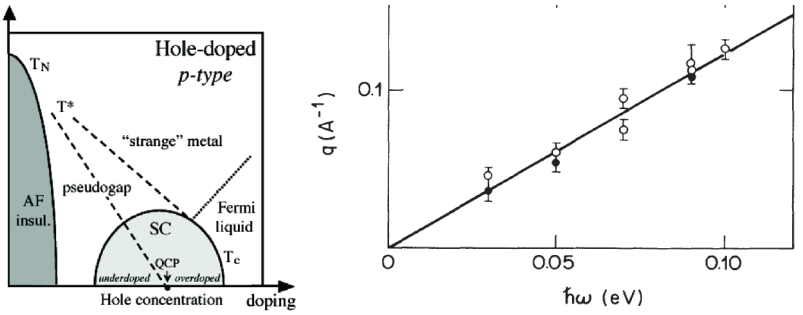

Fig. 13: left) Generic phase diagram of the high temperature superconductors as a function of temperature and hole doping. right) Spin wave dispersion in AF La_2CuO_4 measured with INS. The high spin wave stiffness $\frac{\hbar\omega}{q}$ relates to strong AF coupling $J \approx 160meV$. From [13]

4.2 Antiferromagnet

Antiferromagnetic order results from a negative exchange integral J in eq. 16 The antiparallel alignment of neighboring spins leads to a magnetic unit cell, which is larger than the nuclear one. The dispersion for a antiferromagnetic magnon of a linear spin chain can be expressed as:

$$\hbar\omega(q) = -4JS|\sin(qa)| \tag{21}$$

Fig. 13 shows the dispersion in La_2CuO_4, a antiferromagnetic parent compound of high T_C superconductors. The material becomes superconducting, when charge carriers are doped into it. In an intermediate doping range, a spin glass state appears, until at higher doping the so called superconducting dome appears. Also in the superconducting state antiferromagnetic correlations persist.
The spin wave stiffness $\frac{\hbar\omega}{q}$ is very high. The exchange integral J can be estimated to 135 meV. One can clearly see, that the dispersion remains linear throughout the whole energy range.

The role of the antiferromagnetic correlations, that are still present in the doped superconducting compounds, is still controversially debated. So called kinks in the electronic dispersion have been attributed to either electron phonon or electron magnon coupling. It is clear, that any theory explaining high T_C superconductivity must also take into account the unconventional antiferromagnetic correlations.

4.3 Crystal field excitations

If a magnetic ion is placed in a crystal lattice, the *crystalline electric field* created by the surrounding ions will lift the degeneracy of the free ion ground state, in which the energy depends only on the total angular momentum J and hence the degeneracy is $(2J + 1)$ fold. One can imagine that the strongly anisotropic charge distributions in $3d$ and $4f$ elements have different energies, if they point e.g. to a positive or a negative charge in the crystal lattice. In the case of the $3d$ elements the energy splitting amounts to several eV, because the modest localization gives a large overlap with the orbitals of the surrounding ions. These excitations are usually to high in energy to be investigated by inelastic neutron scattering. The stronger localization of the $4f$ electrons in the rare earth leads to typical energies below 100 meV, which is perfectly suited for the scattering of thermal and cold neutrons. The crystal field splitting is a purely local effect. As long as it is not modified by other interactions, it gives therefore rise to a dispersion less excitation. Time-of-flight methods using polycrystalline sample are the traditional way to establish the crystalline electric field level scheme. The crystal field levels are classified according to the irreducible representations of the site symmetry of the magnetic ion. As an example the level scheme and magnetic excitation spectra of $Yb_{0.9}Er_{0.1}B_{12}$ are shown in Fig. 14. The intensities of the respective lines are mainly determined by the transition probabilities $\Gamma_i \rightarrow \Gamma_j$. The analysis may be used to refine the crystal field parameters, which largely determine the anisotropy in a rare earth system.

5 Concluding remarks

Inelastic scattering of neutrons is an almost unique technique to observe lattice vibrations and magnetic excitations throughout the whole Brillouin zone. Subjects of present interest like high T_C superconductivity, heavy fermions, quasi crystals or frustrated systems demand a detailed analysis of their vibrational dynamics as well as of their magnetism. The increased complexity of novel materials requires therefore a continuous development of the experimental facilities as well as of the analysis methods. Novel functionalities often arise, when different degrees of freedom start to couple. A prominent example is the metal-insulator transition in the colossal-magneto resistance Manganites, where the coupling of ferromagnetic order and charge order leads to magnetic control of the electrical properties. These coupling affects the dynamics either by shifts in energy or by broadening that is due to competing interactions.
Recent developments of time-of-flight techniques, particularly at the new spallation sources,

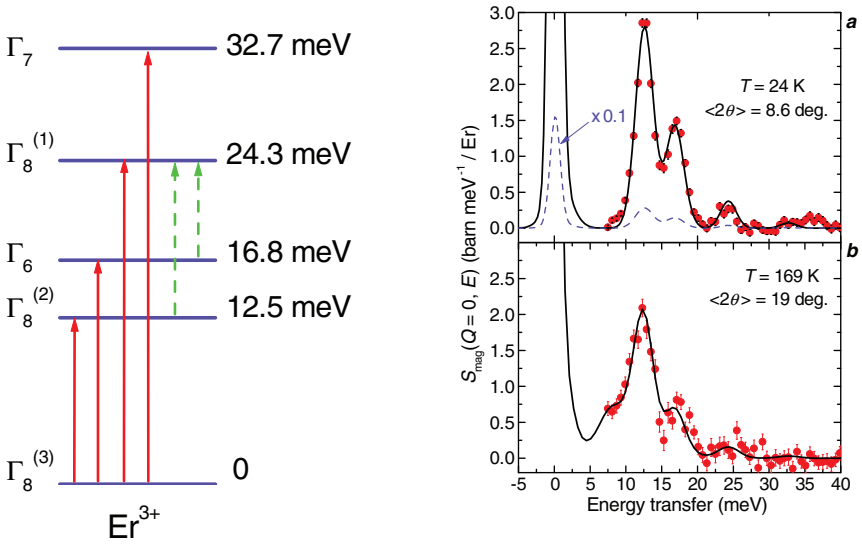

Fig. 14: CEF level scheme and magnetic excitation spectra of the Er^{3+} sites in $Yb_{0.9}Er_{0.1}B_{12}$. From [14]

.

but also at the FRM2 in Munich, aim for a fast mapping of the 4D dispersion landscape. Such instruments become feasible, because the neutron sources and optic systems lower the flux limitations and allow a pixelized data acquisition that covers the full $\boldsymbol{Q}, \omega$ space simultaneously. New TAS instruments are build, which analyse not a single final wave vector, but cover immediately a wide range in $\boldsymbol{k}'$. Both developments require a new generation of data analysis and visualization tools, for human beings finding their way in the reciprocal universe.

References

[1] Léon Van Hove. *Phys. Rev.*, 95(1):249–262, Jul 1954.

[2] Gen Shirane, Stephen M. Shapiro, and John M. Tranquada. *Neutron scattering with a triple axis spectrometer*. Cambridge University Press, Cambridge, 2002.

[3] M. J. Cooper and R. Nathans. *Act. Cryst.*, 23:357, 1967.

[4] M. Popovici. *Act. cryst. A*, 31(JUL1):507 – 513, 1975.

[5] B. Dorner. *Coherent Inelastic Neutron Scattering in Lattice Dynamics*. Springer-Verlag, Berlin, Heidelberg, New York, 1982.

[6] M. T. Dove. *Introduction to lattice dynamics*. Cambridge university press, Cambridge, 1993.

[7] G. l. Squires. *Introduction to the theory of thermal neutron scattering*. Cambridge university press, Cambridge, 1978.

[8] B Dorner, W von der Osten, and W Buhrer. *Jour. Phys. C: Solid State Physics*, 9(5):723–732, 1976.

[9] T. Keller, P. Aynajian, K. Habicht, L. Boeri, S. K. Bose, and B. Keimer. *Phys. Rev. Lett.*, 96(22):225501, 2006.

[10] K. Habicht, R. Golub, F. Mezei, B. Keimer, and T. Keller. *Phys. Rev. B (Condensed Matter and Materials Physics)*, 69(10):104301, 2004.

[11] R. Golub and R. Gahler. *Physics Letters A*, 123:43–48, July 1987.

[12] Jens Jensen and Allan R. MacKintosh. *Rare Earth Magnetism*. Clarendon Press, Oxford, 1991.

[13] G. Aeppli, S. M. Hayden, H. A. Mook, Z. Fisk, S.-W. Cheong, D. Rytz, J. P. Remeika, G. P. Espinosa, and A. S. Cooper. *Phys. Rev. Lett.*, 62(17):2052–2055, Apr 1989.

[14] P A Alekseev, J-M Mignot, K S Nemkovski, E V Nefeodova, N Yu Shitsevalova, Yu B Paderno, R I Bewley, R S Eccleston, E S Clementyev, V N Lazukov, I P Sadikov, and N N Tiden. *Jour. Phys.: Condensed Matter*, 16(15):2631, 2004.

9

Macromolecules and Self Assembly

Henrich Frielinghaus

9. Macromolecules and Self Assembly

Henrich Frielinghaus

9.1 Introduction

The method small angle neutron scattering (SANS) is widely used in the fields of conventional solid state physics, but more intensively in the field of soft matter research. This field embraces polymer melts, solutions, and rubbers, but also complex fluids such as microemulsions, colloidal dispersions, and micellar solutions. The complex fluids often also contain polymers, i.e. macromolecules. Finally the neighborhood to biological systems brings biophysical subjects close to neutron scattering techniques.

The typical length scale of a SANS experiment lies in the range of 1 to 100 nanometers (or 10 to 1000 Angstroems). The developments of ultra SANS enlarged the spatial region to 10 to 100μm. While the scattering techniques observe structures in the reciprocal space, all these length scales are also covered by microscopy techniques (transmission electron microscopy (TEM) and light microscopy). Advantages of SANS experiments will be made clear.

In the following some important properties of polymers shall be introduced and discussed. Then polymer blends and melts will be introduced connected with their typical scattering pattern. Finally, microemulsions are an interesting system where amphiphilic polymers can be added. These polymers modify the phase behaviour and the microscopic structure, which is studied by SANS experiments.

9.2 Homopolymers

Homopolymers are long linear chain molecules consisting of a single repeat unit, the monomer. While there is a local rigidity and a non-vanishing angular correlation of single carbon-carbon bonds, effective longer chain segments can be defined. The Kuhn segment embraces so many monomers that the angular correlation of these effective segments is lost. In the following we assume the polymer physics we want to describe take place on length scales larger than the Kuhn segment length ℓ_K. Especially, the polymer itself is large compared to the single Kuhn element, of which it contains N_K ($\gg 1$) segments. One important observable of a single polymer is the end-to-end distance, which simply is defined as:

$$\mathbf{R}_{ee} = \sum_{i=1}^{N_K} \mathbf{r}_i \tag{9.1}$$

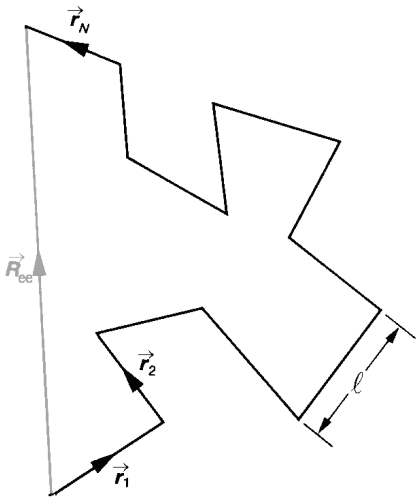

Figure 9.1: Schematic drawing of a chain with independent chain segments. The vectors $\mathbf{r}_i$ specify the individual segments. The segment length is ℓ_K. The end-to-end vector $\mathbf{R}_{ee}$ is a measure for the size of the polymer.

The statistical average of this observable is simply zero, since each segment does not have a preferred orientation ($\langle \mathbf{r}_i \rangle = 0$), and so the whole polymer does not show a preference either. The next higher order moment of this observable is the second moment. We simply can arrange the square of a sum by:

$$\left\langle \mathbf{R}_{ee}^2 \right\rangle = \sum_{i,j=1}^{N_K} \left\langle \mathbf{r}_i \cdot \mathbf{r}_j \right\rangle = \sum_{i=1}^{N_K} \left\langle \mathbf{r}_i^2 \right\rangle + 2 \cdot \sum_{1 \le i < j \le N_K} \left\langle \mathbf{r}_i \cdot \vec{\mathbf{r}}_j \right\rangle \tag{9.2}$$

The diagonal terms appear N_K times and represent the length of a single Kuhn segment ℓ_K^2. The off-diagonal terms would contribute if angular correlations were present. According to our assumptions this is not the case, and we finally obtain:

$$\left\langle \mathbf{R}_{ee}^2 \right\rangle = N_K \cdot \ell_K^2 \quad \text{or:} \quad R_{ee} \equiv \sqrt{\left\langle \mathbf{R}_{ee}^2 \right\rangle} = \sqrt{N_K} \cdot \ell_K \tag{9.3}$$

The radius of gyration is a similar measure for the size of the polymer, which is defined like the moment of inertia normalized to the total mass:

$$\left\langle \mathbf{R}_g^2 \right\rangle = \frac{1}{N_K + 1} \cdot \sum_{i=0}^{N_K} \left\langle \mathbf{s}_i^2 \right\rangle \tag{9.4}$$

The single vectors $\mathbf{s}_i$ specify the distance of a single segment from the centre of mass. It can be shown (as article C1 in reference 4) that the two typical sizes of a polymer are proportional for our assumptions ($N_K \gg 1$):

$$R_g \equiv \sqrt{\left\langle \mathbf{R}_g^2 \right\rangle} = \sqrt{\tfrac{1}{6} N_K} \cdot \ell_K = \sqrt{\tfrac{1}{6}} \cdot R_{ee} \tag{9.5}$$

In this sense, a polymer with negligible segment rigidity has only one length scale, given by either R_g or R_{ee}. This typical size of the polymer is proportional to the length of a single Kuhn length ℓ_K and the square root of the segment number N_K. In practical equations, often some effective monomer length ℓ_{mon} and the real degree of polymerization N, which is the monomer number in a polymer, are used. For relatively rigid chains the monomer length can be larger than the real geometric length, since the equations hold for sizes on the polymer length scale.

9.3 Scattering of homopolymers

We now consider the scattering of a solution of homopolymers without interactions. The macroscopic scattering cross section dΣ/dΩ as a function of the scattering vector $\mathbf{Q}$ is defined rigorously as the squared amplitude of the individual phases of all atoms in the whole macroscopic volume V, and thus:

$$\frac{d\Sigma}{d\Omega}(\mathbf{Q}) = \frac{1}{V} \cdot \left| \sum_j b_j \exp\left(i \mathbf{Q}_j \mathbf{R}_j\right) \right|^2 \tag{9.6}$$

The scattering length b_j determines the amplitude of the outgoing wave from a single atom j. with the position $\mathbf{R}_j$. The symbol i is now the imaginary unit. This elementary formula can be expressed in a handier way:

$$\frac{d\Sigma}{d\Omega}(\mathbf{Q}) = I_{coh}(\mathbf{Q}) = (\Delta\rho)^2 \cdot \phi \cdot \frac{v_K}{N_K} \cdot \left| \sum_j \exp\left(i\mathbf{Q}\mathbf{R}_j\right) \right|^2 = (\Delta\rho)^2 \cdot \phi \cdot \frac{1}{V_{pol}} \cdot \left| \int_{pol} \exp\left(i\mathbf{Q}\mathbf{R}\right) d^3R \right|^2 \tag{9.6}$$

The first assumption is, that we take all monomers of a Kuhn segment as one unit. This unit has a total volume v_K, and so a scattering length density can be defined $\rho_{pol} = (\sum b_j) / v_K$ being a measure of the polymer. In the same way one obtains the scattering length density of the solvent ρ_{sol}. The contrast, i.e. the scattering length density difference, appears when the sum focuses on the solute only. A remaining term considering the solvent as a homogenous matrix results in a delta function $\delta(\mathbf{Q})$, which does not contain information for the typical scattering experiment, and thus is neglected. The concentration ϕ is the volume fraction of the

polymer in solution. It is proportional to the number of polymers, and thus the individual sum in eq. 9.6 over index *j* considers a single homopolymer only. All homopolymers contribute to the scattering independently without interference, which is true for dilute solutions. The second part of eq. 9.6 considers the polymer to be a worm with a finite volume, over which the integration is conducted. The new prefactor contains the volume $V_{\mathrm{pol}} = v_{\mathrm{K}} \cdot N_{\mathrm{K}}$ of a single polymer. It is important to repeat, that we consider length scales above the Kuhn segment length, and atomic structures within the large molecule are neglected.

The chain statistics we have developed for homopolymers will be applied to this final scattering formula (eq. 9.6) now. For the scattering function $S(\mathbf{Q})$, i.e. the structure factor, we obtain now:

$$\begin{aligned} S(\mathbf{Q}) &= \frac{v_K}{N_K} \cdot \left\langle \left| \sum_j \exp\left(i\mathbf{Q}\mathbf{R}_j\right) \right|^2 \right\rangle \\ &= \frac{v_K}{N_K} \cdot \left\langle \sum_{j,k} \exp\left(i\mathbf{Q}(\mathbf{R}_j - \mathbf{R}_k)\right) \right\rangle \\ &= \frac{v_K}{N_K} \cdot \left(\sum_{j,k} 1 + \left\langle \sum_{j,k} i\mathbf{Q}(\mathbf{R}_j - \mathbf{R}_k) \right\rangle + \frac{1}{2} \left\langle \sum_{j,k} \left(i\mathbf{Q}(\mathbf{R}_j - \mathbf{R}_k)\right)^2 \right\rangle + \ldots \right) \end{aligned} \tag{9.7}$$

The vectors $\mathbf{R}_j$ specify the position of a segment relative to a fixed origin (contrary to $\mathbf{r}_i$ which is an individual segment vector). In the first transformation the complex conjugate was explicitly used, and all addends were combined in every possible form. The next transformation uses the Taylor expansion of the exponential function. The linear term has an expected value of zero, since again a first order momentum appears. So the quadratic term determines the *Q*-dependence of the structure factor, and one expresses the expansion as an exponential again:

$$S(\mathbf{Q}) = \frac{v_K}{N_K} \cdot \sum_{j,k} \exp\left\langle -\tfrac{1}{2}\left(\mathbf{Q}(\mathbf{R}_j - \mathbf{R}_k)\right)^2 \right\rangle \tag{9.8}$$

For independent chain segments - as we assumed anyhow - it can be shown, that all higher order terms of eq. 9.7 contribute consistently to the final expression of eq. 9.8. The averaging is carried out inside the exponential now, which simplifies the calculation strongly. For a random orientation relatively to the scattering vector *Q*, one obtains:

$$S(\mathbf{Q}) = \frac{v_K}{N_K} \cdot \sum_{j,k} \exp\left(-\tfrac{1}{6}\mathbf{Q}^2 \left\langle (\mathbf{R}_j - \mathbf{R}_k)^2 \right\rangle\right) \tag{9.9}$$

The inner term $(\mathbf{R}_j - \mathbf{R}_k)^2$ specifies a chain part with $|j - k|$ segments. This chain part behaves like an ideal chain, and so its average length follows the formula of eq. 9.3.

Furthermore, it is helpful to express the sum as integrals, which is a good approximation on larger length scales. So one obtains:

$$\begin{aligned} S(\mathbf{Q}) &= \frac{v_K}{N_K} \cdot \int_0^{N_K} dj \cdot \int_0^{N_K} dk \cdot \exp\left(-\tfrac{1}{6}\mathbf{Q}^2 |j-k| \ell_K^2\right) \\ &= V_{pol} \cdot f_D(\mathbf{Q}^2 R_g^2) \\ f_D(x) &= \frac{2}{x^2}\left(\exp(-x) - 1 + x\right) \end{aligned} \tag{9.10}$$

The Debye function $f_D(\mathbf{Q}^2 R_g^2)$ (see Fig. 9.2) is a monotonously decaying function with the maximum at $\mathbf{Q} = 0$. There are two important limits of the structure factor. For small scattering vectors a Taylor series yields the Zimm approximation:

$$S^{-1}(\mathbf{Q}) = V_{pol}^{-1}(1 + \tfrac{1}{3}\mathbf{Q}^2 R_g^2) \tag{9.11}$$

The extrapolated forward scattering $S^{-1}(\mathbf{Q}\to 0)$ is a measure for the single polymer volume. Of course, as described by eq. 9.6, the scattering contrast $(\Delta\rho)^2$ and the concentration ϕ have to be known beforehand. The slope of a Zimm-plot tells about the typical polymer size, i.e. the radius of gyration. At larger scattering angles (the considered length scales are still large compared to the segmental size $|\mathbf{Q}|^{-1} \gg \ell_K$) another important scattering behaviour is obtained:

$$S(\mathbf{Q}) = 2 \cdot V_{pol} / (\mathbf{Q}^2 R_g^2) \tag{9.12}$$

Here the self similarity of a chain becomes dominant. On these intermediate scales chain parts still look like perfect chains. The corresponding fractal dimension of ideal chains is 2.

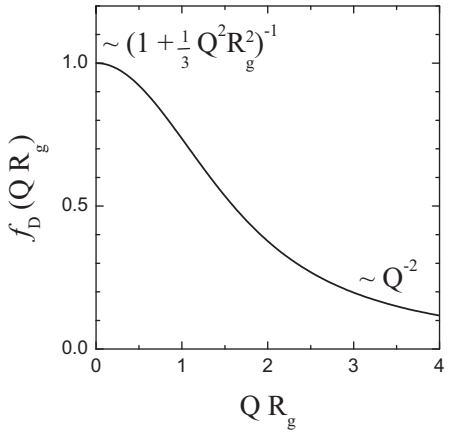

Figure 9.2: The Debye-Function as a function of the scaled scattering vector. Two important limits are given for small and large scattering vectors.

9.4 Scattering of Homopolymer Blends

The formula 9.10 was derived for dilute homopolymers in soultion without interactions. When describing homopolymer blends of two homopolymers, the assumptions of dilution and of negligible interactions do not hold anymore. The concept of the random phase approximation (RPA) bases on the undisturbed chain structure factor (eq. 9.10) and introduces high concentrations and interactions afterwards. Since this short lecture cannot go into details, we simply present the final expression of the RPA:

$$S_{RPA}^{-1}(\mathbf{Q}) = \Delta\rho^2 / \frac{d\Sigma}{d\Omega}(\mathbf{Q}) = \left(\phi_{pol1} V_{pol1} f_D(\mathbf{Q}^2 R_{g1}^2)\right)^{-1} + \left(\phi_{pol2} V_{pol2} f_D(\mathbf{Q}^2 R_{g2}^2)\right)^{-1} + \Gamma \qquad (9.13)$$

The reciprocal structure factor of a homopolymer blend is the sum of the reciprocal structure factors of the undisturbed homopolymers plus the Flory-Huggins interaction parameter Γ. In the limit of identical homopolymers (for instance a blend of protonated and deuterated polymers) and negligible interactions basically the undisturbed chain structure factor is obtained. An example of a real polymer blend is depicted in Fig. 9.3. The basic properties of the Debye function are preserved, but of course the Flory-Huggins interaction parameter is obtained by the detailed analysis. The scattering at small scattering vectors is maximal, which means that on large length scales the thermal composition fluctuations are maximal. The extrapolated forward scattering $S(\mathbf{Q}=0)$ is the reciprocal susceptibility. The peak width is connected with the correlation length ξ telling over which distance the local composition can be assumed constant. At high temperatures $S(0)$ and ξ are small which is connected with a small or even negative interaction parameter Γ. When the interaction parameter comes close to the critical value $\Gamma = 2/V_{\mathrm{pol}}$ the fluctuations become infinitely large, and $S(0)$ and ξ diverge. At this moment the concept of the RPA breaks down, and the system behaves like a 3d-Ising system. This means that the point of criticality is shifted to slightly lower temperatures compared to the RPA estimation. The temperature shift is proportional to the Ginzburg number, which is a measure how strongly fluctuations influence the thermo-dynamics of the system [7].

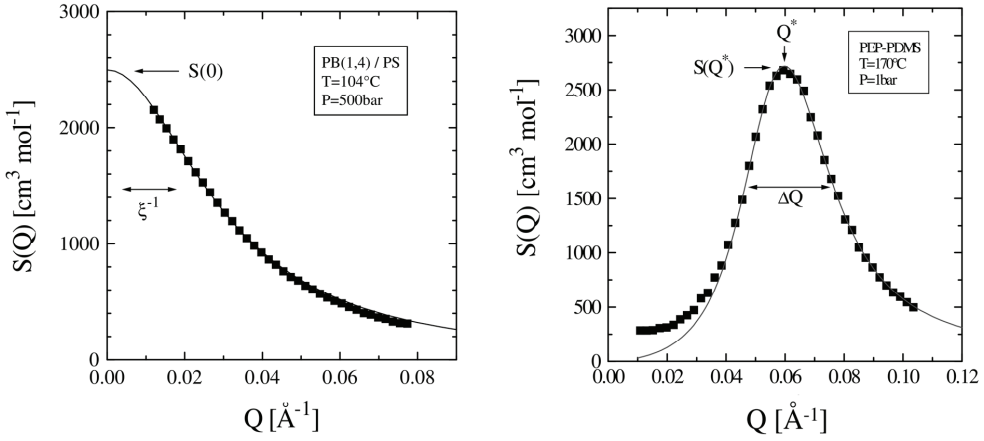

Figure 9.3: The scattering function $S(\mathbf{Q})$ as a function of the scattering vector. On the left the typical scattering of a homopolymer is shown. The sample is a polybutadiene(1,4) / polystyrene blend at 104°C and 500bar. On the right the typical scattering of a diblock copolymer is shown which is a poly-ethylene-propylene-poly-dimethylsiloxane at 170°C and 1bar.

9.4 Scattering of Diblock Copolymers

Diblock copolymers are chainlike molecules with two different kinds of monomers which are placed along the molecule at two different blocks. The RPA is capable to describe the scattering of diblock copolymers at high temperatures. The combination of Debye functions is just slightly more complex as in eq. 9.13, but the interaction parameter is added in the same way [8]. So we simply look on the scattering pattern of a diblock copolymer in Fig. 9.3. At small scattering vectors the ideal intensity vanishes at $\mathbf{Q} = 0$ and increases like $\mathbf{Q}^2$, which is due to the chemical connectivity of the two blocks. Fluctuations on large length scales ideally are impossible. Polydispersity of the block length ratio leads to some finite intensity at $\mathbf{Q} = 0$. At large scattering vectors mainly chain parts are observed, and the connectivity of the blocks does not play a role anymore. Thus the same $\mathbf{Q}^{-2}$ behaviour as for homopolymers is observed. At the intermediate $|\mathbf{Q}^*|$ the pronounced intensity maximum indicates strong fluctuations on length scales $2\pi/|\mathbf{Q}^*|$ similar to the radius of gyration. The peak width again is connected with the reciprocal correlation length, and the maximal intensity is the reciprocal susceptibility. When the temperatures are lowered the fluctuations become much stronger as for homopolymers, and deviations from the RPA concept become much more prominent. The corresponding Ginzburg numbers are much larger.

9.5 Scattering of Homopolymer / Diblock Copolymer blends

For mixtures of A and B homopolymers with an AB diblock copolymer (here polybutadiene and polystyrene) the scattering patterns of the two different systems compete [9]. For small diblock copolymer contents the strong scattering occurs at small scattering angles, while for larger diblock copolymer contents the strong scattering occurs at a finite scattering vector |**Q***|. For intermediate diblock copolymer contents there appears a wide plateau of strong scattering intensity ranging from zero to finite scatting angles. This high temperature phase is interesting by itself to study the critical behaviour of these extremely strong fluctuations.

At lower temperatures a phase separation occurs. While for the homopolymer-like systems with **Q*** = 0 a phase separation takes place on macroscopic length scales (macrophase separation), for the diblock-like systems with finite **Q*** the phase separation leads to ordered structures (microphase separation). For the intermediate diblock copolymer contents discussed here the system forms a bicontinuous phase structure. This means that the A-rich phase forms a sponge-like structure with space for the B-rich phase. Each of the phases is continuously connected. The diblock copolymer acts as a surfactant and thus inhibits the macrophase separation.

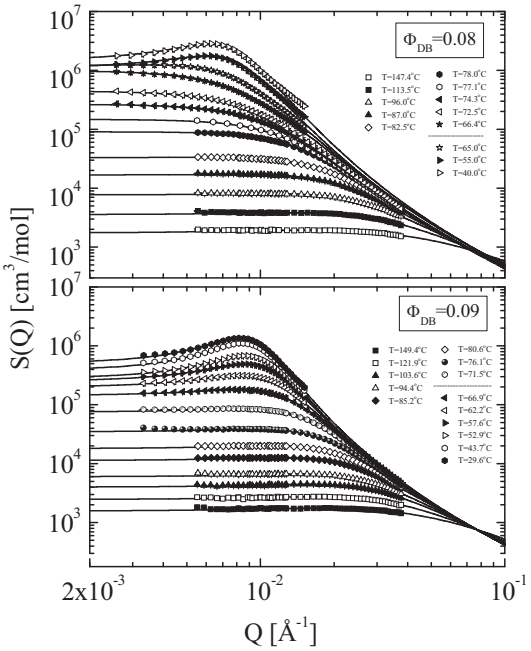

Fig. 9.4: The scattering function of an A/B/AB homopolymer / diblock copolymer blend. At higher temperatures the scattering is less intense, the plateau at small scattering angles is quite broad. At lower temperatures there is a phase transition to the microemulsion phase where a correlation peak appears.

The tailoring of homopolymer domains by small amounts of additives (here: diblock copolymers) is an interesting field of the current research. These systems resemble microemulsions since the mediating component has an A-philic and a B-philic segment. Some systems mimic the microemulsions better others worse. The still open mayor issue is to replace the costly diblock copolymers by less expensive polymers.

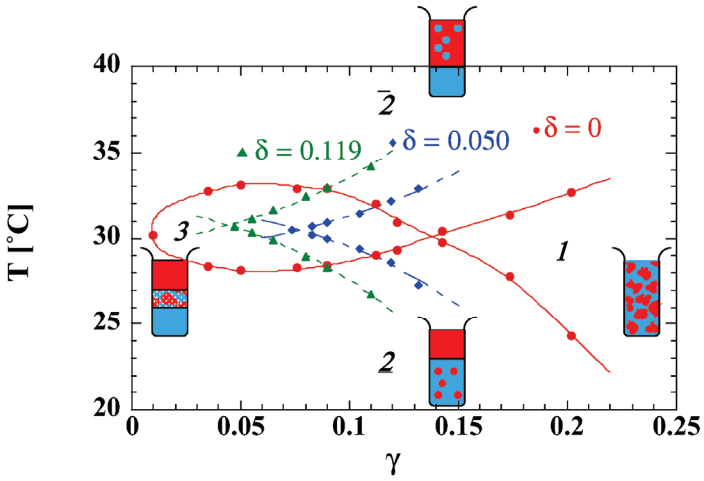

Figure 9.5: A typical fish-phase-diagram (red curve): temperature versus surfactant content for a symmetric water to oil ratio. At high surfactant contents a one-phase microemulsion (1) is observed, while for lower surfactant contents the three-phase coexistance (2) with a microemulsion phase, an excess oil and an excess water phase is found. At low and high temperatures (2 and $\bar{2}$) a two-phase coexistance occurs with excess oil or water phases. When adding aphiphilic diblock copolymers (δ measures the polymer content with respect to the amphiphile) the fish-tail moves to lower surfactant contents. The minimum amount of surfactant of the one-phase region is given by the fish-tail-point and is a measure for the efficiency of the amphiphile. The polymer increases the efficiency dramatically.

9.6 Microemulsions

Microemulsions consist of oil, water and a surfactant. While the microemulsion appears macroscopically homogenous, oil- and water-rich domains form on a microscopic level. The mediating surfactant forms a thin film between these domains. In the following we restrict ourselves to equal amounts of oil and water. A typical phase diagram is shown in Fig. 9.5 in the temperature versus surfactant content γ representation [10]. The most interesting region is the one-phase region (1), where a bicontinuous microemulsion is found. The minimum amount of surfactant is connected to the fish-tail-point, and is a measure for the efficiency of

the surfactant. When adding amphiphilic diblock copolymer, the system becomes more efficient. The polymer amount δ is given in units relative to the total amphiphile, but in absolute units it is less than 0.5%. The dramatically increased efficiency bases on the polymer boosting effect which is described in the following.

By contrast variation measurements it was revealed where the polymer is placed in this four component system. Is was necessary to have each component in a normal protonated and a deuterated version, i.e. normal and heavy water, normal and deuterated decane and normal and deuterated $C_{10}E_4$ surfactant. The minor component polymer was always protonated. The bulk contrast was achieved by using heavy water and protonated components otherwise. Then the water domain is visible against the other components. For the film contrast also deuterated decane was used, and the surfactant film became visible. For the polymer contrast only the protonated polymer was visible. The macroscopic cross section of such a four component system can be written generally as:

$$\begin{aligned}\frac{d\Sigma}{d\Omega}(\mathbf{Q}) = {} & (\rho_O - \rho_W)^2 S_{OO} + (\rho_F - \rho_W)^2 S_{FF} + (\rho_P - \rho_W)^2 S_{PP} \\ & + (\rho_O - \rho_W)(\rho_F - \rho_W) S_{OF} + (\rho_F - \rho_W)(\rho_P - \rho_W) S_{FP} \\ & + (\rho_O - \rho_W)(\rho_P - \rho_W) S_{OP}\end{aligned} \tag{9.14}$$

The first three terms are purely represented by the bulk, film, and polymer contrast (S_{OO}, S_{FF}, S_{PP}). But since the macroscopic cross section is a quadrature of the scattering amplitudes (see eq. 9.6) also cross terms appear. By measuring many contrasts close to the polymer contrast, also the other partial scattering functions (S_{OF}, S_{FP}, S_{OP}) are detectable. These cross terms arise due to a convolution of the real space structures, and thus relative positions of two components are measurable. This valuable information is unavailable by the diagonal terms or a single contrast condition.

For many measurements of macroscopic cross sections at different contrast conditions eq. 9.14 reads $d\vec{\Sigma}/d\Omega = \underline{\underline{\Delta\rho}} \cdot \vec{S}$. Usually, there are many more measurements than the six unknown partial scattering functions, and so the system is over-determined and the experimental noise is reduced. Formally, the inverse matrix of the scattering length densities can be calculated by the Sigular Value Decomposition method, and the partial scattering functions are obtained by $\vec{S} = \underline{\underline{\Delta\rho}}^{-1} \cdot d\vec{\Sigma}/d\Omega$. An example of a cross term S_{FP} is shown in Fig. 9.6. The valuable information of the polymer relative to the surfactant membrane is obtained. The solid line is described by a diblock copolymer decorating the surfactant membrane. Each of the blocks is placed in its pleasant environment and the coils form a mushroom like object.

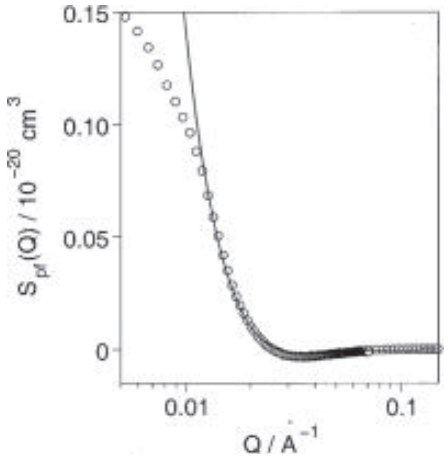

Figure 9.6: The partial polymer-film scattering function as a function of the scattering vector. The fitted function describes a polymer in the presence of a planar wall. The polymer shows a mushroom conformation.

9.7 Bulk Scattering and Phase Diagrams

The bulk scattering also reveals valuable information about the domain structure and finally about the thermodynamics of the microemulsion [11]. An example for the bulk scattering is shown in Fig. 9.7. The macroscopic cross section can be described by the Teubner-Strey theory which bases on a Ginzburg-Landau approach, which considers long wavelength fluctuations of the oil and water domains. The final formula reads:

$$\frac{d\Sigma}{d\Omega}(\mathbf{Q}) = \frac{(\Delta\rho_{OW})^2 \cdot 8\pi\phi_W(1-\phi_W)/\xi}{((2\pi/d)^2+\xi^{-2})^2 - 2((2\pi/d)^2-\xi^{-2})\mathbf{Q}^2 + \mathbf{Q}^4} \tag{9.15}$$

The dominator contains the total fraction of water ϕ_W. Much more interesting are the two structural parameters ξ and d which are obtained as fitting parameters from the measurement. The domain size d is to be understood as the average distance between two consecutive water parts. The correlation length ξ is a measure for the regularity of alternating domains. As indicated in Fig. 9.7 the peak position is mainly given by the domain size d, and the peak width is mainly given by the correlation length ξ. In comparison to diblock copolymers the forward scattering of microemulsions is clearly non-zero. Thermal fluctuations of oil and water can take place easily on large length scales while for the diblock copolymer the bond between the block makes sure that the polymer looks homogenous on large length scales. Many similarities to the polymeric microemulsions become visible (see Fig. 9.4) where the domains become less pure by raising the temperature or the domains even turn to fluctuations at temperatures above the phase boundary.

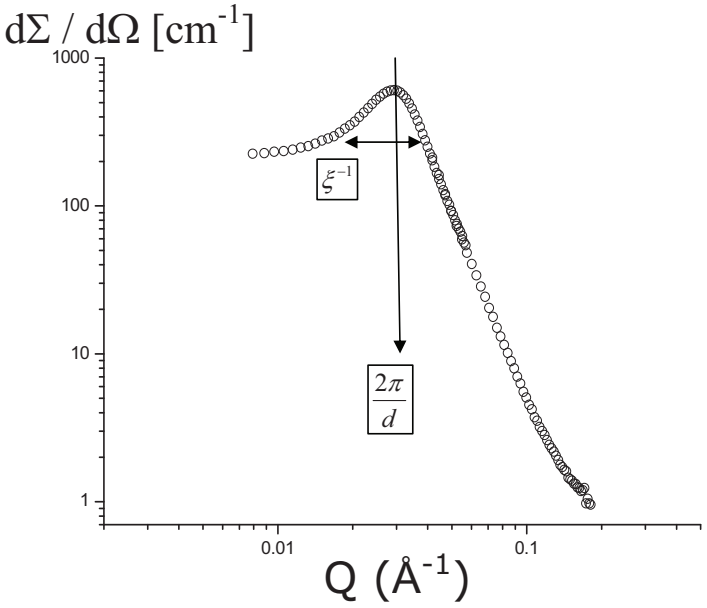

Figure 9.7: A typical scattering pattern of a bicontinuous microemulsion. The peak position is connected to the domain spacing *d*. The peak width is inversely proportional to the correlation length ξ. This kind of data is usually well described by the Teubner-Strey fitting function given in eq. 9.15.

While the structure is described by the concepts above, the thermodynamic properties of a microemulsion shall be discussed now. Phase diagram measurements and SANS measurements can be compared in a unique way. The Helfrich free energy assumes that the free energy of a microemulsion is dominated by the elastic properties of the surfactant film:

$$H = \int dS \left(\tfrac{1}{2}\kappa (c_1 + c_2)^2 + \bar{\kappa} c_1 c_2 \right) \tag{9.16}$$

The integral is conducted along the membrane surface. The two principal curvatures c_1 and c_2 are obtained by a tangential construction of two circles at each membrane point. The curvatures $c_i = 1/R_i$ are the reciprocal radii, and the two circles are perpendicular. The mean curvature $c_1 + c_2$ is connected with the first modulus, the bending rigidity κ. The Gaussian curvature $c_1 c_2$ is connected with the saddle splay modulus $\bar{\kappa}$. The moduli have the following dependence:

$$\begin{aligned} \frac{\kappa_R}{k_B T} &= \frac{\kappa_0}{k_B T} + 0.239 \cdot \ln \gamma + 0.214 \cdot \sigma (R_W^2 + R_O^2) \\ \frac{\bar{\kappa}_R}{k_B T} &= \frac{\bar{\kappa}_0}{k_B T} - 0.265 \cdot \ln \gamma - 0.167 \cdot \sigma (R_W^2 + R_O^2) \end{aligned} \tag{9.17}$$

The logarithmic spatial renormalization (ln γ) lets the membrane appear flabbier on larger length scales. The connected intrinsic modulus (κ_0, $\bar{\kappa}_0$) is the extrapolated modulus for high surfactant contents ($\gamma \to 1$). The analytic theory of diblock copolymers [12] scales with the grafting density σ and the end-to-end distances R_{ee} of the oil- and water-soluble blocks. Please note, that for both moduli the correction terms are very similar except for the sign. As a rule of thumb, the saddle splay modulus $\bar{\kappa}_R$ is basically the negative value of the bending rigidity κ_R.

Now, both moduli are connected with experimentally accessible magnitudes. At the fish tail point of the phase diagram (see Fig. 9.5) the renormalized saddle splay modulus $\bar{\kappa}_R$ is a small constant, and, thus, changes of the minimal surfactant amount are connected with the polymer amount: $\Delta\bar{\kappa}_R / k_B T = -0.167 \cdot \sigma(R_W^2 + R_O^2) = +0.265 \cdot \Delta \ln \gamma$. In a real experiment the sensitivity $\hat{\Xi}$ (i.e. one coefficient) is measured besides the linear dependence, and, thus, $\Delta \ln \gamma = -\hat{\Xi} \cdot \sigma(R_W^2 + R_O^2)$. The bending rigidity is accessible through SANS experiments by the following trick: The Gaussian random field theory describes the statistics of a membrane by a random field, which defines the membrane at the zero of the random field. The fluctuations of the random field are controlled by a parameterized spectral density, which exactly has the appearance of eq. 9.15. In this way the structural parameters d and ξ are connected with the bending rigidity by $\kappa_R / k_B T = 0.85 \cdot \xi / d$. Again, the linear dependence is observed as a function of the scaled polymer amount by: $\Delta\kappa_R / k_B T = 0.85 \cdot \Delta(\xi / d) = \Xi \cdot \sigma(R_W^2 + R_O^2)$.

While this concept proved correct for amphiphilic diblock copolymers it remains to be tested for the newly synthesized sticker polymers. These polymers have only a short hydrophobic unit of 10 carbon atoms, and a polymeric hydrophilic block (90 ethylene oxide units). If all polymers are anchored at the surfactant membrane the same equations should hold, except for the oil soluble end-to-end distance, which simply can be set to zero. The obtained results are shown in Fig. 9.8. The dependencies are linear as predicted by the theory. The coefficients read $\hat{\Xi} = 1.64$ and $\Xi = 0.256$ which agrees exceptionally well with the coefficients of the diblock copolymers. This means, that the polymer boosting effect is successfully transferred to the new sticker polymers which are much easier to synthesize and therefore much cheaper to produce. This polymer is highly water soluble, which is important for formulations of powders. So this polymer is much better for applications than the initially well characterized diblock copolymer.

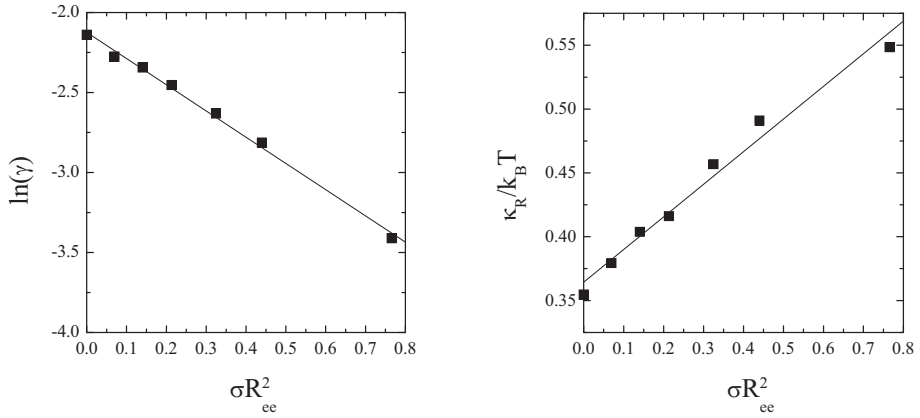

Figure 9.8: The minimum surfactant amount γ as a function of the scaled polymer amount $\sigma \cdot R_{ee}$ for microemulsions with increasing amount of a sticker polymer $C_{12}E_{90}$. The decrease shows that the microemulsion becomes more and more efficient, i.e. the polymer boosting effect is successfully transferred to sticker polymers. On the right the bending rigidity κ_R is plotted as a function of the scaled polymer amount. The increased bending rigidity explains why larger domain structures with a better surface to volume ratio can be formed. On a microscopic scale both diagrams are related through the Helfrich free energy. The polymer effect was described by Lipowsky.

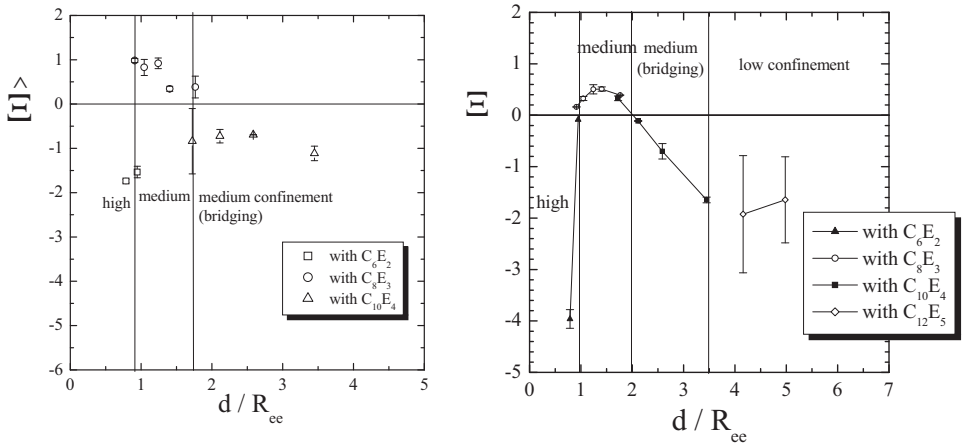

Figure 9.9: The sensitivities of the telechelic polymer on the phase diagram and the bending rigidity for different scaled domain sized d / R_{ee}. At low confinement (large d) a constant limit is reached (for Ξ). At medium confinement there is a region where bridging is continuously switched on (for Ξ) and a region where the sensitivity is almost constant. This constant sensitivity compares well with the confined diblock copolymer. At high confinement a reversed behaviour is found. For this degree of confinement homopolymers, diblock copolymers and telechelic polymers agree. The discontinuous change of $\hat{\Xi}$ at medium confinement might be interesting for applications.

Another aspect of possible additives is addressed with the telechelic polymer. This polymer has two hydrophobic end-groups at each end of the hydrophilic mid-block. So this polymer will connect two spots of the membrane, if both end-groups are anchored safely. This kind of connection can take place between neighbored points, or between opposite points, if the domains are small enough. For the full information of possible conformations, the domain size d has to be changed with respect to the end-to-end distance R_{ee} of the polymer. The sensitivities $\hat{\Xi}$ and Ξ of the saddle splay modulus and the bending rigidity are shown as a function of the scaled domain size d/R_{ee} in Fig. 9.9 (the reciprocal ratio R_{ee}/d can be also interpreted as a degree of confinement). At large domain sizes a constant value is reached (at least for Ξ). Here only neighbored membrane points should be connected, and the dependence on the domain size should vanish. At medium domain sizes a continuous change of Ξ indicates that more and more polymers bridge opposite membrane points. At even lower domain sizes a plateau value of Ξ is reached, which is comparable for diblock copolymers in the same stage (d/R_{ee}). For these medium domain sizes $\hat{\Xi}$ changes discontinuously from negative to positive values. So the bridging does not affect the saddle splay modulus continuously, but the plateau value at lower domain sizes is comparable to diblock copolymers as for Ξ. The plateau value is a sign of medium confinement without differentiating between bridging and connecting neighbored points, since telechelic polymers and diblock copolymers are similar. At the lowest domain sizes a reversed behavior is found. This high confinement stage is universal for homopolymers, diblock copolymers and telechelic polymers. Here the polymer is reflected by the membrane many times, and the anchoring does only play a minor role.

The sudden change of $\hat{\Xi}$ at medium domain sizes is directly connected to the phase behavior, and should be interesting for applications. When dilution of microemulsions plays a role in an industrial process, the polymer supports the emulsification for a concentrated system and a phase separation upon dilution. In metal processing often microemulsions are used, which are cleaned and phase separated after the process in order to be reused for another cycle. The telechelic polymer acts as an intelligent additive which reacts on the environment and supports special purposes. Other polymer architectures may bear many other important properties, which should be uncovered and made suitable for applications. Furthermore, the synthetic polymers mimic biological proteins on cell membranes. The basic research on synthetic polymers thus reveals also valuable information about the functions of biological attachments on membranes, such as the cytoskeleton. Many interesting results are about to come.

9.6 Summary

Many new interesting aspects appear, when certain polymers are added to either polymer blends or microemulsions. All these new polymers are A-philic and B-philic at certain parts, and the architecture can vary. The aim of the polymer additives is always to modify the overall miscibility of the components A and B. Furthermore, the domain size and shape can be influenced by the polymer additive. While the miscibility often can be studies by visual inspection - it is a macroscopic property - the detailed analysis of the nano-scale domain structure is performed best by scattering experiments. The more components are used in the final formulation the more important is the method of contrast variation. This method inevitably leads to neutron scattering. In this way basic research will support the tailoring of next-generation materials.

References

Text books:

[1] R.J. Roe, *Methods of x-ray and neutron scattering in polymer science*. Oxford University Press, Oxford 2000

[2] J.S. Higgins and H.C. Benoit, *Polymers and neutron scattering*. Clarendon Press, Oxford (1994)

IFF Spring Schools:

[3] 33. IFF-Ferienkurs 2002, *Soft Matter - Complex Materials on Mesoscopic Scales*, Schriften des Forschungszentrums Jülich, Jülich 2002

[4] 35th Spring School 2004, *Physics Meets Biology - From Soft Matter to Cell Biology*, Schriften des Forschungszentrums Jülich, Jülich 2004

[5] 38th Spring School 2007, *Probing the Nanoworld - Microscopies, Scattering and Spectroscopies of the Solid State*, Schriften des Forschungszentrums Jülich, Jülich 2007

[6] 22. IFF-Ferienkurs 1991, *Physik der Polymere*, Ferienkurse des Forschungszentrums Jülich, Jülich 1991 (written in German)

Articles:

[7] D. Schwahn *Adv. Polym. Sci.* **183**, 1 (2005)

[8] L. Leibler, *Macromolecules* **13**, 1602 (1980)

[9] V. Pipich, D. Schwahn, L. Willner *J. Chem. Phys.* **123**, 124904 (2005)

[10] H. Endo, M. Mihailescu, M. Monkenbusch, J. Allgaier, G. Gompper, D. Richter, B. Farago, T. Sottmann, R. Strey, I. Grillo, *J. Chem. Phys.* **115**, 580 (2002)

[11] D. Byelov, H. Frielinghaus, O. Holderer, J. Allgaier, D. Richter *Langmuir* **20**, 10433 (2004)

[12] C. Hiergeist, R. Lipowsky *J. Phys. II* **6**, 1465 (1996)

10

Dynamics of Macromolecules

Dieter Richter

10. Dynamics of Macromolecules

D. Richter
Institut für Festkörperforschung
Forschungszentrum Jülich GmbH

Contents

1 Introduction

Polymeric materials are used because they are durable, cheaply to produce, easily to process and because they exhibit very favourable processing and mechanical properties. Polymers may behave like a viscous fluid or rubber elastic, very tough with high impact strength or even brittle. In the simplest case polymers are long linear chain molecules build from a repeating unit: the monomer. Such polymers are called linear homopolymers. Other than synthetic polymers, biopolymers are highly complex molecular structures with a sharp molecular weight and a uniquely defined sequence of building blocks. They are the molecular manifestations of life with a high variety of structure and specific function. Nevertheless, at least in their denaturated state they exhibit similarities with synthetic materials while in their folded state the specific function evolves. Also the general principles of selfassembly in structure formation are common to both species.

The diffusional motions of long flexible polymers constitute fascinating physics and at the same time represent one of the great challenges of modern material science. The drive towards the molecular understanding of the complex viscoelastic properties of polymer liquids is the focal point of rheology and connects the classical chemical engineering approach with modern physics [1]. There the tube model invented by Doi and Edwards [2] and de Gennes [3] has shown itself as the most successful molecular model describing the topological confinement imposed by the mutually interpenetrating polymer chains in the melt. In terms of this so called reptation model a theory of viscoelasticity has been developed that describes the main features of polymer melt rheology.

Large scale protein motions on the other hand are critical for proteins to coordinate precise biological function. Such dynamics are invoked in regulatory proteins, motor proteins, signalling proteins and structural proteins. Structural studies have documented the conformational flexibility in proteins accompanying their activity. Results from macroscopic studies such as biochemical kinetics and single molecule detection have also shown the importance of conformational dynamics and Brownian thermal fluctuations within the proteins or protein complexes. However, the time dependent dynamic processes that facilitate such protein motions remain poorly understood and experimentally nearly untouched [4].

Neutron spin echo spectroscopy is the highest resolution neutron technique and provides time resolution in the 100ns range, enabling thereby the access to molecular motion on a mesoscopic time scale between the atomic picosecond scales and the macroscopic times [5]. At that scale the molecular motions of the polymers take place that underlie their macroscopic viscoelastic behaviour. Similarly, the large scale motions of bio molecules occur on similar space time frames.

This lecture aims to identify general principles of chain motion on a molecular scale which underpin the macroscopic properties and presents concepts and experimental results on these motional mechanisms in space and time. We will mainly address the dynamics of homopolymers and give one example for studies of the molecular dynamics of biopolymers.

2 Neutron scattering and the large scale motion of macromolecules

Neutron scattering with its space time sensitivity on a molecular and atomic scale unravels the space time occurrence of the molecular motions we are interested in. Commencing at the scale of the single bond, where movements take place at a pace as in normal liquids quasielastic neutronscattering (QENS) provides insight into local relaxation processes they are not addressed here. For a reference see [1]. At larger length scales first the entropy driven Rouse motion and at even larger distances the effect of topological confinement due to the mutual interpenetrating chains come into the observation range. The most powerful technique suitable for these investigations, the neutron spin echo spectroscopy (NSE) operates in the time domain and uncovers a time range from about 2ps to several hundred ns and accesses a momentum transfer between about 0.01Å^{-1} and 3Å^{-1}.

Coherent, quasi- and inelastic neutronscattering reveals the dynamic structure factor ($S(Q,t)$) or its Fourier transformed counter part $S(Q,\omega)$.

$$S(Q,t) = \frac{1}{N}\sum_{ij}\left\langle \exp\left(-i\underline{Q}\underline{r}_j(t)\right)\exp\left(-i\underline{Q}\underline{r}_i(0)\right)\right\rangle \tag{1}$$

Where $\underline{r}_j(t)$ and $\underline{r}_j(0)$ are the position vectors of the scatterers at time t and time $t = 0$ respectively. N is the number of scatteres, $\hbar Q = \hbar 4\pi/\lambda * \sin(\theta/2)$ is the momentum transfer during scattering (for elastic or nearly elastic scattering) with θ the scattering angle and λ the neutron wavelength. The brackets denote the thermal average. $S(Q,t)$ reflects the pair correlation function and relates to the collective properties of a material. In the neutron cross section it is weighted by the average scattering length $\left|\overline{b}\right|^2$.

Incoherent scattering is related to the scattering length disorder which may either result from spin dependent scattering lengths like in the case of hydrogen or from isotope mixtures of isotopes with different scattering properties. This disorder prevents constructive interference of partial waves scattered at different atoms and reveals the self correlation function. Eq.[1] provides the self correlation function if in the double sum only terms with $i = j$ are considered. In the cross section $S_{inc}(Q,t)$ is weighted by the average scattering length fluctuation $\left(\left\langle b^2\right\rangle - \left|\overline{b}^2\right|\right)$.

In Gaussian approximation which is commonly used for the calculation of neutron dynamic structure factors for polymer dynamics Eq.[1] is approximated by

$$S(Q,t) = \frac{1}{N}\sum_{ij}\exp\left[-\frac{Q^2}{6}\left\langle\left(\underline{r}_i(t) - \underline{r}_j(0)\right)^2\right\rangle\right] \tag{2}$$

3 Entropy driven dynamics

The dynamics of a generic linear Gaussian chain as described in the Rouse model [6] is the starting point for a standard description of the Brownian dynamics in polymer melts. In this model the conformational entropy of a chain acts as a resource for restoring forces for a chain conformation deviating from thermal equilibrium. In this chapter we deal with this entropy driven dynamics in terms of the Rouse model and present neutron spin echo (NSE) results on the space time evolution of the Rouse relaxation.

3.1 Gaussian chains

The conformation of a flexible linear polymer chain on scales somewhat larger than the main chain bond length ℓ_0 assumes a random walk. The conformations of such a chain are described by a set of segment vectors $\{\underline{r}(n)\} = (\underline{R}(n) - \underline{R}(n\text{-}1))$ where $\underline{R}(n)$ is the position vector of segment n. Following the central limit theorem the length distribution of a vector $\underline{r}$ connecting segments that have a topological distance of n steps is a Gaussian.

$$\phi(R,n) = \left(\frac{3}{2\pi n\ell^2}\right)^{3/2} \exp\left(-\frac{3R^2}{2n\ell^2}\right) \tag{3}$$

with ℓ the segment length. The Rouse model bases on a further idealization of the chain statistics assuming that the bond vector $\underline{\ell}$ of hypothetic connecting points along the chain also has a Gaussian distribution. With $\langle \ell^2 \rangle = b^2$. For simplicity throughout the lecture we will take $b^2 = \ell_0^2 C_\infty$. Keeping, however, in mind that the building block of a Gaussian chain may well contain a larger number of main chain bonds. C_∞ is the characteristic ratio accounting for the local stiffness arising from the non-random bond angle distribution of the bonds of length ℓ_0. The conformational probability of a conformation $\{\underline{r}(n)\}$ follows as

$$P\left(\{\underline{r}(n)\}\right) = \left(\frac{3}{2\pi\ell^2}\right)^{\frac{3}{2}N} \exp\left[-\sum_{n=1}^{N} \frac{3\left(\underline{R}(n) - \underline{R}(n-1)\right)^2}{2\ell^2}\right] \tag{4}$$

with n counting the number of segments of the chain. The free energy of a Gaussian chain is entirely described by its conformational entropy

$$S = k_B \ell n\left[P\left(\{r(n)\}\right)\right] \tag{5}$$

The Gaussian chain model yields a spring constant for the Gaussian segment. $k = 3k_BT/\ell^2$ where k_B is the Boltzmann constant. From Eq.[4] the chain extension between arbitrary points along the chain becomes $|n - m|\,\ell^2$.

3.2 The Rouse model

The Rouse model starts from a Gaussian chain representing a coarse grained polymer model where springs stand for the entropic forces between hypothetic beats [6] (Fig.1).

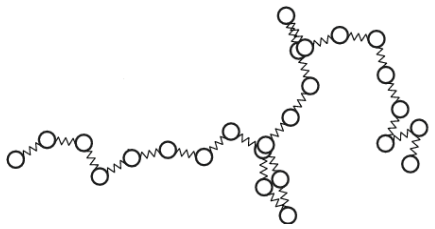

Fig. 1: *Spring-bead model of a Gaussian chain as assumed in the Rouse model. The beads are connected by "entropic springs" and are subject to a frictional force $\zeta_0 \upsilon$, where υ is the bead velocity and ζ_0 the bead friction coefficient*

We are interested in the motion of segments on a length scale $\ell < r < R_E$ where $R_E^2 = N\ell^2$ is the end to end distance of the chain. The segments are subject to an entropic force resulting from the derivative of Eq.[5] (x components).

$$\frac{\partial}{\partial x(n)} \; S = \frac{k_B T}{\ell^2}\left[x(n+1) - 2x(n) + x(n-1)\right] \tag{6}$$

And to a stochastic force $f_x(n,t)$ which fulfils $\langle f_x(n,t)\rangle = 0$ and $\left\langle f_\alpha(n,t) \;\; f_\beta(m,0)\right\rangle = 2k_B T \zeta_0 \; \delta_{nm} \; \delta_{\alpha\beta} \; \delta(t)$. ζ_0 denotes the friction coefficient and α,β the Cartesian components. Regarding the index n as the continuous variable the Langevin equation for segment motion assumes the form

$$\zeta_0 \; \frac{\partial x}{\partial t} = \frac{3k_B T}{\ell^2} \; \frac{\partial x^2(n)}{\partial n^2} + f_x(n,t) \tag{7}$$

The boundary condition of force free ends requires $\left.\frac{\partial^2 x(n)}{\partial n}\right|_{n=0,N} = 0$. The differential equations are solved by Cosine Fourier transformation to normal coordinates fulfilling the boundary conditions.

The normal mode with index p counting the knots of the cosine function relaxes with a characteristic relaxation time τ_p

$$\tau_p = \frac{\zeta_0 N^2 \ell^2}{3\pi^2 k_B T \, p^2} = \frac{\tau_R}{p^2} = \frac{N^2}{W \pi^2 p^2}; \; W = \frac{3k_B T}{\ell^2 \zeta_0} \tag{8}$$

τ_R is the Rouse time – the longest time in the relaxation spectrum – and W is the elementary Rouse rate. The correlation function of the normal coordinates is finally obtained as

$$\left\langle \tilde{x}(p,t)\ \tilde{x}(p,0)\right\rangle = \frac{N\ell^2}{6\pi^2 p^2}\exp\left(-\frac{t}{\tau_p}\right) \tag{9}$$

For the center of mass coordinate one finds

$$\left\langle \tilde{x}(0,t)\ \tilde{x}(0,0)\right\rangle = \frac{2k_BT}{N\zeta_0}t \tag{10}$$

Scattering experiments relate to mean square segment correlation functions which are obtained by back transformation of the normal coordinates.

For the mean square segment displacement we obtain

$$\left\langle r^2(t)\right\rangle = 2\ell^2\left(\frac{3k_BT\,t}{\pi\zeta_0\ell^2}\right)^{1/2} + 6D_Rt \tag{11}$$

In the segmental regime the mean square displacement does not grow linearly in time but with its square root. For the translational diffusion coefficient $D_R = \frac{k_BT}{N\ \zeta_0} = \frac{W\ell^4}{3N\ell^2} = \frac{W\ell^4}{3R_E^2}$ is obtained. D_R is inversely proportional to the number of friction performing segments.

The self correlation function relates directly to the mean square displacement of the diffusing segments. In Gaussian approximation, inserting Eq.[11] into Eq.[2], for $t \ll \tau_R$ we have

$$S_{self}(Q,t) = \exp\left[-Q^2D_Rt\right]\ \exp\left\{-\frac{2}{\sqrt{\pi}}\left(\frac{k_BT\ell^2}{12\zeta_0}Q^4t\right)^{1/2}\right\} \tag{12}$$

For coherent scattering observing the pair correlation function interferences from waves emanating from various segments complicate the scattering function. For long chains and high Q de Gennes [3] provided an approximate formula for the coherent scattering function $S_{chain}(Q,t)$.

$$\begin{aligned} S_{chain}(Q,t) &= \frac{12}{Q^2\ell^2}\int_0^\infty du\exp\left\{-u-\left(\Omega_Rt\right)^{1/2}\ h\left(u\left(\Omega_Rt\right)^{-1/2}\right)\right\} \\ h(y) &= \frac{2}{\pi}\int_0^\infty dx\ \frac{\cos(xy)}{x^2}\left(1-\exp\left(-x^2\right)\right) \end{aligned} \tag{13}$$

Note that this equation only depends on one variable: the Rouse variable.

$$\left(\Omega_Rt\right)^{1/2} = \frac{Q^2}{6}\sqrt{\frac{3k_BT\,\ell^2t}{\zeta_0}} = \frac{Q^2\ell^2}{6}\sqrt{Wt} \tag{14}$$

Aside of the cut off length scales (R_E and ℓ) the Rouse model does not contain an explicit length scale. Therefore for different momentum transfers the dynamic structure factors are predicted to collapse to a single master curve if they are represented as a function of the Rouse variable.

In the regime of validity the form of Ω_R immediately reveals that the intrachain relaxation increases $\approx Q^4$ in contrast to normal diffusion $\approx Q^2$.

3.3 Neutron spin echo results

Recently it became possible to observe directly the incoherent cross section from a protonated chain, thereby measuring the self correlation function. Figure 2 displays the time dependent mean square displacement obtained from a high molecular weight ($M_w = 80000$) monodisperse polyethylene-propylene (PEP) melt at 492K [7]. In Gaussian approximation for negligible translational diffusion Eq.[12] yields

$$\left\langle r^2(t)\right\rangle = -\frac{6}{Q^2}\ell n\, S_{self}(Q,t) \tag{15}$$

As may be seen from Figure 2 the mean square displacement (MSD) follows with high accuracy the predicted square root law in time. Since neutron quasielastic scattering resolves dynamic processes in space and time these measurements give direct information about the segment displacement at a given time. E.g. at 10ns the MSD amounts to 620Å^2 i.e. the average proton has travelled about 25Å during this time interval.

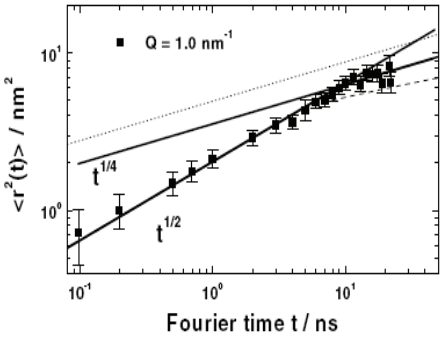

Fig. 2: *Time dependent mean square displacement of a PEP segment in the melt at 492K. The solid line indicates the prediction of the Rouse model. The slowing down at longer times is an indication of a cross over to local reptation (see ref [7]).*

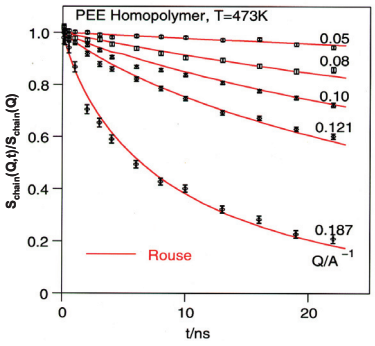

Fig. 3: *Single chain structure factor from a PEE melt at 473K. The numbers along the curves represent the experimental Q-values in [Å^{-1}]. The solid lines are a joint fit with the Rouse model (Eq.[13]).*

The pair correlation function arising from the segment motion within one given chain is observed if some protonated chains are dissolved in a deuterated matrix. Figure 3 displays the observed spectra for polyethylethylene (90% dPEE, 10% hPEE) with the molecular weight of $M_w^h = 21.5kg/mol$; $M_w^d = 24.5kg/mol$ and a narrow molecular weight distribution [8]. The solid lines give the predictions of the dynamic structure factor of Eq.[13]. Obviously very good agreement is achieved.

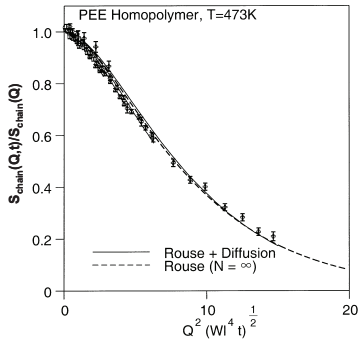

Fig. 4: *Single chain structure factor from PEE melts as a function of the Rouse scaling variable. The dashed line displays the Rouse prediction for infinite chains, the solid lines incorporate the effect of translational diffusion. The different symbols relate to the spectra displayed in Figure 3.*

We now use these data in order to investigate the scaling prediction inherent in Eq.[13]. Figure 4 presents a plot of the data of Figure 4 now as a function of the Rouse scaling variable (Eq.[14]). With satisfactory precision the data follow the scaling prediction. The small deviations are related to the translational diffusion of the chains. This becomes evident from Figure 6 where the obtained relaxation rates $\Omega_R(Q)$ are plotted vs. Q in a double logarithmic

fashion. The dashed line gives the Rouse prediction $\Omega_R \approx W\ell^4 Q^4$ while at larger momentum transfer the experimental results follow very well this prediction, towards lower Q a systematic relative increase of the relaxation rate is observed. Including translational diffusion we have

$$\Omega_R(Q) = Q^2\left[D_R + Q^2\frac{W\ell^4}{6}\right] = Q^2 W\ell^2\left[\frac{\ell^2}{3R_E^2} + \frac{Q^2\ell^2}{6}\right] \tag{16}$$

The solid lines in Figure 5 represent the predictions of Eq.[16] - perfect agreement is obtained. The above expressions provide a universal description of the dynamics of a Gaussian chain and are valid for real linear polymer chains on intermediate length scales. The specific properties of a polymer enter only in terms of two parameters: $N\ell^2 = R_E^2$ and ℓ^2/ζ_0. The friction parameter is governing the Rouse variable (Eq.[14]). As eluded to in Eq.[16] also the center of mass diffusion coefficient may be expressed in these terms. Since the Rouse model does not contain an inherent length scale the parameter N (chain length) and ℓ^2 (segment length squared) are somewhat arbitrary as long as the physical values ℓ^2/ζ_0 and R_E^2 are constant. The NSE experiments measure directly the friction coefficient/length^2.

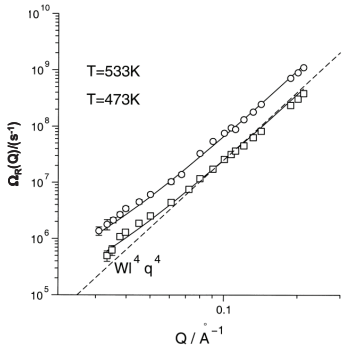

Fig. 5: *Relaxation rates from PEE melts vs. Q for two different temperatures. The dashed line represents the $\Omega_R \sim Q^4$ prediction of the Rouse model. The solid lines include the contribution from translational diffusion (Eq.[24]).*

The Rouse model predicts a mean square center of mass displacement of a diffusing chain which should be strictly linear in time. Recently, the chain center of mass a displacement in a regime where the internal modes do not contribute, was studied on the scale of the chain. This measurement showed that for times shorter than the Rouse time τ_R the Rouse prediction for the center of mass displacement is not fulfilled. Figure 6 displays results for the center of mass MSD for different short chains. For each chain length the corresponding Rouse relaxation time $\tau_R(N)$ is indicated. With increasing length an increasingly important subdiffusive behaviour at short times becomes evident. At longer times a cross over to a center of mass displacement proportional to t with a cross over time around the corresponding Rouse relaxation time takes place. The dashed lines in Figure 6 extrapolate the long time behaviour towards shorter times.

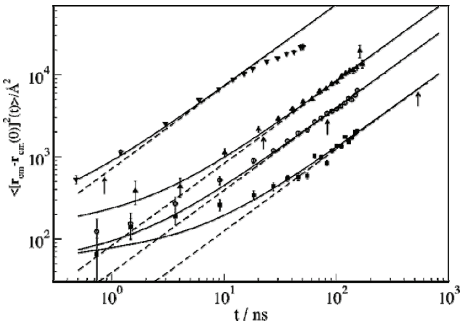

Fig. 6: *The com mean-square displacement, extracted from the data at q = 0.3nm^{-1}. Symbols: experimental data for N = 36 (down triangles), 106 (up triangles), 192 (open circles), and 377 (filled squares). Vertical arrows: decorrelation time, τ_{decorr}. Full lines: cooperative dynamics generalized Langevin equation. Dashed lines: free diffusion.*

While in the Rouse theory local intermolecular interactions are ignored, more realistically in a polymer melt, where a chain spans a volume $V \approx R_g^3$, it may interact with the $n \cong \sqrt{N}$ chains that on average fill the volume of a given chain. Guenza [10] has derived a generalized Langevin equation (GLE) for the resulting cooperative dynamics of such interacting polymers in the melt. Thereby an effective potential acting between the centers of mass of a pair of molecules has been derived to

$$W(r) = \frac{27\sqrt{2}}{4\pi\sqrt{\pi}} \frac{1}{\sqrt{N}\rho^*} \left[1 - \frac{108}{\pi^2 \rho^{*2} N}\right] \exp\left[-\frac{3r^2}{4R_g^2}\right] \tag{17}$$

Where $\rho^* = \rho\ell^3$ with ρ the density. The potential is Gaussian with a range in the order of R_g. An approximate solution of the GLE leads to subdiffusive center of mass MSD. The solid lines in Figure 6 display the result of the GLE approach by Guenza [9]. Thereby the soft interchain potential $W(r)$ (Eq.[17]) was employed using the prefactor as the fitting parameter and introducing the proper R_g into the Gaussian potential. With this approach an adequate description of the experimental data is achieved (solid lines in Figure 6).

4 Topological confinement: Reptation

The dynamic modulus of a polymer melt is characterized by a plateau in frequency which broadens with increasing chain length. In this plateau regime the polymer melt acts like a rubber where the elastic properties are derived from the entropy elasticity of the chains between permanent cross links. The modulus of a rubber is inversely proportional to the mesh size and proportional to the temperature. In analogy, it is suggestive to assume that the entanglement or topological interactions between the chains in a melt lead to the formation of

a temporary network which displays rubber elastic properties. Other than in a rubber for long times the chains may disentangle and the melt flows. This flow process is characterized by a melt viscosity $\eta \approx N^{3.2\ldots3.6}$ and the translational chain diffusion coefficient $D \approx N^{2\ldots2.3}$ [11]. Using the analogy to the modulus of a rubber we may estimate the distances between entanglement points from the value of the plateau modulus G_N^0. For different polymers values between 30Å and 100Å are found. On the basis of such assumptions a number of theories of viscoelasticity have been developed [2,11,12]. The most famous among them is the reptation model by de Gennes [3] and Doi and Edwards [2]. In this model the dominating chain motion is a reptile like creep along the chain profile. The lateral restrictions by the interpenetrating other chains are modelled by a tube with a diameter d parallel to the chain profile. d relates to the plateau modulus of the melt

$$d^2 = \frac{4}{5}\frac{R_E^2}{M}\frac{k_B T}{G_N^0} \tag{18}$$

The restrictions of the motion by the presence of the other chains are not effective on a monomer scale but rather permit lateral freedom on intermediate length scales. The experimental observations for viscosity and diffusion can be made directly comprehensible in this simple model.

4.1 Mean square displacements

We now consider the predictions of the reptation model for the mean square displacements of the chain segments. For short times when the chain segments have not yet realized the topological constraints ($r^2 < d^2$) we expect unrestricted Rouse motion $\langle r^2(t)\rangle \approx t^{1/2}$ (Eq.[11]). Experimentally this was the case for PEP (Figure 3) where for an entangled chain for times up to 20ns and displacements up to 30Å Rouse dynamics was observed. At a time τ_e, $\tau_e = d^4/(\pi^2 W \ell^4)$ the mean square displacement reaches the order of the tube diameter. τ_e is derived as the Rouse time for polymer strand spanning the tube. Then motional restrictions are expected.

For times $t > \tau_e$ one dimensional curve linear Rouse motion along the tube needs to be considered. Displacements along the tube are described by Eq.[11] where we have to change real space coordinates to coordinates $s(t)$ along the tube. If a segment is displaced along the tube by $\langle (s_n(t) - s_n(0))^2\rangle$ then the mean square displacement in 3-d real space is $d\left\langle \left(s_n(t) - s_n(0)\right)^2 \right\rangle^{1/2}$. With that we obtain

$$\left\langle r^2(t)\right\rangle = \begin{cases} 2d\left(\dfrac{k_B T \ell^2 t}{\zeta_0 \pi}\right)^{1/4} & \tau_e < t < \tau_R \\ 2d\left(\dfrac{k_B T t}{N\zeta_0}\right)^{1/2} & \tau_R < t < \tau_d \end{cases} \tag{19}$$

In Figure 7 the two situations correspond to the second and the third process. The second process where the chain performs Rouse motion along the tube is called local reptation while the creep like diffusion along the tube which eventually leads to a complete tube renewal is also termed pure reptation. The terminal time τ_d after which the chain has left its original tube determines to a large extend the viscosity of the melt. Beyond that time reptation diffusion prevails.

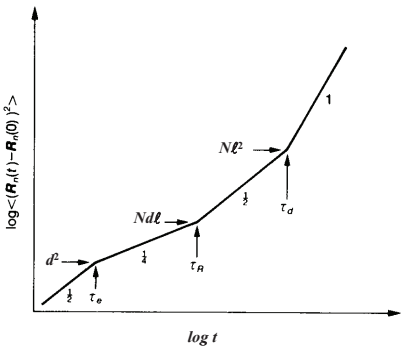

Fig. 7: *Mean-square displacement of a chain segment in the reptation model.*

4.2 Self correlation function

In Gaussian approximation the self correlation function of a reptating chain directly relates to the MSD's of chapter 4.1. This supposes that the widths of the Gaussian function after a diffusion time t of the single segment distribution along the 1-dimensional tube contour may be taken for the time dependent displacement. Projecting this on the Gaussian contorted tube then would again correspond to a Gaussian sublinear diffusion in real space.

However, as Fatkullin and Kimmich have shown [13], the real process has to be modelled by projecting the segment probability distribution due to the Rouse motion with the curve linear coordinate s on the random walk like contour path of the contorted tube. This leads to a non-Gaussian probability distribution of the segment at times $t > \tau_e$,

$$S_{self}\left(Q,t > \tau_e\right) = \exp\left[\frac{Q^4 d^2}{72}\,\frac{\left\langle r^2(t)\right\rangle}{3}\right] erfc\left[\frac{Q^2 d}{6\sqrt{2}}\sqrt{\frac{\left\langle r^2(t)\right\rangle}{3}}\right] \tag{20}$$

invalidating the Gaussian approximation for times longer than τ_e. We note that Eq.[20] is strictly valid only for $t \gg \tau_e$ when $\langle r^2(t)\rangle \gg d^2$. The effect on the scattering function is that if (wrongly) interpreted in terms of the Gaussian approximation the cross over to local reptation appears to occur a significantly lower values of τ_e. A generic asymptotic $t^{1/4}$ law remains untouched.

In the sense of Eq.[20] the MSD of a chain segment may be directly observed by incoherent quasielastic scattering. In the local reptation regime we expect to observe the predicted cross over of the MSD from a $t^{1/2}$ to a $t^{1/4}$ law (Eq.[19]). Experiments were performed on PE and PEP samples at temperatures where also the dynamic structure factors were studied [7]. Figure 8 displays these data in terms of an effective mean square displacement (Eq.[15]), thereby assuming implicitly the Gaussian approximation.

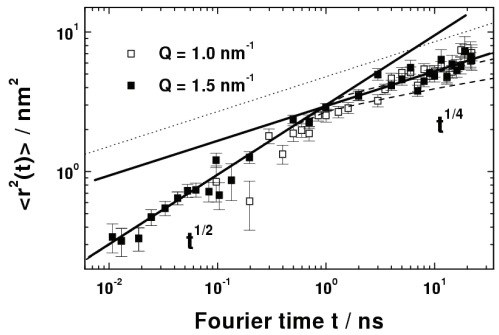

Fig. 8: *NSE data obtained from the incoherent scattering of a fully protonated PE-melt in a representation of* $-6\ell n[S_{self}(Q,t)]/Q^2$ *which is the mean-square displacement* $\langle r^2(t)\rangle$ *as long as the Gaussian approximation holds. Solid lines describe the asymptotic power laws* $\langle r^2(t)\rangle \propto t^{1/2}, t^{1/4}$. *Dotted lines: prediction form the Gaussian approximation, dashed lines: see text.*

Inserting the Rouse rate for PE at 509K, $W\ell^4 = 7 \pm 0.7\text{nm}^4/\text{ns}$ obtained from single chain dynamic structure factor measurements into Eq.[12] the solid line $\approx t^{1/2}$ is obtained. It quantitatively corrobates the correctness of the Rouse descriptions at short times. The data also reveal clearly a transition to a $t^{1/4}$ law, though Eq.[19] would predict the dotted line. The discrepancy explains itself in considering the non-Gaussian character of the curve linear Rouse motion (Eq.[20]). Fixing also the value of the tube diameter to that obtained from single structure factor measurements (see later), the dashed line in Figure 8 presents the prediction of the non-Gaussian treatment. For $Q = 0.1\text{Å}^{-1}$ the unrestricted Rouse regime ($t < \tau_e$) as well as the local reptation regime is perfectly reproduced.

4.3 Single chain dynamic structure factor

Now we turn to the single chain dynamic structure factor $S_{chain}(Q,t)$ which is also strongly effected by the topological tube constraints. Qualitatively, we would expect the following behaviour:

(i) At short times $t < \tau_e$ the chain will perform unrestricted Rouse motion and the dynamic structure factor of Eq.[13] should well describe the dynamics. This e.g. has been exemplified in earlier measurements of the Rouse dynamic structure factor of entangled PDMS melts - in these materials d is large [14].

(ii) In the regime of local reptation the chain has already explored the tube laterally and further density fluctuations of the labelled chain will only be possible via Rouse relaxation along the tube. Under such circumstances the structure factor to a first approximation will mirror the formfactor of the tube $S_{chain}(Q,\tau_R > t > \tau_e)/S_{chain}(Q) \approx \exp\left(-Q^2d^2/36\right)$. In this regime the experiment should reveal the size of the topological constraints without applying any detailed model.

(iii) In the creep regime $t > \tau_R$ the memory of the tube confinement will be gradually lost and the dynamic structure factor should reveal the fraction of the still confined polymer segments.

(iv) Finally, in the diffusive regime at very small Q ($QR_g \ll 1$) the reptation diffusion coefficient will be measured. de Gennes [15] and Doi and Edwards [11] have formulated tractable analytic expressions for the dynamic structure factor. Thereby, they neglected the initial Rouse regime i.e. the derived expression is valid only for $t > \tau_e$ once confinement effects become important. The dynamic structure factor is composed from two contributions S^{loc} and S^{esc} reflecting local reptation and escape processes from the tube.

$$\frac{S_{chain}(Q,t)}{S_{chain}(Q)} = \left[1-\exp\left(-\frac{Q^2d^2}{36}\right)\right] S^{loc} + \exp\left(-\frac{Q^2d^2}{36}\right) S^{esc} \tag{21}$$

The local reptation part was calculated as

$$S^{loc}(Q,t) = \exp\left(\frac{t}{\tau_0}\right) erfc\left(\sqrt{\frac{t}{\tau_0}}\right) \tag{22}$$

Where $\tau_0 = 36/\left(W\ell^4Q^4\right)$ a more general expression for $S^{esc}(Q,t)$ due to pure reptation was given by Doi and Edwards [11]. For short times $S^{chain}(Q,t)$ decays mainly due to local reptation (first term) while for longer times (and low Q) the second term resulting from the creep motion is important. The ratio of the two relevant time scales τ_0 and τ_d is proportional to N^3. Therefore, for long chains at intermediate times a pronounced plateau in $S_{chain}(Q,t)$ is predicted. Such a plateau is a generic signature for confined motion.

Figure 9 compares the dynamic structure factors from 2 PE melts both studied at 509K for two different molecular weights (10a: M_w = 2kg/mol; 10b: M_w = 12.4kg/mol). The solid lines in Figure 10a display a fit with a Rouse dynamic structure factor. Very good agreement is achieved. Figure 10b presents equivalent results from the higher M_w melt with the solid lines again showing the prediction of the Rouse model.

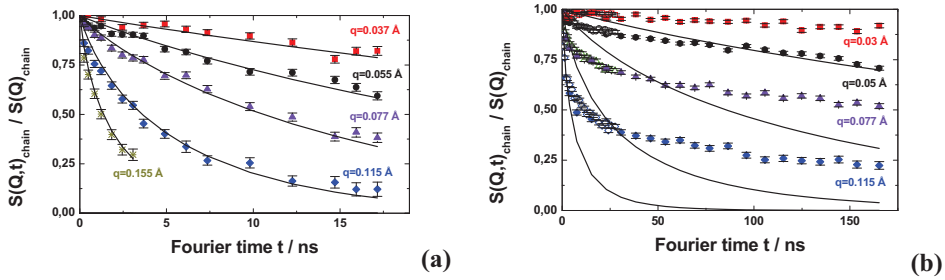

Fig. 9: *Dynamic structure factors from PE-melts at 509K (a) M_w = 2000; (b) M_w = 12400. The solid lines display the predictions of the Rouse model.*

Please note, that the time scale for the 12.4kg/mol sample is extended by one order of magnitude compared to the short chain case. While for the short chain melt the Rouse model describes well the experimental observations, for the longer chains the model fails completely. Only in the short time regime the initial decay of the dynamic structure factor is depicted, while for longer times the relaxation behaviour is strongly retarded signifying the confinement effects.

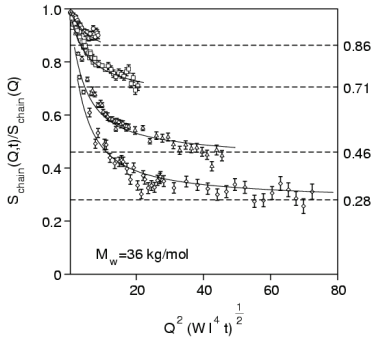

Fig. 10: *Scaling presentation of the dynamic structure factor from a M_w = 36000 PE-melt at 509K as a function of the Rouse scaling variable. The solid lines are a fit with the reptation model (Eq.[21]). The Q-values are from above Q = 0.05, 0.077, 0.115, 0.145Å^{-1}. The horizontal dashed lines display the prediction of the Debye-Waller factor estimate for the confinement size (see text).*

Figure 10 displays the dynamic structure factor from a M_w = 36kg/mol PE-melt as a function of the Rouse variable $Q^2\ell^2\sqrt{Wt}$. Other than in Figure 4, where the scaled data followed a common master curve, here they split into different branches which only at small values of the scaling variable are coming close together. This splitting is a consequence of the existing dynamic length scale invalidating the Rouse scaling properties. We note that this length is of purely dynamical character and cannot be observed in static equilibrium experiments.

In the spirit of Eq.[21] and neglecting the ongoing decay of $S_{chain}(Q,t)$ due to local reptation from the heights of the achieved plateaus we may obtain a first estimate for the amount of

confinement. Identifying the plateau levels with a Debye Waller factor description of the confinement, we get $d = 46$Å, a value which is a lower estimate for the two tube diameter since S^{loc} is not fully relaxed. The horizontal lines in Figure 11 are the predictions from this Debye-Waller factor estimate. A full fit with the reptation structure factor of Eq.[28] yields $d = 48 \pm 1$Å.

4.4 Reptation limiting processes

It is well known that a number of salient properties of entangled polymer melts are only qualitatively in agreement with reptation, indicating the existence of additional processes that release topological confinement [17]. These processes comprise fluctuating chain ends with open a route to escape the tube confinement (contour length fluctuations – CLF) and the lateral tube opening by diffusion processes of confining chains (constraint release – CR). While CLF is an effect of the confined chain itself CR stems from the movements of the chains building the tube which of course undergo the same dynamical processes as the confined chain. Both processes are schematically depicted in Figure 11. In this lecture we restrict ourselves to CLF presses.

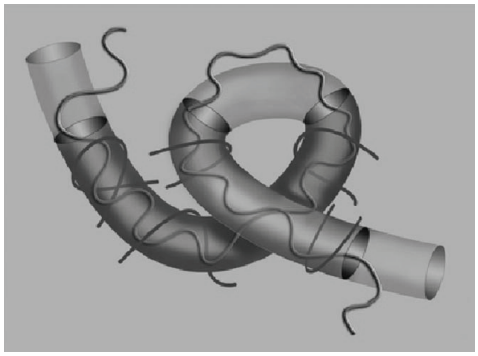

Fig. 11: *Schematic presentation of the CLF and CR mechanisms: chain end fluctuations lead to a shortening of the effective tube length, while the dissolving of entanglements allow chain motions beyond the initial tube constraints [17].*

CLF originate from the fluctuations of the primitive path length of the tube and are a key mechanism for the relaxation at earlier times and are also the basis for hierarchical relaxation processes of branched polymers. There CLF are considered to be the fundamental process facilitating the release of side branches.

The CLF effect evolves from the participation of the chain ends in the local reptation process (Figure 11). Any chain retraction and subsequent expansion leads to a loss of the memory of the original confining tube. Thus, effectively the tube becomes shorter with time. Mathematically the problem may be treated as a first passage problem. Whenever a tube contour is visited by the free end it ceases to exist. The functional form of the tube survival probability $\mu(t)$ was derived from scaling arguments [18].

$$\mu(t) = 1 - \frac{C_\mu}{Z}\left(\frac{t}{\tau_e}\right)^{1/4} \tag{23}$$

The constant $C_\mu = 1.5 \pm 0.02$ was obtained from stochastic simulation. $Z = N/N_e$ is the number of entanglements and N_e the number of segments forming an entanglement strand. Eq.[23] describes quantitatively which chain fraction at a time t is still confined. All parameters are known from the NSE experiments on the dynamics of asymptotically long chains, where the CLF effect does not play a role.

With this knowledge Eq.[23] allows the design of an experiment where the CLF effect may be directly demonstrated [19]. In this experiment the dynamic structure factor of a fully labelled chain is compared with that of an identical chain where the contrast of those segments which are affected by CLF within the experimental time frame was matched. The first case is realized by performing an experiment on a fully protonated chain in a deuterated matrix. Then the full chain dynamics including the CLF effect are observed. The second case is realized in a chain where the inner part is protonated while the outer chain sections of a length which would be affected by CLF are deuterated and thus not visible in a deuterated matrix. In such a case the dynamics should be equal to those of an asymptotically long fully labelled confined chain.

With the known parameters for PE Eq.[23] gives that at the experimental temperature of 509K on average on each side 220 monomers are released during an observation time of 190ns. The above described experiments were performed on two different PE chains of a molecular weight of 25kg/mol^{-1} one of which was fully hydrogenated and the other having deuterated labels of $M_w = 4$kg/mol^{-1} corresponding to 260 monomers on each end.

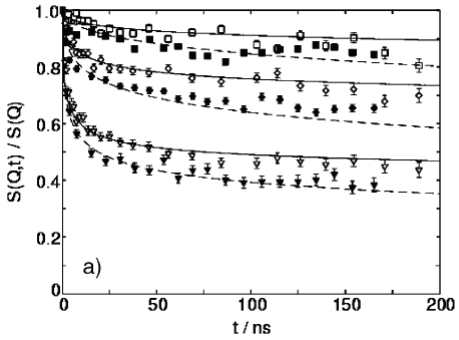

Fig. 12: *Dynamic structure factor of a centre labelled 25kg mol^{-1} PE chain (filled symbols) compared to a fully labelled chain (open symbols) of the same overall molecular weight. Q values (in nm^{-1}): 0.5 (squares), 0.77 (diamonds), 0.96 (circles), 1.15 (triangles). Lines: for center labelled chain, pure reptation model (Eq.[21]); for fully labelled 25kg mol^{-1} chain (dashed) CLF was considered.*

Figure 12 presents the normalized dynamic structure factor $S(Q,t)/S(Q)$ for different Q values for the two chains. In all cases at short times the structure factor displays the strong initial decay which is due to the initial free Rouse motion. For longer times the decay is strongly

reduced transgressing into the confinement related plateau behaviour. Comparing the levels of decay it is clear that the structure factor from the fully labelled chain decays significantly more than that from the corresponding center labelled counter part. Apparently the constraints for the center labelled chain are stronger than those for the chain where the ends are visible. We further note that in the case where the ends were masked the center part of the chains shows exactly the same structure factor as that from a very long chain. This signifies directly the action of CLF at the chain ends and the remaining full confinement of the center. The agreement of these two sets of data means that for a 25kg/mol^{-1} chain the effect of constraint.

The solid lines in Figure 12 are a description of the dynamic structure factor in terms of Eq.[21] yielding the same parameters as for asymptotically long chains. In order to depict the CLF mechanism in the dynamic structure factor the escape term in Eq.[21] needs to be modified. The effective tube shortens with time. The time dependent fraction of escaped monomers may be incorporated into the structure factor following an approach of Clark and McLeish [20]. Assuming that after time t all monomers from both ends up to a contour length $s(t) = (1 - \mu(t))/2$ have been released from the tube without introducing any new parameter a simple analytical expression for the escape term is derived.

$$S_{CLF}^{esc}(Q,t) = A\left(2 + 2\gamma + e^{-2\gamma} - 4\gamma s(t) - 4e^{-\gamma S(t)} + e^{-4\gamma s(t)}\right) \tag{24}$$

With A a normalization constant and $\gamma = Q^2 N\ell^2/12$. Eq.[24] replaces S^{esc} in the original Eq.[21]. This approach is valid as long as $t < \tau_R$ where the Rouse time τ_R for a 35kg/mol chain is in the order 1300ns far beyond the experimental window of 190ns. The dashed lines in Figure 12 present the prediction of Eq.[24]. They describe perfectly the data from the fully labelled chain without any further parameter.

5 Large scale dynamics in biopolymers

While the study of the dynamics of synthetic polymers has reached some maturity, the next challenge will be the investigation of the large scale motion of biopolymers. The goal there will be to find out to what extend these dynamics play a role in bio function. On local scales some insight into the conformational dynamics has been gained e.g. by time dependent crystallography [21]. On the other hand, the large scale dynamics such as protein domain motions remain basically untouched experimentally, because of the lack of techniques to study these large scale correlated motions. In this lecture we present a first study on such dynamics on the example of alcohol dehydrogenase (ADH) [22]. The alcohol dehydrogenases are enzymes that are important for many organisms allowing the interconversion between alcohols and ketones. In humans ADH is present as a dimer and catalyzes the oxidation of ethanol allowing thereby the consumption of alcohol in beverages. In yeast on the hand it is at the basis of the fermentation process converting acetaldehyde into ethanol. In the process the cofactor Nicotinamide Adenine Dinucleotide (NAD) is needed assisting the oxidation reaction at the zinc catalytic side.

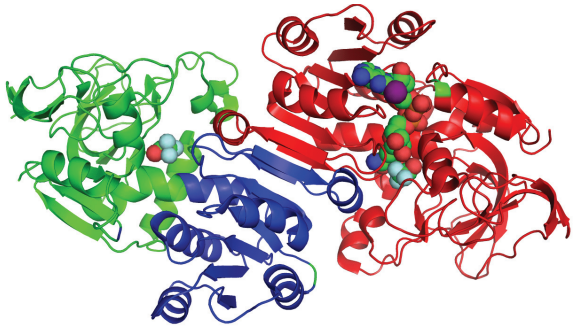

Fig. 13: *Dimer of alcohol dehydrogenase. The molecule presented by spherical caps is the NAD cofactor used in the chemical reaction.*

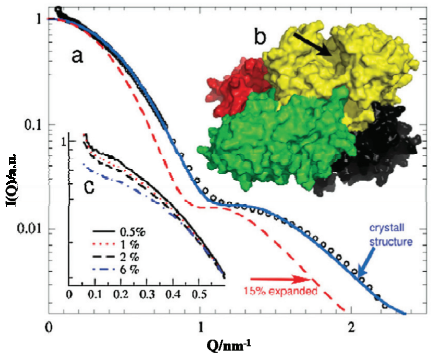

Fig. 14: *(a) SANS intensity from ADH with bound cofactor at 0.5% wt=vol conc. (circles) and protein form factors (lines see text). The shoulder around 1nm^{-1} is characteristic for the tetrameric structure. (b) Illustration of the overall protein structure with two crossed dimers (green/yellow in front, red/black behind). The yellow monomer shows the cofactor binding cleft (arrow) separating the inner cofactor binding domain and the exterior catalytic domain. (c) Concentration scaled, low q scattering intensity of the protein solution.*

Figure 13 displays a schematic structure of the dimer based on crystallographic data. The two monomeric units are clearly visible. Each monomer is build from two domains, the catalytic and the binding domain with a small opening in between, where the cofactor NAD is placed. ADH from yeast forms a tetrameric structure. The crystallographic data suggest a crossed arrangement of the two dimers.

In order to verify whether in solution a similar tetrameric aggregate is present it is important to perform neutron small angle scattering (SANS) experiments. Figure 14 presents SANS data at different concentrations.

The coherent scattering intensity in a solution of equal particles is given by $I(Q) \propto NS(Q)P(Q)$ where the structure factor $S(Q)$ results from the interparticle interactions of N scatterers and depends on concentration, while the concentration independent form factor

$$P(Q) = \sum_{j,k} \left\langle b_j b_k \exp\left(i\boldsymbol{q}\left(\boldsymbol{r}_j - \boldsymbol{r}_k\right)\right)\right\rangle \tag{25}$$

describes the scattering of the single tetramer. b_j are the atomic scattering lengths and $\boldsymbol{r}_j$ the atomic position vectors. For the form factor calculation the coordinates of the crystal structure from the protein data bank are used and hydrogen exchange is considered. As may be seen from Figure 14a the structural model based on the crystal structure (solid line) is in very good agreement with the SANS results. Figure 14c presents the scattering intensities after scaling with concentration. The observed decrease of the scattering intensity at low Q is caused by the structure factor $S(Q)$, which is extracted in dividing by the lowest concentration data.

The dynamics in solution is importantly influenced by the overall translational diffusion of the molecular aggregate. Therefore, in the next step the translational diffusion coefficient needs to be studied. Dynamic light scattering is the proper tool since it investigates the overall dynamics on the proper length scale. Figure 15 displays light scattering results for different ADH concentrations as a function of momentum transfer squared. We note that apparently for all concentrations we observe identical translational diffusion coefficients. At 5°C it amounts to $D_{DLS} = 2.35 \pm 0.2 \times 10^{-2}\text{nm}^2/\text{ns}$.

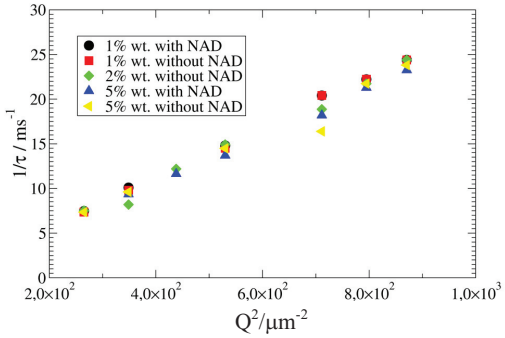

Fig. 15: *Dynamic light scattering results on the translational diffusion of tetrameric ADH in water solution at different concentrations. The characteristic rates* $1/\tau = D*Q^2$ *are plotted vs.* Q^2.

In order to approach the internal dynamics of such an aggregate one has to increase the Q range such that $1/Q$ roughly corresponds to the molecular or aggregate size. This may be achieved implying neutron spin echo spectroscopy to the ADH solutions. Figure 16 displays NSE results for a large number of different momentum transfers Q. The data are presented in a log linear fashion showing directly the nearly single exponential decay observed in all cases. Fits with single exponential decays are included by straight lines. We note however, that at intermediate Q ($Q = 0.68\text{nm}^{-1}$) small but systematic deviations appear indicating a two component structure. This is evident particularly if one fits only data at long times (see dashed line in Figure 16).

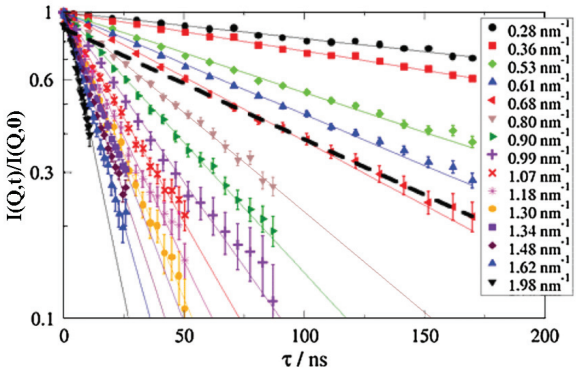

Fig. 16: *Intermediate scattering function measured by NSE for a protein concentration of 5% wt/vol with the bound cofactor. The broken line is a fit to $Q = 0.68nm^{-1}$ for times above 75ns.*

Comparing the covered Q range with the SANS data (Figure 14) we realize that the range of the structure factor, where intermolecular interactions are important as well as the regime of internal structure are covered. Now we approximate the spectra in terms of a first cumulant expansion

$$\ell n \frac{S(Q,t)}{S(Q)} = -\Gamma(Q)t + \frac{1}{2}K_2 t^2 \tag{26a}$$

The decay rate of the dynamic structure factor, also called initial slope, is

$$\Gamma(Q) = -\lim_{t\to 0}\frac{\partial}{\partial t}\,\ell n\left[S(Q,t)\right] \tag{26b}$$

Using the decay rates $\Gamma(Q)$ we may define an effective diffusion coefficient

$$D_{eff}(Q) = \frac{\Gamma(Q)}{Q^2} \tag{26c}$$

For the case of a translational diffusion $D_{eff}(Q)$ would be a constant and giving the translational diffusion coefficient.

Figure 17 displays the thus obtained effective diffusion coefficients as a function of Q for the different concentrations with and without the cofactor NAD. The line at low Q indicates the level of the light scattering results.

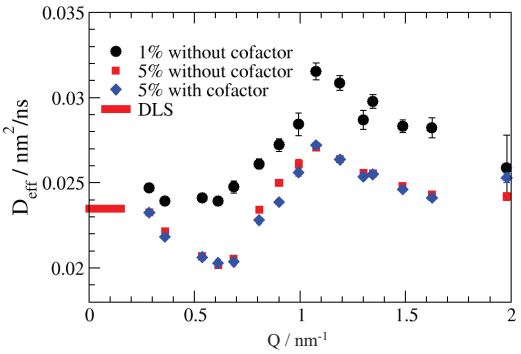

Fig. 17: *(a) Effective diffusion coefficient $D_{eff}(Q)$ for 3 different solutions of ADH.*

The experimental results show a strong Q modulation with a maximum around $Q = 1\text{nm}^{-1}$. Furthermore, we realize that at low Q the data are in agreement with the concentration independent light scattering results. We also see that beyond the statistical error in the low Q flank of the 5% data the relaxation without the cofactor NAD is faster than that including the cofactor. We may conclude that in the dynamics of the ADH tetramer on the scale of the aggregate itself we observe significant contributions beyond translational diffusion.

We now want to interpret the data and commence with the low Q data which are affected by the interactions between the molecules. In this regime the effective diffusion coefficient relates to the diffusion coefficient D_0 at infinite dilution by

$$D_{eff}(Q) = D_0 \frac{H(Q)}{S(Q)} \tag{27}$$

where $H(Q)$ is the hydrodynamic factor. The structure factor may be extracted from the SANS data in dividing the concentration dependent results by the lowest concentration results ($C = 0.25\%$). With this experimental structure factor the data may be corrected. This correction removes the low Q increase of the 5% data but leaves the results at higher Q untouched (see Figure 18a). The hydrodynamic factor cannot be measured directly. A first approximation in terms of a Perkus Yevic model shows that (i) at a 1% level the correction factor $H(Q)/S(Q)$ leaves the experimental data practically untouched and (ii) at 5% the correction is somewhat weaker than the experimentally observed effect. Nevertheless, beyond $Q = 0.6\text{nm}^{-1}$ the ratio of $H(Q)/S(Q)$ remains constant. Thus, the observed higher Q structure is entirely determined by intra aggregate effects.

The prime reason for a Q dependent structure in $D_{eff}(Q)$ are rotational motions of the molecule. In a first cumulant approximation (see Eq.[26]) the effective diffusion coefficient of a rigid bodg undergoing translational and rotational diffusion has the form [23]

$$D_{eff}(Q) = \frac{k_B T}{Q^2} \times \frac{\sum_{jK} \left\langle b_j e^{i\underline{Q}\underline{r}_j} \begin{pmatrix} \underline{Q} \\ \underline{Q} \times \underline{r}_j \end{pmatrix} \ddot{H} \begin{pmatrix} \underline{Q} \\ \underline{Q} \times \underline{r}_K \end{pmatrix} b_K e^{-i\underline{Q}\underline{r}_K} \right\rangle}{\sum_{jK} \left\langle b_j e^{i\underline{Q}\underline{r}_j} \; b_K e^{-i\underline{Q}\underline{r}_K} \right\rangle} \tag{28}$$

Here $\underline{r}_i$ and $\underline{r}_k$ are the atomic coordinates, b_i and b_k the corresponding neutron scattering length and $\ddot{H}$ the mobility tensor. The sum runs over all atoms of the molecule or molecular aggregate and the pointed brackets indicate an ensemble average. The denominator is the aggregate formfactor. The mobility matrix $\ddot{H}$ is a 6×6 tensor involving translational ($\ddot{T}$) rotational ($\ddot{R}$) parts including a translational rotational coupling ($\overrightarrow{TR}$). For the simplest case of an isotropic particle $T = D_{trans}/k_BT$ and $R = D_{rot}/k_BT$. The evaluation of Eq.[27] is importantly complicated by the hydrodynamic interaction between the different parts of the molecule. In the biophysical literature one finds the computer code HYDROPRO which was developed by the group around Garcia de la Torre [24]. In this code a complicated molecule is approximated by a rigid aggregate of little spheres. Its diffusional motion including the hydrodynamic interaction is then calculated by a proper superposition of the motion of the rigidly connected spheres. The calculations with HYDROPRO need as an input the crystallographic coordinates of all atoms.

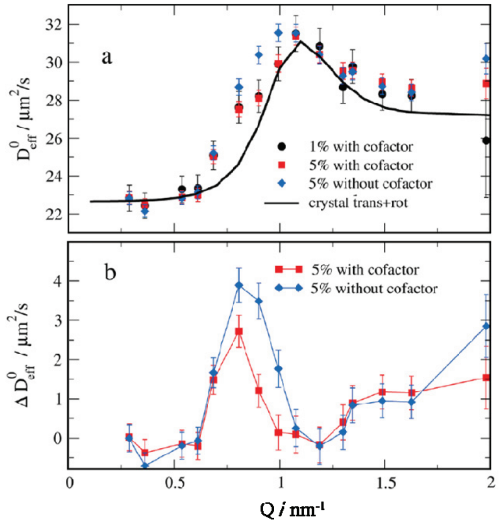

Fig. 18: *(a) Single tetramer diffusion coefficient $D^0_{eff}(Q)$ after corrections with and without the bound cofactor. The black solid line represents the calculated effective diffusion coefficients for the ADH crystal structure, including translational and rotational diffusion. (b) Difference of the corrected diffusion coefficients and the calculated translational or rotational diffusion coefficient.*

In Figure 18a all data sets for $D_{eff}(Q)$ at the different concentrations with and without cofactor are compared. After rescaling with the diffusion coefficients at different concentrations in the

region above $Q = 0.6\text{nm}^{-1}$ all data sets are consistent. We furthermore note that the data at 5% solution are of significantly higher statistical significance. The solid line in Figure 18a displays the result of the HYDROPRO calculations for a rigid molecule. While the line describes the general form of the effective diffusion coefficient data reasonably well, we observe significant deviations at smaller momentum transfers. These differences between the rotational diffusion expectation for a rigid aggregate and the experimental data are displayed in Figure 18b. We note that at Q values below the peak of the rigid body rotational diffusion coefficient significantly faster effective diffusion takes place. This result indicates the presence of internal motion within the molecule which must involve mainly those atoms which are placed in the outer regions of the tetramer emphasizing more strongly the larger distances and within the molecule and therefore giving rise to extra dynamics at low Q.

A first interpretation of this result may be carried out in terms of a normal mode analysis. For this purpose an elastic network model is used where the complicated bonded and non-bonded interactions are replaced by a pair wise Hookian potential controlled by a single parameter. As has been shown, such a simple formulation is sufficient to describe the anomalous low frequency motion of large proteins [25].

In this model two close enough atoms are connected by a spring, if the equilibrium distance between them is sufficiently small. The elastic forces acting on the particles obey Hookes law and depend only on the change in the distances between them. In principle the dynamics of such an elastic network is nonlinear because the distances are nonlinear functions of the coordinates. Close to the equilibrium the equations of motions can however be linearized yielding to an equation of motion

$$m_i \ddot{\underline{r}}_i = -\sum_j \Lambda_{ij}\, \underline{r}_j \tag{29}$$

where Λ is the $3N \times 3N$ dynamical matrix obtained by the linearization process. In this linear approximation the motions are described by a sum of independent oscillating normal modes.

$$\underline{r}_i(t) = \sum_\alpha k_\alpha \sin\omega_\alpha t\ \underline{e}_i^\alpha \tag{30}$$

With ω_α^2 and $\underline{e}_i^\alpha$ representing nonzero eigenvalues and the respective eigenvectors of the matrix Λ and $k_\alpha = \dfrac{k_B T}{\bar{m}\omega_\alpha^2}$ the amplitude factor of the mode. The large scale slow motions we are interested in, are dominated by the soft modes with small eigenvalues. In the case of overdamped modes which are seen in the experiment the oscillating part needs to be replaced by an exponential $\left(e^{(-\lambda_\alpha t)}\right)$. The relaxation rates λ_α contain the unknown friction factors within the molecule and with the surrounding water molecules.

A first approximation for the dynamic form factor may be obtained in analogy to a phonon approximation of the cross section, which in fact is an expansion of the cross section with respect to small displacements.

$$S(Q,t) \simeq P(Q) + \sum_\alpha k_\alpha e^{-\lambda_\alpha t} \sum_{k,\ell} b_k b_e\ e^{i\underline{Q}\underline{r}_k} e^{-i\underline{Q}\underline{r}_e} \left(\underline{Q}\,\underline{e}_k^\alpha\right)\left(\underline{Q}\,\underline{e}_\ell^\alpha\right) \tag{31}$$

In first cumulant approximation (Eq.[26]) we have to take the logarithmic derivative with respect to time at time equal zero. Subtracting the translational and rotational part we finally obtain

$$\Delta D_{eff}(Q) = \frac{\sum_{\alpha} \lambda_\alpha k_\alpha \sum_{k,\ell} b_k b_e \, e^{i\underline{Q}\underline{r}_k} e^{-i\underline{Q}\underline{r}_e} \left(\underline{Q}\underline{e}_k^\alpha\right) \times \left(\underline{Q}\underline{e}_\ell^\alpha\right)}{Q^2 P(Q)} \tag{32}$$

describing the dynamic formfactor of the eigenmodes. Finally, Figure 19 presents the outcome of such a harmonic analysis for the tetrameric aggregate of ADH with and without the cofactor. In an exemplary way we present the contributions from the modes 7 and 11 with and without the cofactor. In all cases the low eigenmodes exhibit a formfactor with the strong peak around $Q = 1\text{nm}^{-1}$. Comparing with Figure 28 qualitatively the experimental observation and the results of the normal mode analysis resemble each other.

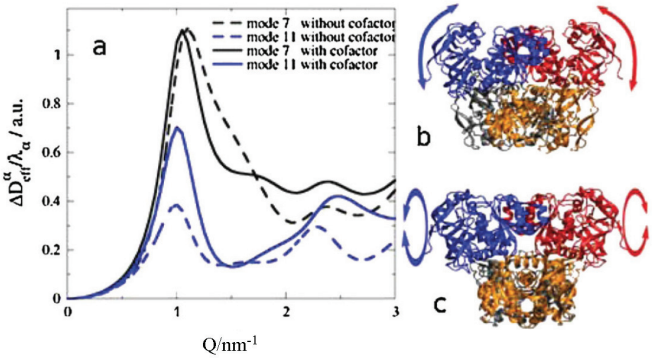

Fig. 19: *(a) Diffusion form factor of the normal modes 7 and 11 for the protein configuration with and without the cofactor. (b) Motional pattern of mode 7: Without cofactor the exterior domain (catalytic domain) tilts outwards and opens the cleft. The inner domain with connection points between the monomers remains stiff. (c) Motional pattern of mode 11: With and without the bound cofactor the monomers within a dimer exhibit torsional motion around the long dimer axis (in the image plane), which is more pronounced with the cofactor.*

Quantitatively the observed experimental feature is shifted towards smaller Q indicating a more pronounced motion of the outer atoms. This difference is not yet fully understood but may result from the anharmonicity of the dynamics or the effect inhomogeneously distributed friction within the molecule or both.

6 Conclusion and outlook

We have presented some representative results from neutron spin echo spectroscopy on the dynamics of macromolecules. In the case of synthetic polymers we have displayed recent

results on the universal dynamics of flexible polymers from the entropy driven Rouse dynamics to confinement and reptation including reptation limiting processes. In the case of biopolymers we have displayed some first experiments on the intra aggregate motion of alcohol dehydrogenase an important enzyme for fermentation and the oxidation of ethanol. The lecture attempted to transmit a flavour of what can be achieved with high resolution neutron spin spectroscopy which permits to access the molecular motion simultaneously in space and time.

The lecture commenced with a description of the standard model of polymer motion, the entropy driven dynamics covered by the so called Rouse model. In the spatial range where the Rouse approximations are valid, the NSE measurements have confirmed most of the predictions of the Rouse model both for the self- and pair correlation function. We also have shown limitations related to the inter chain interactions which reveal themselves in the center of mass selfdiffusion at short times.

Towards larger scales topological interactions resulting from the mutually interpenetrating chains gain dominating influence and confine the chain motion to a tube along the chain profile. We have presented measurements on the dynamic structure factor of a reptating chain which unequivocally confirm the picture of local reptation i.e. Rouse relaxation along the contorted tube. A measurement of the self correlation function corrobates the picture. Finally, we have shown NSE results that quantitatively confirm contour length fluctuations as one of the leading reptation limiting processes.

Compared to the investigations of the dynamics of synthetic polymers the study of the large scale relaxation dynamics of biopolymers is still in its early stages. We have presented some first experimental data on the collective inter aggregate fluctuations of a tetrameric aggregate formed by alcohol dehydrogenase. It became possible to directly measure the Q dependent effective diffusion coefficient which bears information on the detailed rotational diffusion dynamics. Furthermore, additional dynamics appears at low momentum transfers which is related to motions of the outer more flexible parts of each dimer. Employing normal mode analysis these dynamical features have been attributed to the slow large scale collective fluctuations of the domains.

These experiments are a first attempt to directly observe the collective internal dynamics of proteins or protein complexes. In the future experiments will be needed in order to resolve the internal dynamics or further proteins, in order to try to resolve the different relaxation modes. Such experiments need to be accompanied by computer simulations in order to enhance the level of interpretation. Furthermore, the experiments need to address proteins where domain motion is functionally important. We hope that in the future such NSE studies will make an important contribution to a better understanding of protein function based not only on the structure but also on the dynamics.

References

[1] For a recent review see: D. Richter, M. Monkenbusch, A. Arbe, J. Colmenero, Adv. Polymer Sci. 174, Springer, Berlin, Heidelberg, New York (2005)
[2] M. Doi, S.F. Edwards, J. Chem. Soc. Farad. Trans. 274, 1789; 274, 1802; 275, 38 (1978)
[3] P.G. de Gennes, J. Chem. Phys. 55, 572 (1971)
[4] Z. Bu, R. Biehl, M. Monkenbusch, D. Richter, J.E. Callaway, PNAS 102, 17646 (2005)
[5] F. Mezei (Ed.), Neutron spin echo lecture notes in physics 128, Springer, Berlin, Heidelberg, New York (2005)
[6] P.R. Rouse, J. Chem Phys. 21, 1272 (1953)
[7] A. Wischnewski, M. Monkenbusch, L. Willner, D. Richter, B. Farago, G. Kali, Phys. Rev. Lett. 90, 058302 (2003)
[8] H. Montes, M. Monkenbusch, L. Willner, S. Rathgeber, L.J. Fetters, D. Richter, J. Chem. Phys. 110, 10188 (1999)
[9] M. Zamponi, A. Wischnewski, M. Monkenbusch, D. Richter, B. Farago, M. Guenza, J. Phys. Chem. 3112, 16220 (2008)
[10] M. Guenza, Phys. Rev. Lett. 88, 025901 (2002)
[11] M. Doi, S.F. Edwards, The theory of polymer dynamics, Clarendon Oxford (1986)
[12] P.G. de Gennes, Scaling concepts in polymer physics, Cornell University Press, Ithaca (1979)
[13] N. Fatkullin, R. Kimmich, Phys. Rev. E 52, 3273 (1995)
[14] D. Richter, A. Baumgärtner, K. Binder, B. Ewen, J.B. Hayter, Phys. Rev. Lett. 47, 109 (1981)
[15] P.G. de Gennes, J. Phys. (Paris) 42, 735 (1981)
[16] P. Schleger, B. Farago, A. Kollmar, C. Lartigue, D. Richter, Phys. Rev. Lett. 81, 124 (1998)
[17] For a review see e.g. T.C.B. McLeish, Adv. in Polymer Physics 51, 1 (2002)
[18] A.E. Likhtman, T.C.B. McLeish, Macromolecules 35, 6332 (2002)
[19] M. Zamponi, A. Wischnewski, M. Monkenbusch, L. Willner, D. Richter, A. Likhtman, G. Kali, B. Farago, Phys. Rev. Lett. 96, 238302 (2006)
[20] N. Clark, T.C.B. McLeish, Macromolecules 26, 5264 (1993)
[21] F. Schotte, M. Lim, T.A. Jackson, A.V. Smirnov, J. Soman, J.S. Olson, G.N. Jr Philips, M. Wulf, P.A. Aminfrud, Science 300, 1944 (2003)
[22] R. Biehl, B. Hofmann, M. Monkenbusch, S. Prevost, R. Merkel, D. Richter, Phys. Rev. Lett. 101, 138102 (2008)
[23] N. Brown, Dynamic Light Scattering, Monographs of the Physics and Chemistry of Materials, Oxford Science Publications, Oxford 49 (1993)
[24] J. Garcia de la Torre, M.L. Huertas, B. Carrasco, Biophysics J. 78, 719 (2000)
[25] M.M. Tirion, Phys. Rev. Lett. 77, 1905 (1996)

11

Correlated electrons in complex transition metal oxides

Thomas Brückel

11. Correlated electrons in complex transition metal oxides

Thomas Brückel, IFF, Forschungszentrum Jülich

11.1 Introduction

Materials with strong electronic correlations are materials, in which the movement of one electron depends on the positions and movements of all other electrons due to the long-range Coulomb interaction. With this definition, one would naively think that all materials show strong electronic correlations. However, in purely ionic systems, the electrons are confined to the immediate neighborhood of the respective atomic nucleus. On the other hand, in ideal metallic systems, the other conduction electrons screen the long-range Coulomb interaction. Therefore, while electronic correlations are also present in these systems and lead for example to magnetism, the main properties of the systems can be explained in simple models, where electronic correlations are either entirely neglected (e. g. the free electron Fermi gas) or taken into account only in low order approximations (Fermi liquid, exchange interactions in magnetism etc.). In highly correlated electron systems, simple approximations break down and entirely new phenomena appear, possibly with related novel functionalities. These so-called *emergent phenomena* cannot be anticipated from the local interactions among the electrons and between the electrons and the lattice [1]. This is a typical example of *complexity*: the laws that describe the behavior of a complex system are qualitatively different from those that govern its units [2]. This is what makes highly correlated electron systems a research field at the very forefront of condensed matter research. The current challenge in condensed matter physics is that we cannot reliably predict the properties of materials with strong electronic correlations. There is no theory, which can handle this huge number of interacting degrees of freedom. While the underlying fundamental principles of quantum mechanics (Schrödinger equation or relativistic Dirac equation) and statistical mechanics (maximization of entropy) are well known, there is no way at present to solve the many-body problem for some 10^{23} particles. Some of the exotic properties of strongly correlated electron systems and examples of emergent phenomena and novel functionalities are:

- *High temperature superconductivity*; while this phenomenon was discovered in 1986 by Bednorz and Müller [3], who received the Nobel Prize for this discovery, there is still no commonly accepted mechanism for the coupling of electrons into Cooper pairs, let alone a theory which can predict high temperature superconductivity or its transition temperatures. This lack of understanding is the more surprising, the more we consider the large number of solid-state physicists worldwide, which are trying to solve this problem. High temperature superconductivity has already some applications like in so-called SQUID (Superconducting Quantum Interference Device) magnetic field sensors, superconducting generators or motors, high field magnets etc but might in the future have even further applications for loss-free energy storage or -transport.

- *Colossal magnetoresistance effect CMR*, which was discovered in transition metal oxide manganites and describes a large change of the electrical resistance in an applied magnetic field [4]. This effect can be used in magnetic field sensors and could eventually replace the giant magnetoresistance field sensors[1], which are employed for example in the read heads of magnetic hard discs.

[1] The giant magnetoresistance effect [5] is an effect that occurs in artificial magnetic thin film multilayers. It was discovered independently by P. Grünberg and A. Fert, who received the Nobel Prize in 2007 for their discovery.

- *The magnetocaloric effect* [6], which describes a temperature change of a material in an applied magnetic field and can for example, be used for magnetic refrigeration without moving parts or a cooling fluid.

- *The multiferroic effect* [7], which describes the simultaneous occurring of various ferroic orders in one material. This could be ferromagnetism, ferroelectricity or ferroelasticity. If the respective degrees of freedom are strongly coupled, one can switch one of the orders by applying the conjugate field of the other order. In certain multiferroic materials, the application of a magnetic field can switch the ferroelectric polarization or the application of an electric field can switch the magnetization of the material. Future applications of multiferroic materials in computer storage elements are apparent. One could either imagine elements, which store several bits in form of a magnetic- and electric polarization, or one could apply the multiferroic properties for an easier switching of the memory element.

- Metal-insulator-transitions as observed e. g. in magnetite (Verwey transition [8]) or certain vanadites are due to strong electronic correlations and could be employed as electronic switches.

- Negative thermal expansion [9] is just another example of the novel and exotic properties that these materials exhibit.

It is likely that many more such emergent phenomena will be discovered in the near future. This huge potential is what makes research on highly correlated electron systems so interesting and challenging: this area of research is located right at the intersection between fundamental science investigations, striving for basic understanding of the electronic correlations, and technological applications, connected to the new functionalities [10].

11.2 Electronic structure of solids

In order to be able to discuss the effects of strong electronic correlations, let us first recapitulate the textbook knowledge of the electronic structure of solids [11]. The description of the electron system of solids usually starts with the *adiabatic or Born-Oppenheimer approximation*. The argument is made that the electrons are moving so quickly compared to the nuclei that the electrons can instantaneously follow the movement of the much heavier nuclei and thus see the instantaneous nuclear potential. This approximation serves to separate the lattice- and electronic degrees of freedom. Often one makes one further approximation and considers the nuclei to be at rest in their equilibrium positions. The potential energy seen by a single electron in the averaged field of all other electrons and the atomic core potential is depicted schematically for a one dimensional system in figure 11.1.

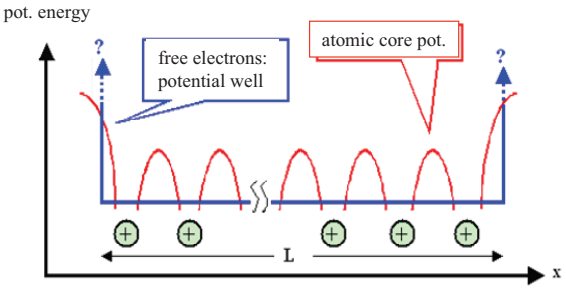

Fig. 11.1: *Potential energy of an electron in the solid; once in the case of free electrons, where the electron is described as moving in a potential well with infinitely high walls; and once taking into account the potential arising from the Coulomb interaction with the atomic cores, which is periodic in the infinite solid.*

The following simple models are used to describe the electrons in a crystalline solid:

- *Free electron Fermi gas*: here a single electron moves in a 3D potential well with infinitely high walls corresponding to the crystal surfaces. All electrons move completely independent, i. e. the Coulomb interaction between the electrons is not considered explicitly, only the Pauli exclusion principle.
- *Fermi liquid*: here the electron-electron interaction is accounted for in a first approximation by introducing quasiparticles, so-called dressed electrons, which have a charge e, and a spin ½ like the free electron, but an active mass m*, which can differ from the free electron mass m.
- *Band structure model*: this model takes into account the periodic potential of the atomic cores at rest i. e. the electron moves in the average potential from the atomic cores and from the other electrons.

Considering the strength of the long-range Coulomb interaction, it is surprising that the simple models of Fermi gas - or better Fermi liquid - already are very successful in describing some basic properties of simple metals. The band structure model is particularly successful to describe semiconductors. But all three models have in common that the electron is described with a single particle wave function and electronic correlations are only taken into account to describe phenomena like magnetism due to the exchange interaction between the electrons or BCS superconductivity [12], where an interaction between electrons is mediated through lattice vibrations and leads to Cooper pairs, which can undergo a Bose-Einstein condensation.

What we have sketched so far is the textbook knowledge of introductory solid state physics courses. Of course there exist more advanced theoretical descriptions, which try to take into account the electronic correlations. The strong Coulomb interaction between the electrons is taken into account in density functional theory in the so-called "LDA+U" approximation or in so-called dynamical mean field theory DMFT or a combination of the two in various degrees of sophistication [13]. Still, all these extremely powerful and complex theories often times fail to predict even the simplest physical properties, such as whether a material is a conductor or an insulator.

Let us come back to the band structure of solids. In the so-called tight binding model one starts from isolated atoms, where the energy levels of the electrons in the Coulomb potential of the corresponding nucleus can be calculated. If such atoms are brought together, the wave

functions of the electrons from different sites start to overlap, leading to a broadening of the atomic energy levels, which eventually will give rise to the electronic bands in solids. The closer the atoms are brought together, the more the wave functions overlap, the more the electrons will be delocalized, and the broader are the corresponding bands. This relationship is depicted graphically in figure 11.2.

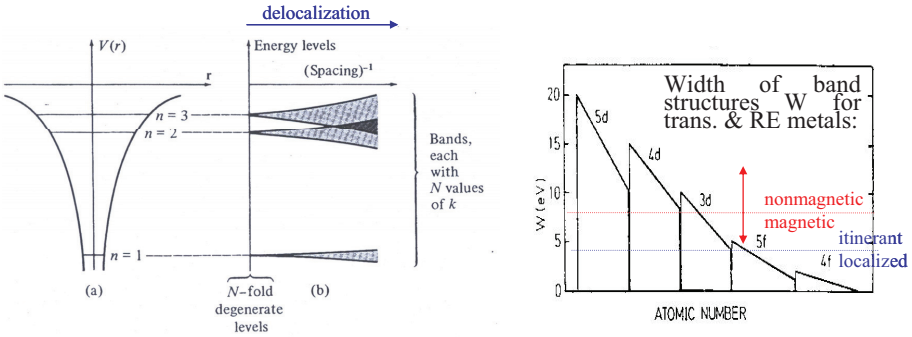

Fig. 11.2: *Left: The figure on the left shows the atomic potential of an electron interacting with the atomic core and the corresponding level scheme, which consists of sharp energy levels. The figure in the middle shows how these atomic energy levels broaden into bands, the more the wave functions of neighboring atoms overlap. Right: The figure on the right shows schematically the band width as a function of atomic number for the rare-earth- and transition metals. Underneath a certain width, the electrons remain localized. For partially filled shells such electrons can be magnetic. But even itinerant electrons can remain magnetic up to a certain band width. At band width over typically 8 eV, the electrons will be itinerant (the material will be metallic) and non-magnetic.*

If electronic correlations are not too strong, the electronic properties can be described by a band structure, which allows one to predict, whether a material is a metal, a semiconductor or an insulator. This is shown in figure 11.3. At $T = 0$ all electronic states are being filled up to the Fermi energy. At finite T the Fermi-Dirac distribution describes the occupancy of the energy levels. If the Fermi energy lies somewhere in the middle of the conduction band, the material will be metallic. If it lies in the middle between valence band and conduction band and these two are separated by a large gap significantly larger than the energy equivalent of room temperature, the material will show insulating behavior. Finally, if the gap is small enough to allow thermal excitations of electrons from the valence band to the conduction band, we have semiconducting behavior. But again, this band structure model describes the electrons with single particle wave functions. Where are the electronic correlations?

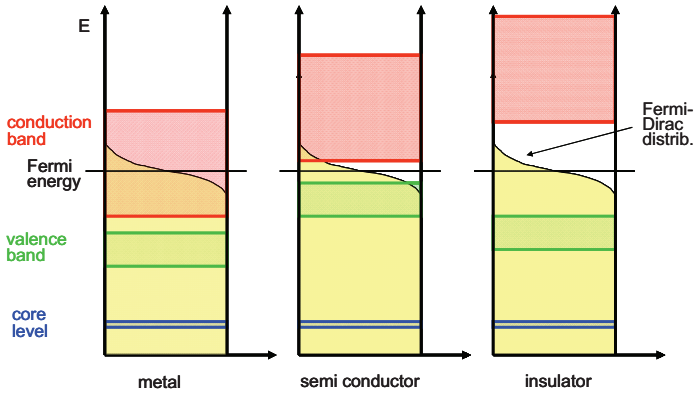

Fig. 11.3: *Schematic band structure for a simple metal, semiconductor and insulator.*

11.3 Electronic correlations

It turns out that electronic correlations are particularly important in materials, which have some very narrow bands. This occurs for example in transition metal oxides or transition metal chalcogenides[2] as well as in some light rare earth intermetallics (heavy fermion systems). Let us chose CoO as a typical and simple example of a transition metal oxide. CoO has the rock salt structure depicted in figure 11.4.

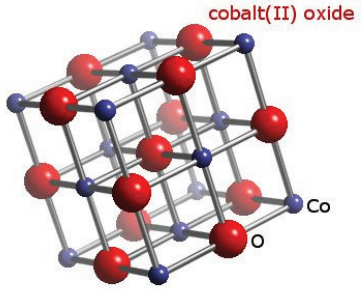

Fig. 11.4: *CoO crystallizes in the rock salt structure.*

The unit cell depicted in figure 11.4 is face centered cubic fcc and contains four formula units. The primitive unit cell of the fcc lattice, however, is spanned by the basis vectors

$$\underline{a}' = \frac{1}{2}a\left(\hat{\underline{e}}_x + \hat{\underline{e}}_y\right) \;;\; \underline{b}' = \frac{1}{2}a\left(\hat{\underline{e}}_y + \hat{\underline{e}}_z\right) \;;\; \underline{c}' = \frac{1}{2}a\left(\hat{\underline{e}}_z + \hat{\underline{e}}_x\right) \qquad (11.1)$$

Here a is the lattice constant, and $\hat{\underline{e}}_x$, $\hat{\underline{e}}_y$, $\hat{\underline{e}}_z$ are the unit basis vectors of the original fcc unit cell. Therefore the primitive unit cell contains exactly one cobalt and one oxygen atom. The electronic configurations of these atoms are: *Co: [Ar]3d^{7}4s^2; O: [He]2s^{2}2p^4*. In the solid, the atomic cores of Co and O have the electronic configuration of Ar and He, respectively. These electrons are very strongly bound to the nucleus and we need not consider them on the usual energy scales for excitations in the solid state. We are left with nine outer electrons for the Co

[2] Chalcogenides are compounds of the heavier chalcogens (group VI elements of the periodic table, particularly sulfides, selenides, tellurides). Even so, oxygen is in the same group of the periodic table, oxides are usually not considered chalcogenides.

and six outer electrons for the O atom in the solid, so that the total number of electrons per primitive unit cell is 9 + 6 = 15. Therefore we have an uneven number of electrons in the primitive unit cell. According to the Pauli principle, each electronic state can be occupied by two electrons, one with spin up and one with spin down. Therefore with an uneven number of electrons, we must have at least one partially filled band and according to figure 11.3, CoO must be a metal.

What does experiment tell us? Well, in fact, CoO is a very good insulator as the resistivity at room temperature amounts to $\rho \sim 10^8\ \Omega cm$. This value can be compared to a good conductor like iron, which has a resistivity of about $10^{-7}\ \Omega cm$. The resistivity of CoO corresponds to activation energies of about *0.6 eV* or a temperature equivalent of *7000 K*, which means there is a huge band gap making CoO a very good insulator. To summarize these considerations: the band theory breaks down already for a very simple oxide consisting of only one transition metal and one oxygen atom!

In order to understand the reason for this dramatic breakdown of band theory, let us consider an even simpler example: the alkali metal sodium. It has the electronic configuration: $Na: [Ne]3s^1 = 1s^2 2s^2 2p^6 3s^1$. Following our argumentation for CoO, sodium obviously has a half-filled 3s band and is therefore a metal. This time our prediction was correct: the electrical resistivity at room temperature is about $5 \cdot 10^{-6}\ \Omega cm$. However, what happens if we pull the atoms further apart and increase the lattice constant continuously? Band theory predicts that for all distances sodium remains a metal, since the 3s band will always be half-filled. This contradicts our intuition and of course also the experiment: at a certain critical separation of the sodium atoms, there must be a transition from a metal to an insulator. It was Sir Nevill Mott (Nobel Laureate in physics of 1977), who predicted this metal-to-insulator transition, which is therefore called the Mott-transition [14]. The physical principle can be made clear with the illustration in figure 11.5.

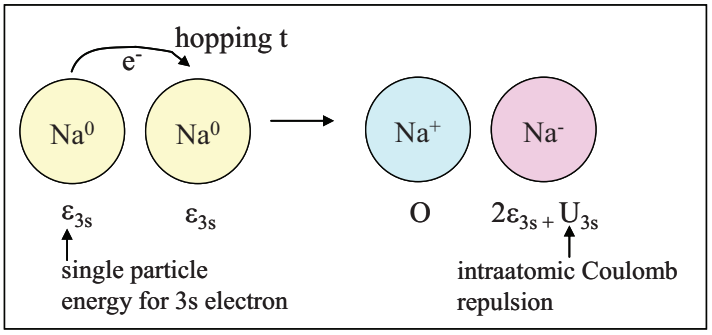

Fig. 11.5: *Illustration of the hopping process of an electron between two neutral sodium ions leading to charge fluctuations.*

On the left of figure 11.5, two neutral sodium atoms are depicted. The atomic energy levels of the outer electrons correspond to an energy ε_{3s}. The wave functions of the 3s electrons will overlap giving rise to a finite probability that an electron can hop from one sodium atom to the other one. Such a delocalization of the electrons is favored according to the Heisenberg uncertainty principle

$$\Delta p \cdot \Delta x \geq \frac{\hbar}{2} \qquad (11.2)$$

(11.2) shows that we can gain kinetic energy, if the electrons become more delocalized. Figure 11.5 on the right shows the situation after the electron transfer. Instead of neutral atoms, we have one Na^+ and one Na^- ion. However, we have to pay a price for the double occupation of the 3s states on the Na^- ion, namely the intra-atomic Coulomb repulsion between the two electrons denoted as U_{3s}. While this is a very simplistic picture, where we assume that the electron is either located on one or the other Na atom, this model describes the two main energy terms by just one parameter: the hopping matrix element *t*, connected to the kinetic energy, and the intra-atomic Coulomb repulsion *U*, connected with the potential energy due to the Coulomb interaction between the two electrons on one site. In this simple model, we have replaced the long range Coulomb potential proportional to $1/r$ with its leading term, an onsite Coulomb repulsion *U*. More realistic models would have to take higher order terms into account but already such a simple consideration leads to very rich physics. We can see from figure 11.5 that electronic conductivity is connected with charge fluctuations and that such charge transfer costs energy, where *U* is typically in the order of 1 or 10 eV. Only if the gain in kinetic energy due to the hopping *t* is larger than the penalty in potential energy *U* can we expect metallic behavior. If the sodium atoms are now being separated more and more, the intra-atomic Coulomb repulsion *U* will maintain its value, while the hopping matrix element *t*, which depends on the overlap of the wave functions, will diminish. At a certain critical value of the lattice parameter *a*, potential energy will win over kinetic energy and conductivity is suppressed. This is the physical principle behind the Mott transition.

More formally, this model can be cast into a model Hamiltonian, the so-called *Hubbard model* [15]. In second quantization of quantum-field theory, one can write down the so-called single band Hubbard Hamiltonian:

$$\mathbf{H} = -t \sum_{\substack{j,l \\ \in n.N.}} \sum_{\sigma} (\mathbf{c}^{+}_{j\sigma}\mathbf{c}_{l\sigma} + \mathbf{c}^{+}_{l\sigma}\mathbf{c}_{j\sigma}) + U \sum_{j} \mathbf{n}_{j\uparrow}\mathbf{n}_{j\downarrow} \tag{11.3}$$

The operator $\mathbf{c}^{+}_{j\sigma}$ creates an electron in the tight binding (Wannier)-state $\Phi(\underline{r} - \underline{R}_j)|\sigma\rangle$, $\mathbf{n}_{j\sigma}$ is the occupation operator $\mathbf{c}^{+}_{j\sigma}\mathbf{c}_{j\sigma}$ of the corresponding Wannier state; *U* is the Coulomb repulsion in one orbital at one site:

$$U = \int dr_1 \int dr_2 \frac{e^2 \left|\Phi(\underline{r}_1 - \underline{R}_j)\right|^2 \left|\Phi(\underline{r}_2 - \underline{R}_j)\right|^2}{4\pi\varepsilon_0 \left|\underline{r}_1 - \underline{r}_2\right|} \tag{11.4}$$

t is the hopping amplitude

$$t = \int d\underline{r}\, \Phi(\underline{r} - \underline{R}_1) \frac{e^2}{4\pi\varepsilon_0 \left|\underline{r} - \underline{R}_2\right|} \Phi(\underline{r} - \underline{R}_2) \tag{11.5}$$

The Hubbard model is a so-called "*lattice fermion model*", since only discrete lattice sites are being considered. It is the simplest way to incorporate correlations due to the Coulomb interaction since it takes into account only the strongest contribution, the onsite Coulomb interaction. Still there is very rich physics contained in this simple Hamiltonian like the physics of ferromagnetic- or antiferromagnetic metals and insulators, charge- and spin density waves and so on [15]. A realistic Hamiltonian should contain many more inter-site terms due to the long range Coulomb interaction and it is quite likely that additional new physics would be contained in such a more realistic model.

The most direct consequence of the onsite Coulomb interaction is that additional so-called Hubbard bands are created due to possible hopping processes. This is illustrated in figure 11.6.

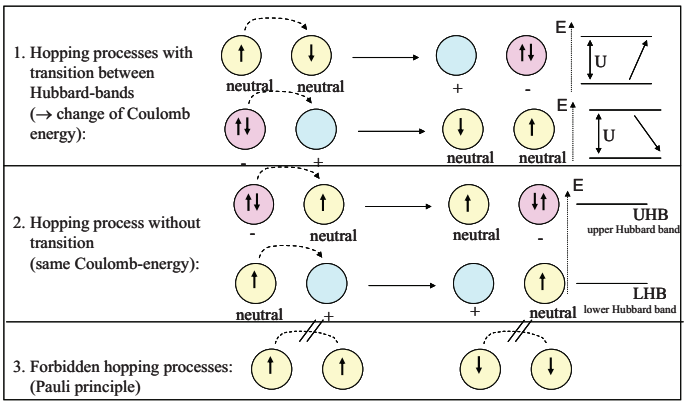

Fig. 11.6: *Illustration of hopping processes between neighboring atoms together with their corresponding energy scales.*

The first row in figure 11.6 shows hopping processes, which are connected with a change of the total Coulomb energy. The second row shows hopping processes without transition. The last row shows hopping processes, which are forbidden due to the Pauli principle. From figure 11.6 we can identify two different energy states. Configurations for which the onsite Coulomb repulsion comes into play have an energy which is higher by the onsite Coulomb repulsion U as compared to such configurations where the electrons are not on the same atom. In a solid these two energy levels will broaden into bands (due to the delocalization of the electrons on many atoms driven by the hopping matrix element t), which are called the *lower Hubbard band* and the *upper Hubbard band*. If these bands are well separated, i. e. the Coulomb repulsion U dominates over the hopping term t, we will have in insulating state, since only the lower Hubbard band is occupied. If the bands overlap, we will have a metallic state. Note however that lower and upper Hubbard band are totally different from the usual band structure of solids as they do not arise due to the interaction of the electrons with the atomic cores but due to electronic correlations. As a result the existence of the Hubbard bands depends on the electronic occupation. Figure 11.6 illustrates how in correlated electron systems the energy terms for simple hopping processes depend of the occupation of neighboring sites and how hopping transports spin information. The apparently simple single electron operator gets complex many body aspects.

11.4 Example: doped CMR manganites

In what follows we will discuss one example of highly correlated electron systems, the mixed valence manganites (see e.g. [16]). Their stoichiometric formula is $A_{1-x}B_xMnO_3$, where A is a trivalent cation (A= *La, Pr, Nd, Sm, Eu, Gd, Tb, Dy, Ho, Er, Y, Bi*) and B is a divalent cation (B = *Sr, Ca, Ba, Pb*). The doping with divalent cations leads to a mixed valence on the manganese sites. If we neglect covalency[3] and describe these compounds in a purely ionic model, charge neutrality requires that manganese exists in two valence states: Mn^{3+} and Mn^{4+} according to the respective doping levels:

$$A_{1-x}B_xMnO_3 \rightarrow \left[A^{3+}_{1-x}B^{2+}_x\right]\left[Mn^{3+}_{1-x}Mn^{4+}_x\right]O_3 \qquad (11.6)$$

[3] an assumption which is often made but certainly not entirely adequate this class of materials!

This is why one speaks of mixed valence manganites as Mn exists in two valence states with the following electronic configurations:

Mn^{3+}: $[Ar]3d^4$ / Mn^{4+}: $[Ar]3d^3$ (11.7)

The structure of these mixed valence manganites is related to the perovskite structure depicted in figure 11.7.

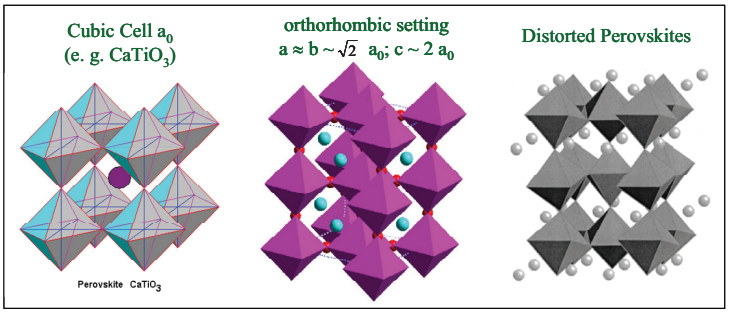

Fig. 11.7: *The perovskite structure. Left: The ideal cubic structure; middle: the cubic structure in orthorhombic setting; right: the distorted perovskite structure with rotated and tilted oxygen octahedra.*

Perovskite is a mineral $CaTiO_3$, which has a cubic crystal structure, where the smaller Ca^{2+} metal cation is surrounded by six oxygen atoms forming an octahedron; these corner sharing octahedra are centered on the corners of a simple cubic unit cell and the larger Ti^{4+} metal cation is filling the interstice in the centre of the cube. This ideal cubic perovskite structure is extremely rare. It only occurs when the sizes of the metal ions match to fill the spaces between the oxygen atoms ideally. Usually there is a misfit of the mean ionic radii of the A and B ions, which leads to sizeable tilts of the oxygen octahedra. The resulting structure is related to the perovskite structure as illustrated in figure 11.7: in the middle of figure 11.7 the cubic perovskite structure is shown in a different, orthorhombic setting. The usually observed perovskite structure is related to this structure by a tilting of the corner shared oxygen octahedra as shown on figure 11.7 on the right. Such an orthorhombic structure is for example realized in $LaMnO_3$ with space group Pbnm. Orthorhombic or rhombohedral structures occur if the so-called *tolerance factor T*, which is the measure for the misfit of the ionic radii deviates significantly from the value 1, where *T* is defined as:

$$T = \frac{1}{\sqrt{2}} \frac{\langle R_{A,B} \rangle + \langle R_O \rangle}{\langle R_{MN} \rangle + \langle R_O \rangle} \qquad (11.8)$$

For the manganites the octahedral surrounding of the Mn ions leads to so-called crystal field effects. To explain these we stay in the ionic model and describe the oxygen atoms as O^{2-} ions. The outer electrons of the Mn ions, the 3d electrons, experience the electric field created by the surrounding O^{2-} ions of the octahedral environment. This leads to a splitting of the electronic levels as depicted in figure 11.8, the so-called *crystal field splitting*. Those 3d orbitals, which have loops of the electron density pointing towards the negatively charged oxygen ions, will have higher energies with respect to those 3d orbitals, where the loops point in directions between the oxygen atoms. This leads to a splitting of the d-electron levels into three so-called t_{2g} and two so-called e_g crystal field levels. For the manganites this crystal field splitting is typically in the order of 2 eV. If we now consider a Mn^{3+} ion, it depends on the ratio between the crystal field splitting and the intra-atomic exchange, how the electrons will occupy these crystal field levels. According to Hunds' rule, electrons tend to maximize the

total spin i. e. occupy energy levels in such a way that the spins of all electrons are parallel as far as Pauli principle permits. This is a consequence of the Coulomb interaction within a single atom and is expressed by the Hunds' rule energy J_H. If the crystal field splitting is much larger than Hunds' coupling, a *low spin state* will result where all electrons are in the lower t_{2g} level and two of these t_{2g} orbitals are single occupied, while one orbital is double occupied. Due to Pauli principle the spins in the doubly occupied orbital have to be antiparallel giving rise to a total spin $S = 1$ for this low spin state. Usually, however, in the manganites Hunds' rule coupling amounts to about 4 eV, and is stronger than the crystal field splitting. In this case the *high spin state* shown in figure 11.8 is realized, where four electrons with parallel spin occupy the three t_{2g} levels plus one of the two e_g levels. The high spin state has a total spin of $S = 2$ and the orbital angular momentum is quenched[4]. This state has an orbital degree of freedom. The e_g electron can either occupy the $3z^2$-r^2 or the x^2-y^2 orbital. Nature does not like such degenerate states. The MnO_3 octahedra will undergo a geometric distortion that removes this degeneracy and lowers the overall energy of the complex. This is called the *Jahn-Teller effect*, which is depicted in figure 11.8 as a further splitting of the d-electron levels. For the case shown in the figure, the c-axis of the octahedron has been elongated thus lowering the energy of the $3z^2$-r^2 orbital with respect to the energy level of the x^2-y^2 orbital. The Jahn-Teller splitting in the manganites has a magnitude of typically some 0.6 eV.

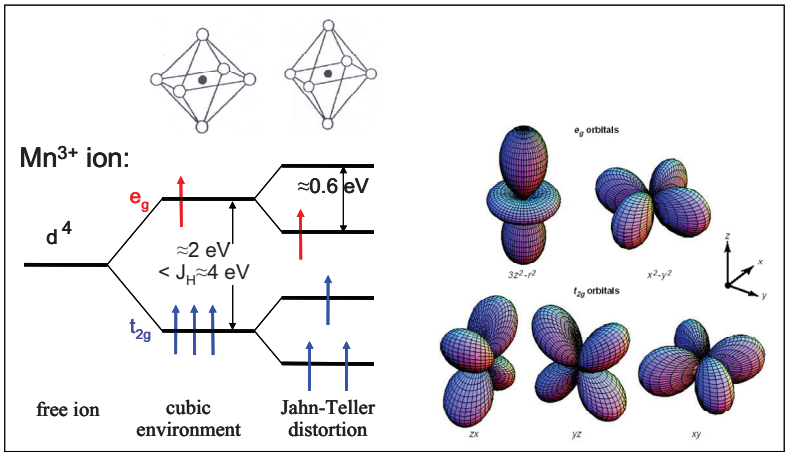

Fig. 11.8: *Energy level diagram for a MnO^{3+} ion in an oxygen octahedron. For the free ion, the four 3d electron levels are degenerate. They split in a cubic environment into t_{2g} and e_g levels. If Hunds' rule coupling is stronger than crystal field splitting, a high spin state results. The degeneracy of the e_g level is lifted by a Jahn-Teller distortion, which results in an elongation of the oxygen octahedra. On the right of the figure, the 3d orbitals corresponding to the different orbital magnetic quantum numbers are depicted.*

The Jahn-Teller effect demonstrates nicely how in these transition metal oxides electronic degrees of freedom and lattice degrees of freedom are coupled. Only the Mn^{3+} ion with an even number of electrons (the so-called *Kramer ion*) exhibits the Jahn-Teller effect, while the Mn^{4+} ion with only three d electrons does not. A transfer of charge between neighboring manganese ions is accompanied with a change of the local distortion of the oxygen octahe-

[4] i.e. vanishes: L=0

dron: a so-called lattice polaron. Due to the Jahn-Teller effect, charge fluctuations and lattice distortions become coupled in these mixed valence transition metal oxides.

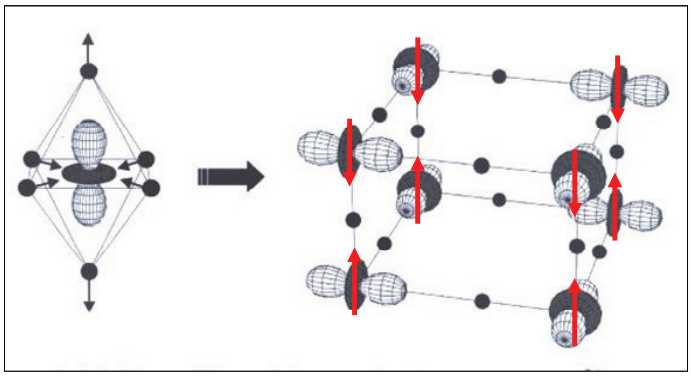

Fig. 11.9: *Orbital order in $LaMnO_3$. Below the Jahn-Teller transition temperature of 780 K, a distinct long range ordered pattern of Jahn-Teller distortions of the oxygen octahedra occurs leading to orbital order of the e_g orbitals of the Mn^{3+} ions as shown. Also shown is the antiferromagnetic spin order which sets in below the Néel temperature $T_N \sim 145$ K. Oxygen atoms are represented by filled circles, La is not shown.*

Having explained the Jahn-Teller effect, we can now introduce an important type of order occurring in these transition metal oxides: *orbital order*. Let us look at the structure of the $LaMnO_3$ parent compound. Here all manganese are trivalent and are expected to undergo a Jahn-Teller distortion. In order to minimize the elastic energy of the lattice, the Jahn-Teller distortions on neighboring sites are correlated. Below the Jahn-Teller transition temperature $T_{JT} \sim 780$ K, a cooperative Jahn-Teller transition takes place, with a distinct pattern of distortions of the oxygen octahedra throughout the crystal lattice as shown in figure 11.9. This corresponds to a long range orbital order of the e_g electrons, which should not be confused with magnetic order of an orbital magnetic moment. In fact, the orbital magnetic moment is quenched i. e. totally suppressed by the crystal field surrounding the Mn^{3+} ions. Orbital ordering instead denotes a long range ordering of an anisotropic charge distribution around the nuclei. As the temperature is further lowered, magnetic order sets in at the Néel temperature of 145 K. In $LaMnO_3$ the spin degree of freedom of the Mn^{3+} ion orders antiferromagnetically in so-called A-type order: spins within the a-b plane are parallel, while spins along c are coupled antiferromagnetically. This d-type orbital ordering and A-type antiferromagnetic ordering results from a complex interplay between structural-, orbital- and spin degrees of freedom and the relative strengths of the different coupling mechanisms in $LaMnO_3$.

The situation becomes even more complex for doped manganites, where the charge on the manganese site becomes an additional degree of freedom due to the two possible manganese valances Mn^{3+} and Mn^{4+}. In order to minimizes the Coulomb interaction between neighboring manganese sites, so-called *charge order* can develop. This is shown for the example of half-doped manganites in figure 11.10.

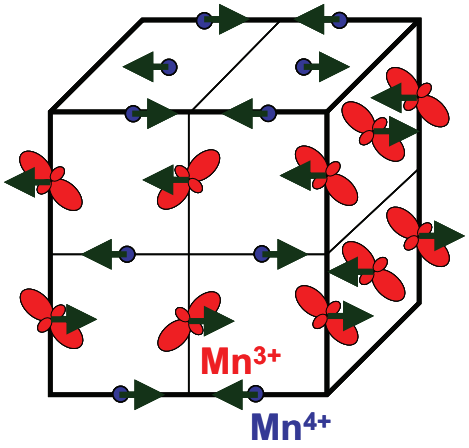

Fig. 11.10: *Charge-, orbital- and spin-order in the half-doped manganite* $\left[La^{3+}_{1/2}Sr^{2+}_{1/2}\right]\left[Mn^{3+}_{1/2}Mn^{4+}_{1/2}\right]O_3$

These half-doped manganites show antiferromagnetic spin order, a checkerboard-type charge order with alternating Mn^{4+} and Mn^{3+} sites and a zigzag orbital order of the additional e_g electron present on the Mn^{3+} sites. This is only one example of the complex ordering phenomena that can occur in doped mixed valence manganites. These ordering phenomena result from a subtle interplay between lattice-, charge-, orbital-, and spin degrees of freedom and can have as a consequence novel phenomena and functionalities like the colossal magnetoresistance effect.

How are these ordering phenomena related with the macroscopic properties of the system? To answer this question, let us look at the resistivity of doped Lanthanum-Strontium-Manganites, see figure 11.11.

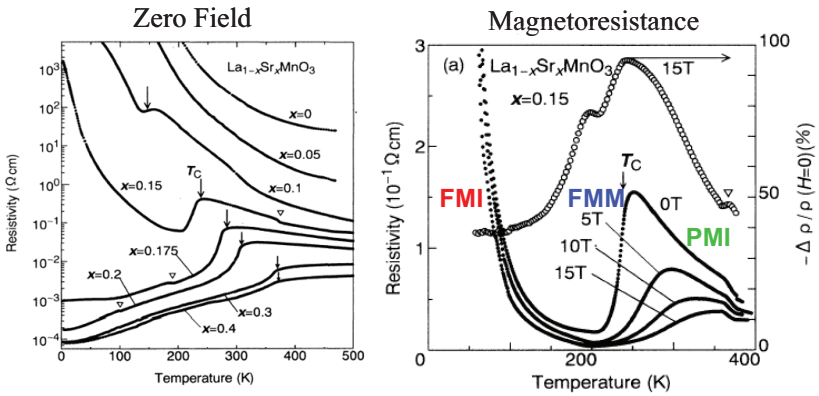

Fig. 11.11: *Resistivity in the $La_{1-x}Sr_xMnO_3$ series, taken from [17]. Left: resistivity in zero field for various compositions from x = 0 to x = 0.5. Right: resistivity for x = 0.15 in different magnetic fields as well as the magnetoresistance defined as the change in resistivity relative to its value for field equal zero.*

The zero field resistance changes dramatically with composition. The x = 0 compound shows insulating - or better semiconducting - behavior as the resistivity increases with decreasing temperature. The higher doped compounds e. g. x = 0.4 are metallic as the resistivity decreases with decreasing temperature. Note however that the resistivity of these compounds is still about three orders of magnitude higher than for typical good metals. At an intermediate composition x = 0.15, the samples are insulators at higher temperatures down to about 250 K, then a dramatic drop of the resistivity indicating an insulator-to-metal transition and again an upturn below about 210 K with typical insulating behavior. The metal-insulator transition occurs at a temperature, where the ferromagnetic long-range order sets in. Around this temperature we also observe a very strong dependence of resistivity on external magnetic field. This is the so-called *colossal magnetoresistance effect*. In order to appreciate the large shift in the maximum of the resistivity curve with field shown in figure 11.11, one should remember that the energy scales connected with the Zeeman interaction of the spin ½ electron in an applied magnetic field are very small: the energy equivalent of 1 Tesla for a spin ½ system corresponds to 0.12 meV, which in turn corresponds to a temperature equivalent of 1.3 K.

Can we understand this strong dependence of the resistance on an external field in simple terms? Indeed there is a mechanism for a magnetic exchange interaction which can give rise to a ferromagnetic order and at the same time is connected with conductivity. This mechanism is called *double exchange* and is depicted schematically in figure 11.12. This exchange interaction can only occur between transition metals of different valences. In the case depicted in figure 11.12, an e_g electron from a Mn^{3+} ion hops into the oxygen 2p orbital while the other oxygen 2p electron hops on the Mn^{4+} site. Since e_g and t_{2g} electrons are strongly coupled through the Hund's rule coupling, this transfer of an electron from Mn^{3+} to Mn^{4+} can only occur if the spins of the t_{2g} electrons are parallel.

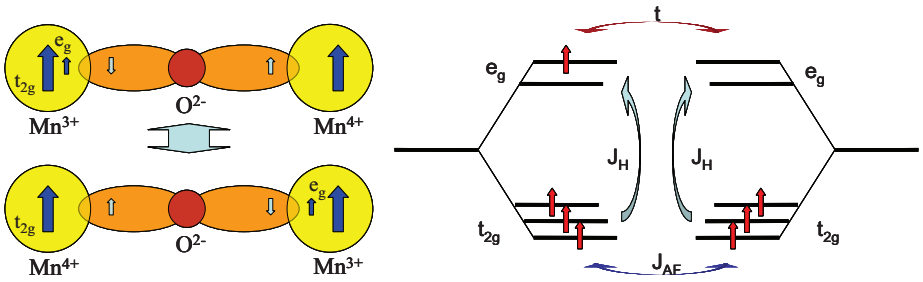

Fig. 11.12: *Schematic representation of the double exchange interaction. On the left, the transfer of an e_g electron through the intervening 2p orbitals from a Mn^{3+} to a Mn^{4+} ion is shown. On the right, this process is illustrated in an energy level diagram for the manganese atoms. There is an antiferromagnetic exchange interaction J_{AF} between the t_{2g} electrons. Within the Mn atoms, Hund's rule coupling J_H is assumed to be larger than the crystal field splitting. t represents the hopping term between the two Mn sites. Only if the t_{2g} spins of both Mn atoms are parallel can the e_g electron hop between the two sites. If the t_{2g} spins are anti-parallel, hopping is suppressed by the strong Hund's rule coupling between e_g and t_{2g} spins. As double exchange is stronger than J_{AF}, the Mn spins tend to align parallel.*

For an anti-parallel orientation of the t_{2g} spins hopping is suppressed due to the penalty of the Hund's rule coupling energy J_H. Therefore the double exchange between Mn^{3+} and Mn^{4+} ions is ferromagnetic and this ferromagnetic exchange is connected with conductivity. In terms of

the double exchange mechanism, we can now explain the insulator-to-metal transition occurring at T_C: in the paramagnetic states, the spins of the t_{2g} electrons fluctuate, thus suppressing the hopping of the e_g electron due to Hund's rule coupling. The system behaves like an insulator. As soon as ferromagnetism sets in, hopping between neighboring manganese sites can occur and the resistivity drops. An applied external field aligns the Mn spins even above the Curie temperature. This induced magnetization permits an increased hopping of the e_g electrons and thus to a decrease of resistivity. Thus in this simple model of the double exchange interaction, magnetoresistance can be explained qualitatively. However, it has been shown [18] that the double exchange interaction alone gives the wrong magnitude for the magnetoresistance effect. Other effects, such as the electron-phonon interaction, have to be taken into account.

It is also clear that our entire discussion starting from ionic states is only a crude approximation to the real system. Therefore we now have to pose the question how can we determine the true valence state? Or more general, which experimental methods exist to study the complex ordering and excitations of the charge-, orbital-, spin- and lattice- degrees of freedom in these complex transition metal oxides?

11.5 Experimental techniques: Neutron and x-ray scattering

In this chapter we will give a first glimpse into how these various ordering phenomena can be studied experimentally. Obviously we need probes with atomic resolution which interact as well with the spins as with the charges in the system. Therefore neutron and x-ray scattering are the ideal microscopic probes to study the complex ordering phenomena and their excitation spectra. The lattice and spin structure can be studied with neutron diffraction from a polycrystalline or single crystalline sample as detailed in the chapter on "Structure determination" of this course. Figure 11.13 shows as an example a powder spectrum of a $La_{7/8}Sr_{1/8}MnO_3$ material.

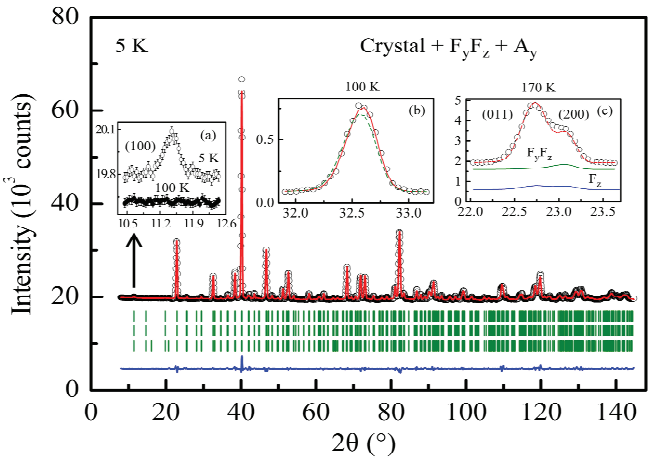

Fig. 11.13: *High resolution neutron powder diffractogram of a powdered single crystal of $La_{7/8}Sr_{1/8}MnO_3$. Circles are the data points, the solid line is the result of the structural refinement. Structural and magnetic Bragg reflections are located at the 2θ values indicated by the vertical lines below the spectrum. The solid line underneath shows the difference between the observed and simulated spectrum. Inserts show details in certain 2θ regions e. g. a magnetic Bragg reflection at very low Q.*

Preferably the structure determination from polycrystalline material is done by a simultaneous refinement of neutron and x-ray powder diffraction spectra, as the two probes have different contrast mechanisms. For example an x-ray spectrum contains less precise information on the structural parameters for the oxygen atoms, since these rather light atoms scatter much weaker than the heavier metal atoms. Neutrons have the added advantage of a vanishing form factor for nuclear scattering and therefore give information up to larger momentum transfer. This is particularly useful for the determination of the thermal parameters (Debye-Waller factors). Neutrons also allow one to determine the magnetic structure from a powder diffraction pattern. As a result of such a refinement, one can show that the low temperature structure of this compound is monoclinic or even triclinic[5], i.e. there exists an additional distortion from the Pnma structure introduced in chapter 11.4. Ferromagnetic order becomes visible by intensity on top of the structural Bragg peak. Antiferromagnetic order is usually (but not always!) connected with an increase in the unit cell dimension, which in turn shows up in the diffractogram by additional superstructure reflections between the main nuclear reflections. It is beyond the scope of this lecture to discuss the experimental and methodological details of such a structure analysis or to present detailed results on specific model compounds. For this we refer to the literature, e.g. [16]. We just want to mention that with detailed structural information, we cannot only determine the lattice- and spin structure, but also the charge- and orbital order and can relate them to macroscopic phenomena such as the CMR effect. At first sight it might be surprising that neutron diffraction is able to give us information about charge order. We have learnt in the introductory chapters that neutrons interact mainly through the strong interaction with the nuclei and through the magnetic dipole interaction with the magnetic induction in the sample. So how can neutrons give information about charge order? Obviously charge order is not determined directly with neutrons. However in a transition metal-oxygen bond, the bond length will depend on the charge of the transition metal ion. The higher the positive charge of the transition metal, the shorter will be the bond to the neighboring oxygen, just due to Coulomb attraction. This qualitative argument can be quantified in the so-called *bond valence sum*. There exists an empirical correlation between the chemical bond length and the bond valence:

$$s_{ij} = \exp\left(\frac{R_0 - R_{ij}}{B}\right) \tag{11.9}$$

Here, the R_{ij} are the experimentally determined bond lengths, B is a constant ($B = 0.37$ according to [19]) and R_0 are tabulated values for the cation-oxygen bonds see e. g. [19]. Table 11.1 reproduces some of these values.

Ions	La^{3+}	Pr^{3+}	Nd^{3+}	Sm^{3+}	Eu^{3+}	Gd^{3+}	Tb^{3+}	Dy^{3+}	Er^{3+}
R_0	2.172	2.138	2.105	2.090	2.074	2.058	2.032	2.001	1.988
Ions	Tm^{3+}	Yb^{3+}	Y^{3+}	Ca^{2+}	Sr^{2+}	Ba^{2+}	Mn^{3+}	Mn^{4+}	
R_0	1.978	1.965	2.019	1.967	2.118	2.285	1.760	1.753	

Tab. 11.1: *R_0 values of cation-oxygen bonds in manganese perovskites needed for the bond valence calculation (11.9); taken from [19].*

[5] Highest resolution synchrotron x-ray powder diffraction is best suited to solve the problem of the metric of the low temperature structure, as peak splitting can be detected much better with this method than with laboratory x-ray- or neutron powder diffraction which has generally less resolution

Finally the valence or oxidation state of the cation can be determined by the sum of the bond valences around the respective atom i according to:

$$V_i = \sum_{ij} s_{ij} \qquad (11.10)$$

Even though this method to determine the valence state is purely empirical, it proves to be rather precise, if compared to other techniques. The values of the valences found with this method differ significantly from a purely ionic model. Instead of integer differences between charges on different transition metal ions, one finds more likely differences of a few tenth of a charge of an electron.

Just like charge order, orbital order is not directly accessible to neutron diffraction techniques since orbital order represents an anisotropic charge distribution and neutrons do not directly interact with the charge of the electron. However, we have seen in the discussion of the Jahn-Teller effect (figure 11.8 and figure 11.9) that an orbital order is connected with a distortion of the local environment visible in different bond lengths within the anion complex surrounding the metal cation. In this way, by a precise determination of the structural parameters from a combined neutron and x-ray powder diffraction experiment, one can determine in favorable cases the ordering pattern of all four degrees of freedom: lattice, spin, charge and orbitals.

One can ask, whether there is not a more direct way to determine charge- and orbital order. The scattering cross section of x-rays contains the atomic form factors, which are Fourier transforms of the charge density distribution of an atom. Naively one would think therefore that charge and orbital order can be easily determined with x-ray scattering. However, as discussed in the last paragraph on bond valence sums, it is usually only a fraction of an elementary charge, which contributes to charge- or orbital ordering. If we take the case of the Mn atom, the atomic core has the Ar electron configuration i. e. 18 electrons are in closed shells with spherical charge distributions. For the Mn^{4+} ion, three further electrons are in the t_{2g} levels. Since in scattering, we measure intensities and not amplitudes, these 21 electrons contribute $21^2 r_0^2$ to the scattered intensity[6]. If the difference in charge between neighboring Mn ions amounts to 0.2e, this will give an additional contribution to the scattered intensity of $0.2^2 r_0^2$. The effect of charge ordering in x-ray scattering is therefore $\frac{0.2^2}{21^2} \sim 1\times10^{-4} = 0.1\,‰$. In this simple consideration, we have completely ignored the scattering from all the other atoms, so that detection of charge- or orbital ordering becomes even more difficult in reality. There is, however, a way to enhance the scattering from non-spherical charge distributions, the so-called *anisotropic anomalous x-ray scattering*. It was first discussed by Templeton and Templeton [20] and applied for orbital order in manganites by Murakami et al. [21]. The principle of this technique is shown in figure 11.14.

[6] The classical electron radius $r_0=e/mc^2=2.82$ fm is the natural unit for the scattering amplitude of x-ray Thomson scattering

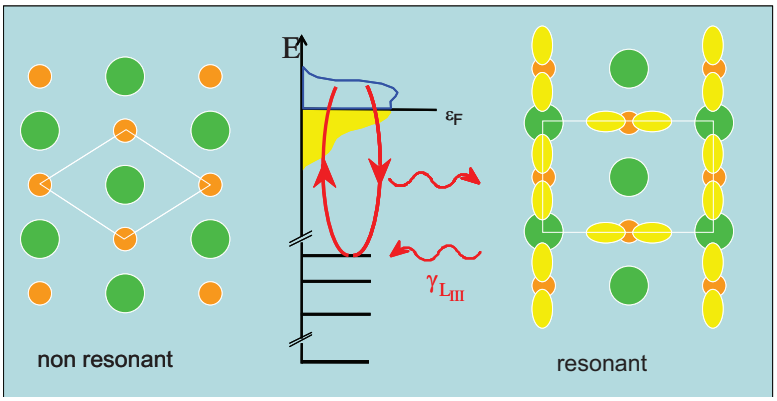

Fig. 11.14: *Illustration of the principle of anisotropic anomalous x-ray scattering for a hypothetical 2-dimensional compound consisting of two atoms with different number of electrons. On the left a possible reconstruction of the charge distribution from a laboratory x-ray source is shown. Non resonant x-ray scattering is sensitive mainly to the spherical charge distribution and a unit cell as shown by the white lines is being deduced from this experiment. In the middle the principles of a resonance x-ray scattering is depicted in an energy level diagram (see text). On the right, the charge distribution deduced from such an anomalous x-ray scattering experiment is shown. Now an orbital ordering pattern becomes apparent, which could not be detected with non-resonant x-ray scattering. The unit cell is evidently larger, giving rise to superstructure reflections which appear at resonance.*

The figure shows scattering from a hypothetical two dimensional compound consisting of two atoms with different number of electrons. Non resonant x-ray scattering as it can be done on a laboratory x-ray source is sensitive mainly to the spherical charge distribution. A reconstruction of the charge distribution done from such an experiment might look schematically as shown on the left of figure 11.4. The corresponding crystal structure can be described with a primitive unit cell indicated by the white lines. In order to enhance the scattering from the non spherical part of the charge distribution, an experiment can be done at a synchrotron radiation source. There the energy of the x-rays can be tuned to the energy of an absorption edge as shown in the middle of figure 11.4. Now second order perturbation processes can occur, where a photon induces virtual transitions of an electron from a core level to empty states above the Fermi energy and back with re-emission of a photon of the same energy as the incident photon. Since second order perturbation processes have a resonant denominator, this scattering will be largely enhanced close to an absorption edge. If the intermediate states in this resonant scattering process are somehow connected to orbital ordering, scattering from orbital ordering will be enhanced. Thus in the resonant scattering experiment, orbital order can become visible as depicted schematically on the right of figure 11.14. With the shown arrangement of orbitals, the true primitive unit cell of this hypothetical compound is obviously larger than the unit cell that was deduced from the non resonant scattering experiment (shown on the left), which was not sensitive enough to determine the fine details of the structure. An increase of the unit cell dimensions in real space, however, is connected with a decrease of the distance of the reciprocal lattice points, i. e. an increase in the number of Bragg reflections. Therefore orbital order is visible by a resonant scattering process in the appearance of additional superstructure reflections. The intensity of these reflections has strong energy dependence as we would expect for a second order perturbation process. This type of

scattering experiment is called anisotropic anomalous x-ray scattering, since it is sensitive to the anisotropic local charge distribution around an atom.

Figure 11.15 shows data from such a resonant scattering experiment [22] together with its interpretation in terms of an orbital polaron lattice [23].

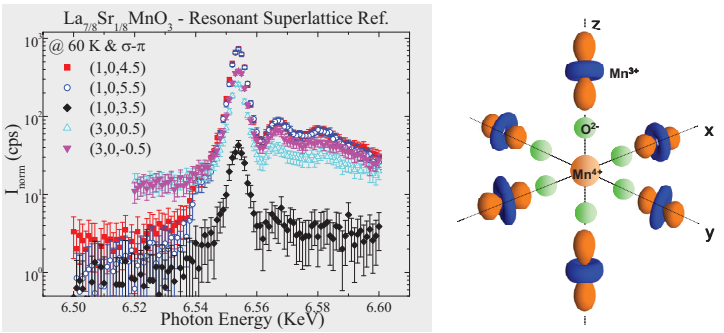

Fig. 11.15: *The figure on the left shows the dependence of the intensity of resonant superlattice reflections from $La_{7/8}Sr_{1/8}MnO_3$ as a function of the energy of the incident photons. Clearly visible is the strong resonant enhancement at the K-absorption edge of Mn (note the logarithmic intensity scale). Several reflections with half indices along c become visible at resonance. The interpretation of this experiment is given in real space on the right of the figure. There is an alternating arrangement of Mn^{3+} and Mn^{4+} ions. The additional electron of the Mn^{3+} ion occupies an e_g orbital, which points towards the Mn^{4+} ion. This arrangement is called an orbital polaron. In the ferromagnetic insulating phase of $La_{7/8}Sr_{1/8}MnO_3$ below 155 K, these orbital polarons arrange into a long ranged ordered orbital polaron lattice.*

The figure gives a nice example of how anisotropic anomalous x-ray scattering gives detailed information on charge- and orbital ordering in solids. Its advantage is that it is element specific (due to the different absorption edge energies for the different elements) and that it combines diffraction and spectroscopy. This can also be seen in figure 11.15: there is a distinct fine structure in the resonance above the absorption edge, which gives information about the density of states of the unoccupied orbitals above the Fermi level.

So far we have discussed some powerful experimental techniques to determine the various ordering phenomena in complex transition metal oxides. Scattering can give much more information than just on the time averaged structure. Quasielastic diffuse scattering gives us information on fluctuations and short range correlations, i. e. short range correlations of polarons above the phase transition, magnetic correlations in the paramagnetic state, local dynamic Jahn-Teller distortions above the Jahn-Teller transition etc. Studying these correlations and fluctuations help us to understand what drives the respective phase transitions into long range order. The relevant interactions, which give rise to these ordering phenomena, can be determined from inelastic scattering experiments as we have learnt in the chapter on "Inelastic neutron scattering". For example, one can determine the exchange interactions from measurements of the spin wave spectra and compare with models for superexchange interactions and double exchange in order to verify or falsify the simple model explanations for the CMR effect discussed in chapter 11.4. Since there is a huge amount of such experiments on highly correlated transition metal oxides and chalcogenides, a review of these experiments definitely goes far beyond the scope of this introductory lecture.

11.6 Summary

This chapter gave a first introduction into the exciting physics of highly correlated electron systems, restricted to the complex transition metal oxides and -chalcogenides. The main message can be summarized in figure 11.16.

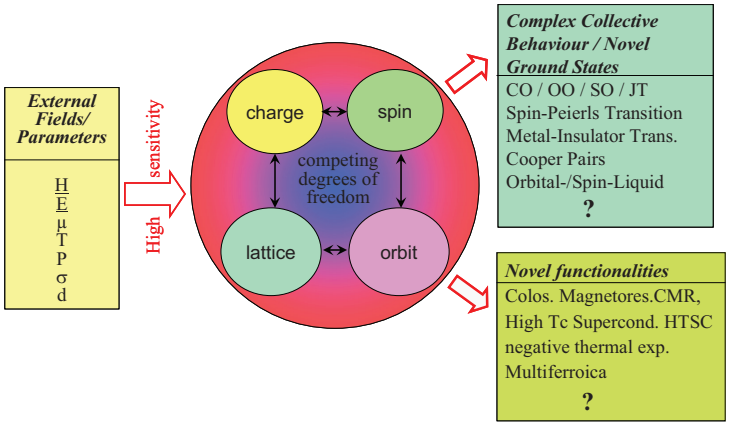

Fig. 11.16: *Illustration of complexity in correlated electron systems. Meaning of the symbols is: H, E: magnetic and electric field, respectively; μ: chemical potential (doping); T: temperature; P: pressure; σ: strain (epitaxial growth); d: dimensionality (e. g. bulk versus thin film systems); CO: charge order; OO: orbital order; SO: spin order; JT: Jahn-Teller transition.*

The complexity in these correlated electron systems arises from the competing degrees of freedom: charge, lattice, orbit and spin. The ground state is a result of a detailed balance between these different degrees of freedom. This balance can be easily disturbed by external fields or other thermodynamical parameters, giving rise to new ground states or complex collective behavior. Examples are the various ordering phenomena discussed, Cooper pairing in superconductors, so-called spin Peierls transitions in one dimensional systems etc. This high sensitivity to external parameters as well as the novel ground states of the systems gives rise to novel functionalities, such as the colossal magnetoresistance effect, high temperature superconductivity, multiferroic behavior and many more. A theoretical description of these complex systems starting from first principles, like Schrödinger equation in quantum mechanics or the maximization of entropy in statistical physics, is bound to fail due to the large number of strongly interacting particles. Entirely new approaches have to be found to describe the emergent behavior of these complex systems. Therefore highly correlated electron systems are a truly outstanding challenge in modern condensed matter physics. We have shown in this lecture that neutron and x-ray scattering are indispensable tools to disentangle this complexity experimentally. They are able to determine the various ordering phenomena as well as the fluctuations and excitations corresponding to the relevant degrees of freedom. No other experimental probe can give so much detailed information on a microscopic level as scattering experiments.

References

[1] R.B. Laughlin and D. Pines; *The theory of everything*; PNAS 97 (2000), 28

[2] T. Vicsek; *The bigger picture*; Nature 418 (2002), 131

[3] J.G. Bednorz, K.A. Müller; *Possible high T_C superconductivity in the Ba-La-Cu-O system*; Z. Phys. B 64 (1986), 189

[4] A-M. Haghiri-Gosnet1 and J-P. Renard; *CMR manganites: physics, thin films and devices (TOPICAL REVIEW)*; J. Phys. D: Appl. Phys. 36 (2003) R127

[5] G. Binasch, P. Grünberg, F. Saurenbach, and W. Zinn, *Enhanced magnetoresistance in layered magnetic structures with antiferromagnetic interlayer exchange;* Phys. Rev. B 39, (1989), 4828
and
M.N. Baibich, J.M. Broto, A. Fert, F. Nguyen van Dau, F. Petroff, P. Eitenne, G. Creuzet, A. Friederich, and J. Chazelas; *Giant magnetoresistance of (001)Fe/(001)Cr magnetic superlattices;* Phys. Rev. Lett. 61 (1988), 2472

[6] MH. Phan, SC. Yu; *Review of the magnetocaloric effect in manganite materials*; JMMM 308 (2007), 325

[7] M. Fiebig; *Revival of the magnetoelectric effect*; J. Phys. D: Appl. Phys. 38 (2005), R123

[8] E. J. W. Verwey; *Electronic conduction of magnetite (Fe_3O_4) and its transition point at low temperatures*; Nature 144 (1939), 327

[9] G.D. Barrera, J.A.O. Bruno, T.H.K. Barron et al.; *Negative thermal expansion*; J. Phys-Condens. Mat. 17 (2005), R217

[10] E. Dagotto; *Complexity in strongly correlated electronic systems*; Science 309 (2005), 257

[11] see e.g.
N.W. Ashcroft, N.D. Mermin; *Solid state physics*; Holt, Rinehart and Winston, 1976
or
H. Ibach, H. Lüth; *Solid-state physics: An introduction to principles of materials science*; Springer, 2003

[12] J Bardeen, L. N. Cooper & J. R. Schrieffer; *Nobel Prize in Physics 1972 for their jointly developed theory of superconductivity, usually called the BCS-theory*; http://nobelprize.org/nobel_prizes/physics/laureates/1972/index.html

[13] e.g. K. Held, O.K. Andersen, M. Feldbacher, A. Yamasaki, Y.F. Yang; *Bandstructure meets many-body theory: the LDA + DMFT method*; J. Phys. – Condens. Mat. 20 (2008), 064202

[14] N.F. Mott; *Metal-insulator transition*; Rev. Mod. Phys. 40 (1968), 677

[15] a good introduction into the physics of correlated electrons and the Hubbard model is provided by:
P. Fazekas; *Lecture notes on electron correlation and magnetism (Series in Modern Condensed Matter Physics, Vol. 5)*; World Scientific, 2003

[16] T. Chatterji (Ed.); *Colossal magnetoresistive manganites*; Kluwer Academic, 2004

[17] A. Urushibara, Y. Moritomo, T. Arima, A. Asamitsu, G. Kido, Y. Tokura; *Insulator-metal transition and giant magnetoresistance in $La_{1-x}Sr_xMnO_3$*; Phys. Rev. B 51 (1995), 14103

[18] A.J. Millis, P.B. Littlewood, B.I. Shraiman ; *Double exchange alone does not explain the resistivity of $La_{1-x}Sr_xMnO_3$* Phys. Rev. Lett. 74 (1995), 5144

[19] G.H. Rao, K. Bärner & I.D. Brown; *Bond-valence analysis on the structural effects in magnetoresistive manganese perovskites*; J. Phys.: Condens. Matter 10 (1998), L757

[20] D. H. Templeton, L. K. Templeton, J. C. Phillips & K. O. Hodgson; *Anomalous scattering of x-rays by caesium and cobalt measured with synchrotron radiation*; Acta Cryst. A 36 (1980), 436
[21] Y. Murakami, J. P. Hill, D. Gibbs, M. Blume, I. Koyama, M. Tanaka, H. Kawata, T. Arima, Y. Tokura, K. Hirota & Y. Endoh; *Resonant x-ray scattering from orbital ordering in $LaMnO_3$*; PRL 81 (1998), 582
[22] Y. Su, Th. Brückel et al., unpublished results
[23] J. Geck, B. Wochner, S. Kiele, R. Klingeler, P. Reutler, A. Revcolevschi & B. Büchner; *Orbital polaron lattice formation in lightly doped $La_{1-x}Sr_xMnO_3$*; PRL 95 (2005), 236401

12

Surfaces, interfaces and thin films investigated by neutron reflectometry

Emmanuel Kentzinger and Ulrich Rücker

12. Surfaces, interfaces and thin films investigated by neutron reflectometry

Emmanuel Kentzinger and Ulrich Rücker

IFF-Scattering Methods

12.1. Introduction

Neutron reflectometry is a relatively new technique that allows determining the nuclear and magnetization profile along the depth of a nanometric thin film system. It has been extensively used for solving soft matter problems like polymer mixing, the structure of liquids at the surface [1] or the structure of bio-mimetic membranes [2,3]. The key property of neutrons for polymer studies is their large contrast in nuclear scattering length between hydrogen and deuterium which allows selective labeling by deuteration.

In the mid 1980's, a new field of application of neutron reflectometry emerged. Following the discovery of new magnetic phenomena in ultra-thin films, interlayer exchange coupling and the giant magneto-resistance effect in multilayered films [4], there has been an interest in the precise measurement of the magnetic moment direction in each layer of a multilayer and at the interface between layers. The large magnetic coupling between the neutron and the magnetic moment makes neutron reflectometry a powerful tool for obtaining information about these magnetic configurations and for measuring magnetic depth profiles.[5]

More recently, the neutron reflectometry technique has been extended to study nuclear and magnetic structures in the sample surface. At grazing incidence, it is possible to distinguish three scattering geometries: specular reflection, scattering in the incidence plane (off-specular scattering) and scattering perpendicular to the incidence plane (grazing incidence SANS). These different scattering geometries probe different mesoscopic length scales and directions in the sample surface, as detailed in section 12.2.

Section 12.3 describes the calculation of specular reflection at flat and homogeneous surfaces, introducing the concepts of scattering length density, index of refraction and critical angle of total reflection. It also shows that reflection at an interface is achieved only when a contrast in scattering length density exists. Sections 12.4 to 12.6 detail three studies of non magnetic systems, two of them demonstrating the advantage of partial deuteration for the enhancement

of the scattering length density contrast along the depth (12.5) and parallel to the surface (12.6) of a thin film.

Section 12.7 presents the polarized neutron reflectometry technique for the determination of magnetization depth profile. It is emphasized that, from a comparison between the spin-flip and non-spin-flip reflectivities, a vector information on the magnetizations can be extracted. Finally, an investigation of the magnetization depth profile in a polarizing supermirror is presented (12.8), followed by a presentation of off-specular scattering data for the study of the nuclear and magnetic correlations along its surface (12.9).

12.2. Reflectivity and scattering under grazing incidence

A monochromatic, well collimated beam impinges under a well defined, small angle $\alpha_i = \theta$ (in most cases $\theta << 5°$) onto the surface of the sample. It is then partly reflected specularly from the surface, i.e. the outgoing angle $\alpha_f = \theta$ as well, and partly refracted into the material (see Fig. 1). As we will derive in section 12.3, the reflection of x-rays or neutrons from a laterally homogeneous medium can be treated according to classical optics. Only the proper index of refraction n for the radiation has to be used.

For most materials, the index of refraction for neutrons and x-rays is slightly smaller than 1, leading to total external reflection for small angles of incidence $\theta < \theta_c$, where θ_c depends on the material and the radiation.

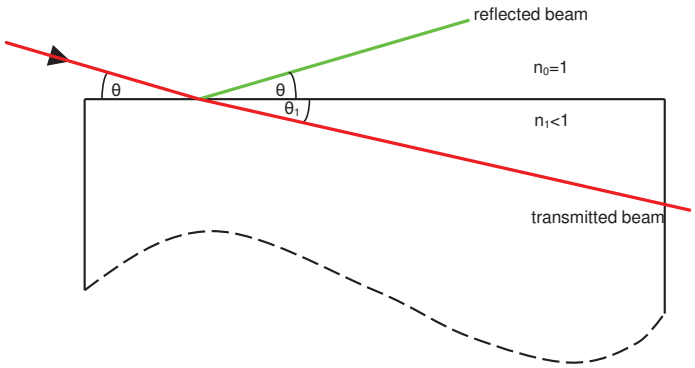

Fig. 1: Reflection and refraction from a free surface

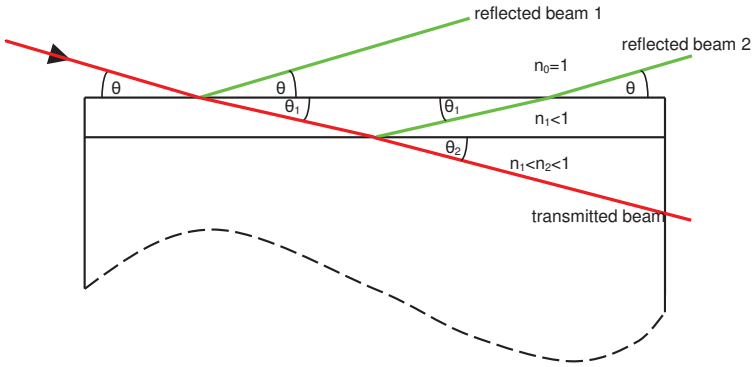

Fig. 2: Reflection and refraction from a single layer on a substrate

In the case of a single layer on the substrate, reflection and refraction take place at both the surface and the interface (Fig. 2). Then, the reflected beams from the different interfaces interfere with each other. Maximum intensity is received, when the path length difference between the two reflected beams is an integer multiple of the wavelength. Fig. 8 shows the reflectivity curve of a real single layer on a substrate. It is discussed in detail in section 12.4.

If surface and interface are laterally ideally homogeneous and flat, the complete beam is either reflected specularly or transmitted after refraction. If the interface is not flat, but e.g. periodical (as sketched in Fig. 3), additional beams are coming up. Their origin is diffraction from the modulated interface, as it is known from an optical grating. This so-called off-specular or diffuse scattering can be observed at $\alpha_f \neq \alpha_i$.

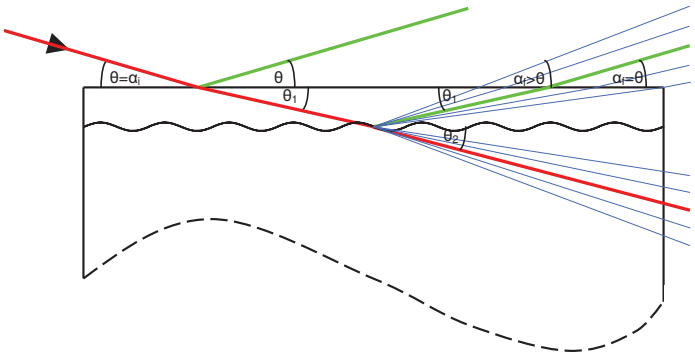

Fig. 3: Specular and offspecular scattering from a laterally modulated interface

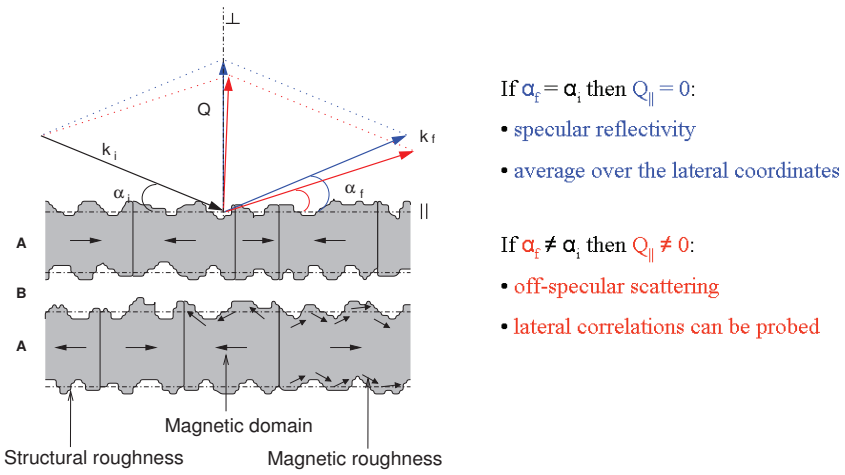

Fig. 4: General geometry of reflectivity and off-specular scattering.

The general principle of a scattering experiment under grazing incidence is depicted in Fig. 4 and the exact geometry is given in Fig. 5. For the mathematical description of the scattering process, it is again convenient to introduce the wave vectors $\mathbf{k_i}$ and $\mathbf{k_f}$ for the incoming and the detected wave, respectively. Neutrons or x-rays impinge on the sample surface under the grazing angle of incidence α_i with wave vector $\mathbf{k_i}$ and are detected with outgoing wave vector $\mathbf{k_f}$ whose direction is defined by the angle α_f in the plane of incidence and by the angle φ perpendicular to it. Let $\mathbf{Q} = \mathbf{k_f} - \mathbf{k_i}$ be the scattering wave vector and $\mathbf{Q}_{//} = (Q_x,Q_y)$ its component in the sample plane. We will restrict the discussion to elastic scattering, i.e. $k_i = k_f = 2\pi/\lambda$ where λ is the wavelength of the radiation.

If the sample can be considered as laterally homogeneous, i.e. invariant by translation along its surface, intensity can only be observed in the specular direction defined by $\mathbf{Q}_{//} = 0$, i.e. at $\alpha_f = \alpha_i$ and $\varphi = 0$. If the sample shows lateral fluctuations like structural roughness, magnetic roughness or magnetic domains, then some intensity can be observed in the directions given by $\mathbf{Q}_{//} \neq 0$, i.e. by $\alpha_f \neq \alpha_i$ and $\varphi \neq 0$. Very often specular reflectivity and scattering under grazing incidence are observed simultaneously. Specular reflectivity then gives information on the order parameters averaged over the lateral coordinates and diffuse scattering gives access to the fluctuations around this mean value.

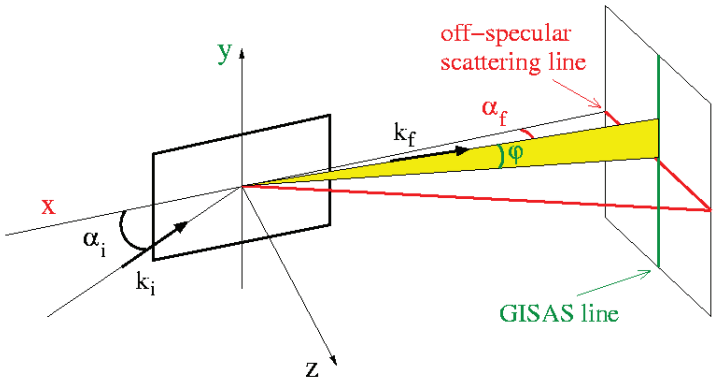

Fig. 5: The different geometries of scattering under grazing incidence. Off-specular scattering probes the lateral correlations along the x-direction, while grazing incidence small angle scattering (GISAS) probes the correlations along the x- and y-directions.

In practice, two types of scattering under grazing incidence geometries can be used (Fig. 5). The first one is obtained by scanning α_i and α_f while integrating the measured intensities along φ. This is called off-specular scattering. For the second one, the experimental conditions are such that φ can be resolved. Recording the intensities along φ as a function of α_i and α_f is called grazing incidence small angle scattering (GISAS).

Taking into account the small values of the angles α_i, α_f and φ the scattering wave vector projects itself on the three axis of the coordinate system of Fig. 5 in the following manner:

$$\mathbf{Q} = \begin{cases} Q_x \approx k \cdot (\alpha_i^2 - \alpha_f^2 - \varphi^2) \\ Q_y \approx k \cdot \varphi \\ Q_z \approx k \cdot (\alpha_i + \alpha_f) \end{cases} \qquad (1)$$

Note that while Q_x is a linear combination of squares of small angles, Q_y is linear in φ. Q_x is then always much smaller than Q_y. Typically, at a neutron source one has $0.5\ \mu m < d_x = 2\pi/Q_x < 20\ \mu m$ and $1\ nm < d_y = 2\pi/Q_y < 300\ nm$. The lower limits are defined by the maximum available intensity and the upper limits are fixed by the reachable resolution in Q_x and Q_y. It appears then that GISANS (grazing incidence small angle neutron scattering) probes much smaller lateral length scales than off-specular scattering. For x-rays the lower limits for d_x and d_y can be brought even smaller thanks to the availability of high intensity synchrotron sources. As GISAS is giving access to the nanometer length scale, one observes at the moment a rush on this method, with both neutrons (GISANS) and x-rays (GISAXS) [6].

Off-specular and GISAS intensities are represented differently. The off-specular data are represented as a function of α_i and α_f (Fig. 6a). Along the main diagonal (where $\alpha_i = \alpha_f$) is the specular line ($Q_x = 0$). Away from this diagonal, off-specular scattering is measured and the lateral correlations are probed along the x-direction ($Q_x \neq 0$). Along lines perpendicular to the specular line (where $\alpha_i + \alpha_f$ = constant), the correlations are probed along Q_x at Q_z constant (cf. eq. (1)).

GISANS and GISAXS measurements are usually performed on a small angle scattering instrument [7] where the data are collected on the 2D position sensitive detector. For a well defined angle of incidence α_i and a well defined sample-to-detector distance, the intensities recorded on the 2D detector give the GISAS signal as a function of $\alpha_i + \alpha_f$ and φ (Fig. 6b). As $Q_y \approx k.\varphi$, the φ axis gives directly access to the correlations along the y-axis. The specular reflectivity peak is centred around the point of coordinates ($\alpha_i + \alpha_f = 2\ \alpha_i$, $\varphi = 0$).

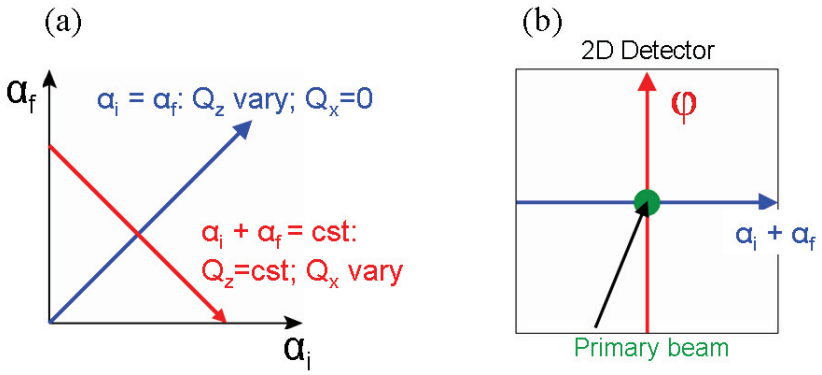

Fig. 6: Data representation of off-specular scattering (a) and GISAS (b)

12.3. Specular reflectivity: optical approach

For the case of a perfectly smooth surface, an exact description of the reflected and transmitted intensity can be deduced from quantum theory. This approach is also valid, if the correlation lengths of the lateral fluctuations exceed largely the coherence lengths of the beam in the respective directions.

As an example, we will show the case for neutrons, although the identical calculus is valid for x-rays. Only some nature constants are different, resulting in a different term describing the index of refraction.

The starting point is the Schrödinger equation for the wave function of the neutron

$$\left[-\frac{\hbar^2}{2m}\Delta + V(\mathbf{r})\right]\Psi(\mathbf{r}) = E\Psi(\mathbf{r}) \qquad (2)$$

The energy of the neutron is given by $E = \hbar^2 k^2/(2m)$ with the modulus $k = 2\pi/\lambda$ of the wave vector **k**. As we assume elastic scattering, the energy of the incident and of the outgoing wave is identical.

Due to the small |**Q**| values that are probed, a reflectometry experiment does not resolve the atomic structure of the sample in any of the three directions. Therefore, it is a valid approximation to describe the potential V_1 of the homogeneous material as proportional to the sum of the scattering length densities of all constituents:

$$V_1 = \frac{2\pi\hbar^2}{m}\sum_j N_j b_j \qquad (3)$$

where b_j are the coherent scattering lengths and N_j are the atomic or nuclear number densities of the different elements (evtl. isotopes) in the material. With that, we receive

$$\left[\Delta + \left(k^2 - 4\pi\sum_j N_j b_j\right)\right]\Psi(\mathbf{r}) = \left[\Delta + k^2\left(1 - \frac{\lambda^2}{\pi}\sum_j N_j b_j\right)\right]\Psi(\mathbf{r}) = \left[\Delta + k_1^2\right]\Psi(\mathbf{r}) = 0 \qquad (4)$$

with the wave vector $\mathbf{k}_1$ inside the medium. From this equation, it is justified to introduce the index of refraction of the material

$$n = \frac{k_1}{k} \qquad n = 1 - \frac{\lambda^2}{2\pi}\sum_j N_j b_j =: 1 - \delta \qquad \delta = \frac{\lambda^2}{2\pi}\sum_j N_j b_j \qquad (5)$$

It is a number very close to 1 for thermal and cold neutrons. The correction δ is called dispersion and is in the order of 10^{-5} to 10^{-6}. For most materials δ is positive (because the coherent scattering length b is positive for most isotopes), so that n is smaller than 1. This means that the transmitted beam is refracted towards the sample surface, which is opposite to the daily experience with light refracted at a glass or liquid surface.

For most materials, such as silicon, aluminium or iron, the absorption of neutrons is negligible. In case it is not negligible, it can be introduced most straightforward by including an imaginary part to the index of refraction:

$$n = 1 - \delta + i\beta \qquad (6)$$

In the case of x-rays the description in the framework of optical refraction inside the material is valid as well. In this case the index of refraction can be calculated as

$$n = 1 - \frac{\lambda^2 r_o}{2\pi} \sum_j N_j (Z_j + f_j' - i f_j'') =: 1 - \delta + i\beta \qquad \delta = \frac{\lambda^2 r_0}{2\pi} \sum_j N_j (Z_j + f_j') \qquad (7)$$

r_0 is the classical electron radius $r_0 = e/m_e c^2 = 2.82$ fm, Z is the number of electrons of the atom and f' and f'' are corrections for dispersion and absorption close to resonance energies. Typically, they can be neglected; only at the absorption edges they become important. Also for x-rays, the dispersion δ is always positive, so that the index of refraction n is smaller than 1.

In analogy to classical optics, we can derive e.g. Fresnel's formulas: For the solution of the wave equation at the sharp interface, we assume the surface of the sample to be at z = 0. The potential is then

$$V(z) = \begin{cases} 0 & \text{for } z > 0 \\ V_1 & \text{for } z \le 0 \end{cases} \qquad (8)$$

As the potential is independent on x and y, the wave vector $\mathbf{k}_1$ in the wave equation (4) is also independent on x and y. Therefore, the wave equation can be separated by the Ansatz

$$\Psi(\mathbf{r}) = \Psi_x(x)\Psi_y(y)\Psi_z(z) \qquad (9)$$

For the z direction we receive the one-dimensional differential equation

$$\Psi_z''(z) + k_z^2(z)\Psi_z(z) = 0 \qquad (10)$$

To solve the differential equation we use the Ansatz

$$\Psi_{zl}(z) = t_l e^{ik_{zl}z} + r_l e^{-ik_{zl}z} \qquad (11)$$

The index l distinguishes between vacuum (l=0) and matter (l=1). The unique solution is determined by the boundary conditions. The incoming wave in vacuum before interaction with the sample is a plane wave of norm of 1, i.e. t_0 is equal to 1. In a half-infinite medium, there is no reflected wave, because there is nothing to reflect from, i.e. r_1 vanishes. In addition, the wave function and its first derivative must be continuous at the interface. So we receive the boundary conditions

$$\begin{aligned} &\Psi_{z0}(z=0) = \Psi_{z1}(z=0) \\ &\Psi_{z0}'(z=0) = \Psi_{z1}'(z=0) \\ &t_0 = 1 \\ &r_1 = 0 \end{aligned} \qquad (12)$$

When we insert (11) into (12), we receive the continuity equations for the wave function

$$\begin{aligned} &1 + r_0 = t_1 \\ &k_{z0}(1 - r_0) = k_{z1}t_1 \end{aligned} \qquad (13)$$

t_1 is the amplitude of the transmitted wave and r_0 of the reflected wave. We can rewrite this set of equations in a matrix equation

$$\begin{pmatrix} 1 \\ r_0 \end{pmatrix} = \mathbf{M_0}\begin{pmatrix} t_1 \\ r_1 \end{pmatrix} = \mathbf{M_0}\begin{pmatrix} t_1 \\ 0 \end{pmatrix} \qquad (14)$$

The reflectivity R is defined as the modulus squared of the ratio of the amplitudes of reflected and incoming waves, the transmissivity T is defined as the modulus squared of the ratio of the amplitudes of transmitted and incoming waves.

$$R = |r_0|^2 \qquad T = |t_1|^2 \tag{15}$$

In conclusion, we arrive at Fresnel's formulas for the reflection at a flat interface

Reflectivity $$R = \left|\frac{k_{z0} - k_{z1}}{k_{z0} + k_{z1}}\right|^2 = \left|\frac{\theta - n_1\theta_1}{\theta + n_1\theta_1}\right|^2 \tag{16}$$

Transmissivity $$T = \left|\frac{2k_{z0}}{k_{z0} + k_{z1}}\right|^2 = \left|\frac{2\theta}{\theta + n_1\theta_1}\right|^2 \tag{17}$$

Taking into account the continuity relation for the wave vector component tangential to the surface

$$k_{x0} = k_{x1} \qquad k_{y0} = k_{y1} \tag{18}$$

together with $k_1 = k_0 n_1$ (eq. 5), Snell's law for refraction follows from trigonometry:

$$\frac{\cos\theta}{\cos\theta_1} = \frac{k_1}{k_0} = n_1 \tag{19}$$

The fact that in most cases the index of refraction is $n_1 < 1$ means that the transmitted beam is refracted towards the sample surface ($\theta_1 < \theta$ in Fig. 1). For angles of incidence θ below the so-called critical angle θ_c with

$$n_1 = \cos\theta_c \qquad \theta_c \approx \sqrt{2\delta} \tag{20}$$

total reflection is observed, i.e. all intensity is reflected and no wave propagating in z-direction exists in the sample. Only an evanescent wave in z-direction with propagation

parallel to the surface is induced. For incident angles above θ_c, the beam can partially penetrate the sample and is only partly reflected.

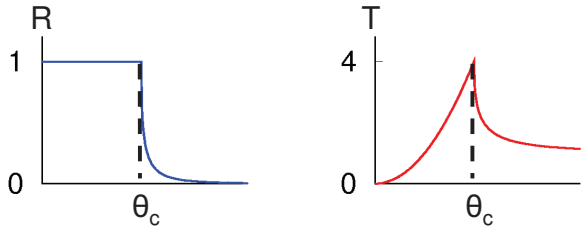

Fig. 7: Reflectivity and Transmittivity as a function of the angle of incidence

In the case of p layers on a substrate, the same calculus can be used. At every interface, the continuity relation can be formulated analogous to (14):

$$\begin{pmatrix} 1 \\ r_0 \end{pmatrix} = \mathbf{M_0} \begin{pmatrix} t_1 \\ r_1 \end{pmatrix} \qquad \begin{pmatrix} t_1 \\ r_1 \end{pmatrix} = \mathbf{M_1} \begin{pmatrix} t_2 \\ r_2 \end{pmatrix} \qquad \ldots\ldots \qquad \begin{pmatrix} t_p \\ r_p \end{pmatrix} = \mathbf{M_p} \begin{pmatrix} t_{p+1} \\ 0 \end{pmatrix} \tag{21}$$

The amplitudes of reflected and transmitted wave then can be calculated by a matrix multiplication of the individual reflection matrices:

$$\begin{pmatrix} 1 \\ r_0 \end{pmatrix} = \mathbf{M_0} \cdot \mathbf{M_1} \cdot \ldots \cdot \mathbf{M_p} \begin{pmatrix} t_{p+1} \\ 0 \end{pmatrix} \tag{22}$$

From equation (16), it becomes obvious, that reflection is only achieved when a difference between the indices of refraction of the adjacent layers exists. If one wants to investigate two layers with neutron or x-ray reflectivity, the contrast of the indices of refraction is the important quantity deciding if the interface is visible or not. The higher the contrast, i.e. the higher the difference between the two indices of refraction, the higher is the contribution of this interface to the reflectivity curve.

The contrast achievable decides which probe is useful to investigate a certain structure. Fig. 19 from lecture 2 of this book gives an impression of the scattering lengths of different elements for neutrons and x-rays. The scattering length density, which is proportional to the

dispersion δ as well for neutrons as for x-rays, is proportional to the density and to the scattering length of the elements contained in the respective layer. For x-rays, the scattering length is generally proportional to the number of electrons, while for neutrons it is quite randomly distributed over the periodic system and over the different isotopes of each element. Light atoms as well as neighbouring atoms in the periodic system cannot be distinguished well with x-rays.

As neutrons interact strongly with the magnetic environment, polarized neutrons also show a contrast between layers with different magnetization (see section 12.7).

In case of low contrast, there might be a chance to enhance the contrast by contrast variation. In the case of neutrons, isotopic substitution is a good way to improve the contrast. Especially for two polymer layers, the contrast can be enhanced substantially by deuteration of one of the polymers, because the scattering lengths of Hydrogen ^{1}H and Deuterium ^{2}H differ strongly from each other (see sections 12.5 and 12.6). In the case of x-rays, one can modify the contrast for one element by tuning the x-ray energy to a resonance [8].

12.4. Neutron reflectivity from a single Ni layer on glass

The first example is a neutron reflectivity measurement from a glass plate coated with a Ni layer. Such Ni coated glass plates are used in the neutron guides at several research reactors to guide cold neutron beams from the reactor to the instruments without losses. Fig. 8 shows the reflectivity curve together with a fit and several simulations.

Despite the experimental artefacts below $2\theta = 0.4°$, where the sample does not yet cover the complete beam, a typical reflectivity curve of a single layer has been measured. Up to the critical angle of $2\theta_c = 0.93°$, all impinging neutrons are reflected. At higher angles, the interference fringes of the reflections at the surface and at the interface are clearly visible. As the reflectivity drops quickly above the critical angle, it is plotted on a logarithmic scale.

It can be seen that the fit takes into account 8 parameters, some of them describe the experimental setup and some of them the sample.

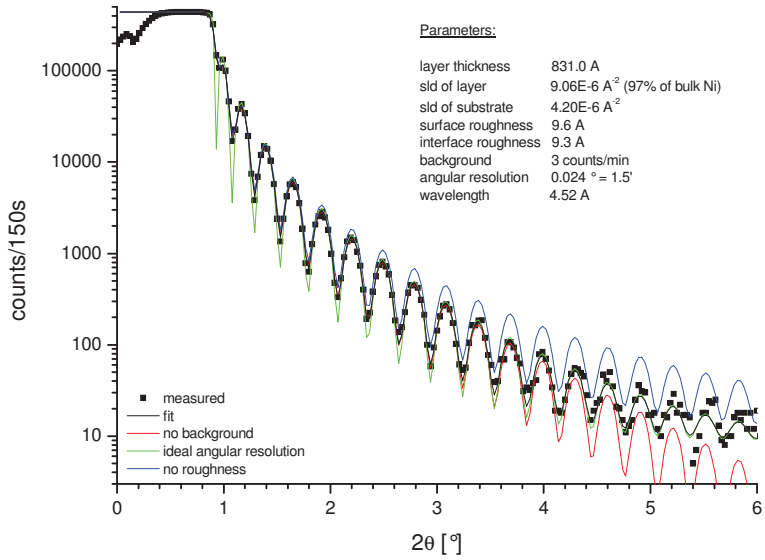

Fig. 8: Specular reflectivity of neutrons from a Ni layer on a glass substrate, as measured with the HADAS reflectometer at the research reactor DIDO in Jülich. The black line shows the best fit, the coloured lines show simulations obtained by ignoring several parameters.

The main parameters from the experimental setup are the wavelength used, the angular resolution of the incoming beam and the background. In the simulation of the green curve, where the resolution has not been taken into account, one can see the minima much more distinct than in the measurement. Due to the limited resolution, the minima are washed out due to the higher reflectivity of neutrons impinging under slightly different angles. The red curve, where the background has been omitted, shows that the signal-to-noise ratio of the instrument is strongly limited by the background, because the incoming intensity is small compared to a x-ray beamline.

The main physical parameters of the sample that have been derived from the measurement are the scattering length densities of the layer and the substrate, the roughnesses of surface and interface and, of course, the layer thickness.

The layer thickness is the easiest; it can be estimated by the distance between the maxima. The highest scattering length density (in this case of the layer) determines the critical angle θ_c, while the difference of the scattering length densities determines the height of the fringes. From the knowledge, that the layer consists of natural Ni, we have been able to determine that the density of the layer is only 97% of the bulk density, i.e. during the sputtering process a

small fraction of voids has been introduced into the layer. The information about the density and the composition are not independent! Only one of the two can be derived from the reflectivity measurement.

The effect of the roughness is a drop of the reflectivity curve at high angles. The blue curve shows a simulation of the reflectivity of perfectly flat surface and interface. The growing uncertainty of the path length between two rough interfaces with growing angle of incidence leads to a decrease of interference quality with higher angles and therefore to a drop in reflectivity.

12.5. Segregation of a polymer mixture under annealing

The second example shows a structure of polymer layers, where a chemical reaction at the interface between the two polymers takes place [9,10]. To increase the sticking between two layers of immiscible polymers, some polymer chains have a functional group ("telechelic") added which finds reaction partners in the other layer to form a multiblock copolymer (see Fig. 9). This multiblock copolymer is then fixed to the interface, with some sections compatible to polymer A and some sections compatible to polymer B.

The chemical reaction changes the sample only at the buried interface; no sign of the modification of the system is present at the surface.

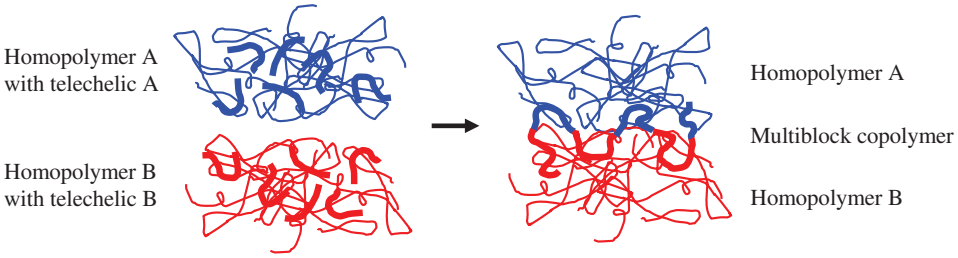

Fig. 9: A schematic of the in situ interfacial reaction of telechelic oligomers in an immiscible polymer blend resulting in the formation of multiblock copolymer

Fig. 10: A schematic of the reaction that takes place between the carboxylic acid and epoxy groups that were present on the reactive polymer chain ends

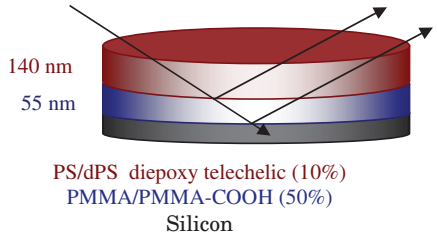

Fig. 11: Sample used for the neutron reflectivity experiment.

Fig. 11 shows the sample used for this investigation. The bottom layer consists of poly methyl methacrylate (PMMA) and PMMA with a carboxylic acid group at the end. The top layer consists of polystyrene (PS) and deuterated PS with epoxy functional groups. The mobility of the polymer chains at room temperature is low, so that only the molecules that meet by chance at the interface react with each other. The reaction scheme is shown in Fig. 10. During annealing in vacuum at 150°C the mobility is increased strongly, so that more reactive groups diffuse towards the interface, where they react and are immobilized.

The strong contrast between the deuterated functionalized PS and all other polymers with natural hydrogen makes the enrichment of the reactive polymer at the interface clearly observable.

Fig. 12 shows the neutron reflectivity data measured on the virgin sample as well as after several annealing steps. It can be seen that the shortest period hardly changes but the modulation of the peak height changes drastically during annealing. The analysis of the data resulted in the scattering length density profile shown in Fig. 13.

The main effect during the first 15 min annealing is a sharpening of the PS/PMMA interface and a slight increase in the density of both polymers. At the same time, the total thickness of the sample is slightly reduced. This leads to the interpretation that voids in the layers have been filled. After the following annealing steps the formation of the interface layer with a high concentration of the reactive compound can be observed due to the high scattering length density of dPS. At the same time, the remaining PS layer is depleted from dPS, so that the scattering length density of this part is reduced.

From the integrated area of the d-PS peak of the scattering length density profile, the amount of immobilized copolymer could be derived and compared to calculations of the diffusion velocity in the polymer melt. It was shown that the kinetics of this reaction does not match the predictions of a purely diffusion-based theory.

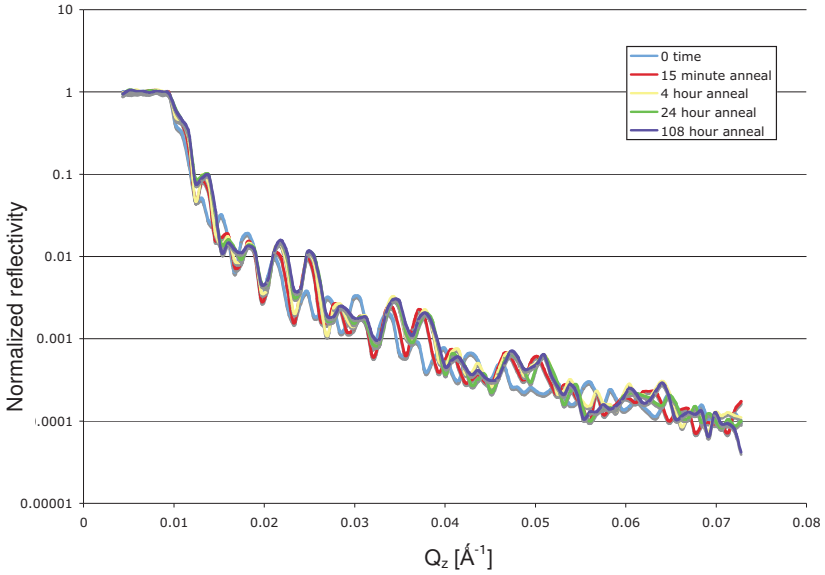

Fig. 12: Neutron reflectivity fits from the sample shown in Fig. 11 as cast (light blue) and after 15 min, 4 hours, 24 hours and 108 hours annealing at 150 °C.

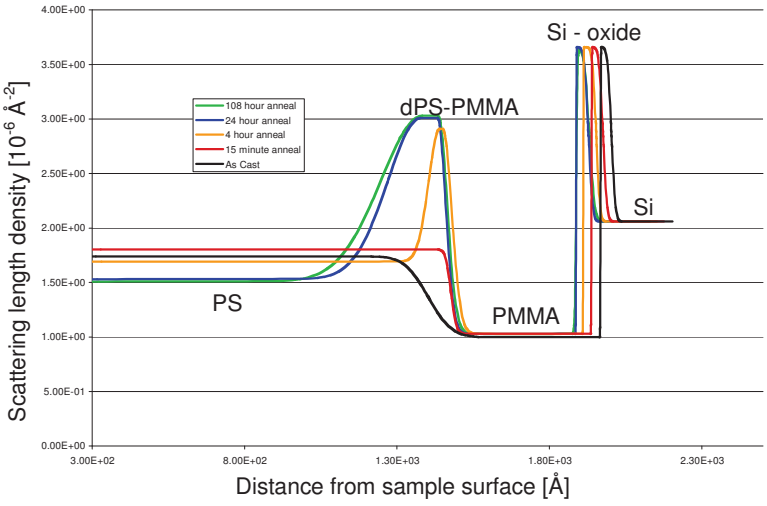

Fig. 13: Scattering length density profile received from fitting the reflectivity data shown in Fig. 12. The sample surface is at distance 0, the Si substrate is continued towards larger distances. The colours indicate the same annealing steps as in Fig. 12

12.6. Ordering of a dPS-PB diblock coplymer on a Si substrate

The last non-magnetic example shows an investigation of the lateral correlations in a partially deuterated polystyrene-polybutadien (PS-PB) diblock copolymer film on a Si substrate investigated by GISANS.

In order to create magnetic nanostructures topologically ordered over large surfaces, several bottom-up routes are possible. One possible route is to produce diblock copolymer templates [11]. A diblock copolymer is made of two polymer blocks attached to each other and that experience repulsive forces between each other, such as PS and PMMA or PS and PB. Depending on the relative lengths of the two blocks, several segregation scenarios can occur, such as formation of spheres or cylinders of one polymer in the matrix of the other, or formation of lamellae [12]. During deposition on a surface, and depending on the molecular weight and on the interactions between the blocks and the substrate and between the blocks and the air, the structures may orient differently parallel or perpendicular to the substrate. Once the diblock copolymer has been deposited, one of the two constituent polymers can then selectively be removed (by acid etching) and the resulting structure can be used as a mask for the structuring of the underlying magnetic medium. The diblock copolymer structure on the surface can be characterized using AFM in the mechanical contrast mode (the contrast is determined by the elasticities of the different constituents as experienced by the oscillating AFM tip). However, this gives almost no information on whether the structure is coherent over the whole thickness of the film. This information is crucial in order to figure out whether the etching process can be successful. It can in principle be obtained by GISANS, varying the angle of incidence α_i of the neutrons. A strong enhancement in neutron contrast between the two polymers can be achieved by substituting the H atoms of one constituent polymer by D atoms.

In order to prove this principle a high molecular weight symmetric dPS-PB diblock copolymer has been prepared (“dPS” means “deuterated PS”). If the two polymers composing the diblock have the same length, they order as lamellae. Due to the high molecular mass of the diblock (150 kg/mol), when spin coated on a Si surface, the lamellae have the tendency to order perpendicular to the substrate [13], at least close to the surface of the film, as verified by the AFM scan shown in Fig. 14.

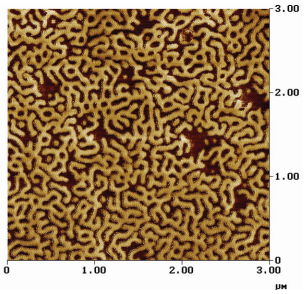

Fig. 14: AFM scan in the mechanical contrast mode on the surface of a 170 nm thick dPS-PB film spin-coated from solution on a Si wafer [14].

GISANS measurements were performed on that sample as a function of the angle of incidence of the neutrons and we show in Fig. 15 such a measurement performed at $\alpha_i = 0.45°$, close above the critical angle of total reflection. Out-of-plane scattering peaks are present in transmission around the direct beam and in reflection around the specular peak. From the position in Q_y of those peaks we deduce an average distance between two PS or PB lamellae of $2\pi/Q_y = 97$ nm, in agreement with the AFM picture.

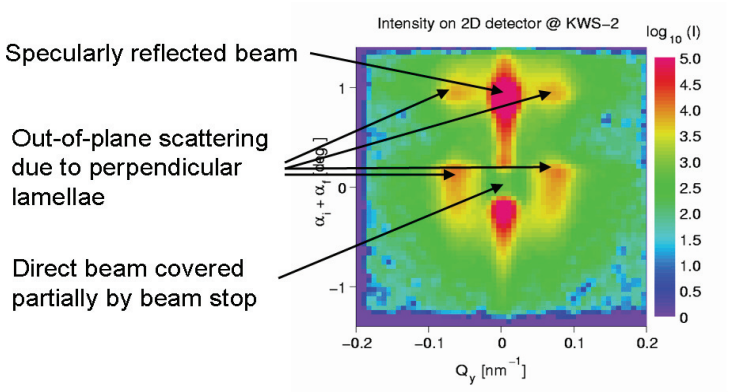

Fig. 15: GISANS performed on the very sample of Fig. 14 at an angle of incidence $\alpha_i = 0.45°$. Contrarily to the geometry depicted in Fig. 6, for this measurement, the sample surface is almost horizontal and the plane of incidence of the neutrons is vertical [14].

12.7. Magnetization depth profile: Specular reflectivity of polarized neutrons.

In this chapter, we would like to have a closer look at the investigation of the magnetization depth profile in magnetic layered structures. The neutron is a spin ½ particle and therefore interacts with the magnetic induction **B**. As reflectometry measurements average over the

atomic structure of the sample, antiferromagnetic structures are not accessible due to the vanishing net magnetization. In contrast to that, magnetization densities of ferromagnetic layers can be measured on an absolute scale with reflectometry of polarized neutrons.

We stay in the approximation of homogeneous layers with flat interfaces, where the potential for the neutron only depends on the z coordinate. In the case of magnetic multilayers, we need to take into account the interaction of the neutron's spin with the magnetic induction inside matter. To treat this properly, we have to work with wave functions in the 2-dimensional quantum mechanical spin space, where the usual space-dependent functions, e.g. the potential, become operators on the neutron's spin.

The potential for the interaction of the neutron with matter in the layer l can be separated into two parts

$$\hat{V}_l = V_l^N \hat{1} + \hat{V}_l^M \qquad (23)$$

where V_l^N is the nuclear interaction from eq. (3), $\hat{1}$ is the unity operator, which does not affect the spin state, and $\hat{V}_l^M = -\mu_n \hat{\boldsymbol{\sigma}} \cdot \mathbf{B}_l$ is the magnetic dipole interaction operator between the neutron magnetic moment operator $\mu_n \hat{\boldsymbol{\sigma}}$ and the magnetic induction $\mathbf{B}_l$.

We assume the direction of the external magnetic field $\mathbf{H}=H\mathbf{e}_x$ to be oriented in the x-direction of the coordinate system defined in Fig. 5. Then it is convenient to choose also the x-axis as quantization axis for the neutron spin, so that the order of the Pauli matrices in the spin operator $\hat{\boldsymbol{\sigma}} = (\sigma_x, \sigma_y, \sigma_z)$ is the following.

$$\sigma_x = \begin{pmatrix} 1 & 0 \\ 0 & -1 \end{pmatrix} \qquad \sigma_y = \begin{pmatrix} 0 & 1 \\ 1 & 0 \end{pmatrix} \qquad \sigma_z = \begin{pmatrix} 0 & -i \\ i & 0 \end{pmatrix} \qquad (24)$$

It is arbitrary to choose the coordinate system for the scattering experiment (Fig. 5) and for the neutron spin to be parallel; the result does not change, if the magnetic field **H**, which defines the quantization axis for the spin, is rotated to any other direction in the x-y-plane of the scattering experiment. This rotation will only change the phase of the spin-flip scattering (eq. 28), which has no influence on the reflectivities and transmissivities. The magnetic induction can be decomposed into terms of applied field and magnetization

$$\mathbf{B} = \mu_0(\mathrm{H}\mathbf{e}_x + (1-\mathrm{D})\mathbf{M}) = \mathbf{B}_0 + \mu_0(1-\mathrm{D})\mathbf{M} \qquad (25)$$

where $\mathbf{B}_0$ is the induction from the external magnetic field, D is the demagnetizing factor and $\mathbf{M}$ the magnetization of the material. In the case of a thin film, (1 – D)$\mathbf{M}$ is equal to the in-plane component of the magnetization.

The magnetization component M_z perpendicular to the film surface cannot induce any magnetic contrast between adjacent layers, because $\nabla \cdot \mathbf{B} = 0$ does not allow B_z to change discontinuously when crossing an interface. In fact, this is the origin of the demagnetizing effect.

$\mathbf{B}_0$ is constant over the sample volume and therefore gives a constant contribution to the index of refraction as well for vacuum as for every material involved. Therefore, all these contributions cancel out when calculating reflectivity R and transmissivity T according to (16) and (17).

The only remaining contributions are M_x parallel to the quantization axis and M_y perpendicular to the quantization axis, but in plane. With that, we can rewrite the total interaction operator in analogy to (3) as

$$\hat{\mathrm{V}}_l = \frac{2\pi\hbar^2}{\mathrm{m}}(\rho_l^{\mathrm{N}}\hat{1} + \rho_l^{\mathrm{M}}\hat{\boldsymbol{\sigma}} \cdot \mathbf{b}_l) \qquad (26)$$

with the nuclear scattering length density ρ_l^{N}, the magnetic scattering length density ρ_l^{M} and the unit vector $\mathbf{b}_l$ along the magnetic induction vector $\mathbf{B}_l$ in layer l. In most cases, if $\mu_0 M >> B_0$, $\mathbf{b}_l$ is approximately parallel to $\mathbf{m}_l$.

In complete analogy to section 12.3, the Schrödinger equation can be solved in coordinate and spin space. The eigenvectors $|+\rangle$ and $|-\rangle$ of the operator $\hat{\boldsymbol{\sigma}} \cdot \mathbf{b}_0 = \sigma_x$ with the eigenvalues +1 and -1, respectively, define states of the neutron with “spin up” and “spin down”. The solution of the Schrödinger equation is the neutron state $|\Psi(\mathbf{r})\rangle$, which is again a linear combination of those two eigenvectors:

$$\left|\Psi(\mathbf{r})\right\rangle = \Psi^{+}(\mathbf{r})\left|+\right\rangle + \Psi^{-}(\mathbf{r})\left|-\right\rangle = \begin{pmatrix}\Psi^{+}(\mathbf{r})\\ \Psi^{-}(\mathbf{r})\end{pmatrix} \tag{27}$$

We end up with a set of two coupled one-dimensional linear differential equations for every layer:

$$\begin{aligned}\Psi_l^{+\prime\prime}(z) + \left[k_{zl}^2 - 4\pi(\rho_l^N + \rho_l^M m_{xl})\right]\Psi_l^{+}(z) - 4\pi\rho_l^M m_{yl}\Psi_l^{-}(z) = 0\\ \Psi_l^{-\prime\prime}(z) + \left[k_{zl}^2 - 4\pi(\rho_l^N - \rho_l^M m_{xl})\right]\Psi_l^{-}(z) - 4\pi\rho_l^M m_{yl}\Psi_l^{+}(z) = 0\end{aligned} \tag{28}$$

The solution of this set of differential equations can be done in analogy to (21). The calculation is straightforward, but lengthy. Its solution can be found in [15]. It ends with the reflection and transmission amplitude operators $\hat{r}_l$ and $\hat{t}_l$, which are again operators in spin space with two different eigenvalues.

Four types of reflectivities can be measured, which are the squares of the projections of the reflection amplitude operator into vacuum onto spin up or down neutron states:

$$R^{\pm\pm} = \left|\left\langle \pm\right|\hat{r}_0\left|\pm\right\rangle\right|^2 \tag{29}$$

These reflectivities have a clear physical meaning. From eq. (28) it is clear that only nuclear scattering and the magnetization component M_x parallel to the field lead to non-spin-flip (NSF) reflectivities. By analysis of the sum and the difference of R^{++} and R^{--}, these two contributions can be separated from each other. Fig. 16 shows the influence of the magnetic scattering length density on the critical angle and the reflectivity for the case of a magnetically saturated surface, where only NSF reflectivity is present.

The spin-flip (SF) reflectivities R^{+-} and R^{-+} are equal to each other and arise from the magnetization component M_y in plane, perpendicular to the field. As the sign of the magnetization is only coded in the phase of the SF reflected wave, it is lost when measuring the intensities. Therefore, only $|M_y|$ can be measured.

In conclusion, polarized neutron reflectivity can measure the nuclear scattering length density ρ^N and the magnetization components M_x and $|M_y|$ for every layer in the thin film structure.

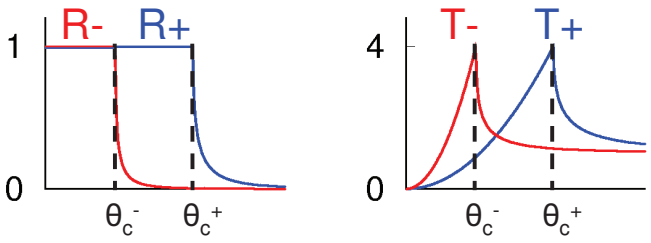

Fig. 16: Reflectivity and Transmissivity for polarized neutrons from a saturated ferromagnetic material

12.8. Layer-by-layer magnetometry: polarizing supermirror

Polarizing supermirrors are commonly used for the polarization of cold neutron beams. For the operation of a polarized neutron instrument, it is of course important to know the performance of the polarizers used and their behaviour in the magnetic field. During the characterization of the device, it turned out that a lot of physics of the layered magnetic structure can be understood by having a closer look at the data, and so we have investigated the polarizing supermirror thoroughly [16,17]. In this section, we will present the laterally averaged data from specular reflectivity, the off-specular measurements are shown in the next section.

A polarizing supermirror is a stack of bilayers of a magnetic and a non-magnetic material. The thickness of the bilayers is gradually increasing to receive constructive interference for a broad range of **Q**-values, what results in an extended plateau of high reflectivity above the total reflection angle. The materials are chosen to have a high contrast for one spin direction and no contrast for the other.

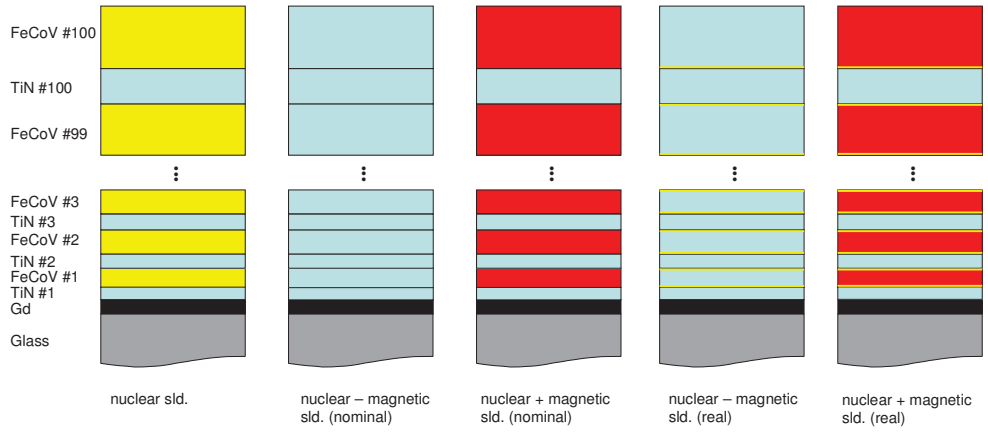

Fig. 17: Colour representation of the scattering length density distribution in a polarizing supermirror. On the left, the nuclear scattering length density distribution is shown. The next two columns show the intended contrast for neutrons with spin antiparallel to the magnetization (no contrast) and for neutrons with spin parallel to the magnetization (high contrast). The two columns on the right show the measured scattering length density profile. We found magnetically dead layers at the interfaces between FeCoV and TiN, so that a 2 – 4 Å of the FeCoV layer show only the nuclear scattering length density, but no magnetic contribution.

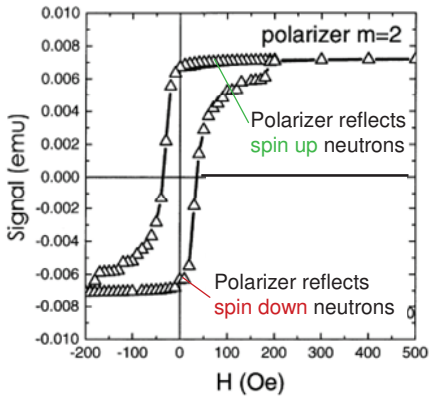

Fig. 18: Magnetization curve of a polarizing supermirror with 40 bilayers [18]

The supermirror we have investigated is a polarizing supermirror produced by Swissneutronics which reflects the neutrons with the proper spin direction up to m=2.5 times the critical angle of Ni. The first three columns of Fig. 17 show the intended scattering length density sequence. 100 bilayers of FeCoV (ferromagnetic) and TiN (nonmagnetic) with gradually increasing thickness are transparent for neutrons with spin antiparallel to the magnetization and reflecting for neutrons with spin parallel to the magnetization. Below the

stack, there is a strongly absorbing Gd layer to kill all spin down neutrons and a glass substrate for mechanical stability.

As our sample cannot be measured in a magnetometer because the back surface is also coated magnetically, we show the magnetization curve of a comparable sample with only 40 bilayers in Fig. 18. After negative saturation, the polarizer remains almost completely saturated at small positive fields. This allows two different working conditions for the polarizer. On the one hand, it can work in saturation, i.e. after exposure to a high positive magnetic field. Then all magnetic layers are magnetized along the field direction, and the supermirror reflects spin-up neutrons, i.e. neutrons with spin along the magnetic field. On the other hand, it can be used in remanence with all layers magnetized opposite to the applied (small) magnetic field. Then the spin-down neutrons are reflected.

Fig. 19 shows the polarized neutron reflectivity measurement at different fields after negative saturation. Fig. 19 a) shows the remanence. In the "working regime" up to α_i = 21 mrad, the reflectivity for spin down neutrons R^{--} is more than two orders of magnitude higher than R^{++}, yielding a good negative polarization of the reflected beam. The reflectivity for the proper polarization channel is close to 1, the increasing slope at small angles is an experimental artefact due to the increasing coverage of the beam's cross section with increasing angle of incidence. The spin-flip signal is completely determined by the imperfect polarization of the incident beam, no spin-flip specular reflectivity is coming from the sample. Fig. 19 d) is measured at saturation and is almost exactly opposite to the remanent state.

In the two intermediate states shown in Fig. 19 b) and c), there is a crossover between R^{++} and R^{--}, showing that some of the layers are magnetized along and some antiparallel to the field. In the fit, we can address the individual magnetization of every layer and find out, which layers have flipped and which stay magnetized opposite to the field direction. It turned out, that the thinner, i.e. lower magnetic layers flip first. In the case of 3.8 mT (Fig. 19 b), 48 layers have flipped, in the case of 5.6 mT (Fig. 19 c), 94 FeCoV layers have flipped in field direction. Fig. 20 shows the number of layers flipped in field direction as a function of the field strength.

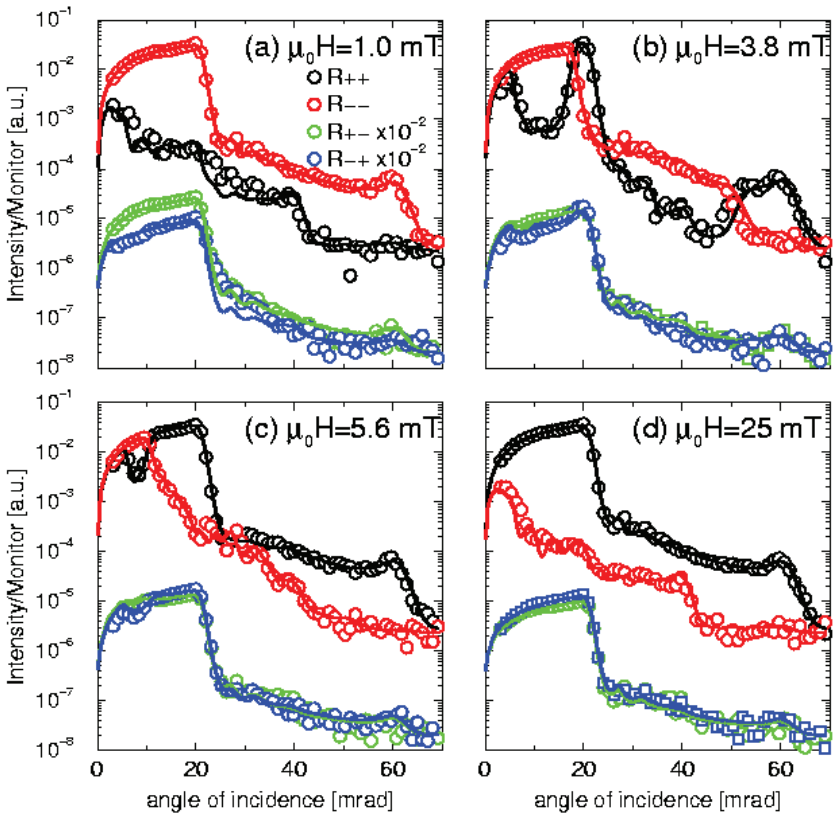

Fig. 19: Polarized neutron reflectivity measurements on the polarizing supermirror at different magnetic fields applied after negative saturation. The dots show experimental data, the lines are fits.

What is striking is the relatively high R^{--} signal in saturation that drops at twice the angle of the end of the supermirror plateau. It shows that spin-down neutrons see a structure that has half the period of the intended supermirror structure for the spin-up neutrons. It turned out, that this feature comes from magnetically dead layers at the interface between FeCoV and TiN. At the top and the bottom of the FeCoV layer, there is a 2 – 4 Å thick nonmagnetic region with the purely nuclear scattering length density of FeCoV. The two pictures on the right side of Fig. 17 show a schematic of the real scattering length density profile, where the reflectivity in R^{--} comes from the yellow – blue bilayers, that have about half the thickness of the red – blue bilayers that result in R^{++}.

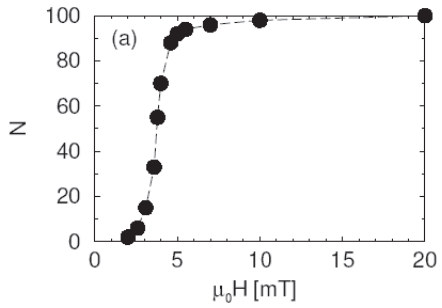

Fig. 20: Number of FeCoV layers flipped in field direction as a function of the positive magnetic field applied after negative saturation

12.9. Lateral correlations in the polarizing supermirror

We stay with the polarizing supermirror of the previous section. We show here the data of off-specular scattering giving access to the nuclear and magnetic structure of the system in the plane of the surface. Reflectivity and off-specular scattering with polarization analysis measured in remanence and under a field of 4.5 mT are shown in Fig. 21 a) and c). Inside the 4 spin channels, one recognizes along the main diagonals ($\alpha_i = \alpha_f$) the specular reflectivities of Fig. 19. Off-diagonal ($\alpha_i \neq \alpha_f$), strong spin-polarized off-specular scattering is also observed. The non-spin-flip off-specular scattering stems mainly from scattering by interfacial roughness correlations and the spin-flip scattering arises from lateral fluctuations of the component of the magnetizations perpendicular to the applied field [17]. Those affirmations are confirmed by the simulations shown in Fig. 21 b) and d), performed within the Distorted Wave Born Approximation (DWBA) [19, 20].

This approximation takes into account the fact that, at the shallow angles α_i and α_f considered here, the projection of the coherence length of the neutron beam on the sample surface can be relatively large, giving a high probability for the neutrons to be scattered more than once when travelling through the sample. In that case, the Born approximation is not valid to describe the scattering.

Note that within the off-specular geometry, it has not been possible to determine accurately the lengths of the structural and magnetic correlations, because they stem from length scales below the micrometer range. They have been determined using polarized neutrons in the GISANS geometry [21].

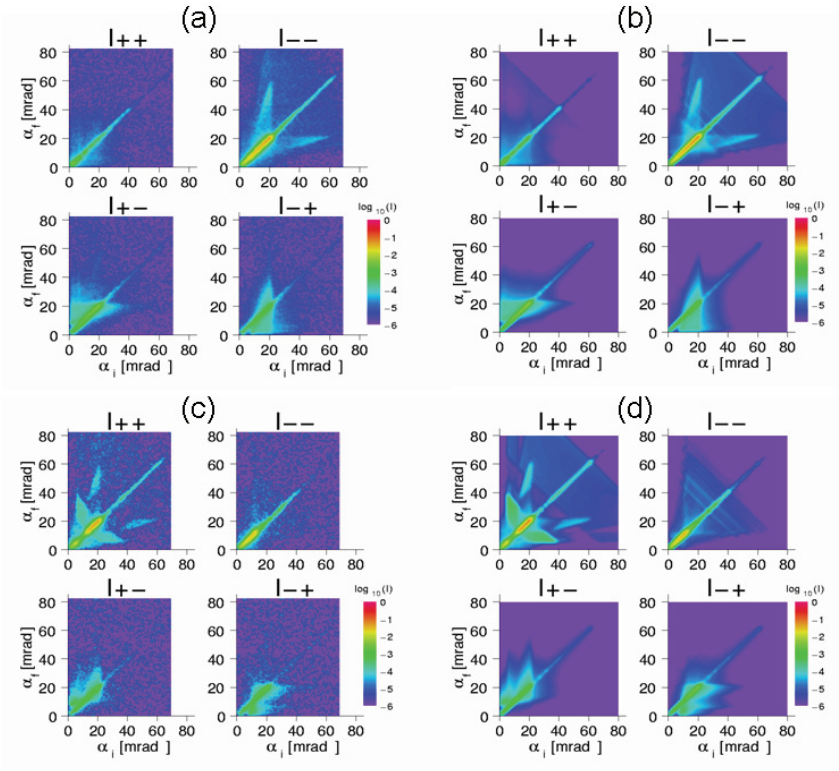

Fig. 21: (a): Reflectivity and off-specular scattering of polarized neutrons with polarization analysis on a remanent polarizing supermirror measured under a field of 1 mT after negative saturation saturation of the sample. (b): Simulation of the data within the DWBA. (c): Data at 4.5 mT and (d): simulation. [17]. .

12.10. Conclusion and outlook

X-ray and neutron scattering under grazing incidence are powerful probes of buried layers and interfaces in multilayers. For a detailed and quantitative investigation it is necessary to use the proper probe to be able to get the best signal by using the most suitable contrast. In addition one should take into account, how well the interactions can be described to avoid additional uncertainties during the data analysis.

For the investigation of morphology and composition, x-rays are in most cases superior to neutrons due to the high signal-to-noise ratio of today's x-ray sources. If the contrast between the different elements is sufficient, the use of a laboratory x-ray source is a good choice, as the wavelength of the radiation and the cross-sections are well known, so that a reliable input for the fitting procedure is available.

If very light elements, e.g. in polymer layers, are included in the sample, the critical angle θ_c for x-rays is very low, the reflectivity is weak and the contrast between different polymers is negligible. With neutrons and partly deuterated materials, a high contrast and a good signal quality can be achieved.

In the case of structures containing several elements in close neighbourhood in the periodic table a detailed weighting of the advantages of the probes needs to be performed. X-rays from a standard x-ray source do not give sufficient contrast between neighbouring elements. One can use synchrotron x-rays and contrast variation by tuning the energy to an absorption edge of one of the constituents. But a problem is that the calculation of the scattering length density and absorption as a function of element and x-ray energy is not reliable close to the absorption edge. It is therefore an additional fitting parameter. Moreover, the high beam intensity can make sample heating a problem.

In contrast, the interaction of neutrons with all materials is well-known, tabulated and independent on the neutron's wavelength. The absorption is usually weak, so that the data analysis is straight-forward.

For the investigation of magnetic structures, there is no way around polarized neutrons, as the interaction of neutrons with magnetic material is well known and can be calculated easily. The interpretation of the measured data is therefore very straight-forward. Anyway it can be very useful to make an additional measurement of the same(!) sample with x-rays to receive a better understanding of the structural parameters and to reduce the number of fitting parameters for the analysis of the polarized neutron measurement. Element specific information about magnetism in layered structures can also be received using resonant magnetic soft-x-ray scattering [22,23], however the penetration depth is very low, the interaction at the resonance energy is not well known and the **Q**-range available is limited.

Nowadays, the major disadvantage of neutrons is the low intensity and the necessity of large sample sizes to obtain data over a sufficient **Q**-range. This leads to a less unique modelling of the data, again giving rise to uncertainties of the data analysis.

Presently, a big effort is made in order to increase the flux of neutron reflectometers. For example, on the new instrument MARIA of the Jülich Center for Neutron Science presently (Spring 2010) being commissioned at FRM-2, an increase in polarized neutron flux of 3 orders of magnitude with respect to HADAS (the instrument on which the measurements presented here have been performed) is expected! A quantitative gain in the measuring time and signal-to-noise ratio for the minimum sample size will be achieved. Qualitative gains

might also be achieved, for example for the study of the interface magnetic structure in oxide multilayers, for investigating magnetically dilute samples and, perhaps, to use neutrons to probe inelastic processes in the field of thin films.

[1] C. Fermon, F. Ott and A. Menelle, *Neutron Reflectometry*, Lect. Notes Phys. **770**, 183 (2009)

[2] S. Krueger, C.W. Meuse, F. Majkrzak, J.A. Dura, N.F. Berk, M. Tarek, A.L. Plant, Langmuir **17**, 511 (2001)

[3] G. Fragneto, M. Rheinstädter, C.R. Physique **8**, 865 (2007)

[4] P. Grünberg, J. Phys. Condens. Matter **13**, 7691 (2001)

[5] U. Rücker, Lecture 13 of this book

[6] G. Renaud, R. Lazzari, F. Leroy, Surface Science Report **64**, 255 (2009)

[7] T. Brückel, Lecture 5 of this book

[8] M. Feygenson, E. Kentzinger, N. Ziegenhagen, U. Rücker, G. Goerigk, Y. Wang, T. Brückel, J. Appl. Cryst. **40**, 532 (2007)

[9] J.K. Rice, "The reaction of telechelic polymers at multicomponent interfaces: A molecular loop study", PhD Thesis, University of Tennessee, Knoxville, USA, Dec. 2006

[10] J.K. Rice, H. Ji, J.W. Mays, M. Dadmun, Proceeding published 2005 by the ACS

[11] J.Y. Cheng, W. Jung, C.A. Ross, Phys. Rev. B **70**, 064417 (2004)

[12] I. W. Hamley, *The Physics of Block Copolymers*, Oxford University Press (1998) and references therein

[13] P. Busch, D. Posselt, D.M. Smilgies, B. Rheinländer, F. Kremer, C.M. Papadakis, Macromolecules **36**, 8717 (2003)

[14] D. Korolkov, "Structural analysis of diblock copolymer nanotemplates using grazing incidence scattering", PhD Thesis, RWTH Aachen (2008)

[15] E. Kentzinger, U. Rücker, B. Toperverg, Physica B **335**, 82 (2003)

[16] U. Rücker, E. Kentzinger, B. Toperverg, F. Ott, T. Brückel, Appl. Phys. A **74**, S607 (2002)

[17] E. Kentzinger, U. Rücker, B. Toperverg, F. Ott, Th. Brückel, Phys. Rev. B **77**, 104435 (2008)

[18] P. Böni, D. Clemens, M. Senthil Kumar, C. Pappas, Physica B **267**, 320 (1999)

[19] B.P. Toperverg, "Polarized Neutron Reflection and Off-Specular Scattering" in *Polarized Neutron Scattering*, Forschungszentrum Jülich, Series "Matter and Materials", Vol. 12 (2002)

[20] B.P. Toperverg, Physica B **297**, 160 (2001)

[21] E. Kentzinger, H. Frielinghaus, U. Rücker, A. Ioffe, D. Richter, Th. Brückel, Physica B **397**, 43 (2007)

[22] J.M. Tonnerre, M. De Santis, S. Grenier, H.C.N. Tolentino, V. Langlais, E. Bontempi, M. García-Fernández, U. Staub, Phys. Rev. Lett. **100**, 157202 (2008)

[23] H.L. Meyerheim, J.M. Tonnerre, L. Sandratskii, H.C.N. Tolentino, M. Przybylski, Y. Gabi, F. Yildiz, X.L. Fu, E. Bontempi, S. Grenier, J. Kirschner, Phys. Rev. Lett. **103**, 267202 (2009)

13

Nanomagnetism

Ulrich Rücker

13. Nanomagnetism

Ulrich Rücker

IFF-Scattering Methods

13.1. Introduction

The physical properties of a layered structure of nanometer size, as it is shown schematically in Fig. 13.1, differs from the bulk properties of the constituents. There are several origins of new effects due to miniaturization:

The ratio between surface and volume is much higher than in bulk. Therefore, the amount of atoms with reduced coordination is significant and can change the crystalline structure as well as the electronic structure of the whole layer. Boundary conditions, e.g. for the magnetic induction **B** become important, introducing shape anisotropies. The magnetization tends to align along the long edges of the magnetic nanostructure because the dipolar fields are smaller then.

At the interface between two layers, the electronic structures and the crystal lattices have to be matched, which leads to structural stress, interfacial disorder and electronically to charge transfer (e.g. Shottky barrier in semiconductor heterostructures) or splitting of the layers' bandstructures.

Nanostructures can be prepared in several dimensions: thin films with a thickness in the nm range are 2D nanostructures, stripes with thickness and width are 1D nanostructures and dots or nanoparticles with all three dimensions in the nm range are 0D nanostructures. The dimension number indicates, in how many directions the dimension remains macroscopic.

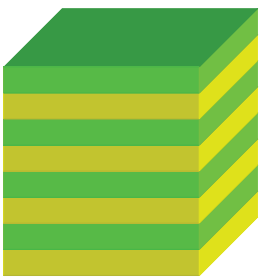

Fig. 13.1: Sketch of a layered structure of two materials

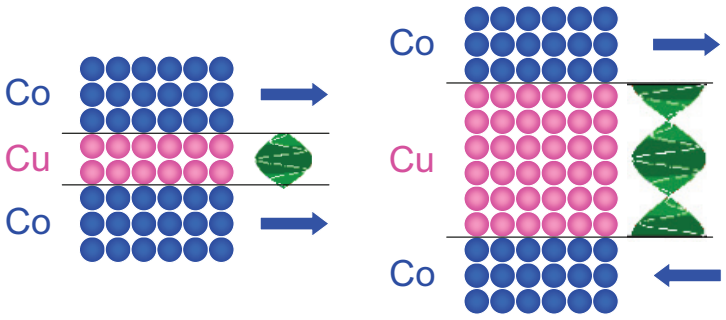

Fig. 13.2: Oscillating interlayer coupling as a function of interlayer thickness

Magnetic nanostructures are nanostructures which contain at least one magnetic constituent. Typical systems are layered structures with ferromagnetic and nonmagnetic layers or arrays of ferromagnetic dots on a nonmagnetic substrate. The interesting aspect of magnetic nanostructures is the fact that two ferromagnetic (FM) layers with a nonmagnetic (NM) spacer in between have a connection between their electronic systems across the spacer layer. This connection influences as well the magnetic behaviour as the electron transport through the system.

The first phenomenon found in magnetic layered structures has been the oscillating magnetic interlayer coupling in FM / NM / FM trilayer structures. Depending on the NM interlayer thickness, the magnetization of the two FM layers tend to align parallel or antiparallel to each other [1]. It turned out that the coupling is mediated by electronic states in the NM interlayer close to the Fermi surface [2]. The oscillation period of the coupling is related to the length of the wavevector of the electrons at the Fermi surface, as is sketched in Fig. 13.2.

Subsequently, the most important discovery followed, the Giant Magnetoresistance Effect (GMR) [3,4]. For this discovery, P. Grünberg and A. Fert were honoured with the Nobel Prize for Physics 2007. They have found out that the resistivity of a layered structure containing more than ferromagnetic layer depends on the mutual orientation of the magnetization directions, see Fig. 13.3. They used the antiferromagnetic coupling in Fe / Cr / Fe trilayer structures to be able to influence the mutual orientation of the magnetization of the Fe layers by changing the applied magnetic field.

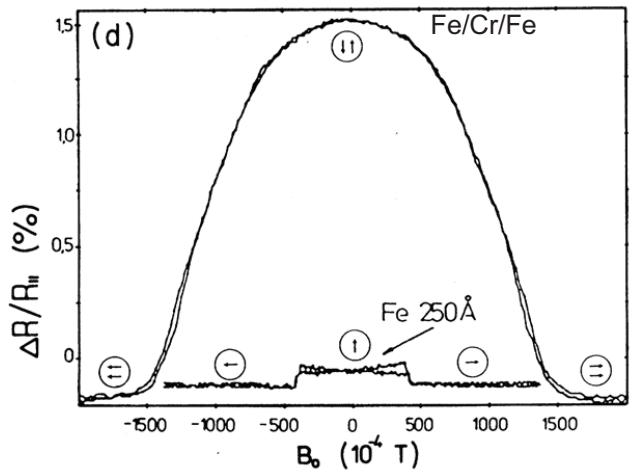

Fig. 13.3: Giant Magnetoresistance effect in an Fe / Cr / Fe trilayer compared to the anisotropic magnetoresistance in a single Fe layer [3]

It turns out that the resistivity is highest in the case of antiparallel alignment of the two magnetization directions. This effect is much stronger and much more sensitive than the anisotropic magnetoresistance effect in single ferromagnetic layers, which was known before. The microscopic origin of the GMR effect is the matching between the spin-split bandstructures of the two ferromagnetic layers. The conductivity of the entire structure is the sum of the conductivities of the two spin channels. As the Fermi surface is different for the two spin channels, the matching between the FM and the NM layer is different.

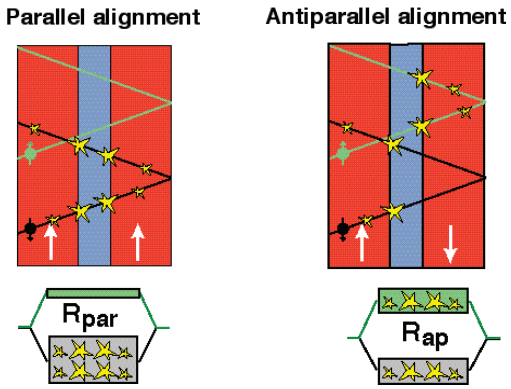

Fig. 13.4: Different matching of the bandstructure between ferromagnetic and nonmagnetic layers changes the resistivity for the different spin channels

As shown in Fig. 13.4, in the case of parallel alignment, the scattering probability of a conduction electron is the same at both interfaces. For one spin channel, the scattering probability is high while for the other it is low. The conductivity is then dominated by the spin channel with the smaller scattering probability. The resistivity of the entire structure, which can be described as a parallel wiring of the two resistors for the two spin channels, is small.
In the case of antiparallel alignment, the scattering probability for both spin channels is high in one of the FM layers. This results in a relatively low conductivity for every spin channel, so that the resulting resistivity is much higher than in the case of parallel magnetization.

As GMR structures are easy to prepare and easy to use, the sensor technology based on this effect quickly became standard in the readout system of computer harddisks and many other applications. Today, it has been replaced by Tunneling Magnetoresistance (TMR), where the nonmagnetic interlayer is insulating and electrons travel across this tunneling barrier while preserving their spin state. Then, the height of the tunneling barrier depends on the spin of the electron and the magnetization direction of both ferromagnetic layers. A detailed overview over the field of spin transport in layered systems is given in Ref. [5].

13.2. Why neutrons are useful for investigating Nanomagnetism

For the investigation of magnetism, many methods are known. They start from classical magnetometry, e.g. using a Vibrating Sample Magnetometer, a Faraday balance, or more recently a SQUID magnetometer, which measure the integral magnetization of a sample. The Magnetooptical Kerr-Effect (MOKE) measures magnetization with light reflected from a magnetic surface, and is therefore surface sensitive in the range of the penetration depth of the light used (typically some 10 nanometers). Magnetic domains can be images using e.g. Magnetic Force Microscopy (surface sensitive), Lorentz microscopy (electrons in transmission through a thin sample), or Kerr microscopy (integrating over the penetration depth of the light, with the spatial resolution of an optical microscope). At synchrotron x-ray sources one can use X-ray Magnetic Circular Dichroism (XMCD), where again the information is integrated over the penetration depth of the x-rays, but it is element specific due to the choice of the x-ray energy in resonance with the magnetic orbitals.
What is missing, is a method that can access the magnetism of buried layers using the depth information. Here, we need a probe that is sensitive to magnetic fields while having a spatial

resolution (at least in depth) in the nm regime. The method of choice is polarized neutron reflectometry with polarization analysis.

In the previous lecture [6] you have been introduced into this method. Here, I would like to repeat the most important formula from this lecture:

The wavefunction has to be treated as a superposition of the two spin states.

$$|\Psi(\mathbf{r})\rangle = \Psi^{+}(\mathbf{r})|+\rangle + \Psi^{-}(\mathbf{r})|-\rangle = \begin{pmatrix} \Psi^{+}(\mathbf{r}) \\ \Psi^{-}(\mathbf{r}) \end{pmatrix}$$

Then, the differential equations for the two components in interaction with the layered sample are the following:

$$\Psi_l^{+''}(z) + \left[k_{zl}^2 - 4\pi(\rho_l^N + \rho_l^M m_{xl})\right]\Psi_l^{+}(z) - 4\pi\rho_l^M m_{yl}\Psi_l^{-}(z) = 0 \quad (1)$$

$$\Psi_l^{-''}(z) + \left[k_{zl}^2 - 4\pi(\rho_l^N - \rho_l^M m_{xl})\right]\Psi_l^{-}(z) - 4\pi\rho_l^M m_{yl}\Psi_l^{+}(z) = 0 \quad (2)$$

As Non-Spinflip (NSF) interaction, one finds in (1) for spin + the sum of the nuclear interaction and the magnetic interaction with the magnetization along the quantization direction and in (2) for spin – the difference. In case of a magnetically saturated layer (all the magnetization is aligned with the external field), the scattering length density for spin + neutrons is enhanced and for spin – neutrons is reduced compared to the nonmagnetic case. This has an influence on the index of refraction, on the total reflection angle, and of course on the reflectivity, which is a function of the change of the index of refraction at a certain interface. Fig. 13.5 shows schematically the splitting of the total reflection angle.

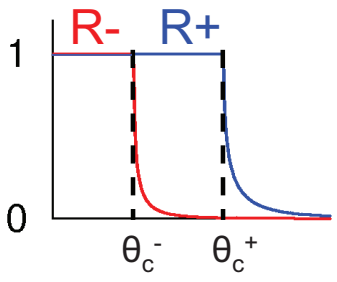

Fig. 13.5: The total reflection angle θ_c of the surface of magnetized material is different for both spins

In the case that the magnetization is not fully aligned with the field, the component along the field direction influences the scattering length density for NSF. The in-plane magnetization component perpendicular to the field induces a spin-flip (SF) interaction that is equally strong for both spin-flip channels +– and –+, as is described in the last term of eq. (2) or (1), resp.

As en example, I would like to show the polarized neutron reflectivity of a [Co / Cu] multilayer. The respective nuclear and magnetic scattering length densities are

Co: $\rho_N = 2.30 \cdot 10^{-6}$ Å^{-2} $\quad \rho_M = 4.24 \cdot 10^{-6}$ Å^{-2}

Cu: $\rho_N = 6.53 \cdot 10^{-6}$ Å^{-2} $\quad \rho_M = 0$.

Obviously, the sum of the magnetic and the nuclear scattering length density of Co is almost equal to the scattering length density of Cu. In the case of magnetic saturation, spin + neutrons will not feel any contrast at the Co / Cu interfaces because they see the sum of nuclear and magnetic scattering length density in the Co layer. The multilayer structure is invisible for spin + neutrons. In contrast, spin – neutrons experience the difference of nuclear and magnetic scattering length density (which is in fact negative), so that the contrast is huge. Fig. 13.6 makes the contrast situation visible by using colours representing the different scattering length densities.

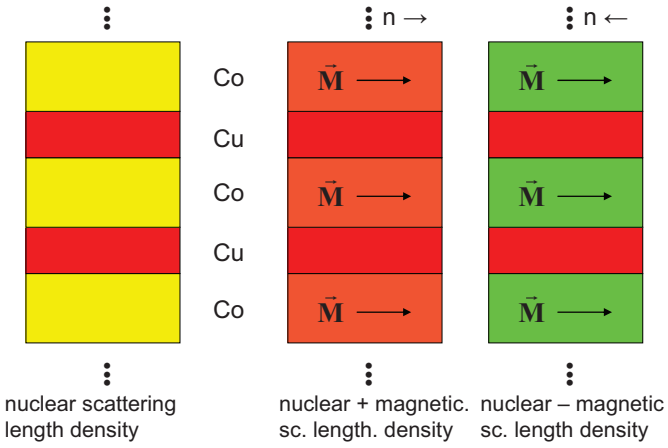

Fig. 13.6: The contrast between Co and Cu depends on the magnetization state. It almost vanishes for spin up neutrons, but is strong for spin down.

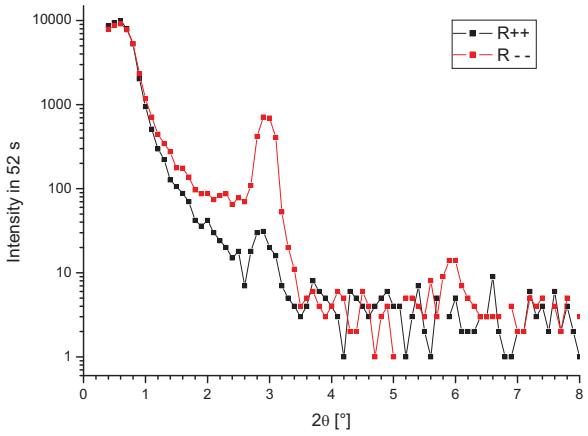

Fig. 13.7: Specular reflectivity of polarized neutrons from a [Co/Cu] multilayer with 20 periods at magnetic saturation

Fig. 13.7 shows the measured polarized neutron reflectivity of such a multilayer. The total reflection edge is identical for both spin channels, because the biggest scattering length density in the layered structure is the one of Cu, which is not magnetic. But the multilayer Bragg peaks at $2\theta = 3°$ and $2\theta = 6°$ are strongly spin split. For spin – neutrons, the Bragg peak is about 30 times stronger than for spin + neutrons. Here, one can see that the contrast is responsible for the reflectivity, not the strength of the scattering potential, as the scattering length density (which describes the scattering potential) is stronger for spin +, but the contrast between the layers is stronger for spin –.

13.3. Vector magnetometry

One important application of polarized neutron reflectometry with polarization analysis is vector magnetometry in layered structures. The ability to distinguish between SF and NSF channels offers an independent access to the in-plane magnetization components perpendicular and parallel to the field direction. As a magnetization direction perpendicular to the sample surface is rare (due to the shape anisotropy) one can determine the full magnetization vector in most cases.

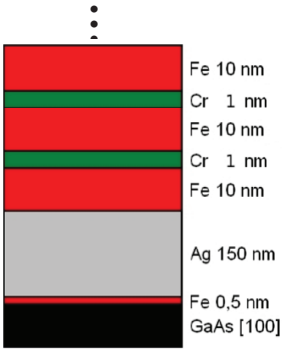

Fig. 13.8: Layer sequence of an epitaxially grown and antiferromagnetically coupled $[Fe / Cr]_{xN}$ multilayer

I would like to explain the power of vector magnetometry using the example of an epitaxially grown and antiferromagnetically (AF) coupled $[Fe / Cr]_{xN}$ multilayer with an odd number of Fe layers [7]. Fig. 13.8 shows the layer sequence of such a sample grown on a GaAs single crystal with a Ag buffer layer to improve the surface quality. The magnetic behaviour is determined by the competition between 3 different interactions (see. Fig. 13.9): The crystalline anisotropy in the single crystalline Fe layers tries to align the magnetization in every Fe layer along one of the in-plane [100] directions. This results in 4 equivalent easy axes. The antiferromagnetic coupling (mediated by the Cr interlayer) has the tendency to align the magnetization of two neighbouring Fe layers antiparallel to each other. The Zeeman term tries to align the magnetization along the applied field.

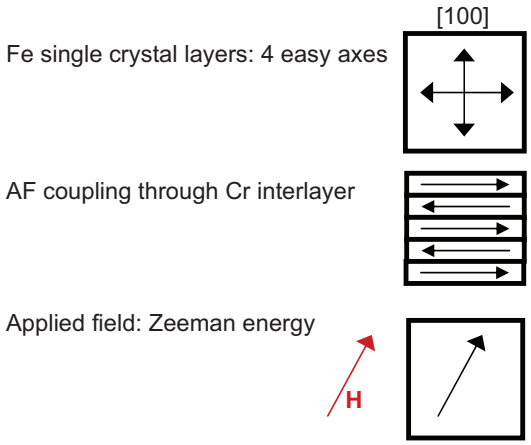

Fig. 13.9: The magnetic behaviour in an applied magnetic field is governed by 3 competing interactions

As the multilayer under investigation has an odd number of Fe layers, the antiparallel orientation of the magnetization in remanence (where the Zeeman term is weak) will leave the magnetization of one layer uncompensated, so that the Zeeman energy does not vanish even at very small fields. This effect is supposed to align the remanent magnetization of all layers along or antiparallel to the field direction.

Fig. 13.10 shows MOKE measurements of such samples with N=7 or N=19 Fe layers in the multilayer sequence. The MOKE signal is a function of the magnetization, but not proportional to it, because it is a superposition of the longitudinal Kerr effect (proportional to the magnetization along the field) and the transverse Kerr effect (proportional to the magnetization perpendicular to the field). Furthermore, the weight of the layers close to the surface is much higher than the weight of lower lying layers. Therefore, one should not worry about the MOKE curve not being monotonous. Nevertheless, a jump in the MOKE curve always indicates a spontaneous change of the magnetization state.

In addition, Fig. 13.10 shows a simulation of the integral magnetization component along the field based on numerical minimization of the three energy terms mentioned above. This kind of simulation cannot reproduce effects of activation barriers leading to hysteresis.

In the case of the multilayer with N=7 Fe layers, the simulation and the MOKE measurement have a good qualitative agreement. In saturation, the magnetic moment of every layer is aligned with the field. In the intermediate field range, the magnetization is alternatingly pointing left or right from the field direction, so that the magnetization component along the field is almost equal for every layer and the magnetization components perpendicular to the field fulfil as much as possible the AF coupling.

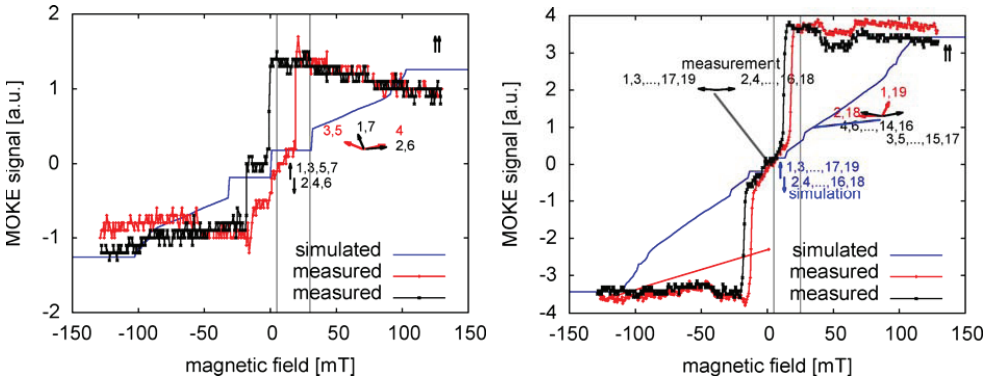

Fig. 13.10: MOKE measurement of $[Fe / Cr]_{xN}$ multilayers with N=7 Fe layers (left) and N=19 Fe layers (right). The simulation of the magnetization curve is based on total energy minimization

At remanence, the magnetization of all layers is turned by 90°, so that 4 layers have the magnetization along the field and 3 layers antiparallel to the field. This configuration fulfils as well the AF coupling condition as the alignment of the net magnetization along the applied field.
In contrast to that, the MOKE measurement of the multilayer with N=19 Fe layers shows a smooth transition through H=0 while the simulation proposes a step comparable to the case described previously. This behaviour is known from AF coupled multilayers with even number of ferromagnetic layers, because there the net magnetization vanishes, so that there is no Zeeman energy that causes the rotation of the entire magnetic configuration at remanence. This contradiction cannot be resolved by magnetometry measurements only.

Fig. 13.11 shows the polarized neutron reflectivity together with the offspecular scattering for the two samples at saturation field. One can see a structured signal with total reflection and several Bragg peaks according to the periodicity in the multilayer structure only in the R++ channel. For spin – neutrons the contrast between fully magnetized Fe and Cr vanishes, so the R– – shows only the total reflection (with a reduced critical angle compared to R++), but no Bragg peaks. As no magnetization component perpendicular to the field direction exists, there is no real spin flip signal. What you see in R+– and R –+ is a parasitic signal due to the limited efficiency of the polarizing equipment of the instrument. The Bragg sheets crossing the specular Bragg peaks are due to vertically correlated roughness of the Fe / Cr interfaces.
No qualitative difference between the two samples can be observed except the fact that the Bragg peaks and Bragg sheets are sharper and more intense for the $[Fe / Cr]_{19}$ sample because of the bigger number of periods.
Fig. 13.12 shows the same in the intermediate field range. Additional Bragg peak of half order appear, which are stronger in SF compared to NSF. This is the indication of the alternation of the magnetization directions due to the antiferromagnetic coupling. Mainly the magnetization component perpendicular to the field oscillates while the component remaining along the field is modulated less. As the sample is no more saturated, the magnetization component in field direction is reduced, so that the contrast for spin – neutrons does not vanish any more. Therefore, the full order Bragg peaks also come up in R– –. They are now mainly induced by the nuclear structure while the magnetic contribution is collected in the half order signal. The strong off-specular signal around the half order Bragg peaks in the SF channels is a signature of magnetic domains.
Again, no distinct qualitative difference between the two samples is observed.

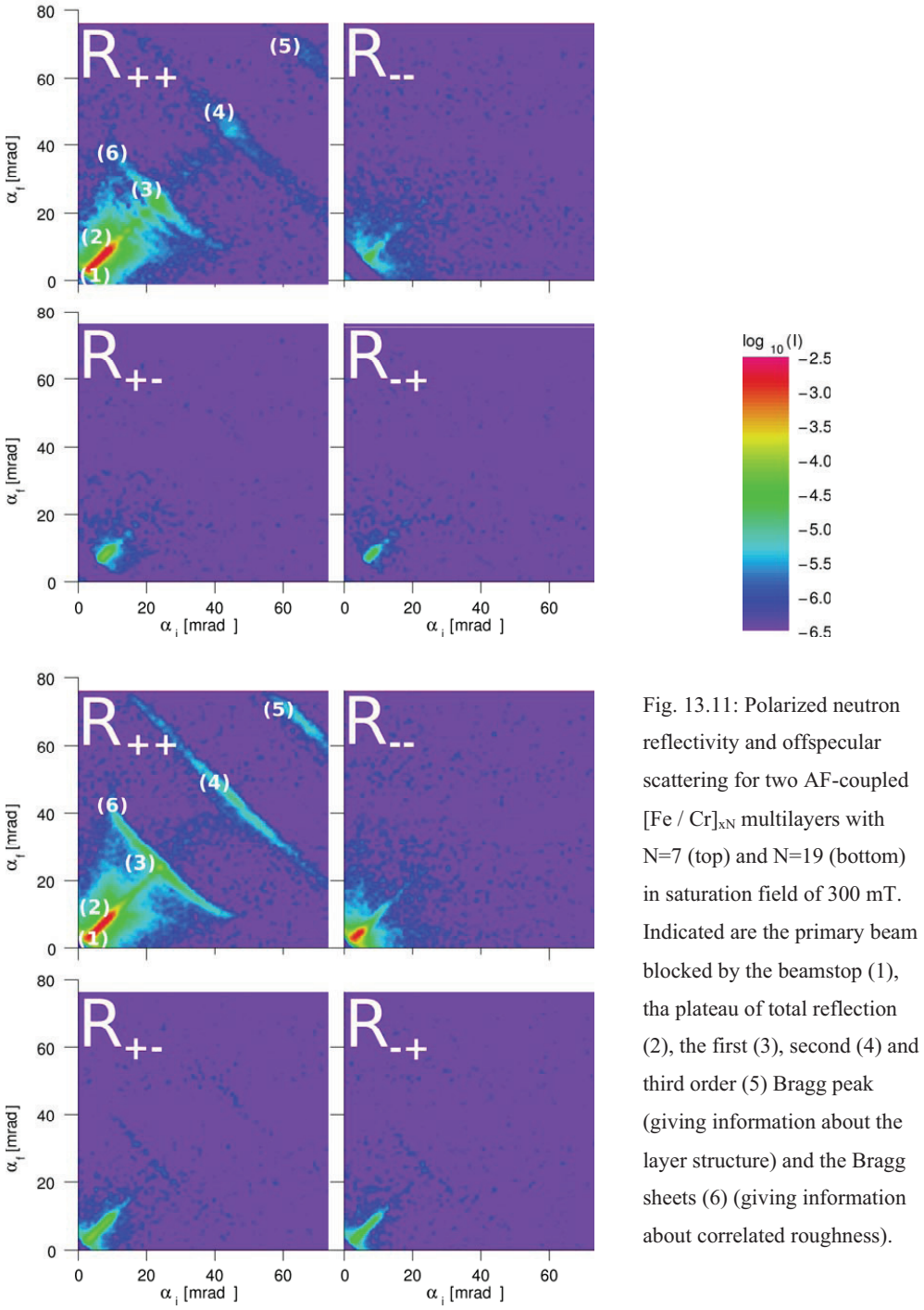

Fig. 13.11: Polarized neutron reflectivity and offspecular scattering for two AF-coupled $[Fe / Cr]_{xN}$ multilayers with N=7 (top) and N=19 (bottom) in saturation field of 300 mT. Indicated are the primary beam blocked by the beamstop (1), tha plateau of total reflection (2), the first (3), second (4) and third order (5) Bragg peak (giving information about the layer structure) and the Bragg sheets (6) (giving information about correlated roughness).

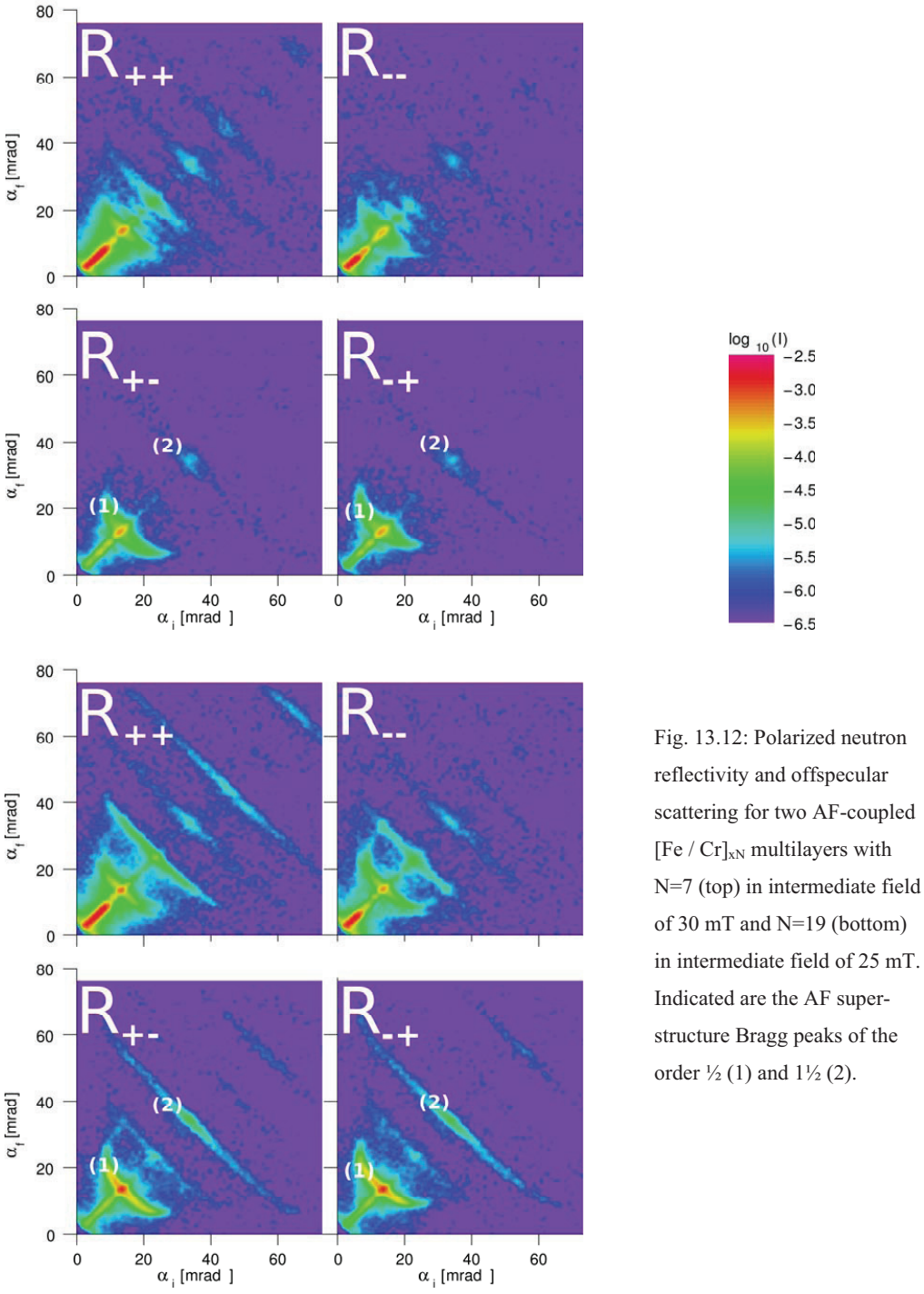

Fig. 13.12: Polarized neutron reflectivity and offspecular scattering for two AF-coupled $[Fe / Cr]_{xN}$ multilayers with N=7 (top) in intermediate field of 30 mT and N=19 (bottom) in intermediate field of 25 mT. Indicated are the AF superstructure Bragg peaks of the order ½ (1) and 1½ (2).

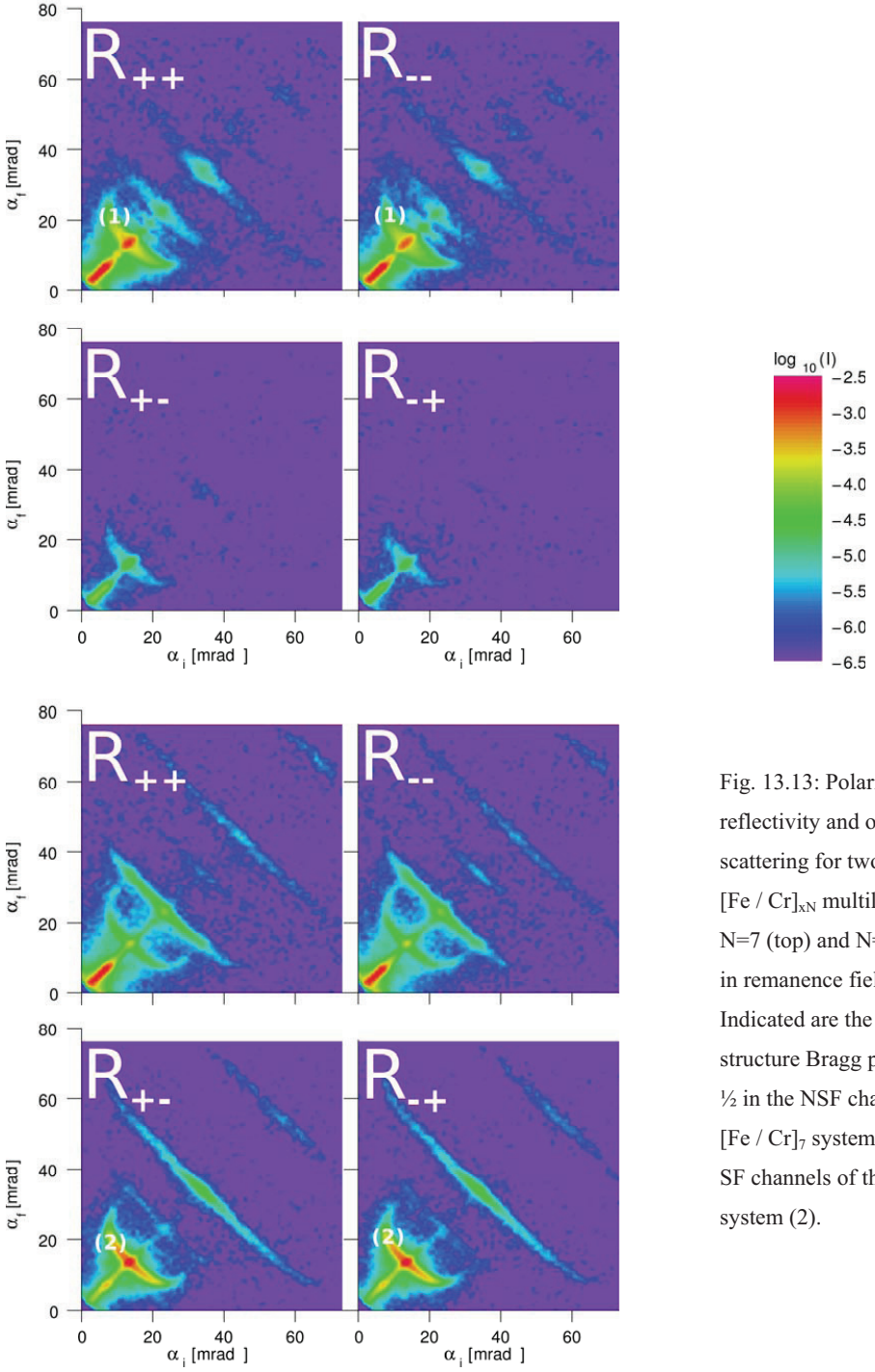

Fig. 13.13: Polarized neutron reflectivity and offspecular scattering for two AF-coupled $[Fe / Cr]_{xN}$ multilayers with N=7 (top) and N=19 (bottom) in remanence field of 5 mT. Indicated are the AF superstructure Bragg peaks of order ½ in the NSF channels of the $[Fe / Cr]_7$ system (1) and in the SF channels of the $[Fe/Cr]_{19}$ system (2).

This is very different at remanence, as shown in Fig. 13.13. The $[Fe / Cr]_7$ sample has all half order peaks in the NSF channels while the $[Fe / Cr]_{19}$ sample has all half order peaks in SF. The small contribution in the other channels can be explained due to the limited polarization of the neutron beam. This shows that the magnetization of all layers of the $[Fe / Cr]_7$ sample is aligned alternatingly parallel and antiparallel to the field direction, as has been proposed by the simulation for the MOKE measurement.
In the case of the $[Fe / Cr]_{19}$ sample, all magnetization is now concentrated perpendicular to the field, no more difference between R++ and R– – can be observed. The measurement clearly shows, that the Zeeman energy contribution equivalent to the magnetization of a single Fe layer is not sufficient to turn the entire magnetization of all 19 layers by 90° across the crystalline anisotropy barrier.

In addition to the qualitative description presented here, a quantitative analysis of the measurements allows to determine the angle of the magnetization vector of every layer independently. This analysis is presented in Ref. [7].

13.4. Layer-by-layer magnetometry

The second important application of polarized neutron reflectometry with polarization analysis is layer-by-layer magnetometry. As an example, I present the magnetization evolution in exchange bias multilayers of the type [IrMn / CoFe] with the number of periods [8]. The exchange bias effect is the coupling between a ferromagnetic layer and a neighboring antiferromagnetic layer. If the antiferromagnet has been cooled below its Néel temperature with the ferromagnet being saturated, it has conserved the interface magnetization without being sensitive to the applied magnetic field. This induces an additional unidirectional anisotropy on the ferromagnetic layer, i.e. the original magnetization direction is preferred over all others. The hysteresis loop is shifted away from H = 0.
The green curve in Fig. 13.14 shows the exchange biased magnetization curve of a IrMn / CoFe double layer shifted left together with the magnetization loop of the NiFe buffer layer, which is not affected by exchange bias and therefore symmetric around H = 0 field. The CoFe layer shows a nice square hysteresis loop, indicating spontaneous magnetization flip at the coercive field.

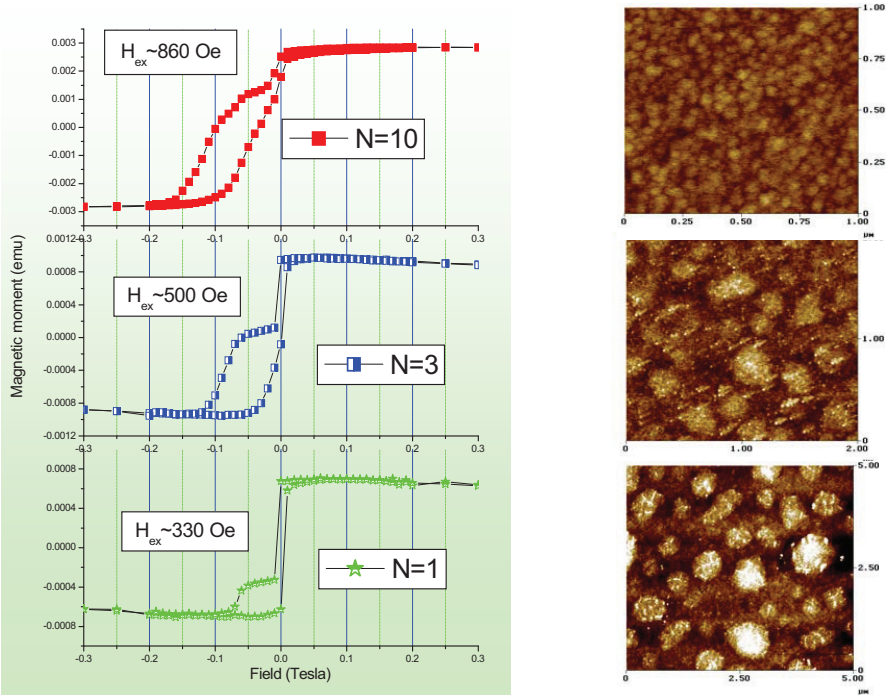

Fig. 13.14: SQUID magnetization measurements (at room temperature, left) and AFM micrographs of the surface (right) of polycrystalline multilayers of the type SiO_2 / 10 nm NiFe / [5 nm IrMn / 3 nm CoFe]$_{x\,N}$ with N = 1, 3, or 10, resp.

Strangely, the shape of the magnetization loop of the exchange biased CoFe layers changes, when the number of [IrMn / CoFe]$_{xN}$ bilayers is increased. In addition, the strength of the exchange bias in increased. An AFM study of the surfaces shows that the grain size of the polycrystalline layers is reduced from layer to layer during the preparation procedure, but not information could be found that justifies the slope of the magnetization curves and that could eventually explain the origin of a magnetization rotation process responsible for the gradual evolution of the magnetization as a function of the applied field.

Therefore, a polarized neutron reflectivity study was performed, to investigate the individual behaviour of the ferromagnetic layers in the multilayer structure. As an example, Fig. 13.15 shows the specular polarized neutron reflectivity at one of the coercive fields (i.e. the net magnetization vanishes) together with the fit.

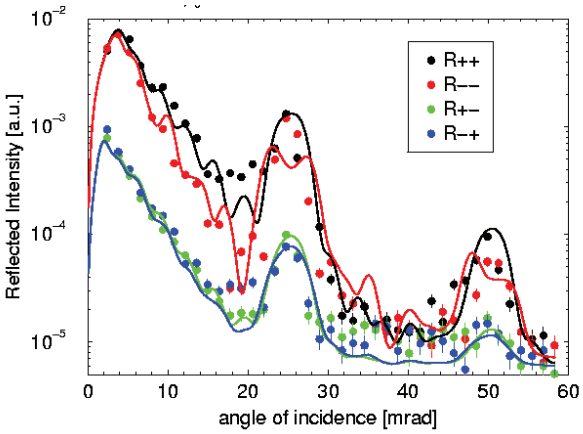

Fig. 13.15: Polarized neutron reflectivity of the sample with N=10 at $\mu_0 H$ = -0.1 mT after positive saturation

The polarized neutron measurement shows no spin flip signal at all, immediately excluding the idea of a magnetization rotation process. Furthermore, it shows that the magnetization of the upper 5 CoFe layers is aligned antiparallel to the field while the magnetization of the lower 5 CoFe layers is still aligned along to the field. I.e., the exchange bias on the upper layers (with smaller grains) still can hold the magnetization in the preferred direction, while the magnetization of the lower layers already has followed the field.

Together with measurements at several magnetic field values on both branches of the hysteresis loop it turned out that every single layer has a square magnetization loop, but the strength of the exchange bias effect (i.e. the shift of the centre of the loop away from H=0) increases with reduced grain size. The overlaying of the differently shifted square loops then results in the inclined net magnetization loop measured with magnetometry.

References

[1] P. Grünberg, R. Schreiber, Y. Pang, M.B. Brodsky, and H. Sowers, Phys. Rev. Lett. **57** (1986), 2442

[2] P.H. Dederichs, "Interlayer Exchange Coupling", chapter C 3 in "Magnetism goes Nano", 36th IFF Spring School, Forschungszentrum Jülich, series Matter and Materials, Vol. 26 (2005)

[3] G. Binasch, P. Grünberg, F. Saurenbach, and W. Zinn, Phys. Rev. B **39** (1989), 4828

[4] M.N. Baibich, J.M. Broto, A. Fert, F. Nguyen Van Dau, F. Petroff, P. Etienne, G. Creuzet, A. Friedrich, and J. Chazelas, Phys. Rev. Lett. **61** (1988), 2472

[5] D.E. Bürgler, "Spin-Transport in Layered Systems" , chapter E 5 in "Magnetism goes Nano", 36th IFF Spring School, Forschungszentrum Jülich, series Matter and Materials, Vol. 26 (2005)

[6] E. Kentzinger, U. Rücker, "Surfaces, interfaces and thin films investigated by neutron reflectometry", chapter 12 of this book

[7] E. Josten, U. Rücker, S. Mattauch, D. Korolkov, A. Glavic, and Th. Brückel, J. Phys: Conf. Ser. **211** (2010), 012023

[8] A. Paul, E. Kentzinger, U. Rücker, D.E. Bürgler, and P. Grünberg, Phys. Rev. B **70** (2004), 224410

1. **Soft Matter**
   From Synthetic to Biological Materials
   Lecture manuscripts of the 39th IFF Spring School March 3 – 14, 2008
   Jülich, Germany
   edited by J.K.G. Dhont, G. Gompper, G. Nägele, D. Richter, R.G. Winkler (2008),
   c. 1000 pages
   ISBN: 978-3-89336-517-3

2. **Structural analysis of diblock copolymer nanotemplates using grazing incidence scattering**
   by D. Korolkov (2008), III, 167 pages
   ISBN: 978-3-89336-522-7

3. **Thermal Nonequilibrium**
   Thermal forces in fluid mixtures
   Lecture Notes of the 8th International Meeting on Thermodiffusion,
   9 – 13 June 2008, Bonn, Germany
   edited by S. Wiegand, W. Köhler (2008), 300 pages
   ISBN: 978-3-89336-523-4

4. **Synthesis of CMR manganites and ordering phenomena in complex transition metal oxides**
   by H. Li (2008), IV, 176 pages
   ISBN: 978-3-89336-527-2

5. **Neutron Scattering**
   Lectures of the JCNS Laboratory Course held at the Forschungszentrum Jülich and the research reactor FRM II of TU Munich
   edited by R. Zorn, Th. Brückel, D. Richter (2008), ca. 500 pages
   ISBN: 978-3-89336-532-6

6. **Ultrafast Magnetization Dynamics**
   by S. Woodford (2008), 130 pages
   ISBN: 978-3-89336-536-4

7. **Role of Surface Roughness inTribology: from Atomic to Macroscopic Scale**
   by C. Yang (2008), VII, 166 pages
   ISBN: 978-3-89336-537-1

8. **Strahl- und Spindynamik von Hadronenstrahlen in Mittelenergie-Ringbeschleunigern**
   von A. Lehrach (2008), II, 171 Seiten
   ISBN: 978-3-89336-548-7

9. **Phase Behaviour of Proteins and Colloid-Polymer Mixtures**
   by C. Gögelein (2008), II, 147 pages
   ISBN: 978-3-89336-555-5

10. **Spintronics – From GMR to Quantum Information**
    Lecture Notes of the 40th IFF Spring School March 9 – 20, 2009
    Jülich, Germany
    edited by St. Blügel, D. Bürgler, M. Morgenstern, C. M. Schneider,
    R. Waser (2009), c. 1000 pages
    ISBN: 978-3-89336-559-3

11. **ANKE / PAX Workshop on SPIN Physics**
    JINR, Dubna, Russia / June 22. – 26, 2009
    Org. Committee: A. Kacharava, V. Komarov, A. Kulikov, P. Lenisa, R. Rathmann,
    H. Ströher (2009), CD-ROM
    ISBN: 978-3-89336-586-9

12. **Entwicklung einer Nanotechnologie-Plattform für die Herstellung Crossbar-basierter Speicherarchitekturen**
    von M. Meier (2009), 135 Seiten
    ISBN: 978-3-89336-598-2

13. **Electronic Oxides –**
    Correlation Phenomena, Exotic Phases and Novel Functionalities
    Lecture Notes of the 41st IFF Spring School March 8 – 19, 2010
    Jülich, Germany
    edited by St. Blügel, T. Brückel, R. Waser, C.M. Schneider (2010), ca. 1000 pages
    ISBN: 978-3-89336-609-5

14. **4th Georgian-German School and Workshop in Basic Science**
    Tbilisi, Georgia / May 3 – 7, 2010
    Org. Committee: E. Abrosimova, R. Botchorishvili, A. Kacharava, M. Nioradze,
    A. Prangishvili, H. Ströher (2010); CD-ROM
    ISBN: 978-3-89336-629-3

15. **Neutron Scattering**
    Lectures of the JCNS Laboratory Course held at Forschungszentrum Jülich and the research reactor FRM II of TU Munich
    edited by Th. Brückel, G. Heger, D. Richter, G. Roth and R. Zorn (2010),
    ca 350 pages
    ISBN: 978-3-89336-635-4

Band | Volume 15
ISBN 978-3-89336-635-4

JÜLICH
FORSCHUNGSZENTRUM